Response of an Embedded Block Impacted by High-Velocity Jets

THÈSE N^{O} 5160 (2011)

PRÉSENTÉE LE 9 SEPTEMBRE 2011

À LA FACULTÉ ENVIRONNEMENT NATUREL, ARCHITECTURAL ET CONSTRUIT
LABORATOIRE DE CONSTRUCTIONS HYDRAULIQUES
PROGRAMME DOCTORAL EN ENVIRONNEMENT

ÉCOLE POLYTECHNIQUE FÉDÉRALE DE LAUSANNE

POUR L'OBTENTION DU GRADE DE DOCTEUR ÈS SCIENCES

PAR

Matteo Paolo Elia Antonio FEDERSPIEL

acceptée sur proposition du jury:

Prof. I. Smith, président du jury
Prof. A. Schleiss, Dr E. Bollaert, directeurs de thèse
Prof. F. Avellan, rapporteur
Prof. L. G. Castillo Elsitdie, rapporteur
Prof. V. Fiorotto, rapporteur

ÉCOLE POLYTECHNIQUE
FÉDÉRALE DE LAUSANNE
Suisse
2011

Dedico questo lavoro di ricerca ai miei genitori,
a mia mamma Eliana ed a mio papà Marco,
alle mie sorelle,
Sonja e Lucia,
ai miei nonni,
Ginetta e Giovanni,
alla mia amata
Nicoletta
che in questi anni mi hanno sostenuto!

Matteo

Abstract

High-velocity plunging jets, issuing from flood release structures of dams, may result in scouring of the rocky riverbed and even endanger the foundation of the dams. Assessment of the scour extent is essential to ensure the safety of the dam and appurtenant structures as well as to guarantee the stability of its abutments.

The existing near-prototype scaled experimental facility developed at the Laboratory of Hydraulic Constructions (LCH) of the École Polytechnique Fédérale de Lausanne (EPFL) has been modified to study the complex interaction between pressures fluctuations acting inside a cylindrical plunge pool and inside a full interconnected 3-dimensional fissure. The present facility allows to simulate near-prototype jets in terms of velocity, turbulence and aeration.

A movable highly instrumented block, simulating an "artificial rock block" founded in a fissured rock mass with one degree of freedom (along the vertical axis), has been inserted in the existing facility. The block and the measured box (new set-up), simulating the fissured rock mass, represent a sophisticated installation allowing to perform several measurements simultaneously. The block, having a cubic shape of 200 mm side and a density similar to in-situ rocks, is equipped with pressure, displacement and acceleration transducers. It is embedded in an artificially created surrounding rock mass equipped as well by pressure transducers. Between the block and the measurement box a 3-dimensional fissure of 1 mm thickness has also been created. The plunge pool and the new experimental set-up have been impacted by high-velocity jets to generate different loading conditions (core, transition or developed jets impacts).

The purpose of the research project is to study the behavior of a single rock block separated from its surroundings by a 3-dimensional fissure and impacted by a high-velocity impinging water jet subjected to a natural aeration.

Pressure fluctuations (pressure field) and block responses (displacements and accelerations) are recorded simultaneously for several jet impacts positions on the block upper face (at the plunge pool bottom level), for different water depths (Y/D ratio between 0 and 9.7) and near prototype jet velocities (2.5 - 27.0 m/s).

The influence of the jet solicitations (symmetrical or asymmetrical jet impacts related to the block center) have been analyzed for several parameters: pressure field surrounding the block, dynamic block impulsion, natural and passive air entrainment, fissure geometries, block degree of freedom and block rotations in the fissured rock mass.

The main conclusions coming from these analyses display interesting results. The pressure field acting on the block upper face follows the distribution found in literature (exponential distribution) whereas the pressures acting inside the 3-dimensional fissure are quite constant. The extreme pressures (positive and negative values) are attenuated inside the fissure. No transient phenomena have been observed inside the fissure.

For the first time, the computation of the dynamic block impulsion has shown the relevance of the added mass and its different behavior whether the block is loaded by a symmetrical or an asymmetrical jet impact. When a body immerged in a fluid is subjected to accelerations, the surrounding fluid must accelerate as well. The inertia of the entrained fluid is the added mass. It influences the amplitudes of the vertical displacements. The added mass values obtained experimentally using the LCH facility are different from the literature values determined for different test conditions (a body moving in a quiet fluid and laterally confined). The highly instrumented block is strongly confined in the measurement box: it is surrounded on five of its six faces by the measurement box with a distance of 1 mm and it is directly loaded by high-velocity jets on its free surface. These conditions may explain this difference between observed and literature values. Theoretical block uplift shows good similitude with the measured uplift when the added mass is integrated in the computation of the dynamic block impulsion. Only the amplitude of the vertical displacements could not be always simulated exactly by the theoretical uplift, but the vertical fluctuations could be well reproduced. The maximum uplift was observed for a jet impacting on a corner of the block ($\sim$160 mm for a block side of 200 mm).

The air entrainment generated by a suction-based passive aeration system, together with the natural jet aeration, seems influence the extreme pressures (maximum and minimum) but not the block responses (displacements) related to a jet only naturally aerated. The influence of the air entrainment needed a more accurate investigation.

To define the geometry of the fissure surrounding the block and to limit the block degrees of freedom to one, two type of lateral guides, fixed on the block lateral faces, have been tested. If the block is loaded symmetrically no differences have been observed, whereas for an asymmetrical jet impact for the same jet impact but on another block side some differences in the block responses (displacements) have been observed.

The degree of freedom of the block influences strongly the pressure field generated inside the 3-dimensional fissure. When the block is fixed inside the measurement box, the pressures increase the hydrodynamic loading generating the propagation of the fissure networks in the rock mass. This pressure increase may reach some Bars of difference between the block free to move or fixed. The largest differences have been observed for a jet impacting on a corner of the block.

Keywords: *High-velocity water jets, plunge pool, fissured rock mass, 3-dimensional fissure, "artificial rock block", scour phenomena, pressure fluctuations, block movements, dynamic block impulsion, added mass, air entrainment, fissure geometry, degree of freedom.*

Résumé

Les jets à hautes vitesses, générés par les évacuateurs de crues des barrages, peuvent entrainer l'érosion du lit rocheux de la rivière et, dans certains cas, endommager les fondations du barrage. L'évaluation de l'érosion et de sa propagation est essentielle pour garantir la sécurité du barrage et de ses ouvrages annexes ainsi que pour assurer la stabilité de ses remblais.

L'installation expérimentale existante, développée au Laboratoire de Constructions Hydrauliques (LCH) de l'École Polytechnique Fédérale de Lausanne (EPFL), a été modifiée afin d'étudier l'interaction complexe entre les fluctuations de pression générées à l'intérieur d'une fosse d'érosion cylindrique et à l'intérieur d'une fissure tridimensionnelle complètement interconnectée. L'installation actuelle permet de simuler des jets à une échelle proche du prototype en termes de vitesse, turbulence et aération.

Un bloc mobile instrumenté, simulant un bloc de roche artificielle encastré dans un massif rocheux fissuré mais ayant un degré de liberté, a été installé sur l'installation expérimentale existante. Le bloc et la boite de mesure, représentant le massif rocheux fissuré, constituent une installation sophistiquée permettant d'effectuer différents types de mesures simultanément. Le bloc de forme cubique de 200 mm de côté et de densité similaire à celle du rocher in-situ, est équipé avec des capteurs de pression, de déplacement et d'accélération. Il est inséré dans une masse rocheuse artificielle équipée également de capteurs de pression. Une fissure tridimensionnelle de 1 mm est également créée entre le bloc et la boite de mesure.

La fosse d'érosion, le bloc et la fissure sont sollicitées par des jets à hautes vitesses afin de générer différents types de comportements en fonction du niveau d'eau dans la fosse (jet noyau, jet de transition et jet développé).

L'objectif de ce projet de recherche est d'étudier le comportement d'un bloc entouré par une fissure tridimensionnelle et sollicité par des jets d'eau à hautes vitesses aérés naturellement.

Les fluctuations de pression et le comportement du bloc sont enregistrés simultanément pour différents points d'impact du jet sur la surface supérieure du bloc (au fond de la fosse d'érosion), niveaux d'eau (rapport Y/D compris entre 0 et 9.7) et vitesses du jet (2.5 - 27.0 m/s).

L'influence des sollicitations, générées par les différentes conditions de jets, a été analysée en fonction de plusieurs paramètres : champ de pression, impulsion du bloc, aération naturelle et passive du jet, géométrie de la fissure, degrés de liberté du bloc et rotations du bloc dans sa fondation.

L'analyse des données montre des résultats très intéressants. Le champ de pression agissant sur la surface supérieure du bloc suit une distribution exponentielle comme cela a été proposé dans la littérature, tandis que les pressions à l'intérieur de la fissure tridimensionnelle sont presque constantes. Les valeurs de pression extrêmes (positives et négatives) sont atténuées à l'intérieur de la fissure. Aucun phénomène transitoire n'a été observé à l'intérieur de la fissure.

Pour la première fois, le calcul de l'impulsion du bloc a montré l'importance de la masse virtuelle (added mass) et ses différents comportements selon le type d'impact du jet (symétrique ou asymétrique). Quand un corps immergé dans un fluide est soumis à une accélération, le fluide qui l'entoure doit se déplacer aussi. L'inertie de cette masse d'eau correspond à la masse virtuelle et influence l'amplitude des déplacements verticaux. Les valeurs de masse virtuelle obtenues expérimentalement avec cette installation sont très différentes de celles pouvant être trouvées dans la littérature avec des conditions expérimentales différentes (un corps se déplaçant dans un milieu calme et confiné latéralement). Dans le cas étudié, le bloc est fortement confiné à l'intérieur de la boite de mesure sur cinq de ses six faces, avec un écartement de 1 mm et, de plus, il est sollicité directement par le jet sur sa face libre. Ces conditions peuvent expliquer l'écart entre les valeurs observées et celles de la littérature. Les déplacements verticaux du bloc calculés à partir des mesures de pressions montrent une bonne similitude avec les valeurs mesurées. L'élévation théorique du bloc montrent de bonnes similitudes avec le déplacement mesuré lorsque la masse virtuelle est intégrée dans le calcul de l'impulsion du bloc. Seule l'amplitude des mouvements verticaux ne peut pas toujours être bien modélisée par l'élévation théorique mais les fluctuations verticales peuvent être bien reproduites. Le déplacement vertical maximal est observé pour un jet impactant sur un coin du bloc.

L'entrainement d'air artificiel, généré par un système d'aération passif basé sur le principe de la succion, en combinaison avec l'aération naturelle du jet, semble influencer les valeurs extrêmes de pression mais pas les déplacements du bloc par rapport un jet qui est seulement aéré naturellement. Une étude de l'influence de l'entrainement d'air approfondie est à prévoir.

Pour définir la forme de la fissure entourant le bloc et, en même temps, pour limiter le degré de liberté du bloc à un, deux différents types de guides latéraux, fixés sur les faces latérales du bloc, ont été développés. Si le bloc est sollicité par un impact symétrique (au centre du bloc) aucune différence n'a été observée, tandis que pour un impact asymétrique le bloc montre des comportements différents selon le type des guides latéraux.

Le degré de liberté du bloc influence profondément le champ de pression généré à l'intérieur de la fissure. Quand le bloc est fixé dans la boite de mesure, les pressions augmentent la charge hydrodynamique provoquant la création d'un réseau de fissures dans la masse rocheuse. Ces pressions peuvent être augmentées de plusieurs Bar par rapport au même cas avec le bloc libre de se déplacer. La plus grande différence de pression a été observée pour un jet impactant sur le coin du bloc.

Mot clés : *Jets d'eau à hautes vitesses, masse rocheuse fissurée, fissure tridimensionnelle, bloc de roche artificielle, érosion, fluctuations de pression, mouvement du bloc, impulsion du bloc, masse virtuelle (added mass), entrainement d'air, géométrie de la fissure, degré de liberté.*

Zusammenfassung

Hochgeschwindikeitswasserstrahlen von z.B. Hochwasserentlastungsanlagen können Kolk im felsigen Flussbett am Fusse einer Talsperre auslösen und somit die Stabilität des Bauwerks gefährden. Um die Sicherheit der Anlagen zu gewährleisten sind Kolkberechnungen notwendig.

Ein bestehender massstabsgetreuer Versuchsstand am Laboratoire de Constructions Hydrauliques (LCH) der École Polytechnique Fédérale de Lausanne (EPFL) wurde so angepasst, dass die komplexen Druckwechselwirkungen sowohl im zylinderförmigen Becken mit 3 m Diameter als auch in der dreidimensional ausgebildeten Kluft untersucht werden können. Die Wasserstrahlen können in Sachen Fliessgeschwindigkeit, Turbulenz sowie Lufteintrag realitätsgetreu nachgebildet werden.

Ein beweglicher mit Messtechnik ausgerüsteter Block wurde im Versuchsstand eingebaut. Dieser künstliche Felsblock simuliert einen Teil des gerissenen Felsmassivs und kann sich nur vertikal bewegen (ein Freiheitsgrad). Der Block mit 200 mm Seitenlänge und einer gesteinsähnlichen Dichte ist mit Druck-, Bewegungs- sowie Beschleunigungssensoren ausgerüstet, was mehrere Messungen gleichzeitig zulässst. Er ist in eine Messnische eingelassen, die ebenfalls mit Druckmessern ausgerüstet ist. Der dreidimensional ausgebildete Zwischenraum zwischen Block und Nische entspricht einem 1 mm breiten Riss resp. Kluft.

In der Versuchsanlage konnten mit den Hochgeschwindigkeitswasserstrahlen verschiedene Lastfälle mit unvollständig sowie voll ausgebildeter Wasserstrahl simuliert werden.

Das Forschungsziel beinhaltete den Aufschluss über das Verhalten eines einzelnen Felsblocks, der vom Muttergestein durch einen Riss abgetrennt ist und einem natürlich belüfteten Hochgeschwindigkeitswasserstrahl ausgesetzt wird.

Druckvariationen sowie die Bewegungen des Blocks (Verschiebung und Beschleunigung) werden für verschiedene Strahlauftreffpunkte auf der Blockoberkante, für unterschiedliche Wassertiefen (Wasserstand / Düsendurchmesser (72 mm) zwischen 0 und 9.7) und für realitätsgetreue Strahlgeschwindigkeiten (2.5 - 27.0 m/s) aufgezeichnet.

Die Reaktion der symmetrisch und asymmetrisch zum Blockzentrum auftreffenden Wasserstrahlen werden für mehrere Eingangsgrössen untersucht: Blocknahes Druckfeld, dynamische Blockimpulsion, natürliche sowie passive Bellüftung, Rissgeometrie, Freiheitsgrade des Blocks sowie Blockrotationen.

Die Ergebnisse erlauben interessante Schlussfolgerungen. Das Druckfeld auf die Blockober-

seite entspricht der in der Literatur beschriebenen exponentiellen Verteilung, wobei die Drücke im dreidimensionalen Riss fast konstant bleiben. Die Extremwerte (positiv und negativ) werden in der Kluft gemessen, wo keine Übergangsphänomene stattfinden.

Zum ersten Mal kann dank der aufgezeichneten dynamischen Blockimpulsion die Relevanz der Blockmasse sowie des Strahlauftreffpunkts aufgezeigt werden. Beschleunigt man einen eingetauchten Körper, so beschleunigt sich auch das umgebende Fluid. Die Trägheit des Fluids entspricht der Trägheitsmasse, was die vertikale Auslenkungsamplitude beeinflusst. Die im Versuchsstand gemessenen Grössen stimmen nicht mit den bisher für verschiedene Randbedingungen gekannten Werten eines lateral gehaltenen, bewegten Körpers in unbewegtem Fluid überein. Der quadratische Block wird von der Messnische auf fünf Seiten durch einen 1 mm breiten Spalt abgegrenzt. Die Oberseite wird direkt dem Wasserstrahl ausgesetzt. Diese erstmals getestete Versuchsanordnung erklärt den Unterschied zwischen gemessenen und aus der Literatur bekannten Werten.

Der theoretische Blockauftrieb stimmt mit dem gemessenen Wert überein, sofern die zusätzliche Masse im Datensatz der dynamischen Blockimpulsion enthalten ist. Einzig die Amplitude der vertikalen Auslenkung kann nicht immer theoretisch nachgewiesen werden. Die vertikalen Fluktuationen können jeweils reproduziert werden. Die maximale Block auslenkung von $\sim$160 mm wird für einen Strahlauftreffpunkt an der Blockecke gemessen.

Die durch das Ansaugen von Luft passiv generierte Belüftung an der Düse, zusammen mit der natürlichen Strahlbelüftung im Becken, beeinflusst die Extremwerte der gemessenen Drücke (Maximum und Minimum), jedoch nicht die Blockauslenkung. Um diese Einflussgrösse jedoch akkurat zu beurteilen, bedürfte es einer erneuten Anpassung des Versuchsstands.

Um die Rissgeometrie zu bestimmen und die Freiheitsgrade auf eins zu begrenzen, werden zwei Typen von seitlich am Block angebrachten Schienen getestet. Bei symmetrischer Belastung werden keine Unterschiede gemessen, wobei bei asymmetrischem Strahlauftreffen mit gleicher Intensität, jedoch auf einer anderen Blockkante, unterschiedliche Blockbewegungen aufgezeichnet werden.

Der Freiheitsgrad des Blocks beeinflusst da Druckfeld im dreidimensionalen Riss. Wenn der Block in der Messnische fixiert ist, erhöhen die Drücke die hydrodynamische Belastung, was eine zunehmende Rissbildung im Felsmassiv auslösen wird. Der Druckunterschied zwischen eingespanntem und freiem Block kann einige bar betragen. Die grössten Differenzen findet man für den Last fall mit dem Wasserstrahl auf die Blockecke.

Schlagwörter: *Hochgeschwindigkeitswasserstrahlen, Tossbecken, gerissener Fels, dreidimenionaler Riss, "künstlicher Felsblock", Kolk, Druckschwankungen, Blockbewegungen, dynamische Blockimpulsion, Trägheitsmasse, Belüftung, Rissgeometrie, Freiheitsgrad.*

Riassunto

I getti ad alta velocità generati dagli sfioratori di piena delle dighe possono erodere il letto fluviale a valle della diga. Una valutazione dell'erosione e della sua evoluzione è essenziale per garantire la sicurezza della diga e degli impianti annessi.

L'installazione sperimentale sviluppata presso il Laboratorio di Costruzioni Idrauliche (LCH) del Politecnico Federale di Losanna (EPFL) è stata modificata per studiare la complessa interazione tra le fluttuazioni delle pressioni generatesi all'interno di una fossa d'erosione e di una fessura tridimensionale. L'installazione attuale permette di ricreare dei getti d'acqua simili alle condizioni reali per quanto concerne la velocità, la turbolenza e l'aerazione.

Un blocco metallico simulante un blocco di roccia situato all'interno di un massiccio roccioso fessurato, rappresentato da un contenitore rettangolare, è stato posto al centro dell'installazione esistente. Il blocco e la struttura circostante permettono di compiere contemporaneamente diversi tipi di misure. Il blocco ha una forma cubica di 200 mm di lato, una densità apparente simile a quella di una roccia ed è equipaggiato con sensori di pressione ed accelerazione. Il contenitore circostante è anch'esso equipaggiato con sensori di pressione e movimento che permettono di ricreare il campo di pressione agente attorno al blocco e i relativi movimenti. Tra il cubo ed il contenitore esterno esiste una fenditura di 1 mm di spessore. La fossa d'erosione, la fessura ed il blocco sono stati sollecitati con dei getti ad alta velocità per generare diversi comportamenti in funzione della profondità dell'acqua all'interno della fossa d'erosione.

L'obiettivo di questo lavoro di ricerca è di studiare il comportamento di un blocco circondato da una fessura tridimensionale, il quale è sottomesso all'azione di getti ad alta velocità aerati naturalmente.

Le fluttuazioni delle pressioni e il comportamento del blocco (movimenti ed accelerazioni) sono registrati simultaneamente per differenti: posizioni d'impatto del getto sulla faccia superiore del blocco, profondità d'acqua nella fossa (rapporto Y/D compreso tra 0 e 9.7) e velocità del getto (2.5 - 27.0 m/s).

L'influenza delle sollecitazioni, generate da tre tipi di getto, sono state analizzate per vari parametri: il campo di pressione, l'impulsione dinamica del blocco, l'aerazione naturale e passiva del getto, la geometria della fessura, il grado di libertà del blocco e la rotazione del blocco nella sua fondazione.

L'analisi delle misure ha mostrato dei risultati interessanti. La pressione che agisce sulla

superficie superiore del blocco segue una distribuzione esponenziale (come proposto nella letteratura) mentre all'interno della fessura tridimensionale è quasi costante. I valori massimi della pressione (positivi e negativi) vengono attenuati all'interno della fessura. Nessun fenomeno transitorio è stato osservato all'interno della fessura.

Per la prima volta, il calcolo dell'impulsione dinamica del blocco (dynamic block uplift) ha mostrato l'importanza della massa virtuale (added mass) e della sua variazione in funzione della posizione d'impatto e della velocità del getto e della profondità d'acqua. Quando un corpo immerso in un fluido è soggetto ad un'accelerazione, anche l'acqua circostante si muove con questo ultimo. L'inerzia di questo volume d'acqua corrisponde alla massa virtuale ed essa influenza l'ampiezza dei movimenti del blocco. I valori trovati mediante l'installazione sperimentale sono molto diversi da quelli trovati nella letteratura (riguardanti principalmente dei corpi che si muovono in un ambiente quasi stazionario e parzialmente confinato). Il blocco è fortemente confinato dal contenitore esterno su cinque delle sue sei facce, con una separazione di 1 mm ed in più è direttamente sollecitato dal getto sulla faccia libera. Queste condizioni possono essere all'origine della differenza tra i valori sperimentali e quelli trovati nella letteratura. I movimenti verticali del blocco calcolati a partire dalle misure di pressione mostrano una buona corrispondenza con i valori misurati dai sensori di movimento. L'ampiezza di questi movimenti non può esser riprodotta correttamente mentre la loro presenza può essere ben ricreata. Lo spostamento massimo del blocco è stato osservato per un getto che colpisce il blocco su di un angolo ($\sim$160 mm per un'altezza del blocco di 200 mm).

Un sistema d'aerazione artificiale, basato sulla creazione di una depressione generata dal getto all'uscita dell'ugello, è stato sviluppato per studiare l'influenza dell'aria sul comportamento della fossa d'erosione e del blocco. L'aggiunta d'aria tramite il sistema artificiale sembra influenzare i valori estremi della pressione ma non i movimenti del blocco.

Per modificare la geometria della fessura che circonda il blocco e, allo stesso tempo, per limitare i gradi di libertà del blocco ad uno soltanto, due tipi differenti di guide laterali fissate sul blocco sono state sviluppate. Nel caso che il blocco sia sollecitato da un getto simmetrico (centro del blocco) nessuna differenza è stata osservata mentre se l'impatto è asimmetrico, un diverso comportamento compare in funzione del tipo di guida laterale usata.

Il grado di libertà del blocco influenza profondamente il campo di pressione che si genera all'interno della fessura. Quando il cubo metallico è bloccato nel contenitore circostante, le pressioni possono essere superiori di vari Bar paragonati allo stesso caso ma con il blocco libero di muoversi. L'impatto sull'angolo del blocco è il caso che genera l'aumento di pressione più consistente.

Parole chiave: *Getti ad alta velocità, fossa d'erosione, massiccio roccioso fessurato, fessura tridimensionale, blocco artificiale di roccia, erosione, fluttuazioni di pressione, movimenti del blocco, impulsione dinamica del blocco, massa virtuale (added mass), aerazione naturale e passiva del getto, geometria della fessura, grado di libertà.*

Contents

Chapter 1

Introduction

1.1 Problem definition

Hydraulic structures that spill excess water from reservoirs as spillways of high head dams, have been a major engineering concern for a long time. The difficulty lies in the transfer of the energy of the water from the upstream reservoir to the downstream river without generation of a dangerous scour of the dam foundation. On the long term, this scour process could create safety problems of the structural stability of the dam. An accurate prediction of scour evolution and the ultimate physical limits is thus required.

1.1.1 Physical processes

Ultimate scour depth is traditionally estimated by use of empirical or semi-empirical formulas that partially neglect the basic physical processes involved in the scouring, especially the fluctuating pressures in plunge pools and inside fissured rock media. Furthermore, these formulas are often only applicable to the specific conditions for which they have been developed (Whittaker and Schleiss (1984) and Bollaert and Schleiss (2003a)).

Since the 1960's, statistical treatment of fluctuating pressures became possible due to development of informatics. Methods taking into account extreme pressures could so clarify the dynamic uplift of concrete slabs in stilling basin and scour hole formation in fissured rock masses. In the 1980's and 1990's, the influence of time-mean (Reinus (1986) and Otto (1989)) or instantaneous pressure differences (Fiorotto and Rinaldo (1992a) and Liu et al. (1998)) was tested on physical models and applied to concrete slabs or rock blocks. However, scouring is a highly dynamic process, governed by the interaction of three main phases (water, rock and air) and characterized by important transient pressure phenomena inside rock fissures, due to their interconnected characteristics (Bollaert and Schleiss (2003a)). This highly unsteady nature is expressed by hydrodynamic fracturing, causing a break-up of the rock mass by a progressive growth of its defaults, and by hydrodynamic uplift, trying to eject the formed blocks outside of their rock foundation (Figure 1.1).

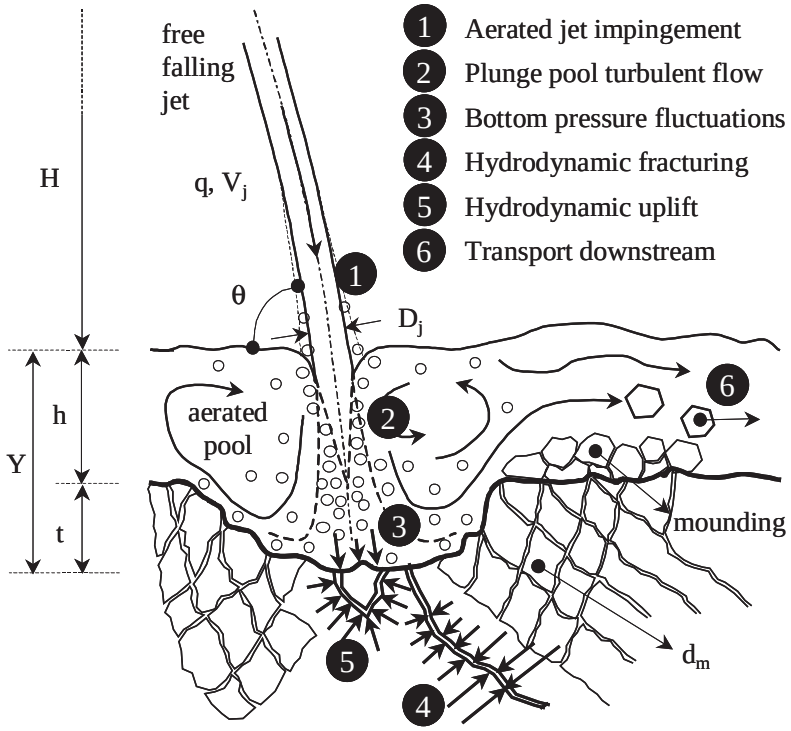

Figure 1.1: Main parameters and physical-mechanical processes involved in the scouring phenomena (Bollaert (2002b)). The present research project focuses on the process of dynamic uplift for an "artificial rock block" founded in the rock mass.

In general, the scour hole development and its propagation can be divided into a series of consecutive physical and/or mechanical processes (Figure 1.1):

1. aerated jet impact at the plunge pool surface;
2. diffuses shear-layer in the plunge pool;
3. dynamic pressures at the water-rock interface;
4. propagation of these pressures inside the fissures and brake-up of the rock mass by hydraulic jacking;
5. dynamic uplift acting on the single rock block presents in the broken rock mass;
6. downstream transportation of the blocks by the main flow.

The overview of existing methods distinguishes between purely empirical approaches (general, based on field and laboratory observations), analytical-empirical methods (combining empiricism with some physics), extreme values of fluctuating pressures at the plunge pool bottom and finally techniques based on time-mean and instantaneous pressure differences.

1.1.2 Existing engineering methods to evaluate scour

The existing engineering methods to evaluate the ultimate scour depth can be divided in four groups (Bollaert (2002b) and Bollaert and Schleiss (2003a)):

- empirical expressions (approach based on laboratory and field observations);
- semi-empirical expressions (methods combining laboratory and field observations with some physics);
- expressions for extreme pool bottom pressures;
- expressions for instantaneous or time-averaged pressure differences over and under rock blocks or concrete slabs.

The parameters of these groups are classified into four types:

- time;
- flow;
- aeration (jet and plunge pool);
- geomechanical parameters (rock mass).

Three methods incorporate the three phases (water, rock and air), but without time evolution: the erodibility index method developed by Annandale (1995) and two methods based on the momentum equation (Fahlbusch (1994) and Hoffmans (1998)). Furthermore, methods determining extreme bottom pressures account for hydraulic and aeration characteristics in detail, but neglect geomechanical aspects. Pressure difference methods provide a good description of hydraulic and geomechanical characteristics, but without valid assumptions regarding the air content.

The only method today that fully describes the four types of parameters (time, hydraulic, aeration and geomechanical parameters) is the method developed by Bollaert (2002b) and Bollaert and Schleiss (2005): the scour model. The scour model is a physically-based method for evaluation of scour formation as a function of time in plunge pools and fissured rock media (Bollaert (2004a) and Bollaert and Schleiss (2005)).

The scour model is based on three main modules: the falling jet, the plunge pool and the rock mass. The module for the falling jet describes the jet trajectory from its point of issuance at the dam down to the impingement of the jet into the plunge pool. The plunge pool module refers to the hydraulic and geometric characteristics of the plunge pool basin downstream of the dam and defines the hydrodynamic loading at the water-rock interface. The rock mass module is used for determination of the hydrodynamic loading inside underlying open- or closed-end rock fissures. The first part of the module for the rock mass defined the characteristics of the hydrodynamic loading inside open- or closed-end rock fissures. The second part of the module

deals with the corresponding failure criteria of the rock mass.

The most common methods used for scour evaluation due to falling high-velocity jets are illustrated in Figure 1.2 (Bollaert (2002b) and Bollaert and Schleiss (2003a)). In the same Figure the principal physical parameters used in the methods for scour evaluation are listed. The parameters can be related to the three phases (water, rock and air) which are involved in the scour process. The time evolution is another important parameter.

Type	Year	Author(s)	Applicability	Time	Hydraulic characteristics										Geomechanical characteristics											Aeration characteristics			
					hydrostatic							hydrodynamic			gran. soil			jointed rock mass											
				T	q	h	H	g	V_j	θ	RMS	Sxx(f)	trans		d_m	w_s	ρ_s	σ_c,σ_t	RQD	N_j	z	α	ϕ_j	C	β	Tu	L_b
				[-]	[m^2/s]	[m]	[m]	[m/s^2]	[m/s]	[°]	[-]	[m^2]	[-]		[mm]	[m/s]	[kg/m^3]	[N/m^2]	[%]	[-]	[-]	[°]	[°]	[-]	[-]	[%]	[m]
empirical	1932	Schoklitsch	plunging jet	-	■	-	■	-	-	-	-	-	-		■	-	-	-	-	-	-	-	-	-	-	-	-	-
	1937	Veronese A	horiz. & plunging jet	-	■	-	■	-	-	-	-	-	-		■	-	-	-	-	-	-	-	-	-	-	-	-	-
	1937	Veronese B	as A, but d_m < 0.005m	-	■	-	■	-	-	-	-	-	-		-	-	-	-	-	-	-	-	-	-	-	-	-	-
	1939	Jaeger	plunging jet	-	■	■	■	-	-	-	-	-	-		■	-	-	-	-	-	-	-	-	-	-	-	-	-
	1953	Doddiah et al.	plunging jet	■	■	-	■	-	-	-	-	-	-		■	■	-	-	-	-	-	-	-	-	-	-	-	-
	1957	Hartung	plunging jet	-	■	-	■	■	-	-	-	-	-		■	-	-	-	-	-	-	-	-	-	-	-	-	-
	1963	Rubinstein	ski-jump, rock cubes	-	-	■	■	■	■	■	-	-	-		-	-	-	-	-	-	■	-	-	■	-	-	-	-
	1966	Damle et al.*	ski-jump	-	■	-	■	-	-	-	-	-	-		-	-	-	-	-	-	-	-	-	-	-	-	-	-
	1967	Kotoulas	plunging jet	-	■	-	■	-	-	-	-	-	-		■	-	-	-	-	-	-	-	-	-	-	-	-	-
	1969	Chee & Padiyar	flip bucket	-	■	-	■	-	-	-	-	-	-		■	-	-	-	-	-	-	-	-	-	-	-	-	-
	1974	Chee & Kung	plunging jet	-	■	-	■	■	-	■	-	-	-		■	-	-	-	-	-	-	-	-	-	-	-	-	-
	1973	Martins A	plunging jet, rock cubes	-	■	■	■	-	-	■	-	-	-		-	-	-	-	-	-	■	-	-	-	-	-	-	-
	1975	Martins B	ski-jump	-	■	-	■	-	-	-	-	-	-		-	-	-	-	-	-	-	-	-	-	-	-	-	-
	1978	Taraimovich	ski-jump	-	-	-	■	-	■	■	-	-	-		-	■	-	-	-	-	-	-	-	-	-	-	-	-
	1981	INCYTH	plunging jet	-	■	-	■	-	-	-	-	-	-		-	-	-	-	-	-	-	-	-	-	-	-	-	-
	1982	Machado A	plunging jet, rocky bed	-	■	-	■	■	-	-	-	-	-		■	-	-	-	-	-	-	-	-	■	-	-	-	-
	1982	Machado B	plunging jet, rocky bed	-	■		■	■	-	-	-	-	-		-	-	-	-	-	-	-	-	-	■	-	-	-	-
	1985	Mason & Arumugam*	plunging jet	-	■	■	■	■	-	-	-	-	-		■	-	-	-	-	-	-	-	-	-	-	-	-	-
	1989	Mason	plunging jet	-	■	■	■	■	-	-	-	-	-		■	-	-	-	-	-	-	-	-	-	■	-	-	-
semi-empirical	1960	Mikhalev	plunging jet	-	■	■	■	■	-	■	-	-	-		■	-	-	-	-	-	-	-	-	-	-	-	-	-
	1967	Mirtskhulava et al.*	plunging jet, rocky bed	-	■	■	■	■	■	■	-	-	-		-	■	■	■	-	-	■	-	-	■	-	-	-	-
	1967	Poreh & Hefez	circ. submerged imp. jet	-	■	-	■	-	■	-	-	-	-		■	-	■	-	-	-	-	-	-	-	-	-	-	-
	1975	Zvorykin	ski-jump	-	-	■	-	-	■	■	-	-	-		-	-	-	-	-	-	-	-	-	-	-	-	-	-
	1983	Mih & Kabir	circ. submerged imp. jet	-	-	■	-	■	■	■	-	-	-		■	-	■	-	-	-	-	-	-	-	-	-	-	-
	1985	Chee & Yuen	plunging jet	-	-	■	-	■	■	■	-	-	-		■	-	■	-	-	-	-	-	-	-	-	-	-	-
	1985	Spurr*	plunging jet	■	■	■	■	■	■	■	-	-	-		■	-	-	■	■	■	■	■	-	-	-	-	-	-
	1991	Bormann & Julien*	grade-control, plung. jet	-	■	-	-	■	■	■	-	-	-		■	-	■	-	-	-	-	-	-	-	-	-	-	-
	1993	Stein et al.	plunging jet	■	-	-	-	■	■	■	-	-	-		■	-	-	-	-	-	-	-	-	-	-	-	-	-
	1994	Fahlbusch	general	-	■	■	-	■	■	■	-	-	-		■	-	-	■	-	-	-	-	-	-	■	-	-	-
	1998	Annandale & al.*	general	-	■	■	■	■	■	■	-	-	-		■	-	■	■	■	■	■	■	■	-	■	-	-	-
	1998	Hoffmans	general	-	■	■	-	■	■	■	-	-	-		■	-	■	-	-	-	-	-	-	-	■	-	-	-
plunge pool pressure fluctuations	1983	Xu Duo Ming	rectang. impinging jet	-	■	■	■	■	■	■	■	■	-		-	-	-	-	-	-	-	-	-	-	-	-	-	-
	1985	Cui Guang Tao	rectang. impinging jet	-	■	■	■	■	■	■	■	■	-		-	-	-	-	-	-	-	-	-	-	-	-	-	-
	1987	Franzetti & Tanda	circular impinging jet	-	■	■	■	■	■	-	■	-	-		-	-	-	-	-	-	-	-	-	-	-	-	-	-
	1991	Armengou	rectang. falling nappe	-	■	■	■	■	■	-	■	■	-		-	-	-	-	-	-	-	-	-	-	-	-	-	-
	1991	May & Willoughby	rectangular slot jet	-	■	■	■	■	■	-	■	■	-		-	-	-	-	-	-	-	-	-	-	■	■	■	■
	1994	Puertas & Dolz	rectang. falling nappe	-	■	■	■	■	■	-	■	■	-		-	-	-	-	-	-	-	-	-	-	-	-	-	-
	1997	Ervine & al.	circular impinging jet	-	■	■	■	■	■	-	■	■	-		-	-	-	-	-	-	-	-	-	-	■	■	■	■
pressure difference techniques	1963	Yuditskii	oblique imp. rect. jet	-	■	-	-	■	-	■	-	-	-		-	-	■	-	-	-	■	-	-	-	-	-	-	-
	1986	Reinius	parallel flow impact	-	-	■	-	■	■	-	-	-	-		-	-	■	-	-	-	-	■	-	-	-	-	-	-
	1989	Otto	oblique imp. rect. jet	-	-	-	-	■	■	■	-	-	-		-	-	■	-	-	-	■	-	■	-	-	-	-	-
	1992	Fiorotto & Rinaldo	concrete slab uplift	-	■	■	■	■	■	-	■	-	-		-	-	■	-	-	-	■	-	-	-	-	-	-	-
	1998	Liu & al.	rock block uplift	-	■	■	■	■	■	■	■	■	-		-	-	■	-	-	-	■	-	-	-	-	-	-	-
	1999	Liu & al.	vibration. slab uplift	-	■	■	■	■	■	■	■	■	-		-	-	■	-	-	-	■	-	-	-	-	-	-	-
	2000	Fiorotto & Salandin	anchored slab uplift	-	■	■	■	■	■	-	■	■	-		-	-	■	-	-	-	■	-	-	-	-	-	-	-
EPFL Project	2002	2-phase transient jacking/uplift		■	■	■	■	■	■	■	■	■	■		-	-	■	■	■	■	■	■	■	■	■	■	■	■

Figure 1.2: Summary of existing engineering methods of ultimate scour depth evaluation, showing the main hydraulic, geomechanical and aeration parameters. Authors names that are marked with * propose an expression based on prototype conditions or observations (Bollaert (2002b) and Bollaert and Schleiss (2003a)).

1.1.3 Field of the research

The scour prediction methods are also presented in Figure 1.3 (Bollaert (2002b), Bollaert and Schleiss (2003a) and adapted by Schleiss and Annandale (2007)). The three phases (water, rock and air) are developed along the three axes of a cubic volume called the "knowledge cube". The precision and accuracy of the prediction methods grow moving along the three axes. For the rock axis, the following methods can be distinguished: simple empirical formulas, initiation of motion theories, rock mass representation by an erodibility index, use of one-dimensional rock fissure, use of 1-dimensional network of rock fissures and finally a more complicated 2-dimensional rock fissure network. Actual knowledge along this axis is restricted to a 2-dimensional rock fissure description. Analogously, the axis that summarizes the hydrodynamic methods incorporates empirical methods, 2-dimensional jet diffusion theory, turbulence measurements, time-averaged and instantaneous pressure differences, fully transient flow (oscillations ...) and finally non-linear flow dynamics that take into account the interaction with the rock mass. Actually, the most valuable developments are situated in the field of instantaneous pressure differences. Finally, the aeration axis shows empirical (mean pressure reduction) coefficients, falling jet aeration, plunge pool aeration and rock fissure air content.

The methods presented at Figure 1.2 are enclosed by the white cubic that is situated inside the main cube in Figure 1.3. This shows the limits of scour description and asks for a physically more refined research. The ultimate description that could be attained is situated in the upper right corner of the main cube and represents a fully interactive, 3-phase transient model. It existing methods consider the fissured rock mass as a sort of "black box". What is happening inside the fissure is rather unknown. This physical reassessment of the situation has to: firstly analyze the fissured rock mass and secondly analyze the water pressures in a microscopic manner (physically based).

Advanced researches performed at the Laboratory of Hydraulic Constructions (LCH) of the École Polytechnique Fédérale de Lausanne (EPFL) have extended the actual knowledge out of the white cube by assessing fully transient two-phase flow effects inside simple rock fissures due to jet impingement on flat plunge pool bottoms (Bollaert (2002b) and Bollaert and Schleiss (2003a)). Also, the influence of realistically shaped plunge pool bottom geometries on dynamic pressure fluctuations at the pool bottom itself has been investigated (Manso (2006) and Manso et al. (2009)). Further progress needs the assessment of fully transient two-phase flow inside complex 3-dimensional networks of rock fissures.

This would for example allow a physical description of the forces acting between the different rock blocks. Especially the following forces need to be quantified:

- pressure forces that let the fissure networks propagate in the rock mass;
- pressure forces that eject the rock blocks from the rock mass (block foundation).

These forces have been described in detail by Bollaert (2002b) for simple single fissure geometries. A real rock mass, however, consists of a 3-dimensional complex fissures, with

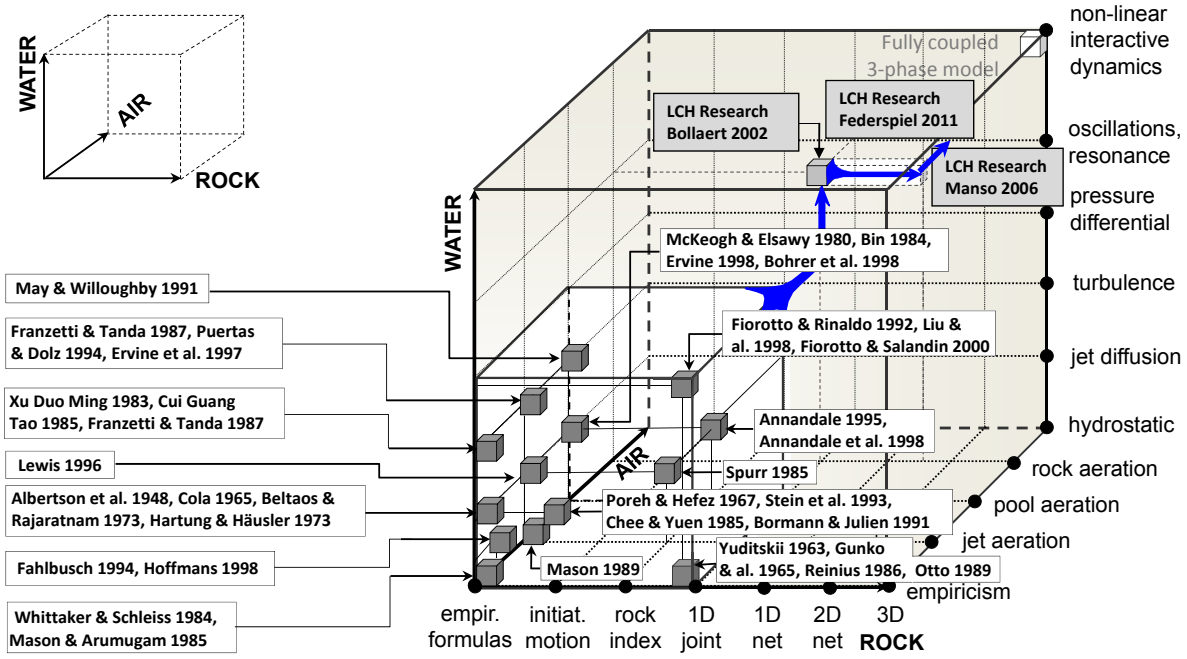

Figure 1.3: 3-dimensional representation of the actual state-of-the-art on scour evaluation methods. The three main axes represent the water, rock and air characteristics (Bollaert (2002b), Bollaert and Schleiss (2003a) and Schleiss and Annandale (2007)).

multiple connection between the different fissures presents in the rock mass. The influence of these connections on the extreme pressure forces and their propagation inside the networks is not clear yet and merits to be investigated in detail.

Simultaneous measurements of pressure fluctuations over and under a block allowed visualizing and assessing the influence of turbulent vortices on the displacement and/or entrainment of the block. Similar research has been performed by Coleman et al. (2003), focusing on the influence of block protrusion on its critical entrainment.

Hence, it becomes obvious that the next major step in the development of scour prediction methods for a fissured rock media (blocky media) consists of a detailed investigation of the main physical-mechanical phenomena that are responsible for block entrainment (ejection) and thus scour formation (responsible for the formation and displacement of blocks of any kind and any dimensions, as example: gravel, rock, concrete slab ...).

By equipping a block with different kind of transducers (pressure, displacement and acceleration), it is possible to record the instantaneous pressure forces acting on the block and the related block vibrations and displacements. This kind of measurements would allow to determine the following aspects:

- net uplift pressure (force) on the block during its vertical displacements;
- pressure force fluctuations underneath the block during its displacements;

- influence of fissure network and connection paths on block displacements/vibrations;
- influence of air entrainment on block displacements/vibrations;
- influence of bottom geometry on block during its displacements/vibrations.

Especially the influence of a moving block on the pressure forces inside the 3-dimensional fissure is of particular interest. When the block begins to move, the pressure acting underneath the block may be released and the block may fall down again. This typically results in block vibrations. For extreme pulses, however, block movement is sufficient to generate entrainment into the main flow.

1.1.4 Field of the research of the Laboratory of Hydraulic Constructions (LCH)

Since 1998, three research projects (Bollaert (2002b), Manso (2006) and the present research) have been performed at the LCH of the EPFL to better understand the complex interaction between the pressures fluctuations acting inside a realistic plunge pool and inside a complex 3-dimensional fissured network of a rock mass. The final goal is to develop a fully interactive 3-phase transient model to predict the rock scouring.

A physically based model to estimate scour has been developed by Bollaert (2002b) and Bollaert and Schleiss (2003a) at the LCH of the EPFL. This experimental installation showed that the high-velocity plunging water jets generated higher pressures inside rock fissures than the entrance pressures. The LCH experimental facility has been used for two research projects before the present research.

The first project was carried out by Erik Bollaert (1998-2002). He studied the behavior of a cylindrical plunge pool with flat bottom equipped with a 1- and 2-dimensional rock fissures (different fissure shapes have been tested: I-, 2D I-, L-, U- and D-fissure, Figure 1.4 on the left). However, a flat bottom happens only in the beginning of the erosion process, with the progression of the rock scour, the geometry of the pool bottom shows a highly irregular shape (Kobus et al. (1979) and Rajaratnam (1981)). This shape is influenced by the fissures distributions and the characteristics of the rock mass.

The second project was carried out by Pedro Manso (2002-2006). He studied the behavior of a more realistic plunge pool with different bottom geometries (different diameter and depths of the scour zone) and a 1- and 2-dimensional rock fissures (the same that have been used by Bollaert (2002b), Figure 1.4 on the center). For these bottom geometries (consisting of laterally confined plunge pool geometries), the pressure fluctuations at the surface and inside a closed-end fissure have been systematically recorded.

For both research projects, the plunge pool bottom and the fissure entrance were loaded by an impinging vertical high-velocity water jet.

The two-phase character of the air-water mixture inside the fissure is essential to the superposition, reflection and propagation of pressure waves. Pressure fluctuations inside rock fissures are caused by the pressure excitation of the jet at the fissure entrance. This excitation depends on the form of the plunge pool and the associated macro-turbulent flow pattern. In fact, the rock fissures have a more complex configuration. Normally the fissures are interconnected (3-dimensional). Some geometrical parameters (thickness and form of the fissure, the angle between the fissure and the water jet, the fissure connections ...) could modify the pressure inside the plunge pool and the fissures. The aeration of the plunge pool and of the fissures could modify the pressure and its propagation inside the fissures.

In the present research project, pressure measurements inside more complex fissure geometries (3-dimensional fissure networks) were performed as a next step to gain more knowledge. The 1- and 2-dimensional fissure shapes will be replaced with a full interconnected 3-dimensional fissure surrounding an "artificial rock block" characterized by one degree of freedom (allowing the block to move along it vertical axis). A new experimental set-up was build and integrated in the existing LCH experimental facility. This facility allows to measure the pressure field surrounding the block and simultaneously measures the respectively block solicitations (vertical displacements and accelerations). Due to the complex passage from a 1- or 2-dimensional fissure to a fully interconnected 3-dimensional fissure, the plunge pool is equipped with a flat bottom.

This research project focus on the response of this single movable rock block surrounded by a 3-dimensional fissure and impacted by high-velocity water jet (Figure 1.4 on the right).

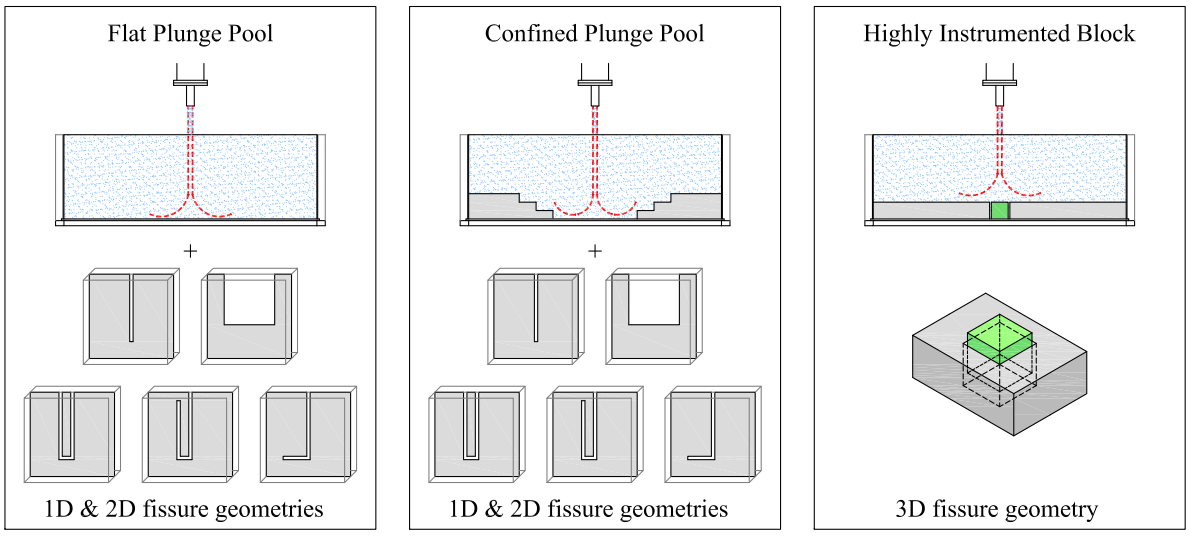

Figure 1.4: Sketch of different pool bottom and rock fissure geometries used for the testing at LCH. Left: flat plunge pool bottom with 1- and 2-dimensional fissure geometries by Bollaert (2002b); Center: confined plunge pool bottom with 1- and 2-dimensional fissure geometries by Manso (2006); Right: flat plunge pool bottom with a full interconnected 3-dimensional fissure and movable block (present research).

1.2 Purpose of the research study

The main purpose of this research project is to study experimentally the behavior of an "artificial rock block" separated from its surroundings by a full interconnected 3-dimensional fissure and impacted by a high-velocity plunging jet.

With this research project it is intended to fill some part the knowledge gap along the rock axis on the "knowledge cube" proposed by Bollaert (2002b) and Bollaert and Schleiss (2003a) (Figure 1.3) with the aim to obtain a better understanding of the response of an embedded block impacted by high-velocity plunging jets.

The following topics are studied:

- the pressure field surrounding the block;
- the block behavior related to the different jet solicitations (symmetrical and asymmetrical jet impacts);
- the dynamic block impulsion;
- the influence of the air entrainment in the jet on the block response;
- the degree of freedom of the block;
- the influence of the lateral guides on the block response (fissure geometry).

The behavior of a highly instrumented block embedded in an artificially created rock mass and solicited by a high-velocity water jet is studied by means of pressure, displacement and acceleration measurements. This block is separated from its surroundings by 1 mm thick fissure and simulates a distinct rock block in a fissured rock mass.

Several test for different configurations (symmetrical and asymmetrical block solicitations), water depths (core, transition and developed jets, Y/D ratio ranging between 0 and 9.7) and near-prototype jet velocities (2.5-27.0 m/s).

Both the block and the cavity are equipped with pressure transducers along their vertical and horizontal faces. The block is equipped by an accelerometer (allowing to measure the block vibrations) and the cavity with two displacement transducers.

1.3 Outline of the work

This report is composed by 9 main chapters.

Chapter 1, the actual chapter, explains the general background and the aim of the research project.

Chapter 2 deals with the literature review in the field of rock scour. Emphasis is given on the added mass concept for a body moving in a fluid.

Chapter 3 describes the experimental facility and the measurement equipment. The facility is at near-prototype scale and is conceived to test an "artificial rock block" surrounded by a 3-dimensional fissure. The test equipment consists of several transducers (pressure, displacement and acceleration) and a data acquisition system that have been used to measure pressure fluctuations at the plunge pool bottom and inside a 3-dimensional fissure. Simultaneously the block displacement and acceleration have been measured.

Chapter 4 describes the methodology of the research project, the fourteen test configurations, the involved test parameters and the type of measurements.

Chapter 5 deals with the theoretical background that has been used in the following chapters.

Chapter 6 shows the results for three of the fourteen configurations that have been tested during this research project. The other configurations are illustrated in the appendices that can be found at the end on this report.

In chapter 7 the performed experiments are analyzed in detailed regarding:

- Dynamic impulsion on a rock block;
- Influence of the "passive" air entrainment by the free falling jet;
- Influence of the lateral guides fixed on the block lateral faces: two or eight contact points;
- Influence of the degree of freedom of the block;
- Investigation on the block rotations.

Chapter 8 shows the practical relevance of the results for different jet configurations.

Chapter 9 summarizes major conclusions that can be drawn for this research project and the possible future research topics.

Chapter 2

Literature review

2.1 Introduction

In the last years, Bollaert (2002b) and Manso (2006) (researchers at the Laboratory of Hydraulic Constructions - LCH) have performed a completely literature review in the field of rock scour.

The literature review performed for this research project is based mostly on the studies of these two previous projects (Bollaert (2002b) and Manso (2006)). Only a short overview of this previous literature researches is given in the following section (Chapter 2.2).

Several papers have been published in the last years in the field of the rock scour and a part of these works are listed in the following (Chapter 2.3).

This research project investigated a new field of literature of particular interest: the added mass (Chapter 2.4) that will be integrated in the computation of the dynamic block impulsion (Chapter 7.1).

2.2 Existing literature reviews

Bollaert (2002b) gives in his literature review emphasis on the methods to evaluate the scouring. The most important empirical expression, semi-empirical expressions, extreme plunge pool bottom pressures and extreme pressure difference techniques have been explained. At the end of each section, some interesting conclusions on the existing methods and on the knowledge gaps are summarized. The existing methods to evaluate the rock scour are illustrated using the "knowledge cube" developed by Bollaert (2002b), Bollaert and Schleiss (2003a) and adapted by Schleiss and Annandale (2007) (Figure 1.3). The same methods but with the main parameters are listed in Figure 1.3.

Bollaert (2002b) performed a review on the scaling effect for the empirical expressions. This review focused on the scaling effect of: rock mass, aeration and time on the standard scouring expressions. The literature research for the semi-empirical expressions focused on: 2-dimensional jet diffusion, initiation of motion concept of the particles, conservation equations and geomechanical characteristics of the scouring rock mass. The extreme plunge pool bottom pressures literature was based on: hydraulic jump pressure fluctuations, plunge pool

bottom pressures fluctuations, aeration effects on the scouring phenomena (aeration of falling jets during its journey in the atmosphere, plunge pool aeration at the jet impact on the water surface and aeration of the rock fissures) and scaling effects between prototype and model. The extreme pressure difference techniques are based on the time-average pressure differences and the instantaneous pressure differences between the upper and lower faces of concrete slabs or rock blocks.

Manso (2006) focused his literature review on the available scour process, on the assessment of pool geometries and the corresponding induced flow patterns generated by the more complex pool shapes. Moreover, he performed a literature review on the plunge pools aeration. In a first time, he gives an overview on the previous studies relevant for the scour that have been performed worldwide and at the LCH. The existing methods for the scour estimation in solid, quasi-fixed and mobile bed have been analyzed (scour profile and influence of the inclination of the impinging jet). The behavior of prototype plunge pools compared to laboratory tested pools have been investigates. Several projects have been analyzed and some conclusions have been proposed. The development of the scour profiles as a function of the time has been investigated and some notes for the pre-excavation have been summarized. The jet diffusion in plunge pool and the air entrainment by undeveloped jets in unbounded pools (smooth and rough turbulent jets) have been investigates.

2.3 Recent research in the field of rock scour

2.3.1 Rock scours in solid, quasi-fixed and mobile beds

Based on Manso (2006) several papers have been published in the last years. These papers discuss the influence of the plunge pool geometries (Manso et al. (2006a), Manso et al. (2008) and Manso et al. (2009)), the air influence on the rock scour (Manso et al. (2006b)), the impact pressures on the plunge pool bottom (Manso et al. (2007a)) and the fissure opening in the rock scour phenomena (Manso et al. (2007b)).

Some works have been published in the field of the rock scour in completely disintegrated rock mass under inclined impinging jets. The jet shape, jet velocity, jet air content, tail water elevation, granulometry, upstream flow to the scour hole and the end scour profile in terms of the basic scour features have been investigated, as an example, by Pagliara et al. (2006), Pagliara et al. (2008), Pagliara and Palermo (2008) and Pagliara et al. (2011).

Several researches for rectangular jets impacting in a plunge pool have been performed by Castillo Elsitdié (2006) and Castillo Elsitdié (2007).

Liu and Li (2007) analyzed analytically and numerically the pressure fluctuations propagation within lining slab joints in stilling basins based on different hydraulic models.

Schleiss and Annandale (2007) and Annandale and Schleiss (2007) gave a state-of-the-art overview on rock scour technologies.

Borgheri and Zarnani (2008) studied the pressure fluctuations acting on the plunge pools side walls for rectangular and circular jets.

Li and Liu (2010) simulated the numerical propagation of a fissure in a rock mass solicited by fluctuating pressure waves. The transient physical and dynamic characteristics of isolated rock blocks and the damage process of the rocky bed have been discussed.

Hoffmans (2010a) proposed an update of a relation for jet scour in the equilibrium phase developed by itself (Hoffmans (1998)).

2.3.2 Influence of air on rock scour

Hence, since the start of this research project, the scientific community has also shown considerable interest in the influence of air entrainment and air concentration in the plunge pool on these dynamic pressures at the pool bottom. An interesting debate actually exists between two different ways of thought:

- Air bubbles entering the pool at the point of impact of the water jet substantially reduce the density of the air-water mixture at the plunge pool bottom and thus reduce mean pressures and risk of block uplift.

- Air bubbles entering the pool at the point of impact of the water jet do not substantially reduce the density of the air-water mixture at the plunge pool bottom because of the high pressure built-up near the bottom. As such, mean pressures and risks of block uplift are not affected.

The following sequence of published papers and discussions point out the actual relevance of this topic: Canepa and Hager (2003), Manso et al. (2004c), Bollaert and Schleiss (2005), Pinheiro and Melo (2008), Bollaert et al. (2009), Manso et al. (2009), Hoffmans (2010a) and Bollaert and Schleiss (2011).

In other words, whether it is found by the experiments that the air content in a pool relates to the dynamic pressures acting above and underneath a rock block, then the air content will also influence the risk of block uplift.

Hence, to benefit from the prototype scaled facility at LCH-EPFL some test with a natural and passive jet aeration have been performed to investigate this aspect and to have a first overview whether air bubbles in plunge pools increase or decrease the risk of block uplift at the plunge pool bottom. A further research projects is on the way at the LCH to study systematically the air influence on the block responses.

2.4 Literature review on added mass of rock block

2.4.1 Introduction

The added mass, also known as virtual mass, is the inertia of the fluid entrained by the accelerating body. When a body immerged in a fluid accelerates (positive or negative accelerations), the fluid surrounding it must accelerate as well. The inertia of the entrained fluid is the added mass. For simplicity this can be modeled as a fluid volume moving with the body, though in reality the entire fluid will be accelerated (but not uniformly).

The first time that the added mass concept appeared was in 1828. Friedrich W. Bessel, a German mathematician and astronomer (1784-1846), proposed the added mass concept to explain the motion of a pendulum oscillating in a fluid. Bessel observed that the pendulum period increased in relation with its period in a vacuum (even after accounting for buoyancy effects), indicating that the surrounding fluid increased the effective mass of the system (Stokes (1851)). Bessel did not perform any numerical computations for the inertia effect on the pendulum but he concluded, from general principles, that a fluid affects the movement of a body by increasing its moment of inertia. Bessel proposed that a mass of n times the displaced fluid volume had to be added to the body inertia.

In the past years, other detailed studies have been performed to better understand the added mass effect on the behavior of a body moving in a fluid (fluids with different density).

Several studies systematically evaluated the added mass for different geometries of 2- and 3-dimensional bodies. A detailed summary of the main formulas can be found in Patton (1965b), Brennen (1982) and Blevins (2001).

2.4.2 Added masses interaction between bodies moving in a fluid

When a body is moving in a fluid close to other bodies (moving or not), the bodies added masses are different from the added masses when the body is moving alone in an infinite fluid.

This difference arises from the boundary conditions: an isolated body in an infinite fluid has only a boundary condition at infinity. Neighboring bodies impose additionally boundary conditions.

Three different cases of interaction of bodies moving in a fluid can be distinguished (Korotkin (2009)):

1. motion of a body composed by several parts rigidly connected among themselves;
2. motion of a body in the presence of one or more stationary bodies;
3. motion of two or more bodies, such that each body is moving independently, possessing (in the general case) six degrees of freedom each.

A typical example of the first case is given by the two-hull vessels (catamarans), where two hulls are rigidly connected to each other and preserve their relative position under arbitrary motion.

The second and third cases of interaction mentioned above are typically classified as cases of variable interaction among bodies in a fluid. The mutual positions of bodies change even if the velocities of the bodies remain constant.

Under a variable motion the mutual positions of bodies in a fluid change continuously, so as the degree of their mutual influence and their hydrodynamic characteristics. Even when they move at constant velocities, all the hydrodynamic characteristics of the fluid flow change (velocities, potentials and pressure). The kinetic energy of the fluid motion changes as well, which leads also to similar changes for the added masses. Under varying interactions between the neighbor bodies, the added masses become variables and depend on the relative positions of the interacting bodies.

This is the principal difference between the motion of many bodies and the motion of a single body in a fluid. For a single body, the added masses forming the added mass matrix (6x6) are constant and are determined only by the shape of the body and choice of the coordinate system.

The common feature between case where a body moves near fixed objects and the one where there are several moving bodies is that in both situations the added masses become time-dependent variables. Simultaneously, there is a significant difference between these types of situations. For example, when a body moves near a rigid wall, there are only the added masses of the body itself, and their number is the same as for a body moving in an infinite fluid. In the case of simultaneous motion of several bodies, the number of added masses is larger. The increase in the number of added masses is not only due to the fact that each body has 36 added masses, but is also due to the appearance of new added masses, called the added masses of interaction.

For 3-dimensional bodies the added masses are difficulty to be determined theoretically but are easier to be determined experimentally.

2.4.3 Body vibration in a fluid

The effect of a surrounding fluid on the natural frequencies and modes shapes of a structure is not significant for relatively compact structures if the fluid density is smaller than the average density of the structure. Thus, the surrounding air does not ordinarily affect the natural frequencies or mode shapes of most structures. However, the surrounding water can play a significant role in the free vibration of the structure. Generally, a body oscillating in a quiescent fluid can be modeled as a 2-dimensional body (Figure 2.1).

The equation of motion of a simple spring-supported damped symmetric body vibrating in a still fluid (Eq. (2.1)) can be written as (Blevins (2001)):

$$m \cdot \ddot{x} + c \cdot \dot{x} + k \cdot x = F \tag{2.1}$$

where m is the mass of the body, c the structural damping, k the spring constant, F the fluid force applied to the body and x the displacement of the body from the equilibrium position.

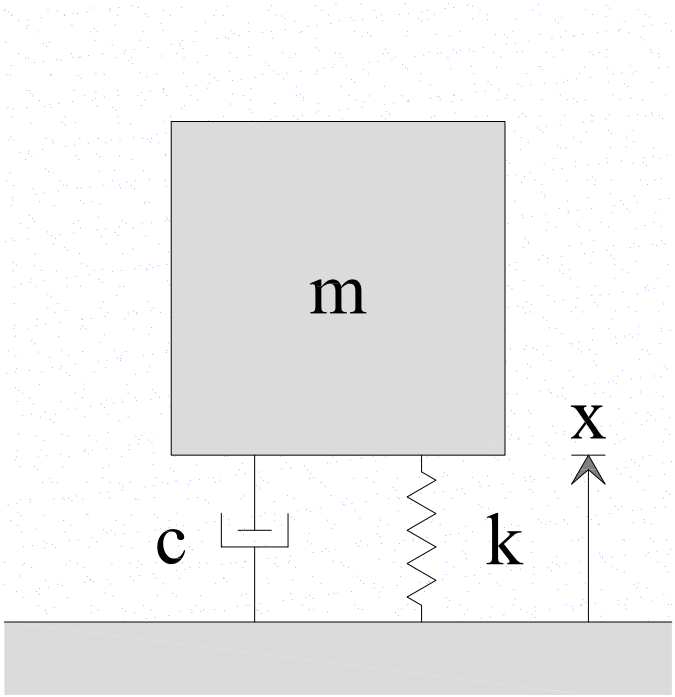

Figure 2.1: 2-dimensional spring supported, damped body in a still fluid.

The fluid force (Eq. (2.2)) acting on the body has two components: the added mass component and the water damping component. The fluid force is given by the following equation (Blevins (2001)):

$$F = -A_{xx} \cdot \ddot{x} - B_{xx} \cdot \dot{x} \tag{2.2}$$

where A_{xx} is the added mass, B_{xx} the water damping and x the block displacement from the equilibrium position.

The added mass (A_{xx}) has units of mass or mass per unit length for cross sections. $-A_{xx} \cdot \ddot{x}$ is the fluid force applied to the structure due to the inertia of the fluid entrained by the moving body. The added mass inertia acts with the same sign, frequency and phase as the inertia of the structural mass.

Equation (2.1) can be rewritten incorporating Equation (2.2) as:

$$m \cdot \ddot{x} + c \cdot \dot{x} + k \cdot x = -A_{xx} \cdot \ddot{x} - B_{xx} \cdot \dot{x} \tag{2.3}$$

which can be also expressed as:

$$(m + A_{xx}) \cdot \ddot{x} + (c + B_{xx}) \cdot \dot{x} + k \cdot x = 0 \tag{2.4}$$

Equation (2.4) describes the free vibrations of a body with an effective mass of $m + A_{xx}$ and an effective damping of $c + B_{xx}$.

The added mass and the added mass moment of inertia increase the effective mass and the effective mass moment of inertia of the structure. The added mass always decreases the natural frequency of the structure that would be measured in a vacuum.

The added mass can be measured experimentally or computed theoretically. The experiments have shown that the added mass of a body vibrating in a still fluid depends on:

I. the geometry of the body surface (including the body geometry, the relative position of the neighboring bodies and the location of the free surface);

II. the amplitude and direction of the vibrations;

III. a Reynolds-number-like parameter.

$$A_{stillfluid} = \rho_w \cdot F\left(geometry, \frac{x_0}{D}, \frac{f \cdot D^2}{\nu_w}\right) \tag{2.5}$$

where ρ_w is the fluid density, x_0 the vibration amplitude acting along one direction, D the characteristics diameter, f the vibration frequency and ν_w the fluid kinetic viscosity.

For an oscillating fluid the point I. of the previous list remains the same but the other two (II. and III.) have to be modified:

I. the geometry of the body surface (including the body geometry, the relative position of the neighbor bodies and the location of the free surface);

II. the amplitude and direction of the fluid oscillations;

III. the maximum Reynolds number achieved during oscillations.

$$A_{oscillanting_fluid} = \rho_w \cdot F\left(geometry, \frac{U_0}{f \cdot D}, \frac{U_0 \cdot D}{\nu_w}\right) \tag{2.6}$$

where U_0 is amplitude of the fluid velocity which oscillates with frequency f in a given plane.

The motion of a 3-dimensional body can be explained using six coordinates: three displacements along the orthogonal axes (x, y and z) and three rotations around these axes (θ_x, θ_y and θ_z). The added mass forces generated on a 3-dimensional body are determinate by a 6x6 matrix.

2.4.4 Added mass for 2-dimensional bodies

In this section the existing formula for 2-dimensional bodies are explained (square and rectangular bodies). All formulas are valid for a body accelerating along the vertical axis.

The added mass of a 2-dimensional body with two perpendicular axes of symmetry is completely specified, using a potential flow theory, by the added mass acceleration along each of the axes of symmetry and the added mass moments of inertia for rotation around the intersection of these axes.

2.4.4.1 Square body immerged in a fluid

The added mass for a square body (where $2a$ is the side length) immerged in a fluid is given as follows (Sedov (1966), Riman and Kreps (1947) and Blevins (2001)):

$$A_{xx} = 1.51 \cdot \pi \cdot a^2 \tag{2.7}$$

where a is the half of the side length.

The added mass is given per unit of length. The above formula was developed theoretically.

2.4.4.2 Square body floating in a fluid

The added mass for a square body (where $2a$ is the side length) floating in a fluid (immerged for half of his side in the fluid: a) is given as follows (Patton (1965b)):

$$A_{xx} = \alpha_{am} \cdot \pi \cdot \rho_w \cdot a^2 \tag{2.8}$$

where α_{am} is the added mass coefficient depending on the e/a ratio (Table 2.1), a the half of the side length and e distance between the water "reservoir" bottom and the lower face of the floating body. The above formula was developed theoretically.

e/a [−]	α_{am} [−]
inf	0.75
2.6	0.83
1.8	0.89
1.5	1.00
0.5	1.35
0.25	2.00

Table 2.1: Added mass coefficient for a square body floating in a fluid where e is the distance between the water "reservoir" bottom and the lower face of the floating body, a the half of the side length and α_{am} the added mass coefficient.

2.4.4.3 Rectangle body immerged in a fluid

The added mass for a rectangular body (where $2a$ is the rectangle width and $2b$ is the rectangle height) immerged in a fluid is given as follows (Patton (1965b), Brennen (1982) and Blevins (2001)):

$$A_{xx} = \alpha_{am} \cdot \pi \cdot \rho_w \cdot a^2 \tag{2.9}$$

where α_{am} is the added mass coefficient depending on the a/b ratio (Table 2.2), a the half of the rectangle width and b the half of the rectangle height.

The acceleration acts along the rectangle longer side ($2b$). The above formula was developed theoretically.

a/b [−]	α_{am} [−]
0.1	2.33
0.2	1.98
0.5	1.70
1.0	1.51
2.0	1.36
5.0	1.21
10.0	1.14
inf	1.0

Table 2.2: Added mass coefficient for a rectangular body immerged in a fluid where a is the half of the rectangle width, b the half of the rectangle height and α_{am} the added mass coefficient.

2.4.5 Added mass for 3-dimensional bodies

In this section the existing formula for 3-dimensional bodies are given (cubic and parallelepipeds bodies). All formulas are given for a body accelerating along the vertical axis.

The added mass and the added mass moments of inertia of symmetric 3-dimensional bodies were determined experimentally due to the difficulty to obtain 3-dimensional theoretical solutions.

2.4.5.1 Cubic body immerged in a fluid

The added mass for a cubic body (where a is the cube side length) immerged in a fluid is given as follows (Blevins (2001)):

$$A_{xx} = \alpha_{am} \cdot \rho_w \cdot a^3 \tag{2.10}$$

where α_{am} is the added mass coefficient and a the cube side length.

Stelson and Mavis (1955) proposes a value of 0.67 for the added mass coefficient, whereas Sarpkaya (1960) and Yu (1945) propose 0.7. Both coefficient values have been determined experimentally.

Vorobjov (1966) has studied the added mass coefficient for a parallelepiped moving in an infinite fluid and having different dimension ratios. For a cubic body immerged in a fluid he proposed the following equation:

$$A_{xx} = \alpha_{am} \cdot \rho_w \cdot \frac{1}{\sqrt[2]{2}} \cdot a^3 \tag{2.11}$$

where α_{am} is the added mass coefficient and a the side length. Vorobjov (1966) proposed 0.9 for the added mass coefficient.

2.4.5.2 Rectangular body immerged in a fluid

The added mass for a rectangular body with a squared base (where a is the side length and b is the body height) immerged in a fluid is given as follows (Sarpkaya (1960) and Blevins (2001)):

$$A_{xx} = \alpha_{am} \cdot \rho_w \cdot a^2 \cdot b \tag{2.12}$$

where α_{am} is the added mass coefficient depending on the b/a ratio (Tables 2.3 and 2.4), a is the side length and b is body height. The added mass coefficients have been determined experimentally.

b/a [−]	α_{am} [−]
0.5	1.32
0.6	1.15
0.8	0.86
1.0	0.70
1.2	0.57
1.6	0.45
2.0	0.35
2.4	0.30
2.8	0.26
3.6	0.22

Table 2.3: Added mass coefficient for a rectangular body with a square base immerged in a fluid where a is the side length, b the body height and α_{am} the added mass coefficient.

Patton (1965b) proposed another formulation for the added mass of a rectangular body having the same geometry and immerged in a fluid. This formulation is the same than has been proposed by Sarpkaya (1960) and Blevins (2001) but the added mass coefficient is different.

2.4.6 Effect of the bottom proximity on added mass

The presence of a solid boundary, near the moving body, can cause a substantial increase in the added mass. If the body is close to the boundary the added mass increases because a narrow gap between the body and the boundary (wall) is developed. Inside this narrow gap the fluid acceleration can be very large. These phenomena can be shown easily for a boat (having a

b/a [−]	α_{am} [−]
1	2.32
2	0.86
3	0.62
4	0.47
5	0.37
6	0.29
7	0.22
10	0.10

Table 2.4: Added mass coefficient for a rectangular body with a square base immerged in a fluid where a is the side length, b the body height and α_{am} the added mass coefficient.

rectangular shape) floating in shallow waters. The same behavior was also observed for deep waters ($c \to$ inf). The rectangular boat has a width of $2a$, a draught of b and the water depth is Y.

Flagg and Newman (1971) and Bai (1977) proposed the following equation:

$$A_{xx} = 2 \cdot \alpha_{am} \cdot \rho_w \cdot a \cdot b \tag{2.13}$$

where α_{am} is an added mass coefficient depending on the Y/b ratio (Table 2.5), a the half boat width and b the boat draught.

Y/b [−]	α_{am} [−]
1.1	5.52
1.2	3.49
1.5	2.11
3.0	1.35
8.0	1.21
inf	1.19

Table 2.5: Added mass coefficients for a rectangular boat floating in shallow waters where Y is the water depth and b the boat draught.

The added mass evolution in function of the Y/b ratio shows (Table 2.5) that: more the boat keel is near to the bottom (river, channel ...) and larger is the added mass that must be considered in the calculation. The same observations have been made for other geometries moving near a solid boundary (i.e. cylinder, plates ...).

2.5 Conclusion on literature review

The literature review in rock scour shows the need to further research in the definition of relevant loading events for fissure propagation and for block uplift solicited by high-velocity jets.

Actually exists only one method to model the fissure propagation underneath a plunge pool loaded by a high-velocity jet (Bollaert (2002b) and Bollaert and Schleiss (2005)). This method required a validation and an improving in terms of fissure characteristics (3-dimensional geometries, opening, roughness ...) and impact pressures generated by the impinging water jet.

Bollaert (2002b) proposed the scour model that is physically-based to evaluate the scour formation as a function of time in plunge pools and fissured rock media (that takes into account the transient pressure regimes inside the fissures). However, it is not clear whether the transient pressure peaks may be generated inside a natural interconnected fissure up to the values observed experimentally by Bollaert (2002b) and Manso (2006) for simples shaped fissures (I-, 2D I-, L-, U- and D-fissures, Figure 1.4). The main physical processes governing rock scour have been identified. However, it is necessary to further research at prototype and model scale. Existing scour assessment methods include important simplifications and do not represent the interactive evolution of the scour as 3-dimensional and 3-phase phenomena (water, rock and air). A further research for more complexes fissure geometries (as an example a full interconnected 3-dimensional fissure) with air entrainment by the impinging water jet have to be performed to improving the existing scour methods.

The literature review on the added mass shows the relevance of the boundary conditions on the evolution of the added mass. More the block is located near to a boundary and more the added mass that has to be considered in the computation increase. The highly instrumented block of the new experimental set-up is strongly confined in the measurement box (Chapter 3.2.2): the block is surrounded on five of its six faces by the measurement box. The distance between the block and its surrounding is 1 mm, that mean the two bodies (block and measurement box) are very close. Moreover, the block is not only strongly surrounded by another body (measurement box) but is directly loaded by the jet on its free surface (block upper face).

In previous studies any similar conditions have been analyzed. Further researches have to be made to estimate the added mass for a cube strongly confined moving in a turbulent flow.

Chapter 3

Test facility

3.1 Introduction

The behavior of a highly-velocity water jet impacting in a plunge pool on a highly instrumented block will be investigated. This section presents the LCH experimental facility and the electrical equipment. The main parts will be described and explained. The facility has been modified for this research project and a new Data Acquisition System (transducers, data acquisition and electrical equipment) has been installed.

3.2 LCH experimental facility

3.2.1 Existing part

The existing experimental facility was built at the Laboratory of Hydraulic Constructions (LCH) of the École Politechnique Fédérale de Lausanne (EPFL) in 1998. The facility was developed by Erik Bollaert for his PhD research project (Bollaert (2002b)) and it was used by Pedro Manso as well for his PhD research project (Manso (2006)).

It aims at reproducing the most important hydrodynamic processes involved in the rock scour. Real-life rock scour being a quite complex process, considerable simplifications are necessary to perform experimental research.

The experimental facility is presented in the following figures (Figures 3.1 to 3.3). This facility consists of five main parts (Bollaert (2002b)). To these main parts a new experimental part will be added (6^{th} main component). This new part has been integrated in the modified existent facility.

The existing five main parts are the following:

I. A 300 mm diameter water supply conduit, with a cylindrical or convergent-shaped jet outlet system at its end, models the jet. Due to constructive limitations, the supply conduit has a 90º bend just upstream of the jet outlet system. The existing nozzle is composed by a cylindrical PVC-tube. A rigid steel frame, consisting of three I-shaped

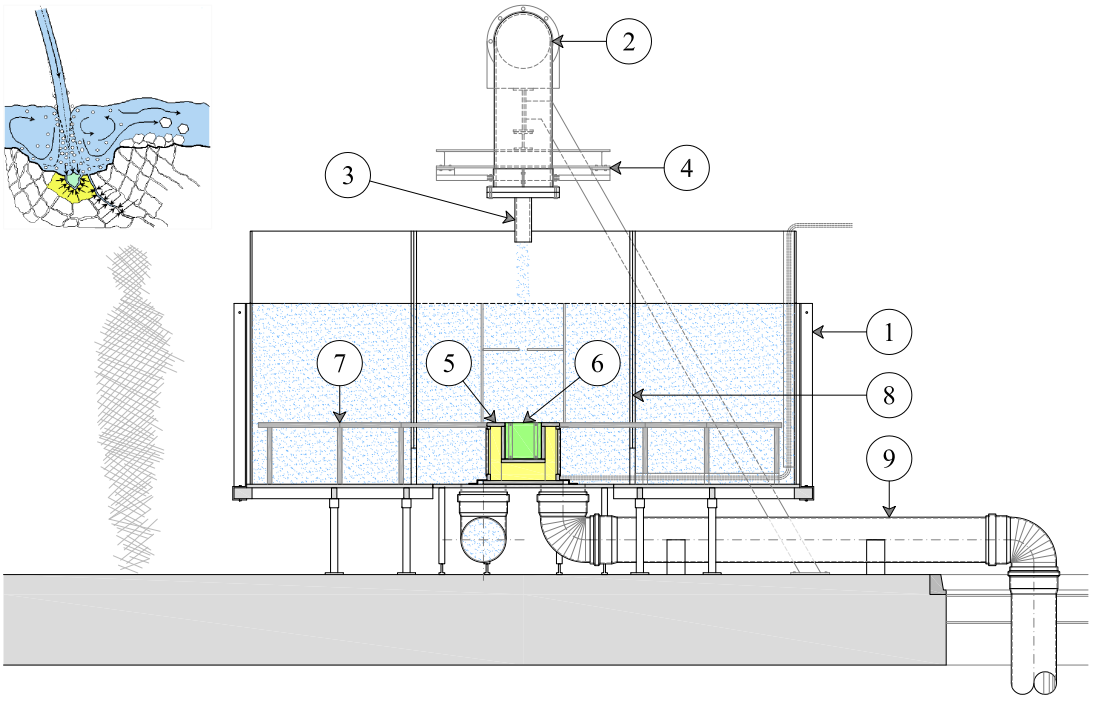

Figure 3.1: Side view of the experimental facility (transversal section): (1) plunge pool, (2) water supply conduit, (3) outlet nozzle, (4) supporting steel structure, (5) measurement box, (6) highly instrumented block, (7) new plunge pool bottom, (8) overflow boxes and (9) water restitution system.

steel profiles that are welded together, guarantees the support of the supply conduit. The jet outlet diameters are 57 or 72 mm.

II. A 3 m diameter cylindrical basin in steel reinforced Lucite simulates the plunge pool. The height of the basin is 1 m, and the steel reinforcement is provided by 10 T-shaped profiles. The bottom of the basin is made of a rigid steel frame, covered by a 10 mm opaque PVC plate. Inside the basin, two rectangular boxes made of PVC adjust the water level by a flat plate that is inserted (overflow boxes). The water that flows over these plates is conducted downstream into four restitution conduits. For the new experimental facility, the height of the basin has been increased to 1.4 m (40 cm higher). The new 40 cm heightening strip is made with transparent Plexiglas. To rigidify the plunge pool two pre-stressed steel cables are fixed along the facility perimeter.

III. A new support for the experimental facility was built. This support has taken the place of the existing pre-stressed steel structure, which modeled the one dimensional fissured rock mass (Bollaert (2002b)). The existing facility was moved down to a new level (50 cm from the laboratory floor). The new support looks like a steel table with four adjustable legs. The horizontal structure is pre-perforated to movement of the new experimental part beside the vertical impinging water jet (Figures 3.1 and 3.2). The water jet position is kept fixed because the water supply conduit cannot be moved. These pre-perforated

holes allow to move the new experimental part (measurement box and highly instrumented block) in 10 different positions.

IV. A restitution system consisting of four conduits of 220 mm of diameter simulates the river downstream. These conduits are connected to the overflow boxes (two conduits for each overflow box) and conduct the water into the main reservoir of the laboratory.

V. Another important element of the installation is the 63 m head pump. This pump is installed in the main reservoir (800 m^3) in the underground floor of the LCH experimental hall, from which the water is pumped into the supply conduit. After restitution through the restitution conduits, the water returns to the main reservoir. A closed water circulation system is therefore obtained. Maximum discharge is 120 l/s.

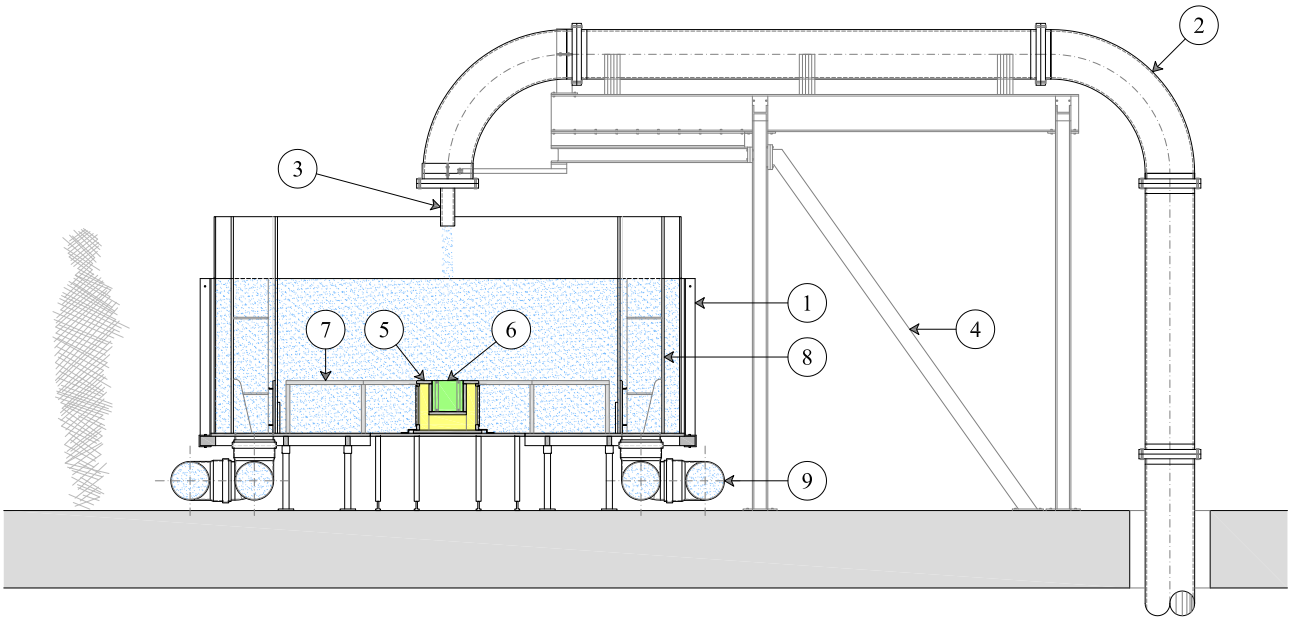

Figure 3.2: Side view of the experimental facility (longitudinal section): (1) plunge pool, (2) water supply conduit, (3) outlet nozzle, (4) supporting steel structure, (5) measurement box, (6) highly instrumented block, (7) new plunge pool bottom, (8) overflow boxes and (9) water restitution system.

Manso (2006) has introduced a honeycomb grid immediately upstream of the last bend of the supply conduit. The grid consists of 10 cm long and 10 cm diameter metallic tubes. This honeycomb grid has the goal to stabilize the flow in the water supply conduit just at the upstream of the outlet (nozzle). The jets produced in the LCH experimental facility show the same behavior as orifices, free-falling high-velocity undeveloped napes and submerged outlets encountered as prototype spillways, in all cases with non-aerated cores at impact into the pool.

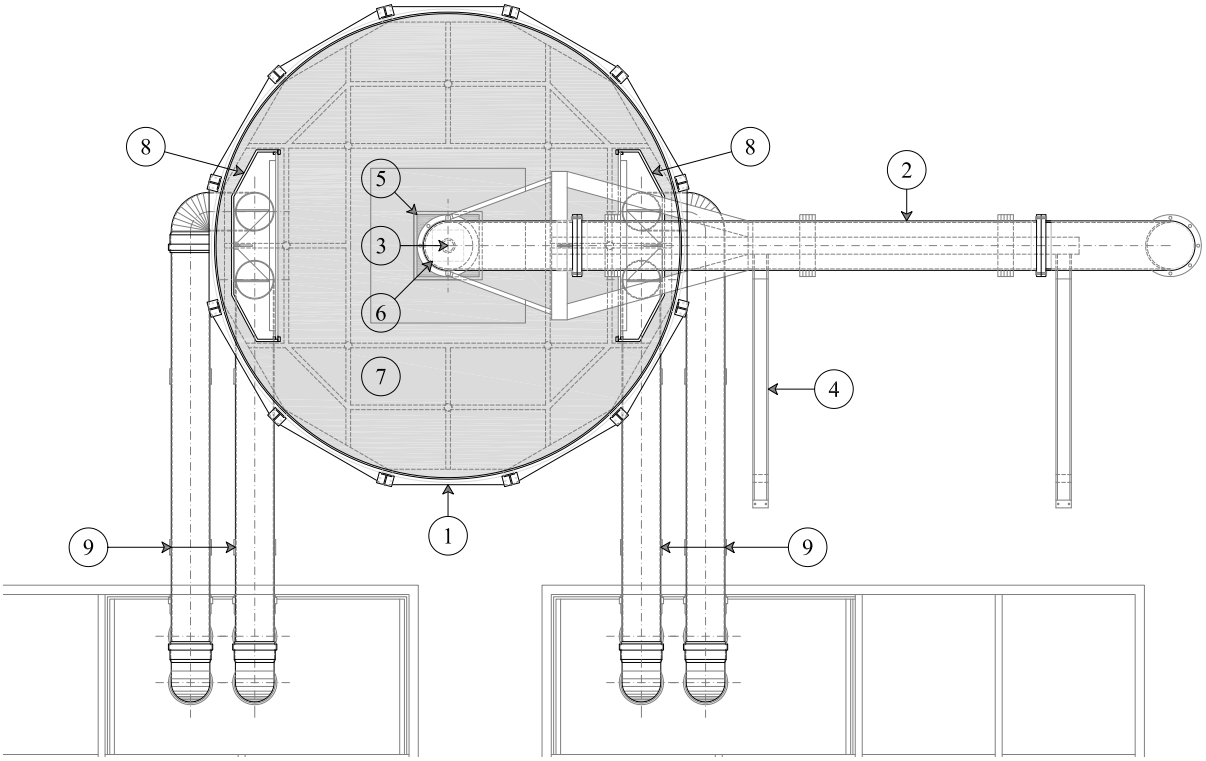

Figure 3.3: Top view of the experimental facility (situation): (1) plunge pool, (2) water supply conduit, (3) outlet nozzle, (4) supporting steel structure, (5) measurement box, (6) highly instrumented block, (7) new plunge pool bottom, (8) overflow boxes and (9) water restitution system.

3.2.2 New experimental set-up: the measurement box and the highly instrumented block

The new experimental set-up is composed by two components: a measurement box and a highly instrumented block (Figures 3.4 to 3.7). The measurement box represents the rock foundation where the highly instrumented block will be inserted. The highly instrumented block represents a single rock block in the rock mass with one degree of freedom (vertical movements).

3.2.2.1 The measurement box

The measurement box is a box build with some steel plates. The dimensions of this box are 402 mm of length, 402 mm of width and 340 mm of height. The thickness of the steel plates is 20 mm. Inside this box, some cavities allow to insert pressure and displacement transducers. All cavities are interconnected (the lateral space between the steel plates is 60 mm and the space under the block is 99 mm). To do some manipulation inside these cavities (modify the transducers position) all external walls have a 250 mm movable lid.

The walls near the block (central cavity) are pre-perforated to allow to change the transducers position (Figure 3.13). The positions were defined in order to cover all measurement opportunities. Thus the pressure inside the fissures between the block and its surroundings as

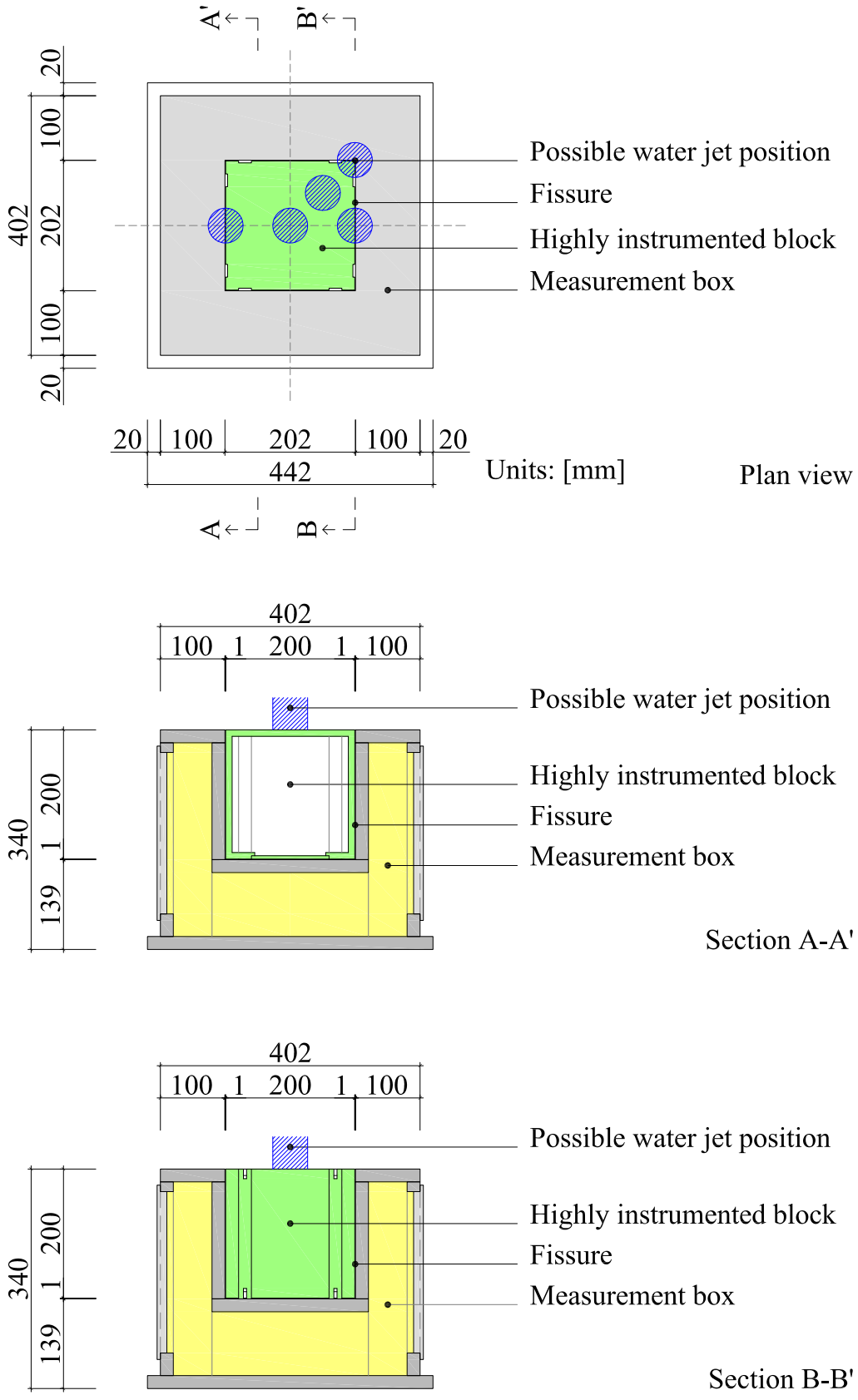

Figure 3.4: Plan view (above) and transversal sections of the new experimental part: measurement box and highly instrumented block.

well as the displacements of the block can be measured.

The box is impermeable to protect the electrical equipment. To allow the transducers cables to be connected at the Data Acquisition System 14 waterproof transducers exits are installed on one vertical wall of the measurement box.

3.2.2.2 The highly instrumented block

In the center of the measurement box, a large cavity allows to insert the highly instrumented block, after called block (Figures 3.4 to 3.7). This cavity has a length of 202 mm, a width of 202 mm and a height of 201 mm. The highly instrumented block has a cubical shape of 200 mm of side and an approximately weight of 22 kg. The width of the steel plates are optimized to have a density similar to the rock (2'400 - 2'500 kg/m^3).

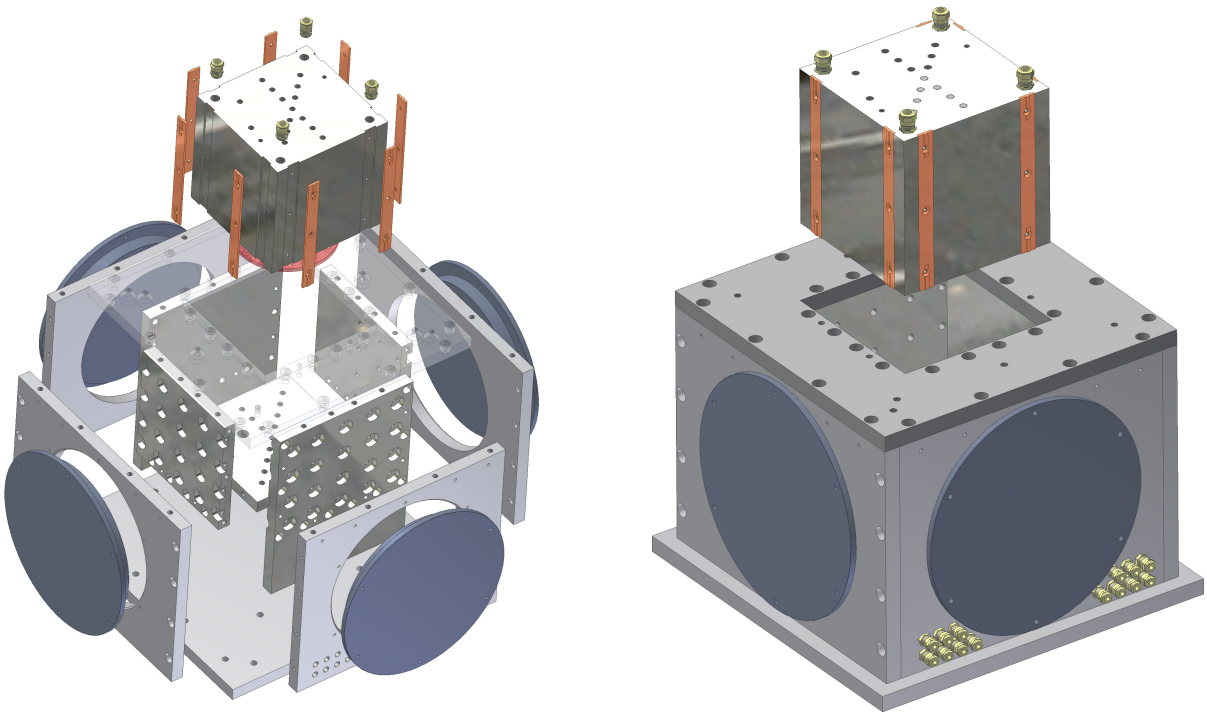

Figure 3.5: Exploded view (left) and axonometric view (right) of the surrounding measurement box of the block.

On the block upper face (at the plunge pool bottom level) some holes are pre-perforated to fix the pressure transducers (Figure 3.13). 93 positions have been pre-perforated for the pressure transducers on the new experimental facility (measurement box and highly instrumented block). The acceleration transducer and the displacement transducers have fixed positions. Between the measurement box and the block, a 3-dimensional fissure of 1 mm width is so created, which extends all around the block. Inside the block, pressure transducers and a vibration transducer (accelerometer) have been inserted in order to measure the pressures at plunge pool bottom under the vertical high-velocities jets and to measure the block vibrations. To do some manipulation inside the block (modify the transducers position) a 150 mm movable lid

is situated on the block lower face. Like in the measurement box four waterproof transducers exits are installed on the block upper face.

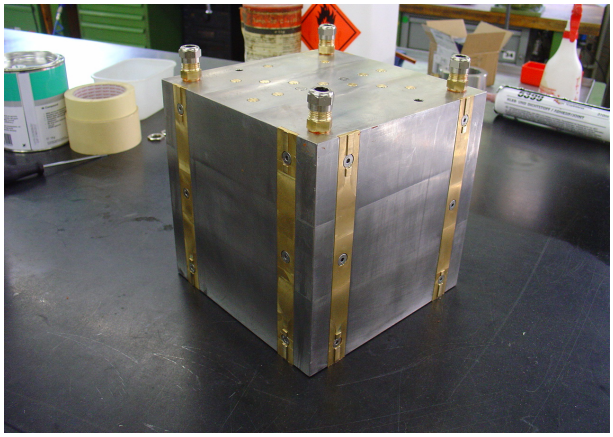
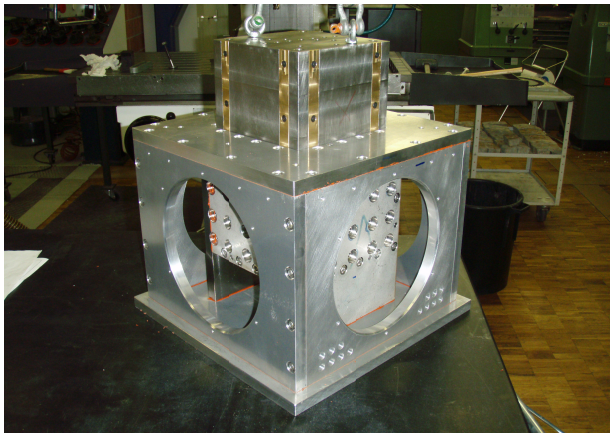

Figure 3.6: The highly instrumented block after construction (left) and being inserted in the measurement box (right).

On the block lateral faces, eight verticals guides have been constructed (two for each lateral face). These guides define the degree of freedom of the block: the vertical axis allowing only the vertical movements (Figure 3.5).

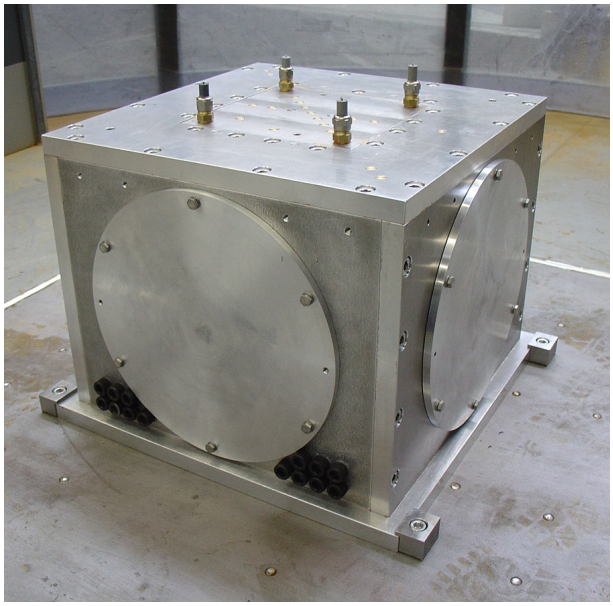
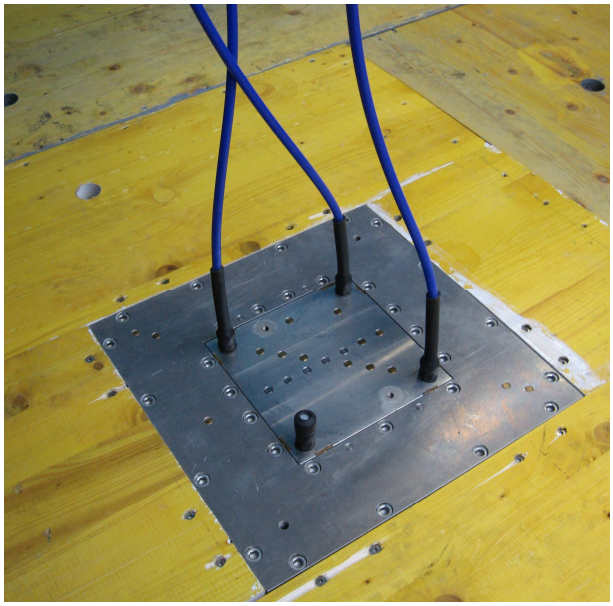

Figure 3.7: The highly instrumented block inserted in the measurement box and fixed in the plunge pool (left) and the new set-up (with the transducers cables) fixed in the plunge pool equipped with the new wooden bottom (right).

The block dimensions were chosen according in-situ rock block size observation, also to allow some manipulations inside the block (change the transducers positions) and at the same time to be representative of a rock block. During the definition of its dimensions the most important characteristic that have to be guaranteed was the block apparent density: it should be similar to the density of a normal rock (i.e. Granite and Gneiss: 2'400 - 2'800 kg/m^3).

Both new parts, the measurement box and the block, have been placed inside the existing 3 m diameter cylindrical basin in steel reinforced PVC, which simulates the plunge pool (Figures 3.1 to 3.3).

In order to have a flat bottom inside the plunge pool, the actual bottom is heightened by 340 mm (level compensation due to the new experimental facility, Figures 3.1 and 3.2). The new bottom is composed of thick wood plates (formed plates) that allow the movement of the new experimental set-up under the vertical impinging jet. This wooden bottom is composed by many plates. When their relative position changes (like a Tetris), a new position for the measurement box is generated in the experimental facility (that changes the jet impact position on the block).

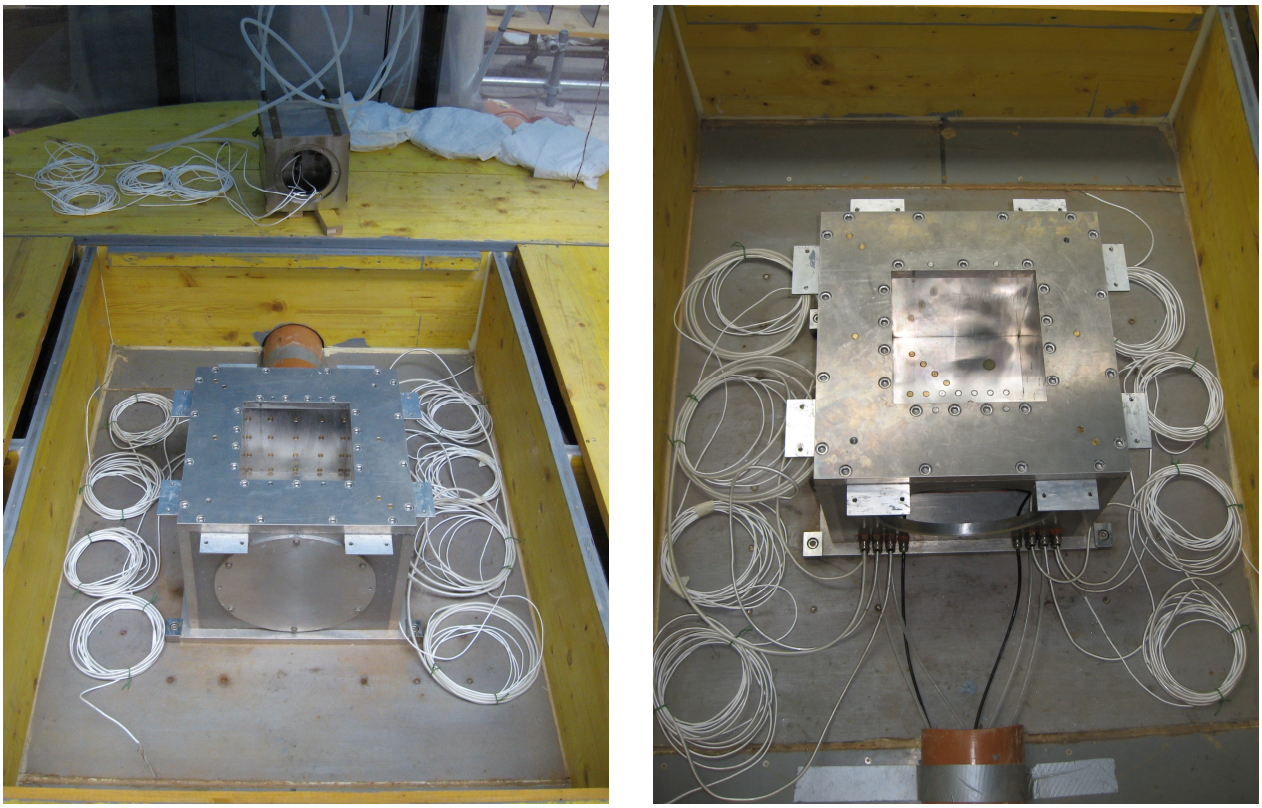

Figure 3.8: The new experimental set-up during the transducers assembly.

3.2.3 Similitude

3.2.3.1 Introduction

The LCH experimental facility was build having into account the impossibility to guarantee the respect of all similitude laws (Bollaert (2002b)) among the free falling jet, the jet aeration, the plunge pool and the rock mass. The water (liquid phase), the air (gas phase) and the rock mass (solid phase) have different predominant similitude laws.

The Froude similitude law ($Fr = U/\sqrt[2]{\rho \cdot D}$ where U is the mean flow velocity, ρ the water density and D the characteristic length) is used to model a free falling water jet. This law focuses on a correct modeling of the ratio of inertial force over gravity force. The diameter

of the jet at impact is highly influenced by the gravitational acceleration, which results in a contraction of the jet and of the jet aeration during its travel in the air before the impact with the bottom.

The air entrainment is a combination of three phenomena: Froude, Reynolds ($Re = U \cdot D/\nu$ where U is the mean flow velocity, ν the water kinematic viscosity and D the characteristic length) and Weber ($We = \rho \cdot U^2 \cdot D/\sigma_w$ where ρ is the water density, U the mean flow velocity, D the characteristic length and σ_w the water surface tension). The aeration characteristics of a free falling water jet are affected by the influences of two opposite forces: the surface tension (that tends to keep the jet together) and is characterized by the Weber number, while the initial turbulence intensity of the jet rather tries to disperse the jet, as described by the Reynolds number.

The rock mass needs similitude laws taking in consideration the fluid-structure interaction effects. These interactions are very difficult to reproduce on a model. The pressurized flow conditions inside the fissures of the rock mass should follow a correct Strouhal similitude ($St = f_{vs} \cdot CL/U$ where f_{vs} is frequency of vortex shedding, CL the characteristic length and U the mean flow velocity), because of their transient and resonating character.

3.2.3.2 Free falling jet and plunge pool scaling

The LCH experimental facility reproduces jet velocity ranging between 2.5 and 30 m/s or 10 to 120 l/s (near-prototype values). These velocities are similar to prototype values and reproduce correctly the aeration of the plunge pool due to jet impact. Nevertheless, the free falling jet travel distance in the air is not long enough to aerate the jet itself. The travel distance in the air ranges from 0.0 to 1.0 m.

The geometry of the jet and the plunge pool are not at prototype scale due to the laboratory limitations (space to build the experimental facility, capacity of the laboratory water circuits: discharge and maximal head, cost ...). To overcome these limitations the ratio Y/D, where Y is the water depth in the plunge pool and D is the nozzle diameter, was used. For ratios that are common in practice and for near-prototype jet velocities, the facility allows to generate frequency spectra of the turbulence intensity of the jet at impact that are very close to reality.

The jet impact impacting on the block upper face only on a small surface is case study poorly academic. In real-life plunge pools the jet impact on the block on the whole upper face and not only on a small part of it.

The generated turbulent excitation and prototype aeration of the water jet are representative for prototype conditions and capable to stimulate a rock fissure to resonance (Bollaert and Schleiss (2001)). These frequency spectra have some limits. The extremely low frequencies that could be present in nature due to large eddies recirculation in real-life plunge pools cannot be simulated (the plunge pool diameter is only 3 m). However, these low frequencies will not excite a fissure to resonance. Therefore, the failure to simulate the extremely low frequency components of the pressures within a prototype plunge pool does not need to be replicated in the facility. The extremely high frequency components of the spectrum do not have to be simulated because they do not influence the transient pressures inside rock fissures.

The model-scaled water depths of the facility (ranging between 0.0 and 0.7 m with 0.1 m steps) are sufficient to produce realistic frequency spectra at the plunge pool bottom and inside the 3-dimensional fissure. By adjusting the water depth, different realistic turbulence levels could be created at the plunge pool bottom and inside the 3-dimensional fissure (this water depths have to be considered as a mean to obtain a correct turbulence modeling).

The experimental facility cylindrical jet outlet (nozzle) generates jets with a low frequency component. The jet turbulence intensities are below 8% for velocities lower than 12 m/s (Manso (2006)). For higher jet velocities the turbulence intensity reaches 3-4% (Manso (2006)). This data confirm the previous observation performed by Bollaert (2002b). Bollaert (2002b) had observed values between 4 and 5% for the longitudinal turbulent intensity and between 1 and 1.3% for the transversal turbulent intensity. According to available literature data (McKeogh and Elsawy (1980) and Ervine and Falvey (1987)) these values correspond to prototype jets that are moderately to roughly turbulent.

It may be concluded that the jet and the plunge pool modeling create realistic plunge pool aeration and turbulence effects and thus can be considered at prototype scale, even with a significant geometric distortion.

3.2.3.3 Rock mass scaling

The rock mass is modeled by the measurement box and the highly instrumented block. The measurement box represent the rock foundation, the block represents a single movable rock block and the 3-dimensional fissure (in between) represents the fissured rock mass (Figures 3.4 to 3.7). The block has only one degree of freedom: the vertical axis. In reality a rock block in the rock mass has more degrees of freedom (displacements and rotations along and across the x-, y- and z-axis) but to simplify the experimental set-up it has been decided to consider just one.

The measurement box did not have particular limitations for its replication of the rock mass. It was important to build the central cavity with small dimensions tolerances (± 0.01 mm). The general dimensions have been optimized to allow the manipulation inside the waterproof space (all around the central cavity).

The block has a cubic shape of 200 mm side, approximately 22 kg weight and an apparent density of 2'600 - 2'700 kg/m^3. The cubic shape has been chosen to have simple block geometry that was representative of a real rock block and "easy" to build.

The size of the block has been chosen according to typical density in prototype rock conditions but also to allow the manipulations inside the block (as an example change the transducers positions) and to have the possibility to install it in the existing experimental facility. To define the block dimensions the most important characteristic to be guaranteed was the apparent density, which had to be similar to a normal rock density (i.e. Granite and Gneiss: 2'400 - 2'800 kg/m^3).

The block is separated from its surroundings by a 3-dimensional fissure with a 1 mm thickness, which is realistic of a natural fissure observed in a fissured rock mass. The 3-dimensional fissure is open and full interconnected. This thickness has been chosen to have the same fissure

width used for the two previous research projects (Bollaert (2002b) and Manso (2006)). The fissure thickness has been adapted to the diameter of the jet at the impact in the plunge pool and to the zone of turbulence generated by the diffusing jet at the plunge pool bottom (Bollaert (2002b)). As a result of the geometric distortion of the jet diameter, this impact zone does not correspond to the prototype conditions. However, as the flow conditions inside the fissures are pressurized, this geometric scaling effect is not of significant importance on the pressure fluctuations inside the fissure.

3.3 Main characteristics of water jet

3.3.1 Jet characteristics of free falling water jet

Table 3.1 summarizes the characteristics of the free falling water jet. These characteristics have been calculated for the 72 mm cylindrical nozzles (the only nozzle used during this research project). The jet turbulence intensity Tu, on the centerline of the jet, has been quantified at 4 to 5 % by Bollaert (2002b). The main jet characteristics are: the discharge Q, the jet velocity at the nozzle V_0, the Froude number Fr, the Reynolds number Re and the Weber number We.

Q $[l/s]$	V_0 [m/s]	Fr [-]	Re [-]	We [-]
10	2.5	2.9	$1.5*10^5$	5'900
20	4.9	5.8	$3.1*10^5$	23'600
30	7.4	8.8	$4.6*10^5$	53'100
40	9.8	11.7	$6.1*10^5$	94'500
50	12.3	14.6	$7.7*10^5$	147'600
60	14.7	17.5	$9.2*10^5$	212'600
70	17.2	20.5	$10.7*10^5$	289'300
80	19.6	23.4	$12.2*10^5$	377'900
90	22.1	26.3	$13.8*10^5$	478'300
100	24.6	29.2	$15.3*10^5$	590'500
110	27.0	32.1	$16.8*10^5$	714'500
120	29.5	35.1	$18.4*10^5$	850'300

Table 3.1: Jet characteristics of the free falling water jet where Q is the discharge, V_0 the jet velocity at the nozzle, Fr the Froude number, Re the Reynolds number and We the Weber number.

3.3.2 Plunge pool characteristics

Table 3.2 summarizes the plunge pool water characteristics for the tested jet velocities. The main plunge pool characteristics are: the water depth in the plunge pool Y, the Y/D geometrical ratio (where D is the nozzle diameter), the length of the jet travel in the air L, the break-up length L_b and the relative degree of jet break-up L/L_b.

Y [m]	Y/D [-]	L [m]	L_b [m]	L/L_b [-]	Jet Type [-]
0.0	0.0	1.0	1.12-1.49	0.65-0.89	Core jet
0.1	1.4	0.9	1.12-1.49	0.58-0.80	Core jet
0.2	2.8	0.8	1.12-1.49	0.52-0.71	Core jet
0.3	4.2	0.7	1.12-1.49	0.45-0.62	Transition jet
0.4	5.6	0.6	1.12-1.49	0.39-0.53	Transition jet
0.5	6.9	0.5	1.12-1.49	0.32-0.44	Developed jet
0.6	8.3	0.4	1.12-1.49	0.26-0.36	Developed jet
0.7	9.7	0.3	1.12-1.49	0.21-0.27	Developed jet

Table 3.2: Plunge pool characteristics where Y is the water depth in the plunge pool, the Y/D geometrical ratio (where D is the nozzle diameter), L the length of the jet travel in the air, L_b the break-up length, L/L_b the relative degree of jet break-up and the jet type (as a function of the Y/D ratio).

3.4 Data acquisition system: electrical equipment

The data acquisition system is composed by the following main components: the transducers with the respective electrical alimentation (pressure, displacement and acceleration), the Data AcQuisition device (DAQ), the computer and the software to drive the DAQ and record the measured data.

3.4.1 Data Acquisition Device

The data acquisition equipment consists of a multifunction DAQ (Data AcQuisition) device. The DAQ device is a National Instruments (NI) card type USB-6259 series M (Figure 3.9). The National Instruments USB-6259 is a USB high-speed M Series multifunction data acquisition module optimized for superior accuracy at fast sampling rates.

This DAQ device is characterized by:

- 32 analog inputs SE (Single Ended) or 16 analog inputs DI (Differential); with a resolution of 16-bit; 1.25 MSamples/second (1.25 x 10^6 Samples/second) = 1.25 MS/s single-channel (1 MS/s aggregate) Analog input: Maximum voltage range from -10 V to 10 V; Minimum voltage range from -50 mV to 50 mV;

- 4 analog outputs (16-bit, 2.8 MS/s); 48 digital I/O (32 clocked) Analog output: Maximum voltage range from -10 V to 10 V; Minimum voltage range from -5 V to 5 V;
- Two 32-bit counters (maximum source frequency 80 MHz).

The NI device is driven by a software developed in-house, based on the LabVIEW© technologies.

Figure 3.9: Data AcQuisition device NI USB-6259 series M [NI].

3.4.2 Pressure transducer

A series of KULITE HKM-350M-17-BAR-A micro pressure transducers are used for the pressure measurements (Figure 3.10). These transducers utilize a flush metal diaphragm as a force collector, with an absolute pressure range between 0 and 17 Bar and a precision of ± 0.1% of the full scale output. A solid state piezoresistive sensing element is located immediately behind this metal diaphragm which is protected by a metal screen. Force transfer is accomplished via an intervening film of non-compressible silicone oil. This sensing sub assembly is welded to a stainless steel body. They have been developed in order to measure highly dynamic pressure phenomena, such as shock waves. Hence, they exhibit a very high resonance frequency (750 kHz). Their measuring membrane has an 8.1 mm diameter. The sensors can be perfectly flush mounted by screwing them into the steel structure. The cable is 7 m long. For the test 12 pressure transducers have been used simultaneously.

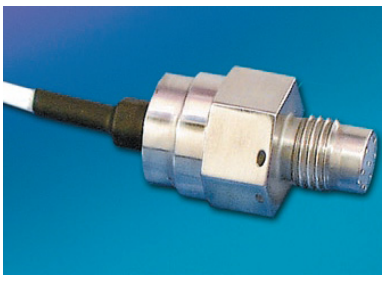

Figure 3.10: Pressure transducer Kulite HKM-350M-17-BAR-A [Kulite].

3.4.3 Displacement transducer

A couple of BAUMER AG IWRM 18I9704/S14 displacement transducers are used for displacement measurements (Figure 3.11). These transducers work with the magnetic field variation (inductive transducer), with an absolute measurement range between 0 and 8 mm and a precision less than 0.005 mm (static) or less than 0.01 mm (dynamic). They are supposed to allow to measure any kind of displacement phenomena.

The cable of type ES33AP10B, with a length of 10 m, is not subjected to the EMI (Electro Magnetic Interference) due to its internal structure. The transducer is supplied with a 24 DVC - 300 mA source. For the test two displacement transducers have been used simultaneously.

Figure 3.11: Displacement transducer Baumer IWRM 18I9704/S14 [Baumer AG].

3.4.4 Acceleration transducer

A PCB PIEZOTRONICS^{INC} 353B14 accelerometer is used for vibration measurements (Figure 3.12). This transducer is high frequency quartz shear accelerometers with a measurement range of $\pm$ 1000 g (acceleration of gravity). The sensitivity of the transducers is 5 mV/g and the frequency range is situated between 1 and 10 kHz. Moreover, they exhibit a very high resonance frequency (>70 kHz).

The cable type 003C20, with a length of 20 ft (6.1 m), is not subjected to the EMI (Electro Magnetic Interference) due to its internal structure. For the test one acceleration transducer has been used.

Figure 3.12: Acceleration transducer PCB PIEZOTRONICS^{INC} 353B14 [PCB].

3.4.5 Personal computer and data acquisition software

The personal computer was a Pentium IV with a 2.53 GHz CPU processor working under Windows XP Pack 3.

The data acquisition was performed with a software developed in the LabVIEW© 8.5 environment. This software drives the data acquisition device (DAQ) and records the data provided by 15 transducers (12 pressure transducers, two displacement transducers and one accelerometer). This software allows to observe on real time the transducers response.

To verify the maximum data flow between the DAQ and the computer some tests have been carried out with different acquisition rates: 1, 5, 10, 15 and 20 kHz. The maximum data flow limit is given by the Universal Serial Bus (USB) capability. In our case a USB 2.0 interface used with a maximum rate of 480 Mbit/s or 57 MB/s.

The computer RAM is another important parameter in the data acquisitions chain. Before the data (coming by the DAQ) are recorded in the output file (file type ASCII: American Standard Code for Information Interchange) they have to be temporarily stored in the computer RAM. If the RAM storage capacity is not large enough, the new data coming by the DAQ will overwrite the stored data, which leads to a loss of data.

The computer record capability was analyzed simultaneously with 15 transducers. The data have been recorded three times (three runs) one after the other. This record technique has been used for the data acquisition during the entire research project. For the lower acquisitions rates (1, 5 and 10 kHz) no limitations have to be fixed for the maximum data sampling, whereas for the higher acquisition rates (15 and 20 kHz) the maximum data sampling has to be limited.

An acquisition rate of 1 kHz has been applied for the most part of the experimental campaign. The tests was carried out with 15 transducers and a sampling of 2^{16} samples/transducer or 65'536 samples/transducer (total: 983'040 samples/run) for each output file (file size: 8-9 MB). The record time for each run was approximately 65.5 s. Some control runs have been performed at different acquisition rates (5 to 20 kHz) in order to check the presences of any transient character of the measured pressure peaks. For these tests the data sampling was the same but the record time was less.

3.5 Transducers positions

To perform the measurement (pressure, displacement and acceleration) the new experimental set-up (measurement box and block) has been pre-perforated to allow to change the transducers position. The block upper face (situated at the plunge pool bottom level) and the walls of the central cavity surrounding the block (vertical fissure) are pre-perforated (Figure 3.13). 93 positions have been chosen for the pressure transducers to cover all measurement opportunities around the block (at the plunge pool bottom and inside the 3-dimensional fissure). These measurement points allow to reconstruct the pressure field surrounding the block. These pre-perforated holes are distributed as follows: 17 on the block upper face, 7 on the measurement box at the plunge pool bottom, 17 on the central cavity bottom of the measurement box and

52 on the walls of the central cavity of the measurement box. The pre-perforated holes on the block upper face and the central cavity bottom have the same locations (on the same vertical axis).

The pre-perforated holes positions have been defined to cover all jet impact possibility at the plunge pool bottom. The jet impact positions are the following: on the block center, on the block left and right hand side, on the block corner and between the center and the block corner (Figure 3.4).

The pre-perforated holes on the block upper faces and at the central cavity bottom are distributed along the transversal and the radial direction. On the transversal direction the transducers positions are the following: the first on the block center, the second at 25 mm, the third at 50 mm and the fourth at 75 mm. For the radial direction the positions are the same with a supplementary position at 100 mm. Two other positions have been chosen on the block surface. The pre-perforated holes on the measurement box have been chosen along the same axis (transversal and radial) than on the block upper face: at 150 and 175 mm from the block center. The pre-perforated holes have a "position code" to find their relative location on the new experimental facility. The "position code" is defined by one letter (U: up and D: down), two numbers (both correspond to one wall of the central cavity), one letter (P: position) and two numbers (transducer location). As an example, the "position code" U34P02 states for: transducer situated at the plunge pool bottom level, in the radial direction between the walls n^o 3 and n^o 4 and it is the third transducer from the block center.

The pre-perforated holes on the measurement box walls allow to measure the pressure field inside the 3-dimensional fissure for all jet impacts. Three walls have been pre-perforated with four rows and three or five columns: each row is separated by 50.25 mm and each column is separated by 50.5 mm.

These pre-perforated holes have as well a "position code". This code is defined with one letter (W: wall), one number (the wall number), one letter (L: row), one number (the row number), one letter (C: column) and one number (the column number). As an example, the "position code" W2L3C1 states for: transducer situated on the second wall, on the third row and on the first column.

The displacement transducers have two fixed position in the measurement box (underneath the block). The acceleration transducer has a fixed position inside the block (on the block lid).

The pressure and displacement transducers are flush-mounted.

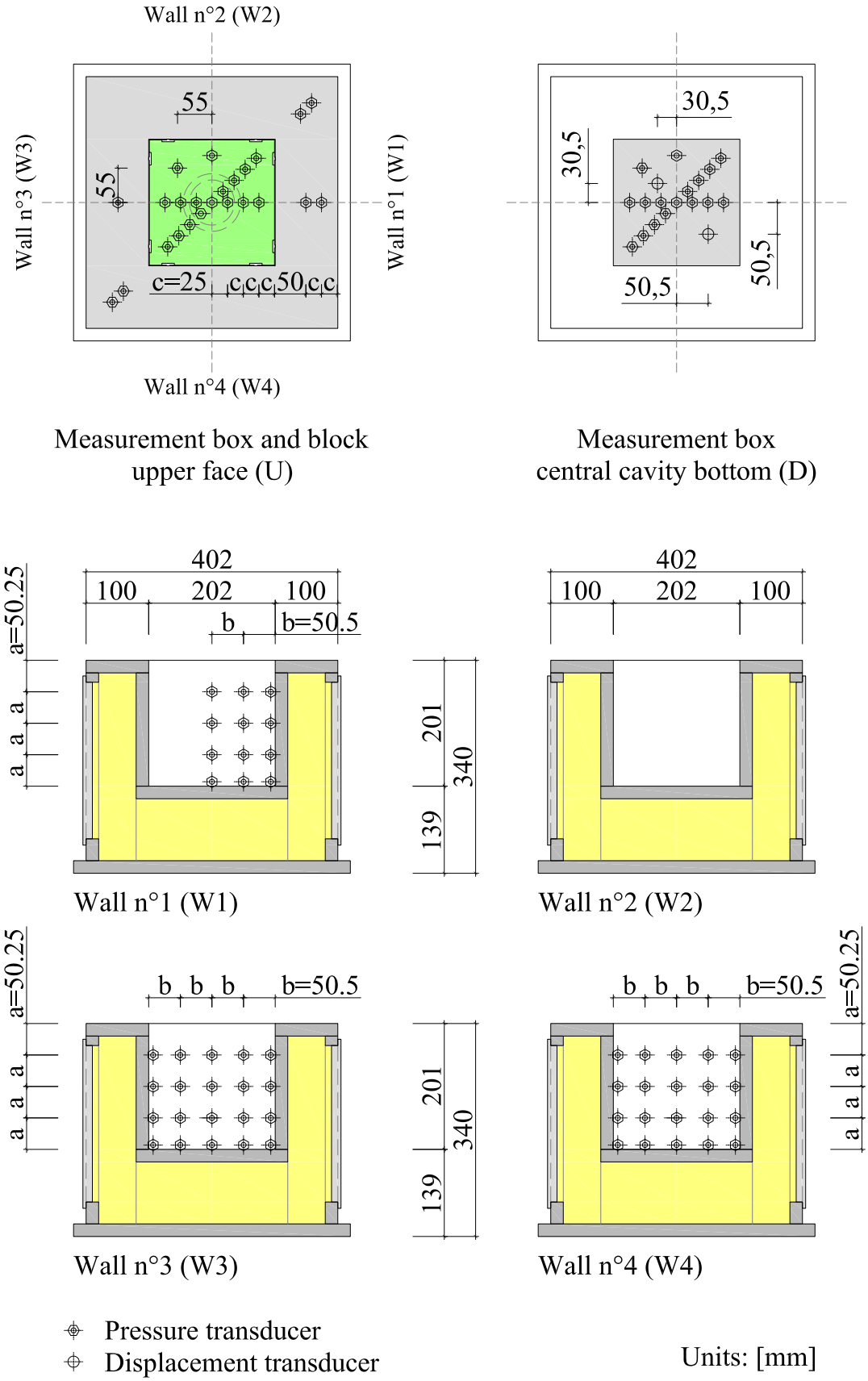

Figure 3.13: Pre-perforated holes positions on the new experimental set-up (measurement box and highly instrumented block). View of the transducers positions at the plunge pool level and inside the central cavity of the measurement box (93 positions for pressure transducer, two positions for displacement transducer. The accelerometer is fixed inside the block (not reproduce on this figure).

3.6 Transducers calibration

3.6.1 Pressure transducer

Pressure transducers (Chapter 3.4.2) have been calibrated at the Laboratory for Hydraulic Machines (LMH) of the EPFL. To perform the transducers calibration a reference transducer has been used: the Huber transducer (Figure 3.14 on the left). The Huber transducer is a high precision pressure transducer (± 0.001 Bar) working with air or liquids.

The transducers calibration has been performed using the 16 Bar LMH compressed air network due to the transducers pressure range (between 0 and 17 Bar). Following the factory instructions the transducers were alimented with a 10 V stabilized electrical alimentation.

Figure 3.14 on the right shows the electrical equipment. On this picture is possible to observe from the left to the right: the DAQ device, the transducers electrical alimentation, the transducers cables and the steel support of the transducers used only for the calibration. The transducers support has been connected to the Huber transducer and to the LMH compressed air network. Between the compressed air network and the transducers support a pressure regulator valve has been installed (not shown on the picture). This pressure regulator valve allows to change the air pressure acting on the transducers in a range between 0 and 16 Bar. The transducers were connected to the DAQ and it was connected to the computer. The software installed in the computer drive the DAQ and record the data for the different calibration pressures (defined using the Huber transducer).

To calibrate the 12 transducers the following procedure has been used:

- measure the atmospheric pressure at the LMH (reference pressure);
- fix the initial relative pressure onto the Hubert transducer (the initial relative pressure correspond to the atmospheric pressure);
- chose a calibration pressure with the air pressure regulator valve (as an example 1 Bar and then increase the pressure with 1 Bar steps);
- measure and record the calibration pressure with the transducers (for each calibration pressure five runs have been performed with a 1 kHz acquisition rate and a record time of 5 seconds);
- repeat the last two points for the calibration range (between 0 and 16 Bar).

The conversion from Volt to Bar was made using a linear equation ($y = m \cdot x + b$ where m is the slope and b the offset). The calibration data allows to plot a calibration curve for each pressure transducer using the mean pressure values computed for each calibration step. These calibration curves showed a perfect overlapping with the factory calibration curves.

3.6.2 Displacement transducer

Displacements transducers (Chapter 3.4.3), called D1D and D2D, have been calibrated at the Laboratory of Hydraulic Construction (LCH) of the EPFL.

Figure 3.14: The Huber transducer (left). The transducer calibration electrical equipment (right) from the left to the right: the DAQ device, the transducers electrical alimentation, the transducers cables and the pressure transducers steel support with the transducers.

To perform this calibration the new experimental set-up has been used (Figure 3.6). The displacement transducers have been fixed in the measurement box (Figure 3.15) and at the same time the block was introduced in the central cavity of the measurement box.

As explained before, these transducers work with the variation of the magnetic field (inductive transducer). The new experimental set-up allows to work with the real modifications of the magnetic field generated by the block displacements.

The calibration procedure was the following:

- introduce a calibrated steel plate (with precise dimensions) underneath the block in the central cavity (Figure 3.15);
- measure and record the distance between the block lower face and the transducers (for each calibrated steel plate three runs have been performed with a 1 kHz acquisition rate and a record time of 5 seconds);
- repeats the two points for the whole measurement range of the transducer with steps of 1 mm.

The conversion from Volt to mm is made using an exponential equation ($y = a \cdot e^{b \cdot x}$ where a and b are two constants). For each displacement transducer a calibration curve has been plotted using the mean pressure values computed for each calibration step. For these transducers a factory calibration curve did not exist, because they are normally used for counting metallic components along a construction chain.

3.6.3 Acceleration transducer

For the acceleration transducer (Chapter 3.4.4) the factory calibration has been used.

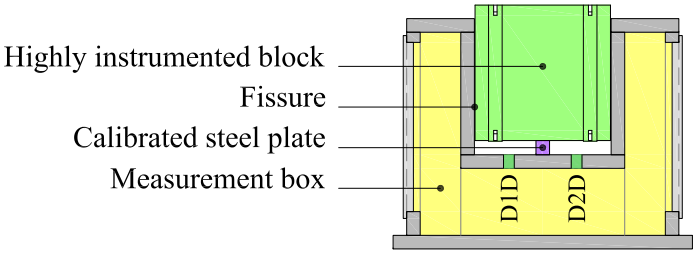

Figure 3.15: Calibration technique used to calibrate the displacement transducers.

3.7 Passive jet aeration

To investigate the air influence in the block reponse, a passive jet aeration system has been developed for the LCH experimental facility ("passive" air entrainment). This passive jet aeration system has been used only for one test configuration (Chapter 4.3.1): jet impact on the block corner with natural and passive jet aeration (configuration ACN, Chapter 4.3).

3.7.1 Design of passive jet aeration system

The existing nozzle was built with a cylindrical PVC-tube with an external diameter of 92 mm and an internal diameter of 72 mm. This tube has a length of 300 mm outside the water supply and 150 mm inside. The entrance of the cylindrical tube has been machined to reduce the flow noise (Figure 3.16 on the left).

The air entrainment in the water jet has been performed with a passive system. A new nozzle has been designed and constructed. The new nozzle, built in PVC, has the same geometry of the existing nozzle but on the external part (outside the water supply) some holes have been perforated. At 50 mm from the water supply lid, six holes of 10 mm diameter have been perforated (Figure 3.16 on the center).

A first test series has been performed with the new nozzle to evaluate the air entrainment in the water jet. The data analysis (pressure coefficients, pressure statistics - maximum, mean, minimum, standard deviation ... - and power spectral density) show that the passive air entrainment did not affect the results (the results are very close to the results obtained for the actual nozzle without the passive air entrainment).

With the aim to improve this jet aeration, a new geometry for the nozzle was proposed: at the previous nozzle, six flexible pipes have been inserted in the perforated holes. These pipes reduce the air flow energy losses at the entrance of the holes.

A second test series has been performed with this enhanced nozzle geometry. The data analysis, the same analysis performed for the previous configuration, showed some difference in the results (notably the lower frequency part of the spectrum).

Finally, the six flexible pipes have been replaced with six aluminum pipes of 10 mm internal diameter and 50 mm length (Figure 3.17). These pipes generate a small depression at the air entrainment point along the inner side of the nozzle (Figure 3.17 on the right). To generate

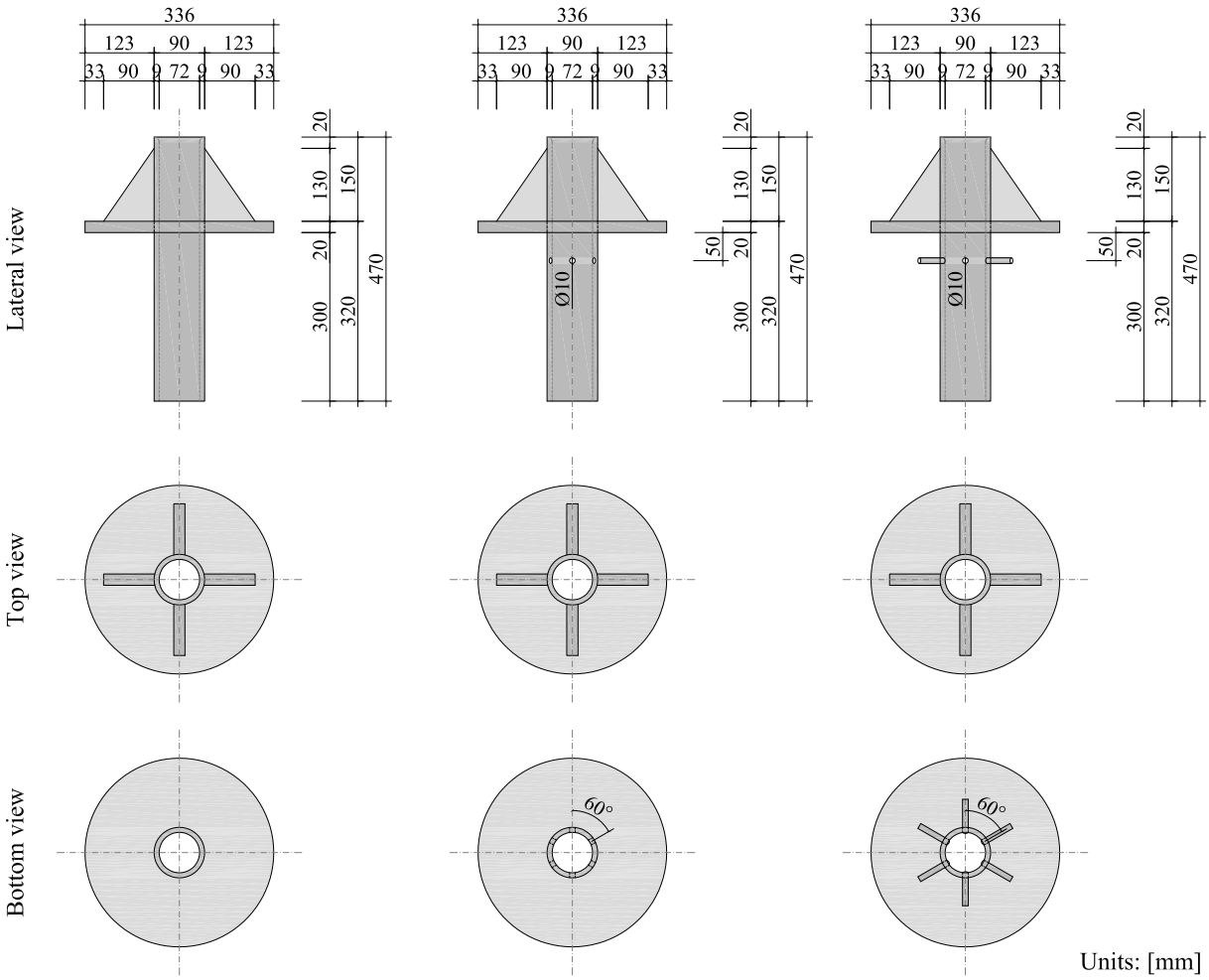

Figure 3.16: Nozzle in its initial configuration (left). Nozzle with the six perforated holes (center). Nozzle with the aluminum pipes (right, see also Figure 3.18).

this depression, the aluminum pipes extremity have been cut with an angle of ∼79° (the higher part of the pipes is 2 mm longer).

3.7.2 Passive air entrainment measurements

The air flow has been measured to quantify the air entrainment in the water jet. The air flow was established by the water jet due to the depression generated along the internal surface of the nozzle (Figure 3.17 on the right).

A 130 mm diameter flexible tube has been sealed onto one pipe. This flexible tube allow to measure the air flow entering in the water jet (Figure 3.19 on the left).

At this entrance, the air flow velocity has been measured with a hot-wire anemometer type Testoterm Testo 491. This device has a precision of ± 0.01 m/s (Figure 3.19 on the right).

When the water discharge was changed, the air flow velocity has been measured. The jet velocity has been varied between 2.5 and 22.1 m/s. For each jet velocity, the air flow velocity has been measured in the middle of the flexible tube and at 100 mm from the tube entrance.

To check the air flow entrained by the water jet another pipe has been used to measure the

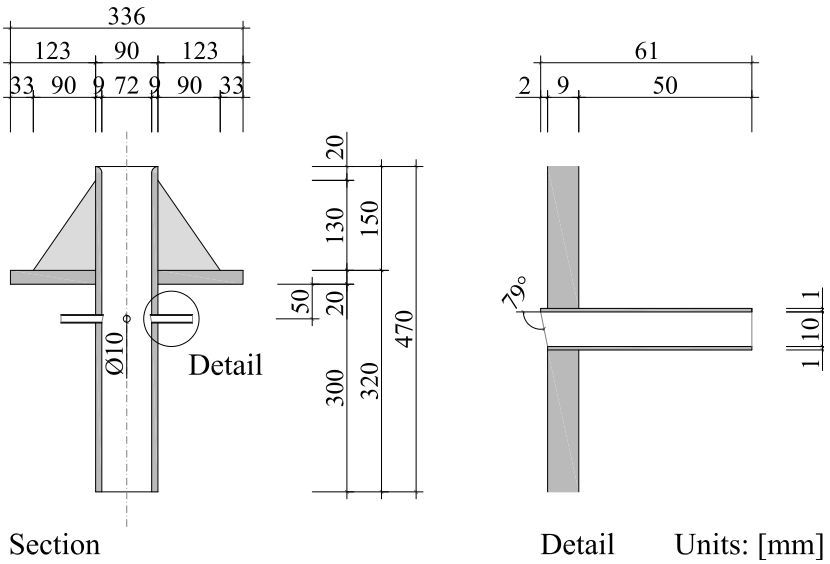

Figure 3.17: Transversal section of the new nozzle (left) and detail of the interface aluminum pipe-nozzle used to generate a small depression at the air entrainment point along the inner side of the nozzle (right).

air flow velocity. This control allows to confirm the following assumptions: the nozzle aeration is symmetrical, the air entering in the water jet from each aluminum pipes is the same. The air flow has been measured for the opposite pipes. The air flow measurement showed similar values. Table 3.3 summarizes the air flow velocity and the jet aeration values (flow velocity V_{air}, air discharge Q_{air}, air-water ratio β and air concentration in the jet C, Chapter 5.6).

Jet discharge Q $[l/s]$	Jet velocity V_0 [m/s]	Air velocity V_{air} [m/s]	Air discharge Q_{air} [l/s]	Air-Water ratio β [-]	Air concentration C [-]
10	2.5	0.04-0.05	3.6	0.36	0.26
20	4.9	0.07-0.08	6.0	0.30	0.23
30	7.4	0.08-0.09	6.8	0.23	0.18
40	9.8	0.10-0.11	8.4	0.21	0.17
50	12.3	0.11-0.12	9.2	0.18	0.15
60	14.7	0.13-0.15	11.2	0.19	0.16
70	17.2	0.22-0.24	18.3	0.26	0.21
80	19.7	0.24-0.25	19.5	0.24	0.20
90	22.1	0.30-0.31	24.3	0.27	0.21

Table 3.3: Air flow data through passive air entrainment pipes.

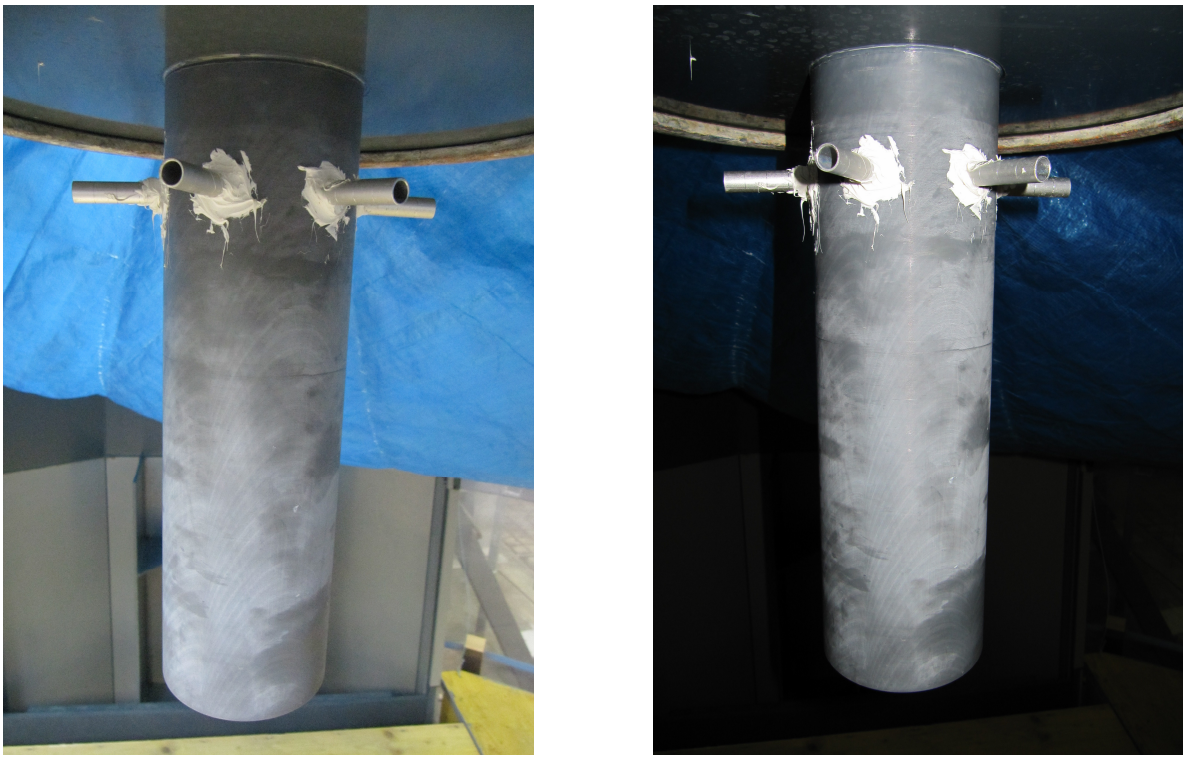

Figure 3.18: Nozzle equipped with passive aeration pipes.

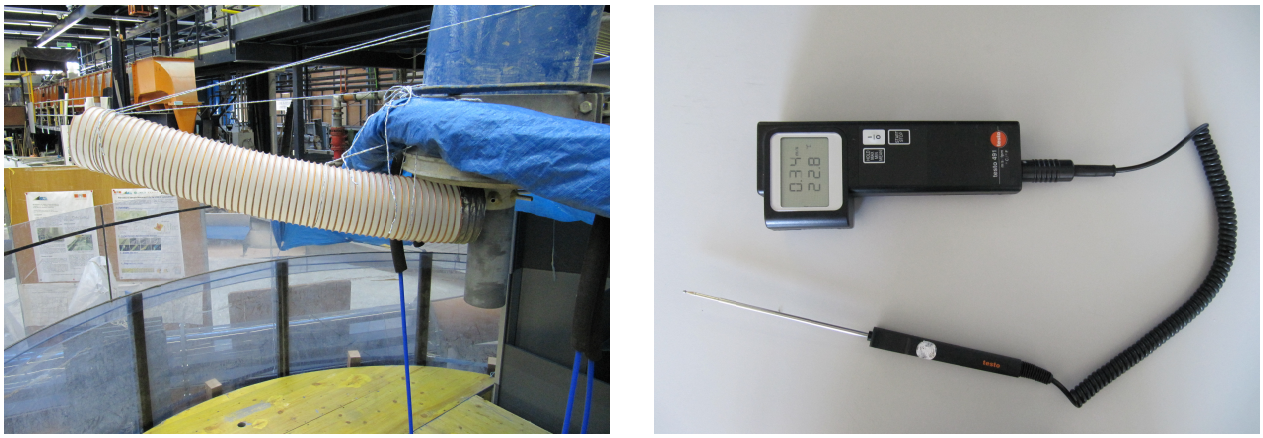

Figure 3.19: Air discharge measurement facility (left) and hot-wire anemometer (right).

3.7.3 Natural jet aeration

The water jet travelling through the atmosphere generates air absorption upon the impact on the plunge pool surface, and then this air is injected in the plunge pool water. The air entrained by the water jet (with the passive aeration system) has to be added to this natural plunge pool aeration. The natural air aeration was the same for all configurations since the test conditions were kept constant.

Chapter 4

Test program

4.1 Introduction

The influence of the jet impact position on the responses of the highly instrumented block will be studied by focusing on the pressure field generated around the block (at the plunge pool bottom and inside the 3-dimensional fissure) and its influence on the block behavior (displacements and accelerations). The aim is to approach real-life conditions for a plunge pool and a fissured rock mass.

To measure the dynamic pressures generated by a high-velocity jet, 12 pressure transducers are flush-mounted at the plunge pool bottom (on the block upper face) and inside a 3-dimensional fissure as illustrate by Figure 4.8. To measure the displacements and the accelerations corresponding to these pressure fields, two displacement transducers are flush-mounted under the block (in the measurement box) and one accelerometer is mounted inside the block (Figure 4.8).

4.2 Involved parameters

The theoretical analyses of the physical process involved in the rock scour phenomena allow to define the following five main parameters for the physical model:

- the jet impact position on the block upper face;
- the degree of freedom of the block (how the block can move in the 3-dimensional space);
- the 3-dimensional fissure structure (how the water can flow inside the fissure);
- the water depth in the plunge pool (core, transition or developed jet generate different solicitations in the plunge pool);
- the jet velocities (jet kinetic energy).

Between these five parameters three of them have been chosen to become configuration parameters and two to become test parameters. In the following sections this five parameters are described (Chapters 4.2.1 and 4.2.2).

4.2.1 Configuration parameters

The three configurations parameters are: the jet impact position on the block upper face, the degree of freedom of the block and the 3-dimensional fissure structure.

4.2.1.1 Jet impact positions on the highly instrumented block

Different jet impact positions on the highly instrumented block have been investigated to study its influence on the pressure field (surrounding the block) and on the block behavior (displacements and accelerations). Five jet impact positions have been tested (Figure 4.1): on the block center (configurations CE and CR), on the block right hand side (configurations SI and SR), on the block left hand side (configuration SL), on the block corner (configurations CO and CN) and an intermediate position between the center and the corner of the block (configuration RR). The configuration name is explained in Chapter 4.3.

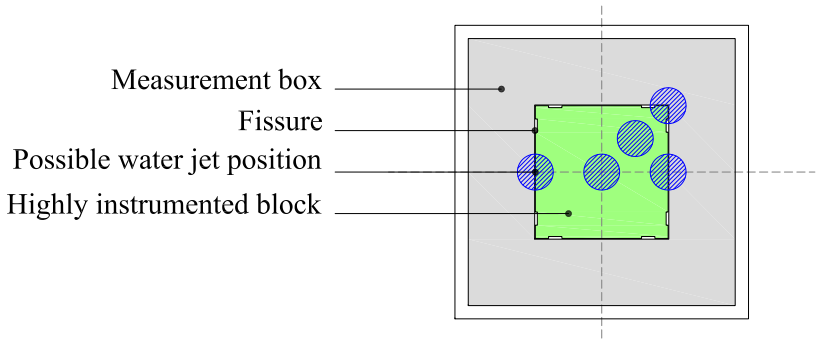

Figure 4.1: Positions of jet impact on the highly instrumented block.

4.2.1.2 Degree of freedom of the highly instrumented block

The fissured rock mass is modeled by the measurement box and the highly instrumented block. The measurement box represents the fissured rock foundation. The block corresponds to one single rock block free to move in the rock mass along his vertical axis (z-axis). To analyze the influence of the degree of freedom of the block on the relationship between pressure fields and block displacements, a system to limit the block vertical movements has been developed. The vertical displacements change the fissure thickness underneath the block (the fissure thickness increases when the block moves up). The lateral fissure did not change its thickness because it is defined by the lateral guides fixed on the block lateral faces (Chapter 4.2.1.3). This change of the fissure thickness may modify the pressure field underneath the block: when the block moves up (the fissure thickness increases) the pressure underneath the block decreases. Vice versa appears the opposite phenomena: when the block moves down (the fissure thickness decreases) the pressure underneath the block increases (Chapter 5.7.3.1).

Figures 4.2 and 4.4 on the left, show the system developed to limit the block vertical displacements. Two steel plates of 10 cm width and 1 cm thick have been constructed. These steel plates have a particular shape to reduce their influence on the jet diffusion near the plunge pool bottom and inside the 3-dimensional fissure. Each steel plate has been fixed on the measurement box with four screws to guarantee the maximum rigidity at the system. To fix the block inside the central cavity and to maintain it in contact with the cavity bottom a screw pro each steel plate has been used. This screw allows to compensate the small construction tolerances between the measurement box and the steel plates.

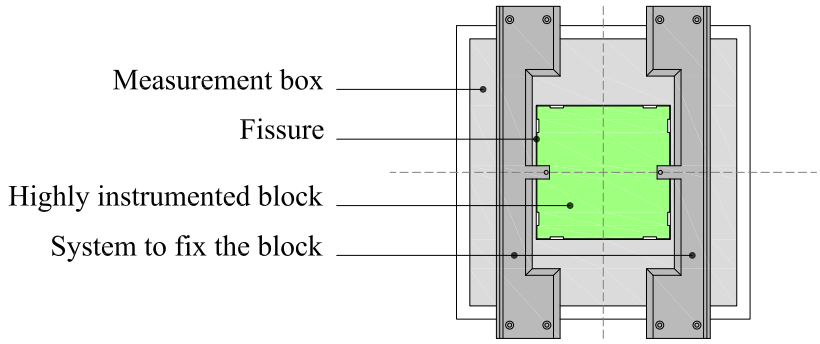

Figure 4.2: System used to fix the block in the central cavity of the measurement box.

4.2.1.3 Lateral guides of the highly instrumented block

To guide the block in its vertical movements a couple of bronze guides have been installed on the block lateral faces (two guides for each face, Figures 3.5 and 4.3). These guides influence the block movements and the water flow inside the 3-dimensional fissure. Moreover, they guaranty the kept of the fissure thickens between the block and the walls of the central cavity. To evaluate their influence, two different types of lateral guides have been tested:

- lateral guide with two contact points (Figure 4.3 on the left);
- lateral guide with eight contact points (Figure 4.3 on the right).

The contact points influence the vertical movements of the block (friction force acting on the block $F_{friction}$): they generate the only contact between the block and the measurement box.

The two guide types have the same main geometrical characteristics: 20 mm width, 201 mm height and 3 mm tick. These dimensions are imposed by the block geometry (two groves along each lateral face of the block) where these guides are flush mounted. To generate the fissure underneath the block, the lower extremity of the guide is 1 mm longer than the block lateral side (200 mm). The block is supported by these parts of the lateral guides (the guides are in contact with the central cavity bottom and not the block lower face). The contact points thickness is 1 mm and 5 mm width for both types.

The difference between the two guide types is situated in the number of contact points (geometry of the contact surface): two or eight.

The first type has two contact points at both extremities: 30 mm length at the upper side and 31 mm length at the lower side (Figures 4.3 on the left and 4.4 on the right). Between this two contact points any other contact exists with the walls of the central cavity.

The second type has the same geometry of the previous guide but between these two contact points, situated at the extremities, six others have been foreseen (Figure 4.3 on the right). These intermediate contact points are disposed in alternation with a contact length of 10 mm.

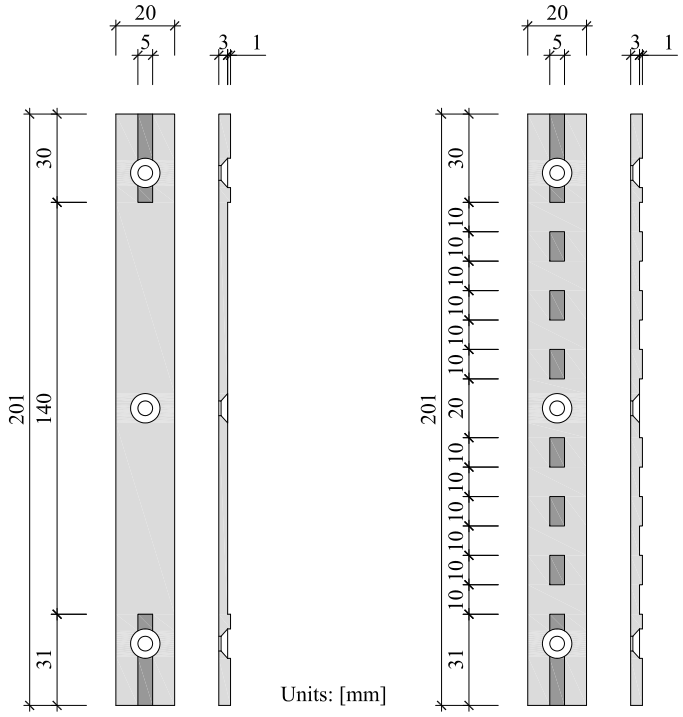

Figure 4.3: Lateral guide with two contact points (left) and lateral guide with eight contact points (right).

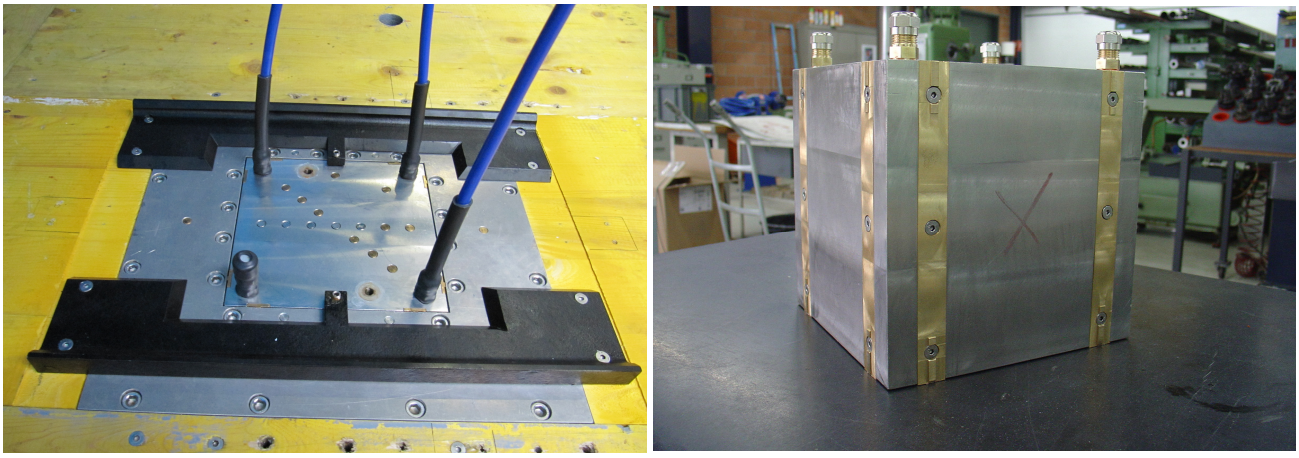

Figure 4.4: System used to fix the block inside the central cavity of the measurement box (left) and lateral guide with two contact points fixed on the block (right).

4.2.2 Test parameters

4.2.2.1 Water depth in the plunge pool

The water depth in the plunge pool is an important parameter to modify the solicitations generated inside the plunge pool by the impinging water jet. The Y/D ratio (where Y is the water depth in the plunge pool and D is the nozzle diameter) has been used to distinguish the different water jets that solicit the plunge pool. Three different jets behavior can be distinguished at the impact with the plunge pool:

- core jet impact (Y/D < 4);
- transition jet impact (4 < Y/D < 6);
- developed jet impact (Y/D > 6).

Figure 4.5 shows the different behavior existing between a core and a developed jet impact on the plunge pool bottom.

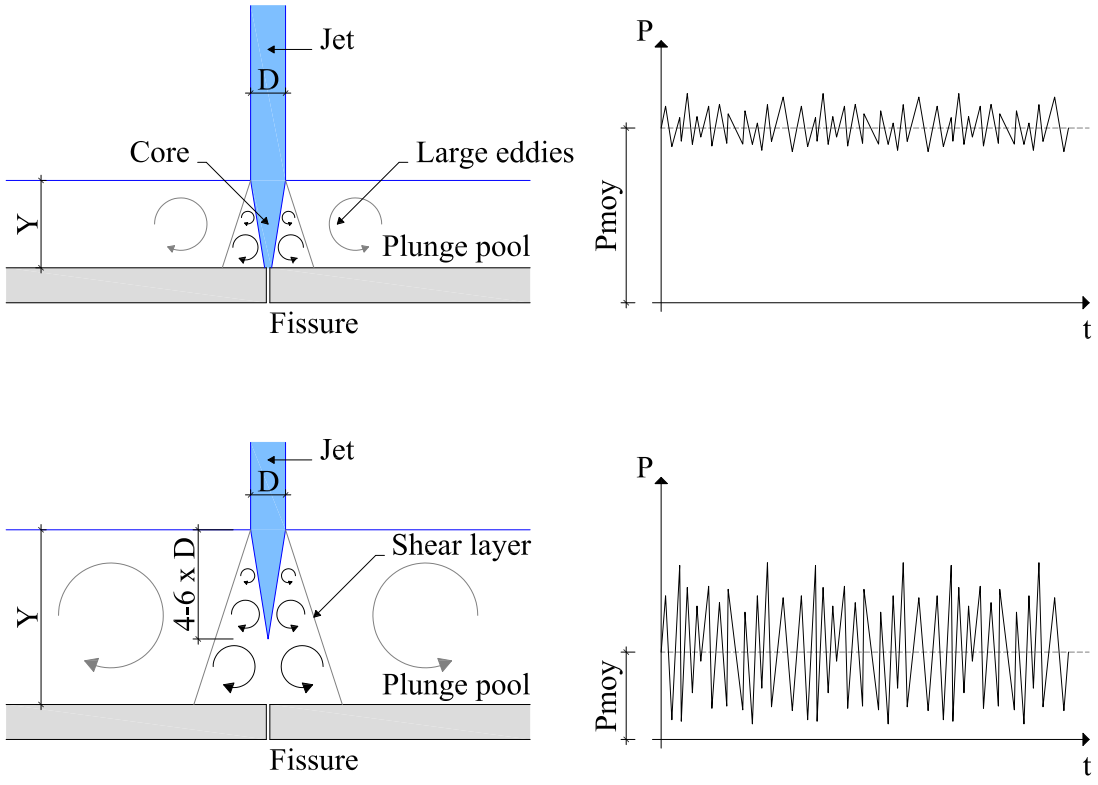

Figure 4.5: Solicitations generated by a core jet impact (Y/D < 4) (top) and generated by a developed jet impact (Y/D > 6) (bottom).

Core jets generate an average pressure higher than a developed jet but with small pressure fluctuations around the average pressure value. Developed jet generates an average pressure lower than a core jet but with larger pressure fluctuations. The instantaneous pressure peaks generated by a developed jet (the sum of the pressure average and the pressure fluctuations)

could be larger than the maximum pressure observed for a core jet, due to the pressure fluctuations generated by large eddies in the plunge pool. These eddies are generated by the interaction between the impinging jet and the water in the plunge pool. When the jet goes through the water cushion and after its deflections near the bottom, some recirculation cells will be generated inside the plunge pool that produces these large eddies.

Due to the limitations of the LCH experimental facility and to avoid the nozzle submersion, the water depth (Y) was limited at 0.7 m. Plunge pool water depths between 0.0 and 0.7 m with 0.1 m steps have been tested.

Only the 72 mm diameter (D) cylindrical nozzle has been used for the tests.

Table 3.2 summarizes the Y/D ratios computed with these water depths and this nozzle diameter. A core jet is generated for plunge pool water depths (Y) of 0.0, 0.1 and 0.2 m, (Y/D ratios: 0.0, 1.4 and 2.8). A transition jet is generated for a 0.3 and 0.4 m water depths (Y/D ratios: 4.2 and 5.6). A developed jet is generated for water depths of 0.5, 0.6 and 0.7 m (Y/D ratios: 6.9, 8.3 and 9.7).

4.2.2.2 Jet velocities

The jet velocity (or the jet discharge) is the tool that has been used to modify the plunge pool solicitations (in collaboration with water depth). The increase of the jet velocity increases the system energy (plunge pool energy). The kinetic energy generated by the jet ($V_0^2/2 \cdot g$) is transformed in pressure solicitations on the plunge pool bottom (on the block upper face) and inside the 3-dimensional fissure.

Eleven different jet outlet velocities (V_0) have been tested: 2.5, 4.9, 7.4, 9.8, 12.3, 14.7, 17.2, 19.6, 22.1, 24.6 and 27.0 m/s. These velocities are associated at the following discharges: 10, 20, 30, 40, 50, 60, 70, 80, 90, 100 and 110 l/s. The jet velocities are near-prototype. Table 3.1 summarizes the jet characteristics.

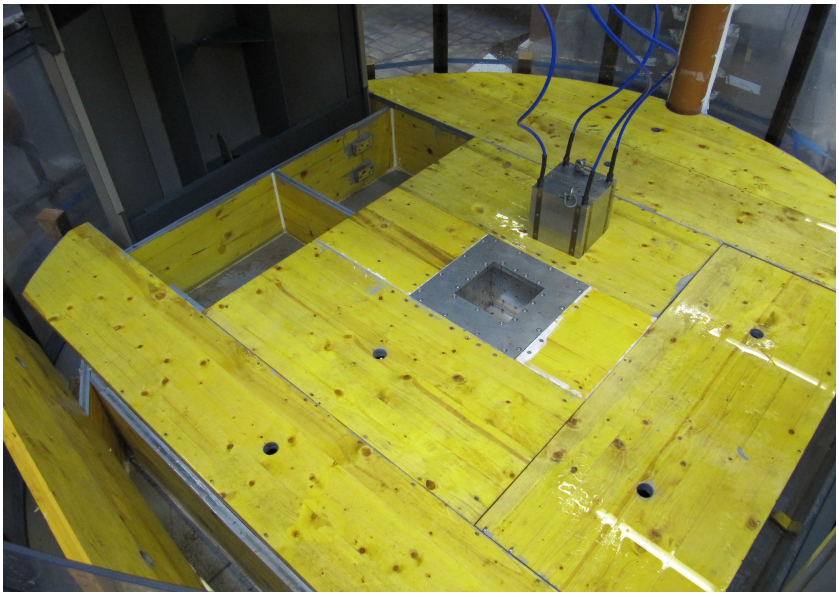

Figure 4.6: View of the plunge pool with the new experimental set-up on the center and the overflow boxes near the wall of the plunge pool.

4.3 Description of test configurations and parameters

4.3.1 Test configurations

The test configurations are a combination of the parameters explained in Chapter 4.2.1. Each configuration is characterized by: the jet impact position on the block upper face, the degree of freedom of the block and the type of the lateral guide. Figure 4.7 and the following lists summarize the configurations that have been tested in this research project:

- Two contact points at lateral guides
  - Jet impact position on the block center with the block free to move (CE);
  - Jet impact position on the block right hand side with the block free to move (SI);
  - Jet impact position on the block corner with the block free to move (CO).
- Eight contact points at lateral guides
  - Jet impact position on the block center with the block free to move (CR);
  - Jet impact position on the block center with the block fixed (CR_F);
  - Jet impact position on the block right hand side with the block free to move (SR);
  - Jet impact position on the block right hand side with the block fixed (SR_F);
  - Jet impact position on the block left hand side with the block free to move (SL);
  - Jet impact position on the block left hand with the block fixed (SL_F);
  - Jet impact position on the block corner with the block free to move (CN);
  - Jet impact position on the block corner with the block fixed (CN_F);
  - Jet impact position radial (between the center and the corner of the block) with the block free to move (RR);
  - Jet impact position radial (between the center and the corner of the block) with the block fixed (RR_F).
- Passive air entrainment and eight contact points at lateral guides
  - Jet impact position on the block corner with the block free to move (ACN).

The configuration CO (jet impact position on the block corner with the block frees to move and equipped with lateral guides having two contact points) has been omitted after the first tests due to the fast block movements. The block moves during the time necessary to change the jet velocity. At the same time, when the vertical movements are larger than 30 mm (the length of the upper contact point on the lateral guide, Figure 4.3), the block has some small rotations and it becomes stocked in the central cavity. To avoid these small rotations the eight contact points lateral guide has been developed. The tests with the configuration CO could not be performed for this reason.

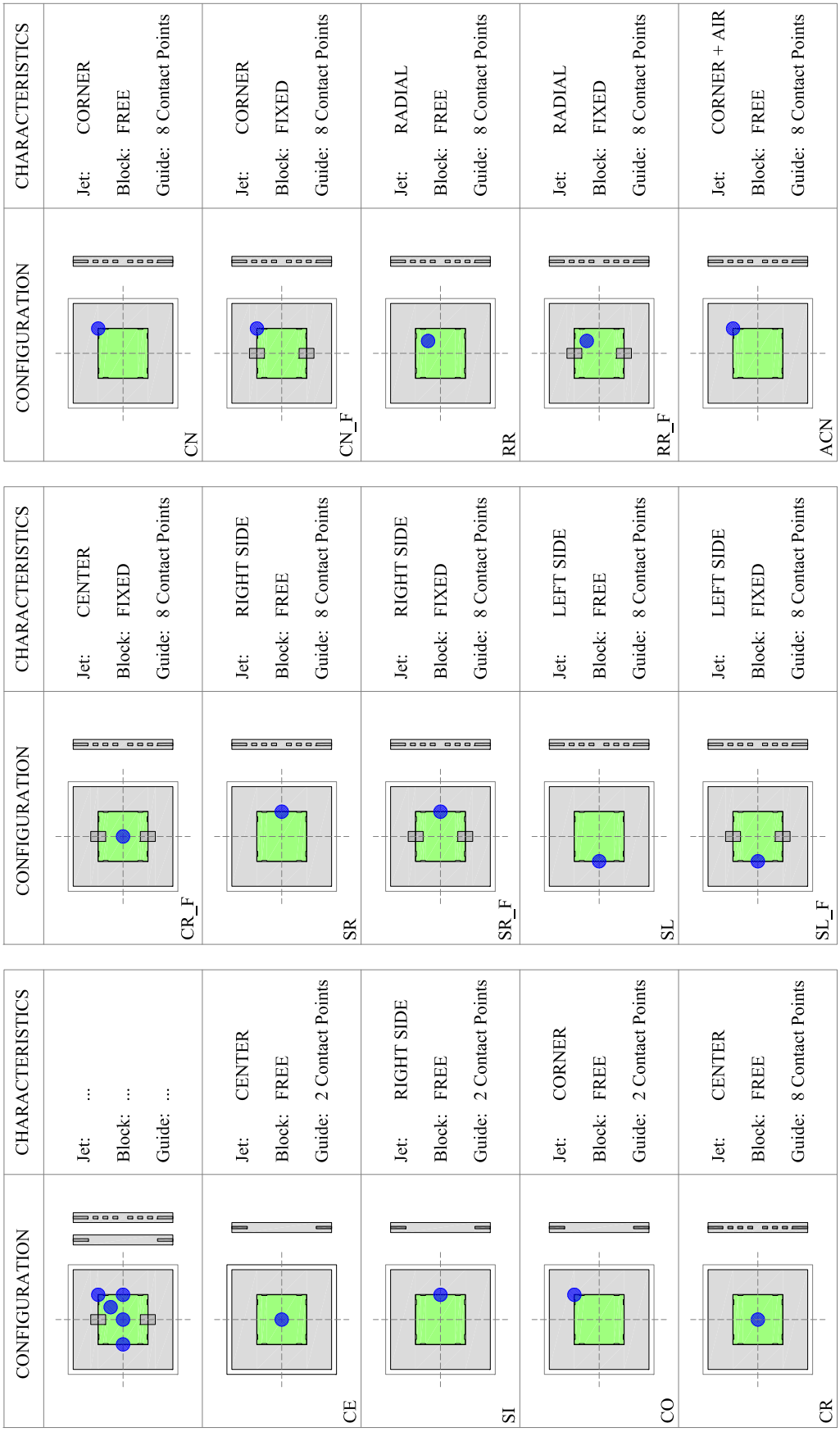

Figure 4.7: Main parameters of test configurations.

4.3.2 Test parameters

All water depths (Y) and some impinging jet velocities or discharges (V_0 or Q) have been tested with the 13 configurations. Table 4.1 summarizes the main characteristics of the performed tests.

Configuration	Water depth Y	Y/D ratio	Discharge Q	Jet velocity V_0
[−]	[m]	[-]	[l/s]	[m/s]
CE	0.0-0.7	0.0-9.7	10-110	2.5-27
SI	0.0-0.7	0.0-9.7	10-110	2.5-27
CO	0.0	0.0	10-60	2.5-14.7
CR	0.0-0.7	0.0-9.7	10-110	2.5-27
CR_F	0.0-0.7	0.0-9.7	10-110	2.5-27
SR	0.0-0.7	0.0-9.7	10-110	2.5-27
SR_F	0.0-0.7	0.0-9.7	10-110	2.5-27
SL	0.0-0.7	0.0-9.7	10-70	2.5-17.2
SL_F	0.0-0.7	0.0-9.7	10-110	2.5-27
CN	0.0-0.7	0.0-9.7	10-80	2.5-19.6
CN_F	0.0-0.7	0.0-9.7	10-110	2.5-27
RR	0.0-0.7	0.0-9.7	10-110	2.5-27
RR_F	0.0-0.7	0.0-9.7	10-110	2.5-27
ACN	0.0-0.7	0.0-9.7	10-80	2.5-19.6

Table 4.1: Overview of tests performed. Configurations are shown in Figure 4.7.

4.3.3 Position of transducers

The transducer positions were the same for all configurations (independently from the jet impact position on the block upper face).

The 12 pressure transducers were fixed on the same vertical plan to reconstruct the pressure field surrounding the block (Figure 4.8). Four transducers were installed inside the block and measure the pressure at the plunge pool bottom or on the block upper face radially outwards from the block center (N°s 309 to 312): the first on the block center, the second at 25 mm, the third at 50 mm and the fourth at 75 mm from the center. Four transducers were installed on one vertical wall of the central cavity of the measurement box (N°s 313 to 317): the first at 50 mm from the plunge pool bottom and the following with a 50 mm interval. Four transducers were installed underneath the block (N°s 318 to 321): they have the same relative position as the four transducers installed on the block upper face. The displacement transducers (D1D and D2D not shown on Figure 4.8) and the accelerometer (ACC) have a fix position: the displacement transducers underneath the block in the measurement box and the accelerometer inside the block.

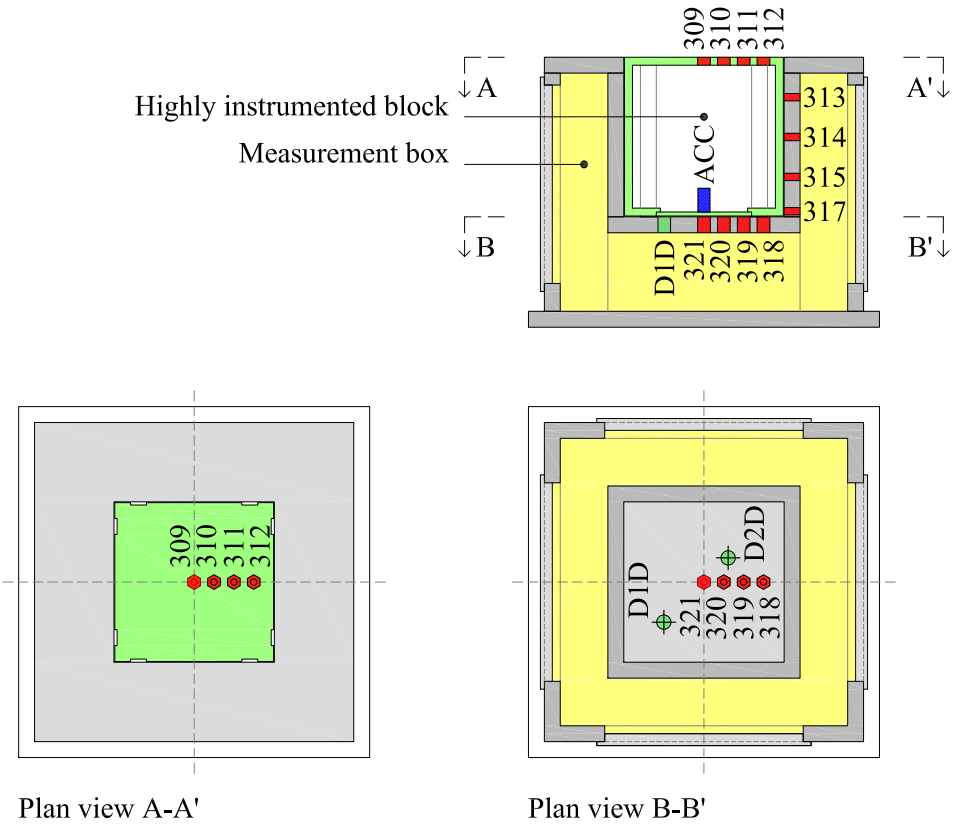

Figure 4.8: Transducer positions on the new experimental set-up for the 15 transducers: 12 pressure transducers (309-321), two displacement transducers (D1D and D2D is not shown on the figure) and one accelerometer (ACC). New experimental set-up section (top), view of the block upper face (bottom left) and view of the central cavity bottom (bottom right).

4.3.4 Data acquisition frequency

For each water depth and jet velocity, three test runs have been performed. The data acquisition frequency was 1 kHz and the recording time was approximately 65.5 seconds, providing 2^{16} or 65'536 samples for each transducer. For each test run, about 983'040 samples (output file dimension: 8-9 MB) are so being recorded (15 transducers: 12 pressure transducers, two displacement transducers and one acceleration transducer).

Some control tests have been performed with higher data acquisition frequencies (5 and 10 kHz).

4.3.5 Recorded data and database storage

Approximately 1'200 tests have been performed for the 14 configurations (13 configurations plus the omitted configuration CO).

To identify the correct data file in this huge database (approximately 3'500 data files) a codification has been used to naming the recorded files. The name of the data files were standardized and contained the following main information: plunge pool bottom configuration

(flat or confined), jet impact position on the block upper face (center, left hand side, right hand side, corner or radial), water depth in the plunge pool (Y), discharge (Q), data acquisition frequency and test run number. The output file is an ".lvm" file (ASCII file). For example the following file FB_CR_F_Y030_Q050_01kHz_2.lvm means: flat plunge pool bottom (FB), jet impact position on the block center with the block fixed and equipped with lateral guides having eight contact points (CR_F), 0.3 m of water depth (Y030), 50 l/s discharge (Q050), 1 kHz data acquisition frequency and it is the second test run.

Each water depth generates a minimum of 300 MB data files and each configuration approximately 2.3 GB of data files. This corresponds to a total storage capacity of ∼30 GB for the 14 configurations.

4.3.6 Measurement procedure

To perform the tests with all configurations (Chapter 4.3.1) the following procedure has been used:

1. prepares the test configuration: moves the measurement box in the correct position for the actual test configuration (position of the jet impact on the block upper face);
2. fixes the new wooden plunge poll bottom (to have a flat bottom);
3. put the block in the measurement box;
4. set the PVC plates in the overflow boxes to have the request water depth (Y) in the plunge for the actual test;
5. measures the atmospheric pressure and the initial block position with the transducers;
6. switches on the pump to generate the water jet;
7. fill up the plunge pool up to the request water depth (slowly to stabilize the experimental facility);
8. perform the test for the whole range of jet velocity: for each jet velocity the record time for the tree runs was roughly 10 minutes. The time necessary to perform the measures for a water depth was approximately two hours.

The electrical equipment has been always switched on minimum 1 hour before starting the tests. Some tests have been performed to analyze the influence of the electrical equipment warming up. The electrical equipment reached the stabilized temperature after approximately half hour. The measurements performed before half hour show some fluctuations due to the electrical equipment warming up. These fluctuations disappear after this minimum time and it is for this reason that the electrical equipment has been always switched on at minimum 1 hour before starting the tests.

4.4 Type of measurements

Pressure, displacement and acceleration measurements have been performed simultaneously for a 3-dimensional rock fissure and for a flat plunge pool bottom.

Four different types of measurements can be distinguished:

- pressure fluctuations at the plunge pool bottom (flat bottom situated at the same level of the block upper face);
- pressures fluctuations inside an artificially simulated full interconnected 3-dimensional rock fissure;
- corresponding block displacements;
- corresponding block vibrations.

4.5 Validation test of experimental facility

A first test has been carried out to validate the experimental facility (integration between the existing LCH experimental facility and new experimental set-up: measurement box and highly instrumented block) whit the following purpose (Figure 4.9):

- check the waterproofness of the experimental facility structure (plunge pool, measurement box and block);
- checks the performances and the precision of the new electrical equipment (transducers and data acquisition system).

The performance and the precision of the new electrical equipment have been validated with the previous measurements performed with the LCH experimental facility by Bollaert (2002b) and Manso (2006). Both research projects have used the same experimental facility but without the new experimental set-up (measurement box and block) and the new electrical equipment.

Figure 4.9: Experimental facility before (left) and during the validation test (right).

Chapter 5

Theoretical background

5.1 Dynamic pressures on a rock block

5.1.1 Dynamic pressure at the plunge pool bottom and inside a 3-dimensional fissure

5.1.1.1 Dynamic pressure at the plunge pool bottom

The jet turbulence intensity Tu is the major parameter that influences the turbulent fluctuations of a jet during its fall through the air to reach the plunge pool. The jet turbulence is at the base of jet spread, jet aeration and eventual jet break-up into distinct water particles. The LCH experimental facility generates compact jets and has a relatively small traveling distance through the air (maximum 1 m). The jet turbulence for this facility has been investigated by Bollaert (2002b) and Manso (2006).

As explained in Chapter 4.2.2.1, the Y/D geometrical ratio (the plunge pool water depth Y over the jet diameter D) has a great importance for the jet diffusion in the plunge pool (jet diffusion during its travel through the plunge pool from the water surface to the plunge pool bottom). Based on the theory of two-dimensional jet diffusion (many textbooks describe these mathematical developments in detail: as an example Abramovich (1963) and Rajaratnam (1976)) the geometrical ratio Y/D is directly related to the turbulence conditions that govern the plunge pool. As explained before (Chapter 4.2.2.1), three different jets behavior can be distinguish at the impact with the plunge pool:

- core jet impact (Y/D $<$ 4);
- transition jet impact (4 $<$ Y/D $<$ 6);
- developed jet impact (Y/D $>$ 6).

These three jet types generate different plunge pool solicitations and different responses of the 3-dimensional fissure as well of the block.

Bollaert (2002b) performed a good literature review in the domain of the dynamic pressures acting at the plunge pool bottom. Four important topics have been investigated by many

authors on the dynamic solicitations generated by the impinging water jet at the plunge pool bottom: the mean dynamic pressure, the root-mean-square (RMS) value of the fluctuations, the extreme instantaneous pressure values and the power spectral content.

The mean dynamic pressure under the jets axis has been already investigated by many authors studying a two-dimensional jets impact at the plunge pool bottom. The C_p value is defined as the mean pressure head divided by the total incoming kinetic energy, as a function of the Y/D ratio. Several authors studied the mean dynamic pressure at the plunge pool for impinging or submerged circular and rectangular jets (as an example: Cola (1965), Hartung and Häusler (1973), Franzetti and Tanda (1987a), Beltaos and Rajaratnam (1973, 1974), Puertas (1994), Ervine et al. (1997), Bollaert (2002b) and Manso (2006)).

The root-mean-square (RMS) value of the fluctuations is expressed by the $C_{p'}$ coefficient and is defined as the ratio of RMS value over the incoming jet kinetic energy. In general, three effects strongly influence the RMS values: the initial jet turbulence intensity Tu, the degree of break-up of the jet and finally aeration effects. The degree of break-up of the jet is defined as the ratio of the jet fall length to the jet break-up length. The root-mean-square (RMS) value of the pressure fluctuations at the plunge pool for impinging or submerged circular and rectangular jets was studied by several authors (for example: Franzetti and Tanda (1984), Toso and Bowers (1988), May and Willoughby (1991) and Ervine et al. (1997)).

The extreme instantaneous pressure values represent the maximum and the minimum pressure values over the incoming kinetic energy of the jet. Most authors found values up to 2 to 4 times the corresponding RMS value (Bollaert and Schleiss (2003a)). The root-mean-square value of the fluctuations for the same conditions was studied by several authors (as an example: Lencastre (1961), Xu-Duo-Ming (1983), Franzetti and Tanda (1987a), May and Willoughby (1991), Castillo Elsitdié (1989), Ervine et al. (1997), Bollaert (2002b) and Manso (2006)).

The last relevant dynamic aspect is the power spectral content, which provides important information concerning the cyclic nature and the energy content of the pressure fluctuations. The power spectral is defined as a decomposition of the pressure fluctuations variance as a function of the frequency. The power spectral signal was studied by Lencastre (1961), Ramos (1979), Xu-Duo-Ming (1983), Tao et al. (1985), May and Willoughby (1991), Puertas (1994), Ervine et al. (1997), Bollaert (2002b) and Manso (2006).

Ervine et al. (1997) developed four envelop curves for mean, turbulent and maximum/minimum pressure coefficients (mean pressure coefficient C_p, turbulent pressure fluctuation coefficient $C_{p'}$, positive extreme pressure fluctuation coefficient C_p^+ and negative extreme pressure fluctuation coefficient C_p^-). Theses curves are normalized by the kinetic energy of the incoming jet. In the field of the rock scour, the Ervine's paper (Ervine et al. (1997)) is considered as reference for the pressure fluctuations at the plunge pool bottom loaded by a cylindrical vertical impinging

water jet. These curves have been developed experimentally by analyzing the recorded data at the plunge pool radially outwards from the stagnation point (jet impact position at the plunge pool bottom).

The jet diffusion through the plunge pool may influence the flow penetration inside the 3-dimensional fissure. Moreover, the jet impact position on the block may influence as well the flow penetration inside the fissure. Only a few studies investigated the pressure propagation inside a fissure. Bollaert (2002b) and Manso (2006) have studied the pressure propagation inside a 1- and 2-dimensional fissure with different geometries (I-, 2D I-, L-, U- and D-fissure, Figure 1.4).

The presence of air in the water influences strongly the hydrodynamic variables. The air penetrates in the system in three different moments: jet aeration during the jet travel in the air from the nozzle to the water surface, plunge pool aeration at the jet impact on the water surface and penetration of air bubbles into rock fissure.

The experimental facility is subjected to a natural air entrainment: jet aeration and plunge pool aeration. The air entrainment was the same for the previous research projects (Bollaert (2002b) and Manso (2006)) and for the actual work.

5.1.1.2 Dynamic pressure inside a 3-dimensional fissure

The 3-dimensional fissure corresponds to a full open boundary system, in which the jet excitation depends on the relative jet impact position on the block upper face and the jet diffusion in the plunge pool. The pressure propagation inside the fissure depends on different geometrical parameters as spacing, opening and interconnection of fissures as well on the characteristics of the fluid in the fissure. Standing pressure waves and resonance conditions inside the fissure may be generated by the superposition of waves. These waves enter the 3-dimensional fissure and then travel forwards and backwards throughout it. The values presents in the literature (pressure field, pressures coefficients, power spectral ...) have been developed for jet impacts at the plunge pool level (Cola (1966), Beltaos and Rajaratnam (1973) and Ervine et al. (1997)) and 1- and 2-dimensional fissure (Bollaert (2002b) and Manso (2006)) but not for jets penetrating inside a 3-dimensional fissure. The computed data inside the fissure can be compared to the literature values (measured at the plunge pool bottom) having in mind that they have been obtained for different conditions (flow, turbulence, geometry and confinements).

5.1.1.3 Pressure distribution at plunge pool bottom and inside the 3-dimensional fissure

The pressure distribution acting at the plunge pool bottom from the stagnation point radially outwards and its conversion in wall flow near the bottom has been investigated by several authors (as an example: Schwartz and Cosart (1961), Häusler (1966), Cola (1966) (Figure 5.2), Aki (1988), Beltaos and Rajaratnam (1973) (Figure 5.1) and Hartung and Häusler (1973)).

They propose a bell-shape distribution (normal distribution) for the pressure acting on the block upper face. This distribution is an exponential function according Equation (5.1).

$$p(x) = A \cdot e^{-B \cdot \left(\frac{x}{Y}\right)^2} \tag{5.1}$$

where A corresponding to the maximum pressure value p_{max} at the stagnation point, B a calibration factor and x/Y the normalized distance from the stagnation point (Y water depth).

Cola (1966) propose the following equation based on his own observations (Figure 5.2):

$$\Delta_p(x) = \rho \cdot \frac{V_0^2}{2} \cdot \frac{1}{\sqrt{\pi} \cdot C_1} \cdot \frac{D}{Y} \cdot \frac{1}{1-\eta_A} \cdot e^{-\frac{1}{4 \cdot C_1^2 \cdot (1-\eta_A)^2} \cdot \left(\frac{x}{Y}\right)} \tag{5.2}$$

where ρ is the water density, V_0 the jet velocity, D the jet diameter, Y the water depth, C_1 and η_A two variables depending on the position of the boundary between the free jet region and the impingement region, x/Y the normalized distance from the stagnation point.

Beltaos and Rajaratnam (1973) propose the following equation (Figure 5.1):

$$p_w(x_1) = p_s \cdot e^{-38.5 \cdot \left(\frac{x}{Y}\right)^2} \tag{5.3}$$

where p_s is the pressure at the stagnation point and x/Y the normalized distance from the stagnation point.

Figure 5.1 shows the two dimensional jet diffusion and impingement on a flat smooth surface. In this figure, three main regions (free jet region, impingement region and wall jet region) and the velocity and pressure distribution are explained.

Figure 5.2 shows the pressure distribution and the flow velocity evolution along the plunge pool bottom radially outwards from the stagnation point (jet impact position).

Armengou (1991) plotted the different curves of the pressure distribution on plunge pool floors, for jets with or without air entrainment. The inflection points of non-dimensional Gaussian type curves (Figure 5.3) are further away from the stagnation point in the cases in which the air entrainment is considered, revealing greater diffusion angles in these cases.

The pressure distribution inside a 3-dimensional fissure has not yet been investigated in detail. Bollaert (2002b) and Manso (2006) have studied the pressure propagation and distribution only inside a 1- and 2-dimensional fissure with different geometries (I-, 2D I-, L-, U- and D-fissure, Figure 1.4).

The present research study allows obtaining new information on the pressure field acting inside a full interconnected 3-dimensional fissure.

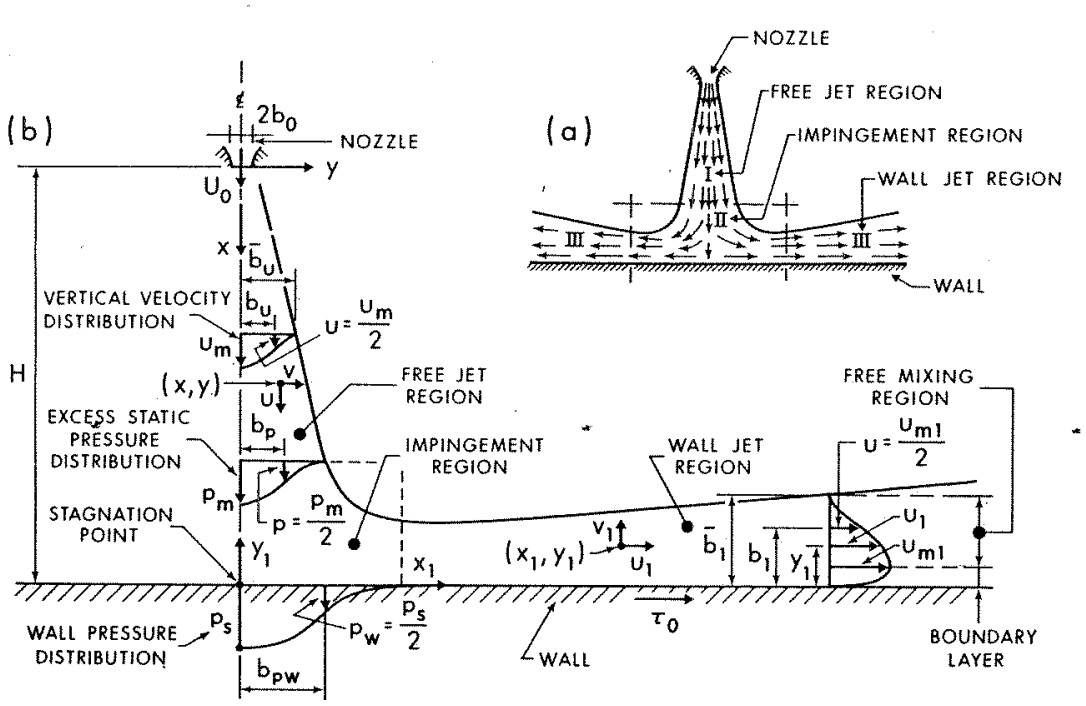

Figure 5.1: Two-dimensional jet diffusion and impingement on a flat smooth surface: a) main jet regions; b) velocity and pressure distributions in each region (according Beltaos and Rajaratnam (1973)).

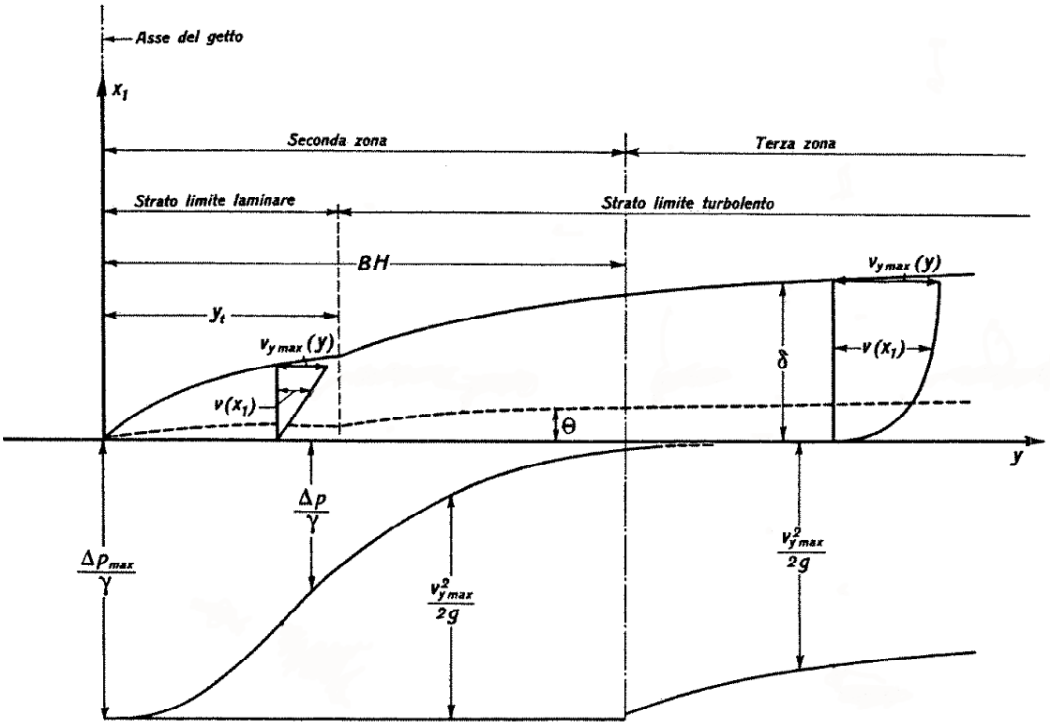

Figure 5.2: Development of the boundary layer at the plunge pool bottom and the evolution of the over pressure (Δp) and velocity (V) along the bottom (according Cola (1966)).

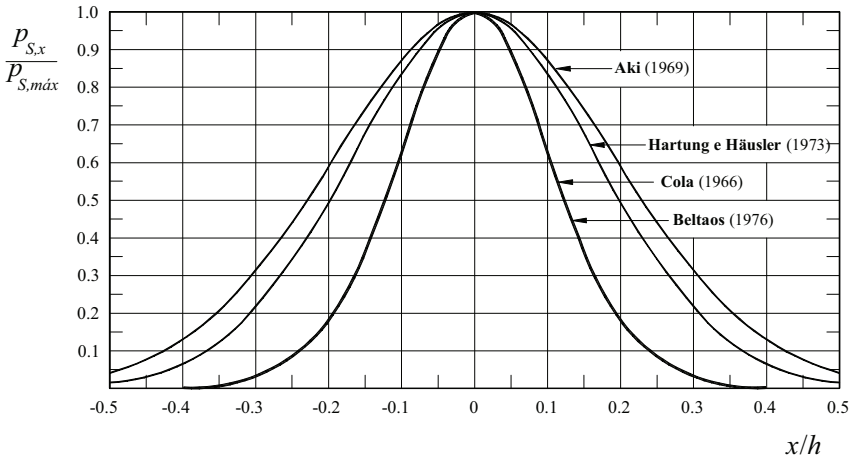

Figure 5.3: Dynamic pressures on the pool floors for one phase flow (Cola (1966) and Beltaos (1976b)) and two phase flow (Aki (1988) and Hartung and Häusler (1973)) as presented by Castillo Elsitdié (1989) and Armengou (1991) where $p_{s,x}$ is the pressure along the x-axis, $p_{s,max}$ the pressure at the stagnation point, x the distance along the x-axis and h the water depth.

5.2 Methods for pressure analysis

To analyses and understand the pressure field acting around the block (at the plunge pool bottom and inside the 3-dimensional fissure) different mathematical tools have been used:

- statistical pressure analysis;
- pressure coefficients;
- spectral analysis.

The statistical and the spectral analysis have been used to analyze the block displacements and as well the block accelerations.

5.2.1 Pressure analysis

The recorded signals have been analyzed to determine the main statistical data for all transducers (pressure, displacement and acceleration). Using the converted signal (from Volt to Bar/mm/g) the following data have been computed:

- maximum value;
- mean value;
- minimum value;
- standard deviation;
- variance;

- skewness;
- kurtosis.

Maximum, mean and minimum values give an overview of the pressure field.

The standard deviation is a measure of the data dispersion from its mean. The standard deviation shows how much variation or "dispersion" there is from the "mean". A low standard deviation indicates that the data points tend to be very close to the mean, whereas a high standard deviation indicates that the data are spread out over a large range of values. The standard deviation is computed as follows:

$$\sigma = \sqrt[2]{\frac{1}{N} \cdot \sum_{i=1}^{N} (x_i + \overline{x})^{\,2}} \tag{5.4}$$

where x_i is a value in the data set, $\overline{x}$ the mean value of the data set and N the total number of values in the data set.

The variance is used as a measure to determine how far a data set is spread out from each other. The variance is one of the moments of a distribution. If the random variable X is discrete with probability mass function $x_1 \to p_1, \ldots, x_n \to p_n$, the variance is computed by the following equation:

$$Var(X) = \sum_{i=1}^{N} \left(p_i \cdot \left(x_i - \sum_{i=1}^{N} (p_i \cdot x_i) \right) \right) \tag{5.5}$$

where x_i is a value in the data set, $\overline{x}$ the mean value of the data set, p_i the probably for the data and N the total number of values in the data set.

The skewness and kurtosis parameters reflect the importance of extreme pressure values in the probabilistic pressure distribution.

The skewness is a measure of the asymmetry of the probability distribution of a real-valued random variable. The skewness value can be positive or negative, or even undefined. Qualitatively, a negative skewness indicates that the tail on the left side of the probability density function is longer than the right side and the bulk of the values (including the median) lie to the right of the mean. A positive skewness indicates that the tail on the right side is longer than the left side and the bulk of the values lie to the left of the mean. A zero value indicates that the values are relatively evenly distributed on both sides of the mean, typically but not necessarily implying a symmetric distribution.

The skewness C_s of a random variable X is the third standardized moment and is computed as follows:

$$C_s = \frac{\sum_{i=1}^{N} (x_i - \overline{x})^{\,3}}{(N-1) \cdot RMS\,(x')^{\,3}} \tag{5.6}$$

where x_i is a value in the data set, $\overline{x}$ the mean value of the data set, x' the fluctuation part of the data, $RMS(x')$ the root-mean-square of the data fluctuations and N the total number of values in the data set.

The kurtosis Ku is a measure of the "peakedness" (having or ending in a peak; pointed) of the probability distribution of a real-valued random variable. Higher kurtosis means more of the variance is the result of infrequent extreme deviations, as opposed to frequent modestly sized deviations. The kurtosis of a random variable X is the fourth standardized moment and is computed by the following equation:

$$Ku = \frac{\sum_{i=1}^{N} (x_i - \overline{x})^4}{(N-1) \cdot RMS\,(x')^4} - 3 \tag{5.7}$$

where x_i is a value in the data set, $\overline{x}$ the mean value of the data set, x' the fluctuation part of the data, $RMS(x')$ the root-mean-square of the data fluctuations and N the total number of values in the data set.

5.2.2 Pressure coefficients

The pressure coefficients are a representation of the loads transmitted by the air-water mixture at the "rock" interface (maximum, mean, minimum, fluctuations, extreme positive and negative, and turbulence) and are function of the jet kinetic energy at the plunge pool entrance. The jet velocity up to the impact on the water surface of the plunge pool is computed as follows:

$$V_I = \sqrt[2]{{V_0}^2 + 2 \cdot g \cdot L} \tag{5.8}$$

where V_0 is the jet velocity at nozzle exit, g the gravity acceleration and L the vertical drop of the jet travel in the air (distance between the nozzle and the water surface in the plunge pool).

The different pressure coefficients have been computed with the following Equations (5.9) to (5.14).

Mean pressure coefficient:

$$C_p = \frac{(\overline{p} - p_{atm}) - Y}{\alpha \cdot \dfrac{V_I^2}{2 \cdot g}} \tag{5.9}$$

Turbulent pressure fluctuation coefficient:

$$C_{p'} = \frac{\sqrt{\sigma_p}}{\alpha \cdot \dfrac{V_I^2}{2 \cdot g}} \tag{5.10}$$

Positive extreme pressure fluctuation coefficient:

$$C_p^+ = \frac{p_{max} - \overline{p}}{\alpha \cdot \frac{V_I^2}{2 \cdot g}} \tag{5.11}$$

Negative extreme pressure fluctuation coefficient:

$$C_p^- = \frac{\overline{p} - p_{min}}{\alpha \cdot \frac{V_I^2}{2 \cdot g}} \tag{5.12}$$

Positive extreme pressure coefficient:

$$C_{p,max} = \frac{p_{max}}{\alpha \cdot \frac{V_I^2}{2 \cdot g}} \tag{5.13}$$

Negative extreme pressure coefficient:

$$C_{p,min} = \frac{p_{min}}{\alpha \cdot \frac{V_I^2}{2 \cdot g}} \tag{5.14}$$

where p_{max} is the maximum pressure, $\overline{p}$ the mean pressure, p_{min} the minimum pressure, Y the water depth in the plunge pool, V_I the jet velocity at the impact on the water surface in the plunge pool, σ_p the standard deviation of the pressure fluctuations, g gravity acceleration and α is a velocity profile correction parameter that has been considered equal to 1.

Several authors have studied the pressure coefficients generated by jet impinging on a flat plunge pool bottom (Chapter 5.1.1.1).

5.2.3 Power Spectral Density

5.2.3.1 Introduction

Pressure fluctuations may also be analyzed by means of spectral analysis. Spectra of turbulent fluctuations present three main features from low to high frequencies (Chassaing (2000)):

I. the production zone, related to the mean characteristics of the energy source (the jet);

II. the energy redistribution zone from large eddies at low frequencies to progressively smaller vortices (cascade of energy);

III. the dissipation or viscous zone, where the energy of the small turbulent structures (high frequencies) is dissipated by viscosity.

The spectral analysis of pressure fluctuations allows identifying the energetic content of each frequency.

A time series of turbulent pressures may be seen as a superposition of different sinusoidal functions with different amplitude A and phase ϕ. The energy content of each frequency is A^2. The power spectra represent the cumulated series of given frequencies and the corresponding energy contents. The variance of p' (fluctuations part of the pressure signal) is the total energy of the fluctuations. The power spectra can be defined as a decomposition of the variance per frequency, inversely the variance is the integral of the power spectra. Bendat and Piersol (1971), Lyons (1997) and Stearns (2003) give detailed information for the spectral analysis of digital signals.

The power spectrum can also be seen as the Fourier transform of the correlation function. In order to identify the relevant sinusoidal functions (the energy-carrying frequencies) for the measured data series, the Fourier analysis is performed. For this research, two approaches have been used but only the second has been presented:

1. the direct computation of the Fourier transform terms using the FFT (Fast Fourier Transformation) algorithm;

2. the lumped computation of the Fourier terms using the algorithm called the "Periodogram of Welch".

The signal data post-processing is performed with in-house routines written in the Matlab© environment.

5.2.3.2 Computation parameters of power spectral density

Power spectral density P_{xx} (PSD) is computed using the Welch periodogram method for the Fast Fourier Transforms (FFT) with a 50% overlapping, a Hamming window and a maximum of 3 x 65'536 samples or 2^{16} samples (196'608 samples) acquired at 1 kHz and cut into 64 blocks. PSD is expressed as a function of frequency f and represents the decomposition of the pressure fluctuations with frequency. This allows visualizing the relative importance of each frequency compared to the total spectral content. Care should be taken when using the ready-made algorithms of the different software for digital signal treatment (as an example: Matlab©, Labview©, ...) since the definition of the outcome is not always the same, in terms of units, number of terms, one-sided or two-sided spectra, with/without the mean, frequency resolution, and so forth. One small example of this is the fact that Welch's PSD estimates are presented in [unit^2/Hz] instead of [unit^2] and the number of one-sided PSD Fourier terms is $k_{Welch} = N/N_b/2 + 1$ instead of $N - 1$ (where N_b is the number of data sub-sets selected).

5.3 Dynamic forces on a rock block

5.3.1 Introduction

The principal force that acts on a rock block can be subdivided into two families: the stabilizing forces and the destabilizing forces (Bollaert (2002b)). The stabilizing forces are the following:

- the immerged weight of the block (W_b).
- the force resulting from the time and space pressure distribution acting on the block at the plunge pool bottom (F_{up}). It appends from the macro turbulent pressure pattern at the plunge pool bottom and when reaches negative values become destabilizing.
- the friction force ($F_{friction}$) which depends on several parameters such: the fissure roughness, the fissure geometry, the fissure aperture and the filling material. It was being assumed to depend on fissure width and time.
- the virtual force generated by the added mass (F_{am}). This virtual force is applied to the fluid mass (along the movement axis) that must be accelerated in order to allow at the block to move. This force depends block geometry, buoyancy, Reynolds number and other variables (such as the proximity of the plunge pool bottom: boundary conditions, Chapter 2.4). This force is not take into account for the structural design.

The destabilizing forces are generated by the transfer of pressures at the plunge pool bottom into underlying rock fissures. The transient two-phase flow conditions inside the fissures create a pressure pattern that is completely different from the pressure pattern at the plunge pool bottom itself. It is this difference between turbulent surface pressures and transient rock fissure pressures that produce the net uplift pressures on a rock block. The destabilizing force corresponds to:

- the time, space and fissure width dependent pressure distribution acting inside the 3-dimensional fissure underneath the block (F_{down}). The lateral pressure is considered as stabilizing due to the limited degree of freedom of the block (only the vertical movements).

5.3.2 The block immerged weight

The immerged block weight is given by the block weight G_b and the buoyancy F_{ar} acting on the block. The immerged block weight is obtained by the following equation:

$$W_b = G_b - F_{ar} = \rho_b \cdot V_b \cdot g - \rho_w \cdot V_b \cdot g = V_b \cdot g \cdot (\rho_b - \rho_w) \tag{5.15}$$

where G_b is the block weight, F_{ar} the buoyancy force, ρ_b the block density, ρ_w the water density and g the gravity acceleration.

The experimental block, equipped with the transducers (pressure and acceleration) and the transducer cables, has a mass of 21.7 kg (m_b), providing an immerged weight of ∼135 N.

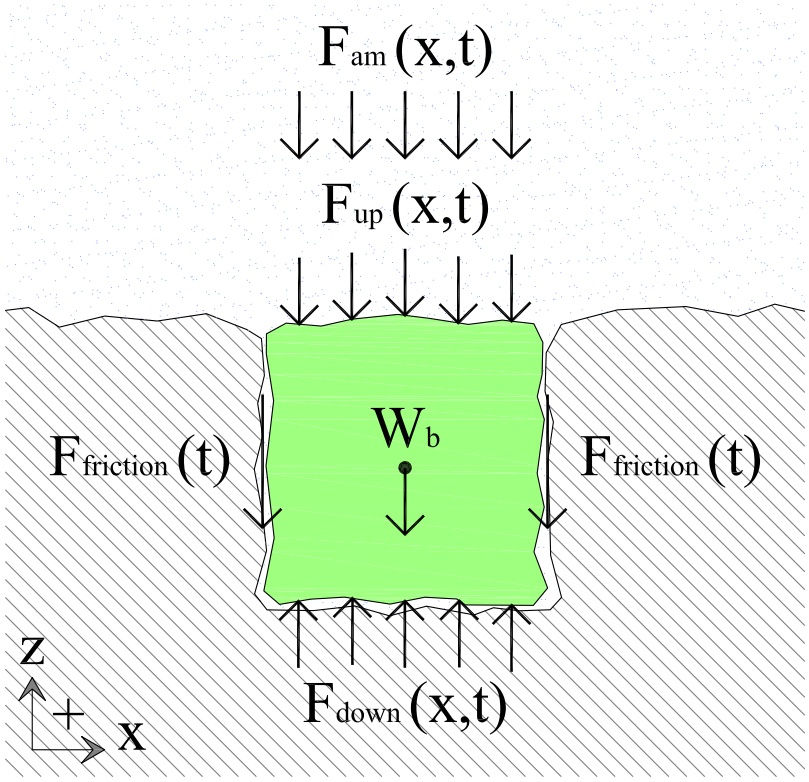

Figure 5.4: Main forces acting on a rock block during its vertical movements in the rock foundation (according Bollaert (2002b)).

5.3.3 Pressure force acting on the block surface

The resulting pressure force acting on the block upper face is generated by the jet impacting on the block. To evaluate this force, the pressure measurements on the block upper face have been used. For jet impacts at the plunge pool bottom, the pressure distribution follows an exponential function. According to Cola (1966) (Figure 5.2) and Beltaos and Rajaratnam (1973) (Figure 5.1) the pressure distribution at the bottom has a bell-shape distribution (normal distribution). This pressure distribution will be fitted to the pressure measurements performed on the block (four pressure transducers, Chapter 4.3.3) according Equation (5.1). Between the impingement region and the wall jet region, the wall pressure distribution decreases and the jet energy is converted into velocity (deflected flow in the wall jet region) as explained by Cola (1966).

The pressure force acting on the block upper face is computed by the integration of the pressure distribution (exponential distribution) on the block surface (Eq. (5.16)).

$$F_{up} = \int \int p(r,\theta,t) \cdot r \cdot \mathrm{d}r \, \mathrm{d}\theta \tag{5.16}$$

Therefore, to compute the force acting on the block upper face (F_{up}), the integration has not been solved and another approach has been chosen. The pressure field, characterized by

this exponential distribution, has been replaced with a discrete linear function. The discrete linear function connects the pressure measurements on the block upper face by a simple line.

The surface under this linear function has been computed and by a revolution around the vertical axis (situated on the stagnation point, for 2π), the force acting on the block upper face F_{up} was obtained. For different jet impact positions on the block (center, left and right hand side, corner and radial) different integration schemes have been used and are illustrated in Figure 5.5. The dark grey region corresponds to the region where the pressures have been measured with the transducers and the dotted region is the region where an assumption has been made to estimate the pressure acting on the block.

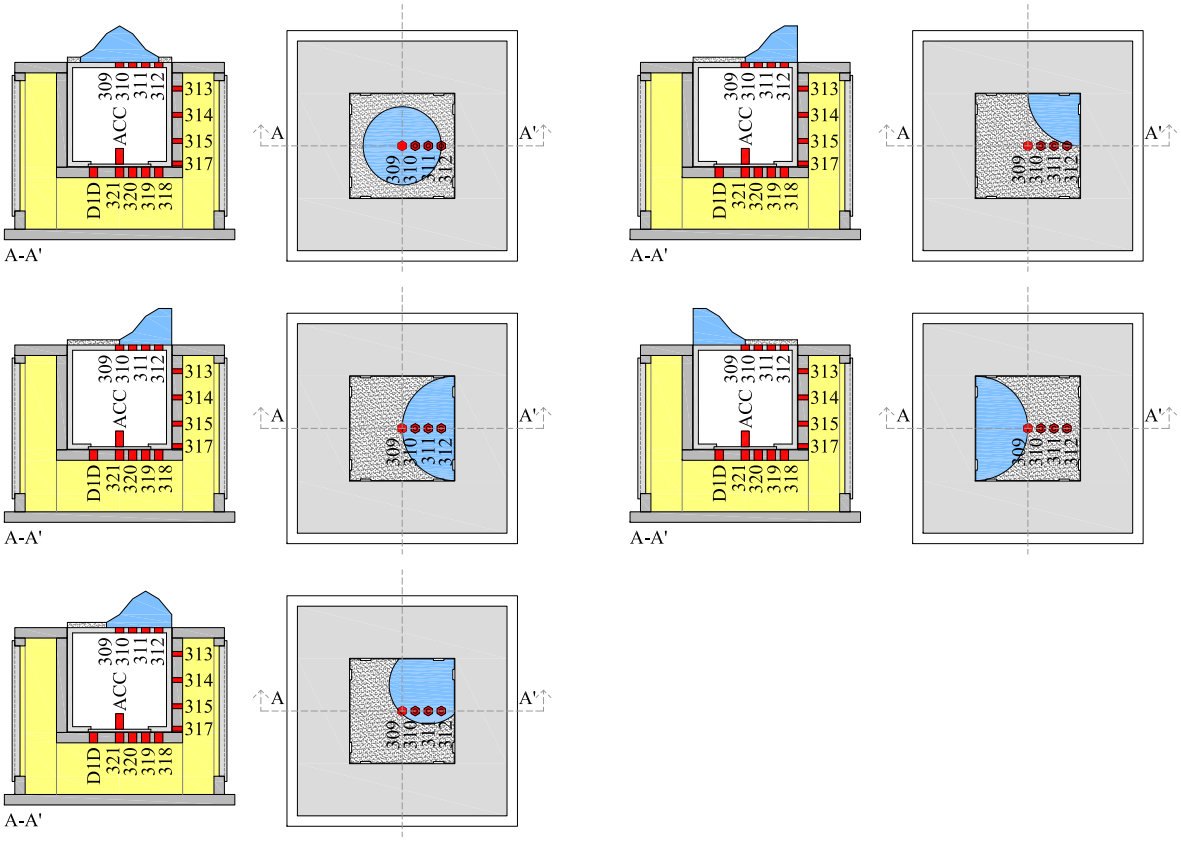

Figure 5.5: Assumption for integrating pressure on the block upper face. Jet impact on the block center (top left); jet impact on the block corner (top right); jet impact on the block right side (middle left); jet impact on the block left side (middle right); jet impact between the center and the corner of the block (bottom left).

5.3.4 The friction force

The friction force $F_{friction}$ is generated by the friction acting between the block and the surrounding fissure. The lateral guides, fixed on the block, provide the contact with the central cavity walls in the middle of the measurement box (Figure 3.5). The friction force is the result of their relative displacements. This force is computed as follows:

$$F_{friction} = \mu_k \cdot G_b \tag{5.17}$$

where μ_k is the kinetic friction coefficient and G_b the block weight.

The friction coefficient is a dimensionless scalar value which describes the ratio of the force of friction between two bodies and the force pressing them together. The static friction is the friction between two objects that are not moving one related to the other. The static friction force must be overcome by an applied force before an object can move. The kinetic friction occurs when two objects are moving relative to each other and rub together. The coefficient of kinetic friction is typically denoted as μ_k and is usually less than the coefficient of static friction μ_s for the same materials.

The lateral guides are composed of bronze and the measurement box is composed of steel. For a bronze-steel greasy interface, the static friction coefficient is $\mu_s = 0.16$.

Due to the complex interface between the block and the measurement box the real kinetic friction coefficient has been determined for the experimental facility and the two types of lateral guides (two or eight contact points, Chapter 4.2.1.3).

The following procedure has been used to quantify the kinetic friction coefficient:

- the block is inserted in the central cavity of the measurement box;
- the block is forced to move up (the block is pulled out from the central cavity) and the resulting force is recorded with a dynamometer (the static and the dynamic force).

This procedure was repeated 20 times with and without water in the surrounding fissure. When this procedure was executed with water inside the fissure, the water was present as well in the plunge pool (Y = 0.2 m) to be more realistic. The complete procedure was repeated three times to obtain representative average values. The coefficients for both lateral guides are summarized in Table 5.1.

	Two contact points		Eight contact points	
Condition	Static friction	Kinetic friction	Static friction	Kinetic friction
	μ_s	μ_k	μ_s	μ_k
[-]	[-]	[-]	[-]	[-]
Dry	0.08	0.34	0.12	0.38
Wet	0.07	**0.29**	0.10	**0.32**

Table 5.1: Static and kinetic friction coefficient for the experimental facility equipped with lateral guides having two or eight contact points.

The computation of the block dynamic impulsion has been made using the kinetic friction coefficient for the wet condition (Chapter 7.1): lateral guide with two contact points $\mu_k = 0.29$ and lateral guide with eight contact points $\mu_k = 0.32$.

5.3.5 Added mass

The added mass is explained in Chapter 2.4. When a body immerged in a fluid is subject to acceleration, the surrounding fluid must accelerate as well. The inertia of the entrained fluid is the added mass. The added mass is computed with the following equation:

$$m_{am} = \alpha_{am} \cdot \pi \cdot \rho_w \cdot V_b \tag{5.18}$$

where m_{am} is the added mass, α_{am} the added mass coefficient, ρ_w the water density and V_b the block volume.

The added mass force is the force necessary to accelerate the fluid near the body. This force is computed as follows:

$$F_{am} = m_{am} \cdot a \tag{5.19}$$

where m_{am} is the added mass and a the block acceleration.

5.3.6 Pressure force acting underneath the block

The destabilizing force is generated by the transfer of pressures from the plunge pool bottom into the 3-dimensional fissure. The flow conditions inside the fissure create a pressure pattern completely different from the pressure pattern at the plunge pool bottom.

To evaluate this force the pressure measurements underneath the block have been used. The data shows that the pressure distribution underneath the block is quite constant (Chapters 6.2.2, 6.3.2 and 6.4.2) for the four pressure transducers (Chapter 4.3.3). The pressure force is computed by the following equation:

$$F_{down} = \overline{p} \cdot S_b \tag{5.20}$$

where $\overline{p}$ is the mean pressure of the four pressure transducers situated underneath the block and S_b the block surface.

5.4 Dynamic impulsion on a rock block

5.4.1 Introduction

Several research works have analyzed the dynamic pressures acting on a rock block or on concrete slabs of stilling basin. The first works focused on the time-averaged dynamic pressure. Montgomery (1984) and Reinus (1986) studied the behavior of planar joints of concrete elements subjected on a horizontal flow. Otto (1989) performed dynamic pressure measurements in fissures solicited with vertical and oblique impinging jets. It was observed that the jet impact position, related to the fissure positions and the jet impact inclination is an important factor. These three studies (Montgomery (1984), Reinus (1986) and Otto (1989)) showed that

the time-averaged forces acting on a block or a concrete slab may eject the blocks/slabs from their foundation.

The relevance of the instantaneous uplift force was observed during the analysis of the damage that occurs in some stilling basins (Malpaso, Tarbela and Karnafuli dams). In this case the time-averaged pressure has played only a small role in the basin damage (Bower and Tsai (1969), Toso and Bowers (1988), Fiorotto and Rinaldo (1992a), Fiorotto and Rinaldo (1992b) and Bellin and Fiorotto (1995)). A laboratory analysis of instantaneous net forces has been made by Liu et al. (1998). They studied the instantaneous net forces acting on a single rock block in a plunge pool. The net uplift pressures or forces are generated by assuming an instantaneous propagation of the pressure waves inside the joints. This generates a constant pressure field under the block. The upper pressure field is governed by turbulent flow conditions and is time-and space dependent. Fiorotto and Salandin (2000) have performed a similar analysis but for the persistence time of the pressures underneath the concrete slabs.

Bollaert (2002b) studies instantaneous uplift generated by the pressure propagation at the jet impact point and inside a 1- and 2-dimensional fissures. Different fissure geometries have been tested. The proposed scour model evaluates the ultimate scour depth in intermittently or completely fissured rock under the impact of high-velocity plunging jets. The scour model is completely physically based and represents a comprehensive assessment of the two major physical processes that govern the rock scour: the hydrodynamic fracturation of close-end fissures and the dynamic uplift acting on a so formed rock block. The model consists of three modules: the falling jet, the plunge pool and the rock mass.

Manso (2006) studied the persistence of the pressure pulse at the jet impact point and inside a 1-dimensional fissure for different confined plunge pool geometries, in view of the definition of a probably-based model for rock block uplift.

Melo et al. (2006) studied the forces acting on a blocky floor solicited by a vertical impinging jet. The floor was composed of 36 metallic parallelepiped blocks covering an area of 0.6 m^2. To simulate the joints between the blocks and the foundation, each block is equipped with vertical adjustable bolts and was connected to neighboring blocks by two steel bars anchored to the floor frame.

Pinheiro and Melo (2008) studied the forces acting on a flat floor solicited by an aerated vertical impinging jet.

5.4.2 Computation of block net impulse

The net impulse $I_{\Delta pulse}$ acting on the block, corresponding to a pressure pulse of time $\Delta t_{\Delta pulse}$, is defined by the integration of the net force at every time step dt. This time step has to

be chosen small enough so that no significant pressure changes occur during each step. This computation gives as result an uplift velocity $V_{\Delta pulse}$. The total force acting on the block is given by the following equation:

$$\sum F = F_{down} - F_{up} - W_b - F_{friction} = (m_b + m_{am}) \cdot a_{\Delta pulse} \tag{5.21}$$

where F_{down} is the pressure force acting underneath the block, F_{up} the pressure force acting on the block upper face, W_b the block immerged weight, $F_{friction}$ the friction force, m_b the block weight, m_{am} the added mass and $a_{\Delta pulse}$ the uplift acceleration.

The net impulse is computed by this equation:

$$I_{\Delta pulse} = \int_0^{\Delta pulse} \sum F \cdot \mathrm{d}t = \int_0^{\Delta pulse} (F_{down} - F_{up} - W_b - F_{friction}) \cdot \mathrm{d}t = (m_b + m_{am}) \cdot V_{\Delta pulse} \tag{5.22}$$

where F_{down} is the pressure force acting underneath the block, F_{up} the pressure force acting on the block upper face, W_b the block immerged weight, $F_{friction}$ the friction force, m_b the block weight, m_{am} the added mass and $V_{\Delta pulse}$ the uplift velocity.

A positive $I_{\Delta pulse}$ means that the block moves up (ejected from the rock foundation) and a negative means that the block moves down in the central cavity of the measurement box.

Due to transient effects, the pressure derivative in time is generally much higher than the pressure gradient in space. Therefore, as a first approach, a space-averaged value can be chosen. The kinetic energy given to the block is transformed into potential energy as a function of the mass of the block. The total uplift of the block h_{up} (for each $\Delta t_{\Delta pulse}$) is defined by the following Equations (5.23) and (5.24):

$$V_{\Delta pulse} = \frac{h_{up}}{\Delta t_{\Delta pulse}} \tag{5.23}$$

which may be rewritten as:

$$h_{up} = V_{\Delta pulse} \cdot \Delta t_{\Delta pulse} \tag{5.24}$$

where $V_{\Delta pulse}$ is the uplift velocity, h_{up} the block uplift and $\Delta t_{\Delta pulse}$ the time interval where the pressure pulse is applied to the block.

The vertical displacement evolution is given by the following equation:

$$h_{up_{i+1}} = h_{up_i} + \Delta h_{up_{i+1}} \tag{5.25}$$

where $h_{up_{i+1}}$ is block uplift at the time $i+1$, h_{up_i} the block uplift at the time i and $\Delta h_{up_{i+1}}$ the vertical displacement between time $i+1$ and time i.

5.5 Interaction between displacement and acceleration of block and the acting net impulse

The block response (displacements and accelerations) is the results of the dynamic loading of the block. The two displacement transducers and the accelerometer allow to measure these solicitations (for the transducer positions see Chapter 4.3.3). The measured displacements and the accelerations may be considered as redundant measurement allowing to compute the dynamic block impulsion.

The displacements allow to compute the total force acting on the block by the uplift velocity Equation (5.23) and the block impulse Equation (5.22).

The accelerations allow to compute the total force acting on the block by the total weight of the system (block mass m_b and added mass m_{am}).

The block impulse $I_{\Delta pulse}$ and the block vertical uplift h_{up} results obtained by the pressure measurements can then be compared with the results obtained by the displacement and acceleration measurements.

5.6 Natural period of an open-ended fissure

The pressure fields, generated by the impinging jet, acting over and underneath the block are not independent and have to be correlated. The pressures acting on the block are able to create standing and resonance pressure waves inside the fissure (large pressure gradient with small time period could be generated). The presence of air bubbles in the fissure reduces the wave celerity. The net instantaneous pressure and the time period acting on the block are very important for block uplift. The integration over time determines the net impulse on the block.

The natural period of an open-ended fissure can be obtained as follows (Bollaert (2002b)):

$$T_c = \frac{2 \cdot L_F}{c_{mix}} \tag{5.26}$$

where c_{mix} is the pressure wave celerity and for a mixed fluid, like a mixture of water containing air, can be estimated using Equation (5.27) (valid for $\beta \leq 50\%$ where β is the volumetric air-to-water ratio: $\beta = Q_{air}/Q_w$).

The pressure wave celerity for a mixed fluid is computed with the following equation:

$$c_{mix} = \sqrt[2]{\frac{1}{\rho_{mix}} \cdot \frac{2 \cdot L_F}{\frac{(1-\beta)}{\rho_w \cdot {c_w}^2} + \frac{\beta}{\rho_{air} \cdot {c_{air}}^2}}} \tag{5.27}$$

where c_w is the pressure wave celerity in the liquid (assume 1000 m/s for water), c_{air} the pressure wave celerity in air (assume 340 m/s), ρ_w the density of the liquid (assume 1000 kg/m^3) and ρ_{air} the density of the air (assume 1.29 kg/m^3).

The mixed fluid density ρ_{mix} can be estimated as follows:

$$\rho_{mix} = \rho_{air} \cdot \beta + \rho_w \cdot (1 - \beta) \tag{5.28}$$

L_F is the characteristic fracture length and can be evaluated as follows:

$$L_F = x_b + 2 \cdot z_b \tag{5.29}$$

where x_b and z_b are length and height of the block, respectively.

The air content inside the 3-dimensional fissure cannot be measured directly. However, several indirect methods exist (Bollaert (2002b)). For high jet velocities (maximum 30 m/s), the mean air content inside the fissure can fluctuates between 1 and 10%. These huge differences in air content are related to the variety of flow conditions in the plunge pool: for developed jets, a turbulent shear layer containing a lot of free air bubbles impacts the fissure entrance, while for core jets the air is only present during low-frequency turbulences that temporarily diffuse the jet and so entrain air into the fissure. It exist two mechanisms of air bubble transfer from the plunge pool into a 3-dimensional fissure: convective air bubble transfer and air bubble transfer by release and/or resolution from the water (Bollaert (2002b)). The first mechanism is based on the ideal gas law (Henry's law) and depends on the free air presents in the water. The second mechanism correspond to the air dissolved in the water that come out from the solution (water-air) when the pressure as a sudden decrease. Vice versa, the opposite phenomena happen when the pressure show a sudden increase, the air is dissolved in the water. This phenomenon depends on the pressure present in the liquid.

Manso (2006) performed air concentration (C_{air}) measurements at the plunge pool bottom in the LCH experimental facility. Three measurement points have been analyzed: close to the stagnation point (in the center of the jet impact), in the transition zone from the impinging to the wall jet region (10 cm away from the jet impact center) and in the transition zone from the free jet region to the impinging region (in the center of the jet impact but 10 cm higher than the plunge pool bottom). For these measurements points, three water depths Y (0.2, 0.4 and 0.67 m) and 15 jet velocities V_0 (between 6 and 28 m/s) have been analyzed.

The air concentration is computed with the following equation:

$$C_{air} = \frac{\beta}{1 + \beta} \tag{5.30}$$

where β is the volumetric air-to-water ratio.

For the measurements close to the stagnation point, the air concentration (C_{air}) covers a range between 0.02 and 0.08 for all water depths (Y). The data dispersion is very small for the whole jet velocity range. For the transition zone, from the impinging region to the wall jet region, the air concentration C_{air} covers a range between 0.04 and 0.4 for all water depths. The

highest values correspond to 0.2 m and the lower values to 0.67 m water depth. Furthermore the data follow the same trend line (increase in air concentration with the jet velocity). The measurements performed in the transition zone, from the free jet region to the impinging region, the air concentration behavior is similar to the one observed for the previous measurement points. The air concentration C_{air} covers a range between 0.03 and 0.28 for all water depths.

For the estimation of the natural frequency of the fissure it was assumed that the air concentration inside the fissure is the same than at the plunge pool bottom. If the extreme air concentration values (C_{air}) were used to compute the fissure natural frequency, the following results were found: for the lower air concentration ($C_{air} = 0.02$) the computed frequency was $f \sim 72$ Hz and for the highest air concentration ($C_{air} = 0.4$) the computed frequency was $f \sim 22$ Hz. Intermediate air concentration values give results between this two extreme boundary values.

5.7 Natural frequency of highly instrumented block

Each natural frequency of a linear structure can be associated with a mode shape that characterizes the form of the free vibrations of the structure. The mode shape gives the relative displacement of points on a structure as the structure vibrates in a given mode. The total displacement is the sum of the modal displacement (Blevins (2001)).

The fundamental frequency is defined as the lowest frequency of a periodic waveform. In terms of a superposition of sinusoids (Fourier series), the fundamental frequency is the lowest frequency sinusoidal in the sum.

All sinusoidal and many non-sinusoidal waveforms are periodic, which repeat exactly over time. A single period is thus the smallest repeating unit of a signal, and one period describes the signal completely.

5.7.1 Single degree of freedom (SDoF) of an oscillator without damping effects

A free oscillating body and not damped can be modeled as a 2-dimensional spring supported body. This would be a single degree of freedom (SDoF) oscillator without damping according Gruber and Willy (1998). The equation of motion of a simple 2-dimensional spring supported body without external solicitation can be written as:

$$m \cdot \ddot{x} + k \cdot x = 0 \tag{5.31}$$

where m is the mass of the body, k the system stiffness and x the displacement of the body from the equilibrium position.

The solution of Equation (5.31) becomes:

$$x(t) = C \cdot \cos(\omega_n \cdot t + \phi) \tag{5.32}$$

where C and ϕ are constants and ω_n the angular frequency.

Once set into motion it will oscillate at its natural frequency. For a single degree of freedom oscillator, a system in which the motion can be described by a single coordinate, the natural frequency depends on two system properties: the body mass and the system stiffness. The angular frequency ω_n can be found using the following equation:

$${\omega_n}^2 = \frac{k}{m} \tag{5.33}$$

where k is the system stiffness, m the body mass and ω_n the angular frequency.

The body natural frequency f_n can be found by simply dividing the angular frequency ω_n by 2π. Without first finding the angular frequency, the body natural frequency can be found directly using the following equation:

$$f_n = \frac{1}{2 \cdot \pi} \cdot \sqrt[2]{\frac{k}{m}} \tag{5.34}$$

where f_n is the body natural frequency, k the system stiffness and m the body mass.

In the modal analysis of structures, the frequency of 1^{st} mode is called fundamental frequency. The natural period T_n is the length of time taken by one cycle, and is the reciprocal of the frequency f_n.

$$T_n = \frac{1}{f_n} = 2 \cdot \pi \cdot \sqrt[2]{\frac{m}{k}} \tag{5.35}$$

5.7.2 Single degree of freedom (SDoF) of an oscillator with damping effects

A free oscillating body can be modeled as a 2-dimensional spring supported body. This would be a single degree of freedom (SDoF) oscillator with damping according Gruber and Willy (1998). In real oscillators the friction is considered as a damping effect. The damping effect slows down the body motion: it tends to reduce the amplitude of the body oscillations. In an oscillating system, the frictional force can be modeled as being proportional to the body displacement velocity (Eq. (5.36)).

$$F_f = -c \cdot v = -c \cdot \dot{x} \tag{5.36}$$

where c is the viscous damping coefficient and v the body displacement velocity.

The equation of motion of a simple 2-dimensional spring-supported body without damping (Eq. (5.31)) must be modified and can be written as:

$$m \cdot \ddot{x} + c \cdot \dot{x} + k \cdot x = 0 \tag{5.37}$$

where m is the mass of the body, c the viscous damping coefficient, k the system stiffness and x the displacement of the body from the equilibrium position.

The solution of Equation (5.37) becomes:

$$\ddot{x} + 2 \cdot \xi \cdot \omega_n \cdot \dot{x} + {\omega_n}^2 \cdot x = 0 \tag{5.38}$$

where ω_n is the undamped angular frequency of the oscillator and ξ the damping ratio.

The solution of Equation (5.37) becomes:

$$x\,(t) = C \cdot e^{-\lambda \cdot t} \tag{5.39}$$

where C and λ are constants. λ is given by the following equation:

$$\lambda = \xi \pm \sqrt[2]{\xi^2 - {\omega_n}^2} \tag{5.40}$$

where ξ is the damping ratio and ω_n the angular frequency.

The angular frequency ω_n is computed with the same equation (Eq. (5.33)) that has been used for a single degree of freedom (SDoF) oscillator without damping. The damping ratio is computed with the following equation:

$$\xi = \frac{c}{2 \cdot m} \tag{5.41}$$

where c is the viscous damping coefficient and m the mass of the body.

The value of the damping ratio ξ determines the behavior of the system. A damped harmonic oscillator can be:

- Overdamped ($\xi > \omega_n$): The system returns (exponentially decays) to equilibrium without oscillating. Larger values of the damping ratio ξ return to equilibrium slower.
- Critically damped ($\xi = \omega_n$): The system returns to equilibrium as quickly as possible without oscillating.
- Underdamped ($0 < \xi < \omega_n$): The system oscillates (at reduced frequency compared to the undamped case) with the amplitude gradually decreasing to zero.
- Undamped ($\xi = 0$): The system oscillates at its natural resonant frequency (ω_n).

The damped natural (angular) frequency ω_d is the frequency of the oscillations occurring when the system is underdamped ($0 < \xi < \omega_n$) and under free vibration with regards to the damping factor ξ and the undamped natural (angular) frequency ω_n is given by the following equation:

$$\omega_d = \sqrt[2]{{\omega_n}^2 - \xi^2} = \omega_n \cdot \sqrt[2]{1 - \frac{c^2}{4 \cdot m \cdot k}} \tag{5.42}$$

where ω_n is the angular frequency, ξ the damping ratio, c the viscous damping coefficient, k the system stiffness and m the mass of the body.

This has not to be confused with the resonant frequency Ω_{peak}. Mechanical resonance is the tendency of a mechanical system to absorb more energy when the frequency of its oscillations matches the system's natural frequency of vibration than it does at other frequencies.

The quality factor Q of a damped oscillator is defined as:

$$Q = \frac{1}{2} \cdot \frac{\omega_n}{\xi} = \frac{m}{c} \cdot \omega_n \tag{5.43}$$

where ω_n is the angular frequency and ξ the damping ratio.

A big quality factor corresponds to lower energy dissipation. The resonant frequency is given by the following equation:

$$\Omega_{peak} = \omega_n \cdot \sqrt[2]{1 - \frac{1}{2 \cdot Q^2}} = \omega_n \cdot \sqrt[2]{1 - \frac{\xi^2}{2 \cdot m \cdot k}} \tag{5.44}$$

where ω_n is the angular frequency, c the viscous damping coefficient, k the system stiffness and m the mass of the body.

For a constant friction coefficient the following expression is valid $\omega_n > \omega_d > \Omega_{peak}$. The three frequencies are related as follows:

$$\omega_d^2 - \Omega_{peak}^2 = \omega_n^2 - \omega_d^2 = \left(\frac{c}{2 \cdot m}\right)^2 \tag{5.45}$$

where ω_n is the angular frequency, ω_d the damped natural frequency and Ω_{peak} the resonant frequency.

5.7.3 Block natural frequency

The highly instrumented block can be modeled as a simple spring-supported damped symmetric 2-dimensional body vibrating in a fluid (Figure 5.6). The block natural frequency $f_{n,b}$ is:

$$f_{n,b} = \frac{1}{2 \cdot \pi} \cdot \sqrt[2]{\frac{k}{m_b + m_{am}}} \tag{5.46}$$

where k is the system stiffness, m_b the body mass and m_{am} the added mass.

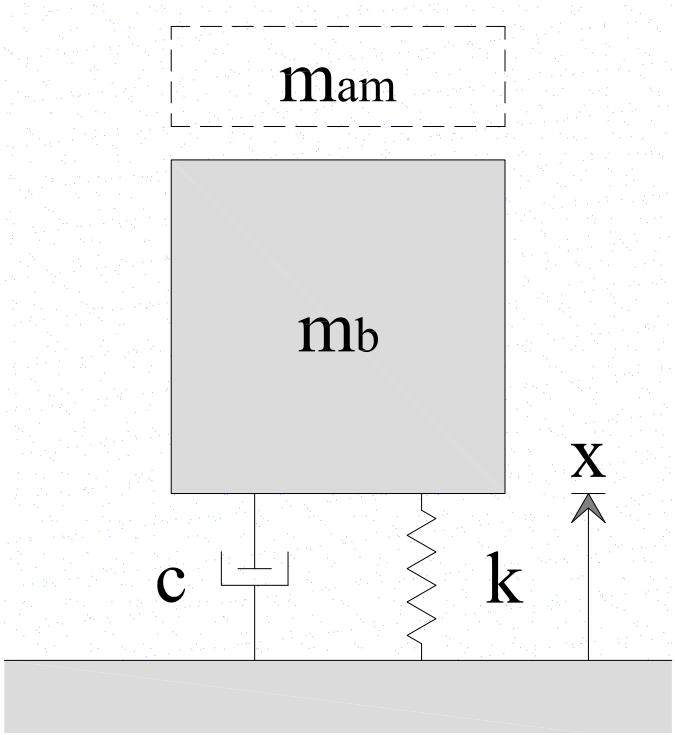

Figure 5.6: 2-dimensional spring supported, damped body in a still fluid where m_b is the body mass, m_{am} the added mass, c the viscous damping coefficient and k the system stiffness.

The block natural frequency was obtained experimentally. To obtain this frequency, the highly instrumented block has been solicited with an external oscillator. The block was inserted in the central cavity of the measurement box and has been solicited by a hammer. The block and the measurement box have been alternatively impacted by the hammer to generate external oscillations. Different points on the block and on the measurement box have been impacted to investigate if a different behavior in frequency response exists. These solicitations have been made without and with water inside the surrounding fissure. When the fissure was filled up with water in the plunge pool the water depth reaches 20 cm. A spectral analysis allows to observe the dominant frequencies. For all solicitations the frequency range is situated between 5 and 9 Hz, with a peak around 7 Hz. This frequency corresponds to the eigenfrequency of the measurement box and the block.

The following three parameters are unknown in Equation (5.46) and have to be estimated:

- the system stiffness (k);
- the damping coefficient (c);
- the added mass (m_{am}).

The system stiffness and the damping coefficient for the block depend on the fissure geometry, the water inside the surrounding fissure and the water level in the plunge pool. The added mass depends on the block geometry, the water level in the plunge pool and the boundary conditions near the block.

5.7.3.1 Imposed displacements on block

To evaluate the system damping a series of tests has been performed. The block has been inserted in the measurement box and the surrounding fissure has been filled up with water. A vertical displacement (approximately 6 mm) has been imposed on the block. It has been moved up and the pressures have been recorded during the block displacement. Then it has been moved down and the pressures have been again recorded. The recorded signals have been analyzed. This procedure has been repeated several times. Figure 5.7 shows the pressure and the displacement evolution when the block was moved up and Figure 5.8 shows the evolution when the block was moved down.

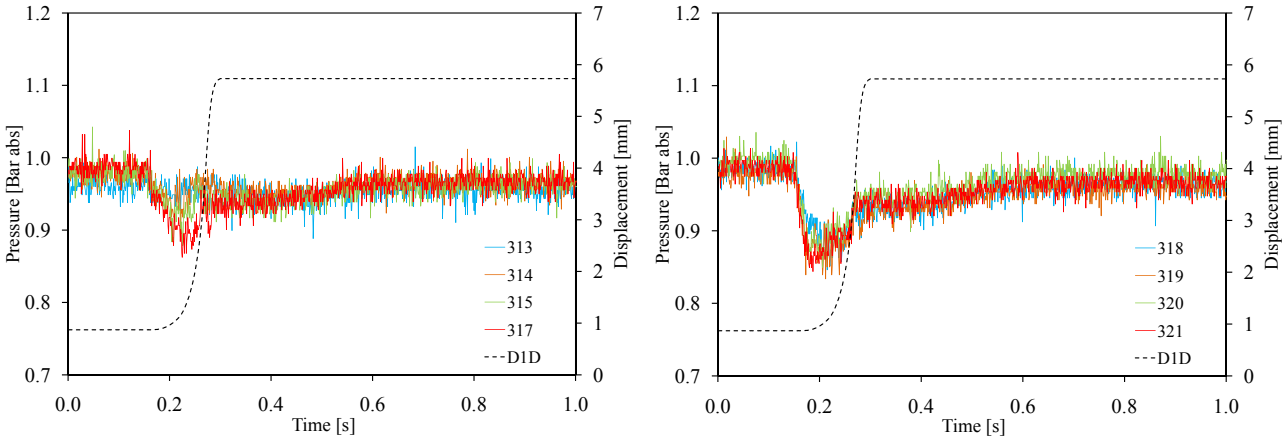

Figure 5.7: Pressure and displacement (D1D) evolution when the block was moved up. Along the vertical fissure for the four pressure transducers N°s 313-317 (left) and underneath the block for the four pressure transducers N°s 318-321 (right).

When the block moves up, the pressure inside the fissure decreases shortly to return approximately at the initial pressure value after a small time interval. This pressure drop appears along the vertical fissure and underneath the block. The pressure drop increases along the vertical fissure, however underneath the block is the same for the four transducers. This pressure drop occurs very fast (< 0.03 s).

When the block moves down, the pressure inside the fissure increase until the block touch the central cavity bottom then return approximately at the initial pressure value. Some peaks appear when the block touches the bottom but are dissipated very fast. The maximal "positive" peak reaches 120% of the initial pressure and the "negative" peach reaches 70% of the initial value. These peaks may be generated by the impact of the block on the bottom of the measurement box and are not related to the block displacements.

When the block moves up the fissure underneath the block (cavity) increases its thickness. This gap has to be filled up with the water situated inside the vertical fissure surrounding the block. At the same time, a pressure decrease occurs around the block (along the vertical fissure and underneath the block). This pressure decrease tries to keep the block near the bottom: a suction effect is generated underneath the block. This suction effect is generated by the water flowing from the vertical fissure to underneath the block. When this cavity is filled up, the

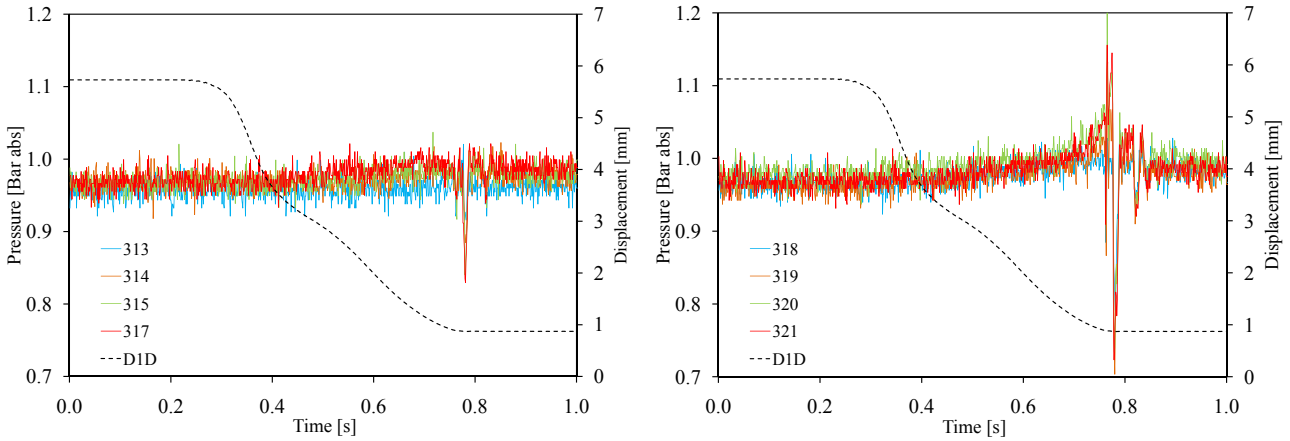

Figure 5.8: Pressure and displacement (D1D) evolution when the block was moved down. Along the vertical fissure for the four pressure transducers N°s 313-317 (left) and underneath the block for the four pressure transducers N°s 318-321 (right).

pressure returns to the normal water head. For small vertical displacements this phenomena reduce the block vertical movements. With an increase of the fissure thickness (underneath the block) this suction effect disappears and the block is more free to move. When the block moves down, the fissure underneath the block decreases its thickness and reaches the initial dimension (∼0.85 mm). The water situated in this cavity must flow back into the surrounding fissure (vertical fissure).

When the block reaches the central cavity bottom some pressure oscillations have been observed. These peaks are generated by the impact of the block with the central cavity bottom and by a pressure wave generated underneath the block. The pressure fluctuations disappear after a time interval of ∼0.1 s. The first pressure oscillation propagates inside the fissure (underneath the block and along the vertical fissure).When this pressure wave reaches the plunge pool bottom it is not reflect by the water in the plunge pool and can flow outside the 3-dimensional fissure: the pressure wave is dissipated. Underneath the block the pressure wave continues its oscillations for a small time and decreases rapidly.

These observations have been made for a 3-dimensional fissure filled up with water but without water in the plunge pool. In real-life conditions the water flow through the fissure and the plunge pool is the boundary condition. The water flow inside the fissure modifies the pressure field surrounding the block. This pressure drop has not been observed during the test because the block displacements are very small and happen very fast (as well they change direction every time increments).

Therefore, the damping effect may be neglected for the computation of the dynamic block impulsion (Chapter 7.1).

5.7.3.2 Estimation of the facility stiffness

The system stiffness can be estimated from the natural frequency $f_{n,b}$ Equation (5.46). The structure eigenfrequency and the block mass are known but the added mass is unknown. In

literature (Chapter 2.4) does not exist a situation similar to our experimental set-up (block strongly confined loaded by high-velocity impinging jet). The added mass has to be estimated for the block impulse computation. The added mass is the variable that has to be calibrated to fit the theoretical uplift (computed with the pressures) with the measured uplift (measured with the displacement transducers). The added mass coefficient changes each time increment and it is not possible to estimate facility stiffness for a time interval.

5.8 Conclusions

The proposed methods for the pressure analysis (Chapter 5.2) are used as a tool to compare and to analyze the different configurations that have been tested (Chapter 4.3.1).

The core of the theoretical background are the tools necessary to compute the dynamic block impulsion with the integration of the added mass concept proposed in Chapter 2.4.

Chapter 6

Test results

6.1 Introduction

In this chapter, the results of only three configurations are explained. The three discussed configurations are the following:

- Eight contact points at lateral guides
  - Jet impact position on the block center with the block free to move (CR);
  - Jet impact position on the block right hand side with the block free to move (SR);
  - Jet impact position on the block corner with the block free to move (CN).

The location of the transducers (pressure, displacement and acceleration) can be seen in Figures 6.1, 6.24 and 6.46 (for more detail see Chapter 4.3.3).

Only the results for the most representative pressure transducers are explained: two on the block upper face (N° 309 and N° 312), two along the vertical fissure (N° 313 and N° 317) and two underneath the block (N° 318 and N° 321).

Only the results of one displacement transducer (D1D) have been explained because the recorded data are very close for both transducers.

The accelerations have been recorded with the accelerometer (ACC) located inside the block.

In this chapter, the pressure values are expressed as relative pressures (without the atmospheric pressure).

6.2 Jet impact position on the block center with the block free to move and equipped with lateral guides having eight contact points (CR)

6.2.1 Configuration description

This configuration is characterized by the following three parameters:

- Jet impact position: *on the center of the block*;
- Degree of freedom: *the block is free to move along the vertical axis*;
- Lateral guides: *eight contact points per lateral guide and two guides per vertical face on the block.*

Figure 6.1 shows the configuration parameters and the transducers positions.

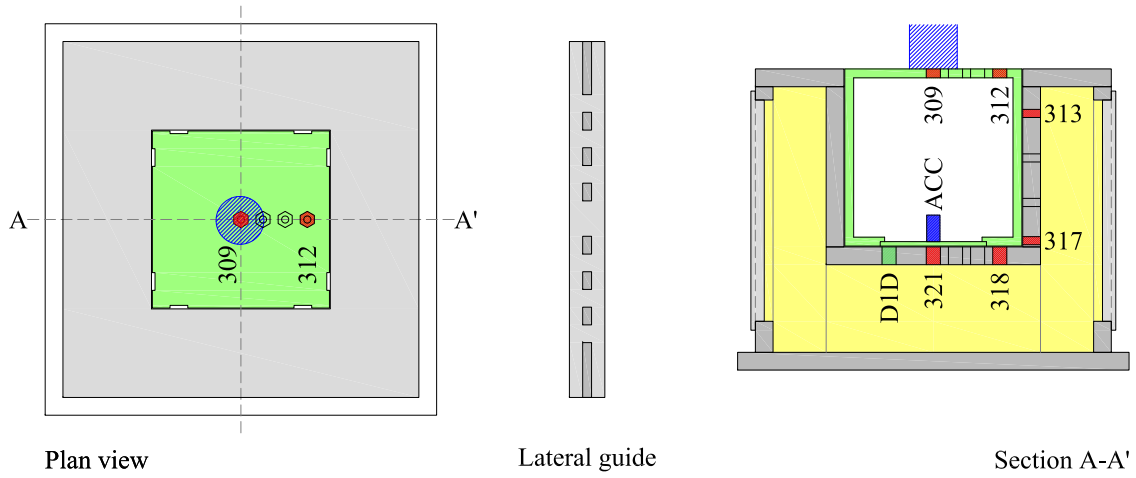

Figure 6.1: New experimental set-up for test configuration CR. Top view with jet impact position (cylinder) and pressure transducers positions (left), lateral guide fixed on the block lateral faces (center) and transversal section with jet impact position (cylinder) and transducers positions (pressure transducers N° 309 to N° 321, displacement transducer D1D and accelerometer ACC.

Table 6.1 summarizes the parameter combinations (water depth Y, jet discharge Q, jet velocity V_0, Y/D ratio and jet type) that have applied to this configuration.

6.2.2 Pressure field surrounding the block

The pressure field surrounding the block (at the plunge pool bottom and inside the 3-dimensional fissure) is explained in this section. The pressures are relative and have been normalized by

Water depth Y [m]	Discharge Q [l/s]	Jet velocity V_0 [m/s]	Y/D ratio [-]	Jet Type [-]
0.0	10-110	2.5-27.0	0.0	Core jet
0.1	10-110	2.5-27.0	1.4	Core jet
0.2	10-110	2.5-27.0	2.8	Core jet
0.3	10-110	2.5-27.0	4.2	Transition jet
0.4	10-110	2.5-27.0	5.6	Transition jet
0.5	10-110	2.5-27.0	6.9	Developed jet
0.6	10-110	2.5-27.0	8.3	Developed jet
0.7	10-110	2.5-27.0	9.7	Developed jet

Table 6.1: Main parameters that have been tested with configuration CR: water depth Y, jet discharge Q, jet velocity V_0, Y/D ratio and jet type.

the kinetic energy of the jet ($V_0^2/2 \cdot g$). The small jet velocities show the largest values due to the small kinetic energy.

Transducer 309 (at the center of the block upper face: stagnation point)
Following Beltaos and Rajaratnam (1973) (Figure 5.1) transducer N° 309 is located at the stagnation point (block center) in the impinging region. The pressure acting on the block center shows the same trend for the three jet types (core, transition and developed jets, Figure 6.2).

Maximum pressures grow quadratically as a function of the jet velocity but the normalized pressure decreases due to be normalized by kinetic energy. With an increase of jet velocity, some small differences can be observed for maximum pressures. These differences are related to the jet type. Core jets (Y/D $<$ 4) show the highest pressure values: the water jet impacts directly on the block and the jet energy is converted into pressure with few energy lost during the jet travel through the plunge pool (due to the small water depths $<$ 0.2 m). Developed jets (Y/D $>$ 6) show the smaller maximum pressures. The difference between core and developed jets grows as a function of the jet velocity and reaches approximately 1 Bar for a jet velocity of 27.0 m/s.

Mean pressures grow with the same trend (quadratically) for all water depths along the whole range of jet velocities. Mean pressure increases as a function of the Y/D ratio. Only the 0.7 m water depth (Y/D = 9.7) shows a different behavior: between 9.8 and 24.6 m/s mean pressure is approximately 0.2 Bar lower than for the other water depths. For the largest jet velocity this difference reaches ∼0.5 Bar.

Minimum pressures are almost constant for the three jet types with some small fluctuations but the normalize pressure did not shows clearly this behavior.

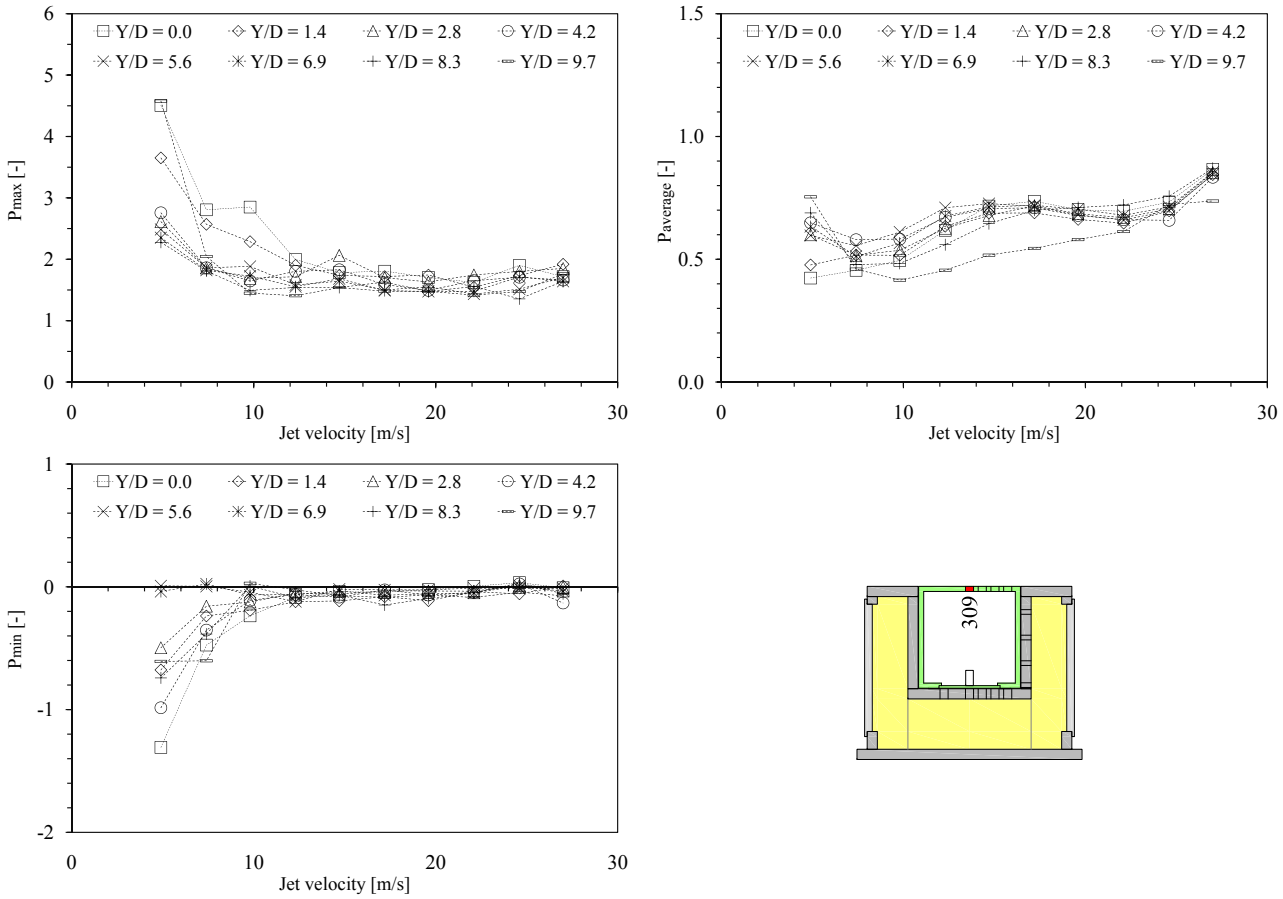

Figure 6.2: Normalized pressure measured with transducer N° 309 for configuration CR as a function of jet velocity (2.5-27.0 m/s) and Y/D ratio (0-9.7). Maximum pressure (top left), mean pressure (top right), minimum pressure (bottom left) and transducer location (bottom right).

Transducer 312 (near the fissure entrance on the block upper face)

Transducer N° 312 is located at the boundary between impingement region and wall jet region (Figure 5.1) where the jet is deflected after the impact with the plunge pool bottom (at 75 mm from the stagnation point). As before, the pressures acting on the block show the same trend and similar behaviors for core, transition and developed jets (Figure 6.3).

Maximum pressures grow quasi-linearly up to the second-last jet velocity (24.6 m/s) where the pressure increase is stronger: maximum pressure for the largest jet velocity (27.0 m/s) is almost the double of the previous jet velocity. Core jets show the highest pressures: as before the jet impacts directly on the block and the energy is converted into pressure (small water depths).

With an increase of the jet velocity, an oscillating hydraulic jump appears between the plunge pool wall and the plunge pool center (stagnation point). The oscillating hydraulic jump moves to the plunge pool center and generates some pressure fluctuations at the bottom. With the largest jet velocity the hydraulic jump reaches the block (schematic movements of the hydraulic jump see Figure 6.4). This hydraulic jump may generate this highest pressures measured near the fissure entrance.

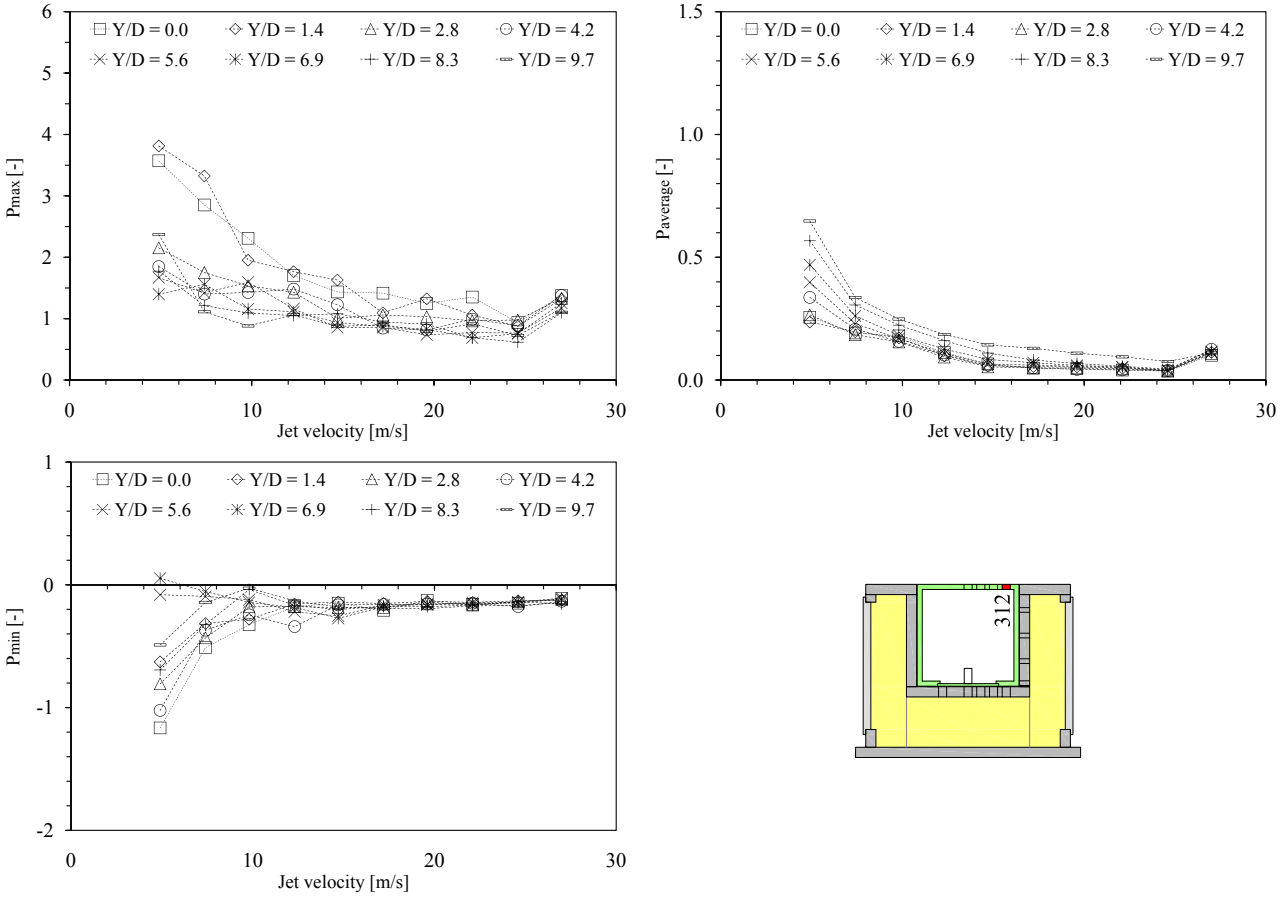

Figure 6.3: Normalized pressure measured with transducer N° 312 for configuration CR as a function of jet velocity (2.5-27.0 m/s) and Y/D ratio (0-9.7). Maximum pressure (top left), mean pressure (top right), minimum pressure (bottom left) and transducer location (bottom right).

Mean pressures grow weakly along the whole range of jet velocities and depends by the Y/D ratio (influence of the water load). As observed for maximum pressures, mean pressures for the largest jet velocity show a significant pressure increase corresponding to ∼0.2-0.3 Bar.

Minimum pressures decrease with increasing jet velocity and show negative values for core, transition and developed jets. An increase of the bottom flow velocity, generated by the jet deflection, reduces the minimum pressure at the plunge pool bottom and generates these negative values.

The pressures recorded at 75 mm from the stagnation point (transducer N° 312) are lower than at the block center (transducer N° 309) as we can aspect. If the pressures (maximum, mean and minimum) measured with the four transducers situated on the block upper face (N°s 309 to 312) are plotted together, the pressure field acting on the block upper face (Figure 6.9) shows a exponential distribution as explained in literature (Chapter 5.1.1.3).

Transducer 313 (inside the vertical fissure near the plunge pool bottom)

Transducer N° 313 is located inside the vertical fissure at 50 mm from the plunge pool bottom. Maximum pressures increase quasi-linearly as a function of the jet velocity (Figure 6.5). The

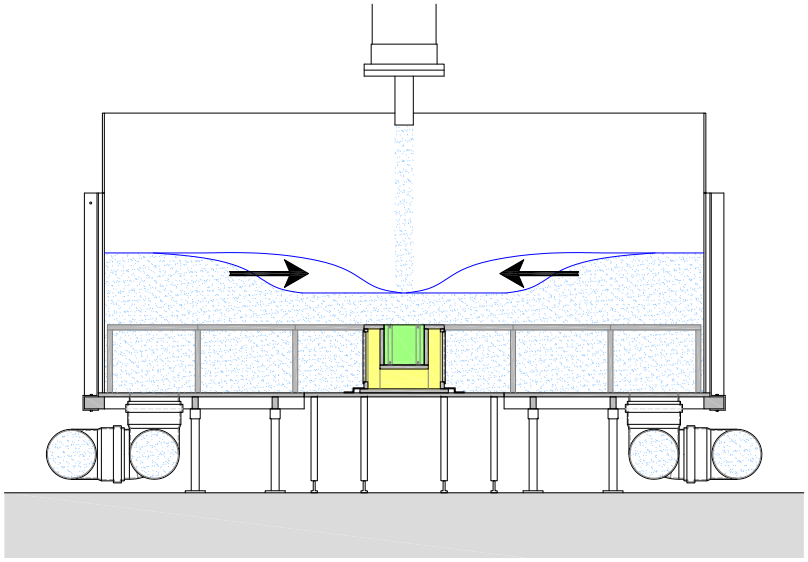

Figure 6.4: Sketch of the oscillating hydraulic jump generated inside the plunge pool.

three jet types show the same trend: for the largest jet velocity (27.0 m/s) suddenly the pressure increase approximately of 1.5 Bar. A similar behavior was observed for transducer N° 312 situated near the fissure entrance. The growth of the maximum pressure, relate to the largest jet velocity, may be explained by the oscillating hydraulic jump moving from the plunge pool wall to the plunge pool center. For a jet velocity of 27.0 m/s, the hydraulic jump reaches the block and the pressure fluctuations generate by itself penetrates inside the 3-dimensional fissure (Figure 6.4) and produce this particular behavior. Or this behavior may be generated by compression-decompression phenomenon of the air bubbles present in the water near the fissure entrance.

Mean pressures grow quadratically and are almost the same for all water depths until the 24.6 m/s jet velocity where the same phenomenon, that has been observed for the maximum pressure, is observable. Mean pressure increases as a function of the Y/D ratio.

Minimum pressures are almost constants for all water depths and all jet velocities with some small pressure fluctuations.

Transducer 317 (inside the vertical fissure near the central cavity bottom)

Transducer N° 317 is located 7 mm from the bottom of the central cavity (or 194 mm from the plunge pool).

Maximum pressures grow quadratically for all water depths (Figure 6.6). Maximum pressures are smaller than near the fissure entrance (Figure 6.5) and the suddenly pressure increase for the 27.0 m/s jet velocity disappears. The pressure fluctuations generated by the oscillating hydraulic jump have been attenuated inside the vertical fissure.

Mean pressures grow quadratically for all water depths and are similar at the values recorded near the fissure entrance (mean pressures change weakly inside the vertical fissure).

Minimum pressures are similar to the pressures recorded near the fissure entrance with some small pressure fluctuations.

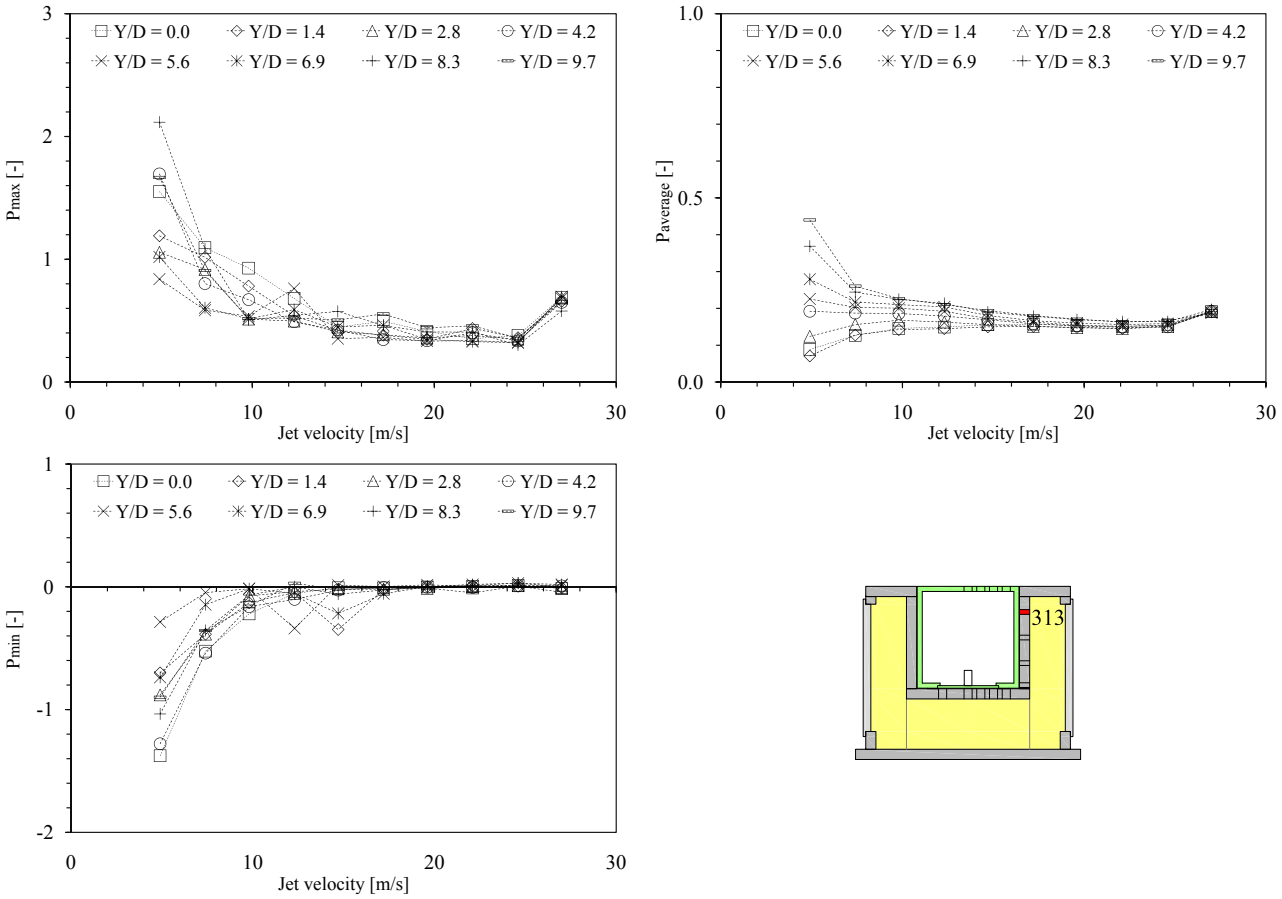

Figure 6.5: Normalized pressure measured with transducer N° 313 for configuration CR as a function of jet velocity (2.5-27.0 m/s) and Y/D ratio (0-9.7). Maximum pressure (top left), mean pressure (top right), minimum pressure (bottom left) and transducer location (bottom right).

Transducer 318 (underneath the block near the vertical fissure)

Transducer N° 318 is located underneath the block, at 25 mm from the vertical fissure on the same vertical axis than transducer N° 312.

The passage from the vertical fissure to the fissure situated underneath the block did not affect the pressure values (Figure 6.7). Maximum, mean and minimum pressure values show exactly the same trend and have almost the same values than transducer N° 317 situated at the end of the vertical fissure (Figure 6.6).

Transducer 321 (underneath block in the center of the measurement box)

Transducer N° 321 is located underneath the block, in the center of the measurement box on the same axis of the stagnation point (N° 309).

The pressure propagation underneath the block (Figure 6.8) shows an increase of maximum pressures and a small decrease of minimum pressures for jet velocities larger than 14.7 m/s. This increase of the maximum pressures was not observed for the other transducers situated underneath the block (not only for transducer N° 318). This increase of pressures may be the

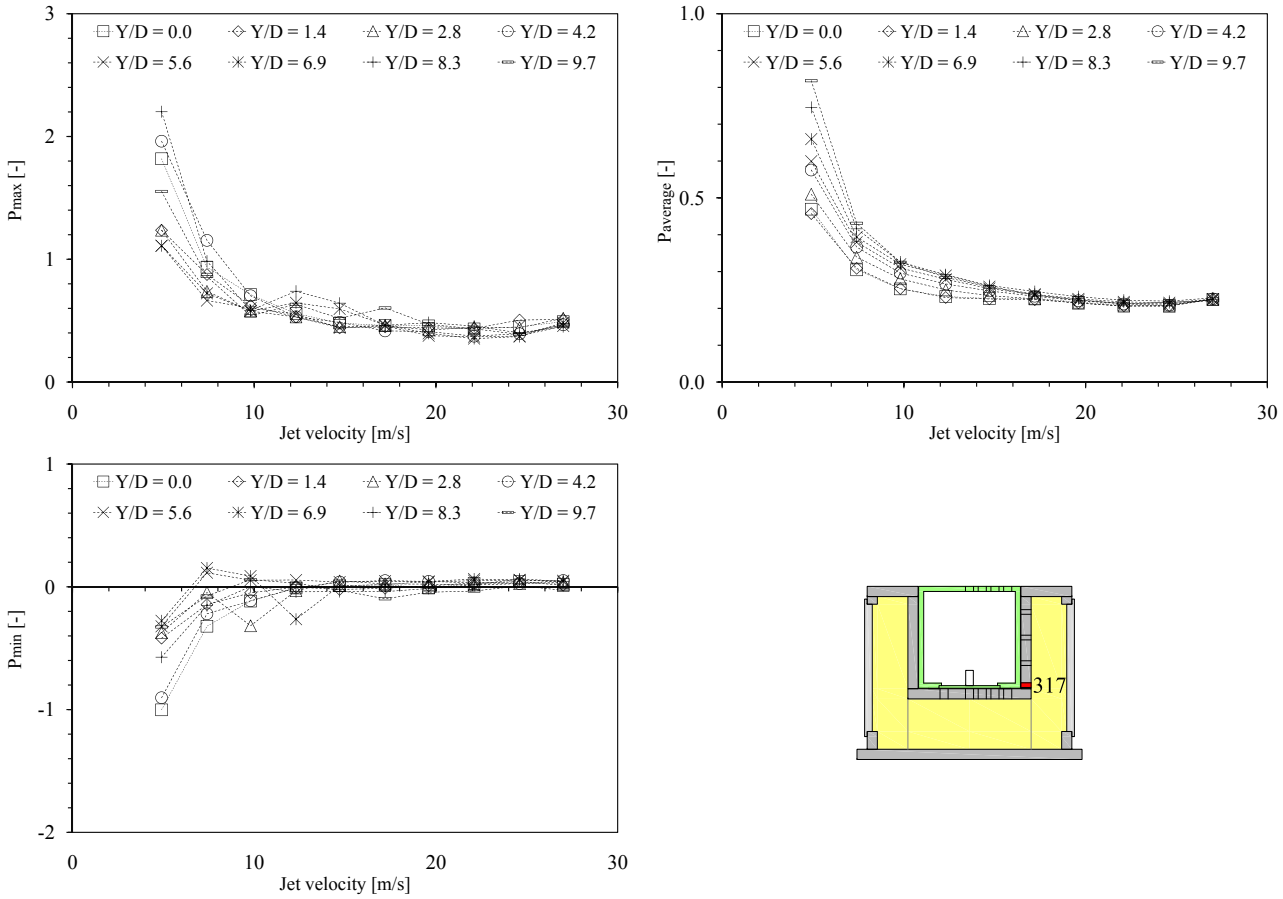

Figure 6.6: Normalized pressure measured with transducer N° 317 for configuration CR as a function of jet velocity (2.5-27.0 m/s) and Y/D ratio (0-9.7). Maximum pressure (top left), mean pressure (top right), minimum pressure (bottom left) and transducer location (bottom right).

result of a sum of different pressure waves travelling underneath the block and linked to the block vertical displacements (Figure 6.16). Not only the pressures acting underneath the block are important to generate block displacements, but also the pressures acting on the block upper face. Mean pressures are almost similar to the pressure values recorded near the vertical fissure (N° 318).

Pressure field surrounding the block

Figure 6.9 gives an example of the pressure field acting on the block for a Y/D ratio of 8.3 and a jet velocity of 27.0 m/s. The pressures are expressed as absolute pressures [Bar abs].

On the block upper face the pressure decreases following the exponential distribution proposed in literature (as an example by Cola (1966) or Beltaos and Rajaratnam (1973), Chapter 5.1.1.3). Inside the vertical fissure the mean pressure increases weakly from the plunge pool to the central cavity bottom. The evolution of maximum and minimum pressures along the vertical fissure follows a conic-shape: the larger values have been recorded near the fissure entrance and the smaller values near the central cavity bottom (at the end of the vertical fissure). Underneath the block the pressures (maximum, mean and minimum) are almost constant. The

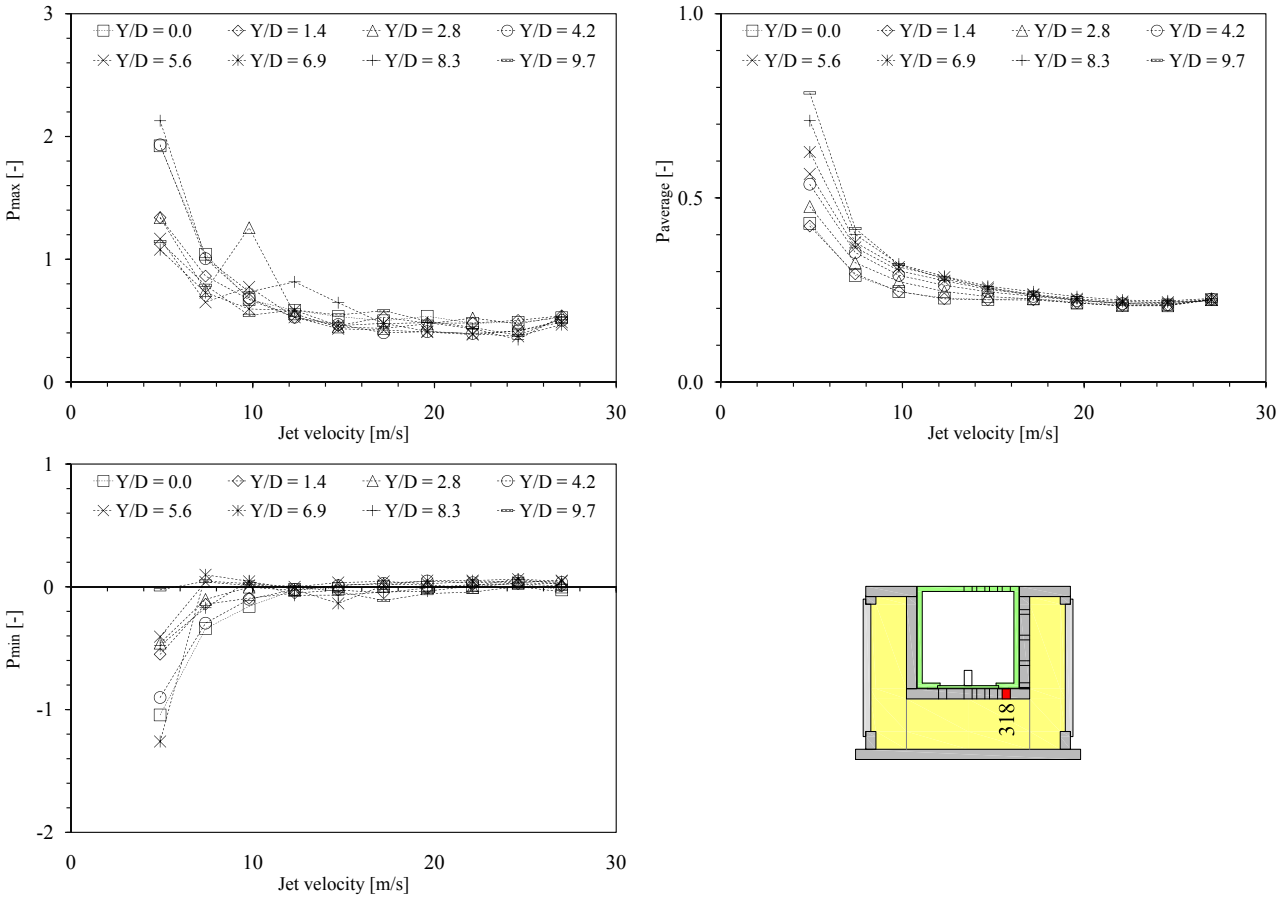

Figure 6.7: Normalized pressure measured with transducer N° 318 for configuration CR as a function of jet velocity (2.5-27.0 m/s) and Y/D ratio (0-9.7). Maximum pressure (top left), mean pressure (top right), minimum pressure (bottom left) and transducer location (bottom right).

same behavior has been observed for the other water depths (core, transition and developed jets) and jet velocities. The difference in the pressure values is only related to the jet velocity: more the jet is faster and more the pressures inside the fissure increase.

6.2.3 Pressure coefficients

In this section non-dimensional pressure coefficients are presented (the formulas have been described in Chapter 5.2.2). These pressure coefficients have been computed using the pressures measured on the block upper face (at the plunge pool bottom) and inside the 3-dimensional fissure surrounding the block.

6.2.3.1 Mean pressure coefficient C_p

The mean pressure coefficients (C_p, Figure 6.10) computed directly on the block at the plunge pool bottom (transducers N° 309 and N° 312) are in reasonable agreement with the theoretical curves developed by Ervine et al. (1997) and with previous pressure records made by Bollaert (2002b) and Manso (2006). The theoretical curves proposed by Ervine et al. (1997) have been

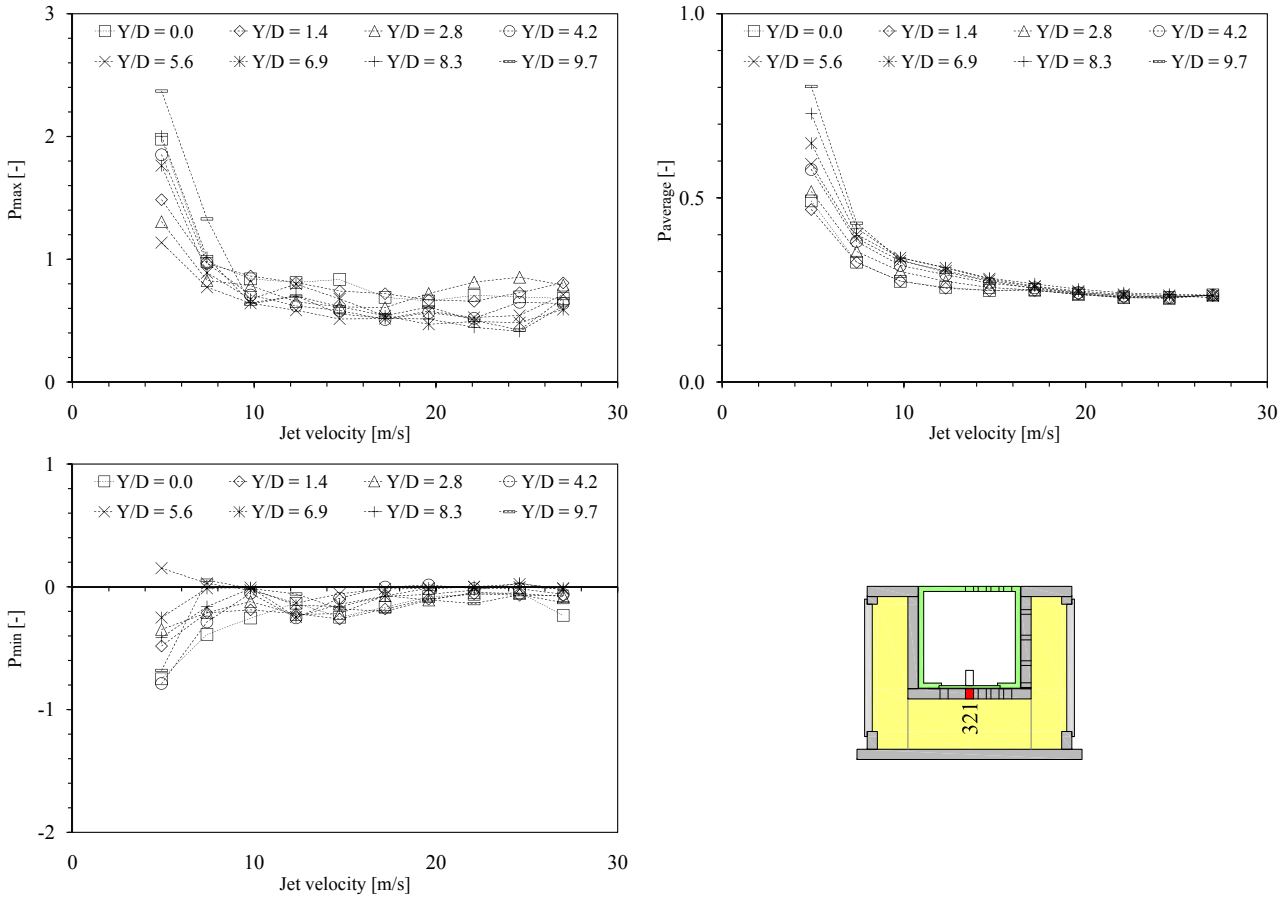

Figure 6.8: Normalized pressure measured with transducer N° 321 for configuration CR as a function of jet velocity (2.5-27.0 m/s) and Y/D ratio (0-9.7). Maximum pressure (top left), mean pressure (top right), minimum pressure (bottom left) and transducer location (bottom right).

developed using measurements performed at the plunge pool bottom only.

Transducer N° 309, located at the stagnation point, shows a good correlation with the theoretical curves for all Y/D ratios. Transducer N° 312, located at 75 mm from the stagnation point near the vertical fissure entrance, shows lower coefficient values than transducer N° 309 (as observed in the pressure field): the pressure acting on the block decreases from the stagnation point radially outwards following a exponential distribution. Hence, the mean pressure coefficient is less than in the center of the block. The coefficient values ranges between 0.03 and 0.15.

The mean pressure coefficients computed inside the 3-dimensional fissure are lower than the corresponding coefficients computed directly under the jet. The coefficient values inside the fissure are more similar to the values observed near the fissure entrance (transducer N° 312) as could reasonably be expected. However, the coefficient values computed inside the fissure are slight higher. Along the vertical fissure transducer N° 317 located near the central cavity bottom shows higher values than transducer N° 313 situated near the fissure entrance, but similar values to the data recorded underneath the block (transducers N° 318 and N° 321). The mean pressure coefficients for transducers located inside the fissure range between 0.15

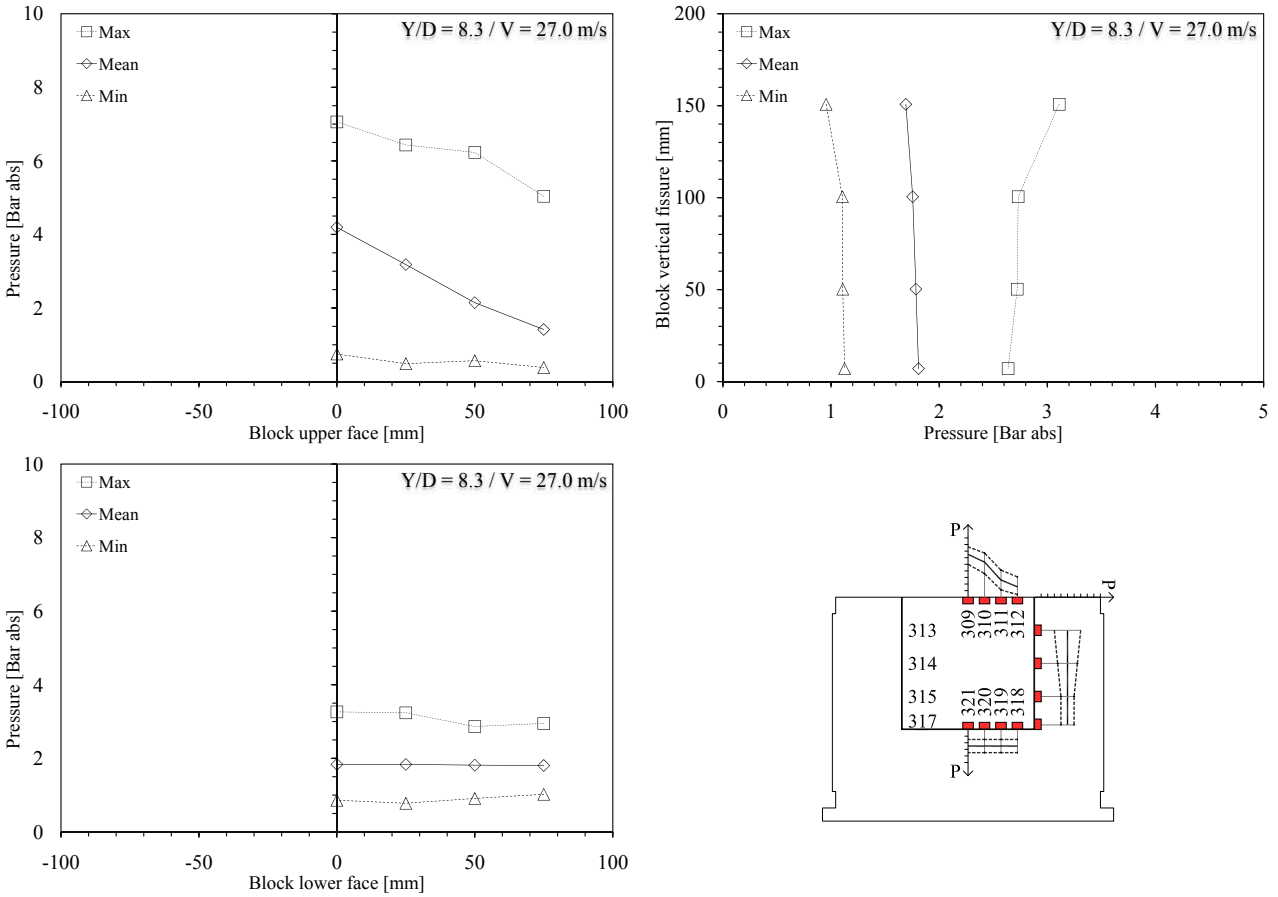

Figure 6.9: Pressure field acting around the block for configuration CR, a developed jet (Y/D = 8.3) and a jet velocity of 27.0 m/s. Pressure acting on the block upper face (top left), along the vertical fissure (top right), underneath the block (bottom left) and pressure filed sketch (bottom right). Pressures are expressed in absolute Bar.

and 0.25. Nevertheless transducer N° 313 located near the fissure entrance shows a different limit of only 0.05.

On the block upper face and near the stagnation point the coefficient values follow the curves proposed by Ervine et al. (1997). Far away from this point and inside the fissure are almost constant for a given jet velocity and did not show this degrowth of coefficients for Y/D ratios larger than 6. The kinetic energy used to normalize the coefficient in the mathematical formula, influence the computed values: the larger jet velocities show the smaller coefficients.

6.2.3.2 Turbulent pressure fluctuation coefficient $C_{p'}$

The turbulent pressure fluctuation coefficients ($C_{p'}$, Figure 6.11) recorded all around the block are in reasonable agreement with the theoretical curves developed by Ervine et al. (1997). However, for core jets (Y/D $<$ 4) generated by jet velocities up to 12.3 m/s, the coefficient values are slightly higher than the theoretical curves. Transition and developed jets (Y/D $>$ 4) follow the theoretical curves. The coefficient values computed with the transducers situated inside the fissure are lower than the coefficient values recorded at the plunge pool bottom for the same jet velocity. The coefficients computed at the stagnation point (transducer N° 309)

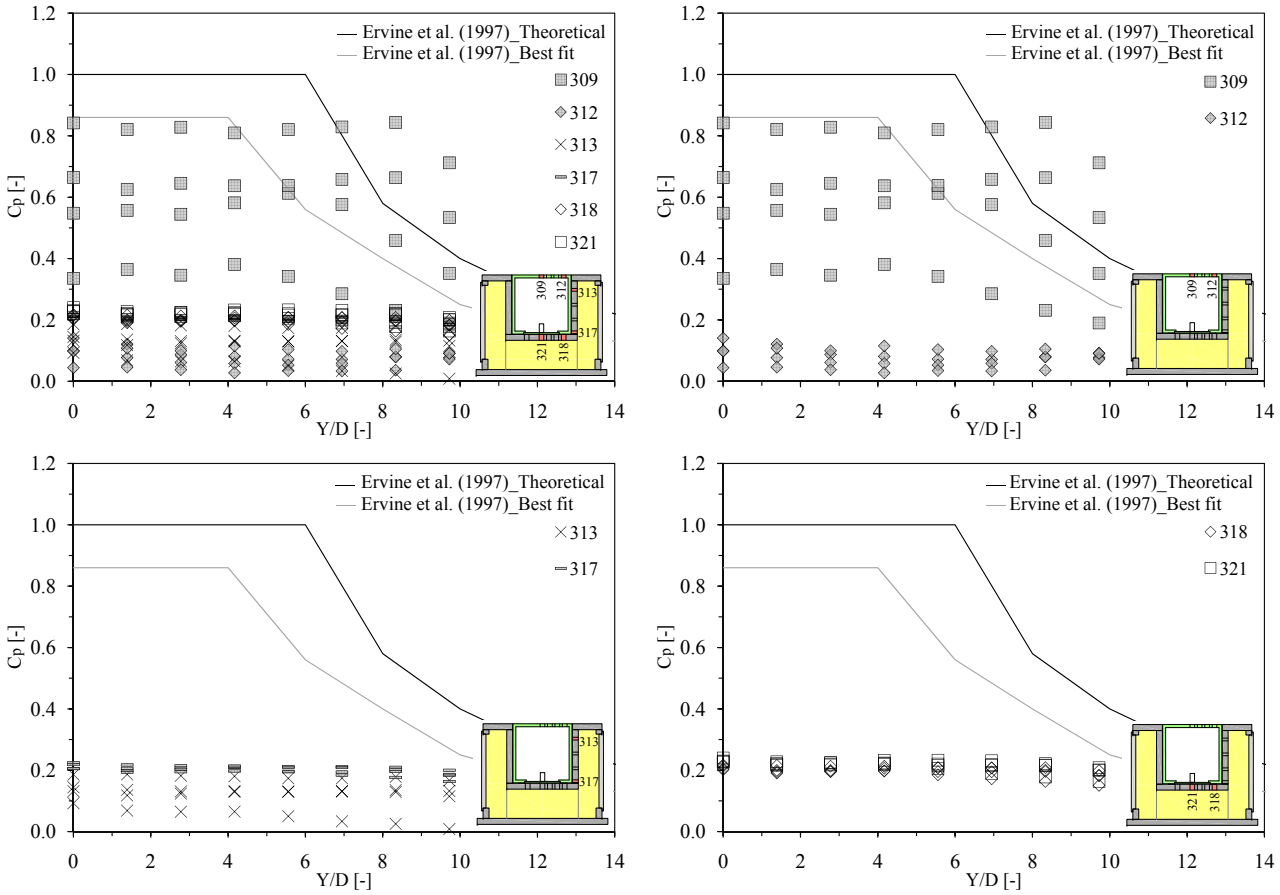

Figure 6.10: Mean pressure coefficient C_p computed for configuration CR as a function of jet velocity (4.9, 12.3, 19.6 and 27.0 m/s) and Y/D ratio (0-9.7). Overview of the six pressure transducers (top left), on the block upper face or at the plunge pool bottom (top right), along the vertical fissure (bottom left) and underneath the block (bottom right).

are always higher than the coefficients recorded at 75 mm from the stagnation point (transducer N° 312). Far away from the stagnation point the pressure fluctuations are less intense for the same jet velocity.

Along the vertical fissure, the transducers N° 313 and N° 317 show the same values. Underneath the block, transducer N° 321 situated at the block center shows higher values than transducer N° 318 situated near the vertical fissure as observed in the pressure field (Figures 6.7 and 6.8). These differences disappear with an increase of the jet velocity. The coefficient values range between 0.03 and 0.16. As before, the normalizing kinetic energy influence the coefficient values (a larger jet velocity generated small coefficients).

6.2.3.3 Positive extreme pressure fluctuation coefficient C_p^+

The positive extreme pressure fluctuation coefficients (C_p^+, Figure 6.12), for transducers situated on the block upper face (N° 309 and N° 312) are higher than the theoretical curve proposed by Ervine et al. (1997). The coefficient values, for these transducers, decrease with an increase of the Y/D ratio. The positive extreme fluctuations are more intense for core jets (Y/D < 4).

For the three jet types the coefficients computed inside the 3-dimensional fissure show a weak

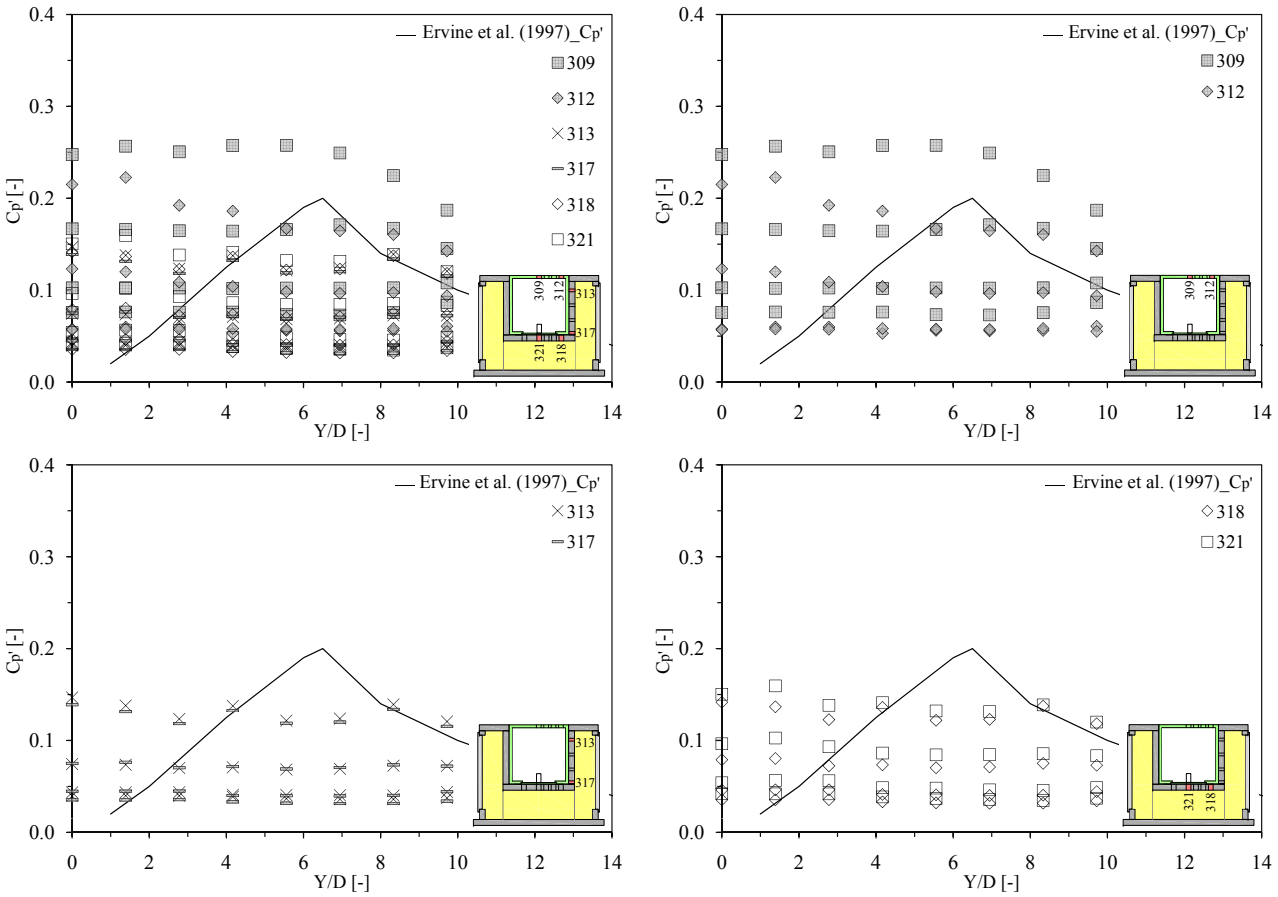

Figure 6.11: Turbulent pressure fluctuation coefficient $C_{p'}$ computed for configuration CR as a function of jet velocity (4.9, 12.3, 19.6 and 27.0 m/s) and Y/D ratio (0-9.7). Overview of the six pressure transducers (top left), on the block upper face or at the plunge pool bottom (top right), along the vertical fissure (bottom left) and underneath the block (bottom right).

decrease as a function of the Y/D ratio and are situated in the same range of values. Along the vertical fissure, transducer N° 317 situated near the central cavity bottom shows lower values than transducer N° 313 situated near the fissure entrance for the same jet velocity. This difference is related to the pressure field acting along the vertical fissure. Underneath the block transducer N° 321 situated at the block center shows higher coefficient values than transducer N° 318 situated near the vertical fissure. These differences disappear with an increase of the jet velocity. The coefficients range between 0.15 and 0.7.

6.2.3.4 Negative extreme pressure fluctuation coefficient C_p^-

The negative extreme pressure fluctuation coefficients (C_p^-, Figure 6.13) are in good agreement with the theoretical curve proposed by Ervine et al. (1997) except for transducer N° 309 situated at the stagnation point. This transducer shows higher coefficient values than transducer N° 312 situated near the fissure entrance. The negative pressure values increase radially outwards from the stagnation point and, for this reason, the coefficient values recorded far away from the stagnation point decrease. This trend is valid for core, transition and developed jets.

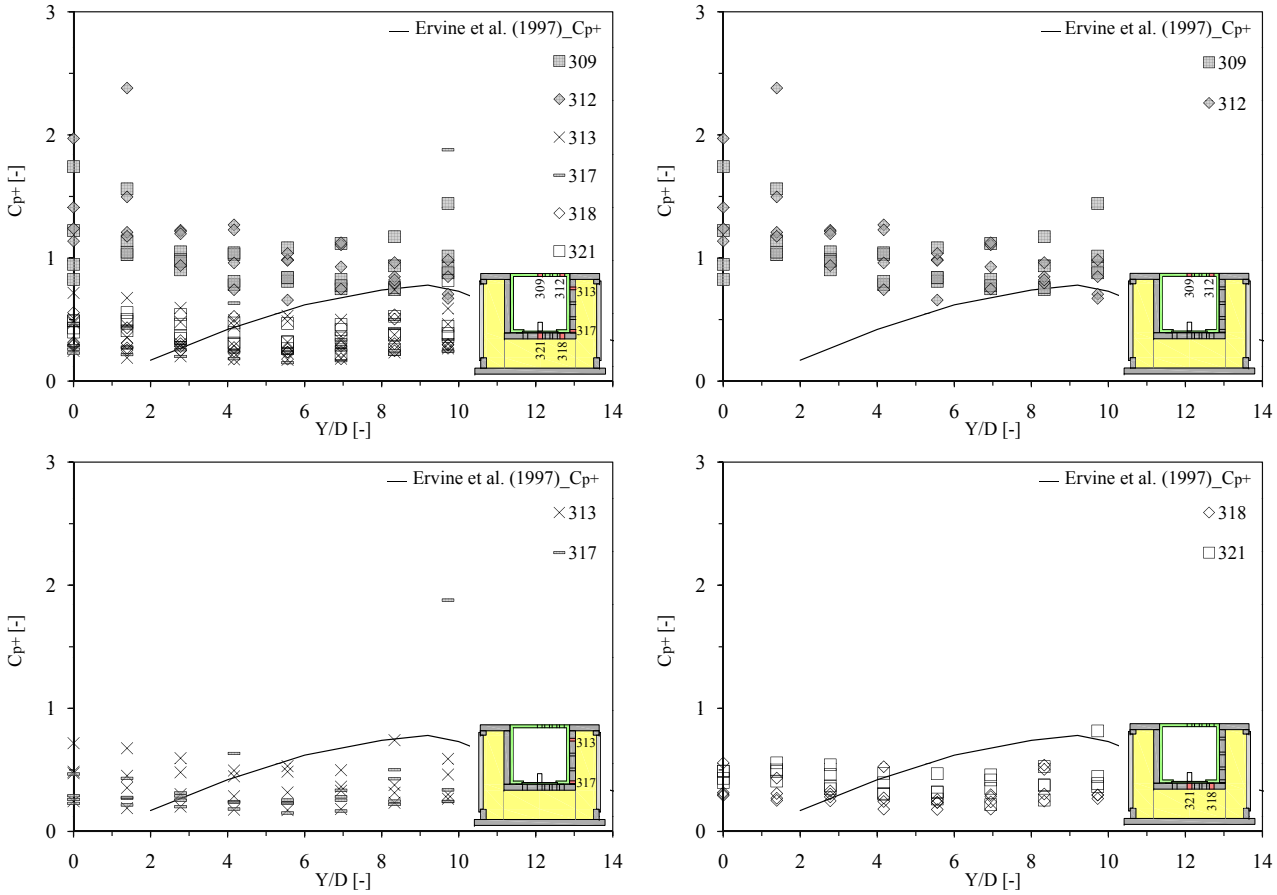

Figure 6.12: Positive extreme pressure fluctuation coefficient C_p^+ computed for configuration CR as a function of jet velocity (4.9, 12.3, 19.6 and 27.0 m/s) and Y/D ratio (0-9.7). Overview of the six pressure transducers (top left), on the block upper face or at the plunge pool bottom (top right), along the vertical fissure (bottom left) and underneath the block (bottom right).

The coefficients computed for transducer N° 309 range between 0.4 and 1.0 but transducer N° 312 shows a lower limit of only 0.5. Inside the 3-dimensional fissure the negative extreme fluctuations coefficient values are in reasonable agreement with the theoretical curve. The trend is similar along the vertical fissure and underneath the block. The coefficient values are lower than 0.6. The coefficients computed inside the fissure are similar to the coefficients recorded near the fissure entrance (N° 312).

6.2.3.5 Positive extreme pressure coefficient $C_{p,max}$

The positive extreme pressure coefficients ($C_{p,max}$, Figure 6.14) computed at the plunge pool bottom are higher than inside the fissure, for the same jet velocity. Transducer N° 309 (situated at the stagnation point) shows normally higher coefficient values than transducer N° 312 (situated near the fissure). The coefficient values decrease with an increase of the jet velocity and with the distance from the stagnation point (pressure distribution on the block). For the three jet types, the coefficients computed inside the fissure are almost constant for the same jet velocity. Along the vertical fissure (N° 313 and N° 317) and underneath the block (N° 318

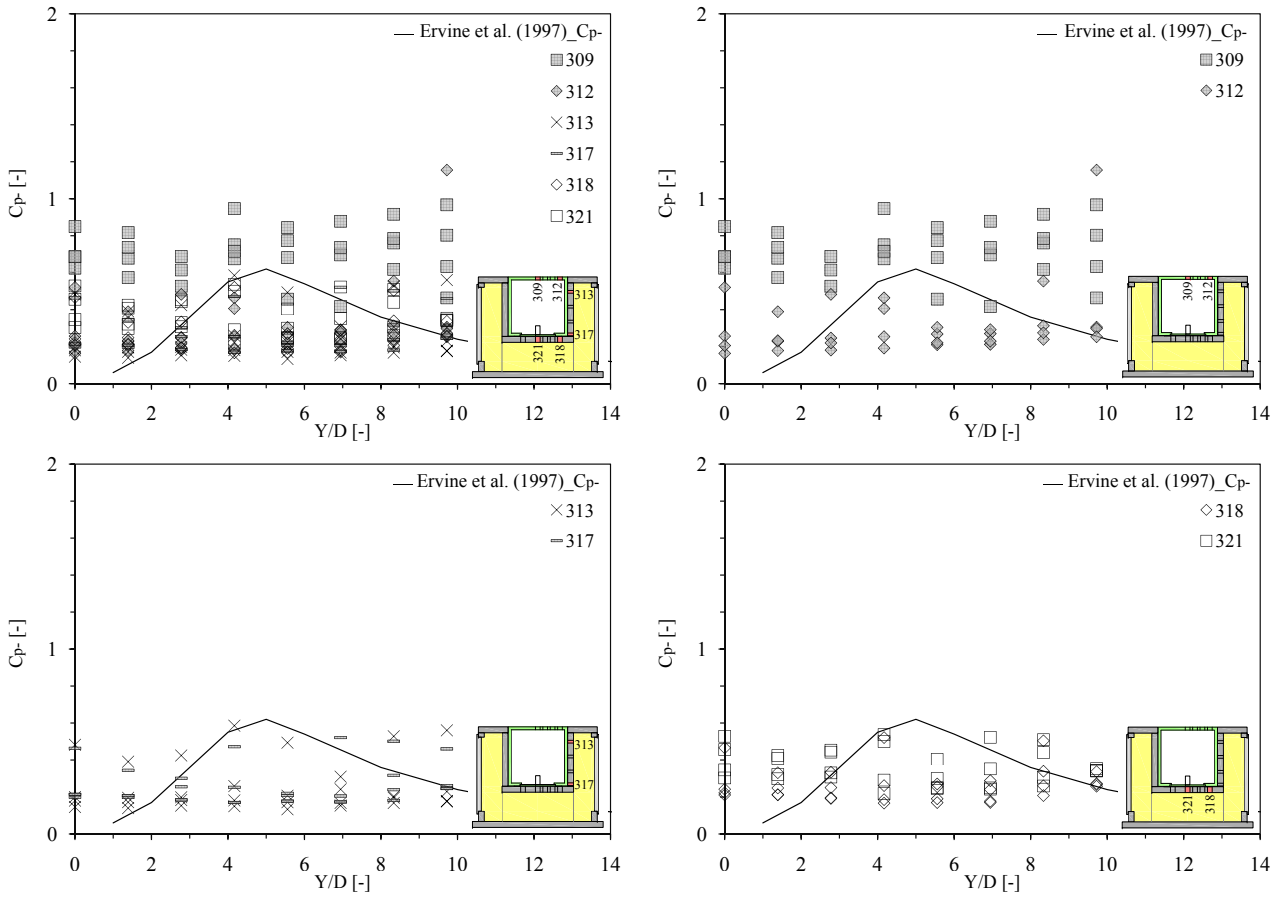

Figure 6.13: Negative extreme pressure fluctuation coefficient C_p^- computed for configuration CR as a function of jet velocity (4.9, 12.3, 19.6 and 27.0 m/s) and Y/D ratio (0-9.7). Overview of the six pressure transducers (top left), on the block upper face or at the plunge pool bottom (top right), along the vertical fissure (bottom left) and underneath the block (bottom right).

and N° 321) the coefficients are situated in the same values range. The higher coefficient values are generated by small jet velocities. The coefficient is computed using the formula explained in Chapter 5.2.2 where the kinetic energy of the jet velocity is used to normalize the maximal pressure: small jet velocities generate larger coefficients. If velocities smaller than 7.4 m/s are omitted, the coefficients are less than 1.9.

6.2.3.6 Negative extreme pressure coefficient $C_{p,min}$

The negative extreme pressure coefficients ($C_{p,min}$, Figure 6.14) show similar values for core, transition and developed jets, except for jet velocities up to 7.4 m/s. The coefficient values are almost constant for all Y/D ratios and for all jet velocities. The lower jet velocities show a rising trend for the coefficient values as a function of the water depth (Y/D ratio), but with an increase of the jet velocity this trend disappears. No apparent differences can be recognized between the coefficient computed at the plunge pool bottom and inside the fissure. As observed before, the larger coefficient values are generated by small jet velocities. If jet velocities smaller than 7.4 m/s are omitted the coefficient values are less than 1.1.

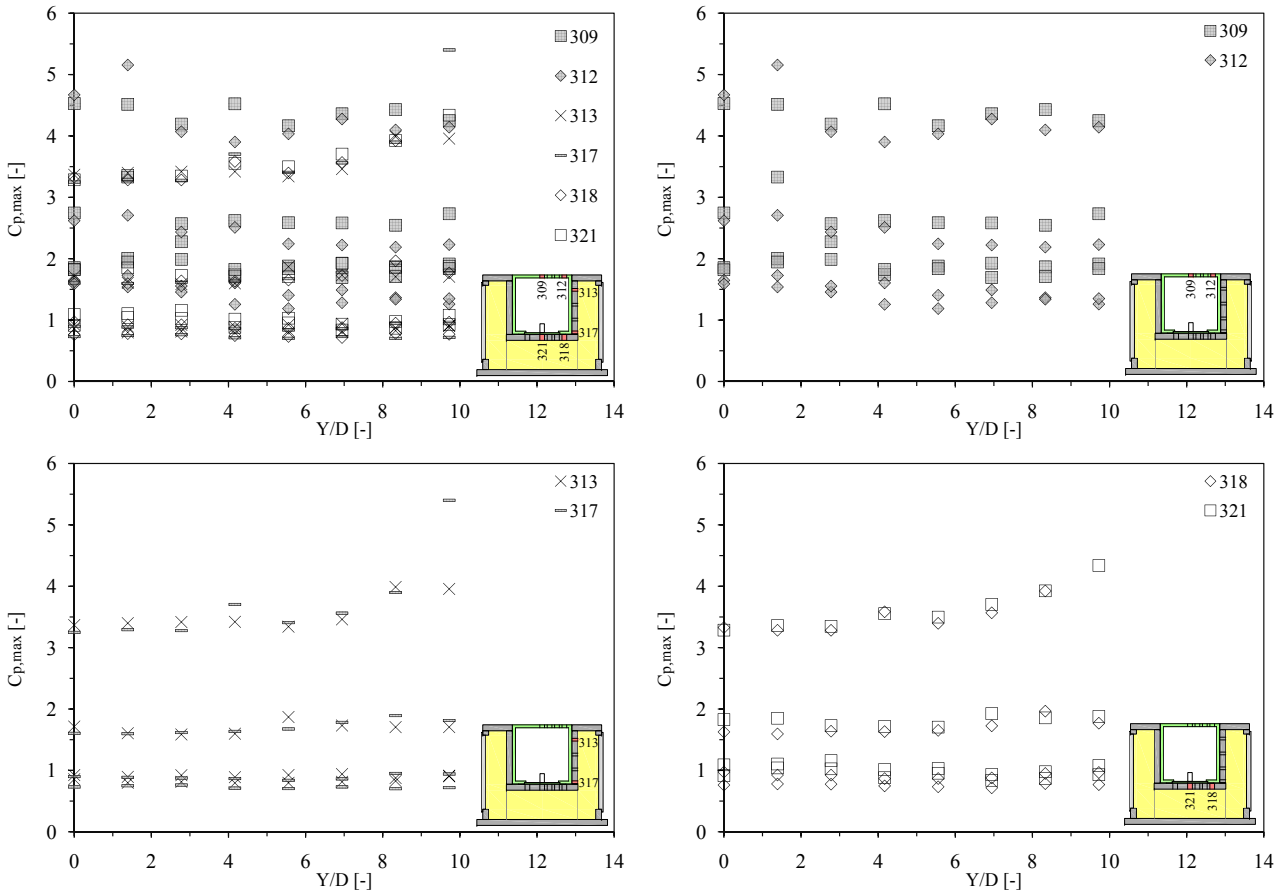

Figure 6.14: Positive extreme pressure coefficient $C_{p,max}$ computed for configuration CR as a function of jet velocity (4.9, 12.3, 19.6 and 27.0 m/s) and Y/D ratio (0-9.7). Overview of the six pressure transducers (top left), on the block upper face or at the plunge pool bottom (top right), along the vertical fissure (bottom left) and underneath the block (bottom right).

6.2.4 Displacements and accelerations of block

In this section, displacements and accelerations of block are explained. The transducers location is shown in Figure 6.1. The block responses (displacements and accelerations) have been recorded simultaneously at the pressures with the same acquisition rate (frequency of 1 kHz). The initial distance between the bottom of the central cavity and the block lower face is approximately 0.85 mm (block initial position).

6.2.4.1 Displacements of block

The block displacement is characterized by a series of vertical fluctuations: first the block moves up, and second the block moves down again and returns into the initial position. The frequency of these fluctuations is very low.

The block begins to move up (Figure 6.16) with jet velocities of 4.9-7.4 m/s. The block is subjected to small fluctuations and the mean displacement correspond to the block initial position (∼0.85 mm). At 7.4 m/s the amplitude of this vertical displacements increases and the

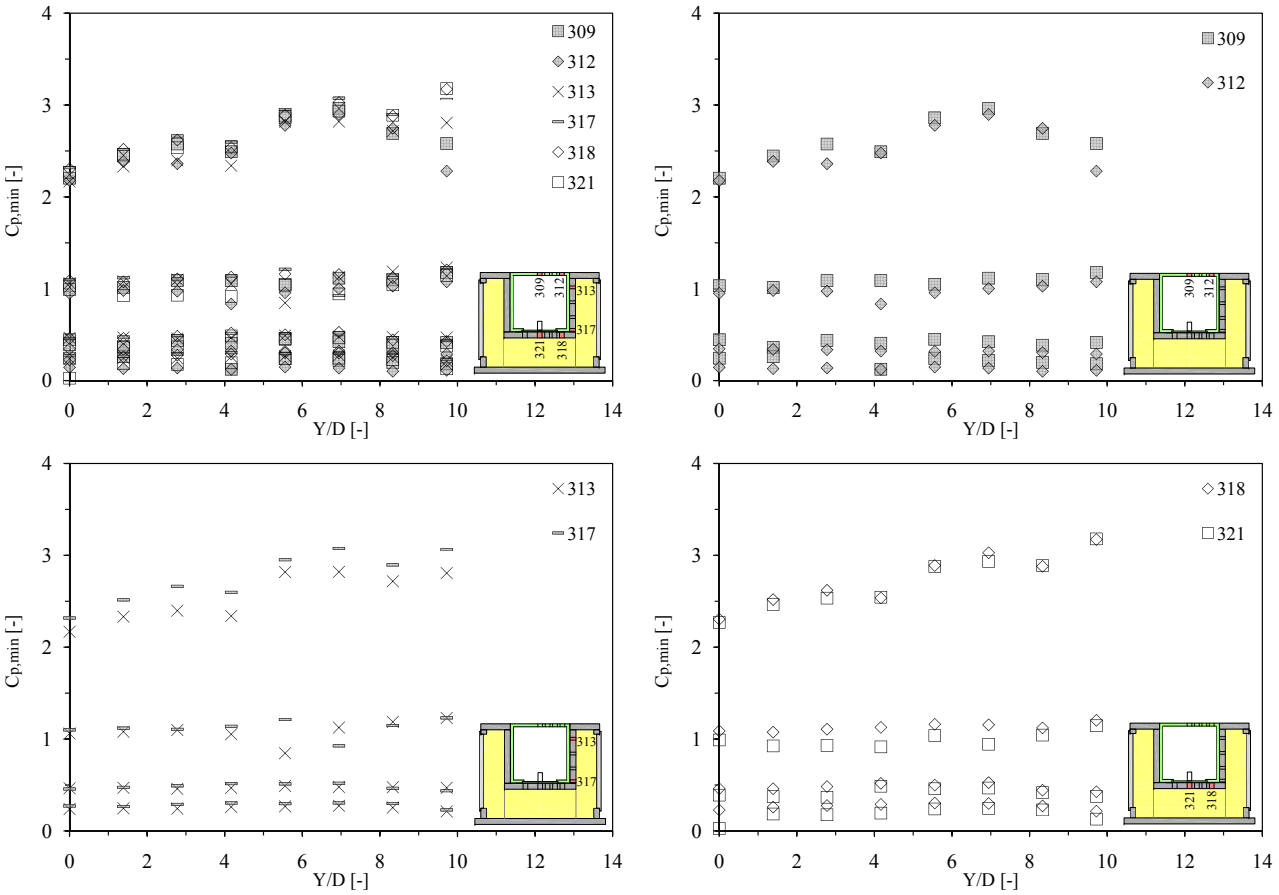

Figure 6.15: Negative extreme pressure coefficient $C_{p,min}$ computed for configuration CR as a function of jet velocity (4.9, 12.3, 19.6 and 27.0 m/s) and Y/D ratio (0-9.7). Overview of the six pressure transducers (top left), on the block upper face or at the plunge pool bottom (top right), along the vertical fissure (bottom left) and underneath the block (bottom right).

block did not return to its initial position: the block reaches a new equilibrium position. This equilibrium position changes with the jet velocity. Transition ($4 < Y/D < 6$) and developed jets ($Y/D > 6$) generate maximum vertical displacements. The same remarks can be made for mean displacements. Core jets ($Y/D < 4$) generate minimum displacements. The 0.7 m water depth ($Y/D = 9.7$) generates largest vertical displacement, corresponding to 1.07 mm (block initial position 0.85 mm). Mean displacement ranges between 0.91 and 0.96 mm for all water depths. Minimum displacement is equivalent to the block initial position.

6.2.4.2 Accelerations of block

The accelerations are related to the block displacements. Accelerations (positive or negative) generate a vertical displacement. If the block is in contact with the measurement box (block initial position) eventually negative accelerations cannot occur because forces are transmitted to the measurement box. In this case the block cannot move down. If the accelerations are positive the block moves up. To generate the measured vertical displacements, maximum and minimum accelerations (Figure 6.17) are not the most important values because their action is

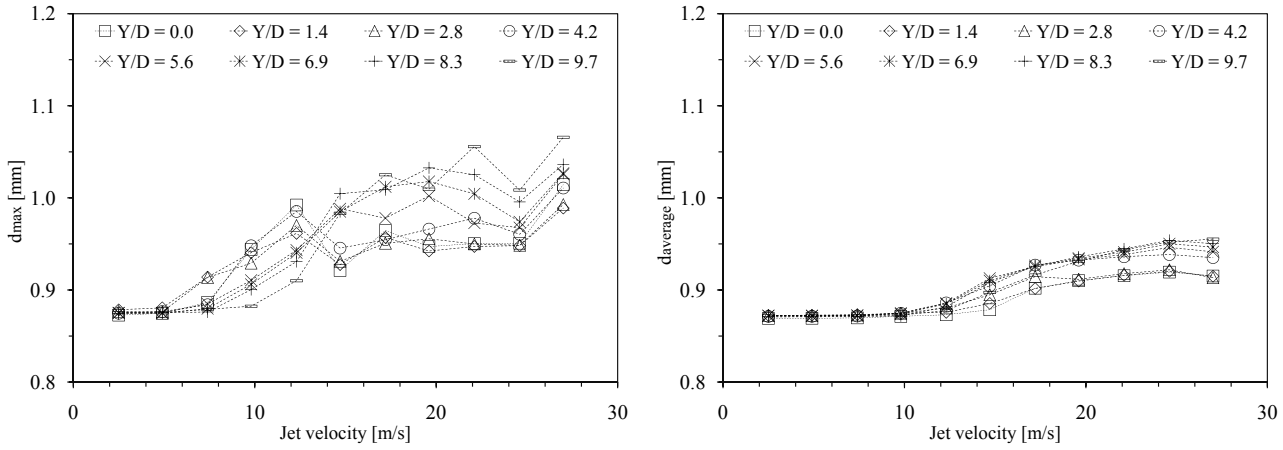

Figure 6.16: Block displacements measured for configuration CR as a function of jet velocity (2.5-27.0 m/s) and Y/D ratio (0-9.7). Maximum (left) and mean (right) displacements of block. The block initial position corresponds to a distance of ∼0.85 mm.

concentrated in a very small interval of time (local impulsion). The most important value is the acceleration that is present for a long time period (constant impulsion).

Maximum vertical acceleration increases with the jet velocity and reaches ∼45 g. Core jets show the highest accelerations. Mean accelerations show a weakly increase as a function of the jet velocity. Mean acceleration ranges between 1.7 and 2.6 g for the three jet types. Minimum accelerations showed measurement problems for jet velocities larger than 14.7 m/s: electrical noises (appears during the measurements) generate incongruous values that reach the acceleration lower limits (-1000 g). This problem is present for several jet velocities.

6.2.5 Power Spectral Density

In this section only the results for a core (Y/D = 2.8 or 0.2 m), a transition (Y/D = 5.6 or 0.4 m) and a developed jet (Y/D = 8.3 or 0.6 m) and four of the eleven jet velocities are explained (4.9, 12.3, 19.6 and 27.0 m/s).

When the jet discharge increases, the energy associated to each frequency increases proportionally. The Power Spectral Density (PSD) may be subdivided into two groups:

I. transducers situated at the plunge pool bottom on the block upper face (N°s 309 to 312);

II. transducers situated inside the 3-dimensional fissure (N°s 313 to 321).

These observations are valid for core, transition and developed jets (Figures 6.18, 6.19 and 6.20).

Pressure transducers fixed on the block upper face have a behavior similar to the previous observations performed by Bollaert (2002b) and Manso (2006) during their PhD research projects. The low frequency part of the PSD signal ($f < 10$ Hz) looks quite similar for all jet velocities. The energy correlated to each frequency decreases slowly with a slope of approximately -2/3. For higher frequencies ($f > 10$ Hz) the spectral content decreases with a -1 slope.

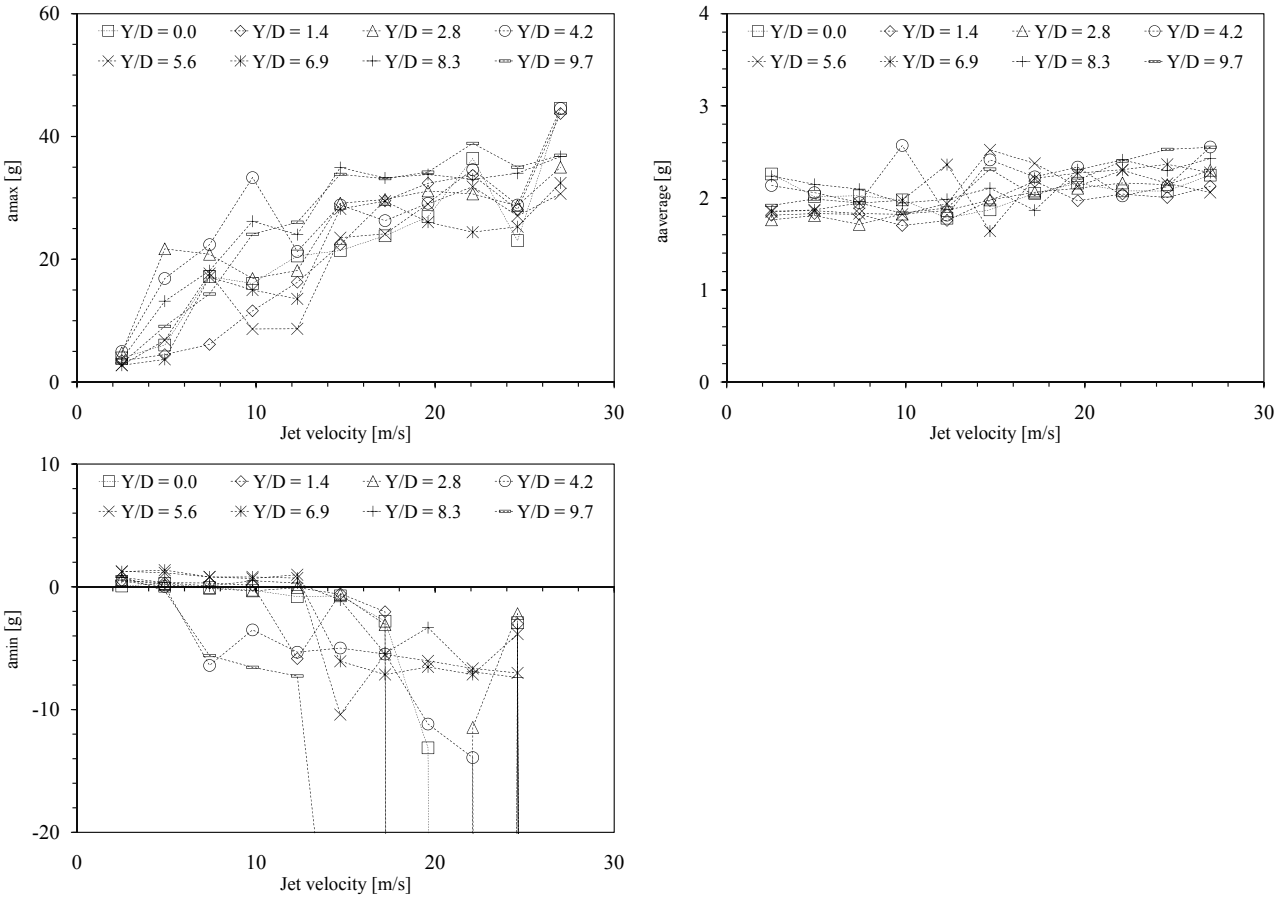

Figure 6.17: Block accelerations measured for configuration CR as a function of jet velocity (2.5-27.0 m/s) and Y/D ratio (0-9.7). Maximum (top left) and mean accelerations of block (top right). Minimum accelerations (bottom left) show some electrical noises that affect the measured values (reach the acceleration lower limit of -1000 g).

The pressure transducers situated inside the 3-dimensional fissure (along the vertical fissure and underneath the block) show a different behavior. The energy correlated to each frequency is lower than at the plunge pool bottom for the same jet velocity as can be expected. With increasing frequencies, two zones can be distinguished: a first zone lowers than 8-10 Hz and a second zone for frequency higher than 8-10 Hz. In the first zone, the energy decreases slowly with a slope approximately situated between -1/3 and -2/3. In the second zone, two different peaks may be detected in the PSD signal: the first peak between 10-20 and 80-100 Hz and the second peak between 80-100 and 200-300 Hz. At low jet velocities, the first peak appears but not the second. When the jet velocity increases, the first peak disappears and the second peak appears.

The two peaks appear in the PSD signal for core, transition and developed jet. The second peak (at higher frequency) is stronger than the first peak. The two peaks are more visible on the PSD signal for transducers situated far away from the plunge pool bottom (N° 317, N° 318 and N° 321). None of the two peaks appear in the PSD of the surface pressure signal; as such they are not present at the plunge pool bottom.

At first sight, the peaks might be related to the fundamental resonance frequencies of the

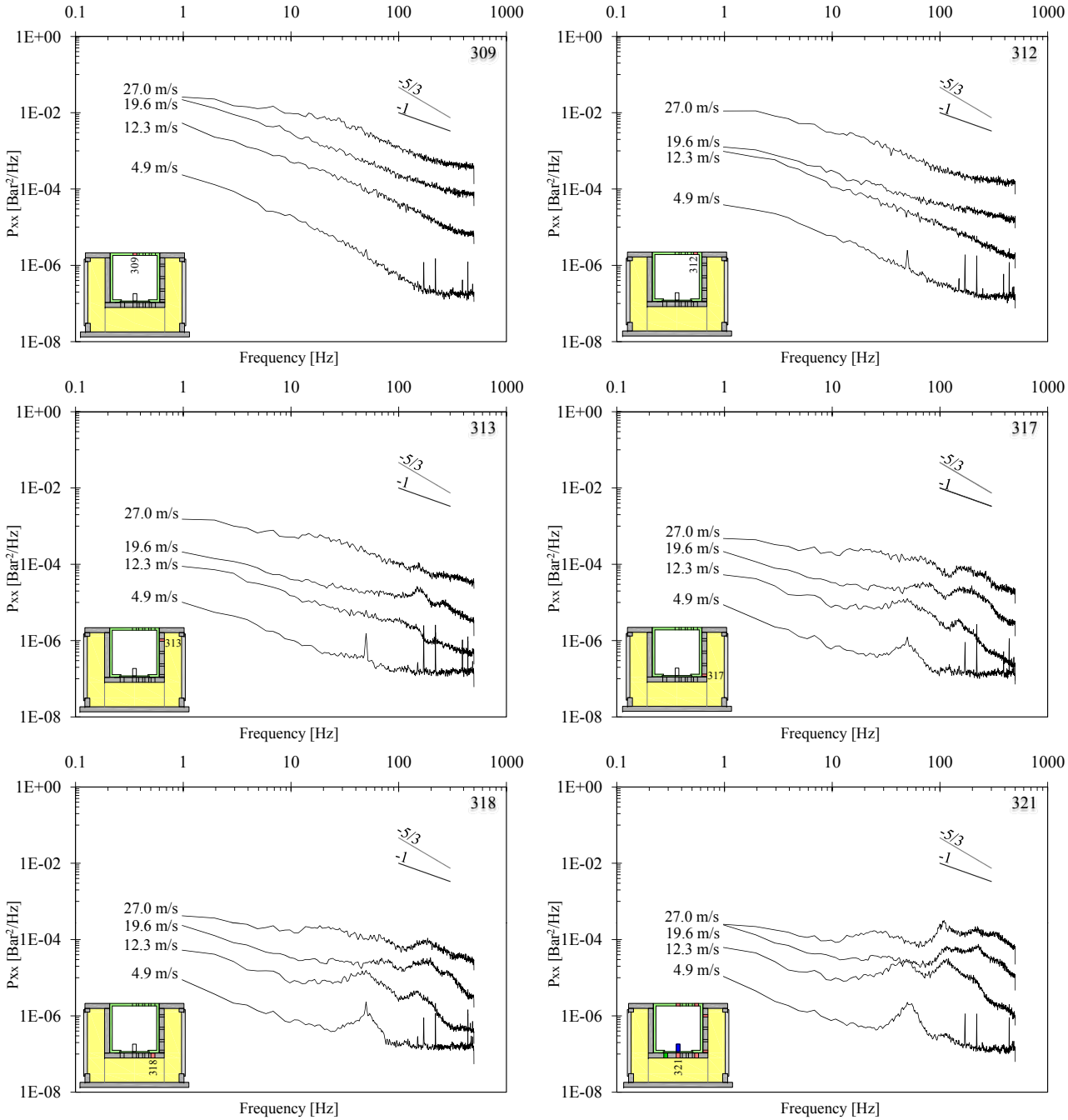

Figure 6.18: Non-dimensional spectral content (PSD) computed for configuration CR. Core jet (Y/D = 2.8) and different jet velocities (4.9, 12.3, 19.6 and 27.0 m/s): on the block upper face pressure transducers N° 309 (top left) and N° 312 (top right); along the vertical fissure pressure transducers N° 313 (center left) and N° 317 (center right); underneath the block pressures transducers N° 318 (bottom left) and N° 321 (bottom right).

travelling pressure waves in the 3-dimensional fissure around the block or even to eigenfrequencies of the block itself due to its inertia. In Chapter 5.6 the natural period of an open ended fissure has been computed. The fissure eigenfrequency is situated in a range of 22-72 Hz. The eigenfrequency of the block has been measured in Chapter 5.7.3 and is situated in a range of 5-9 Hz. The first peak could correspond to the fissure natural frequency but the

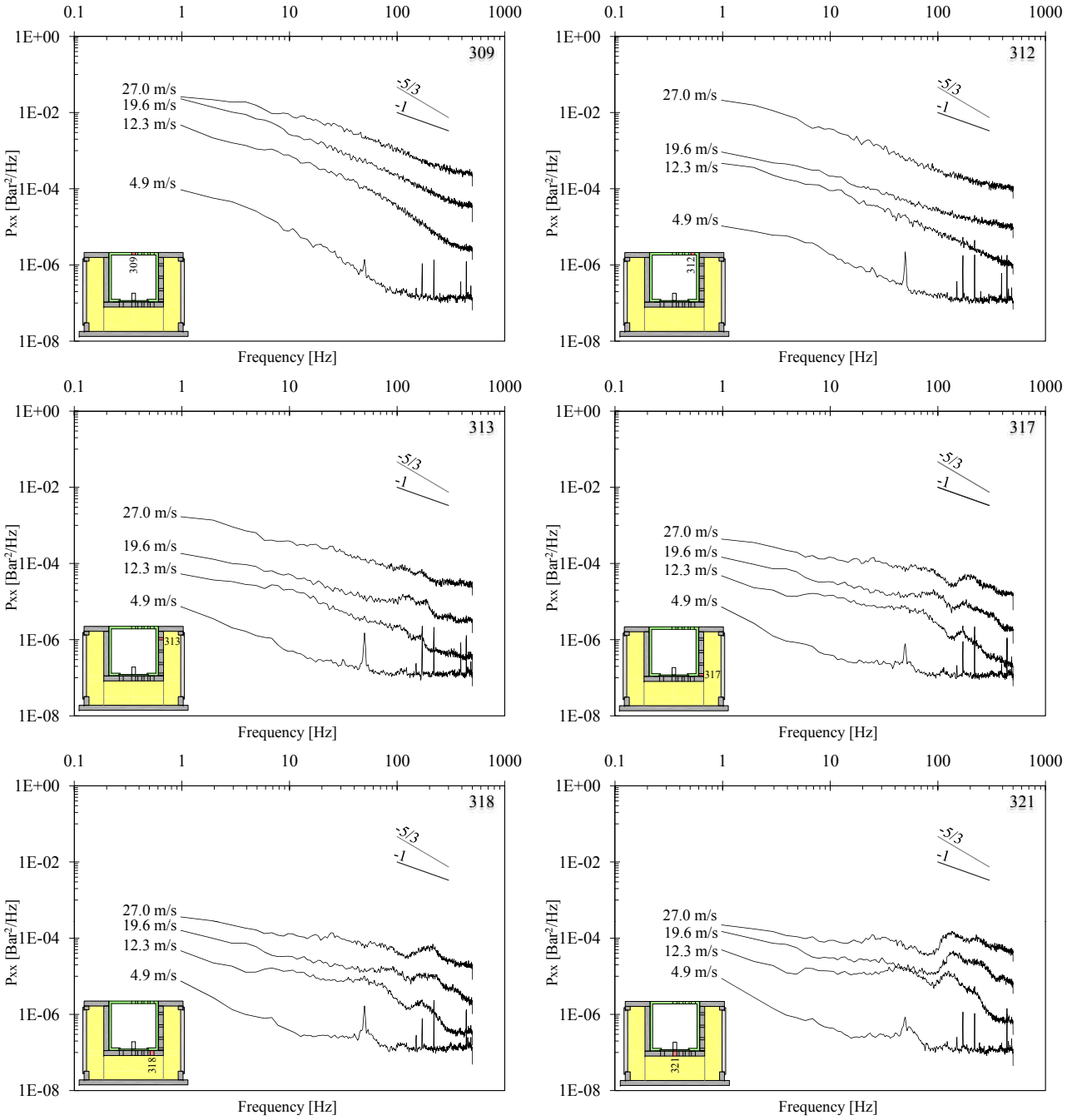

Figure 6.19: Non-dimensional spectral content (PSD) computed for configuration CR. Transition jet (Y/D = 5.6) and different jet velocities (4.9, 12.3, 19.6 and 27.0 m/s): on the block upper face pressure transducers N° 309 (top left) and N° 312 (top right); along the vertical fissure pressure transducers N° 313 (center left) and N° 317 (center right); underneath the block pressures transducers N° 318 (bottom left) and N° 321 (bottom right).

second peak did not correspond to the block eigenfrequency. The first peak was observed as well by Bollaert (2002b). The second peak is characterized by high frequencies and is very different from the block eigenfrequencies. That may be correlated with the interaction block displacements-pressure waves travelling inside the fissure or with a resonance phenomenon inside the 3-dimensional fissure.

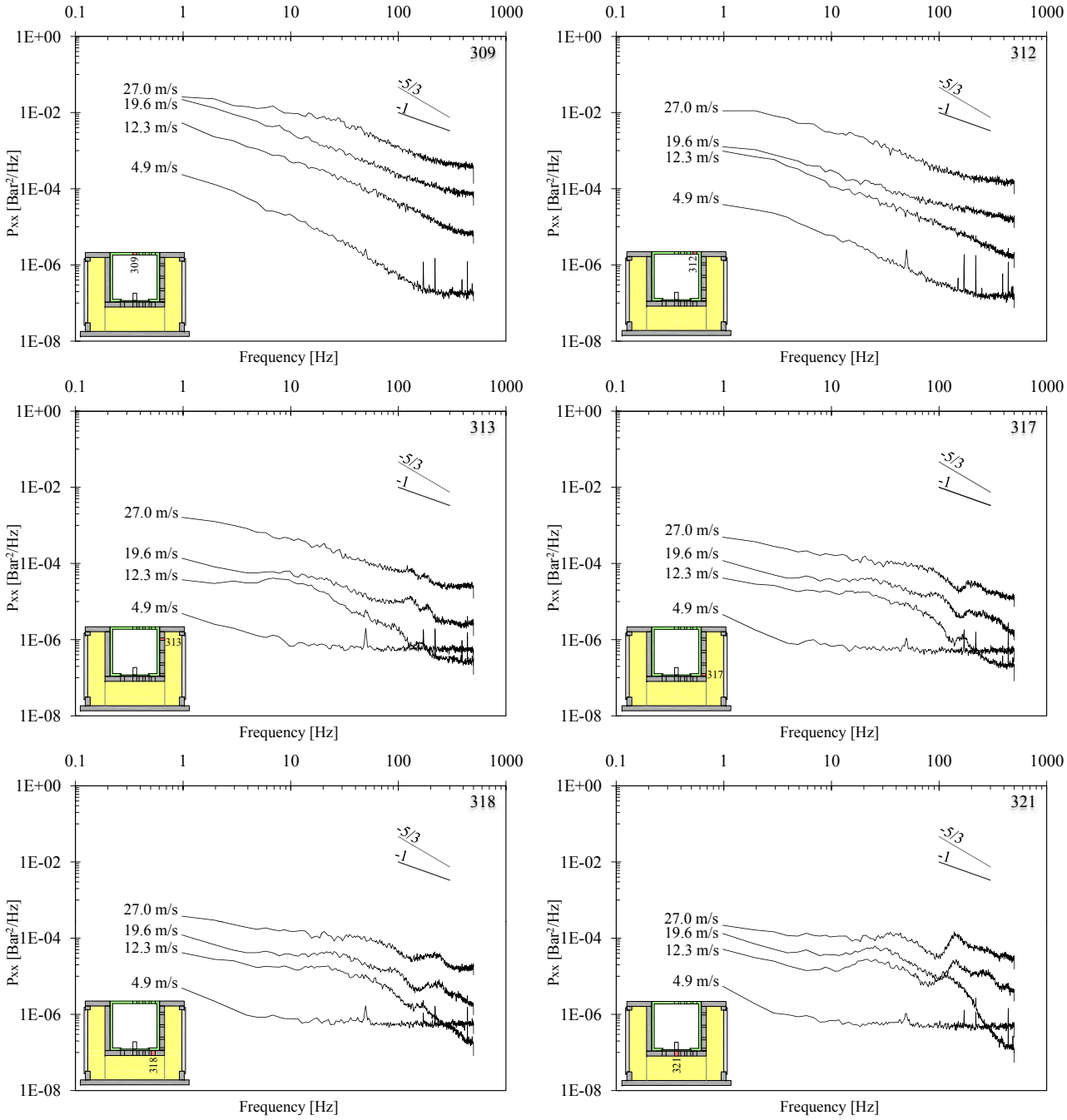

Figure 6.20: Non-dimensional spectral content (PSD) computed for configuration CR. Developed jet (Y/D = 8.3) and different jet velocities (4.9, 12.3, 19.6 and 27.0 m/s): on the block upper face pressure transducers N° 309 (top left) and N° 312 (top right); along the vertical fissure pressure transducers N° 313 (center left) and N° 317 (center right); underneath the block pressures transducers N° 318 (bottom left) and N° 321 (bottom right).

6.2.6 Dynamic block impulsion

The dynamic block impulsion and the respective block uplift have been computed following the theoretical method explained in Chapter 5.4. In this section only the results for a core (Y/D = 2.8 or 0.2 m), a transition (Y/D = 5.6 or 0.4 m) and a developed jet (Y/D = 8.3 or 0.6 m) and

four of the eleven jet velocities (4.9, 12.3, 19.6 and 27.0 m/s) are explained. Figures 6.21, 6.22 and 6.23 show the comparison between theoretical and measured uplift. The dynamic block impulsion is analyzed in Chapter 7.1.

The theoretical uplift (theoretical displacements of block) has been computed from the block initial position that corresponds to the distance between the central cavity bottom and the block lower face (∼0.85 mm). The measured uplift (measured block vertical displacements) is the distance between the displacement transducer and the block lower face. The measured displacements have been adjusted with the block initial position to have the same reference as the theoretical displacements (at the measured displacements the block initial position has been subtracted).

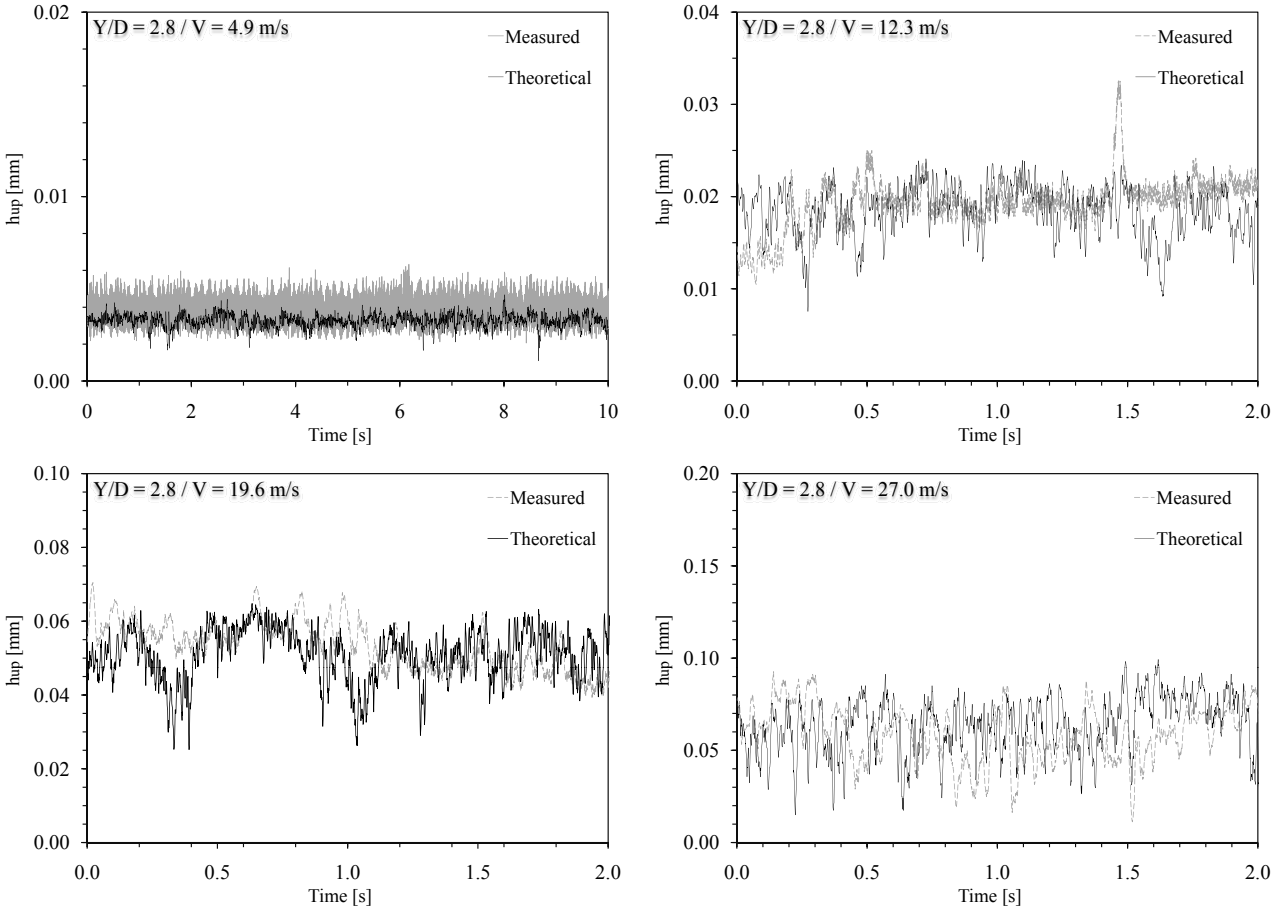

Figure 6.21: Time evolution of dynamic block impulsion for configuration CR. Comparison between theoretical and measured uplift for a core jet (Y/D = 2.8) and four jet velocities (4.9, 12.3, 19.6 and 27.0 m/s).

Two coefficients have to be calibrated to fit the theoretical uplift to the measured uplift: the added mass coefficient (Chapter 2.4) and the pressure reduction coefficient (Chapter 5.3.3) corresponding to the pressure acting on the block upper face where no pressures have been measured. The added mass coefficient influences the amplitude of displacements and the pressure reduction coefficient influences the slope of the time evolution of displacements.

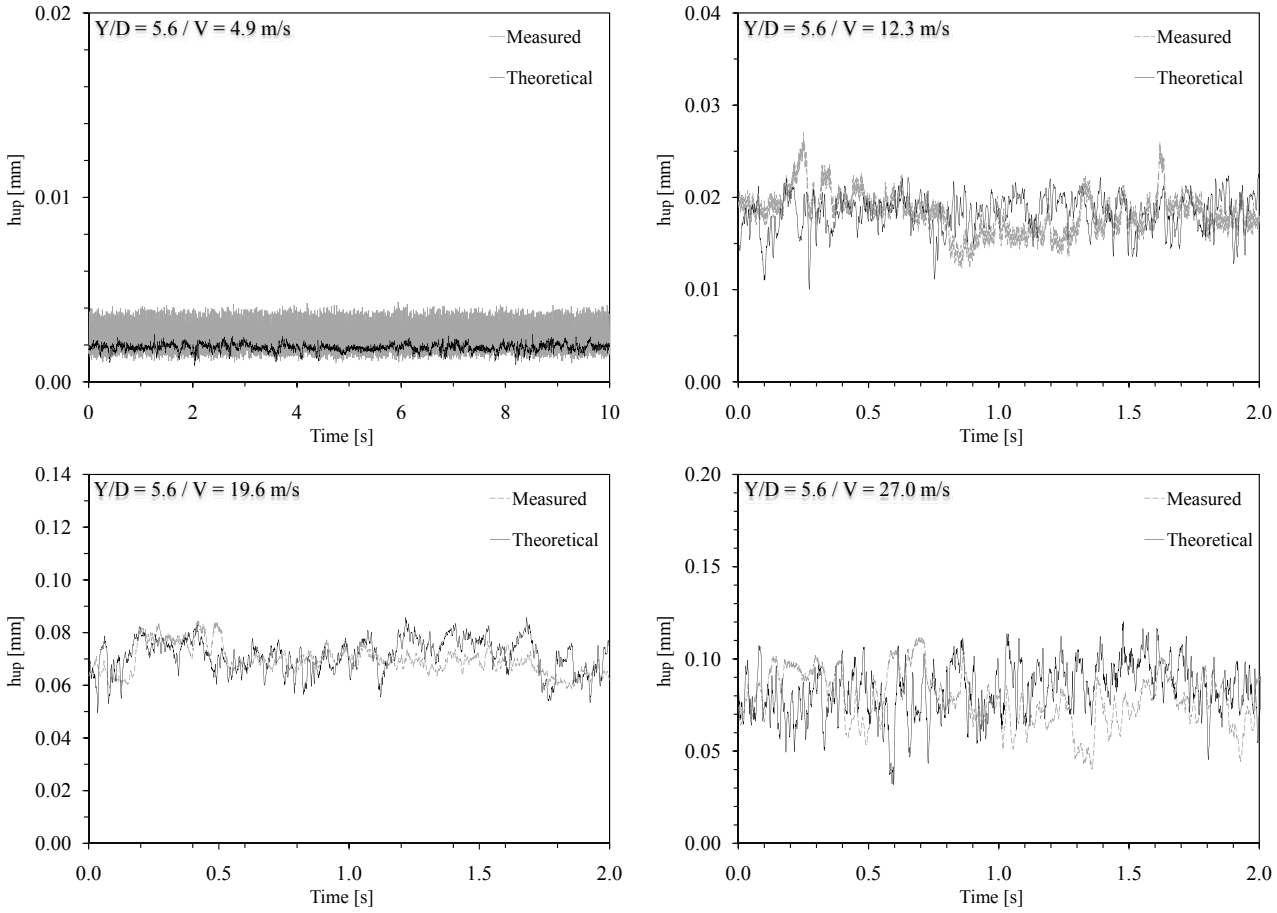

Figure 6.22: Time evolution of dynamic block impulsion for configuration CR. Comparison between theoretical and measured uplift for a transition jet (Y/D = 5.6) and four jet velocities (4.9, 12.3, 19.6 and 27.0 m/s).

By analyzing the time evolution of block uplift (theoretical and measured, Figures 6.21, 6.22 and 6.23), it is possible to observe that the block vertical fluctuations (recorded with the displacement transducer) can be easily reproduced theoretically. Almost all vertical fluctuations are present in the theoretical uplift but the amplitude is not always the same: sometimes they are larger and sometimes smaller than the measured uplift. This amplitude difference is more visible for instantaneous peaks (in the order of magnitude of 10^{-3}-10^{-2} mm). The theoretical uplift cannot be shifted exactly on the measured uplift but the similitude between the two uplifts is very strong for the 30 seconds analyzed time interval.

Table 6.2 summarizes the added mass coefficients and the pressure reduction coefficients that have been used to obtain the similitude between theoretical and measured uplift.

6.2.7 Conclusions

The pressure field acting on the block upper face (at the plunge pool bottom) has an exponential distribution with the center at the stagnation point according to the literature (Chapter 5.1.1.3). The geometry of the bell-shape pressure distribution changes as a function of the jet velocity. The pressure field inside the 3-dimensional fissure is almost constant for all water

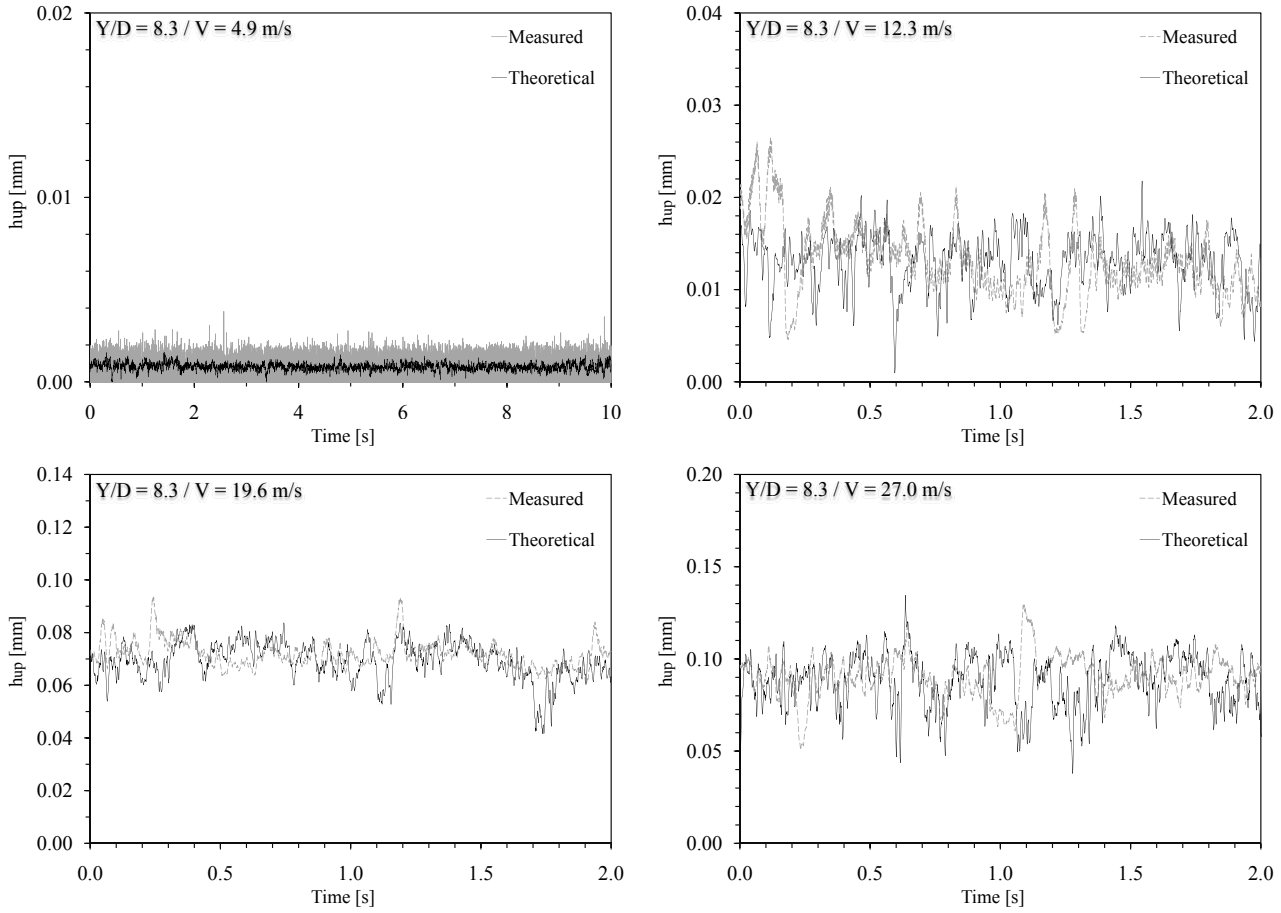

Figure 6.23: Time evolution of dynamic block impulsion for configuration CR. Comparison between theoretical and measured uplift for a developed jet (Y/D = 8.3) and four jet velocities (4.9, 12.3, 19.6 and 27.0 m/s).

Coefficient	Y/D ratio	Jet velocity V_0						
		4.9	7.4	9.8	12.3	14.7	19.6	27.0
[-]	[-]	[m/s]	[m/s]	[m/s]	[m/s]	[m/s]	[m/s]	[m/s]
AMC	2.8	4	3.5	3	3	3	2	2.5
	5.6	4	3.5	2.5	3	2	2.5	1.5
	8.3	4	3.5	3	2	1.5	2	2.5
PRC	2.8	0	0	0	0.5	0.5	0.5	0.5
	5.6	0	0	0	0.5	0.5	0.5	0.2
	8.3	0	0	0	0.5	0.5	0.5	0.5

Table 6.2: Added mass coefficient (AMC, α_{am}) and pressure reduction coefficient (PRC) for configuration CR.

depths. The pressure values change with an increase or a decrease of the jet velocities. Mean pressures acting along the vertical fissure increase weakly with the depth of the fissure, whereas the extreme values (maximum and minimum) decrease for the same conditions. Underneath the block the pressure field is almost constant (maximum, mean and minimum). The pressure

values recorded inside the fissure are smaller than on the block upper face.

The pressure coefficients, for the transducers situated on the block upper face are in reasonable agreement with the literature values. The pressure coefficients computed for transducers located inside the 3-dimensional fissure show lower values than at the plunge pool bottom. Mean, turbulent, positive/negative extreme fluctuations and positive/negative extreme pressures did not solicit the fissure as at the plunge pool bottom. The extreme values are attenuated inside the fissure. Jet velocities lower than 7.4 m/s generate high coefficient values that did not match with the previous measurement present in the literature (Chapter 5.1.1.1).

The block begins to move up and reaches a new equilibrium position for jet velocities greater than 7.4-9.8 m/s. For jet velocities lower than 7.4-9.8 m/s, the block, after its vertical displacements, systematically returns to its initial position (in contact with central cavity bottom) but for jet velocities greater than 7.4-9.8 m/s, the block finds a new equilibrium position (not in contact with central cavity bottom). During its vertical movements the block sometimes touches the bottom of the central cavity. The largest displacement reaches ∼0.2 mm. Maximum and mean accelerations increase as a function of the jet velocity. Mean accelerations increase very slowly and maximum accelerations increases faster along the whole range of jet velocity. Minimum accelerations are affected from electrical noises generating incongruous values that reach the acceleration lower limits.

The Power Spectral Density (PSD) shows a different behavior between transducers situated on the block upper face and inside the 3-dimensional fissure. The pressure transducers fixed on the block upper faces have behavior similar to the previous literature observations. At the plunge pool bottom the low frequency part of the PSD signal ($f < 10$ Hz) looks quite similar for all jet discharges. The energy content decreases slowly with a slope of approximately -2/3 and faster for higher frequencies with a -1 slope. Inside the fissure, with increasing frequencies, two zones can be distinguished: a first zone up to 8-10 Hz and a second zone for frequency higher than 8-10 Hz. In the first zone, the energy decreases slowly with a slope situated between -1/3 and -2/3. In the second zone, two different peaks may be detected in the PSD signal: the first peak (between 10-20 and 80-100 Hz) is related to the fissure natural frequency and the second peak (between 80-100 and 200-300 Hz) is not so clearly definable but it may be related with the interaction block vertical movements-pressure waves travelling inside the fissure or with a resonance phenomenon inside the 3-dimensional fissure. The second peak (at high frequency) is stronger than the first peak.

The dynamic block impulsion shows a good similitude between theoretical and measured values. Only the amplitude of the vertical displacements could not be always simulated exactly by the theoretical uplift, but the vertical fluctuations could be well reproduced. The added mass is an important parameter that has to be integrated in the dynamic block impulsion computation to obtain a good similitude between theoretical and measured uplift.

6.3 Jet impact position on the block right hand side with the block free to move and equipped with lateral guides having eight contact points (SR)

6.3.1 Configuration description

This configuration is characterized by the following three parameters:

- Jet impact position: *on the block right hand side*;
- Degree of freedom: *the block is free to move along the vertical axis*;
- Lateral guides: *eight contact points per lateral guide and two guides per vertical face on the block.*

Figure 6.24 shows the configuration parameters and the transducers positions.

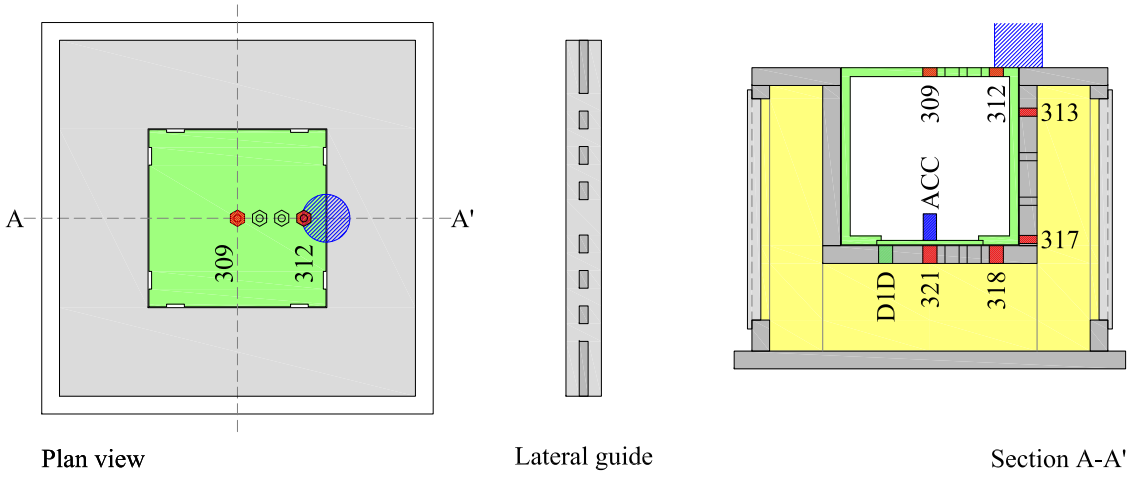

Figure 6.24: New experimental set-up for the configuration SR. Top view with jet impact position (cylinder) and pressure transducers positions (left), lateral guide fixed on the block lateral faces (center) and transversal section with jet impact position (cylinder) and transducers positions (pressure transducers N° 309 to N° 321, displacement transducer D1D and accelerometer ACC.

Table 6.3 summarizes the parameter combinations (water depth Y, jet discharge Q, jet velocity V_0, Y/D ratio and jet type) that have applied to this configuration.

6.3.2 Pressure field surrounding the block

As explained in Chapter 6.2.2, the pressures are relative and have been normalized by the kinetic energy of the jet ($V_0^2/2 \cdot g$).

Water depth Y [m]	Discharge Q [l/s]	Jet velocity V_0 [m/s]	Y/D ratio [-]	Jet Type [-]
0.0	10-110	2.5-27.0	0.0	Core jet
0.1	10-110	2.5-27.0	1.4	Core jet
0.2	10-110	2.5-27.0	2.8	Core jet
0.3	10-110	2.5-27.0	4.2	Transition jet
0.4	10-110	2.5-27.0	5.6	Transition jet
0.5	10-110	2.5-27.0	6.9	Developed jet
0.6	10-110	2.5-27.0	8.3	Developed jet
0.7	10-110	2.5-27.0	9.7	Developed jet

Table 6.3: Main parameters that have been tested with configuration SR: water depth Y, jet discharge Q, jet velocity V_0, Y/D ratio and jet type.

Transducer 309 (at the center of the block upper face)

Transducer N° 309 is located at the boundary between the impingement region and the wall jet region where the jet is deflected after the impact with the plunge pool bottom (at 100 mm from the stagnation point situated on the axis of the vertical fissure).

Core, transition and developed jets show a different behavior as a function of the jet velocity (Figure 6.25): maximum pressure grows quadratically for the three jet types (with the same trend) but core jets (Y/D $<$ 4) show constantly higher pressure values than transition (4 $<$ Y/D $<$ 6) and developed jets (Y/D $>$ 6). Maximum pressures change as a function of water depths and jet velocity: when the jet velocity increases, maximum pressure increases as well but when the water depth increases, maximum pressure decreases. Core jets (Y/D = 0.0 and 1.4) show an evolution of maximum pressure similar to the data recorded by transducer N° 312, located at 25 mm from the stagnation point (they have a similar maximum pressure range). This behavior may be related to the water depth: when the water depth grows, the deflected flow, near the plunge pool bottom, is influenced by the thickness of the water in the plunge pool (backward flow near the water surface). Maximum pressures of core jets follow a trend similar to transition and developed jets but with some fluctuations along the whole range of jet velocities. The difference between maximum pressures for core jets and the other two jets type is approximately 1.5 Bar.

Mean pressures show a weakly increase for all water depths as a function of the jet velocity. It grows until the second-last jet velocity (24.6 m/s) where a weak decrease is observable for the largest jet velocity.

Minimum pressures decrease with an increase of the jet velocity with some small fluctuations. All water depths show the same trend.

As observed for the previous configuration (Chapter 6.2.2), with an increase of the jet velocity, an oscillating hydraulic jump appears between the wall and the center of the plunge pool. For the largest jet velocity the hydraulic jump reaches the block (Figure 6.4).

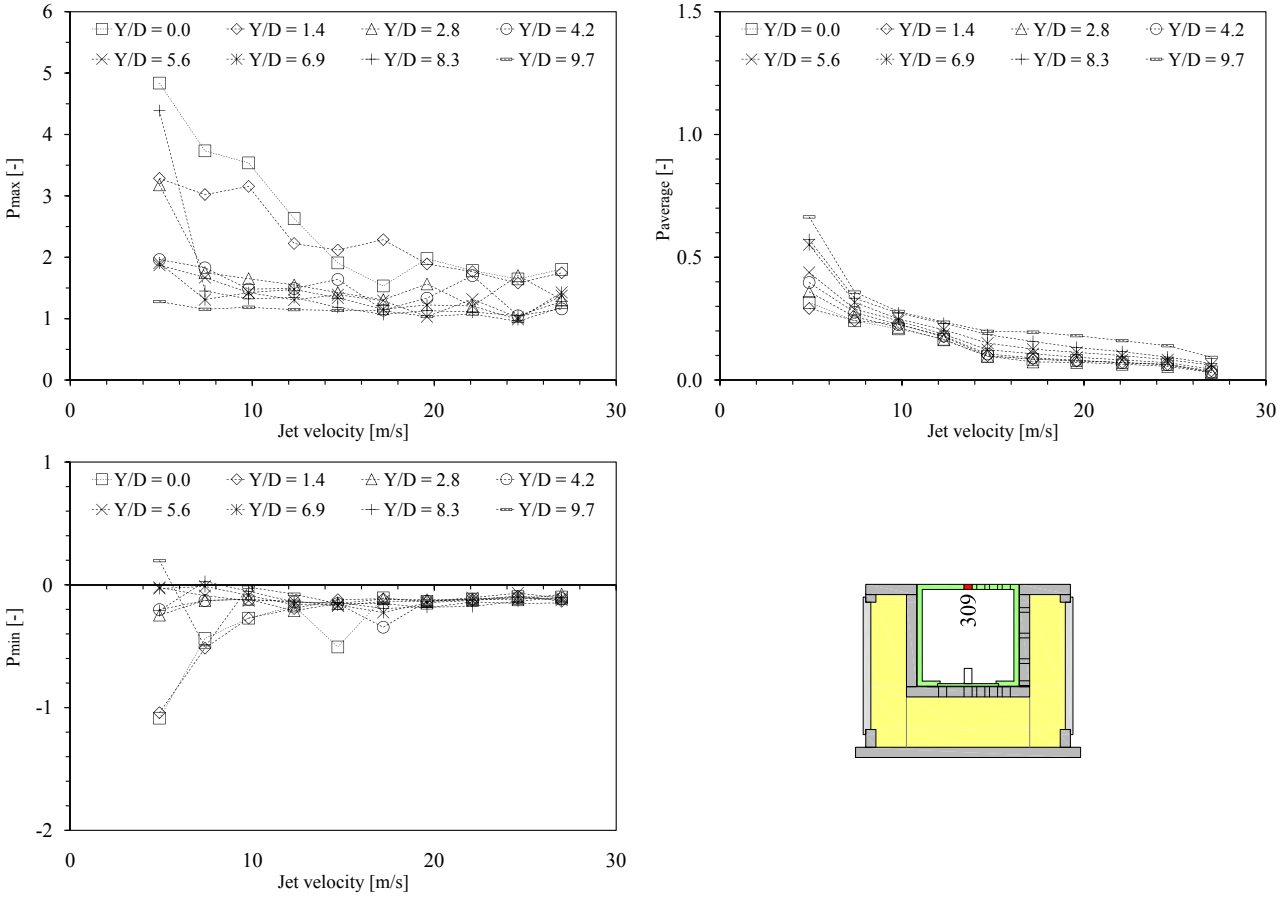

Figure 6.25: Normalized pressure measured with transducer N° 309 for configuration SR as a function of jet velocity (2.5-27.0 m/s) and Y/D ratio (0-9.7). Maximum pressure (top left), mean pressure (top right), minimum pressure (bottom left) and transducer location (bottom right).

Transducer 312 (near the fissure entrance on the block upper face at 25 mm from the stagnation point)

Transducer N° 312 is located at 25 mm from the stagnation point in the impinging region. Maximum pressure acting near the entrance of the vertical fissure shows the same trend and behavior for all water depths and jet velocities (Figure 6.26).

Maximum pressures grow quadratically, but between core jets and transition and developed jets some differences exist: the two groups (core jets and transition/developed jets) show the same evolution as function of the jet velocity but with a vertical shift. Core jets show highest maximum pressures for all jet velocities: the water jet impact directly on the block and the jet energy is converted into pressure with small energy lost. The interaction between the jet and the water depth reduce the maximum pressure acting on the bottom for transition and developed jets. This vertical shift is more visible for jet velocities larger than 12.3-14.7 m/s and reaches a difference of ∼0.7 Bar for the largest jet velocity (27.0 m/s).

Mean pressures grow with the same trend (quadratically) as observed for maximum pressures. Mean pressures are almost the same for all water depths and all jet velocities. Only the 0.7 m water depth (Y/D = 9.7) shows a different behavior: between 9.8 and 24.6 m/s the mean

pressure is approximately 0.3-0.4 Bar smaller than for the other water depths. For the largest jet velocity this difference reaches ∼0.7 Bar.

Minimum pressures evolve with the same trend for all water depths. Up to 19.6-22.1 m/s, minimum pressures are almost constant with some fluctuations. When the jet velocity increases, minimum pressured show a peak for the second-last velocity (24.6 m/s) corresponding at ∼0.4-0.6 Bar. For the largest jet velocity, minimum pressure decreases and reaches again approximately the initial value.

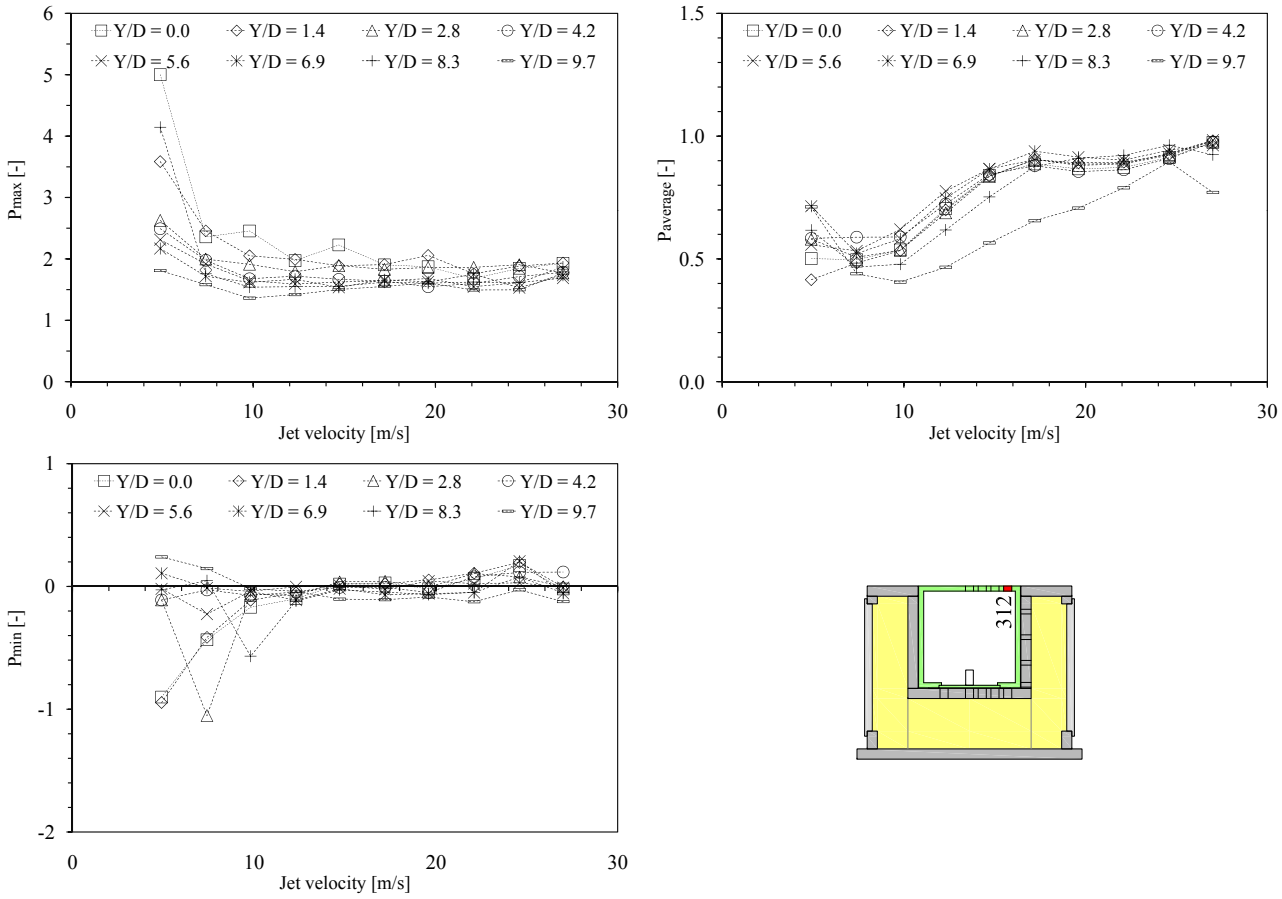

Figure 6.26: Normalized pressure measured with transducer N° 312 for configuration SR as a function of jet velocity (2.5-27.0 m/s) and Y/D ratio (0-9.7). Maximum pressure (top left), mean pressure (top right), minimum pressure (bottom left) and transducer location (bottom right).

Transducer 313 (inside the vertical fissure near the plunge pool bottom)

Transducer N° 313 is located inside the vertical fissure at 50 mm from the plunge pool bottom.

Maximum pressures increase quadratically as a function of the jet velocity (Figure 6.27). Core, transition and developed jets show the same trend: up to 12.3-14.7 m/s maximum pressures are similar for all water depths. Whereas for jet velocities larger than 14.7 m/s, core and transition jets show a significant pressure increase. The difference between maximum pressures, for core and transition jets and developed jets, grow as a function of the jet velocity. When the jet velocity increases, the difference between the three jet types increase as well (largest value

for Y/D = 1.4 and smaller value for Y/D = 9.7) reaching ∼6 Bar for a jet velocity of 27.0 m/s.

Transducer N° 313 recorded some extreme pressures that have not been recorded by transducer N° 317 located at the end of the vertical fissure (Figure 6.28). The jet penetrates directly inside the 3-dimensional fissure (jet axis aligned to the vertical fissure axis) and loaded directly the transducer. The high-velocities of the water flow near the fissure entrance can generated this extreme pressure values by "cavitation" phenomenon or by a compression-decompression phenomenon of the air bubbles present in the water near the fissure entrance. The water flow is strongly perturbed by the impact on the plunge pool bottom and by its penetration inside the vertical fissure (the jet is deflected and partially penetrates inside the fissure). The pressure fluctuations may generate some negative pressures inside the fissure and generating this phenomenon. Cavitation occurs when a liquid is subjected to a rapid pressure changes, causing the formation of cavities (bubbles) in the lower pressure regions of the water. When these bubbles enter high pressure areas, they collapse causing a cyclic stress on the near surface with generations of some extreme pressure peaks. At the same time the compression and decompression phenomenon of the air bubbles present in the water may contribute at these pressure peaks. These peaks could be the peaks that have been recorded with transducer N° 313 (as observed in Figure 6.27).

Mean pressures grow with the same trend and are almost the same for all water depths and all jet velocities. Mean pressures are lower than near the fissure entrance at the plunge pool bottom (N° 312).

Minimum pressures decrease with the same trend for all water depths. Up to 14.7-17.2 m/s, minimum pressures are almost constant, but for higher jet velocities they show a significant decrease reaching the smaller value for the largest jet velocity. These two phenomenons may generate these extreme pressure values that have been recorded with this transducer.

Transducer 317 (inside the vertical fissure near the central cavity bottom)

Transducer N° 317 is located 7 mm from the bottom of the central cavity (or 194 mm from the plunge pool).

Maximum pressures grow quadratically for core, transition and developed jets (Figure 6.28). Maximum pressures recorded with this transducer are lower than the pressures recorded near the fissure entrance (N° 313, Figure 6.27). Up to 12.3-14.7 m/s maximum pressures are almost the same for the two transducers but for higher jet velocities (larger than 14.7 m/s) the difference is visible. These extreme pressure values disappear along the vertical fissure: the previous "cavitation" phenomenon and the compression-decompression phenomenon of air bubbles present into the water are only concentrated near the fissure entrance. The two intermediate transducers (N° 314 and N° 315, Figure 4.8) show pressure values similar to transducer N° 317 located at the end of the vertical fissure.

Mean pressures grow with the same trend for the three jet types. Mean pressure values are similar to the values recorded near the fissure entrance (mean pressures change weakly inside the vertical fissure). They are lower than near the fissure entrance at the plunge pool bottom (N° 312).

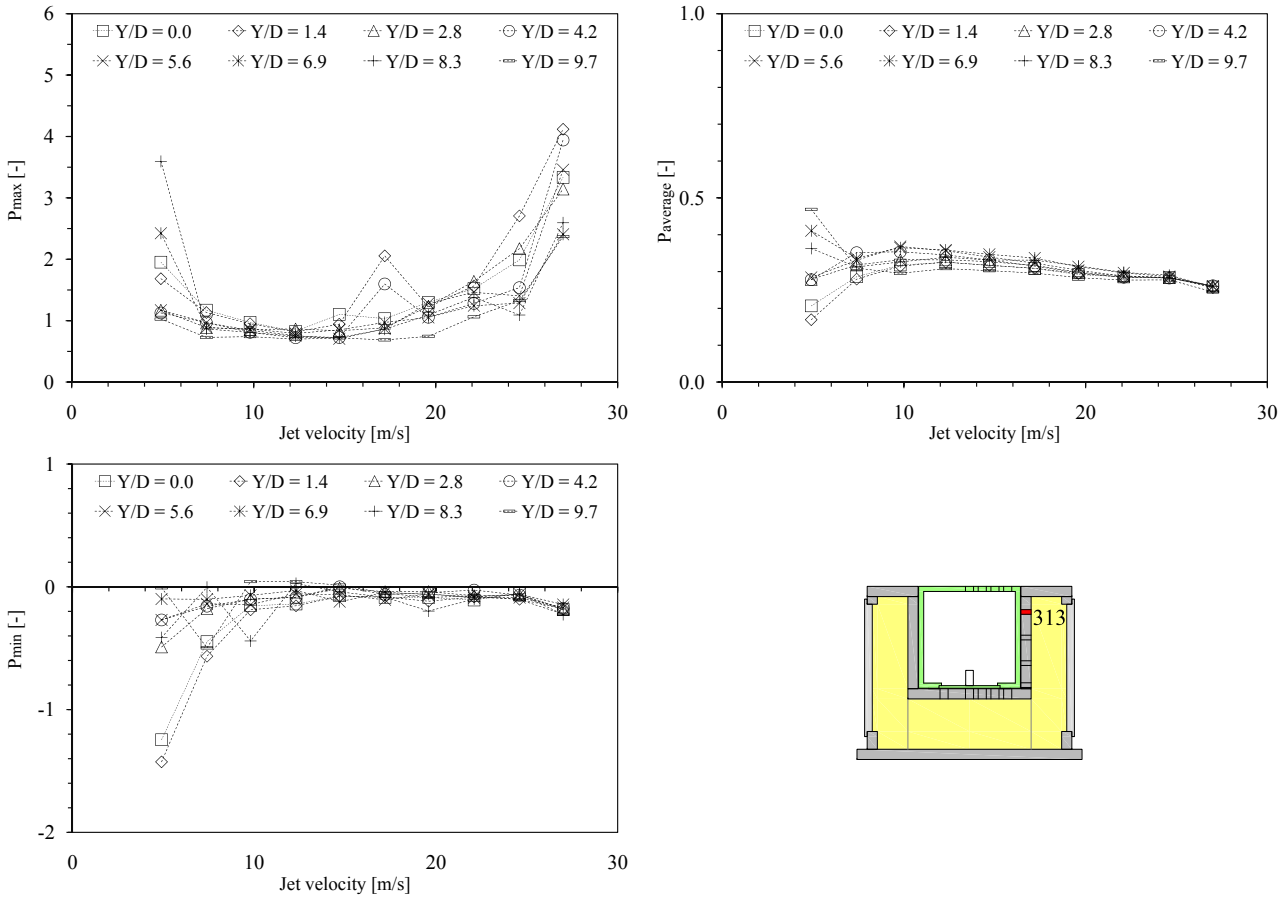

Figure 6.27: Normalized pressure measured with transducer N° 313 for configuration SR as a function of jet velocity (2.5-27.0 m/s) and Y/D ratio (0-9.7). Maximum pressure (top left), mean pressure (top right), minimum pressure (bottom left) and transducer location (bottom right).

Minimum pressures grow slowly until the second-last jet velocity where a pressure drop is observable for the largest jet velocity. Core, transition and developed jets show the same behavior.

Transducer 318 (underneath the block near the vertical fissure)

Transducer N° 318 is located underneath the block, at 25 mm from the vertical fissure on the same vertical axis than transducer N° 312.

As observed for the previous configuration (Chapter 6.2.2), the passage from the vertical fissure to the fissure located underneath the block affect weakly the pressure values (Figure 6.29). Maximum, mean and minimum pressure values show exactly the same trend and almost the same values than transducer N° 317 located at the end of the vertical fissure (Figure 6.28). These weakly differences, between the two transducers, reach 0.2-0.3 Bar for a jet velocity of 27.0 m/s. These differences are irrelevant for the lower velocities.

Transducer 321 (underneath block in the center of the measurement box)

Transducer N° 321 is located underneath the block, in the center of the measurement box on the same vertical axis of transducer N° 309.

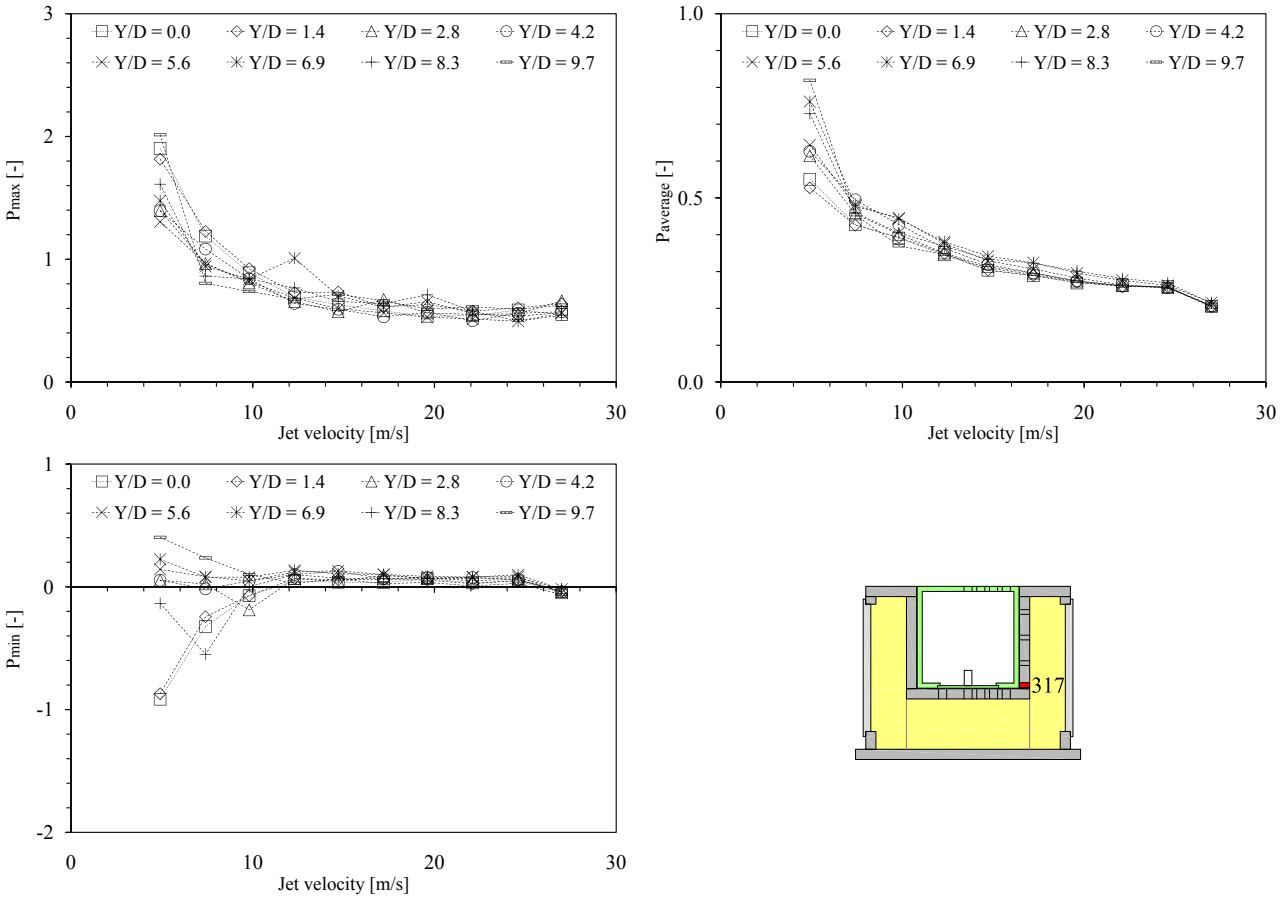

Figure 6.28: Normalized pressure measured with transducer N° 317 for configuration SR as a function of jet velocity (2.5-27.0 m/s) and Y/D ratio (0-9.7). Maximum pressure (top left), mean pressure (top right), minimum pressure (bottom left) and transducer location (bottom right).

The pressure propagation underneath the block affects weakly the pressure values (Figure 6.8). Maximum, mean and minimum pressure values show exactly the same trend and almost the same values than transducer N° 318 located near the vertical fissure (Figure 6.29). These weakly differences reaches 0.1-0.2 Bar for the largest jet velocity. These differences are irrelevant for the lower velocities.

These differences, between the transducer situated at end of the vertical fissure and the transducers situated underneath the block, may be related to the energy loss inside the 3-dimensional fissure (a change of 90° in the direction). The propagation of the water flow inside the 3-dimensional fissure presents some zone where it lost some energy: along the vertical fissure, at the direction change between the vertical fissure and the fissure underneath the block and underneath the block.

Pressure field surrounding the block

As observed for the previous configuration (jet impact on the block center, Chapter 6.2.2) when the pressures recorded with the four transducers situated on the block upper face are plotted together, the pressure distribution looks similar an exponential distribution proposed in the

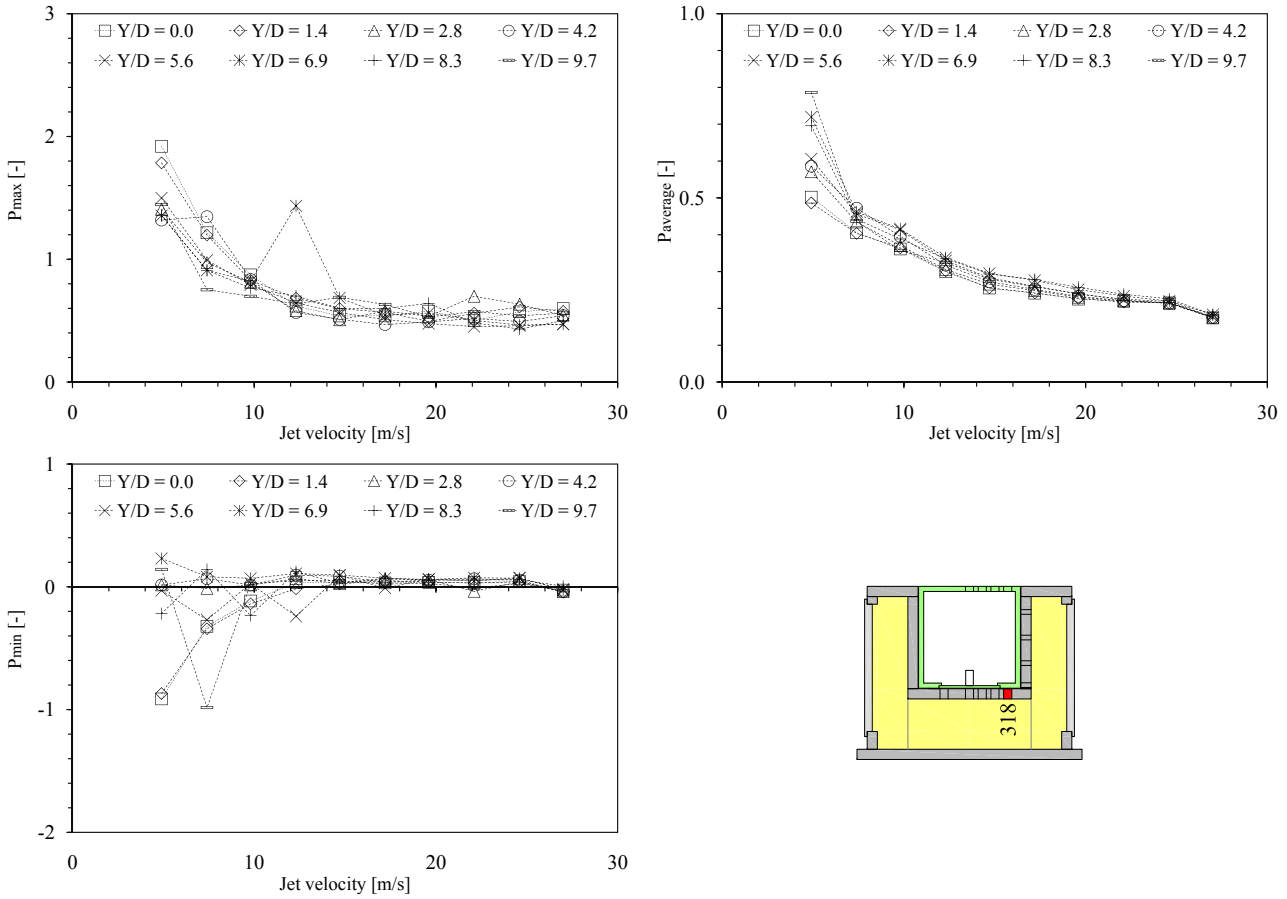

Figure 6.29: Normalized pressure measured with transducer N° 318 for configuration SR as a function of jet velocity (2.5-27.0 m/s) and Y/D ratio (0-9.7). Maximum pressure (top left), mean pressure (top right), minimum pressure (bottom left) and transducer location (bottom right).

literature (Chapter 5.1.1.3).

Inside the fissure, the observations made for configuration CR can be applied: along the vertical fissure mean pressure increases weakly, maximum and minimum pressures have a conic-shape (larger values have been recorded near the fissure entrance and smaller values near the central cavity bottom) and underneath the block the pressures are almost constant (maximum, mean and minimum).

Figure 6.31 shows the pressure field acting on the block for a Y/D ratio of 8.3 and a jet velocity of 27.0 m/s.

The same behavior has been observed for the other water depths (core, transition and developed jets) and jet velocities.

6.3.3 Pressure coefficients

As before the non-dimensional pressure coefficients (the formulas have been described in Chapter 5.2.2) have been computed using the pressures measured on the block upper face and inside the 3-dimensional fissure.

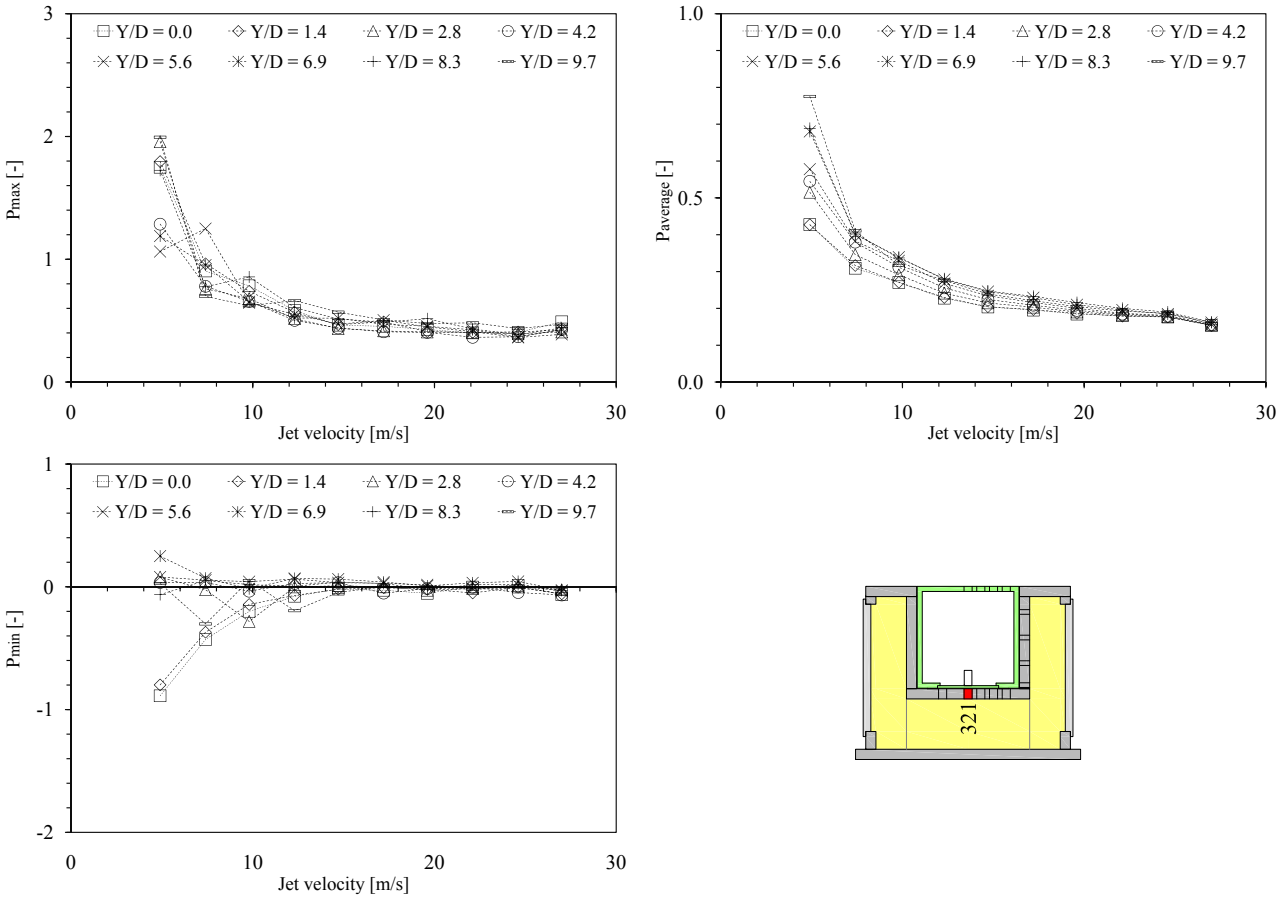

Figure 6.30: Normalized pressure measured with transducer N° 321 for configuration SR as a function of jet velocity (2.5-27.0 m/s) and Y/D ratio (0-9.7). Maximum pressure (top left), mean pressure (top right), minimum pressure (bottom left) and transducer location (bottom right).

6.3.3.1 Mean pressure coefficient C_p

The mean pressure coefficients (C_p, Figure 6.32) computed on the block upper face (transducer N° 312) are in reasonable agreement with the theoretical curves developed by Ervine et al. (1997) and with previous pressure records made by Bollaert (2002b) and Manso (2006). The mean pressure coefficients computed at the plunge pool bottom for core and transition jets (Y/D $<$ 6) are almost constant for the same jet velocity. Developed jets (Y/D $>$ 6) show a trend similar to these curves. Transducer N° 312 (situated at 25 mm from the stagnation point) shows a good correlation with the theoretical curves than transducer N° 309 situated on the block center (at 100 mm from the stagnation point). The pressure field decreases radially outwards from the stagnation. Hence, the mean pressure coefficients recorded at the block center is less than near the stagnation point and range between 0.02 and 0.18. With an increase of the jet velocity the coefficient becomes smaller due to the kinetic energy used to normalize the mathematical expressions (Chapter 5.2.2).

The coefficients computed inside the 3-dimensional fissure are lower than the corresponding coefficients computed directly under the jet. For core and transition jets (Y/D $<$ 6), the coefficient is almost constant for the same jet velocity, but developed jets (Y/D $>$ 6) show a

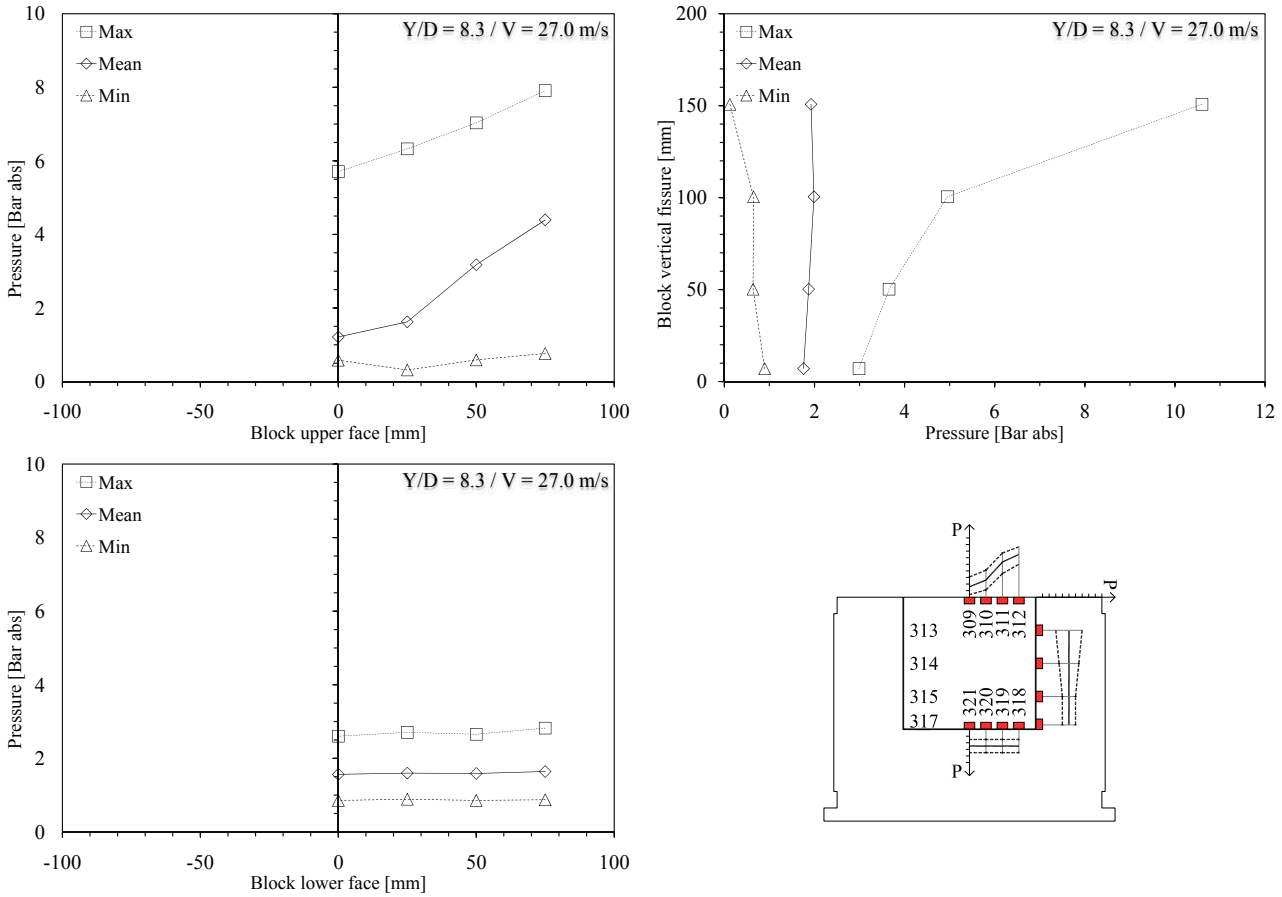

Figure 6.31: Pressure field acting around the block for configuration SR, a developed jet (Y/D = 8.3) and a jet velocity of 27.0 m/s. Pressure acting on the block upper face (top left), along the vertical fissure (top right), underneath the block (bottom left) and pressure filed sketch (bottom right). Pressures are expressed in absolute Bar.

decrease of its values. Along the vertical fissure transducer N° 317 situated near the central cavity bottom shows higher values than transducer N° 313 situated near the fissure entrance due to the direct fissure loading performed by the jet. Underneath the block, transducer N° 318 situated near the vertical fissure show higher values than transducer N° 321 situated at the block center (these differences are generated by the energy lost inside the fissure). The mean pressure coefficients for transducers situated inside the fissure range between 0.14 and 0.32. Transducer N° 313 situate near the fissure entrance shows a lower limit of 0.05.

6.3.3.2 Turbulent pressure fluctuation coefficient $C_{p'}$

The turbulent pressure fluctuation coefficients ($C_{p'}$, Figure 6.33) recorded all around the block are in reasonable agreement with the theoretical curve developed by Ervine et al. (1997). Core jets (Y/D $<$ 4) generated by jet velocities up to 12.3 m/s show coefficient values slightly higher than the theoretical curve. Transition and developed jets (Y/D $>$ 4) follow better this curve. The coefficients computed near the stagnation point (transducer N° 312) are always higher than the coefficients computes at the block center (transducer N° 309). Far away from the stagnation point, the pressure fluctuations are less intense for the same jet velocity. The

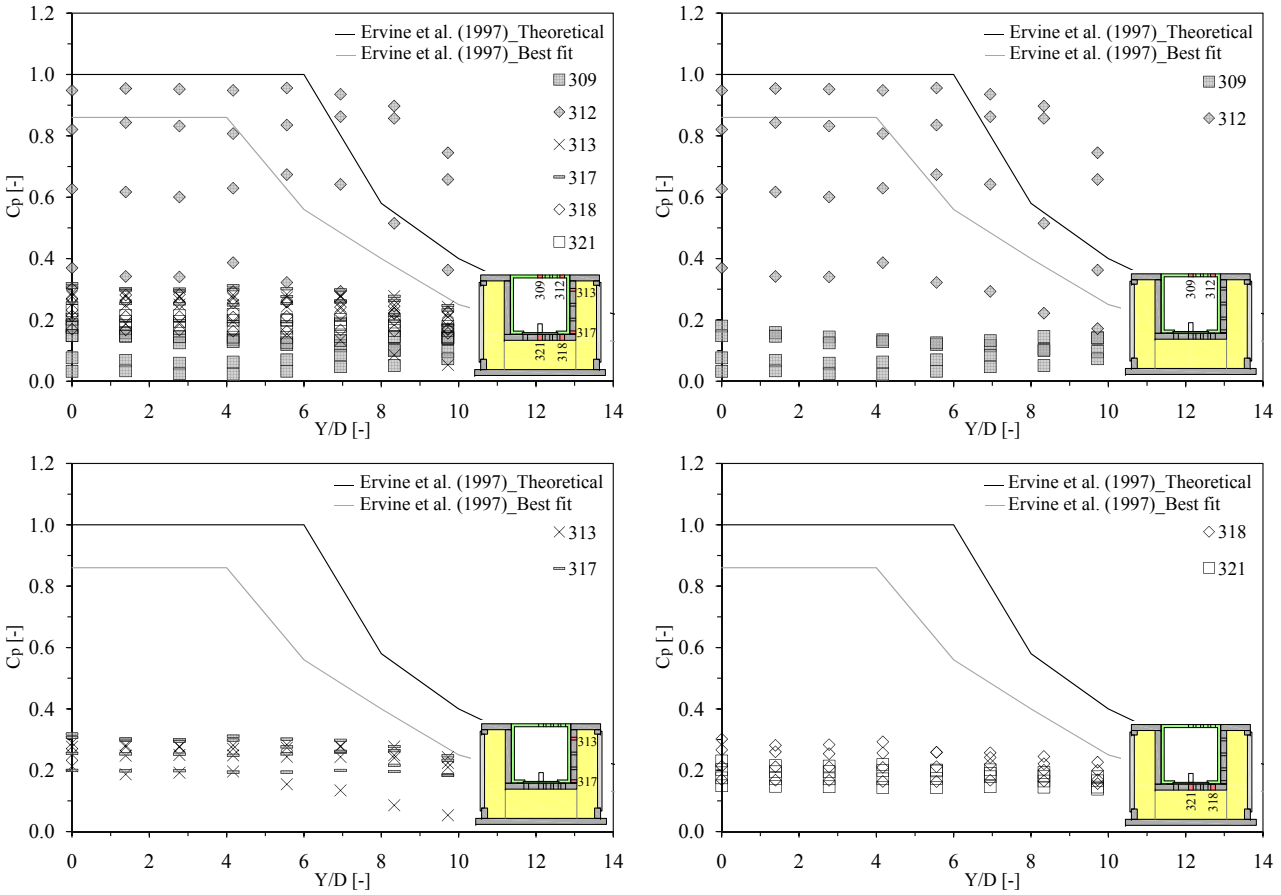

Figure 6.32: Mean pressure coefficient C_p computed for configuration SR as a function of jet velocity (4.9, 12.3, 19.6 and 27.0 m/s) and Y/D ratio (0-9.7). Overview of the six pressure transducers (top left), on the block upper face or at the plunge pool bottom (top right), along the vertical fissure (bottom left) and underneath the block (bottom right).

turbulence decrease radially outward from the stagnation point and as a function of the water depth.

Inside the fissure, the three jet types show approximately a constant coefficient value for the same jet velocity. Along the vertical fissure, transducer N° 317 situated near the central cavity bottom shows smaller values than transducer N° 313 situated near the fissure entrance. The turbulence is higher near the entrance and it is reduced inside the fissure. Underneath the block transducer N° 318 situated near the vertical fissure shows higher values than transducer N° 321 situated at the block center. However, these differences are small and disappear with an increase of the jet velocity. The pressure fluctuations coefficients computed inside the fissure are lower than at the plunge pool bottom for the same velocity. The coefficient values are almost constant for the same jet velocity and range between 0.03 and 0.19.

6.3.3.3 Positive extreme pressure fluctuation coefficient C_p^+

The positive extreme pressure fluctuation coefficients (C_p^+, Figure 6.34), for transducers situated on the block upper face (N° 309 and N° 312) are higher than the Ervine's curve. The coefficient values, for the two transducers, decrease with an increase of the Y/D ratio. Transducer N° 312

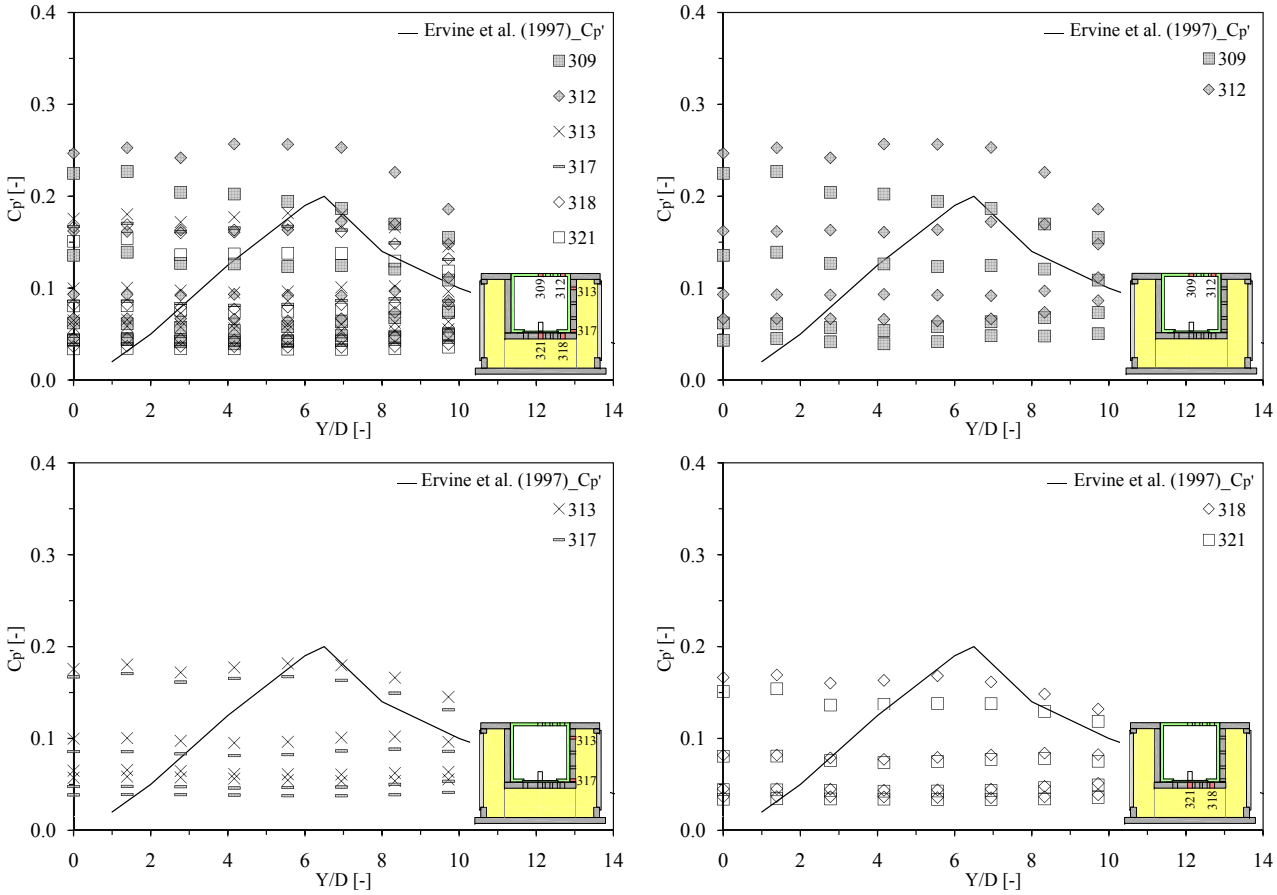

Figure 6.33: Turbulent pressure fluctuation coefficient $C_{p'}$ computed for configuration SR as a function of jet velocity (4.9, 12.3, 19.6 and 27.0 m/s) and Y/D ratio (0-9.7). Overview of the six pressure transducers (top left), on the block upper face or at the plunge pool bottom (top right), along the vertical fissure (bottom left) and underneath the block (bottom right).

shows values smaller than transducer N° 309: it seems that the positive extreme fluctuations are more intense when the coefficient values are computed far away from the stagnation point for core and transition jets (Y/D < 6).

For the three jet types, coefficients computed inside the fissure are almost constant for the same jet velocity except for transducer N° 313 situated near the fissure entrance. Along the vertical fissure transducer N° 317 situated near the central cavity bottom did not show the same peaks. These peaks are dissipated inside the fissure. The extreme pressure recorded with this transducer generates this larger coefficient values (Figure 6.27). Underneath the block, both transducers (N° 318 and N° 321) are situated in the same range of values and this range is more compact for higher Y/D ratios. Underneath the block they are almost constant with weak differences and are similar to values recorded at the end of the vertical fissure. The small pressure differences, recorded between transducers situated inside the fissure, are the origin of these small differences. The coefficients range between 0.2 and 1, excepts the maximum value observed for transducer N° 313 that reaches ∼3.8.

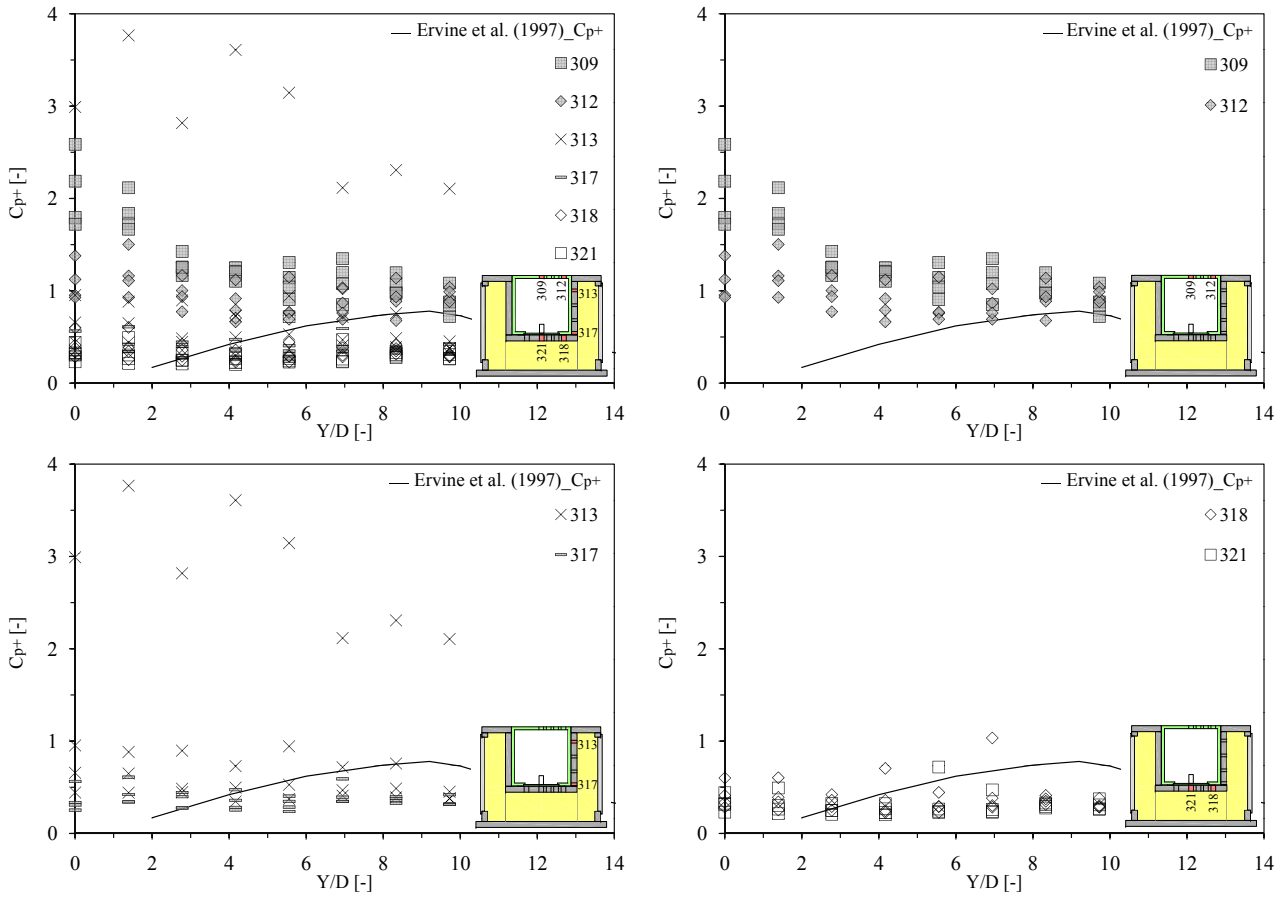

Figure 6.34: Positive extreme pressure fluctuation coefficient C_p^+ computed for configuration SR as a function of jet velocity (4.9, 12.3, 19.6 and 27.0 m/s) and Y/D ratio (0-9.7). Overview of the six pressure transducers (top left), on the block upper face or at the plunge pool bottom (top right), along the vertical fissure (bottom left) and underneath the block (bottom right).

6.3.3.4 Negative extreme pressure fluctuation coefficient C_p^-

The negative extreme pressure fluctuation coefficients (C_p^-, Figure 6.35) are in reasonable agreement with the theoretical curve proposed by Ervine et al. (1997). The transducer situated near the stagnation point shows higher values than this curve and they are almost constant (between 0.4 and 1.0 with some values outside of this range). This trend is valid for core, transition and developed jets. Transducer N° 309, situated at 100 mm from the stagnation point, shows values smaller than transducer N° 312, except for jet velocities lower than 7.4 m/s where some coefficient values are situated outside of this range. The coefficient values are lower than 0.5.

Along the vertical fissure transducer N° 313 situated near the fissure entrance shows values constantly higher than the coefficients computed at the end of the vertical fissure (N° 317). This difference is more accentuate for Y/D ratios lower than 2 and greater than 8. Transducer N° 317 shows values almost constant for the same jet velocity but transducer N° 313 shows fluctuating values for the same jet velocity. The coefficients computed underneath the block are almost constant, except for jet velocities lower than 7.4 m/s, for Y/D ratios lower than 2 and greater than 9 where the coefficients are higher (between 0.2 and 0.6).

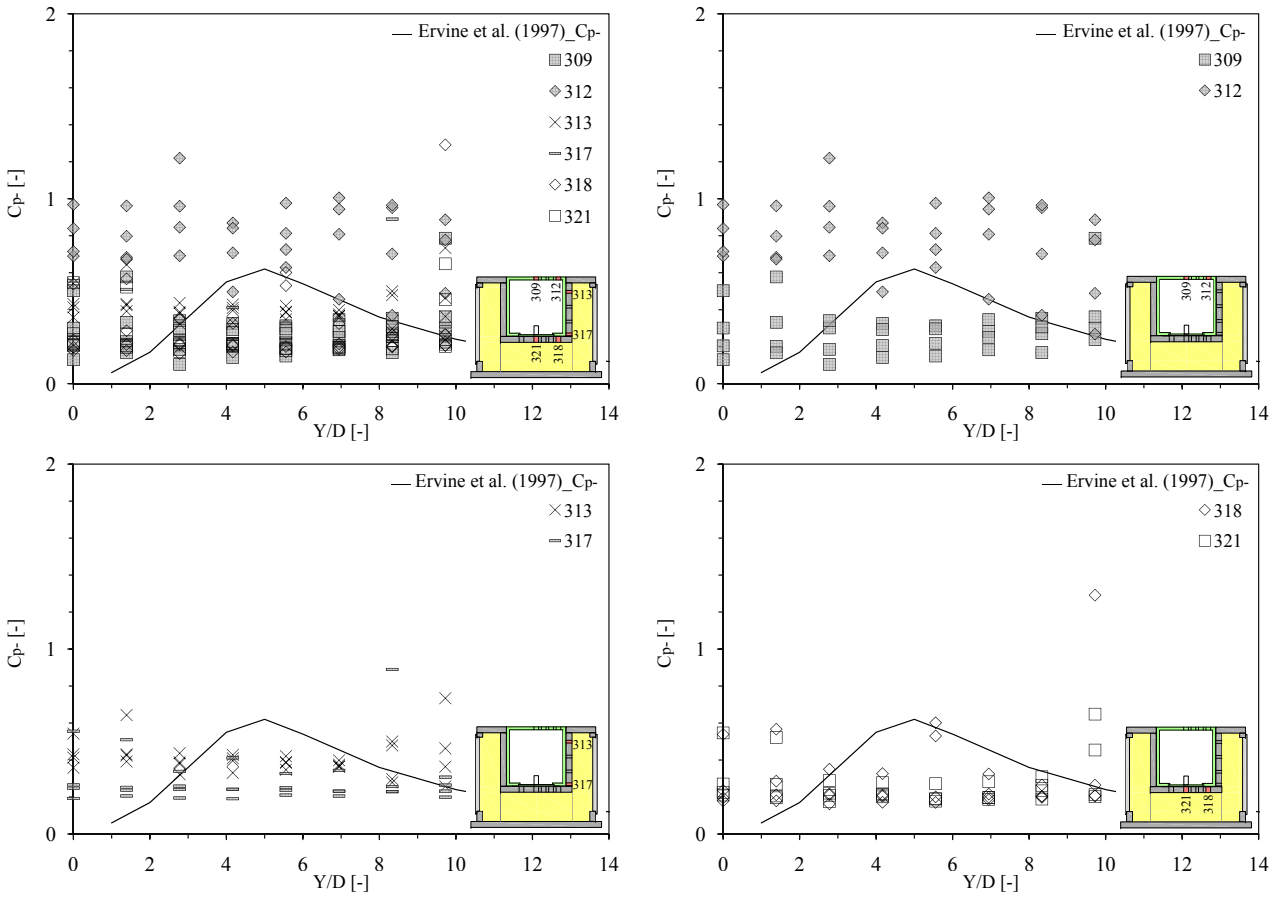

Figure 6.35: Negative extreme pressure fluctuation coefficient C_p^- computed for configuration SR as a function of jet velocity (4.9, 12.3, 19.6 and 27.0 m/s) and Y/D ratio (0-9.7). Overview of the six pressure transducers (top left), on the block upper face or at the plunge pool bottom (top right), along the vertical fissure (bottom left) and underneath the block (bottom right).

6.3.3.5 Positive extreme pressure coefficient $C_{p,max}$

The positive extreme pressure coefficients ($C_{p,max}$, Figure 6.36) computed at the plunge bottom are higher than inside the fissure for the same jet velocity. Core jets (Y/D < 4) shows higher values than transition and developed jets (Y/D > 4). The largest difference reaches 0.5. The two transducers (N° 309 and N° 312) show similar values even if transducers are not located in the same position (the distance between the two transducers is 75 mm).

Inside the fissure, core, transition and developed jets show values almost constant for the same jet velocity, except for transducer N° 313 situated near the fissure entrance, as has been observed for the previous pressure coefficient. Along the vertical fissure, transducer N° 317 situated near the central cavity bottom shows lower values than the transducer situated near the fissure entrance for the same jet velocity. The positive extreme pressure recorded with this transducer generates these largest values. Underneath the block both transducers (N° 318 and N° 321) are situated in the same range of values and are almost constant with weak differences for the same jet velocity. The coefficient values are similar to the values computed at the end of the vertical fissure. Small differences are generated by the pressure differences observed in

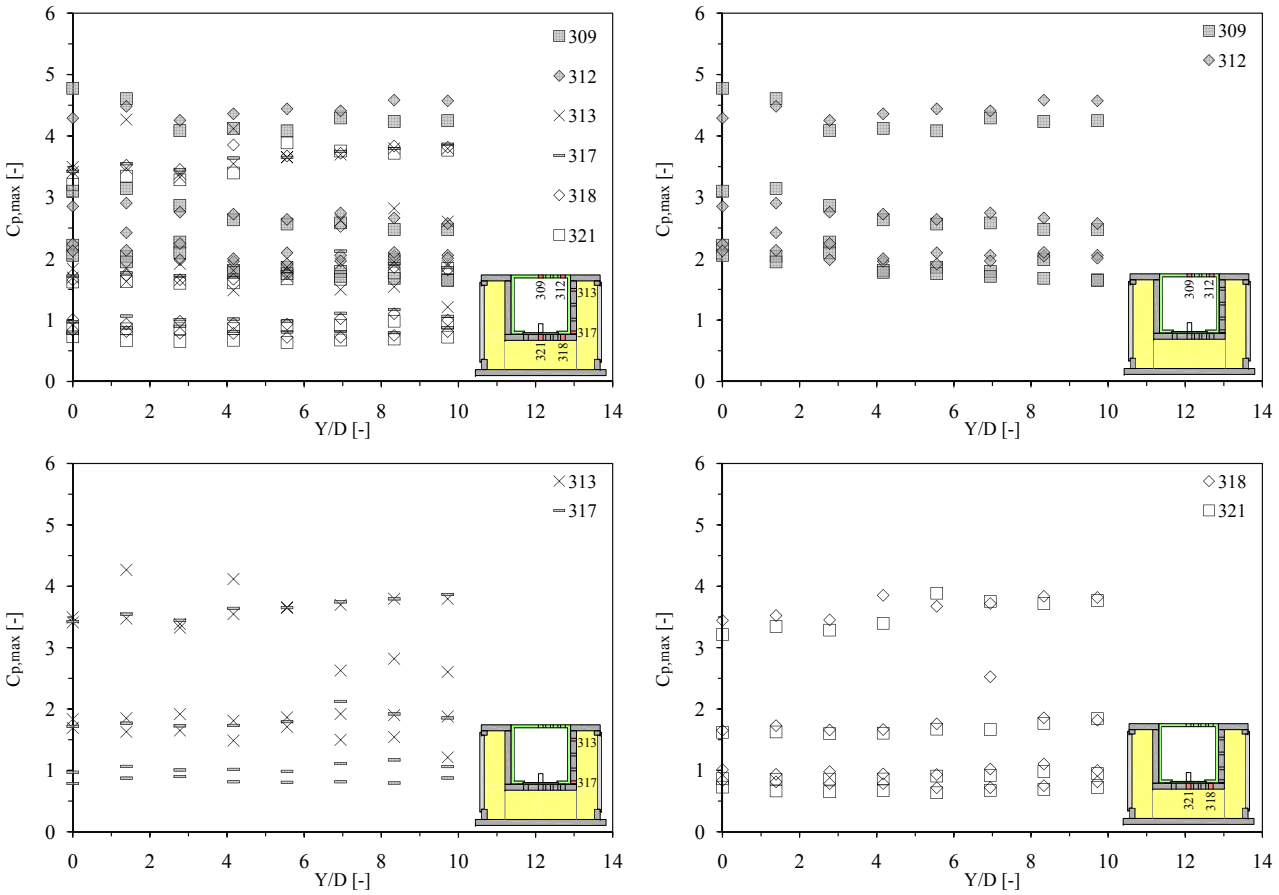

Figure 6.36: Positive extreme pressure coefficient $C_{p,max}$ computed for configuration SR as a function of jet velocity (4.9, 12.3, 19.6 and 27.0 m/s) and Y/D ratio (0-9.7). Overview of the six pressure transducers (top left), on the block upper face or at the plunge pool bottom (top right), along the vertical fissure (bottom left) and underneath the block (bottom right).

the pressure field surrounding the block.

The highest coefficient values are generated by small jet velocities. A small kinetic energy (small jet velocities), used to normalize the pressure, generates a larger coefficient as observed before for the other coefficients.

6.3.3.6 Negative extreme pressure coefficient $C_{p,min}$

The negative extreme pressure coefficients ($C_{p,min}$, Figure 6.36) show similar values for the three jets types and all jet velocities. At the plunge pool bottom and inside the fissure, with an increase of the jet velocity the coefficient values show a decreasing trend. The higher coefficient values are generated by small jet velocities. As explained before, due to the small kinetic energy generated by the jet, the coefficients are higher than for high-velocity jet. The coefficient values, computed for small jet velocities show a rising trend as a function of the water depths. However, with an increase of the jet velocity the coefficients tend to be almost constant for all Y/D ratios.

Along the vertical fissure the transducer situated near the central cavity bottom (N° 317) shows higher value than the transducer situated near the fissure entrance for the same jet

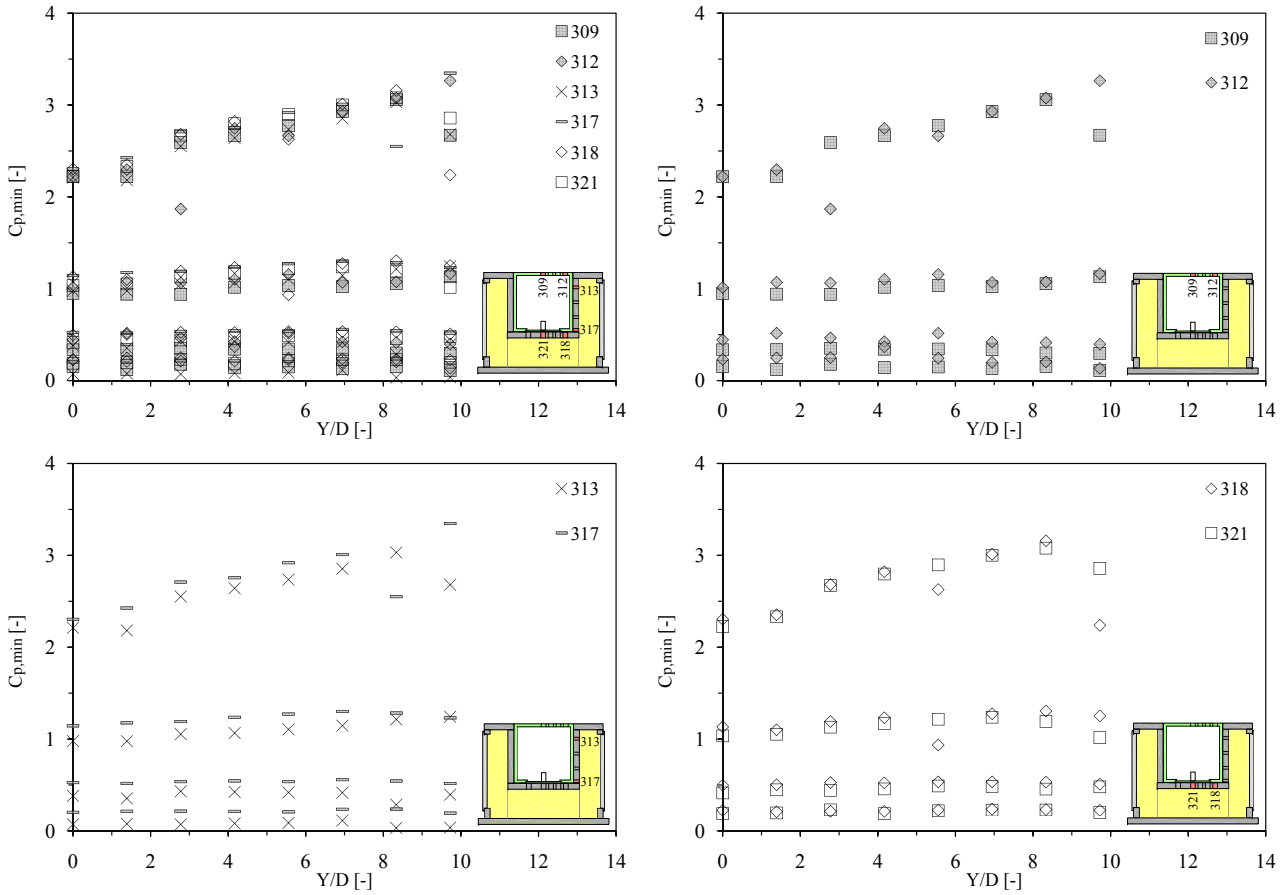

Figure 6.37: Negative extreme pressure coefficient $C_{p,min}$ computed for configuration SR as a function of jet velocity (4.9, 12.3, 19.6 and 27.0 m/s) and Y/D ratio (0-9.7). Overview of the six pressure transducers (top left), on the block upper face or at the plunge pool bottom (top right), along the vertical fissure (bottom left) and underneath the block (bottom right).

velocity and for all Y/D ratios. Underneath the block both transducers (N° 318 and N° 321) show the same values with some small differences.

6.3.4 Displacements and accelerations of block

The transducers location is shown in Figure 6.24. As explained in Chapter 6.2.4, the block responses have been recorded simultaneously at the pressures with the same acquisition rate. The initial distance between the bottom of the central cavity and the block lower face is ∼0.85 mm (block initial position).

6.3.4.1 Displacements of block

The block moves up (Figure 6.38) with jet velocities of 7.4 m/s. The block is subjected to small fluctuations and the mean displacements correspond to the block initial position. At 7.4 m/s the amplitude of this vertical displacements increases and the block did not return to its initial position: the block reaches a new equilibrium position that change as a function of jet velocity.

For jet velocities larger than 14.7 m/s, the block shows a stable equilibrium position until the largest jet velocity (27.0 m/s) where the block suddenly moves up again. This equilibrium position corresponds approximately at two times of the equilibrium position reached with the previous jet velocity (24.6 m/s). This evolution of the equilibrium position can be observed as well for the mean displacement. Developed jets generate largest vertical displacements, corresponding to ∼1.8 mm. Mean displacement is almost the same for all water depths and for a jet velocity of 27.0 m/s reaches ∼1.25 mm. Minimum displacement is equivalent at the block initial position.

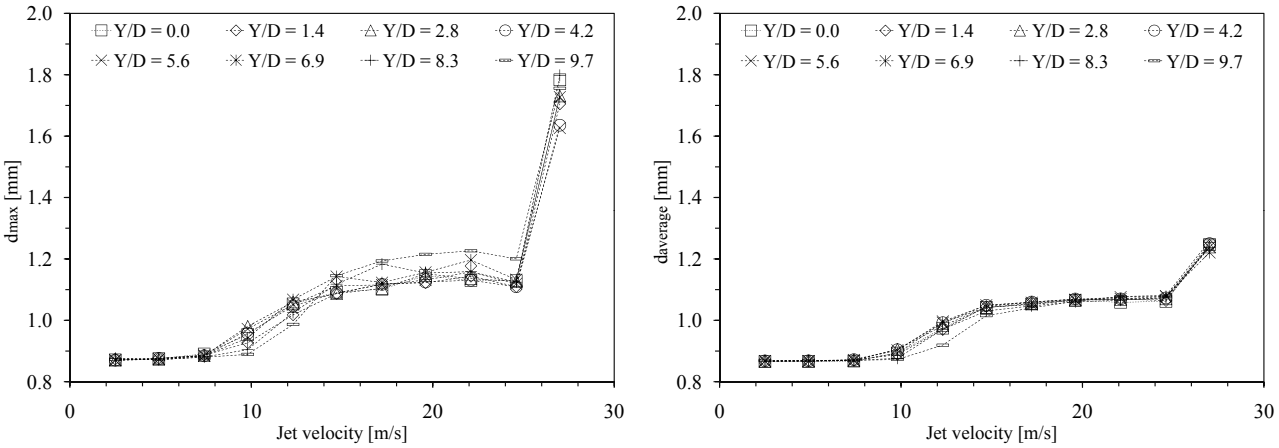

Figure 6.38: Block displacements measured for configuration SR as a function of jet velocity (2.5-27.0 m/s) and Y/D ratio (0-9.7). Maximum (left) and mean displacements of block (right). The block initial position corresponds to a distance of ∼0.85 mm.

6.3.4.2 Accelerations of block

Core jets (Y/D > 4) show the highest accelerations fluctuations (Figure 6.39). The block is directly loaded by the jet and the small water depths influence the block accelerations. Transition and developed jets show an evolution similar to block displacements with some local peaks.

Mean accelerations show as well an evolution as a function of the jet velocity similar to the displacements of block (Figure 6.38). At 7.4 m/s the accelerations are almost constant (∼2.1 g), between 7.4 and 14.7 m/s grow and reach ∼2.9 g and for the maximum jet velocity reach ∼3.9 g. The 0.7 m water depth (Y/D = 9.7) shows some differences: above 12.3 m/s mean acceleration is higher than the other water depths. That may be related to the larger eddies generate inside the plunge poll soliciting the block.

Minimum accelerations showed measurement problems: electrical noises (appears during the measurements) generate incongruous values that reach the acceleration lower limits (-1000 g). This problem is presents for several jet velocities. It may possible that these electrical noises perturb as well maximum and mean accelerations (large difference between core jets and transition and developed jets) and the accelerations are very different from the data recorded with the previous configuration (Figure 6.17).

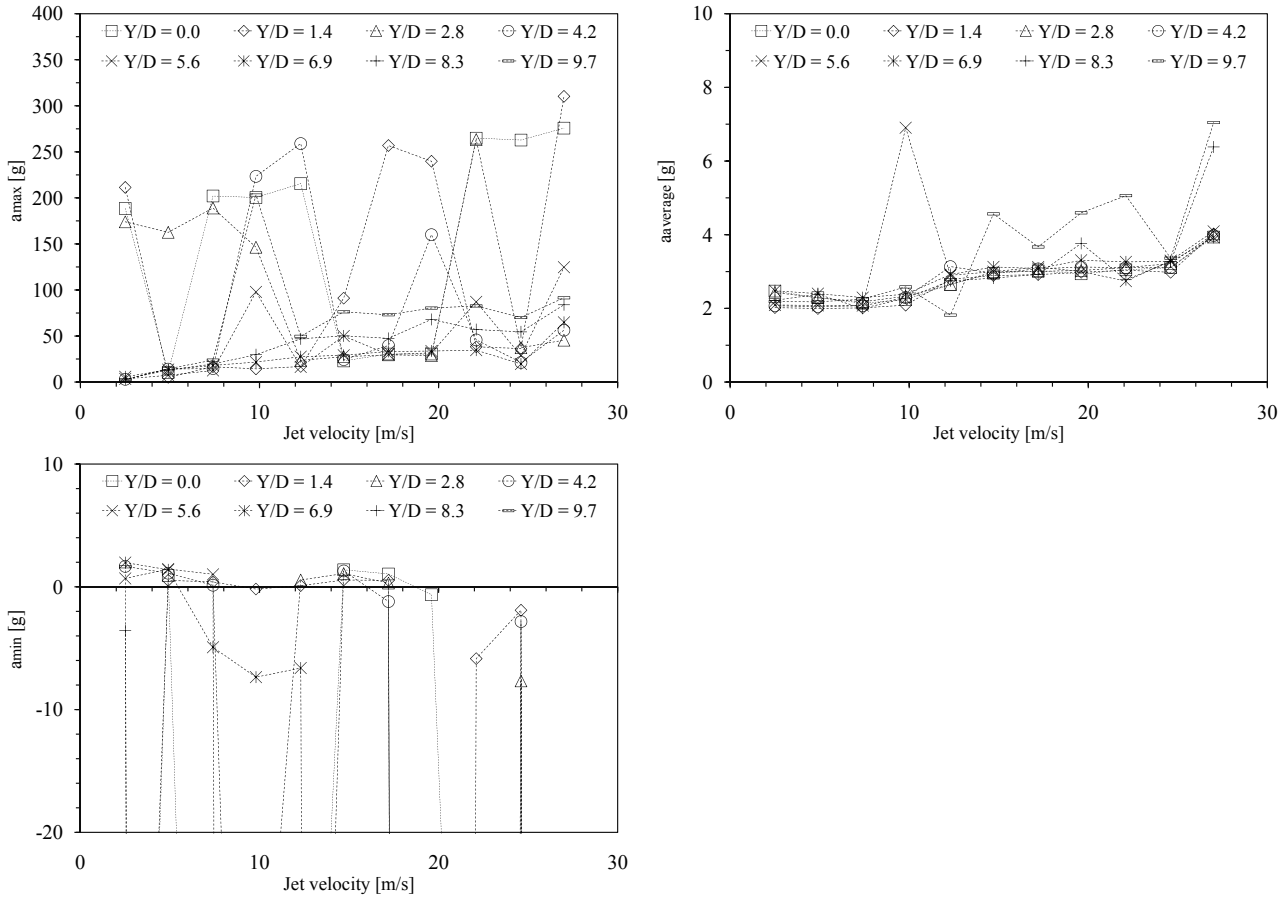

Figure 6.39: Block accelerations measured for configuration SR as a function of jet velocity (2.5-27.0 m/s) and Y/D ratio (0-9.7). Maximum (top left) and mean accelerations of block (top right). Minimum accelerations (bottom left) show some electrical noises that affect the measured values (reach the acceleration lower limit of -1000 g).

6.3.5 Power Spectral Density

In this section only the results for a core (Y/D = 2.8 or 0.2 m), a transition (Y/D = 5.6 or 0.4 m) and a developed jet (Y/D = 8.3 or 0.6 m) and four of the eleven jet velocities are explained (4.9, 12.3, 19.6 and 27.0 m/s).

As observed for the configuration with the jet impact on the block center (CR, Chapter 6.2.5), the energy content increases as a function of the jet velocity. As before, the Power Spectral Density (PSD) may be subdivided into two groups:

I. transducers situated at the plunge pool bottom on the block upper face (N°s 309 to 312);

II. transducers situated inside the 3-dimensional fissure (N°s 313 to 321).

These observations are valid for core, transition and developed jets (Figures 6.40, 6.41 and 6.42).

Pressure transducers fixed on the block upper face have a behavior similar to the previous observations. The low frequency part of the PSD signal ($f < 10$ Hz) looks quite similar for all jet velocities. The energy correlated to each frequency decreases slowly with a slope of

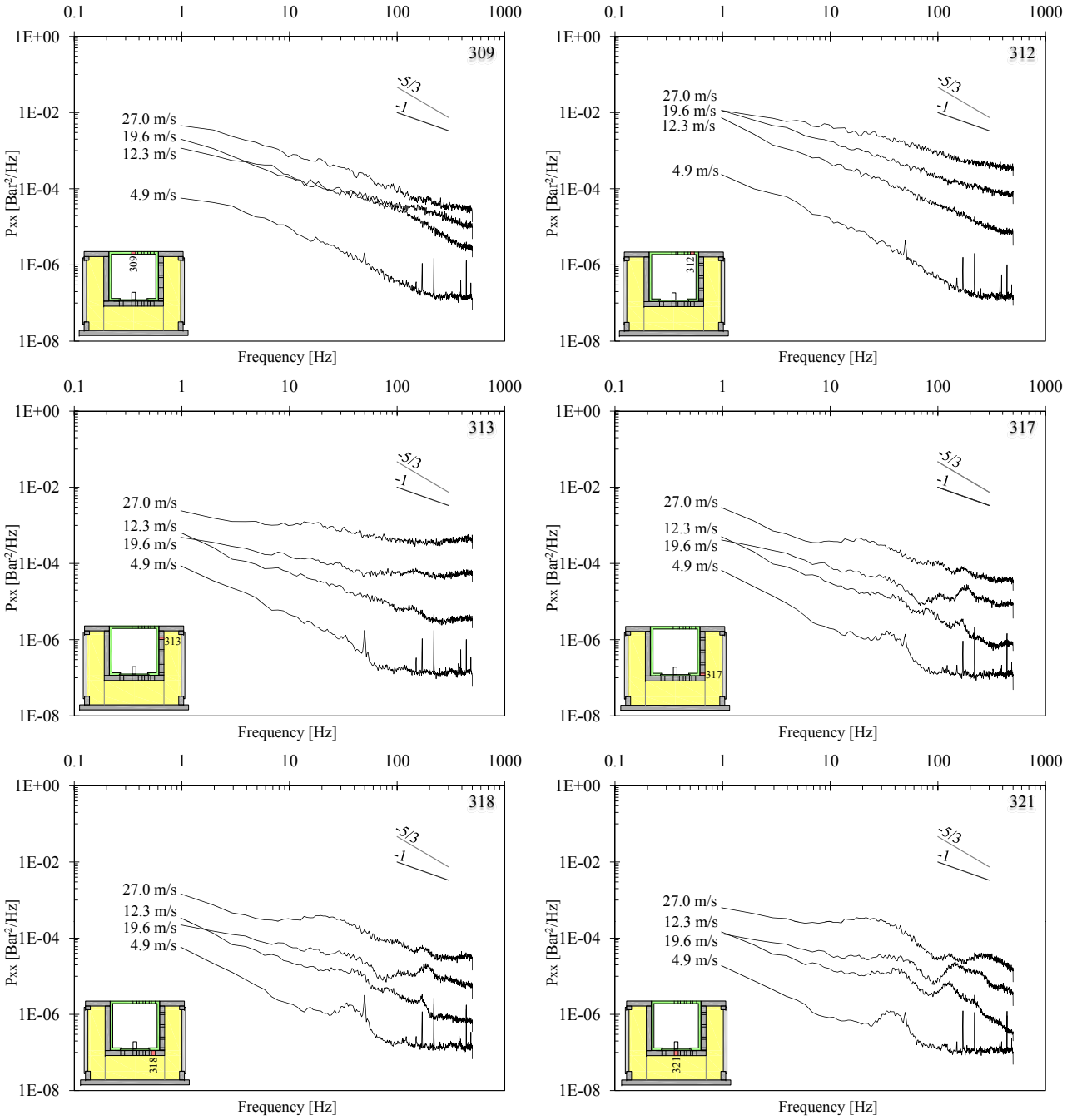

Figure 6.40: Non-dimensional spectral content (PSD) computed for configuration SR. Core jet (Y/D = 2.8) and different jet velocities (4.9, 12.3, 19.6 and 27.0 m/s): on the block upper face pressure transducers N° 309 (top left) and N° 312 (top right); along the vertical fissure pressure transducers N° 313 (center left) and N° 317 (center right); underneath the block pressures transducers N° 318 (bottom left) and N° 321 (bottom right).

approximately -2/3. For higher frequencies ($f > 10$ Hz) the spectral content decreases with a -1 slope.

The pressure transducers situated inside the 3-dimensional fissure show a different behavior. The energy correlated to each frequency is lower than at the plunge pool bottom for the same jet velocity as can be expected. With increasing frequencies, two zones can be distinguished:

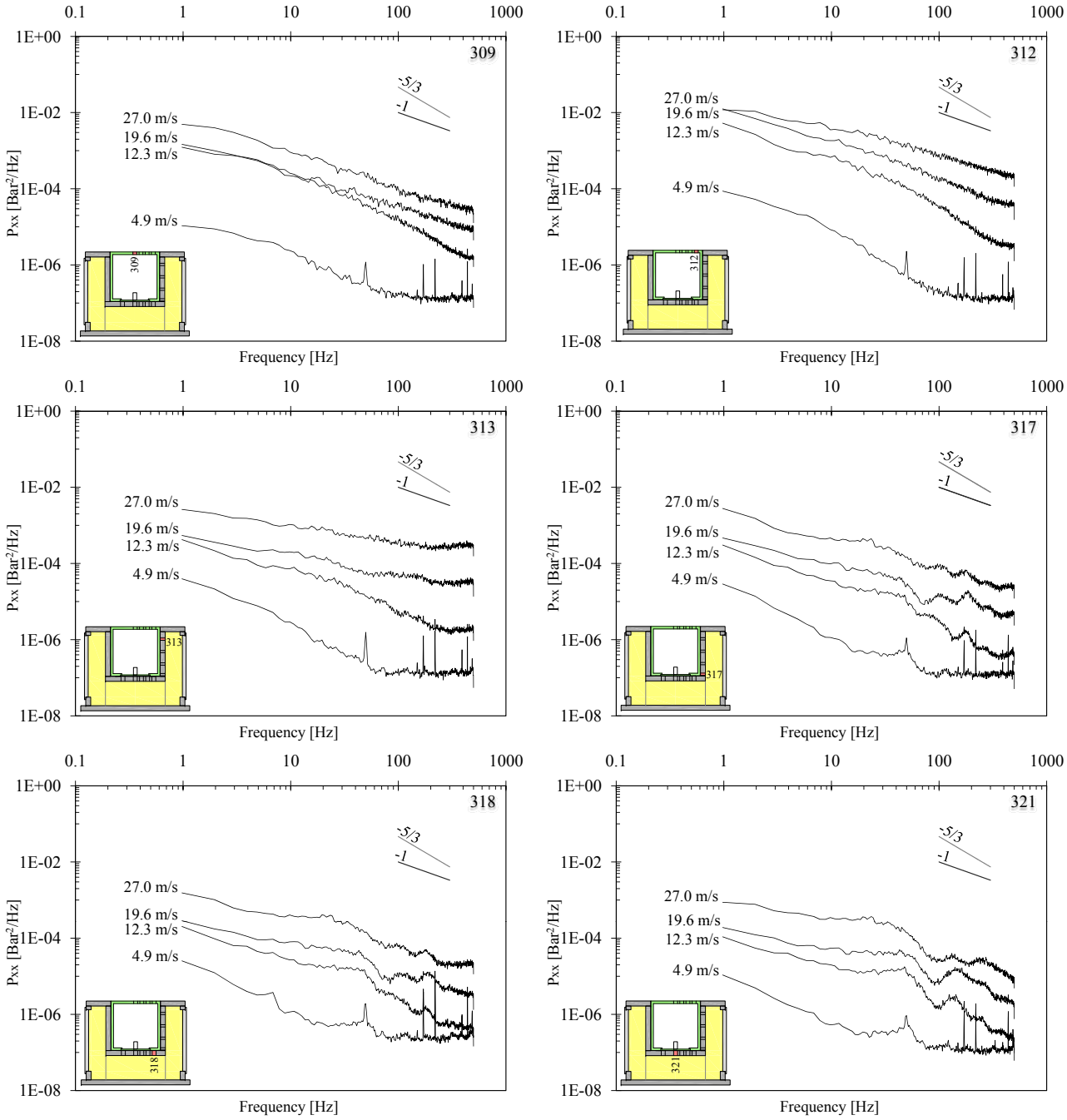

Figure 6.41: Non-dimensional spectral content (PSD) computed for configuration SR. Transition jet (Y/D = 5.6) and different jet velocities (4.9, 12.3, 19.6 and 27.0 m/s): on the block upper face pressure transducers N° 309 (top left) and N° 312 (top right); along the vertical fissure pressure transducers N° 313 (center left) and N° 317 (center right); underneath the block pressures transducers N° 318 (bottom left) and N° 321 (bottom right).

a first zone lowers than 8-10 Hz and a second zone for frequency higher than 8-10 Hz. In the first zone, the energy decreases slowly with a slope approximately situated between -1/3 and -2/3. In the second zone, two different peaks may be detected in the PSD signal: the first peak between 10-20 and 80-100 Hz and the second peak between 80-100 and 200-300 Hz. At low jet velocities, the first peak appears but not the second. When the jet velocity increases, the first

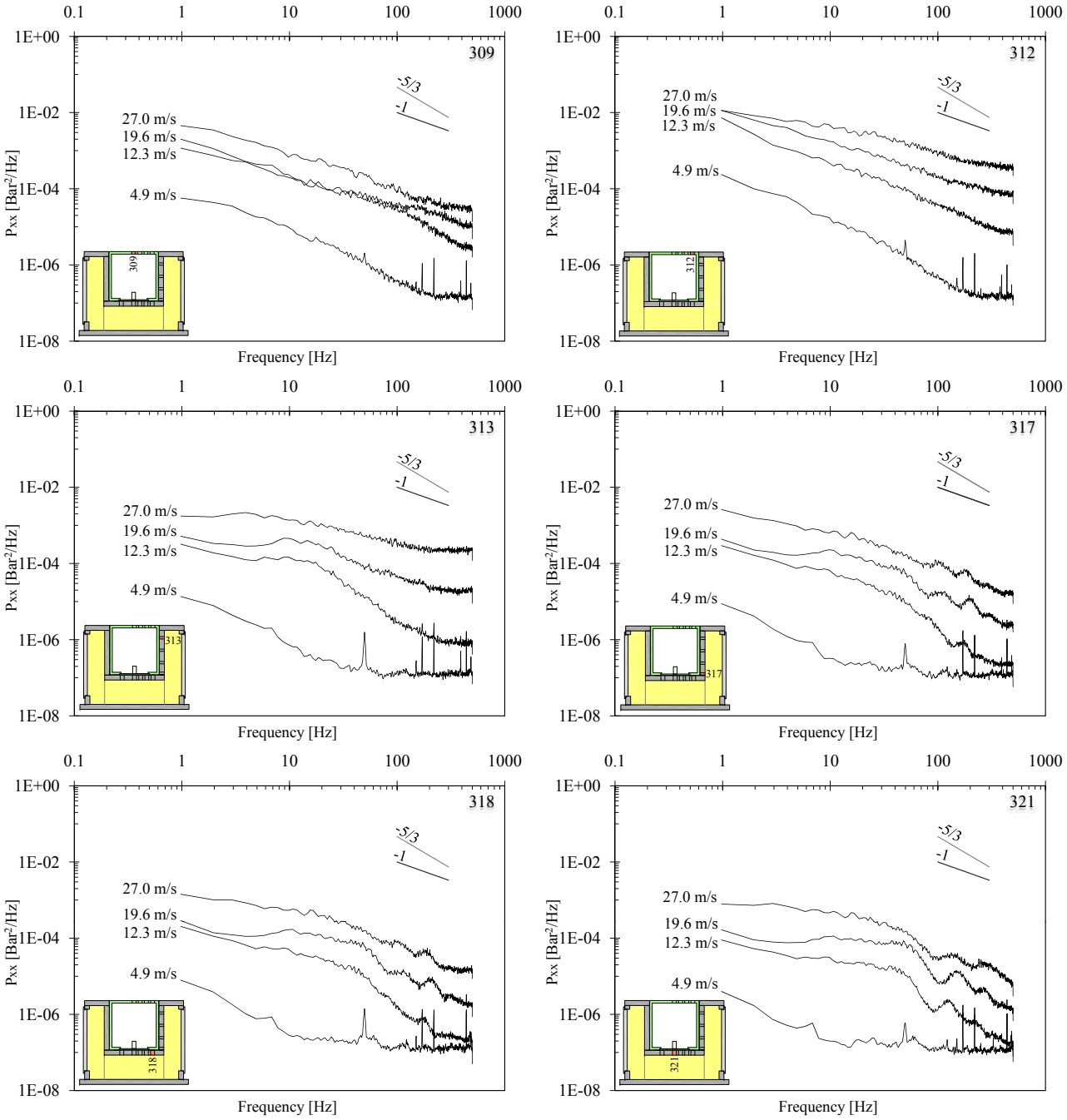

Figure 6.42: Non-dimensional spectral content (PSD) computed for configuration SR. Developed jet (Y/D = 8.3) and different jet velocities (4.9, 12.3, 19.6 and 27.0 m/s): on the block upper face pressure transducers N° 309 (top left) and N° 312 (top right); along the vertical fissure pressure transducers N° 313 (center left) and N° 317 (center right); underneath the block pressures transducers N° 318 (bottom left) and N° 321 (bottom right).

peak disappears and the second peak appears.

As before, the two peaks appear in the PSD signal for core, transition and developed jet. The first peak (at low frequency) is stronger than the second peak. For the previous configuration (CR) the second peak was the stronger (Figures 6.18, 6.19 and 6.20). The two peaks are more visible on the PSD signal for transducers situated far away from the plunge pool bottom.

None of the two peaks appear in the PSD signal computed on the block upper face, as such they are not present at the plunge pool bottom. The same observations made for configuration CR are valid for this configuration. The first peak could correspond to the fissure natural period (Chapter 5.6: range 22-72 Hz) but the second peak did not correspond to the block eigenfrequencies (Chapter 5.7.3: range of 5-9 Hz). The second peak is characterized by high frequencies and is very different from the block eigenfrequencies and is not clearly definable. As explained for the previous configuration, this peak may be correlated with the interaction displacements of block and pressure wave travelling inside the fissure or resonance phenomenon inside the 3-dimensional fissure.

6.3.6 Dynamic block impulsion

The dynamic block impulsion and the respective block uplift have been computed following the theoretical method explained in Chapter 5.4. In this section only the results for a core (Y/D = 2.8 or 0.2 m), a transition (Y/D = 5.6 or 0.4 m) and a developed jet (Y/D = 8.3 or 0.6 m) and four of the eleven jet velocities are explained (4.9, 12.3, 19.6 and 27.0 m/s). Figures 6.43, 6.44 and 6.45 show the comparison between theoretical and measured uplift. The dynamic block impulsion is analyzed in Chapter 7.1.

As explained before (Chapter 6.2.6), two coefficients (added mass and pressure reduction coefficient) have been calibrated to fit theoretical and measured uplift.

By analyzing the time evolution of the block uplift (theoretical and measured, Figures 6.43, 6.44 and 6.45), it is possible to observe that the recorded vertical fluctuations of block can be reproduce theoretically. Almost all vertical fluctuations are present in the theoretical uplift but the amplitude is not always the same: sometimes they are larger and sometimes smaller than the measured uplift.

Table 6.4 summarizes the added mass coefficients and the pressure reduction coefficients that have been used to obtain the similitude between theoretical and measured uplift.

Coefficient	Y/D ratio	Jet velocity V_0						
		4.9	7.4	9.8	12.3	14.7	19.6	27.0
[-]	[-]	[m/s]	[m/s]	[m/s]	[m/s]	[m/s]	[m/s]	[m/s]
AMC	2.8	300	300	140	140	120	90	40
	5.6	300	300	140	140	120	90	40
	8.3	300	300	300	160	140	110	40
PRC	2.8	0	0.41	0.75	0.27	0.06	0.01	0.17
	5.6	0.18	0.61	0.83	0.42	0.26	0.16	0.09
	8.3	0.33	0.55	0.77	0.60	0.49	0.20	0.30

Table 6.4: Added mass coefficient (AMC, α_{am}) and pressure reduction coefficient (PRC) for configuration SR.

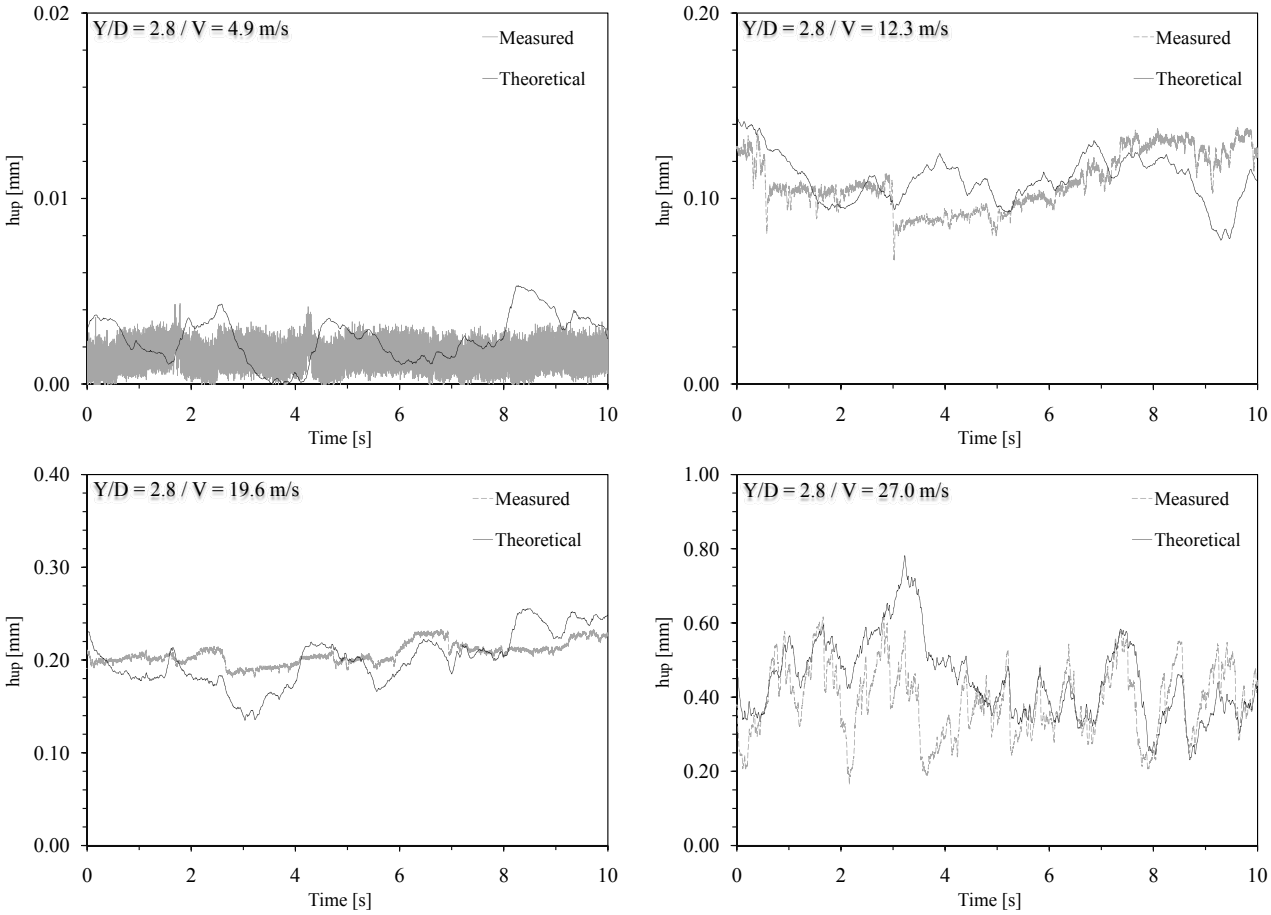

Figure 6.43: Time evolution of dynamic block impulsion for configuration SR. Comparison between theoretical and measured uplift for a core jet (Y/D = 2.8) and four jet velocities (4.9, 12.3, 19.6 and 27.0 m/s).

6.3.7 Conclusions

As observed for the configuration with the jet impact on the block center (CR), the pressure field acting on the block upper face follows an exponential distribution with the center at the stagnation point according to the literature. The geometry of the bell-shape pressure distribution changes as a function of the jet velocity. The pressure field inside the fissure is almost constant for all water depths. The pressure values change with an increase or a decrease of the jet velocities. Mean pressures acting along the vertical fissure increase weakly with the depth of the fissure and the extreme values (maximum and minimum) decrease with an increase of the distance from the plunge pool. The first transducer situated inside the vertical fissure (at 50 mm from the plunge pool bottom) shows some pressure peaks that may be generate by a "cavitation" phenomenon or by a compression-decompression phenomenon of the air bubbles present in the water near the fissure entrance. These extreme pressures have not been recorded with the other transducers located along the vertical fissure. These two phenomena are concentrated near the fissure entrance. Underneath the block the pressure field is almost constant (maximum, mean and minimum). The pressure values recorded inside the fissure are lower than on the block.

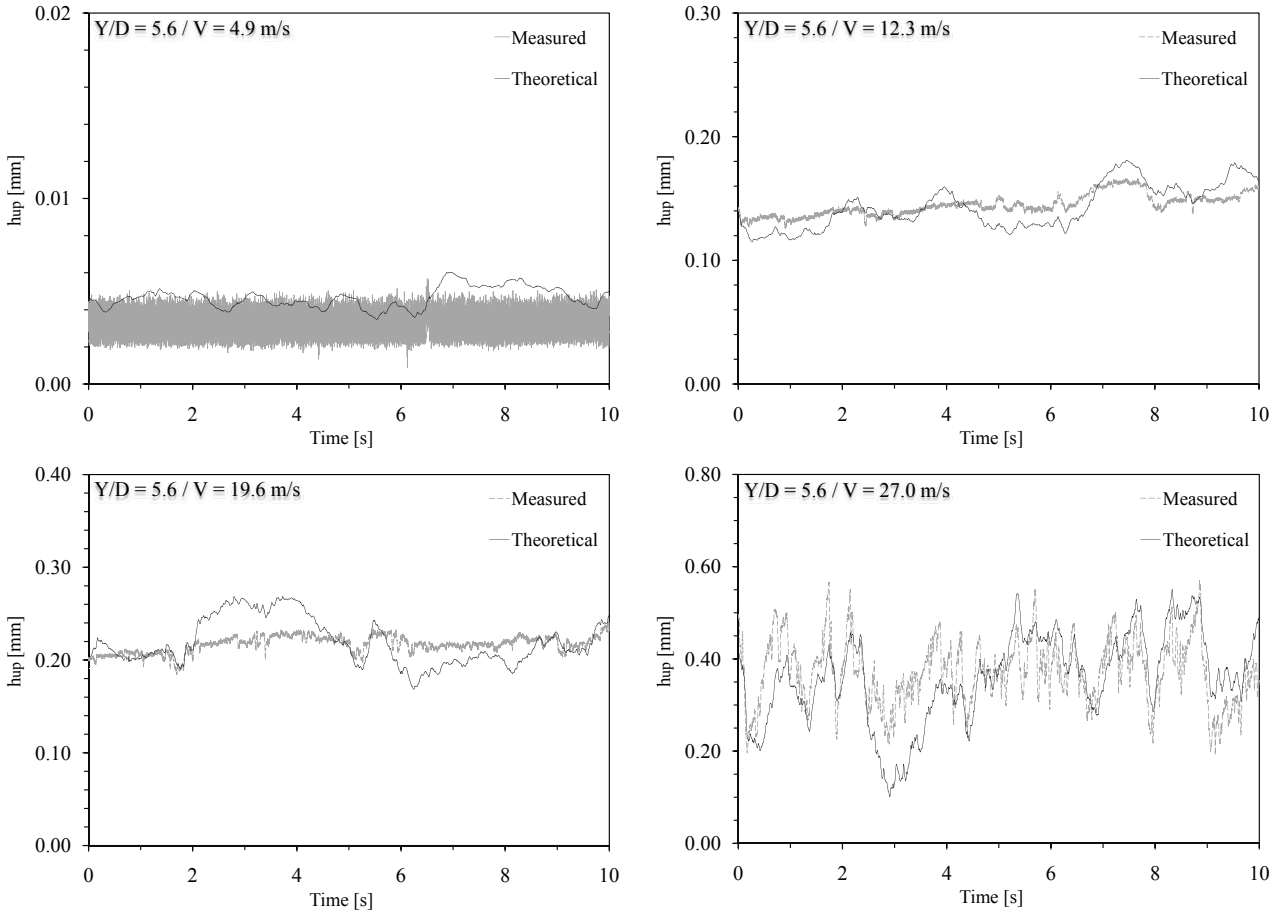

Figure 6.44: Time evolution of dynamic block impulsion for configuration SR. Comparison between theoretical and measured uplift for a transition jet (Y/D = 5.6) and four jet velocities (4.9, 12.3, 19.6 and 27.0 m/s).

The pressure coefficients, for the transducers situated on the block upper faces are in reasonable agreement with the literature values (recorded at the plunge pool bottom). The pressure coefficients computed for the transducers situated inside the 3-dimensional fissure show lower values than at the plunge pool bottom. As observed before, jet velocities lower as 7.4 m/s generate high coefficient values that did not match with the previous measurement present in the literature. Generally core jets show higher coefficients than the literature values.

The block moves up and reaches a new equilibrium position for jet velocities greater than 7.4 m/s. For jet velocities lower than 7.4 m/s systematically the block returns to its initial position. For jet velocities larger than 14.7 m/s, the block shows a stable equilibrium position until the last jet velocity (27.0 m/s) where the block suddenly moves up.

Core jets show the highest accelerations fluctuations. Mean accelerations follow a behavior similar to the block displacements and change as a function of the jet velocity. Minimum accelerations showed measurement problems that generates incongruous values. This problem is presents for several jet velocities and it may possible that this electrical noise perturb as well maximum and minimum accelerations (large difference between core jets and transition and developed jets).

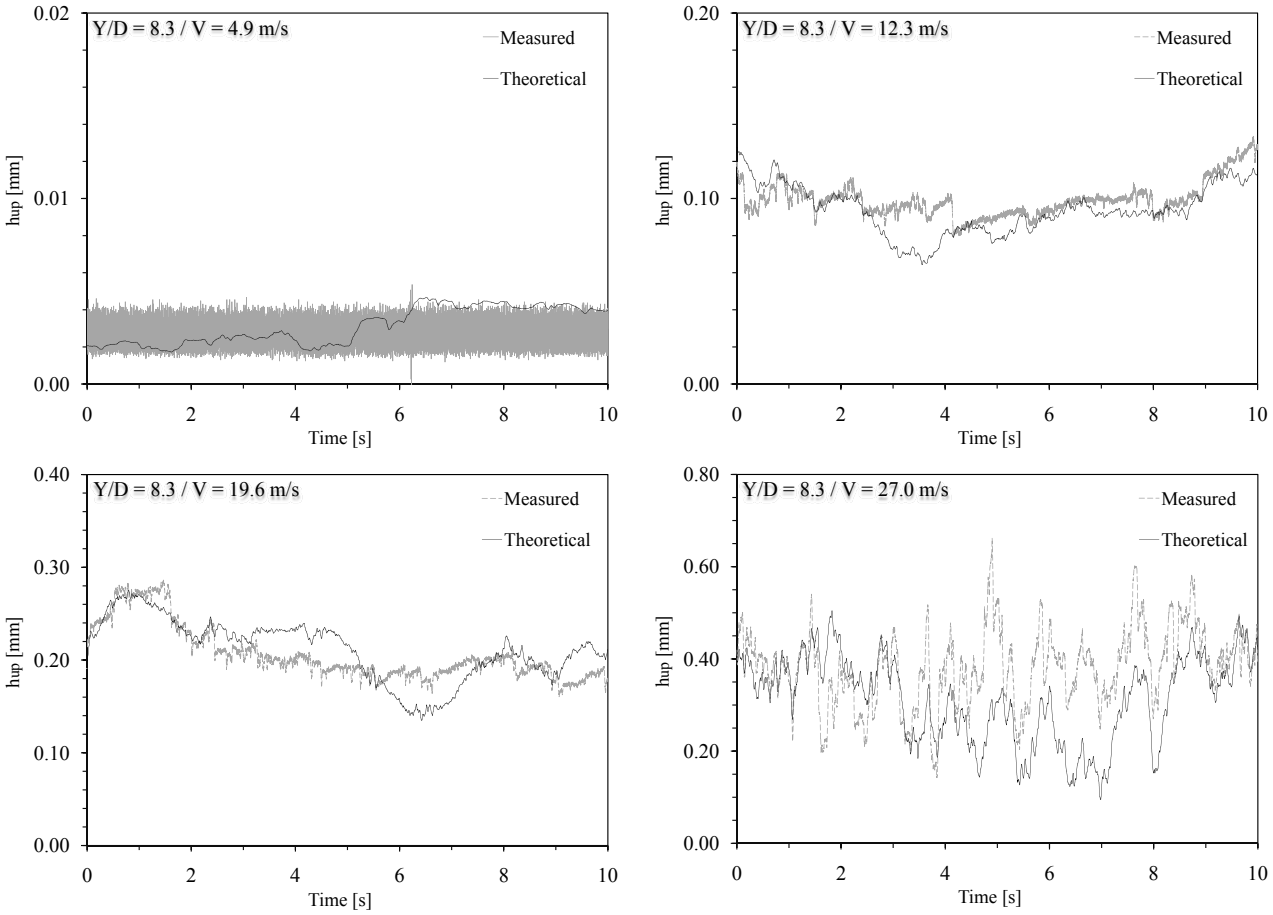

Figure 6.45: Time evolution of dynamic block impulsion for configuration SR. Comparison between theoretical and measured uplift for a developed jet (Y/D = 8.3) and four jet velocities (4.9, 12.3, 19.6 and 27.0 m/s).

As observed for the configuration CR, the Power Spectral Density (PSD) show a different behavior between transducers situated on the block upper face and inside the fissure. At the plunge pool bottom the PSD signal shows a change in the behavior when the frequency reaches 8-10 Hz: for lower frequencies the energy content decreases slowly (slope -2/3) and faster for higher frequencies (slope -1). Inside fissure, the PSD signal show a another behavior: for frequencies lower than 8-10 Hz the energy decreases slowly (with a slope of approximately -1/3 and -2/3) and for higher frequencies two peaks could be observed: the first peak (between 10-20 and 80-100 Hz) is related to the natural fissure frequency and the second peak (between 80-100 and 200-300 Hz) is not so clearly definable. None of the two peaks appear in the PSD signal at the plunge pool. The first peak (at low frequency) is stronger than the second peak.

As observed before, the dynamic block impulsion shows a good similitude between theoretical and measured uplift. Only the amplitude of the vertical displacements could not be always simulated exactly by the theoretical uplift, but the vertical fluctuations could be well reproduced. The added mass has to be integrated in the computation of the dynamic block impulsion.

6.4 Jet impact position on the block corner with the block free to move and equipped with lateral guides having eight contact points (CN)

6.4.1 Configuration description

This configuration is characterized by the following three parameters:

- Jet impact position: *on the block corner*;
- Degree of freedom: *the block is free to move along the vertical axis*;
- Lateral guides: *eight contact points per lateral guide and two guides per vertical face on the block.*

Figure 6.46 shows the configuration parameters and the transducers positions.

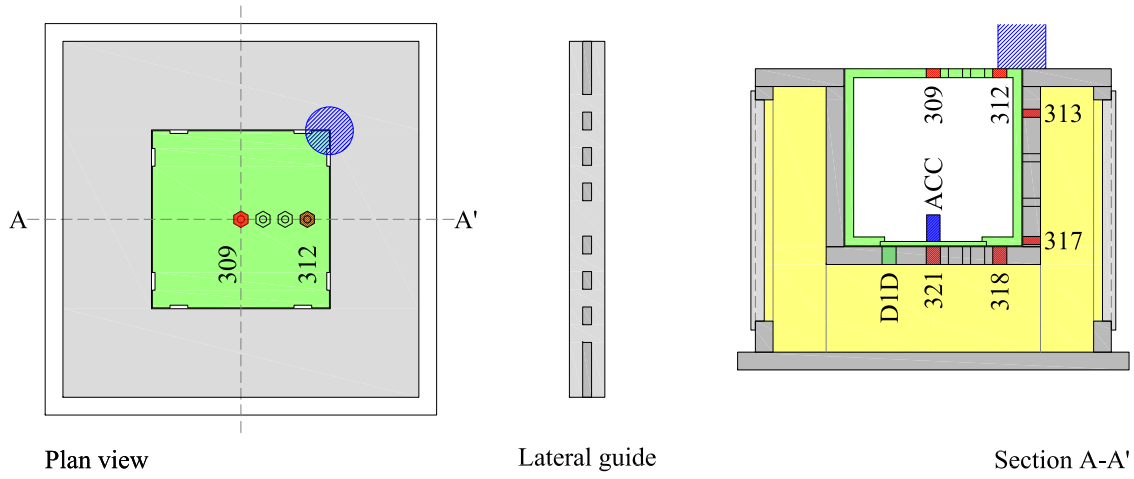

Figure 6.46: New experimental set-up for the configuration CN. Top view with jet impact position (cylinder) and pressure transducers positions (left), lateral guide fixed on the block lateral faces (center) and transversal section with jet impact position (cylinder) and transducers positions (pressure transducers N° 309 to N° 321, displacement transducer D1D and accelerometer ACC.

Table 6.5 summarizes the parameter combinations (water depth Y, jet discharge Q, jet velocity V_0, Y/D ratio and jet type) that have applied to this configuration.

The jet velocity was limited at 19.6 m/s due to the displacement of the block. For this jet velocity the largest vertical displacement has been reached (∼160 mm). For larger jet velocities, it may eject from the measurement box and the transducers cables fixed on the block may be torn away.

Water depth Y [m]	Discharge Q [l/s]	Jet velocity V_0 [m/s]	Y/D ratio [-]	Jet Type [-]
0.0	10-80	2.5-19.6	0.0	Core jet
0.1	10-80	2.5-19.6	1.4	Core jet
0.2	10-80	2.5-19.6	2.8	Core jet
0.3	10-80	2.5-19.6	4.2	Transition jet
0.4	10-80	2.5-19.6	5.6	Transition jet
0.5	10-80	2.5-19.6	6.9	Developed jet
0.6	10-80	2.5-19.6	8.3	Developed jet
0.7	10-80	2.5-19.6	9.7	Developed jet

Table 6.5: Main parameters that have been tested with configuration CN: water depth Y, jet discharge Q, jet velocity V_0, Y/D ratio and jet type.

6.4.2 Pressure field surrounding the block

As explained in Chapter 6.2.2, the pressures are relative and have been normalized by the kinetic energy of the jet.

Transducer 309 (at the center of the block upper face)

Transducer N° 309 is situated in the wall jet region at 142 mm from the stagnation point on the block corner.

Maximum pressures increase as a function of the jet velocity, but decrease with the water depth (Figure 6.47). Core jets (Y/D $<$ 4) show the highest pressure values. Transition (4 $<$ Y/D $<$ 6) and developed jets (Y/D $>$ 6) show similar values. The pressure differences between core jets and transition and developed jets reach approximately 0.5 Bar.

Mean pressures are almost constant for the three jet types, for all jet velocities and depend on the water depths. Developed jets have the highest pressure values and core jets the smaller pressure values. The pressure difference is approximately 0.1 Bar corresponding to the range of water depths used for the tests. Mean pressures are similar to the values recorded with the previous configurations (jet impact on the block center CR and jet impact on the block right hand side SR) and for transducers located approximately at the same distance from the stagnation point (as an example transducer N° 311 for configuration SL where the jet impact is located on the block left hand side).

Configuration CN shows maximum pressures smaller than the previous configurations because transducer N° 309 is located at the maximum distance from the stagnation point (142 mm, 100 mm for configuration SR and 0 mm for configuration CR).

Minimum pressures are subject to a weakly pressure decrease with an increase of the jet velocity.

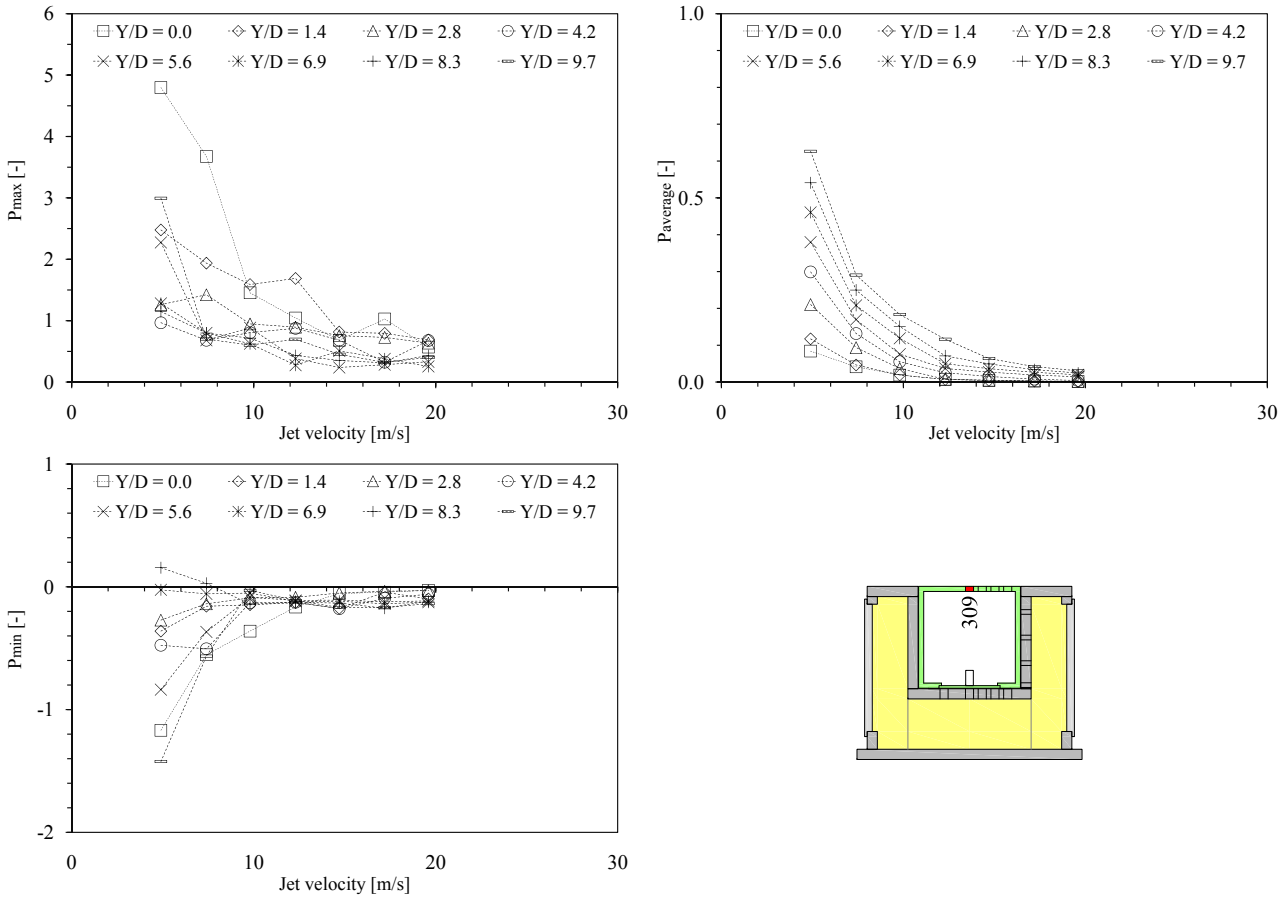

Figure 6.47: Normalized pressure measured with transducer N° 309 for configuration CN as a function of jet velocity (2.5-19.6 m/s) and Y/D ratio (0-9.7). Maximum pressure (top left), mean pressure (top right), minimum pressure (bottom left) and transducer location (bottom right).

Transducer 312 (near the fissure entrance on the block upper face)

Transducer N° 312 is located at the boundary between impingement region and wall jet region at 104 mm from the stagnation point on the block corner.

The pressures acting near the fissure entrance show the same trend for core, transition and developed jets (Figure 6.48). Maximum pressures increase as a function of the jet velocity, but decrease with the water depth. Core and transition jets show the highest pressure values. The pressures recorded with this transducer have been compared to transducer N° 309 used with configuration SR (both transducers are located at the same distance from the stagnation point: 100 mm). The pressures recorded are similar for both configurations but, with some small differences. These differences may be generate by the cable waterproof exit located near the block corner (for this configuration any cable exits from this waterproof exit) or by the hydraulic jump moving from the plunge pool wall to the block center (Figure 6.4).

Mean pressures are almost constant for all jet velocities and increases as a function of the water depth. The pressure differences between the largest mean value (Y/D = 9.7) and the small mean value (Y/D = 0.0) is ∼0.1 Bar.

Minimum pressures show a weakly pressure decrease with an increase of the jet velocity.

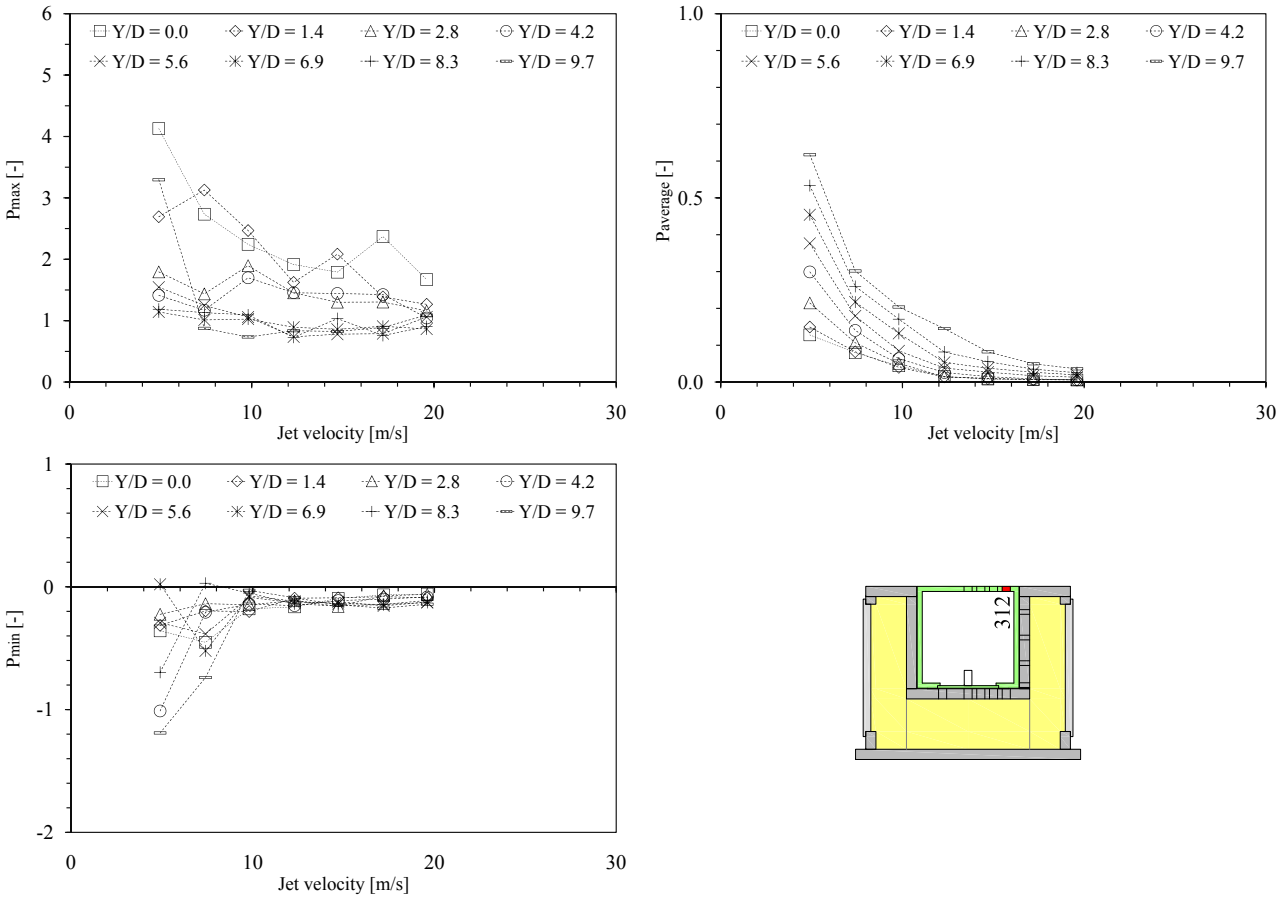

Figure 6.48: Normalized pressure measured with transducer N° 312 for configuration CN as a function of jet velocity (2.5-19.6 m/s) and Y/D ratio (0-9.7). Maximum pressure (top left), mean pressure (top right), minimum pressure (bottom left) and transducer location (bottom right).

Transducer 313 (inside the vertical fissure near the fissure entrance)

Transducer N° 313 is located inside the vertical fissure at 50 mm from the plunge pool bottom.

Maximum pressures increase quasi-linearly as a function of the jet velocity with some small pressure fluctuations (Figure 6.49). Some core (Y/D = 0.0 and 1.4) and developed jets (Y/D = 9.7) show higher pressure values between 4.9 and 14.7 m/s. The pressure differences relate to the other water depths reach ∼0.2 Bar.

Mean pressures increase as a function of jet velocity and water depth. The pressure differences between the larger and the smaller value is equal at ∼0.1 Bar.

As at the plunge pool bottom, minimum pressures are almost constant for all jet velocity.

Transducer 317 (inside the vertical fissure near the central cavity bottom)

Transducer N° 317 is located 7 mm from the bottom of the central cavity (or 194 mm from the plunge pool).

Maximum, mean and minimum pressures (Figure 6.50) show the same behavior of transducer N° 313 situated near the fissure entrance (Figure 6.49). Water depth 0.7 m (Y/D = 9.7) shows a peak between 4.9 and 9.8 m/s: ∼0.4 Bar higher than the maximum pressures generated

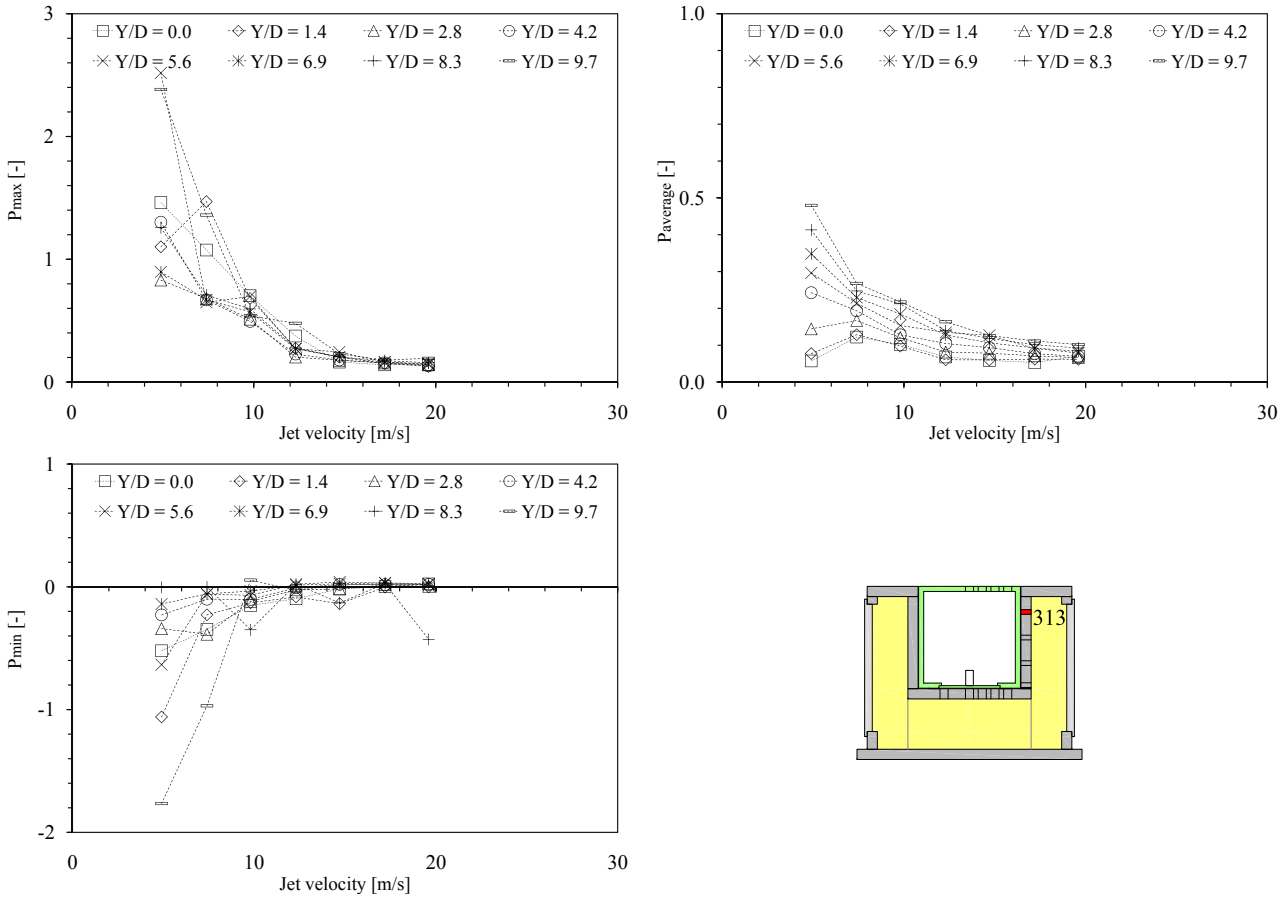

Figure 6.49: Normalized pressure measured with transducer N° 313 for configuration CN as a function of jet velocity (2.5-19.6 m/s) and Y/D ratio (0-9.7). Maximum pressure (top left), mean pressure (top right), minimum pressure (bottom left) and transducer location (bottom right).

by other water depths.

For mean and minimum pressure the same observation made for transducer N° 317 are valid.

Transducer 318 (underneath the block near the vertical fissure)

Transducer N° 318 is located underneath the block, at 25 mm from the vertical fissure on the same vertical axis than transducer N° 312.

As observed for the previous configurations (CR and SR), the passage from the vertical fissure to the fissure situated underneath the block did not affect the pressures (Figure 6.51). Maximum, mean and minimum pressures show exactly the same trend and almost the same values than transducer N° 317 situated at the end of the vertical fissure (Figure 6.50).

Maximum pressures increase linearly for the three jet types. Water depths 0.6 and 0.7 m (Y/D = 8.3 and 9.7) show some peaks between 4.9 and 12.3 m/s: ∼0.4 Bar higher than the maximum pressure generated by the other water depths. These peaks may be generated by a superposition of pressure waves travelling inside the 3-dimensional fissure.

Mean pressure increases as well linearly and minimum pressure is almost constant for three jet types.

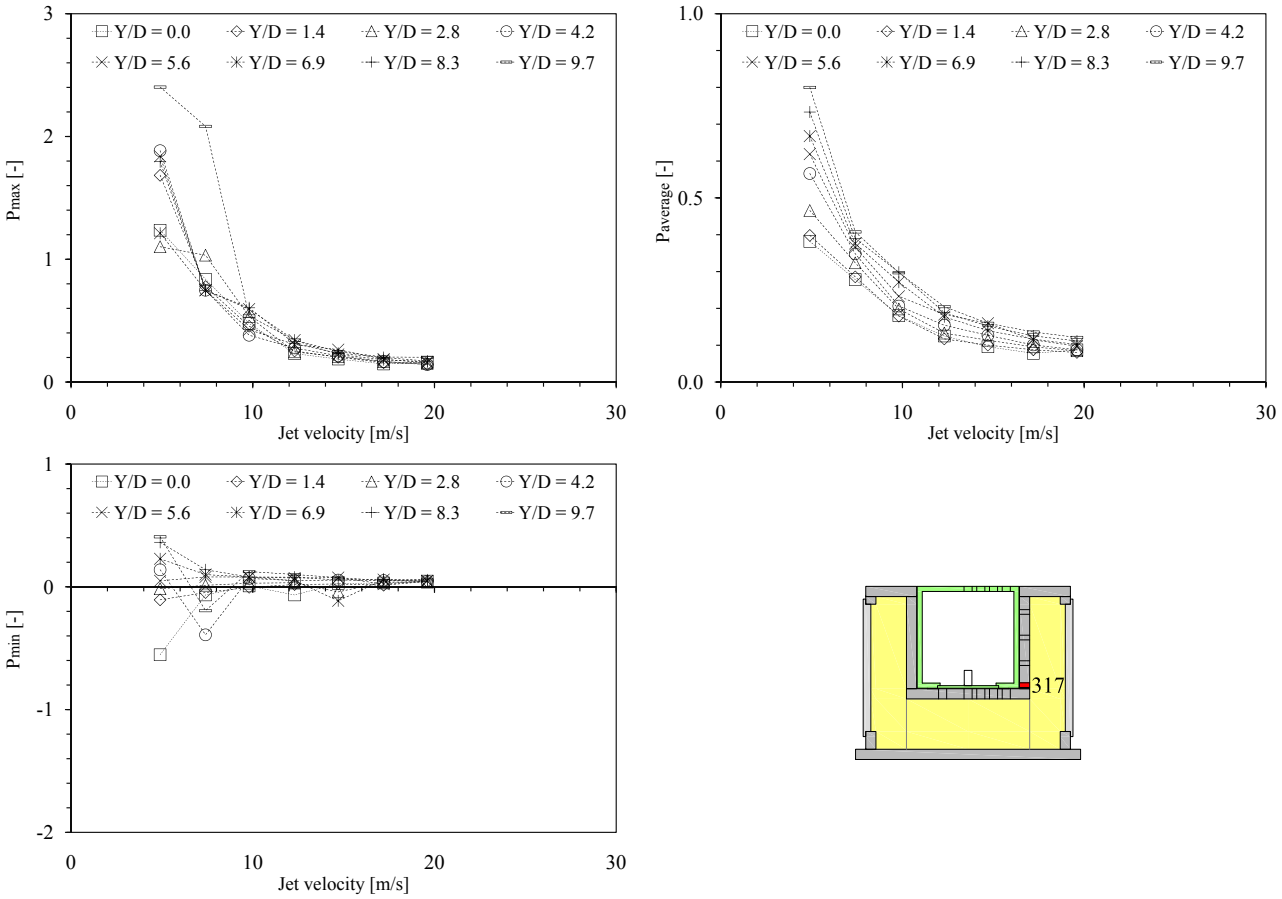

Figure 6.50: Normalized pressure measured with transducer N° 317 for configuration CN as a function of jet velocity (2.5-19.6 m/s) and Y/D ratio (0-9.7). Maximum pressure (top left), mean pressure (top right), minimum pressure (bottom left) and transducer location (bottom right).

Transducer 321 (underneath block in the center of the measurement box)

Transducer N° 321 is located underneath the block, in the center of the measurement box on the same vertical axis of transducer N° 309.

Maximum, mean and minimum pressures (Figure 6.52) show practically the same trend and almost the same values, with some small differences, than pressures recorded near the vertical fissure (N° 318, Figure 6.51).

Pressure field surrounding the block

The pressure distribution on the block upper face did not follow the exponential distribution observed for the two previous configurations (Chapters 6.2.2 and 6.3.2). The four transducers are not aligned radially outwards from the stagnation point but are aligned perpendicularly from a side of the block (with distances between 104 and 142 mm from the stagnation point). Hence, is not possible to obtain the correct pressure distribution acting on the block.

Figure 6.53 shows the pressure field acting on the block for a Y/D ratio of 8.3 and a jet velocity of 19.6 m/s.

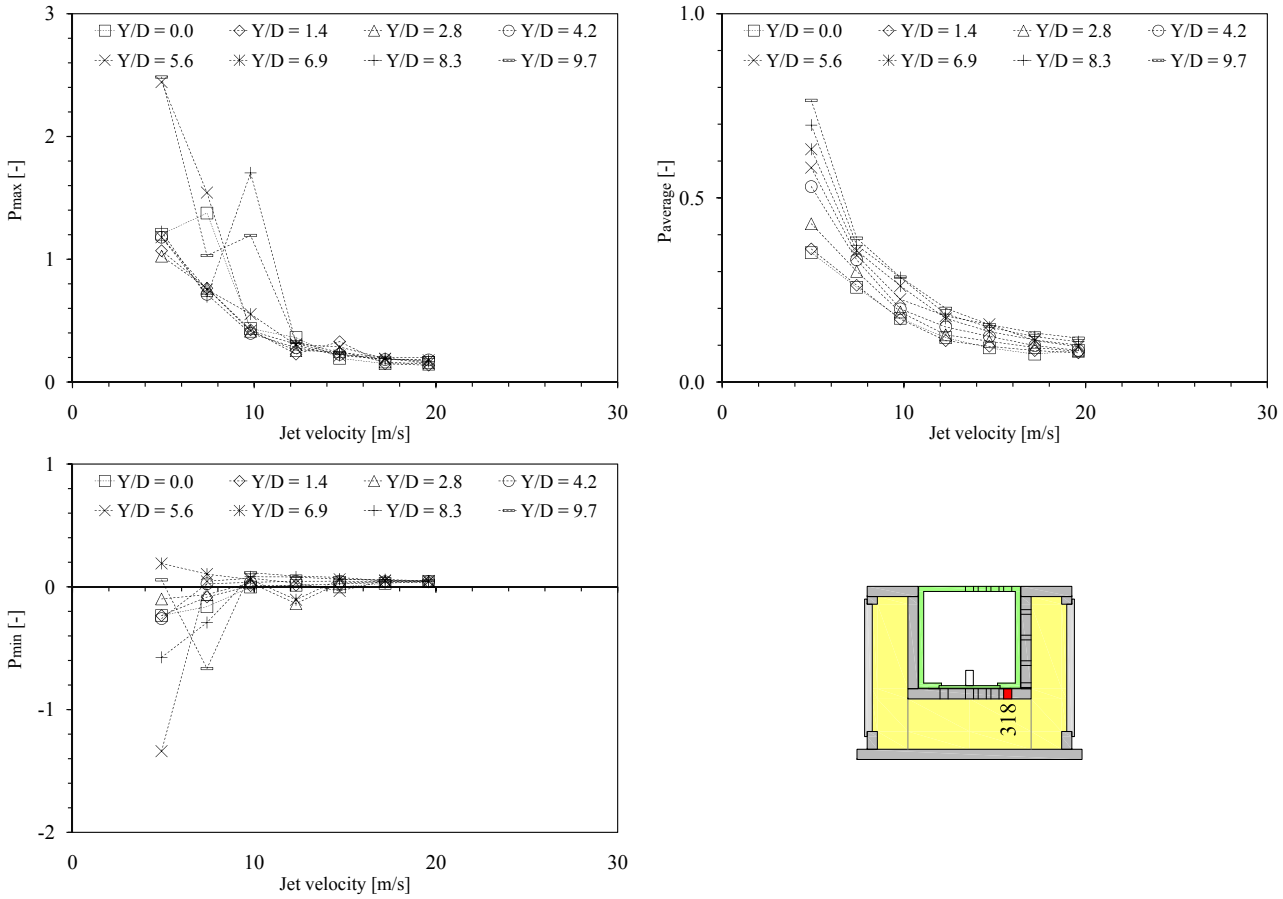

Figure 6.51: Normalized pressure measured with transducer N° 318 for configuration CN as a function of jet velocity (2.5-19.6 m/s) and Y/D ratio (0-9.7). Maximum pressure (top left), mean pressure (top right), minimum pressure (bottom left) and transducer location (bottom right).

On block upper face the pressure is quite constant due to the transducers location: perpendicularly at the stagnation point and not radially outwards (Figure 6.46). Inside the fissure the same observation made for configurations CR and SR are valid (Chapters 6.2.2 and 6.3.2).

6.4.3 Pressure coefficients

As before the non-dimensional pressure coefficients (the formulas have been described in Chapter 5.2.2) have been computed using the pressures measured on the block upper face and inside the 3-dimensional fissure.

6.4.3.1 Mean pressure coefficient C_p

The mean pressure coefficients (C_p, Figure 6.54) computed on the block upper face (transducers N° 309 and N° 312) show values smaller than the theoretical curves proposed by Ervine et al. (1997). The two transducers are situated in the wall jet region where the pressure exponential distribution reaches minimum values. Far away from the stagnation point, the subtraction between mean pressure, atmospheric pressure and hydraulic head decrease and approaches a

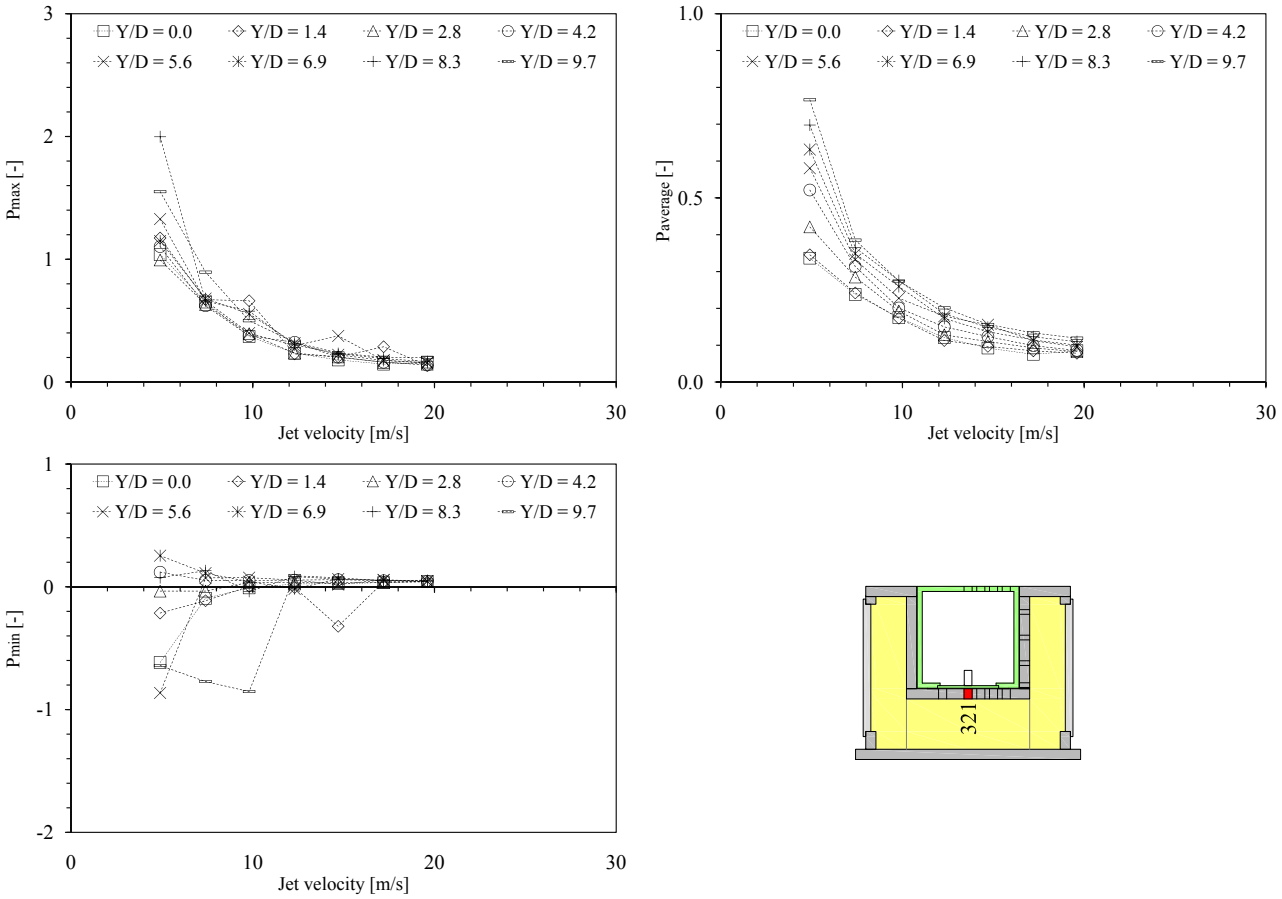

Figure 6.52: Normalized pressure measured with transducer N° 321 for configuration CN as a function of jet velocity (2.5-19.6 m/s) and Y/D ratio (0-9.7). Maximum pressure (top left), mean pressure (top right), minimum pressure (bottom left) and transducer location (bottom right).

zero value (the formula is explained in Chapter 5.2.2). Hence, the mean pressure coefficients approach zero.

Inside the 3-dimensional fissure the mean pressure coefficient is almost constant for core and transition jets (Y/D $<$ 6) and decrease for developed jets (Y/D $>$ 6). Along the vertical fissure transducer N° 317 situated near the central cavity bottom shows higher coefficient values than transducer N° 313 situated near the fissure entrance. Underneath the block the two transducers (N° 318 and N° 321) show the same values and are similar to the values computed at the end of the vertical fissure (N° 317).

6.4.3.2 Turbulent pressure fluctuation coefficient $C_{p'}$

The turbulent pressure fluctuation coefficients ($C_{p'}$, Figure 6.55) computed all around the block are in reasonable agreement with the theoretical curve proposed by Ervine et al. (1997). However, for core jets (Y/D $<$ 4) generated by jet velocities lower than 12.3 m/s, the coefficients are slightly higher than the Ervine's curve.

At the plunge pool bottom, the two transducers show some differences as a function of the jet type: for core jets (Y/D $<$ 4), transducer N° 312 (located at 104 mm from the stagnation

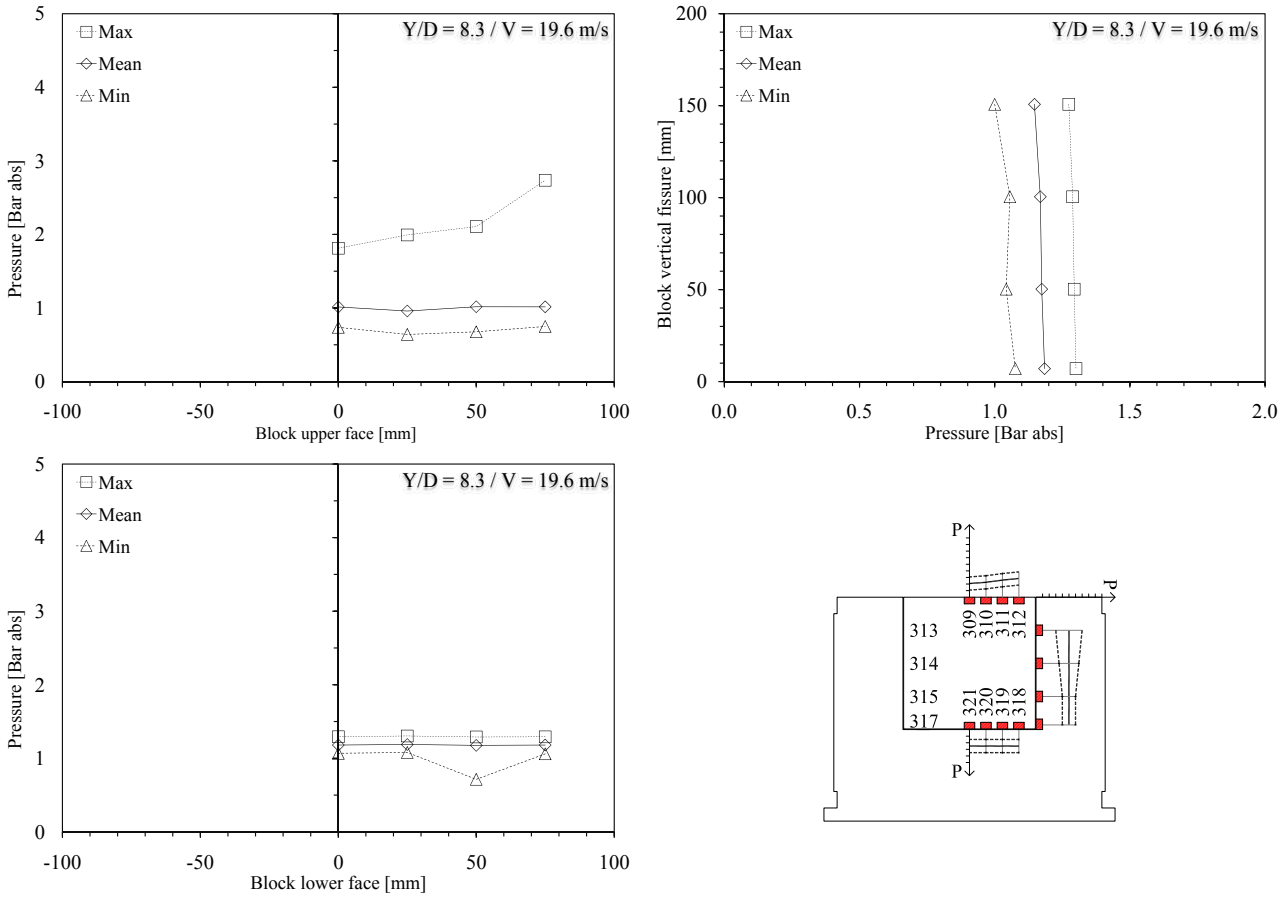

Figure 6.53: Pressure field acting around the block for configuration CN, a developed jet (Y/D = 8.3) and a jet velocity of 19.6 m/s. Pressure acting on the block upper face (top left), along the vertical fissure (top right), underneath the block (bottom left) and pressure filed sketch (bottom right). Pressures are expressed in absolute Bar.

point) shows higher coefficient values than transducer N° 309 (located at 142 mm from the stagnation point). This difference disappears with an increase of the water depth (transition and developed jets: Y/D > 4). The nearest transducer to the stagnation point (N° 312) shows higher pressure values (pressure distribution on the block).

Inside the fissure the coefficients are almost constant for the same jet velocity and practically superposed. Jet velocities lover than 9.8 m/s, show a small decrease of coefficient values related to an increase of the Y/D ratio.

6.4.3.3 Positive extreme pressure fluctuation coefficient C_p^+

The positive extreme pressure fluctuation coefficients (C_p^+, Figure 6.56), for transducers located on the block upper face (N° 309 and N° 312) decrease with the Y/D ratio. Core jets (Y/D < 4) show highest coefficient values for all jet velocities. When the Y/D ratio growth, the values are in reasonable agreement with the Ervine's curve. Transducer N° 312 (nearest to the stagnation point) shows higher values than transducer N° 309 (on the block center): maximum pressures decrease with the distance from the stagnation point.

Inside the 3-dimensional fissure the coefficient is almost constant for the three jet types and

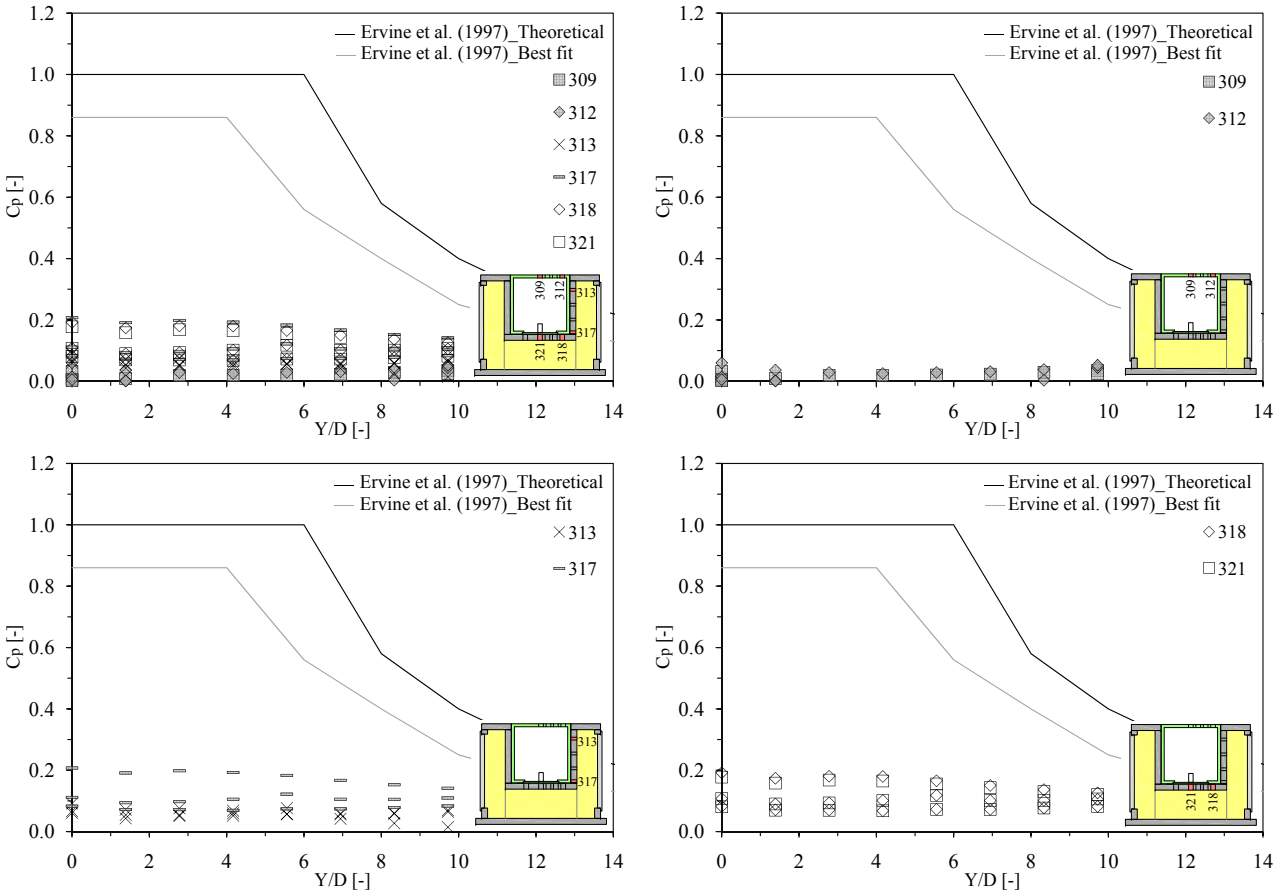

Figure 6.54: Mean pressure coefficient C_p computed for configuration CN as a function of jet velocity (4.9, 12.3 and 19.6 m/s) and Y/D ratio (0-9.7). Overview of the six pressure transducers (top left), on the block upper face or at the plunge pool bottom (top right), along the vertical fissure (bottom left) and underneath the block (bottom right).

for the same jet velocity. However, along the vertical fissure for jet velocity up to 9.8 m/s, some higher coefficient values have been computed for Y/D ratios lower than 3 and greater than 9. The coefficient values have an upper limit of 1.1.

6.4.3.4 Negative extreme pressure fluctuation coefficient C_p^-

The negative extreme pressure fluctuation coefficients (C_p^-, Figure 6.57) are in good agreement with the Ervine's curve for core, transition and developed jets. Some higher values have been computed for core (Y/D $<$ 4) and developed jets (Y/D $>$ 8). These values are related to the jet velocities lower than 9.8 m/s. The coefficients computed inside the fissure are similar at the values computed inside the plunge pool.

6.4.3.5 Positive extreme pressure coefficient $C_{p,max}$

The positive extreme pressure coefficients ($C_{p,max}$, Figure 6.58) computed at the plunge bottom are higher than inside the fissure for the same jet velocity. At the plunge pool bottom, the coefficients decrease with an increase of Y/D ratio and jet velocity. The pressure field acting

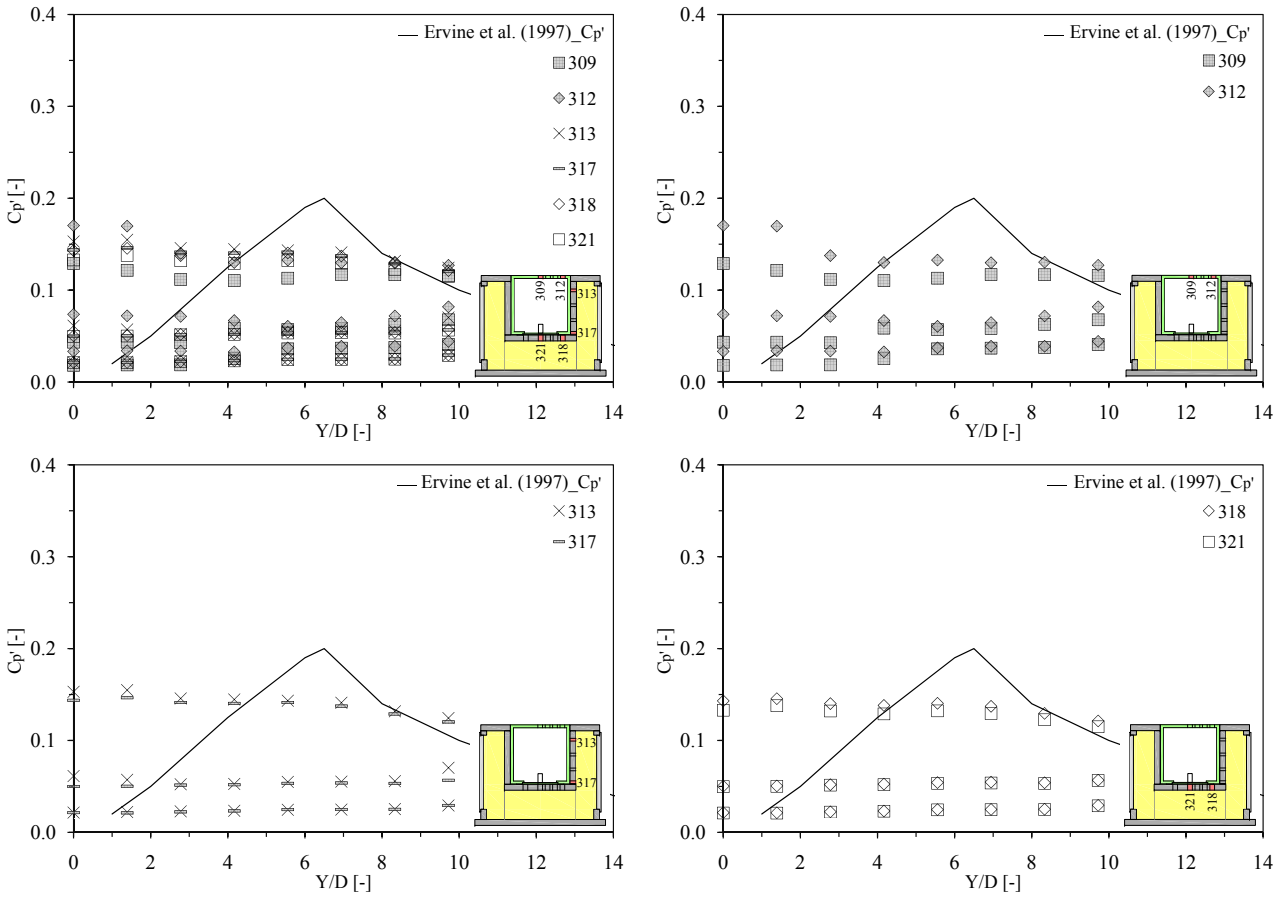

Figure 6.55: Turbulent pressure fluctuation coefficient $C_{p'}$ computed for configuration CN as a function of jet velocity (4.9, 12.3 and 19.6 m/s) and Y/D ratio (0-9.7). Overview of the six pressure transducers (top left), on the block upper face or at the plunge pool bottom (top right), along the vertical fissure (bottom left) and underneath the block (bottom right).

on the block upper face (Chapter 6.4.2) shows a pressure reduction radially outwards from the stagnation point that generates some differences between the computed coefficient values (transducers N° 309 and N° 312 are both located at the extremities of the pressure exponential distribution).

For the three jet types, the coefficients computed inside the fissure are almost constant for the same jet velocity. Along the vertical fissure (N° 313 and N° 317) and underneath the block (N° 318 and N° 321) the coefficients are situated in the same range of values. The higher values are generated by small jet velocities. If jet velocities smaller than 7.4 m/s are omitted, the coefficient values are less than 1.7.

6.4.3.6 Negative extreme pressure coefficient $C_{p,min}$

The negative extreme pressure coefficients ($C_{p,min}$, Figure 6.59) show similar values for the three jet types, except for jet velocities smaller than 7.4 m/s. The coefficients are almost constant for all Y/D ratios and all jet velocities. The small jet velocities show a rising trend for the coefficient as a function of the water depth, but with an increase of the jet velocities this trend

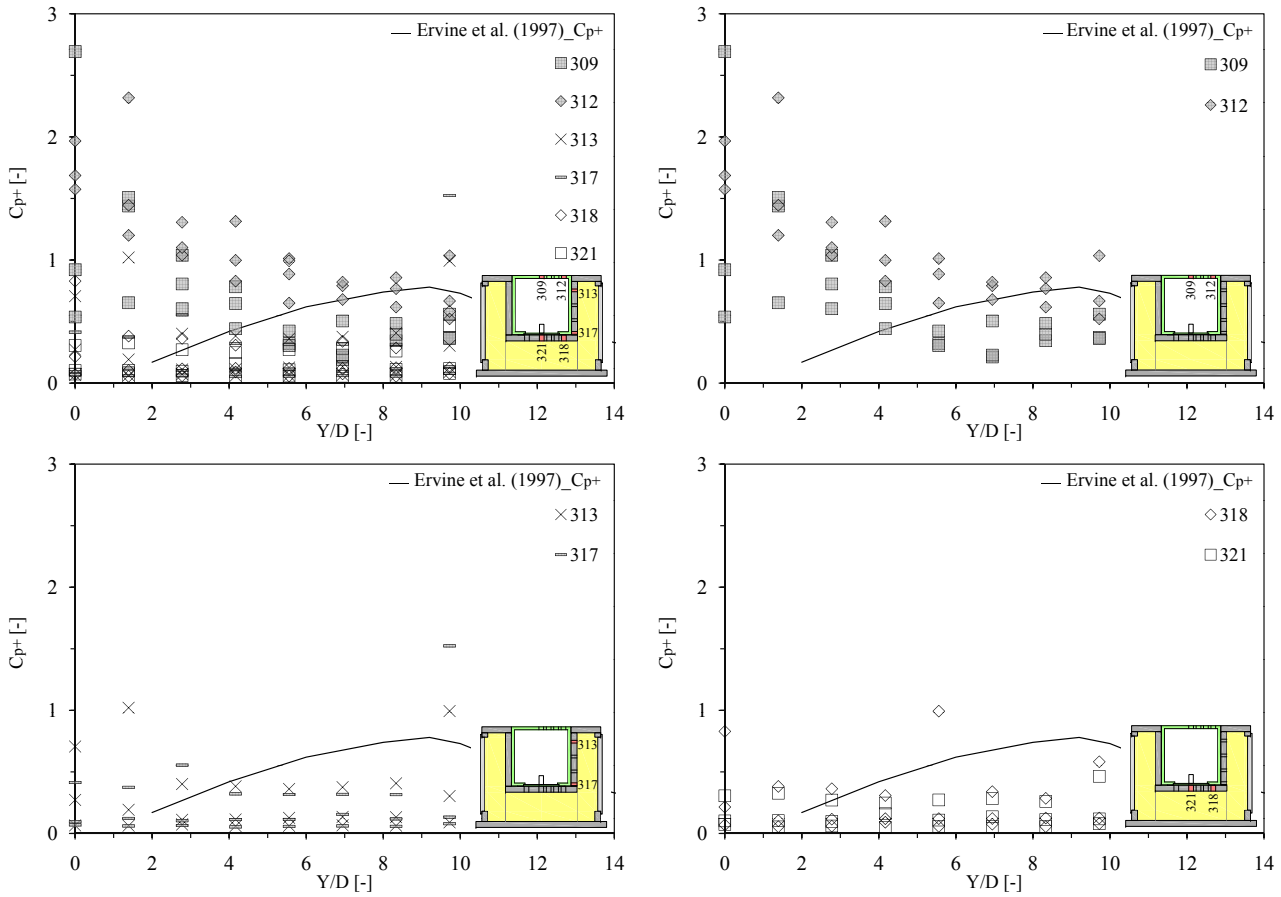

Figure 6.56: Positive extreme pressure fluctuation coefficient C_p^+ computed for configuration CN as a function of jet velocity (4.9, 12.3 and 19.6 m/s) and Y/D ratio (0-9.7). Overview of the six pressure transducers (top left), on the block upper face or at the plunge pool bottom (top right), along the vertical fissure (bottom left) and underneath the block (bottom right).

disappears. No apparent differences are recognizable between the coefficient computed at the plunge pool bottom and inside the fissure. As observed before, the higher values are generated by small jet velocities. If jet velocities smaller than 7.4 m/s are omitted the coefficients are less than 1.3.

6.4.4 Displacements and accelerations of block

The transducers location is shown in Figure 6.46. As explained in Chapter 6.2.4, the block responses have been recorded simultaneously at the pressures. The initial distance between the bottom of the central cavity and the block lower face is ∼0.85 mm (block initial position).

6.4.4.1 Displacements of block

The block begins to move up (Figure 6.60) for a jet velocities greater than 4.9 m/s. The block is subjected to small fluctuations and the mean displacements correspond to the block initial position (∼0.85 mm). At 7.4 m/s the amplitude of this vertical displacements increases and

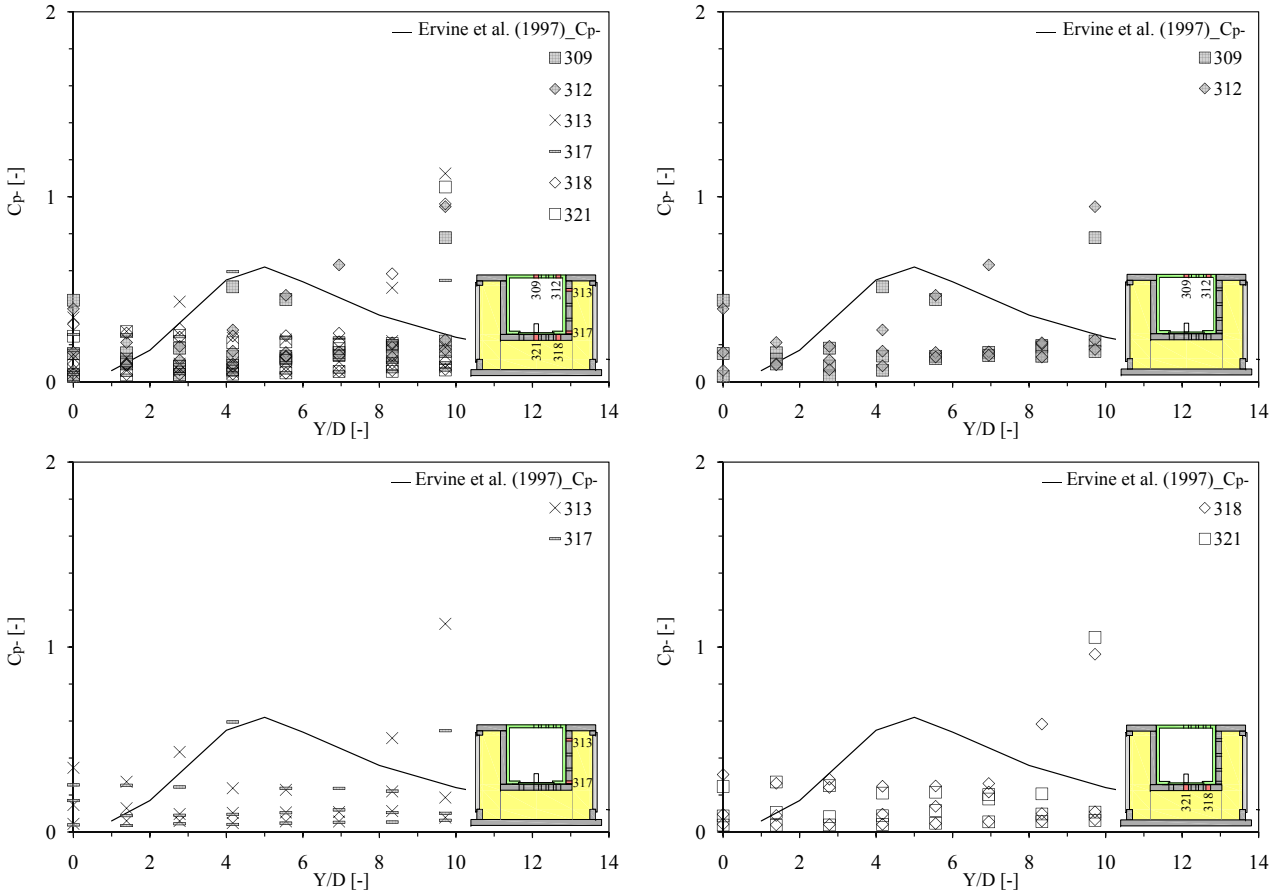

Figure 6.57: Negative extreme pressure fluctuation coefficient C_p^- computed for configuration CN as a function of jet velocity (4.9, 12.3 and 19.6 m/s) and Y/D ratio (0-9.7). Overview of the six pressure transducers (top left), on the block upper face or at the plunge pool bottom (top right), along the vertical fissure (bottom left) and underneath the block (bottom right).

the block did not return to its initial position: as before the block reaches a new equilibrium position that change as a function of the jet velocity. For jet velocities larger than 12.3 m/s, the vertical movements are so large that the transducer cannot measure anymore the displacements (maximum measurement range: ∼5.5 mm). Maximum displacement was reached for jet velocities of 17.2-19.6 m/s and corresponds to ∼160 mm. This value was estimated using the lateral guides fixed on the block lateral faces. Visually it was possible to observe how many contact points were visible on the lateral guide. Knowing the lateral guide geometry the vertical displacement was estimated. The same maximum displacement was observed for core, transition and developed jets.

The block vertical displacements for jet velocities larger than 9.8 m/s happen quickly (but with a constant uplift velocity) and normally in the interval of time necessary to change the jet velocity.

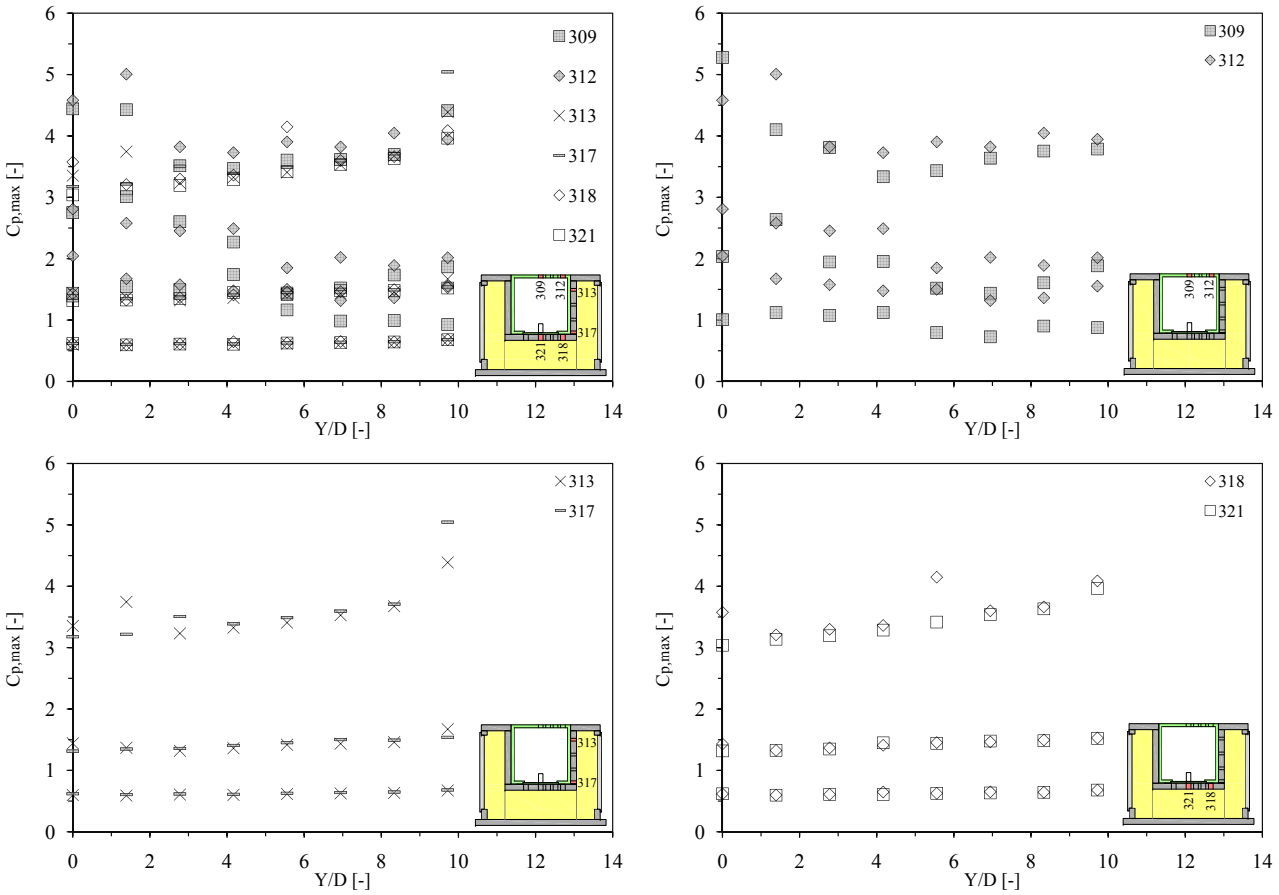

Figure 6.58: Positive extreme pressure coefficient $C_{p,max}$ computed for configuration CN as a function of jet velocity (4.9, 12.3 and 19.6 m/s) and Y/D ratio (0-9.7). Overview of the six pressure transducers (top left), on the block upper face or at the plunge pool bottom (top right), along the vertical fissure (bottom left) and underneath the block (bottom right).

6.4.4.2 Accelerations of block

The block accelerations are related to the recorded displacements. Mean accelerations show a trend similar to the vertical displacements (Figure 6.61): for jet velocities up to 7.4 m/s they are almost constant, than they increase and reach a new constant value for jet velocities larger than 12.3 m/s. Mean accelerations for jet velocities lower than 7.4 m/s is ∼2.5 g and above 12.3 m/s is ∼11 g.

Maximum accelerations show a similar trend but the recorded values are higher and for the 0.7 m water depth (Y/D = 9.7) reaches a maximum value of ∼30 g.

As observed for the two previous configurations, minimum acceleration increases as a function of the jet velocity, but shows some measurement problems for jet velocities larger than 7.4 m/s. Electrical noise generates incongruous values that reach the acceleration lower limits (-1000 g). This problem is presents for several jet velocities. As observed for configuration SR (Chapter 6.3.4.1), it may possible that this electrical noise perturb as well maximum and minimum accelerations.

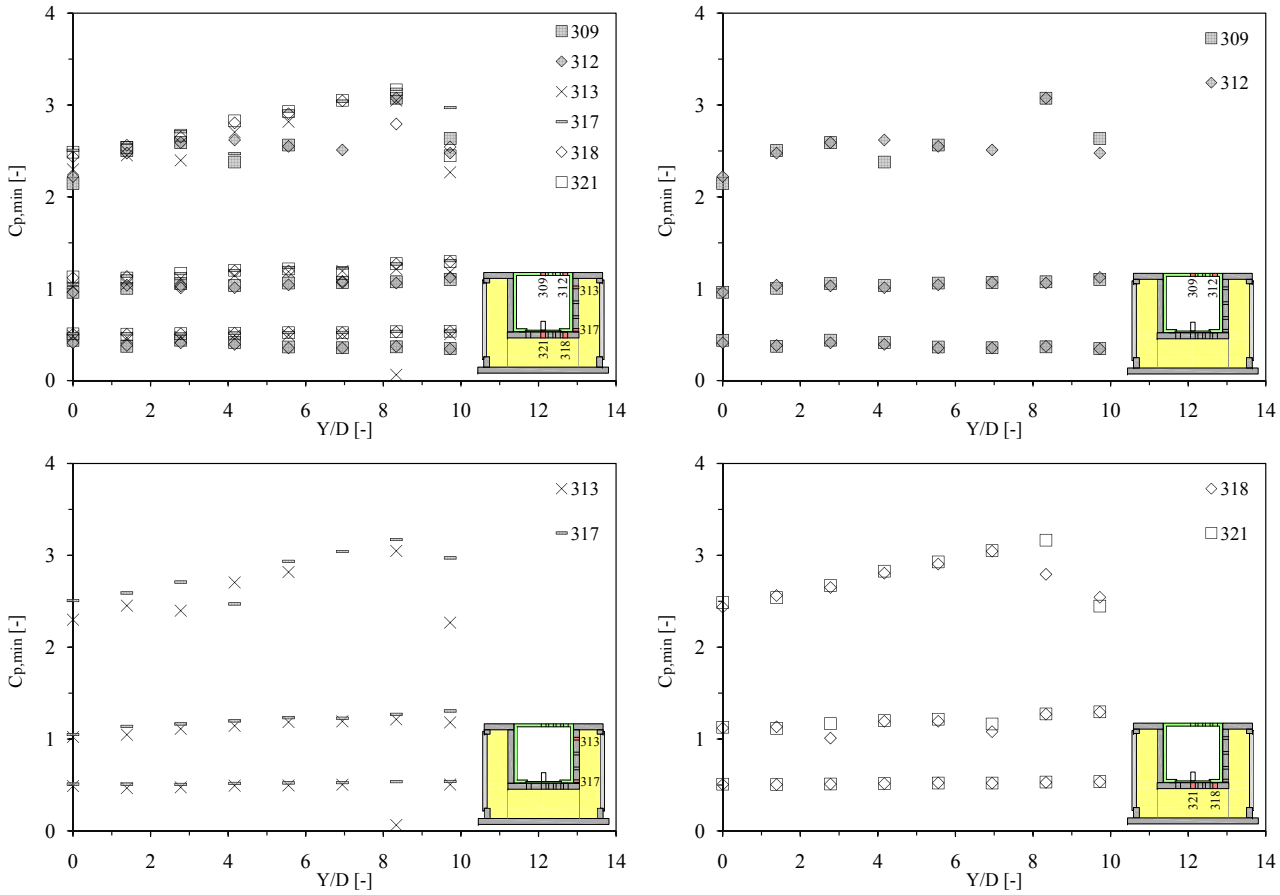

Figure 6.59: Negative extreme pressure coefficient $C_{p,min}$ computed for configuration CN as a function of jet velocity (4.9, 12.3 and 19.6 m/s) and Y/D ratio (0-9.7). Overview of the six pressure transducers (top left), on the block upper face or at the plunge pool bottom (top right), along the vertical fissure (bottom left) and underneath the block (bottom right).

6.4.5 Power Spectral Density

In this section only the results for a core (Y/D = 2.8 or 0.2 m), a transition (Y/D = 5.6 or 0.4 m) and a developed jet (Y/D = 8.3 or 0.6 m) and three of the eleven jet velocities are explained (4.9, 12.3 and 19.6 m/s).

As observed for the two previous configurations (CR and SR), the energy content increases as a function of the jet velocity and as before, the Power Spectral Density (PSD) may be subdivided into two groups:

I. transducers situated at the plunge pool bottom on the block upper face (N°s 309 to 312);

II. transducers situated inside the 3-dimensional fissure (N°s 313 to 321).

These observations are valid for core, transition and developed jets (Figures 6.62, 6.63 and 6.64).

The main difference with the two previous configurations is the energy content (Chapters 6.2.5 and 6.3.5). The distance between transducers and the stagnation point is greater and

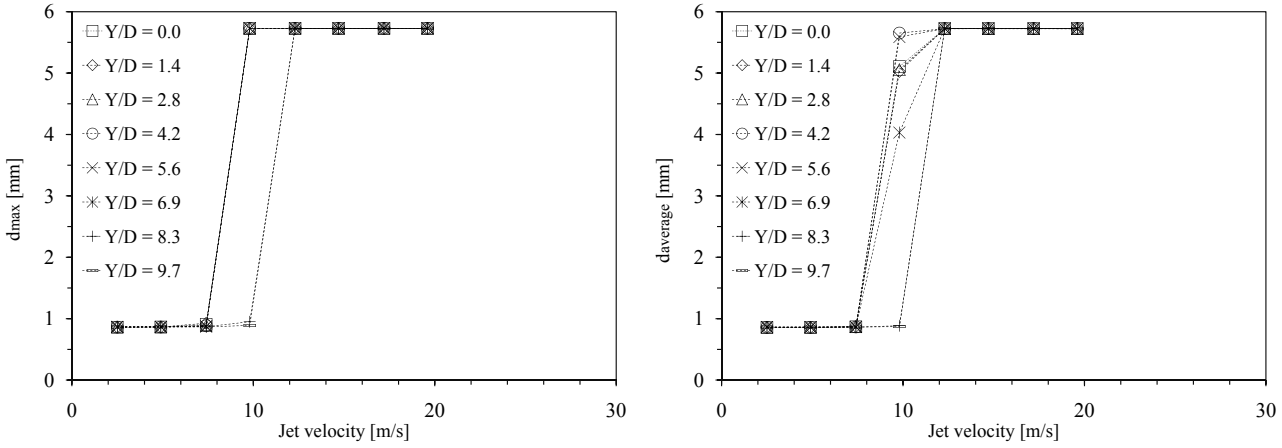

Figure 6.60: Block displacements measured for configuration CN as a function of jet velocity (2.5-19.6 m/s) and Y/D ratio (0-9.7). Maximum (left) and mean displacements of block (right). The block initial position corresponds to a distance of ∼0.85 mm.

they are located in another region: in the wall jet region and not in the impinging region (N° 309 at 142 mm and N° 312 at 104 mm from the stagnation point). The pressure acting on the block upper face decreases with distance from the stagnation point. An energy content difference is easy to observe for the two transducers situated on the block upper face: transducer N° 309 shows less energy than transducer N° 312 due to their relative position from the stagnation point. The low frequency part of the PSD signal ($f < 10$ Hz) looks quite similar for all jet velocities. The energy correlated to each frequency decreases slowly with a slope of approximately -2/3. For higher frequencies ($f > 10$ Hz) the spectral content decreases with a -1 slope. As observed for the previous configurations (CR and SR), when a jet velocity increases the energy content increases proportionally.

Pressure transducers situated inside the 3-dimensional fissure show a different behavior from the transducers situated at the plunge pool bottom. Some differences with the previous configurations (CR and SR) are observables. The energy content is lower than at the plunge pool bottom for the same jet velocity. With an increase of the frequency, three zones can be distinguished: a first zone up to 8-15 Hz, a second zone between 8-15 and 100 Hz and a third zone above 100 Hz. In the first zone, the energy decreases slowly with a slope approximately situated between -2/3 and -1. In the second zone the energy decreases with a different slope, approximately situated between -5/3 and -6/3 in a small frequency range (between 8-15 and 40-60 Hz). In the third zone, the energy reaches a constant value similar for all jet velocities. Between the second and the third zones two peaks may be detected in PSD signal as in the previous configurations: the first peak between 30 and 80 Hz and the second peak between 100 and 200-300 Hz. Their magnitude is lower than in the previous configurations (CR and SR) due to the less pressure acting in the fissure. The two peaks appear in the PSD signal for core, transition and developed jet. The first peak is centred on 50 Hz (the frequency of the electrical distribution). All transducers show an energy peak at 50 Hz for a jet velocity of 4.9 m/s, but disappears for jet velocities larger than 7.4 m/s. The second peak is more difficulty to be observed. The transducers situated near the end of the vertical fissure and underneath

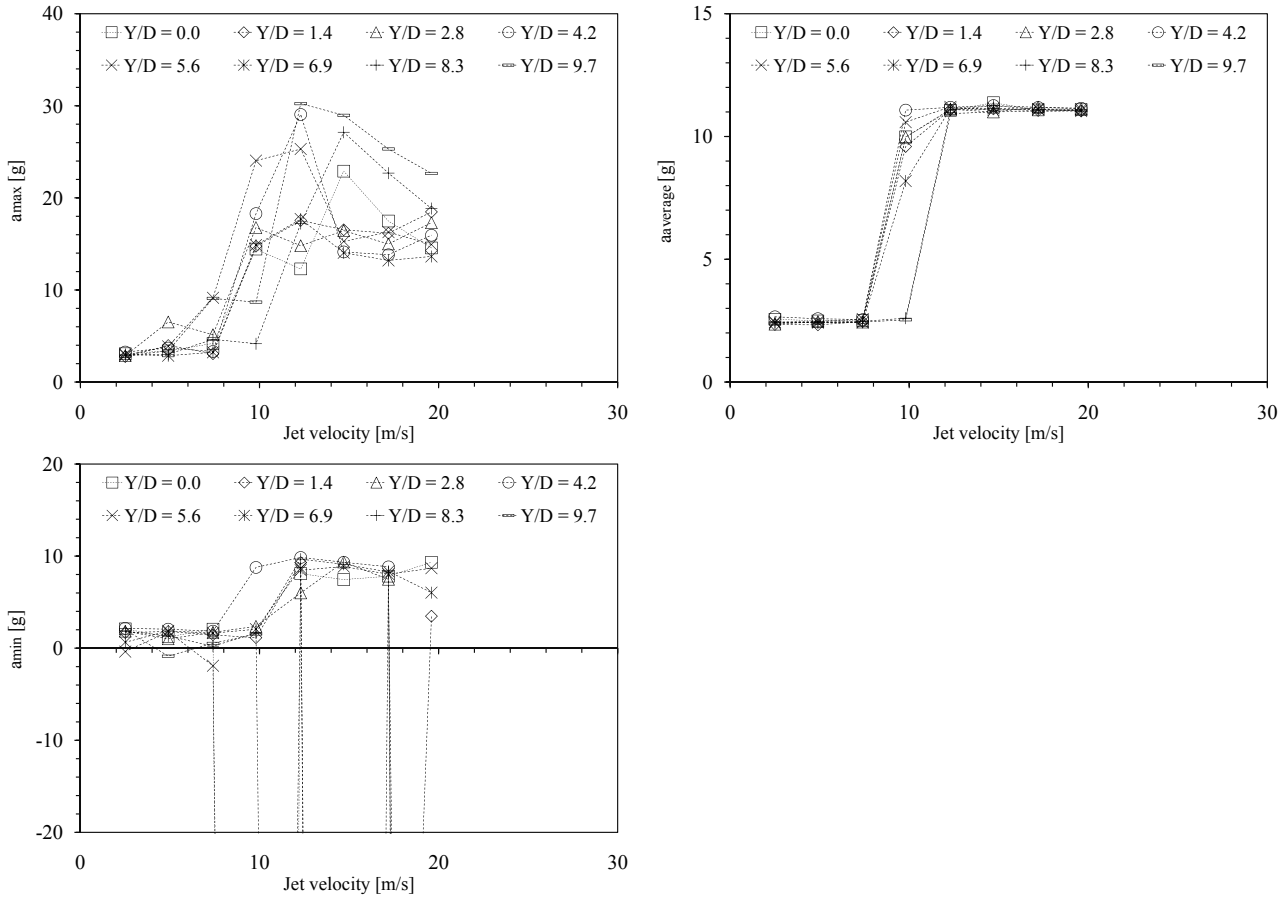

Figure 6.61: Block accelerations measured for configuration CN as a function of jet velocity (2.5-19.6 m/s) and Y/D ratio (0-9.7). Maximum (top left) and mean accelerations of block (top right). Minimum accelerations (bottom left) show some electrical noises that affect the measured values (reach the acceleration lower limit of -1000 g).

the block (near the vertical fissure) show better this peak (N° 317 and N° 318).

None of the two peaks appear in the PSD signal on the block upper face. As observed before, the first peak could correspond to the fissure natural period but the second peak did not correspond to the block eigenfrequencies.

6.4.6 Dynamic block impulsion

The dynamic block impulsion and the respective block uplift have been computed following the theoretical method explained in Chapter 5.4. In this section only the results for a core (Y/D = 2.8 or 0.2 m), a transition (Y/D = 5.6 or 0.4 m) and a developed jet (Y/D = 8.3 or 0.6 m) and two of the eleven jet velocities are explained (4.9 and 9.8 m/s) due to the larger displacement of block. Figures 6.65, 6.66 and 6.67 show the comparison between theoretical and measured uplift. The dynamic block impulsion is analyzed in Chapter 7.1.

As explained before (Chapter 6.2.6), two coefficients (added mass and pressure reduction coefficient) have been calibrated to fit theoretical and measured uplift.

By analyzing the time evolution of the block uplift (theoretical and measured, Figures 6.65,

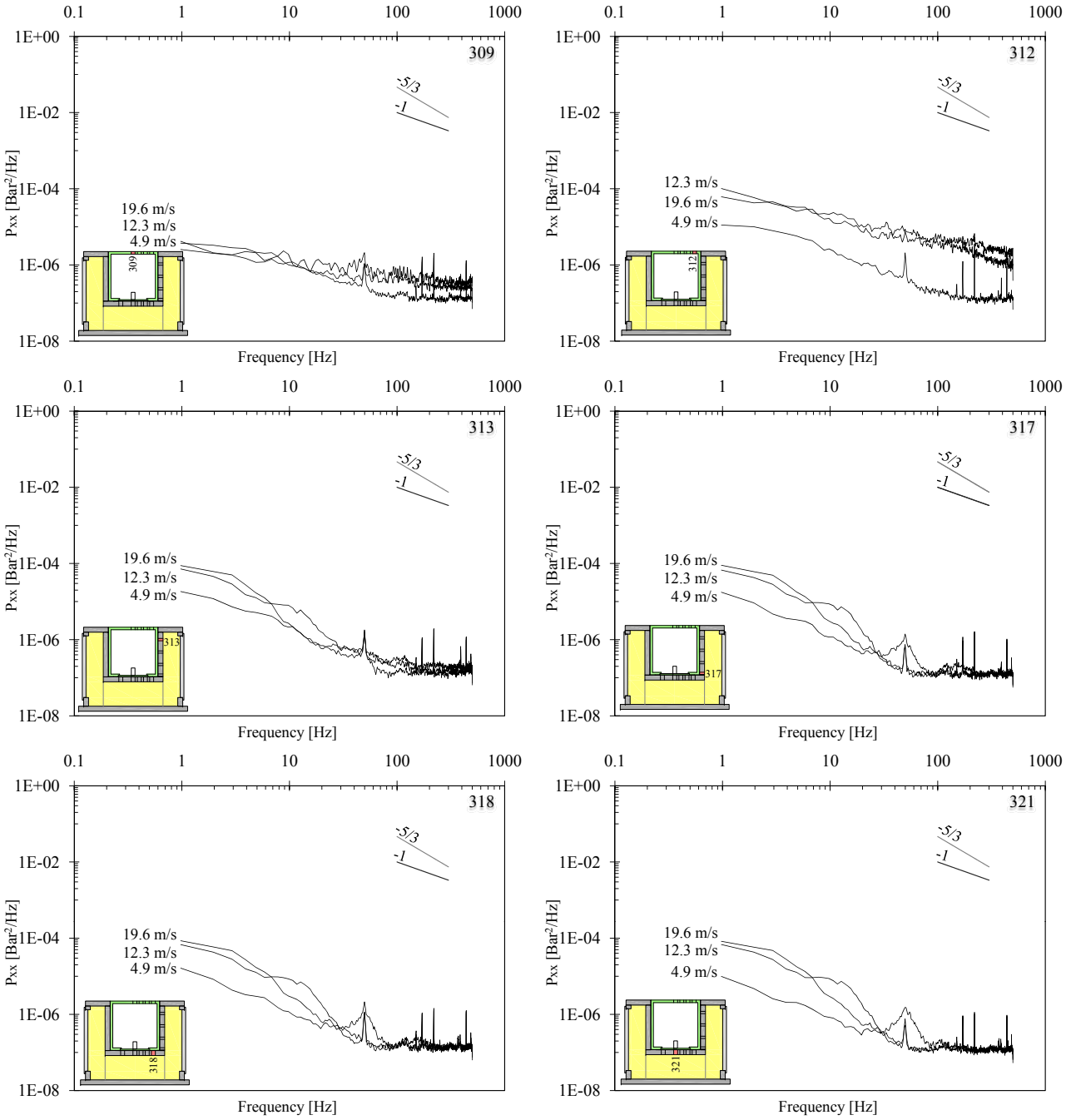

Figure 6.62: Non-dimensional spectral content (PSD) computed for configuration CN. Core jet (Y/D = 2.8) and different jet velocities (4.9, 12.3 and 19.6 m/s): on the block upper face pressure transducers N° 309 (top left) and N° 312 (top right); along the vertical fissure pressure transducers N° 313 (center left) and N° 317 (center right); underneath the block pressures transducers N° 318 (bottom left) and N° 321 (bottom right).

6.66 and 6.67), it is possible to observe that the block vertical fluctuations can be reproduce theoretically even though the pressures used to define the forces acting on the block upper and lower faces come from two different configurations (see Chapter 7.1 for more explanations).

Jet velocities lower than 4.9-7.4 m/s generate displacements in the order of magnitude of 10^{-4}-10^{-3} mm. Jet velocities of 4.9-7.4 m/s generate displacements of 10^{-3}-10^{-2} mm and for

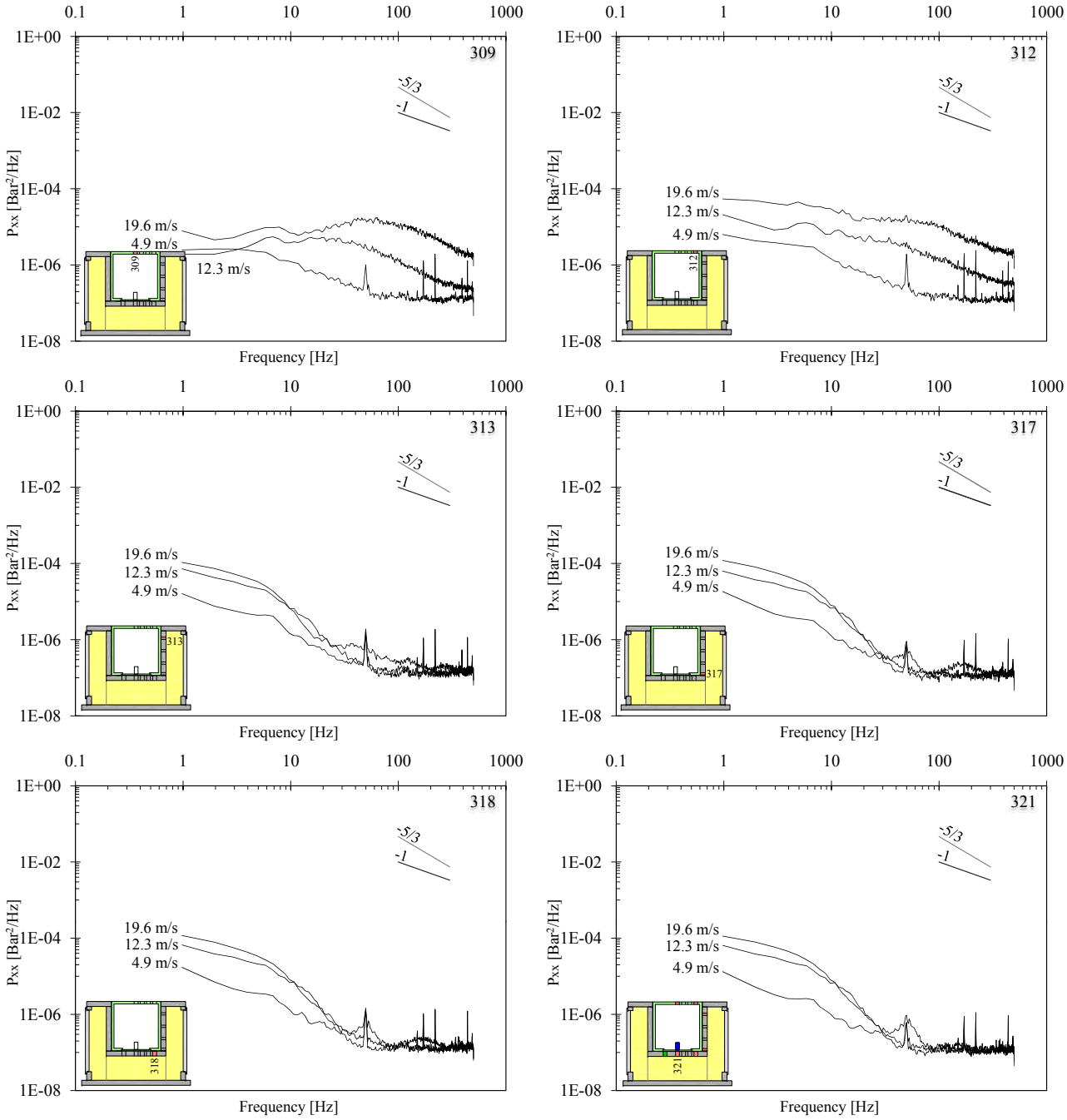

Figure 6.63: Non-dimensional spectral content (PSD) computed for configuration CN. Transition jet (Y/D = 5.6) and different jet velocities (4.9, 12.3 and 19.6 m/s): on the block upper face pressure transducers N° 309 (top left) and N° 312 (top right); along the vertical fissure pressure transducers N° 313 (center left) and N° 317 (center right); underneath the block pressures transducers N° 318 (bottom left) and N° 321 (bottom right).

higher velocities the block displacements reach millimeters and centimeters. The block reaches a maximum uplift (∼160 mm) for jet velocities of 17.2-19.6 m/s.

Table 6.6 summarizes the added mass coefficients and the pressure reduction coefficients that have been used to obtain the similitude between theoretical and measured uplift.

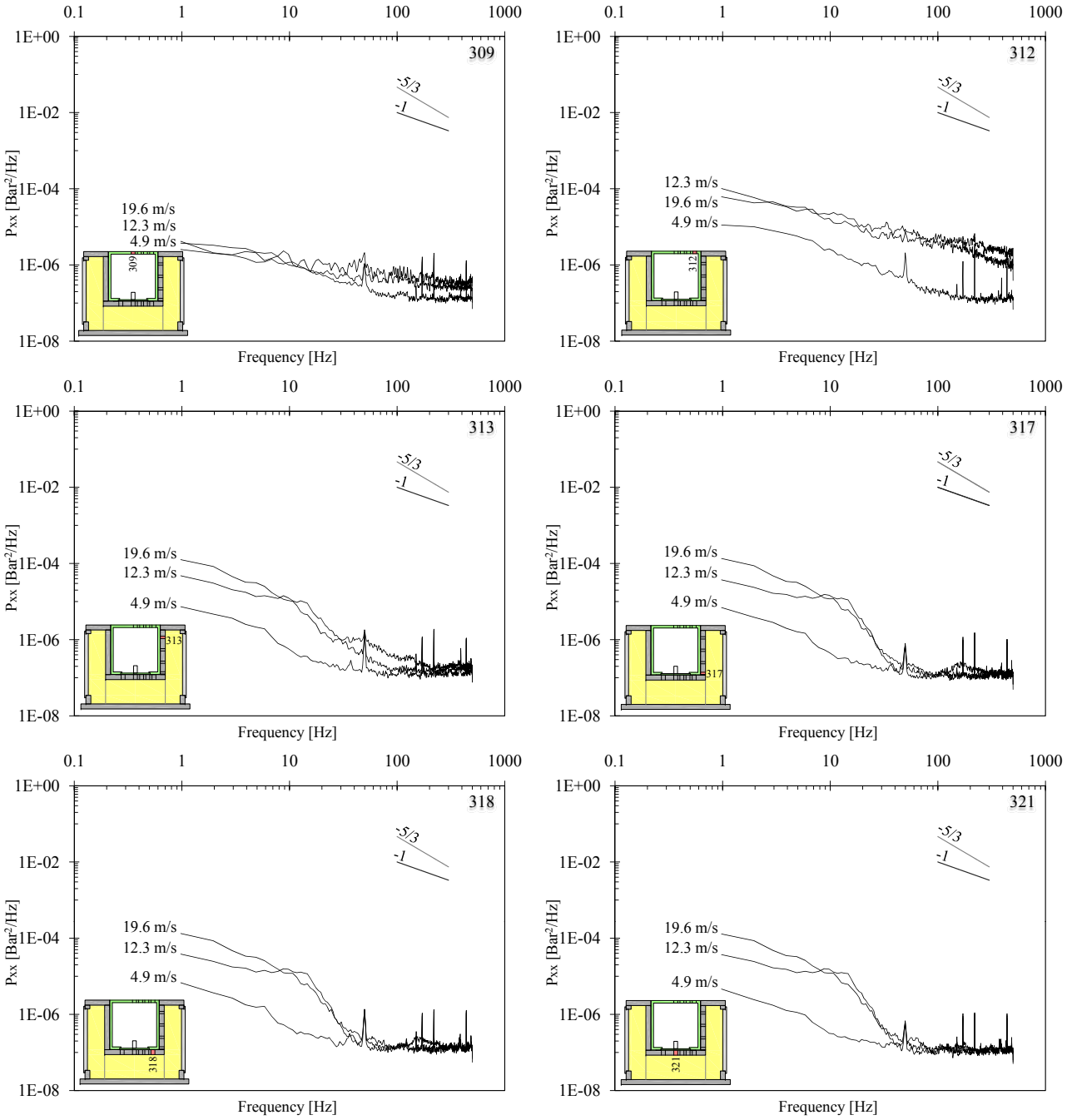

Figure 6.64: Non-dimensional spectral content (PSD) computed for configuration CN. Developed jet (Y/D = 8.3) and different jet velocities (4.9, 12.3 and 19.6 m/s): on the block upper face pressure transducers N° 309 (top left) and N° 312 (top right); along the vertical fissure pressure transducers N° 313 (center left) and N° 317 (center right); underneath the block pressures transducers N° 318 (bottom left) and N° 321 (bottom right).

6.4.7 Conclusions

The pressure field acting on the block for the configuration with the jet impact on the block corner cannot be reproduced correctly as has been observed for the two previous configurations (CR and SR). The four transducers located on the block upper face are not aligned radially outwards from the stagnation point but are located perpendicularly at one side of the block

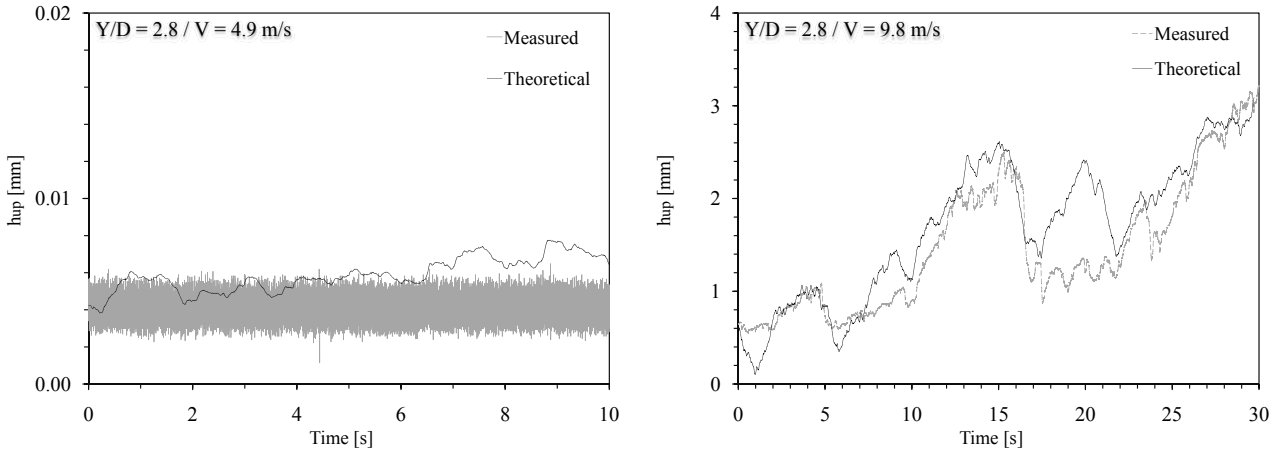

Figure 6.65: Time evolution of dynamic block impulsion for configuration CN. Comparison between theoretical and measured uplift for a core jet (Y/D = 2.8) and two jet velocities (4.9 and 9.8 m/s).

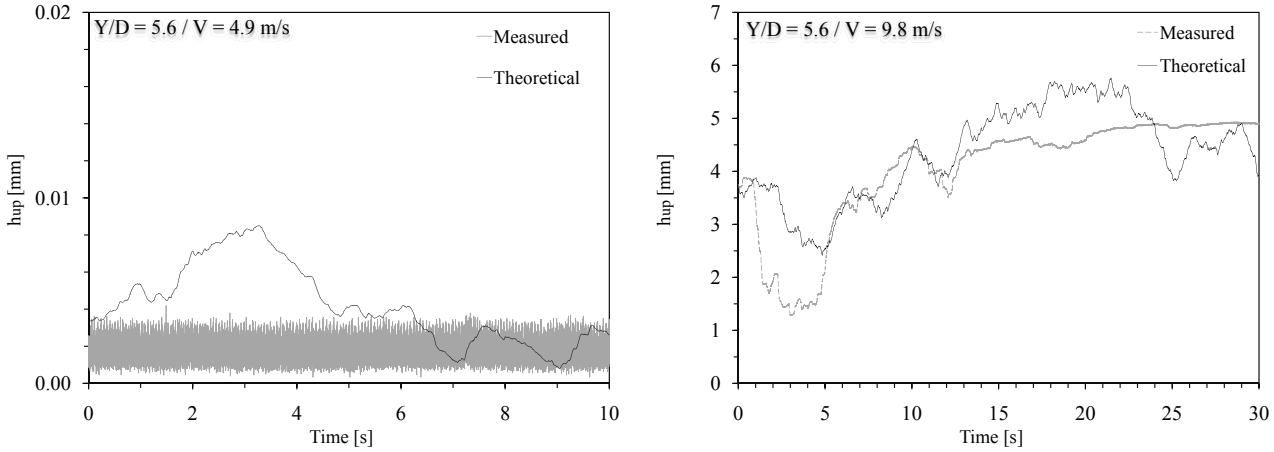

Figure 6.66: Time evolution of dynamic block impulsion for configuration CN. Comparison between theoretical and measured uplift for a transition jet (Y/D = 5.6) and two jet velocities (4.9 and 9.8 m/s).

Coefficient	Y/D ratio	Jet velocity V_0						
		4.9	7.4	9.8	12.3	14.7	19.6	27.0
[-]	[-]	[m/s]	[m/s]	[m/s]	[m/s]	[m/s]	[m/s]	[m/s]
AMC	2.8	300	200	5	-	-	-	-
	5.6	300	200	4	-	-	-	-
	8.3	250	200	70	-	-	-	-
PRC	2.8	-0.22	0.20	0.23	-	-	-	-
	5.6	0.30	0.41	0.34	-	-	-	-
	8.3	0.47	0.49	0.54	-	-	-	-

Table 6.6: Added mass coefficient (AMC, α_{am}) and pressure reduction coefficient (PRC) for configuration CN.

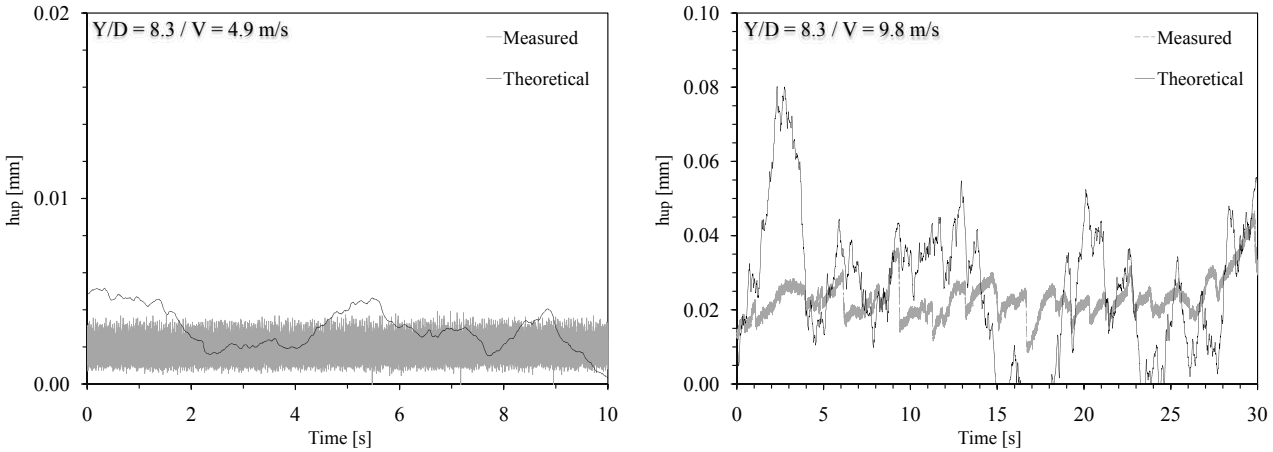

Figure 6.67: Time evolution of dynamic block impulsion for configuration CN. Comparison between theoretical and measured uplift for a developed jet (Y/D = 8.3) and two jet velocities (4.9 and 9.8 m/s).

(between 104 and 142 mm from the stagnation point). Hence, is not possible to obtain the pressure exponential distribution. To control the pressure acting on the block upper face, the pressure recorded with another configuration but with a transducers located at the same distance from the stagnation point, has been used as references. This control allows to affirm that the pressures recorded with the actual configurations are correct for this distance from the stagnation point. Inside the vertical fissure the mean pressures increase weakly with the approach of the central cavity bottom. Maximum and minimum pressures along the vertical fissure show a quite constant evolution. Underneath the block the pressures (maximum, mean and minimum) are almost constant. The same behavior has been observed for the other water depths (core, transition and developed jets) and jet velocities.

The pressure coefficients recorded for transducers situated on the block upper face and inside the fissure are in reasonable agreement with the previous measurements. Jet velocities lower than 7.4 m/s generates high coefficient values that did not match with the literature values.

The block begins to move up with small fluctuations for a jet velocity greater than 4.9 m/s but returns always at its initial position (in contact with the central cavity bottom). For a jet velocity of 7.4 m/s, the amplitude of this vertical displacements increases and the block did not return to its initial position. For jet velocities larger than 12.3 m/s, the vertical movements are so large that the transducer cannot measure the displacements (maximum displacement $\sim$160 mm). The same maximum displacement has been observed for core, transition and developed jets.

The block accelerations are related to the recorded displacements and show a similar behavior: for jet velocities lower than 7.4 m/s they are almost constant, than they increase and reach a new constant value for jet velocities larger than 12.3 m/s. Maximum accelerations show a similar trend but the recorded values are higher. Minimum acceleration increase as a function of the jet velocity, but show some measurement problems for jet velocities larger than 7.4 m/s.

As observed for previous configurations, it may possible that this electrical noise perturb as well maximum and minimum accelerations.

As observed for the two previous configurations (CR and SR), the Power Spectral Density (PSD) show a different behavior between the transducers situated on the block upper face and inside the 3-dimensional fissure. The two transducers situated on the block upper face show a similar behavior with the previous configurations but the energy content related to each frequency is lower. This difference is generated by the different solicitation acting on the transducers due to their distance from the stagnation point. At the plunge pool bottom the PSD signal shows a change in the behavior when the frequency reaches 10 Hz: for lower frequencies the energy content decreases slowly (slope -2/3) and faster for higher frequencies (slope -1). As observed for the two previous configurations, when the jet velocity increases, the energy content increases proportionally. Inside the 3-dimensional fissure, the PSD signal shows a different behavior than at the plunge pool bottom. Some differences with the previous configurations are observables. The energy content is lower than at the plunge pool bottom for the same jet velocity. For frequencies lower than 8-15 Hz the energy decreases slowly (with a slope of approximately -2/3 and -1), between 8-15 and 100 Hz the energy decrease with a different slope (situated between -5/3 and -6/3 in a small frequency range: from 8-15 to 40-60 Hz) and for higher frequencies the energy reaches a constant value similar for all jet velocities. As before, two peaks could be observed: the first peak (between 30 and 80 Hz) is related to the natural fissure frequency and is centred on the 50 Hz frequency for lower jet velocities, the second peak (between 100 and 200-300 Hz) is not so clearly definable. None of the two peaks appear in the PSD signal of the surface pressure signal.

As observed before, the dynamic block impulsion shows a good similitude between theoretical and measured values theoretically even though the pressures used to define the forces acting on the block upper and lower faces come from two different configurations. Only the exact amplitude of the vertical displacements could not be always simulated exactly by the theoretical uplift, but the vertical fluctuations could be well reproduced.

6.5 Overall considerations on test

For the first time the pressure field surrounding a 3-dimensional block loaded by a high-velocity jet and the corresponding responses of an artificial block of rock (displacements and accelerations) have been measured simultaneously.

The pressure field acting on the block upper face has an exponential distribution centred at the stagnation point independently of the jet impact position as proposed in literature. The pressure field acting inside the 3-dimensional fissure is almost constant for a given water depth and jet velocity. The pressure increases as a function of the water depth and jet velocity. The pressure acting inside the vertical fissure shows a weak increase as a function of the distance

from the plunge pool. Maximum and minimum extreme pressures are localized near the fissure entrance where a weak a "cavitation" phenomenon or by a compression-decompression phenomenon of air bubbles present into the water may appear for jets loading directly the vertical fissure. Underneath the block the pressure acting on the whole lower face of the block is almost constant (maximum, mean and minimum pressure) and increases as a function of the jet velocity.

The pressure values recorded inside the fissure are lower than the values recorded on the block upper face and no transient amplifications have been detected.

The block displacements increase as a function of the jet asymmetries. More the jet is move far away from the block center and reaches the entrance of the surrounding fissure and larger are the vertical displacements of the block. Generally the block begins to move up for jet velocities larger than 7.4 m/s. The block finds always a new equilibrium position those changes as a function of the jet velocity. The jet impact on the block corner is the jet configuration that generates the larger vertical displacement independently from the water depth in the plunge pool, which corresponds at approximately 160 mm for a block height of 200 mm. For jet velocities larger than 17.2-19.6 m/s it is possible that the block is completely ejected from the rock foundation and being transported downstream from the main flow (propagation of the scour).

The block acceleration related to these displacements show a similar evolution for maximum and minimum values. Some electrical noises affect minimum values that reach the acceleration lower limits. It may be that these electrical noises affect as well maximum and mean accelerations.

Core, transition and developed jets show the same behavior.

Chapter 7

Influence of parameters

7.1 Dynamic impulsion on a rock block

7.1.1 Introduction

The dynamic block impulsion and the related block uplift have been computed for the configurations where the block is free to move along its vertical axis. The eight configurations are:

- Two contact points at lateral guides
    1. Jet impact position on the block center (CE);
    2. Jet impact position on the block right hand side (SI);
- Eight contact points at lateral guides
    3. Jet impact position on the block center (CR);
    4. Jet impact position on the block right hand side (SR);
    5. Jet impact position on the block left hand side (SL);
    6. Jet impact position on the block corner (CN);
    7. Jet impact position between the center and the corner of the block (RR);
- Passive air entrainment and eight contact points at lateral guides
    8. Jet impact position on the block corner (ACN).

The results for configurations CR, SR and CN have been explained in Chapter 6.

The dynamic block impulsion has been computed following the theoretical method proposed in Chapter 5.4 with the forces explained in Chapter 5.3.

Theoretical uplift (displacements of block computed from pressure measurements) has been computed from the block initial position (distance between the bottom of the central cavity

and the block lower face, approximately 0.85 mm). Measured uplift is the distance between the displacement transducer and the lower face of the block. The measured displacements have been corrected with the block initial position to use a reference similar to the theoretical displacements.

For some configurations, the pressures recorded at the plunge pool bottom (on the block upper face with transducers N°s 309 to 312, see Figure 4.8) cannot be used to compute the dynamic block impulsion because the pressure transducers are situated far away (> 100 mm) or not radially outwards from the stagnation point (jet impact point on the block). The pressure measured for these configurations did not represent a correct pressure distribution on the block upper face from the stagnation point to the block limits.

To overcome this problem, the pressures recorded by the same transducers (N°s 309 to 312) but for another configuration (different jet impact position on the block) have been used. The pressures recorded for the following configurations have been used for the dynamic impulsion computation: jet impact on the block center (CR) and jet impact on the block right side (SR). For both configurations, the transducers are located radially outwards from the stagnation point. As assumption these measurements are considerate to be able to generate a correct pressure distribution on the block upper face (Chapters 6.2.2 and 6.3.2). In any case, pressures acting underneath the block, displacements and accelerations correspond to the analyzed configuration.

As an example, the dynamic block impulsion for the configuration with the jet impact on the block left side (SL) has been computed as follows (Figure 7.1):

- Pressure on the block upper face: measured with the configuration having the jet impact on the block right side (SR);
- Pressure underneath the block: measured with the analyzed configuration (SL);
- Displacements and accelerations: measured with the analyzed configuration (SL).

This method (combing pressures from two different configurations) has been applied to four configurations:

1. Jet impact on the block left hand side (SL);
2. Jet impact between the center and the corner of the block (RR);
3. Jet impact on the block corner without passive jet aeration (CN);
4. Jet impact on the block corner with passive jet aeration (ACN).

Combining pressures may affect the theoretical uplift results. The pressures acting on the block upper face have not been recorded simultaneously than the pressures recorded underneath the block, as well the block displacements and accelerations. This time difference breaks the direct relationship between pressures acting on the block and displacement and accelerations of block.

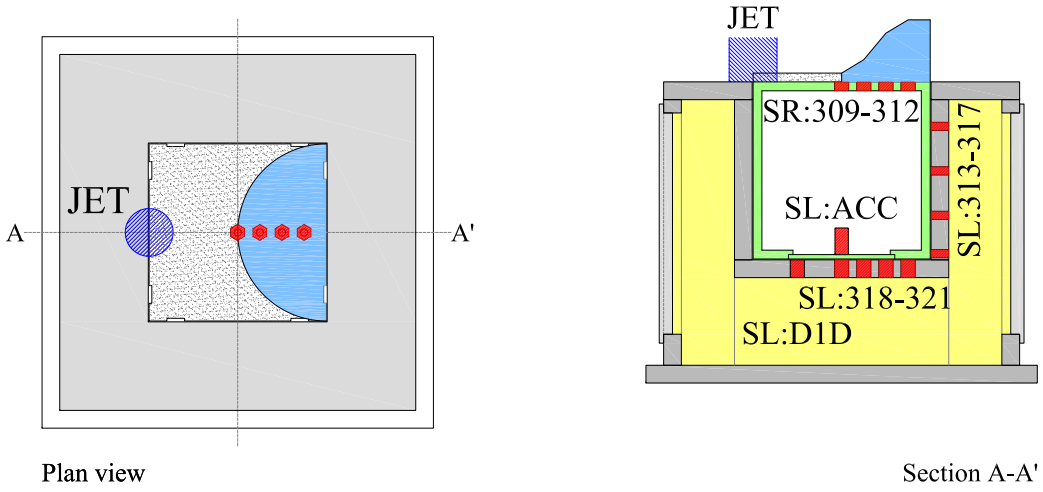

Figure 7.1: Integration sketch for the computation of dynamic block impulsion for configuration SL. Block upper face with jet impact position (cylinder) and integration schema (dark grey region where pressures are know and dotted region where pressures are unknown for configuration SR) (left) and transversal section of the new set-up showing the transducers reparation between the two configurations: block upper face configuration SR and inside the fissure configuration SL (right).

The computation of the block dynamic impulsion has been made with the following assumptions:

- for a given water depth and jet velocity the pressure distribution follows an exponential distribution centred at the stagnation point (as observed in Chapter 6) that can be generated by pressures recorded with another configuration (another jet impact on the block);
- the pressure distribution is the same following any direction from the stagnation point.

The theoretical block uplift shows similar results, independently if the pressures acting on the block upper face have been recorded with configuration CR or SR.

Configurations with the jet impact on the block center (CE and CR) and with the jet impact on the right side (SI and SR) did not need this combination of pressure measurements to compute the dynamic impulsion.

7.1.2 Analysis of dynamic impulsion

The dynamic block impulsion is analyzed for a core (Y/D = 2.8), a transition (Y/D = 5.6) and a developed jet (Y/D = 8.3). The dynamic block impulsion has been computed for different jet velocities until the block uplift reaches the upper limit of the displacement transducers (∼5.5 mm). For some configurations, this maximum jet velocity was 27.0 m/s and for other

configurations it was only 7.4 m/s.

Two coefficients have to be calibrated to fit theoretical uplift to measured uplift: the added mass coefficient (α_{am}) and the pressure reduction coefficient (PRC). The pressure reduction coefficient corresponds to the pressures acting on the block upper face in the region where no pressures have been measured. The added mass has been computed using Equation (5.18) ($m_{am} = \alpha_{am} \cdot \pi \cdot \rho_w \cdot V_b$ where α_{am} is the added mass coefficient, ρ_w the water density and V_b the block volume).

The pressure acting on the block has to be defined. On the block upper face, two different surfaces could be observed: the surface where the pressure measurements have been made (near the stagnation point) and the surface where no pressure measurements have been made for the same test (Chapter 5.3.3). The integration method to compute the force acting on the block upper face is illustrated by Figure 5.5. The dark grey surface (complete, a half or a quarter of the circle surface) is the surface where pressures have been measured, and the dotted surface (the remaining surface on the block upper face) is the surface where an assumption has to be made to estimate the pressures acting on the block. The pressure reduction coefficient has to be calibrated to estimate the force applied to the block upper face in the dotted surface (Figure 5.5). The pressure reduction coefficient matches a percentage of the pressure recorded at the boundary between dark grey and dotted surface on Figure 5.5. Then, the force acting on this region is obtained by multiplication with the dotted surface.

A time interval of 30 seconds has been used to calibrate both coefficients. The dynamic block impulsion has been computed for a time interval of 30 s and, as a result, the theoretical uplift has been obtained. The two coefficients have been calibrated to obtain the best agreement between theoretical and measured uplift. The calibration of the two coefficients has been made for each water depth and for each jet velocity (some test runs have been analyzed for the same water depth and jet velocity). For three configurations, it was not possible to calibrate the two coefficients for jet velocities larger than 9.8 m/s (configurations CN and ACN) and 12.3 m/s (configuration SL) because the block displacement reached the upper limit of the displacement transducers (∼5.5 mm).

Table 7.1, Figures 7.2 and 7.3 summarize the added mass coefficient (α_{am}) that has been calibrated to obtain a good correlation between theoretical and measured uplift.

Table 7.2, Figures 7.4 and 7.5 summarize the pressure reduction coefficient (PRC) that has been calibrated to obtain a good correlation between theoretical and measured uplift.

7.1.2.1 Jet impact on the block center

The two configurations with the jet impact in the center of the block (CE and CR) show similar values for the added mass coefficient and for the pressure reduction factor. As shown in Chapter 6.2.6 for configuration CR, the theoretical uplift shows good correlation with measured uplift.

By analyzing the time evolution of the uplift (theoretical and measured), it is possible to

Configuration	Y/D ratio	Jet velocity V_0						
		4.9	7.4	9.8	12.3	14.7	19.6	27.0
[-]	[-]	[m/s]	[m/s]	[m/s]	[m/s]	[m/s]	[m/s]	[m/s]
CE	2.8	3	3	2.5	3	2.5	3	3
	5.6	3	2.5	3	2	1.5	2	3
	8.3	3	3	2.5	3	2.5	2	3
SI	2.8	350	300	100	70	65	60	50
	5.6	300	300	80	65	60	50	25
	8.3	300	300	80	70	40	40	15
CR	2.8	4	3.5	3	3	3	2	2.5
	5.6	4	3.5	2.5	3	2	2.5	1.5
	8.3	4	3.5	3	2	1.5	2	2.5
SR	2.8	300	300	140	140	120	90	40
	5.6	300	300	230	160	150	100	45
	8.3	300	300	300	160	140	110	40
SL	2.8	300	300	60	15	-	-	-
	5.6	300	150	50	13	-	-	-
	8.3	300	300	60	15	-	-	-
RR	2.8	300	500	200	300	250	400	250
	5.6	300	500	180	200	250	350	120
	8.3	250	500	400	150	100	200	100
CN	2.8	300	200	5	-	-	-	-
	5.6	300	200	4	-	-	-	-
	8.3	250	200	70	-	-	-	-
ACN	2.8	300	200	-	-	-	-	-
	5.6	300	250	-	-	-	-	-
	8.3	250	250	130	-	-	-	-

Table 7.1: Added mass coefficient (α_{am}) for a 3-dimensional block strongly confined as a function of jet configuration, Y/D ratio and jet velocity V_0.

observe that the block vertical fluctuations recorded by the displacement transducer can be reproduced theoretically (using pressures acting on the block upper and lower face and the other forces acting on the block). Almost all vertical fluctuations are present in the theoretical uplift but the amplitude is not always the same (sometimes it is larger and sometimes it is smaller related to the measured uplift). This difference of amplitude is more visible during peaks (in order of magnitude of some 10^{-3}-10^{-2} mm). Theoretical uplift cannot be shifted exactly onto the measured uplift, but the similitude between the two uplifts is very strong for the 30 s analyzed time interval (the differences are very small).

As an example, Figure 7.6 on the left shows theoretical and measured uplift for a small time interval (2 s) for configuration CR, a Y/D ratios of 5.6 and 8.3 and a jet velocity of 27.0 m/s.

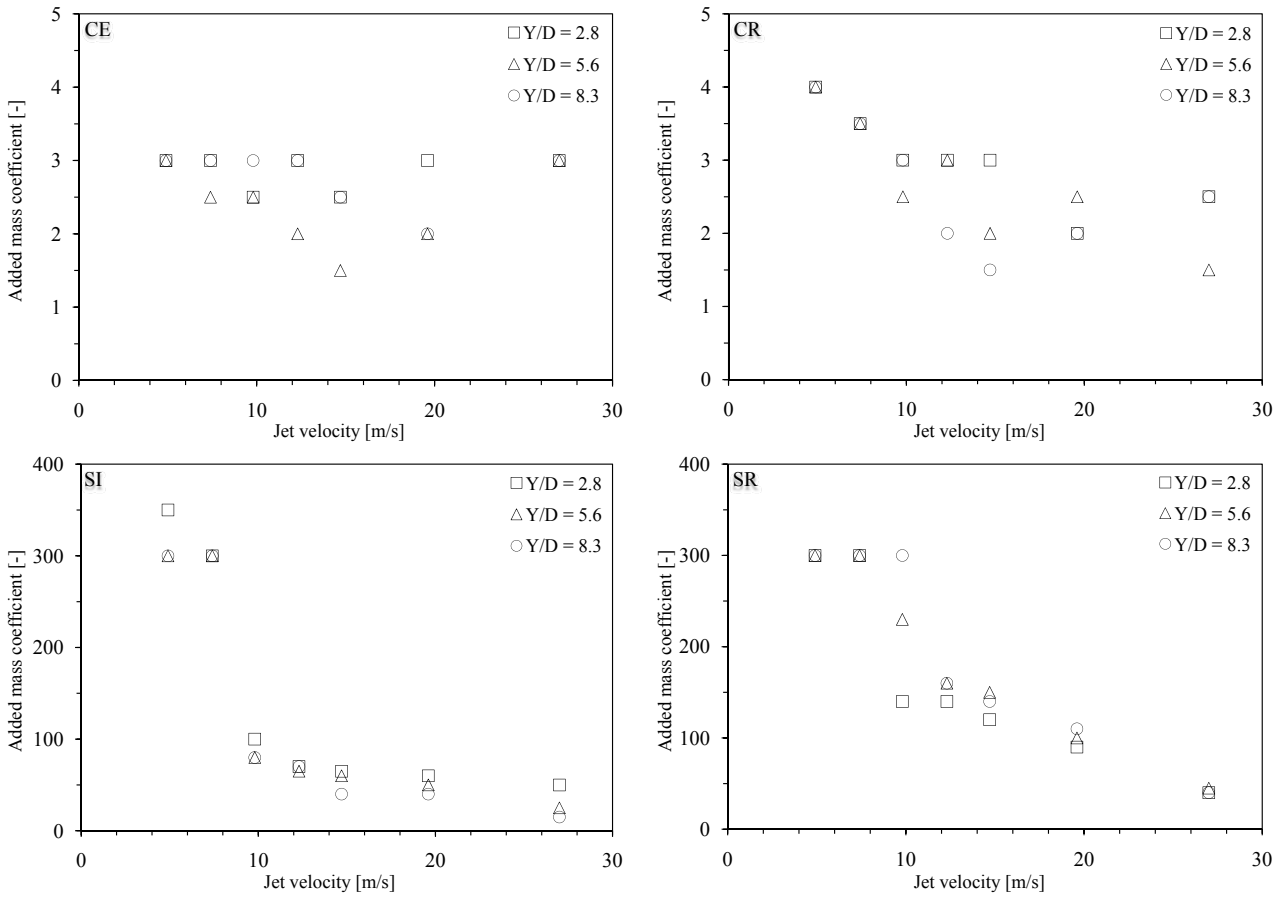

Figure 7.2: Added mass coefficient (α_{am}) for a 3-dimensional block strongly confined as a function Y/D ratio and jet velocity. Configuration CE (top left), configuration CR (top right), configuration SI (bottom left) and configuration SR (bottom right).

The distribution of the uplift values for the analyzed time interval (histogram) is illustrated in the same figure on the right. The histogram shows a similar distribution of the uplift values (theoretical and measured) centred on the mean uplift value. This figure allows to confirm the previous remarks: the two uplifts signal show a good agreement (when a peak appears in the measured uplift, it also appears in the theoretical uplift, but not always with the same amplitude).

Table 7.3 summarizes the statistical values for theoretical and measured uplift illustrated by Figure 7.6. The statistical analysis (maximum, mean, minimum, standard deviation and variance) performed for theoretical and measured uplift shows a similar behavior: the values are similar for the same Y/D ratio and jet velocity. The same behavior has been observed for the other Y/D ratios and jet velocities.

The added mass coefficient influences the amplitudes of the vertical displacement and the pressure reduction coefficient influences the slope of the time evolution of the vertical displacement. Large added mass coefficients generate small amplitude of displacements. A pressure reduction coefficient showing small values ($\rightarrow 0$ or negative) increases the vertical displacement and vice versa, a pressure reduction coefficient showing values higher than 0 reduce the vertical displacements. The added mass coefficient is almost constant for all water depths and jet ve-

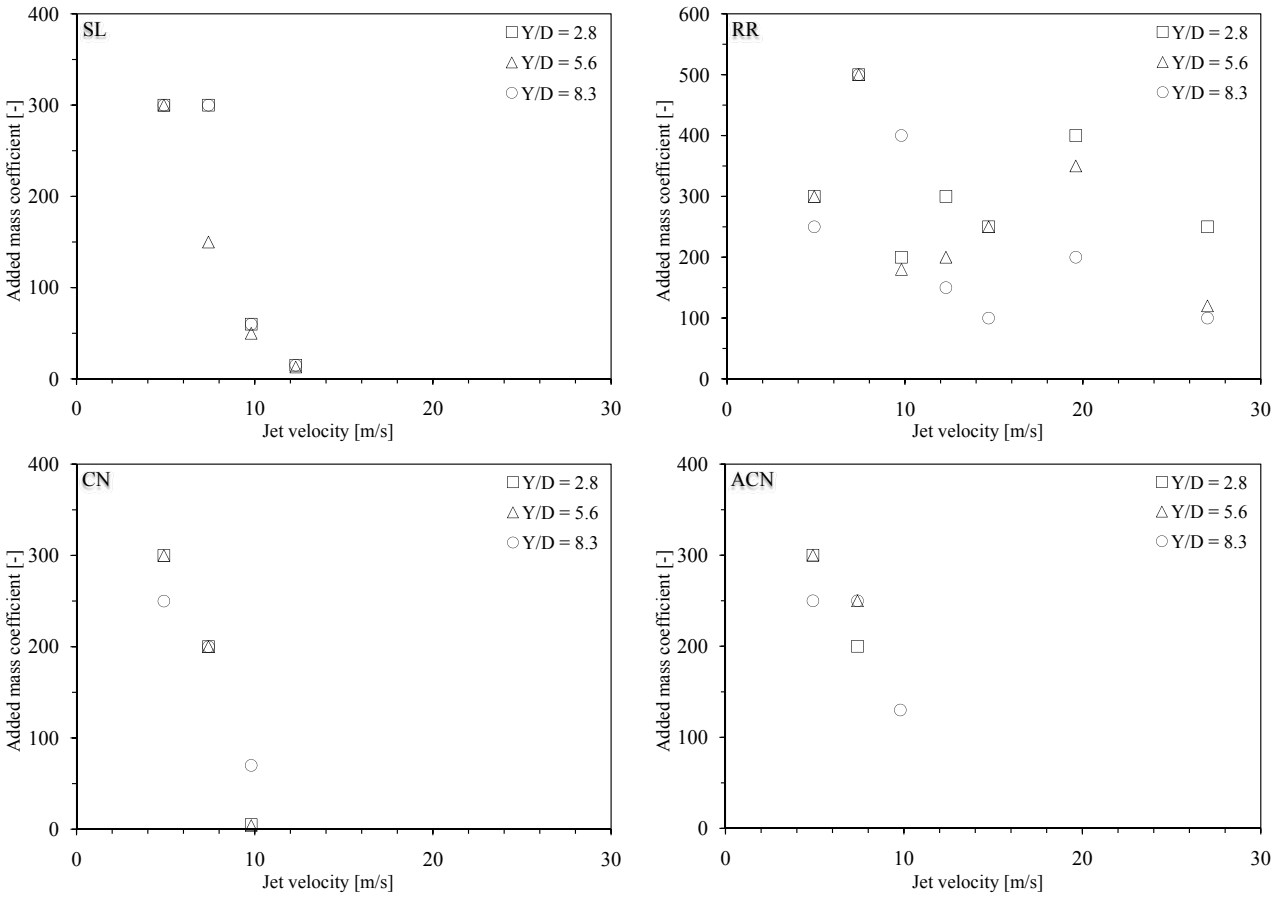

Figure 7.3: Added mass coefficient (α_{am}) for a 3-dimensional block strongly confined as a function Y/D ratio and jet velocity. Configuration SL (top left), configuration RR (top right), configuration CN (bottom left) and configuration ACN (bottom right).

locities. The added mass concept allows obtaining a good agreement between theoretical and measured uplift.

For both configurations (CE and CR), the influence of the pressure reduction coefficient is negligible because the block surface where the pressures are unknown (dotted surface) is small related to the surface where the pressures are known (grey region, Figure 5.5).

For configurations with the jet impacting on the block center, the added mass coefficient α_{am} is situated between 2 and 4 and the pressure reduction coefficient can be assumed equal to 0.5.

The previous remarks are valid for core, transition and developed jets and for all jet velocities.

7.1.2.2 Jet impact on the block right hand and left hand side

Configurations with the jet impact on the block hand right (SI and SR) or left hand side (SL) show a similar behavior for the added mass coefficient and for the pressure reduction coefficient. This behavior is similar for core, transition and developed jets and for all jet velocities.

The added mass coefficient decreases with an increase of the jet velocity. This is the same behavior that has been observed for the block displacements. As show in Chapter 6.3.6 for

Configuration	Y/D ratio	Jet velocity V_0						
		4.9	7.4	9.8	12.3	14.7	19.6	27.0
[-]	[-]	[m/s]	[m/s]	[m/s]	[m/s]	[m/s]	[m/s]	[m/s]
CE	2.8	0	0	0	0	0	0.5	0.5
	5.6	0	0	0	0	0	0.5	0.5
	8.3	0	0	0	0.5	0	0.5	0
SI	2.8	-0.25	0.26	0.36	0.03	-0.27	-0.87	-0.96
	5.6	0.02	0.36	0.46	0.13	-0.13	-0.56	-0.86
	8.3	0.25	0.37	0.54	0.36	0.14	-0.27	-0.46
CR	2.8	0	0	0	0.5	0.5	0.5	0.5
	5.6	0	0	0	0.5	0.5	0.5	0.2
	8.3	0	0	0	0.5	0.5	0.5	0.5
SR	2.8	0	0.41	0.75	0.27	0.06	0.01	0.17
	5.6	0.18	0.61	0.83	0.42	0.26	0.16	0.09
	8.3	0.33	0.55	0.77	0.60	0.49	0.20	0.30
SL	2.8	-0.64	-0.41	-0.35	-0.73	-	-	-
	5.6	-0.04	-0.04	-0.13	-0.59	-	-	-
	8.3	0.22	0.22	0.13	-0.15	-	-	-
RR	2.8	-0.26	0.16	0.30	-0.51	-1.55	-3.63	-4.12
	5.6	0	0.40	0.37	-0.34	-1.14	-2.70	-2.74
	8.3	0.16	0.23	0.45	0.11	-0.23	-1.48	-1.40
CN	2.8	-0.22	0.20	0.23	-	-	-	-
	5.6	0.30	0.41	0.34	-	-	-	-
	8.3	0.47	0.49	0.54	-	-	-	-
ACN	2.8	-0.03	0.21	-	-	-	-	-
	5.6	-0.03	0.46	-	-	-	-	-
	8.3	0.47	0.54	0.50	-	-	-	-

Table 7.2: Pressure reduction coefficient (PRC) for a 3-dimensional block strongly confined as a function of jet configuration, Y/D ratio and jet velocity V_0.

configuration SR, the block begins to move up for jet velocities larger than 7.4-9.8 m/s. Jet velocities lower than 4.9-7.4 m/s generate vertical displacements in the order of magnitude of 10^{-3}-10^{-2} mm. Higher jet velocities generate displacement of 10^{-2}-10^{-1} mm. Maximum uplift was observed for the configuration with jet impact on the left side (SL) that reaches ∼160 mm for a jet velocity of 17.2 m/s.

The dynamic block impulsion for configuration SL (jet impact on the block left side) has been computed using the pressures measured on the block upper face with configuration SR (jet impact on the block right side). For jet velocities larger than 12.3 m/s the upper limit of the displacement transducers is reached and it is impossible to calibrate the two coefficients.

The three configurations show good agreement between theoretical and measured uplift. The

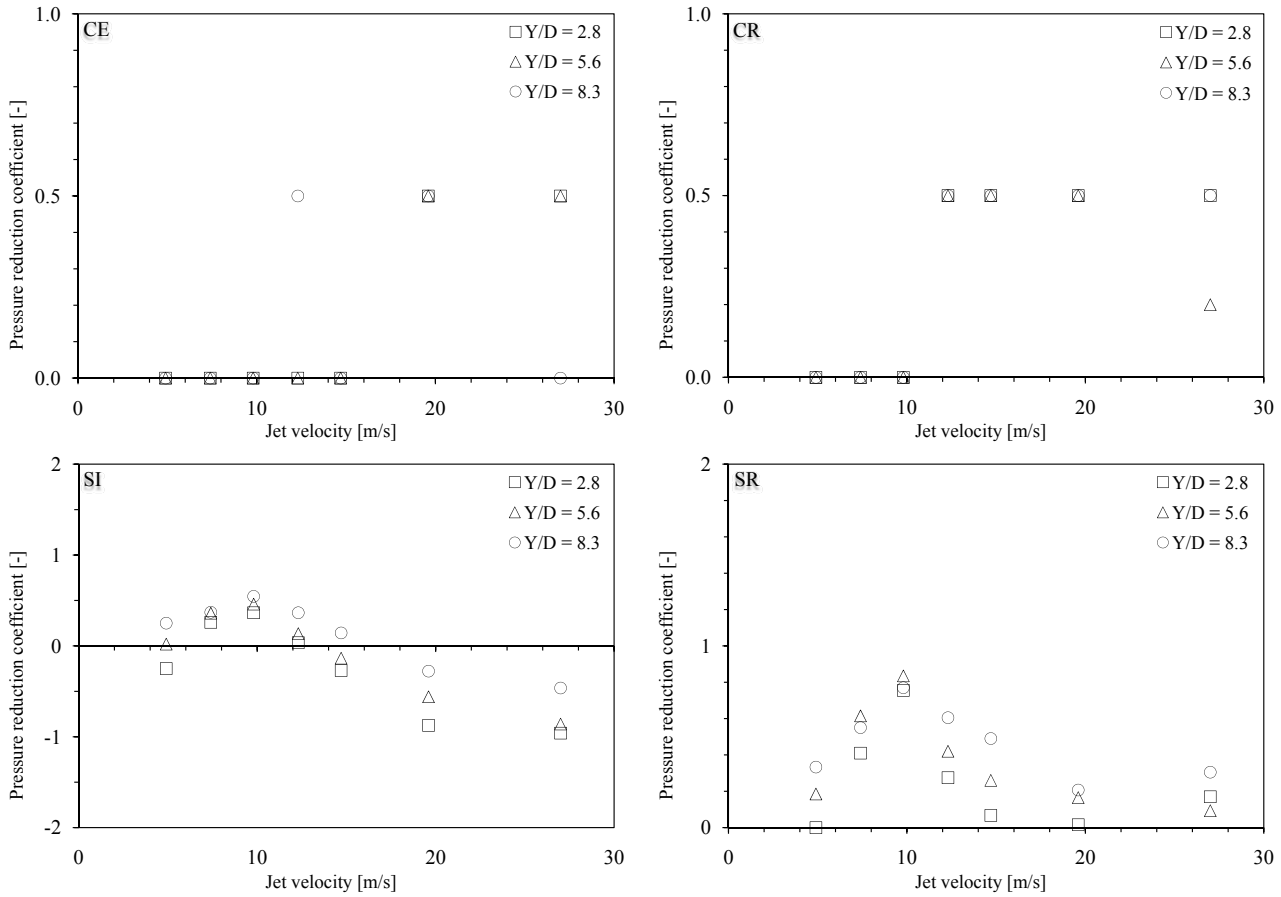

Figure 7.4: Pressure reduction coefficient (PRC) for a 3-dimensional block strongly confined as a function of Y/D ratio and jet velocity. Configuration CE (top left), configuration CR (top right), configuration SI (bottom left) and configuration SR (bottom right).

parameters of the two configurations SR and SL are the same, only the side of the jet impact on the block change. However, the block shows a different behavior for these configurations: with the jet impact on the left side the block uplift is larger than with the jet impact on the right side. To verify this strange behavior, additional tests have been performed for the same water depths and jet velocities. The analysis of these additional tests produces similar results.

To explain this difference in the block behavior, the following remarks can be made: it is possible that the block does some small rotations inside the central cavity when it is solicited by the jet on the block right side. These rotations might be different if the jet impact on the block left side, which might influence the block vertical displacement. By changing the jet impact on the block, these small rotations change or disappear.

The added mass coefficient decreases as a function of the jet velocity. Before any block movement, the coefficient is constant (approximately 300). For jet velocities larger than 7.4 m/s, the coefficient decreases but with a slope depending on the water depths and jet configurations. The larger vertical displacements are related to the lower coefficients.

The pressure reduction coefficient shows a different behavior as a function of the jet velocity: up to 7.4-9.8 m/s the coefficient increases but for higher jet velocities it decreases and reaches some negative values. For the same jet velocity, the pressure reduction coefficient increases as

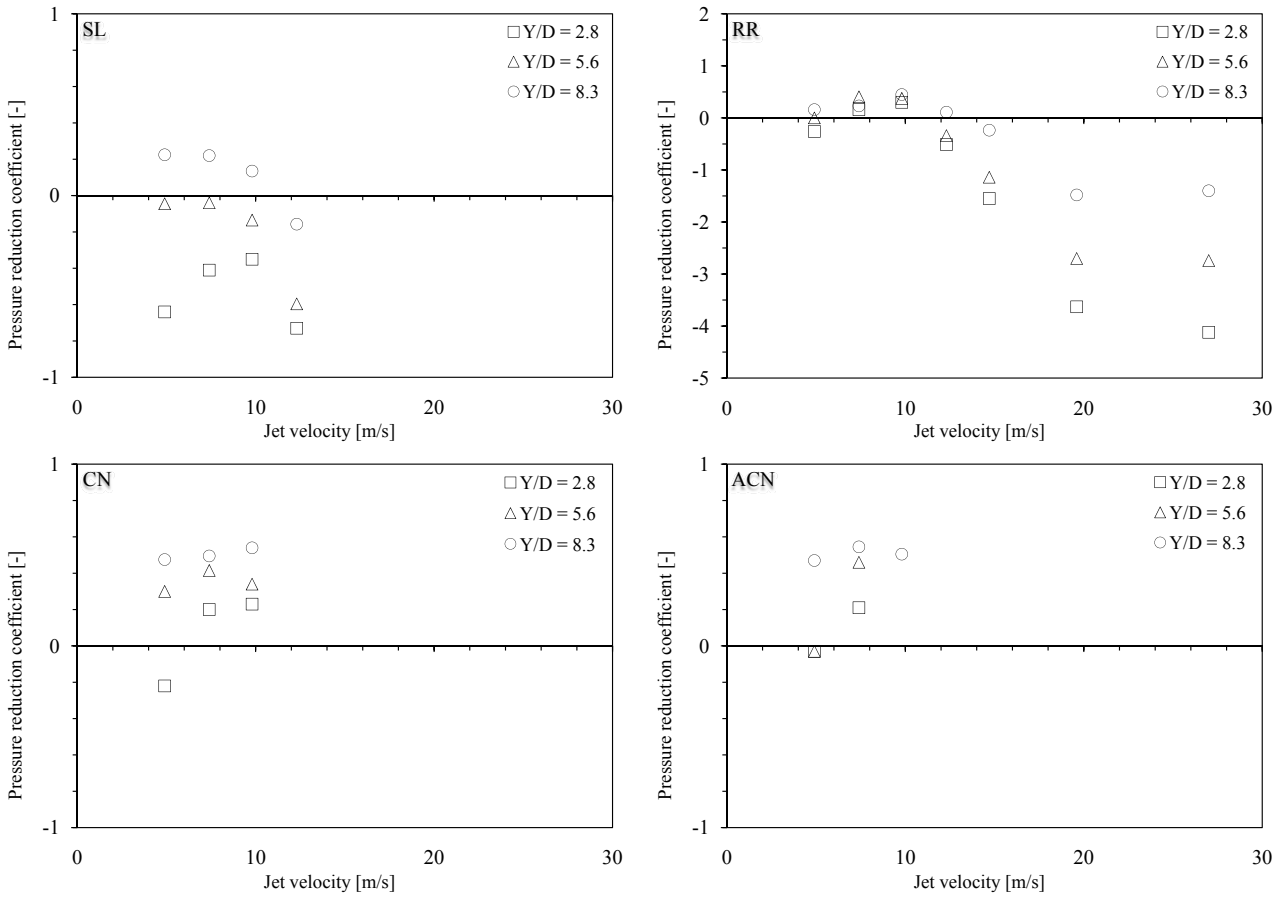

Figure 7.5: Pressure reduction coefficient (PRC) for a 3-dimensional block strongly confined as a function of Y/D ratio and jet velocity. Configuration SL (top left), configuration RR (top right), configuration CN (bottom left) and configuration ACN (bottom right).

a function of the water depth. This behavior is related to an increase of the water load at the plunge pool bottom and was observed for all jet velocities. The deflected flow near the plunge pool bottom (generate by the jet impact on the block) increases as function of the jet velocity. The jet crossing the plunge pool and the deflected flow near the bottom interact with the water in the plunge poll. This interaction generates some large eddies that could generate this negative pressures on the block upper face (negative values for the pressure reduction coefficients). As observed by analyzing the pressure field acting on the block (Chapter 6.3.6) the pressure decrease from the stagnation point radially outwards. At the extremities of the pressure distribution (bell-shape) acting on the block, pressures could reach negatives values. The influence of the pressure reduction coefficient is more important for configurations with the jet impacting not on the block center. For these configurations, the surface where the pressures are unknown is larger than the surface where the pressures are known. This surface is situated in the wall jet region where some negative pressures could appear.

As observed in Chapter 7.1.2.1 for configurations with the jet impact on the block center (CE and CR), theoretical and measured uplift show a good agreement. By analyzing the time evolution of the uplift (theoretical and measured), it is possible to observe that the block vertical fluctuations recorded by the displacement transducer can be reproduced theoretically.

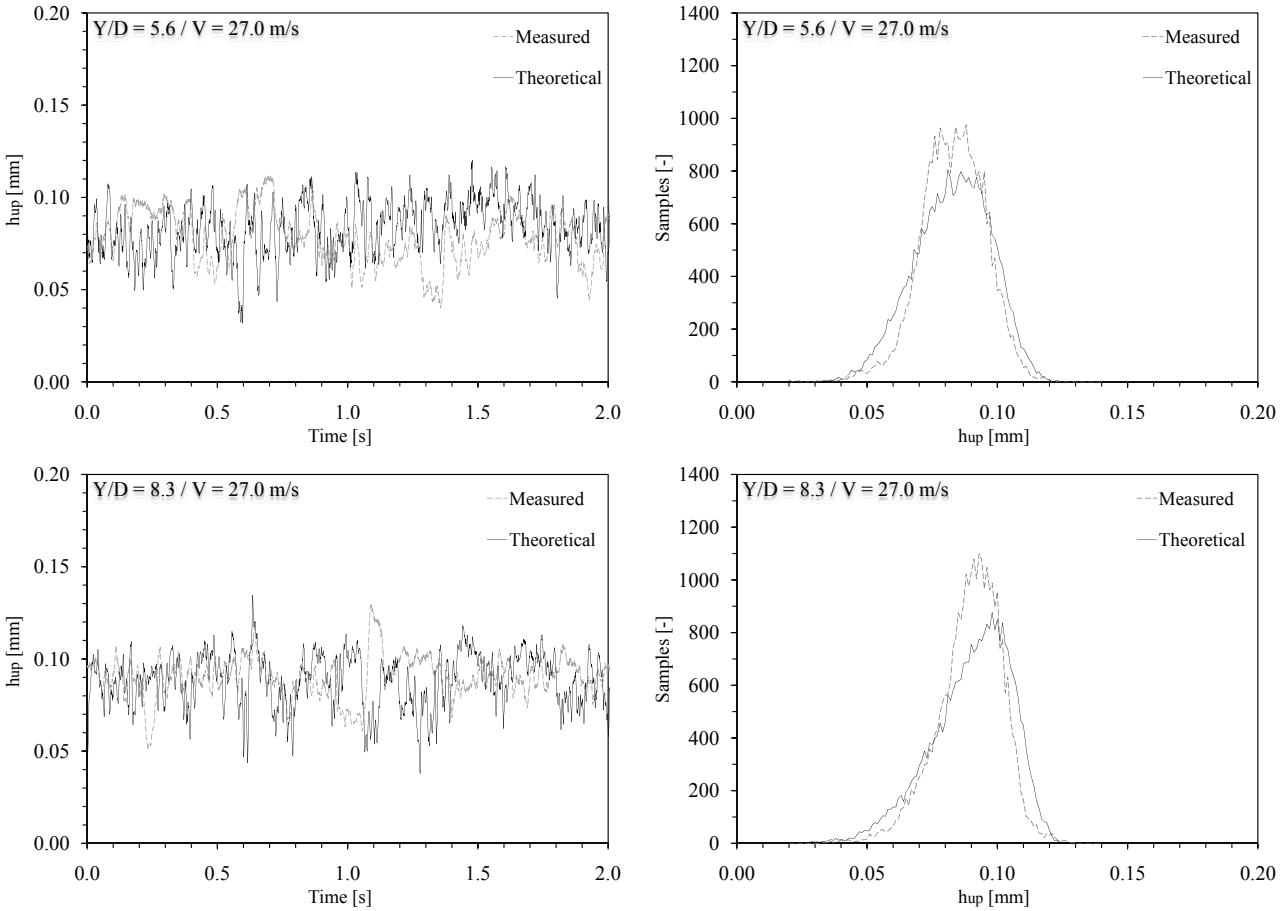

Figure 7.6: Time evolution of vertical uplift of block due to dynamic uplift pressures for configuration CR. Comparison between theoretical and measured uplift (left) and uplift histogram for the 30 s time interval (right). Transition jet Y/D = 5.6 (top) and developed jet Y/D = 8.3 (bottom) with a jet velocity of 27.0 m/s.

Almost all vertical fluctuations are present in the theoretical uplift but the amplitude is not always the same. The theoretical uplift cannot be shifted exactly to the measured uplift, but the similitude between the two uplifts is very strong for the 30 s analyzed time interval.

As an example, Figure 7.7 on the left shows theoretical and measured uplift for a small time interval (2 s) for configuration SR, a Y/D ratios of 5.6 and 8.3 and a jet velocity of 27.0 m/s. The distribution of the uplift values for the analyzed time interval (histogram) is illustrated in the same figure on the right.

Configuration SR (Figure 7.7), for a Y/D ratio of 5.6 shows a similar distribution of the uplift values (theoretical and measured) around the mean uplift. The histogram, for a Y/D ratio of 8.3, shows a different distribution of the uplift values: the theoretical uplift distribution is flatter (this distribution shows small and higher values than are not presents in the measured uplift distribution). The computation of dynamic block impulsion generates smaller and higher uplift values than the measured uplift. Looking the statistical data (Table 7.4), the differences between the two uplift signal are very small. This configuration needed more time to find the appropriate coefficients (added mass and pressure reduction coefficients) to fit theoretical and measured uplift. As explained before, the two uplift signals show good agreement. Sometimes,

Displacement	Maximum	Mean	Minimum	Standard deviation	Variance
[-]	[mm]	[mm]	[mm]	[mm]	[mm]
5.6: Measured	0.13	0.83	0.02	0.012	0.00015
5.6: Theoretical	0.13	0.82	0.02	0.015	0.00021
8.3: Measured	0.13	0.09	0.02	0.015	0.00024
8.3: Theoretical	0.14	0.09	0.03	0.012	0.00015

Table 7.3: Statistical comparison between theoretical and measured uplift for configuration CR. Transition (Y/D = 5.6) and developed jet (Y/D = 8.3) with a jet velocity of 27.0 m/s.

when a peak appears in the measured uplift signal this peak does not appears in the theoretical uplift, and not always the theoretical uplift can reproduce the same peak amplitude.

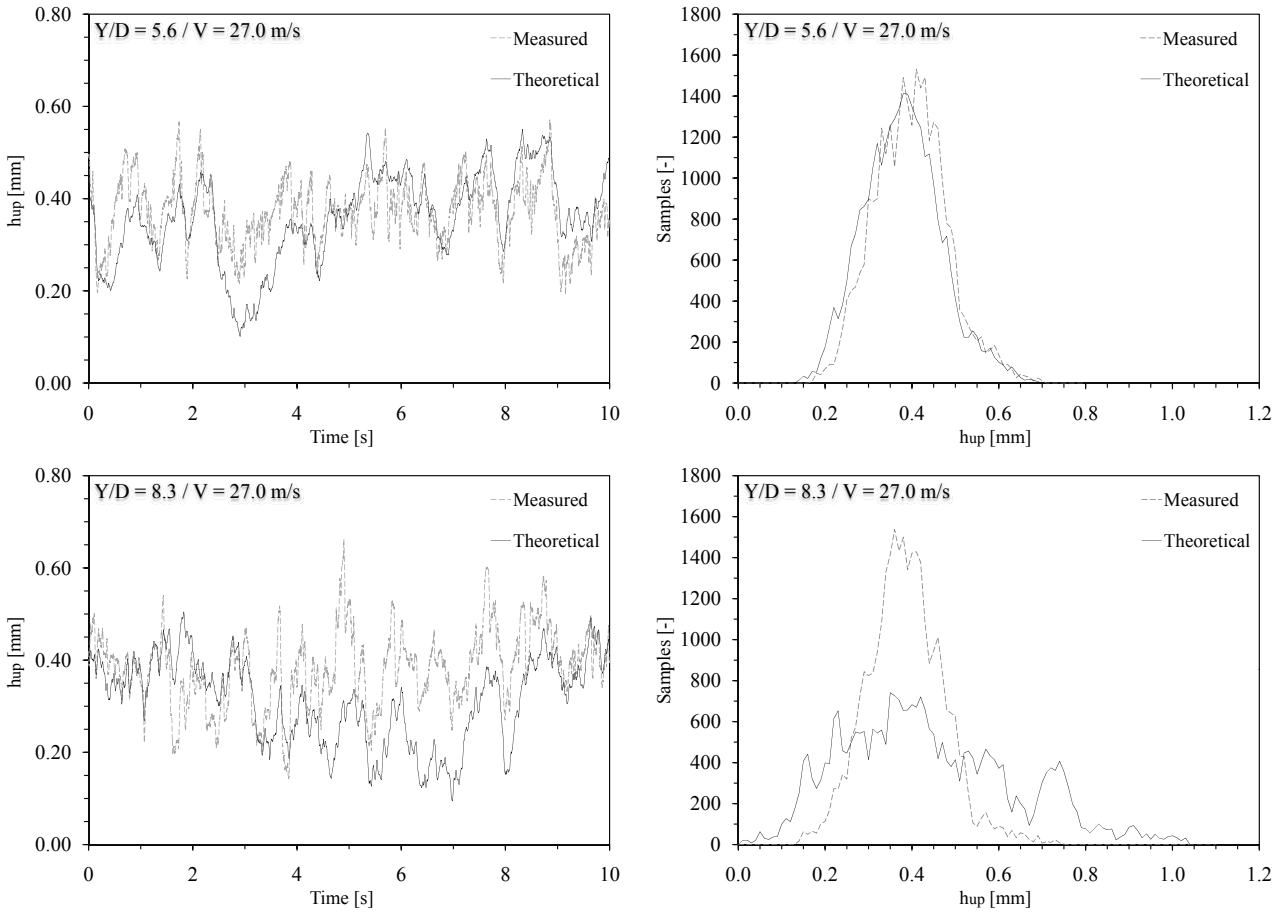

Figure 7.7: Time evolution of vertical uplift of block due to dynamic uplift pressures for configuration SR. Comparison between theoretical and measured uplift (left) and uplift histogram for the 30 s time interval (right). Transition jet Y/D = 5.6 (top) and developed jet Y/D = 8.3 (bottom) with a jet velocity of 27.0 m/s.

Table 7.4 and Figure 7.7 summarize the statistical values for theoretical and measured uplift for configuration SR and Table 7.5 and Figure 7.8 summarize the statistical values for configuration SI. The statistical analysis (maximum, mean, minimum, standard deviation and

variance) performed for configuration SR shows a similar behavior for theoretical and measured uplift: the values are similar for the same water depth and the same jet velocity. The same behavior has been observed for the other water depths and jet velocities.

Displacement	Maximum	Mean	Minimum	Standard deviation	Variance
[-]	[mm]	[mm]	[mm]	[mm]	[mm]
5.6: Measured	0.69	0.37	0.07	0.12	0.015
5.6: Theoretical	0.70	0.39	0.14	0.09	0.007
8.3: Measured	1.03	0.43	0	0.20	0.039
8.3: Theoretical	0.94	0.39	0.14	0.09	0.008

Table 7.4: Statistical comparison between theoretical and measured uplift for configuration SR. Transition (Y/D = 5.6) and developed jet (Y/D = 8.3) with a jet velocity of 27.0 m/s.

As observed for configuration SR, configuration SI shows good agreement between theoretical and measured uplift (both with jet impacting on the right side but different lateral guides). For configuration SI is more complicated to generate the same amplitude of vertical displacements (Figure 7.8). The histograms show a similar shape but sometimes there is a shift along the x-axis.

The statistical analysis performed for configuration SI, shows a similar behavior to configuration SR but is more difficult to obtain the same maximum displacement.

Displacement	Maximum	Mean	Minimum	Standard deviation	Variance
[-]	[mm]	[mm]	[mm]	[mm]	[mm]
5.6: Measured	0.94	0.46	0.04	0.21	0.043
5.6: Theoretical	1.19	0.51	0.10	0.17	0.028
8.3: Measured	1.70	0.62	0.10	0.28	0.079
8.3: Theoretical	1.26	0.65	0	0.28	0.079

Table 7.5: Statistical comparison between theoretical and measured uplift for configuration SI. Transition (Y/D = 5.6) and developed jet (Y/D = 8.3) with a jet velocity of 27.0 m/s.

For jet velocities lower than 4.9-7.4 m/s, the added mass coefficient α_{am} is constant (approximately 300) and the pressure reduction coefficient could be assumed equal to 0.5. Due to the small displacements (10^{-3} mm), the dynamic block impulsion could be neglected (concretely the block does not move). For jet velocities larger than 9.8 m/s, the added mass coefficient α_{am} decrease as a function of the jet velocity. This decreasing trend is not the same if we are looking the same water depth but for different configurations.

To compute the dynamic block impulsion and the respectively block uplift, the coefficients summarized in Tables 7.1 and 7.2 have been used. Each water depth (core, transition and

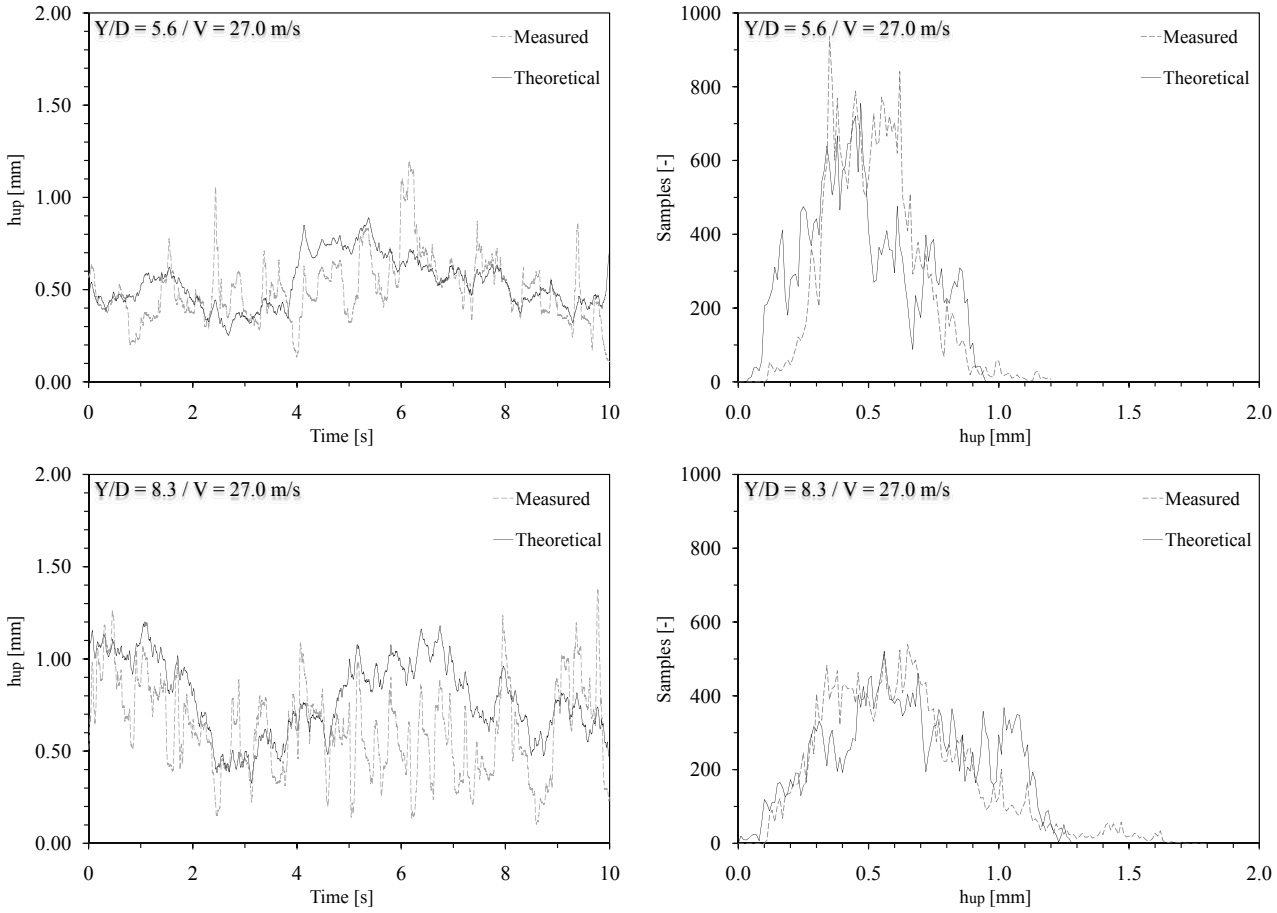

Figure 7.8: Time evolution of vertical uplift of block due to dynamic uplift pressures for configuration SI. Comparison between theoretical and measured uplift (left) and uplift histogram for the 30 s time interval (right). Transition jet Y/D = 5.6 (top) and developed jet Y/D = 8.3 (bottom) with a jet velocity of 27.0 m/s.

developed jets) and configurations had its own equation to estimate the added mass coefficient. Hence, a unique equation could not be defined.

7.1.2.3 Jet impact between the center and the corner of the block

The configuration with jet impact between the center and the corner of the block (RR) shows a different behavior between theoretical and measured uplift: the two uplifts signal did not match.

The dynamic block impulsion for configuration RR has been computed using the pressures measured on the block upper face with configuration SR (jet impact on the block right side). The theoretical uplift computed with this pressures combination does not show a good correlation with the measured uplift. To verify the results, the dynamic block impulsion has been computed as well using the pressures recorded with configuration CR (jet impact on the block center). Anyway, the results were similar. The similitude between theoretical and measured uplift is poor. The amplitude of the displacements cannot be reproduced and some peaks that appear in the measured uplift did not appear in the theoretical uplift (sometimes they appear

but with a time shift).

The added mass coefficient shows a fluctuating behavior when the jet velocity increase. The coefficient evolution, as a function of the jet velocity, is very different from the previous configurations (jet impact on the block center and on the block right/left hand side).

Did not exist any rules that norm the coefficient evolution: the coefficient increase and decrease randomly as a function of jet velocity and water depth (Table 7.1).

As observed for the configurations with the jet impacting on the block side, the pressure reduction coefficient shows a different behavior as a function of the jet velocity: up to 7.4-9.8 m/s the coefficient increases but for greater jet velocities it decreases and reaches some negative values. For the same jet velocity, the pressure reduction coefficient increases as a function of the water depth. This behavior is related to an increase of the water load at the plunge pool bottom and was observed for all jet velocities. The influence of the pressure reduction coefficient is more important for configurations with the jet impacting not on the block center. For these configurations, the surface where the pressures are unknown is larger than the surface where the pressures are known. This surface is situated in the wall jet region where some negative pressures could appear as observed with the pressure measurements.

As an example, Figure 7.9 on the left shows theoretical and measured uplift for a small time interval (2 s) for configuration RR, a Y/D ratios of 5.6 and 8.3 and a jet velocity of 27.0 m/s. The distribution of the uplift values for the analyzed time interval (histogram) is illustrated in the same figure on the right.

As explained before, the theoretical uplift did not follow well the measured uplift. The peaks that have been measured did not appear in the theoretical uplift and sometimes when they appear show a time shift. However, the histograms show a good similitude between the two uplift signals. The most important stuff is the similitude between theoretical and measured uplift time evolution and not only the statistical values, but for this configuration is not the case. The dynamic block impulsion for configuration RR has been computed using the pressures measured on the block upper face with configuration SR.

Table 7.6 and Figure 7.9 summarize the statistical values for theoretical and measured uplift for configuration RR. The statistical analysis shows s good similitude between statistic values of theoretical and measured uplift, but there are other parameters (uplift time evolution) to affirm if theoretical and measured uplift have good correlation.

For this configuration any recommendation for the added mass and the pressure reduction may be made.

7.1.2.4 Jet impact on the block corner

The configurations with the jet impact on the block corner, without passive jet aeration (CN) and with passive jet aeration (ACN), has a behavior similar to the configurations with the jet impacting on the block side (right and left side: SI, SR and SL). This behavior is similar for core, transition and developed jets and for all jet velocities

The added mass coefficient decreases with an increase of the jet velocity. This is the same behavior that has been observed for the displacements of block. As shows in Chapter 6.4.6

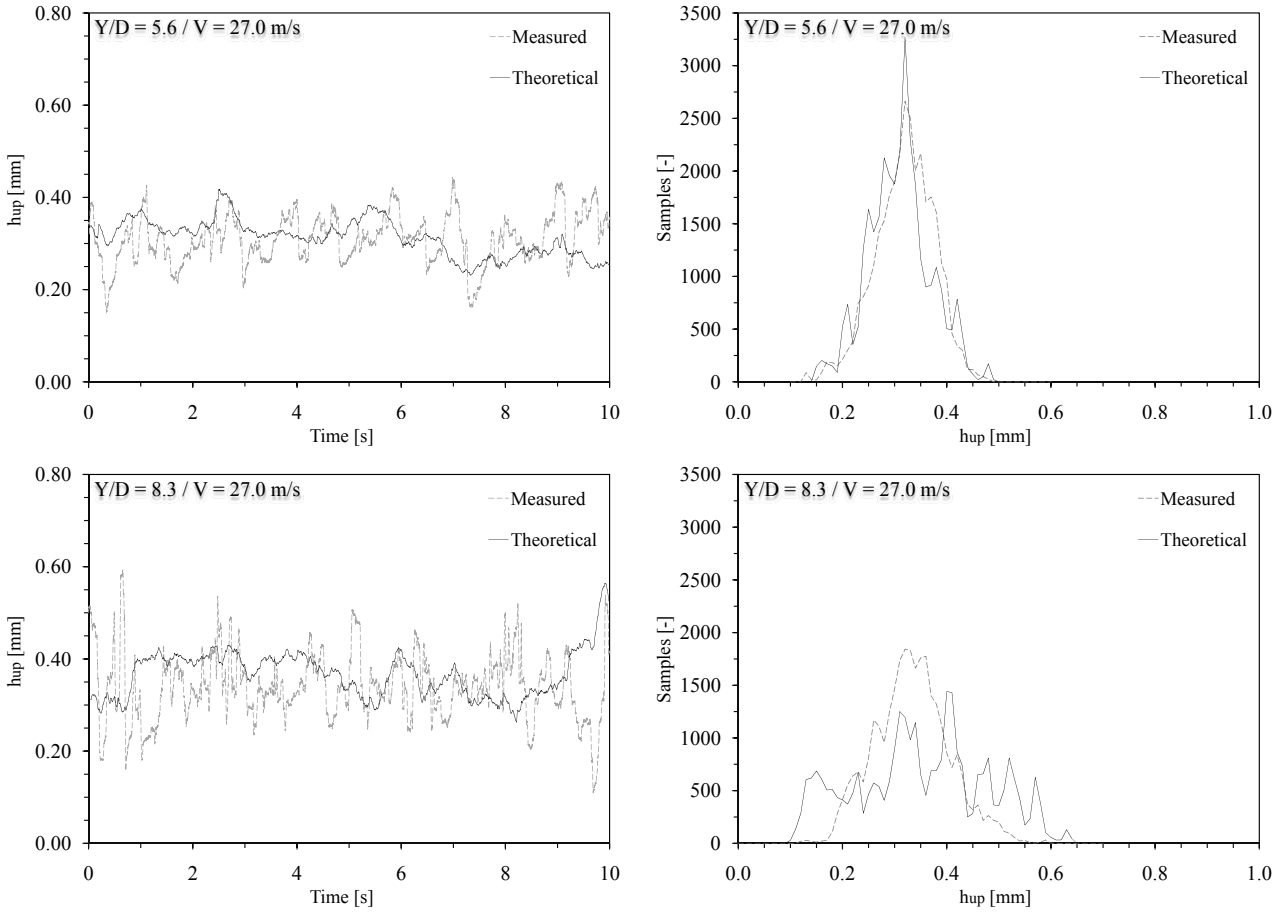

Figure 7.9: Time evolution of vertical uplift of block due to dynamic uplift pressures for configuration RR. Comparison between theoretical and measured uplift (left) and uplift histogram for the 30 s time interval (right). Transition jet Y/D = 5.6 (top) and developed jet Y/D = 8.3 (bottom) with a jet velocity of 27.0 m/s.

for configuration CN, the block moves up for jet velocities larger than 9.8-12.3 m/s for the configuration without passive jet aeration (CN) and larger than 7.4-9.8 m/s with passive jet aeration (ACN). Jet velocities lower than 4.9-7.4 m/s generate vertical displacements in the order of magnitude of 10^{-3}-10^{-2} mm. Jet velocities of 4.9-7.4 m/s generates displacement of 10^{-2}-10^{-1} mm and for higher velocities the displacements reach millimeters and centimeters. Maximum uplift was the same for both configurations: ∼160 mm. The added mass coefficient decreases as function of the jet velocity, but it decreases very fast when the displacements of block growth. Both configurations show this behavior. The block moves up fast when the jet velocity is larger than 7.4 m/s and reaches the upper limit of the displacement transducers. These displacements happen in the time interval necessary to change the jet velocity and cannot be recorded. Hence, there are only few values for the two coefficients.

The pressure reduction coefficient increase as function of the jet velocity but, due to the large displacements of block, it was not possible to observe its evolution for jet velocities larger than 12.3 m/s. For the same jet velocity, the pressure reduction coefficient increases as function of the water depth. This behavior can be observed for all jet velocities.

As an example, Figure 7.10 on the left shows theoretical and measured uplift for a time

Displacement	Maximum	Mean	Minimum	Standard deviation	Variance
[-]	[mm]	[mm]	[mm]	[mm]	[mm]
5.6: Measured	0.49	0.30	0.14	0.06	0.004
5.6: Theoretical	0.48	0.31	0.12	0.06	0.003
8.3: Measured	0.64	0.35	0.09	0.13	0.016
8.3: Theoretical	0.60	0.33	0.11	0.07	0.005

Table 7.6: Statistical comparison between theoretical and measured uplift for configuration RR. Transition (Y/D = 5.6) and developed jet (Y/D = 8.3) with a jet velocity of 27.0 m/s.

interval of 10 s for configuration ACN a Y/D ratio of 8.3 and a jet velocity of 9.8 m/s. The distribution of the uplift values for the analyzed time interval (histogram) is illustrated in the same Figure on the right.

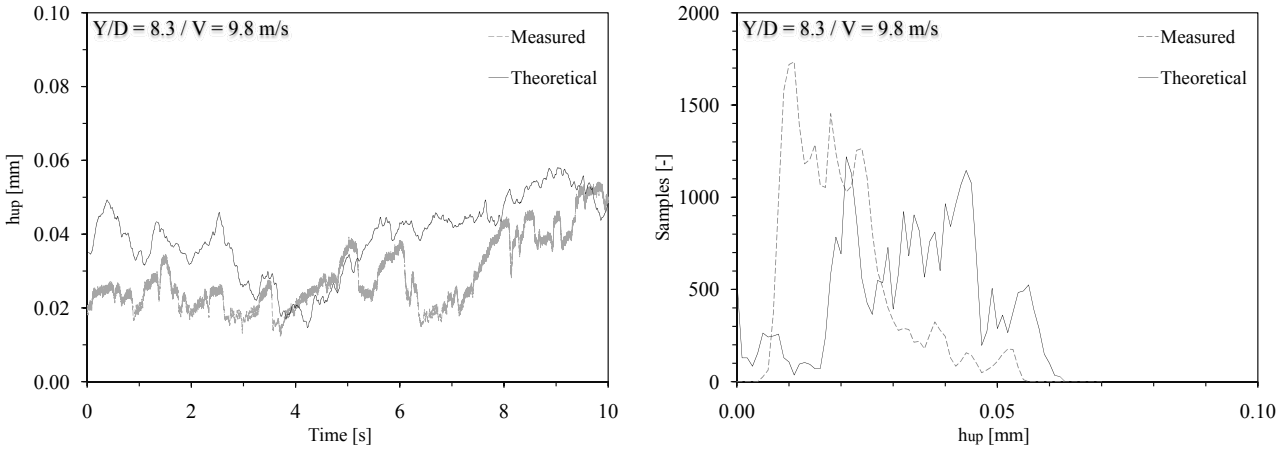

Figure 7.10: Time evolution of vertical uplift of block due to dynamic uplift pressures for configuration ACN. Comparison between theoretical and measured uplift (left) and uplift histogram for the 30 s time interval (right). Developed jet (Y/D = 8.3) with a jet velocity of 9.8 m/s.

Table 7.7 and Figure 7.10 summarize the statistical values for theoretical and measured uplift for configuration ACN. The statistical analysis shows a similar behavior for theoretical and measured uplift: the values are similar for the same water depth and the same jet velocity.

For jet velocities up to 4.9-7.4 m/s, the added mass coefficient α_{am} ranges between 200 and 300, the pressure reduction coefficient ranges between 0.2 and 0.5. For jet velocities larger than 9.8 m/s, the two coefficients for core (Y/D = 2.8) and transition jets (Y/D = 5.6) could be approximate as: added mass coefficient α_{am} equal to 4-5 and pressure reduction coefficient could be assumed as 0.2-0.5. For developed jets (Y/D = 8.3), the added mass coefficient α_{am} is approximately 100 and the pressure reduction coefficient could be assumed as 0.5.

To test the added mass coefficient and the pressure reduction coefficient an uplift simulation has been done: try to estimate the final uplift starting from the displacement of block observed for the second-last jet velocity (17.2 m/s). For both configurations, maximum uplift

Displacement	Maximum	Mean	Minimum	Standard deviation	Variance
[-]	[mm]	[mm]	[mm]	[mm]	[mm]
Measured	0.06	0.03	0	0.014	0.00020
Theoretical	0.06	0.02	0	0.010	0.00010

Table 7.7: Statistical comparison between theoretical and measured uplift for configuration CR. Developed jet (Y/D = 8.3) with a jet velocity of 9.8 m/s.

was estimate using the lateral guides fixed on the block and it reaches approximately 160 mm. The uplift observed for the second-last discharge was approximately 100-110 mm. Figure 7.11 shows this attempt to find the two coefficients starting from maximum observed uplift. Theoretical uplift (Figure 7.11) has been computed with the following values: added mass coefficient α_{am} equal to 4 and pressure reduction coefficient equal to -0.3. The uplift computation has been made with the same coefficients for both configurations (the configuration parameters were the same except the passive jet aeration). These coefficients values are situated along the decreasing trend observed for the other configurations (jet impact on the block side). With these coefficients values it was possible to estimate the block uplift evolution starting from a known position (using the pressure measurements).

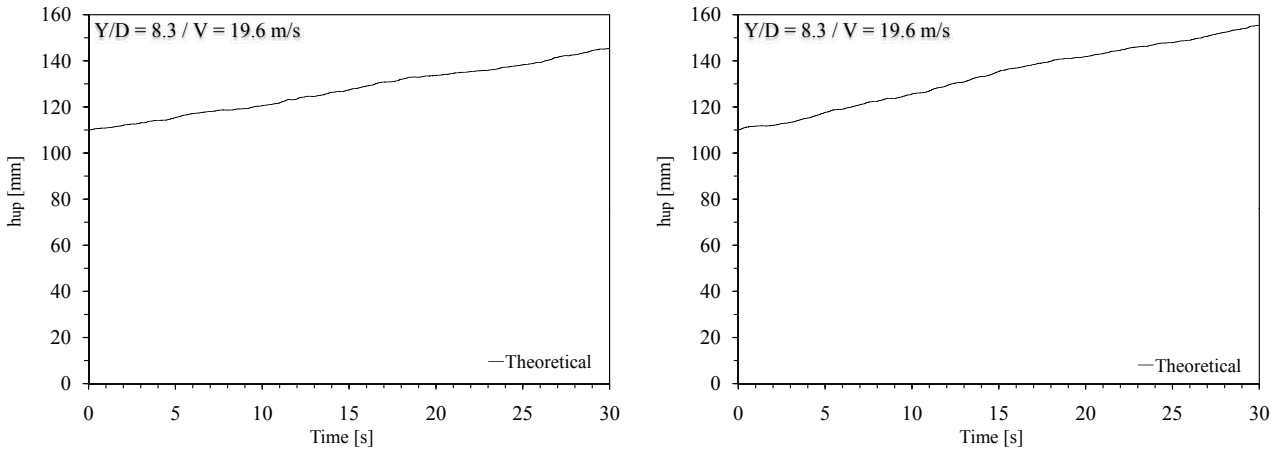

Figure 7.11: Attempt to estimate the block uplift starting from known vertical displacements using the same coefficient values. Configuration CN with natural air entrainment (left) and configuration ACN with natural and passive air entrainment (right) for a developed jet (Y/D = 8.3) and a jet velocity of 19.6 m/s.

7.1.2.5 Block dynamic uplift computed with the mean pressure acting on the block

The time evolution of the dynamic block uplift has been computed in Chapters 7.1.2.1, 7.1.2.2, 7.1.2.3 and 7.1.2.4 with the fluctuating pressure signal as recorded during the test runs.

The dynamic impulsion may also be computed by using only the mean pressure values. The mean pressure has been computed for each test run and for each transducer separately.

As an example, in this section the block uplift has been computed with the mean pressure, for three configurations (CR, SR and CN), three water depths (Y/D = 2.8, 5.6 and 8.3) and for a jet velocity (CR and SR 27.0 m/s and CN 9.8 m/s) The dynamic block uplift has been computes, as in the previous chapters, following the theoretical method proposed in Chapter 5.4 but using the mean pressure.

Figures 7.12, 7.13 and 7.14 show the mean pressure acting around the block for the previous Y/D ratios and jet velocities.

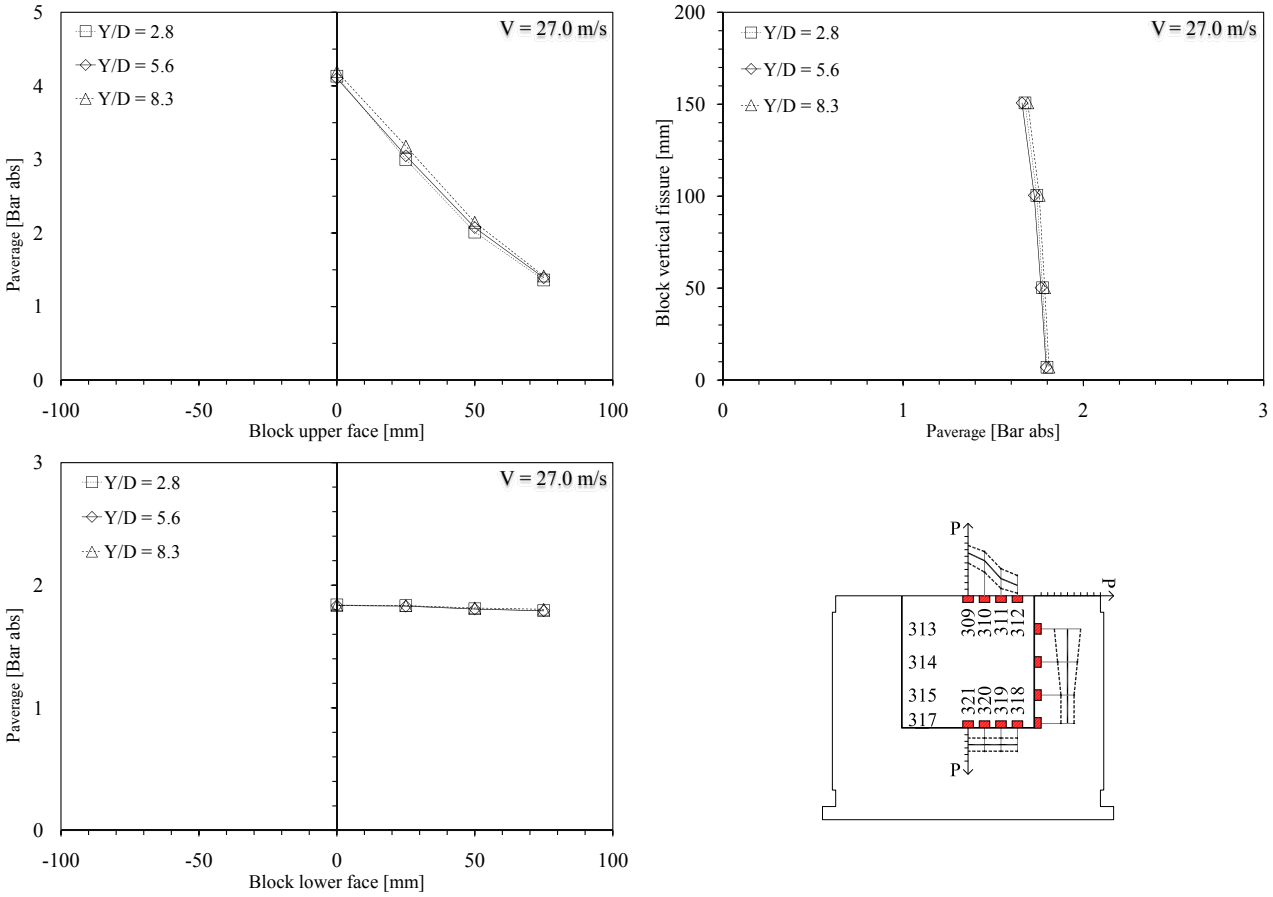

Figure 7.12: Pressure field acting around the block for configuration CR. Core (Y/D = 2.8), transition (Y/D = 5.6) and developed jets (Y/D = 8.3) with a jet velocity of 27.0 m/s. Pressure acting on the block upper face (top left), along the vertical fissure (top right), underneath the block (bottom left) and pressure filed sketch (bottom right). Pressures are expressed in absolute Bar.

The block uplift has been computed using the added mass coefficient and the pressure reduction coefficient summarized in Tables 7.1 and 7.2.

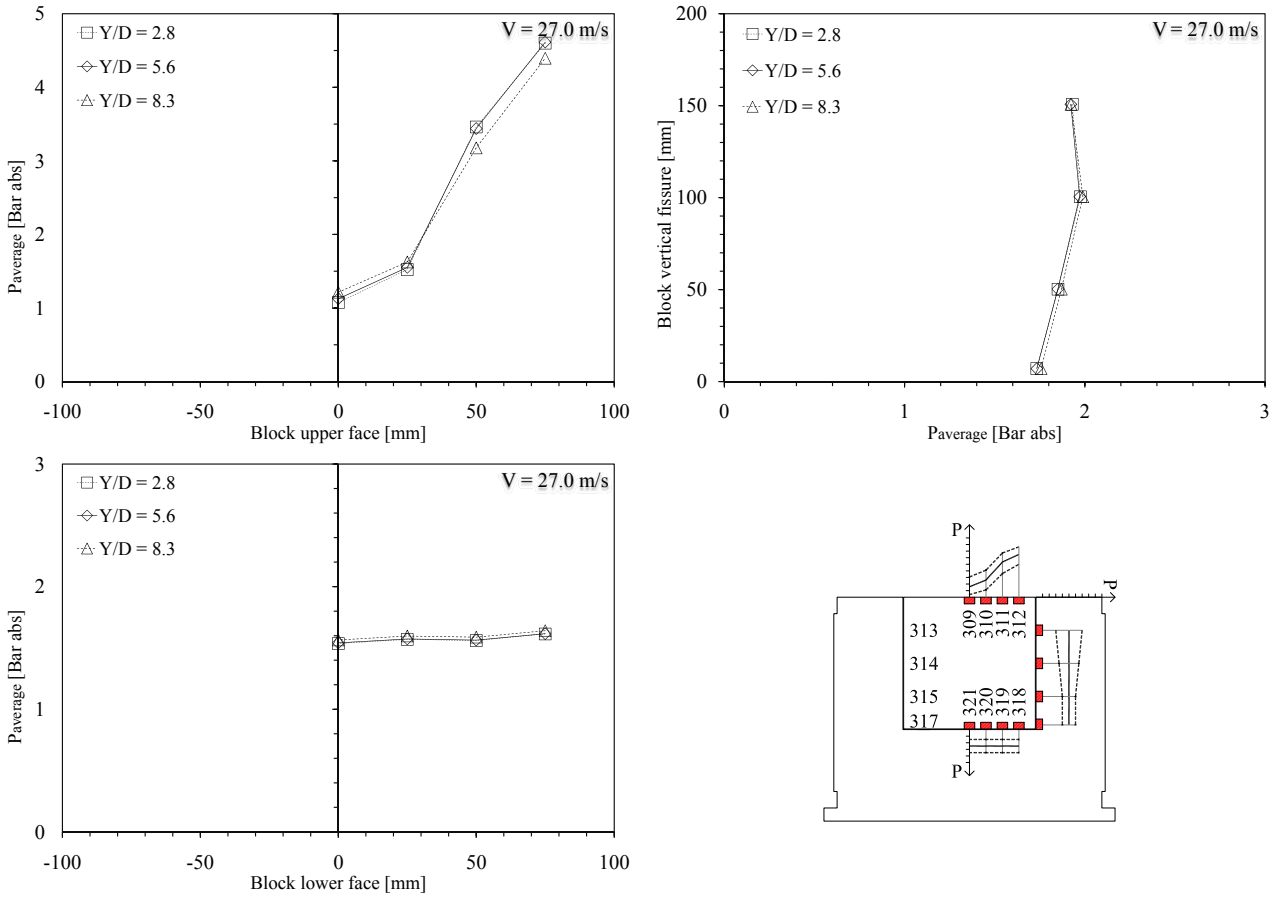

Figure 7.13: Pressure field acting around the block for configuration SR. Core (Y/D = 2.8), transition (Y/D = 5.6) and developed jets (Y/D = 8.3) with a jet velocity of 27.0 m/s. Pressure acting on the block upper face (top left), along the vertical fissure (top right), underneath the block (bottom left) and pressure filed sketch (bottom right). Pressures are expressed in absolute Bar.

The forces and the block uplift that have been computed with mean pressure are summarized in Tables 7.8, 7.9 and 7.10 where F_{up} is the pressure force acting on the block upper face, F_{down} the pressure force acting underneath the block, $I_{\Delta pulse}$ the net impulse, $V_{\Delta pulse}$ the uplift velocity, h_{up} the block uplift and h_{mes} the measured uplift. A positive value for the net impulse ($I_{\Delta pulse}$), respectively for the uplift velocity ($V_{\Delta pulse}$) and block uplift (h_{up}) means that the block moves up.

The friction force (two contact points lateral guide $F_{friction} \cong 62N$ and eight contact points lateral guide $F_{friction} \cong 68N$) and the immerged block weight ($W_b \cong 135N$) are always the same.

The computation performed with mean pressure provides a stationary result for the block uplift because the computation input was only a pressure value.

For all jet configurations, all water depths and all jet velocities the computed uplift provide very small values (as summarized for some examples in Tables 7.8, 7.9 and 7.10), in the order of 10^{-3} to 10^{-5} mm. Following these results the block may moves up for some combinations of water depths and jet velocities. These values did not correspond to the block position after a

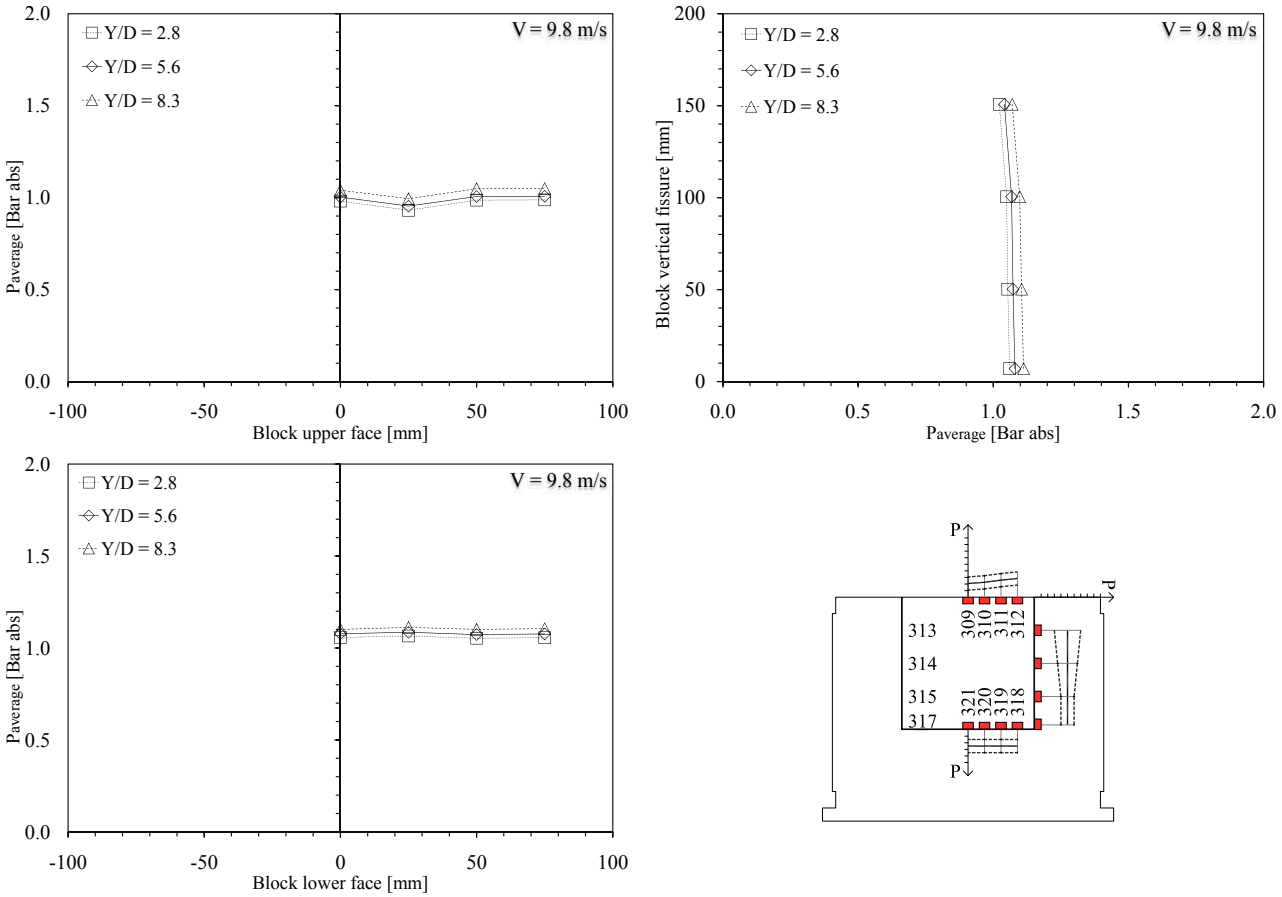

Figure 7.14: Pressure field acting around the block for configuration CN. Core (Y/D = 2.8), transition (Y/D = 5.6) and developed jets (Y/D = 8.3) with a jet velocity of 9.8 m/s. Pressure acting on the block upper face (top left), along the vertical fissure (top right), underneath the block (bottom left) and pressure filed sketch (bottom right). Pressures are expressed in absolute Bar.

defined time interval because they did not take into account the real block solicitations.

The uplift time evolution may be estimate by multiplying the computed uplift value for a certain time interval. If the time interval used to compute the mean pressure (30 s) was used, maximum uplift is overestimate for configuration with the jet impacting on the block center CR (but in the same order of magnitude) and underestimate for the other configurations (but in this case in another order of magnitude: the computed values are smaller). Bollaert (2002b) proposed to use the time interval necessary for one pressure wave to travel inside the fissure form and back. The pressure wave celerity for a mixed fluid (water-air) can be computed with Equation (5.27). However, the wave celerity depends of the air concentration inside the fissure. For this experimental facility any measurements have been done. To estimate the eigenfrequency of the 3-dimensional fissure the air concentration values as proposed by Manso (2006) were used (Chapter 5.6). If these values are used to compute the wave celerity the time intervals corresponds to 0.028 s (minimum air concentration) and 0.093 s (maximum air concentration). If these time intervals are used the theoretical uplift is always smaller than the measured values.

Y/D ratio [−]	F_{up} [N]	F_{down} [N]	$I_{\Delta pulse}$ [Ns]	$V_{\Delta pulse}$ [mm/s]	h_{up} [mm]	h_{mes} [mm]
2.8	2'460	3'400	0.74	9	0.009	0.14
5.6	2'335	3'415	0.88	15	0.015	0.18
8.3	2'780	3'450	0.47	6	0.006	0.19

Table 7.8: Dynamic block impulsion computed with the mean pressure for configuration CR. Core (Y/D = 2.8), transition (Y/D = 5.6) and developed jets (Y/D = 8.3) with a jet velocity of 27.0 m/s. F_{up} is the pressure force acting on the block upper face, F_{down} the pressure force acting underneath the block, $I_{\Delta pulse}$ the net impulse, $V_{\Delta pulse}$ the uplift velocity, h_{up} the block uplift and h_{mes} the measured uplift.

Y/D ratio [−]	F_{up} [N]	F_{down} [N]	$I_{\Delta pulse}$ [Ns]	$V_{\Delta pulse}$ [mm/s]	h_{up} [mm]	h_{mes} [mm]
2.8	2'225	2'420	-0.01	0.01	0.00001	0.88
5.6	2'255	2'455	-0.01	0.01	0.00001	0.78
8.3	2'315	2'535	0.02	0.02	0.00002	0.95

Table 7.9: Dynamic block impulsion computed with the mean pressure for configuration SR. Core (Y/D = 2.8), transition (Y/D = 5.6) and developed jets (Y/D = 8.3) with a jet velocity of 27.0 m/s. F_{up} is the pressure force acting on the block upper face, F_{down} the pressure force acting underneath the block, $I_{\Delta pulse}$ the net impulse, $V_{\Delta pulse}$ the uplift velocity, h_{up} the block uplift and h_{mes} the measured uplift.

Y/D ratio [−]	F_{up} [N]	F_{down} [N]	$I_{\Delta pulse}$ [Ns]	$V_{\Delta pulse}$ [mm/s]	h_{up} [mm]	h_{mes} [mm]
2.8	200	405	0.003	0.02	0.00002	> 6
5.6	260	465	0.002	0.01	0.00001	> 6
8.3	345	540	-0.006	-0.03	-0.00003	> 6

Table 7.10: Dynamic block impulsion computed with the mean pressure for configuration CN. Core (Y/D = 2.8), transition (Y/D = 5.6) and developed jets (Y/D = 8.3) with a jet velocity of 9.8 m/s. F_{up} is the pressure force acting on the block upper face, F_{down} the pressure force acting underneath the block, $I_{\Delta pulse}$ the net impulse, $V_{\Delta pulse}$ the uplift velocity, h_{up} the block uplift and h_{mes} the measured uplift.

To analyze the influence of the type of pressure field (maximum, mean and minimum), the same computation has been made with maximum pressures acting around the block. Figure 7.15 shows maximum pressure acting around the block.

Table 7.11 summarizes the forces and the block uplift that have been computed with maximum pressures for the configuration SR.

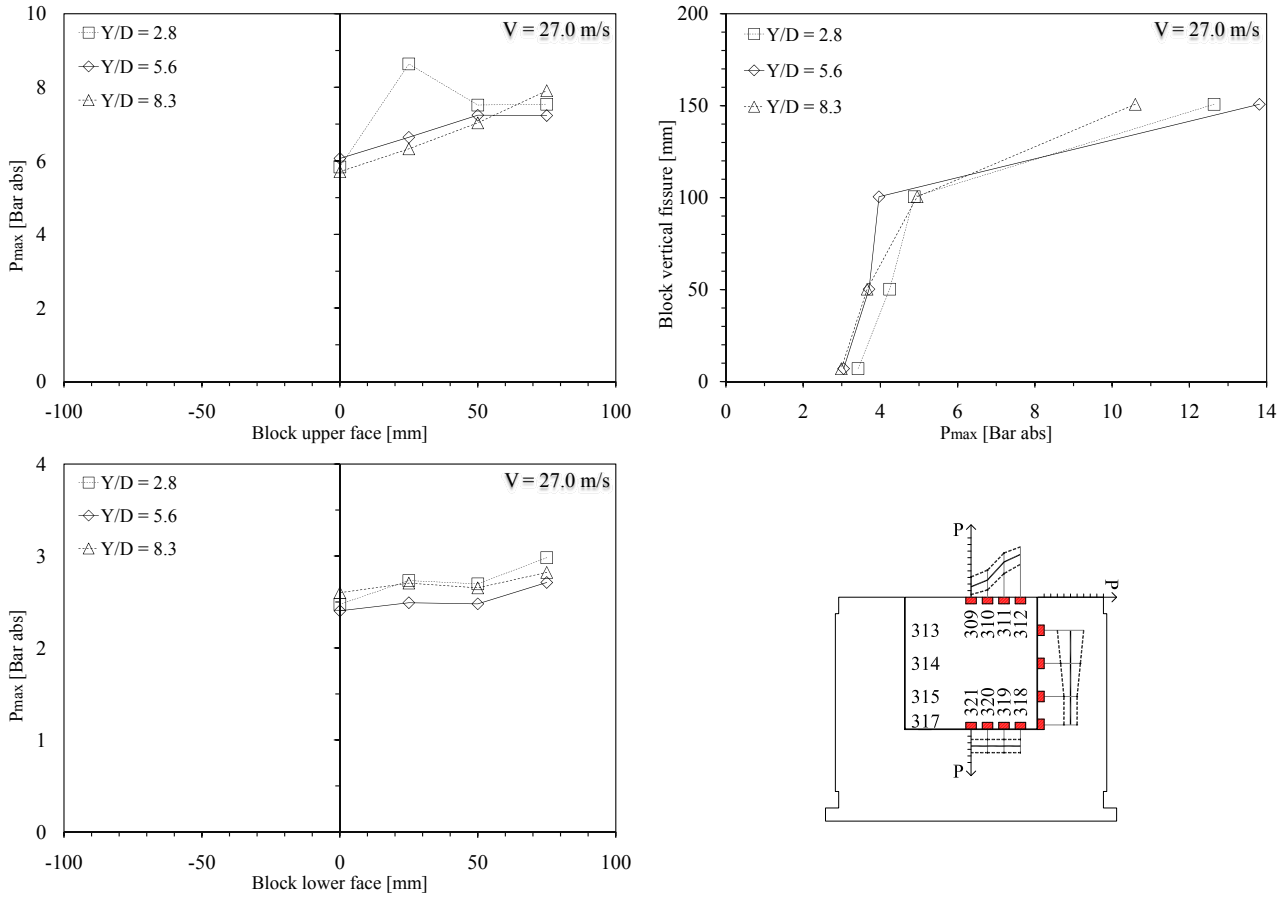

Figure 7.15: Maximum pressure field acting around the block for configuration SR. Core (Y/D = 2.8), transition (Y/D = 5.6) and developed jets (Y/D = 8.3) with a jet velocity of 27.0 m/s. Pressure acting on the block upper face (top left), along the vertical fissure (top right), underneath the block (bottom left) and pressure filed sketch (bottom right). Pressures are expressed in absolute Bar.

Y/D ratio [−]	F_{up} [N]	F_{down} [N]	$I_{\Delta pulse}$ [Ns]	$V_{\Delta pulse}$ [mm/s]	h_{up} [mm]	h_{mes} [mm]
2.8	11'225	6'870	-4.56	-4	-0.004	0.88
5.6	9'600	5'970	-3.82	-3	-0.003	0.78
8.3	11'675	6'755	-5.12	-5	-0.005	0.95

Table 7.11: Dynamic block impulsion computed with the maximum pressures for configuration SR. Core (Y/D = 2.8), transition (Y/D = 5.6) and developed jets (Y/D = 8.3) with a jet velocity of 27.0 m/s. F_{up} is the pressure force acting on the block upper face, F_{down} the pressure force acting underneath the block, $I_{\Delta pulse}$ the net impulse, $V_{\Delta pulse}$ the uplift velocity, h_{up} the block uplift and h_{mes} the measured uplift.

Independently from the jet configurations, for some combinations of water depths and jet velocities the block uplift, computed with the mean pressure, could be positive: that's means the block moves up. If the block uplift is computed with maximum pressures, the block stay always in contact with the bottom of the central cavity (the impulsion is always negative

because the force acting on the block upper face F_{up} is always larger than the force acting on the block lower face F_{down}).

The uplift increase or decrease as a function of the time and depends onto sign of the computed uplift (positive the block moves up and negative the block remains in contact with central cavity bottom) and on the time interval apply to estimate the final uplift.

For configurations with the jet impacting on the block center the time interval used to estimate mean value can be used, but for the other jet configurations a larger time interval is needed. The uplift time evolution did not reconstruct the evolution that has been measured.

7.1.2.6 Block dynamic uplift computed with components of pressure fluctuations

To analyze if the pressure fluctuations are able to move the block, the dynamic impulsion has been computed by using the fluctuations components of pressures (positive and negative components). The fluctuating components allow to compute the uplift with own time evolution, which was not possible with the mean pressure.

The pressure fluctuations ($p_{fluctuations,i} = p_i - \overline{p}$) are obtained subtracting the mean pressure ($\overline{p}$) from the dynamic total pressure signal (p_i).

As before, the computation has been made following the theoretical method proposed in Chapter 5.4 using the added mass coefficient and pressure reduction coefficient summarized by Tables 7.1 and 7.2.

Figure 7.16 shows the dynamic block uplift computed for four different jet configurations, as an example: jet impact in the block center (CR), jet impact on the block right side (SR), jet impact on the block corner (CN) and jet impact on the block left side (SL).

The block uplift computed with the fluctuating components for the configuration with the jet impact on the block center (CR, Figure 7.16 top left) shows a good similitude between theoretical and measured uplift. The uplift time evolution can be well estimated with the fluctuating component of the pressure. The same observations are valid for the other configuration with the jet impacting on the block center (CE).

The configuration with the jet impact not in the block center (Figure 7.16 top right (SR), bottom left (CN) and bottom right (SL)) did not show the same behavior: the theoretical uplift diverged from the measured uplift. Theoretical uplift is negative and the block remains in contact with the bottom of the central cavity. The block is maintained in this position by the forces acting on it (Chapter 5.3): there are not only the forces generated by the pressures acting on the block upper and lower face (F_{up} and F_{down}) but also the block immerged weight (W_b) and the friction force ($F_{friction}$). As well, is important to not forget the influence of the added mass on the block vertical movements. These forces are now predominant in the dynamic uplift because generally are larger than the forces generated by the pressure difference between the block upper and lower face. The forces acting on the block upper and lower face are now only generated by fluctuating components of the pressure.

If the immerged block weight and the friction force were not considerate (but are not realistic) the block uplift was positive and the block moves up (continue to increase).

This different behavior may be related to the way that the block is solicited: symmetrical

for the jet impacting on the block center and asymmetrical for the other jet impacts. When the jet impacts on the block center, the block is maintained in contact with the bottom of the central cavity (small displacements) and any rotations can be generated due the symmetric solicitation. When the jet impacts on another point on the block: the block moves and it is possible that it does some small rotations inside the central cavity that affect the block displacements. These small rotations may affect the pressures acting on the block and influence the pressure fluctuations. The uplift computation show that: to have the same time evolution of the measured uplift the complete pressure signal has to been used in combination with the added mass and the pressure reduction coefficient.

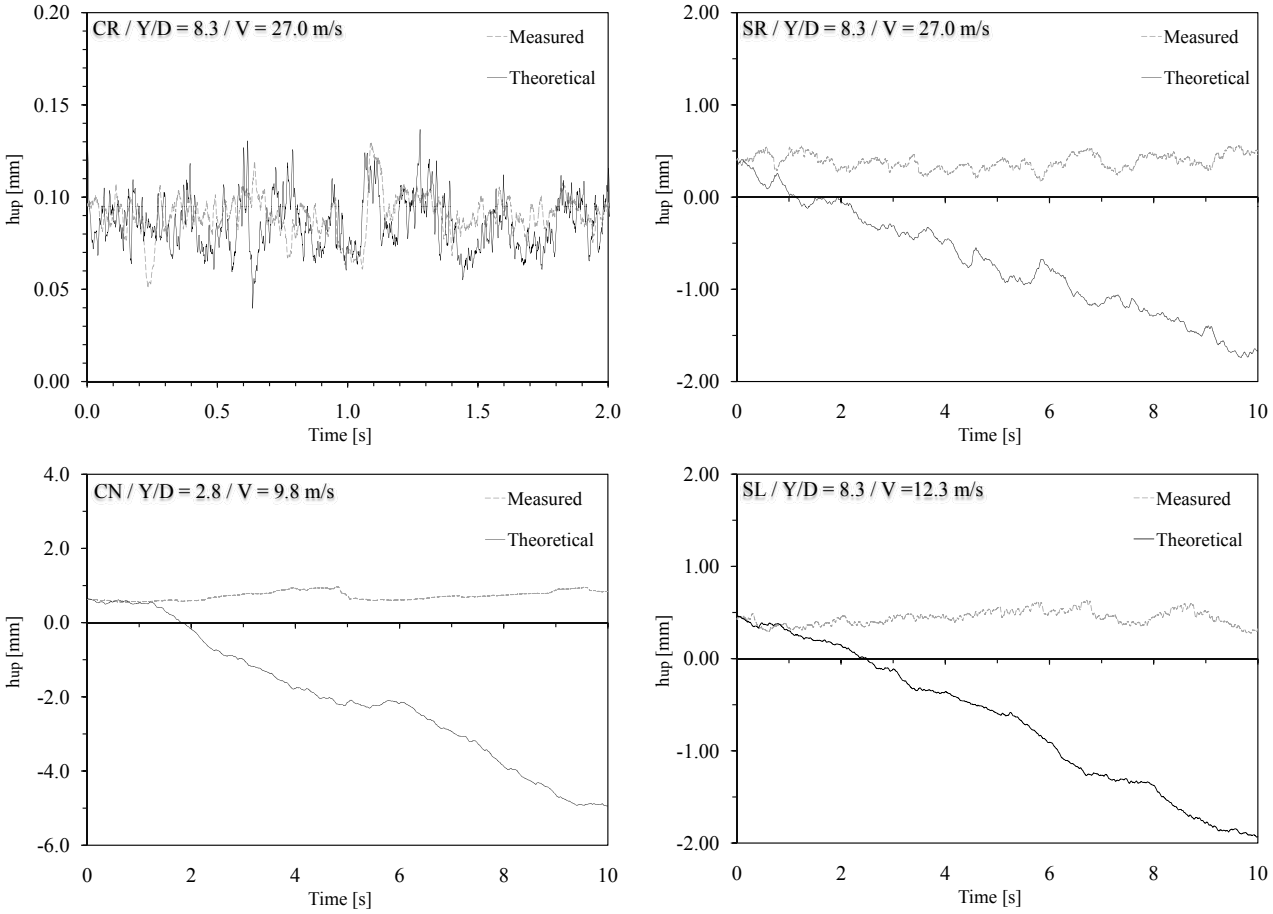

Figure 7.16: Dynamic block impulsion computed by using the fluctuating component of the pressures. Configuration CR with a Y/D ratio of 8.3 and a jet velocity of 27.0 m/s (top left); Configuration SR with a Y/D ratio of 8.3 and a jet velocity of 27.0 m/s (top right); Configuration CN with a Y/D ratio of 2.8 and a jet velocity of 9.8 m/s (bottom left); Configuration SL with a Y/D ratio of 8.3 and a jet velocity of 12.3 m/s (bottom right).

7.1.2.7 Relationship between the net uplift force and the block vertical displacements

The measured uplift should be related to the block dynamic impulse. This relationship has been analyzed for different configurations.

Figure 7.17 shows some examples of relationship between block impulsion (computed with the pressures acting on the block) and vertical displacements recorded with the displacement transducer. Figure 7.17 shows the block impulsion and the block displacements for four configurations: jet impact on the block center (CR, top left), jet impact on the block right side (SR, top right), jet impact on the block corner (CN, bottom left) and jet impact on the block left side (SL, bottom right). The jet velocity corresponds to maximum observed uplift for the corresponding configuration.

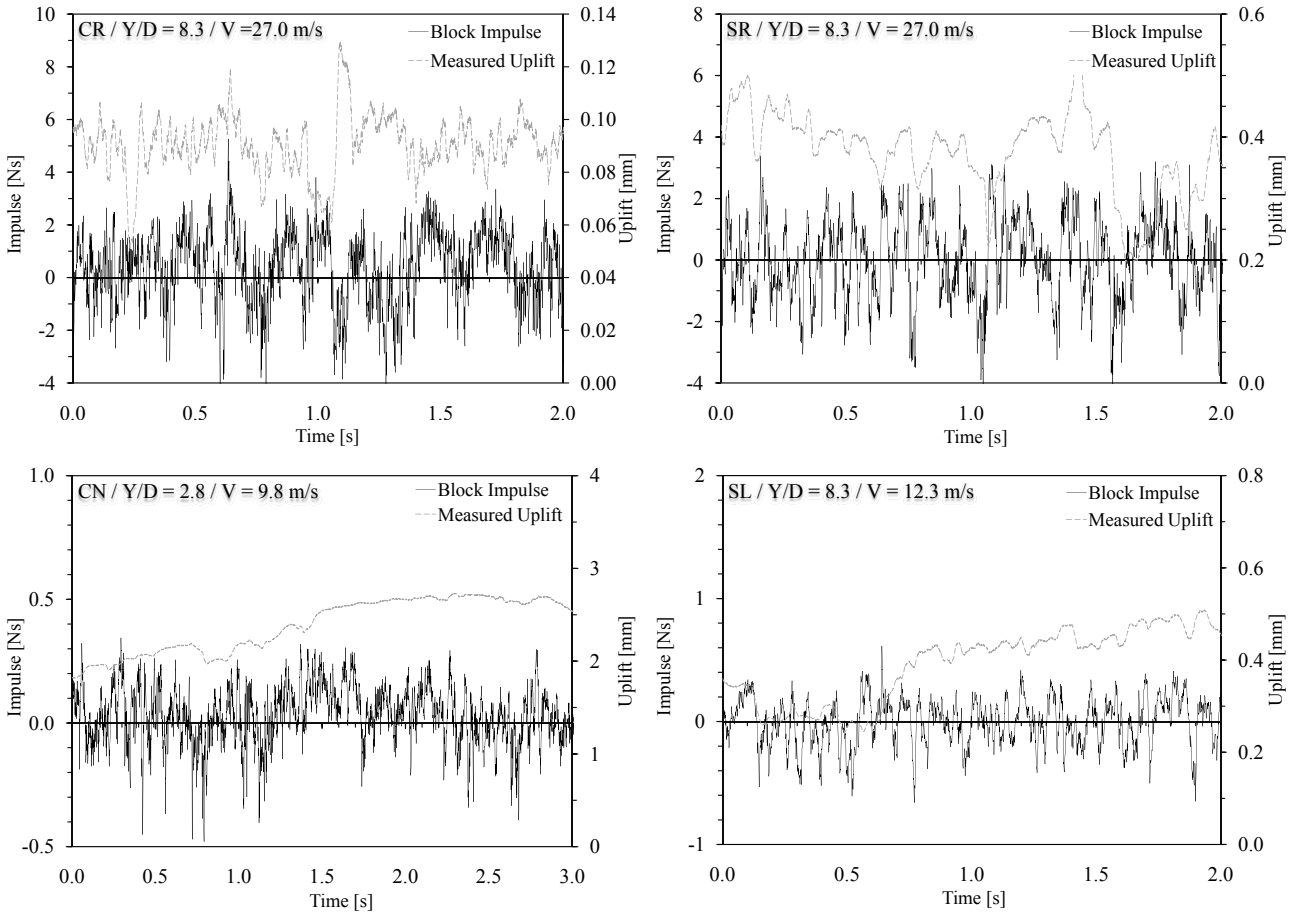

Figure 7.17: Relationship between block impulsion and measured displacements. Configuration CR with a Y/D ratio of 8.3 and a jet velocity of 27.0 m/s (top left); Configuration SR with a Y/D ratio of 8.3 and a jet velocity of 27.0 m/s (top right); Configuration CN with a Y/D ratio of 2.8 and a jet velocity of 9.8 m/s (bottom left); Configuration SL with a Y/D ratio of 8.3 and a jet velocity of 12.3 m/s (bottom right).

Normally, when the block impulsion is positive, the block displacements should be positive (the block is ejected from the central cavity) and, vice versa, when the impulsion is negative, the block should moves down (the block is pushed inside the central cavity). This behavior has

been observed for configurations where the pressures have been recorded simultaneously with the displacements: jet impact on the block center (configurations CE and CR) and jet impact on the block right side (SI and SR). Figure 7.17 shows this behavior (top left configuration CR and top right configuration SR). The configuration with the jet impacting on the block center (CR) generated small displacements. The block impulsion is more related to the displacement fluctuations, oscillating around the mean value. The configuration with the jet impact on the block right side (SR) shows larger displacements than for the previous configuration. The relationship between block impulsion and vertical displacement is more visible. However, sometimes the block impulsion is not directly related to the displacements. This might be related to the block inertia in its vertical movements. If the block impulsion changes direction very fast, the block does not have time to realize this change of direction and continues its preceding vertical movement.

The same behavior has been observed for configurations that do not have a direct relationship between pressures and displacements (as an example, configurations with jet impact on the left side (SL) and jet impact on the corner (CN)). In this case, it is not only the effect of the block inertia but also the non-simultaneously of time when pressures have been recorded on the block upper face and inside the 3-dimensional fissure. This different behavior has been observed due to the block impulsion was not computed with the correct pressure field.

As can be expected, the theoretical block impulsion is directly related to the measured uplift, but sometimes some small time shifts appear.

7.1.2.8 Evaluation of the total force acting on the block

The dynamic block impulsion has been computed using two methods: based on acceleration measurements and based on displacement measurements.

Estimation of the total force with acceleration measurements

The accelerations recorded by the accelerometer (situated inside the block) allow to check the dynamic block impulsion and the related total force acting on the block (all forces: known and unknown). The recorded accelerations and forces, should comply Equation (7.1).

$$\sum F_{measured} = (m_b + m_{am}) \cdot a_{measured} \tag{7.1}$$

where m_b is the block mass, m_{am} the added mass and $a_{measured}$ the measured accelerations.

The theoretical total force is computed following Equation (5.21) (the main sources are the pressure measurements). The comparison between theoretical and measured total force, for the same water depth and jet velocity, does not give satisfactory results. The measured total force is always larger than the theoretical total force: the mean value is always larger but there are some peaks that are smaller than the theoretical total force. If the added mass is not used in the computation, the mean value of the measured total force decreases but is always different from the theoretical value. The added mass influences strongly the total force: larger is the

added mass and larger is the total force. Sometimes the accelerometer has recorded strange values that correspond to the accelerometer measurements limits (±1000 g). These values have been generated by electrical noises and are omitted from the analysis.

As an example, Figure 7.18 shows theoretical and measured total forces for two different configurations (jet impact on the block center (CR) and jet impact on the block right side (SI)) but for the same Y/D ratio (8.3) and jet velocity (27.0 m/s). Figure 7.18 shows larger difference between theoretical and measured total forces acting on the block.

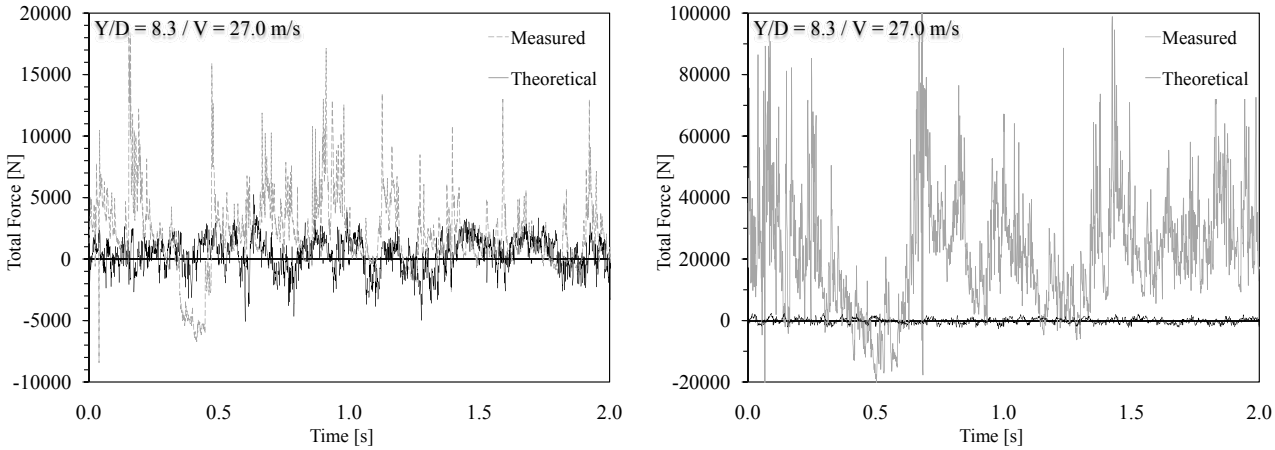

Figure 7.18: Comparison between theoretical total force (computed with pressures acting on the block) and measured total force (computed with accelerations of block) for a Y/D ratio of 8.3 and a jet velocity of 27.0 m/s. Configuration CR (left) and configuration SI (right).

The method based on the acceleration measurements cannot be used because the recorded accelerations are not precise enough to compute the total force acting on the block and due to the larger added mass values. For this computation, the accelerometer shows its limitations. From the beginning of the tests, the accelerometer shows a special behavior: it needs a certain time to "heat" and reaches a stable horizontal asymptote, from where it was possible to record the accelerations properly. Knowing this behavior (and after discussing with the acceleration dealer) some modifications at the data acquisition code have been made. The accelerations have been recorded approximately after 2 minutes from the data acquisition beginning. This interval of time allows at the accelerometer to reach its stability. This procedure has been applied for all tests.

It was possible that, sometimes, the accelerometer needed another interval of time to reach a new stabilization during the measurements, which may have affected the recorded accelerations.

Estimation of the total force with displacement measurements

The displacements recorded by the displacement transducer allow to check the dynamic block impulsion and the related total force acting on the block.

This method is based on the computation of the dynamic block impulsion, explained in Chapter 5.4.2, but using the other way around: the dynamic block impulsion is computed

starting from the measured uplift and not from the forces acting on the block. This method allows to obtain the difference between the force acting on the block upper face (F_{up}) and the force acting on the block lower face (F_{down}). These two forces are the only unknown forces in the reverse computations.

Theoretical total force is computed using the pressure measurements and the measured total force is computed from the displacement measurements. Theoretical total force is always smaller than measured total force. This result is valid for all jet configurations, water depths and jet velocities.

As an example, Figure 7.19 shows theoretical and measured total forces for two different configurations (jet impact on the block center (CR) and jet impact on the block right side (SI)) but for the same Y/D ratio (8.3) and jet velocity (27.0 m/s). Figure 7.19 shows larger differences between theoretical and measured total forces acting on the block.

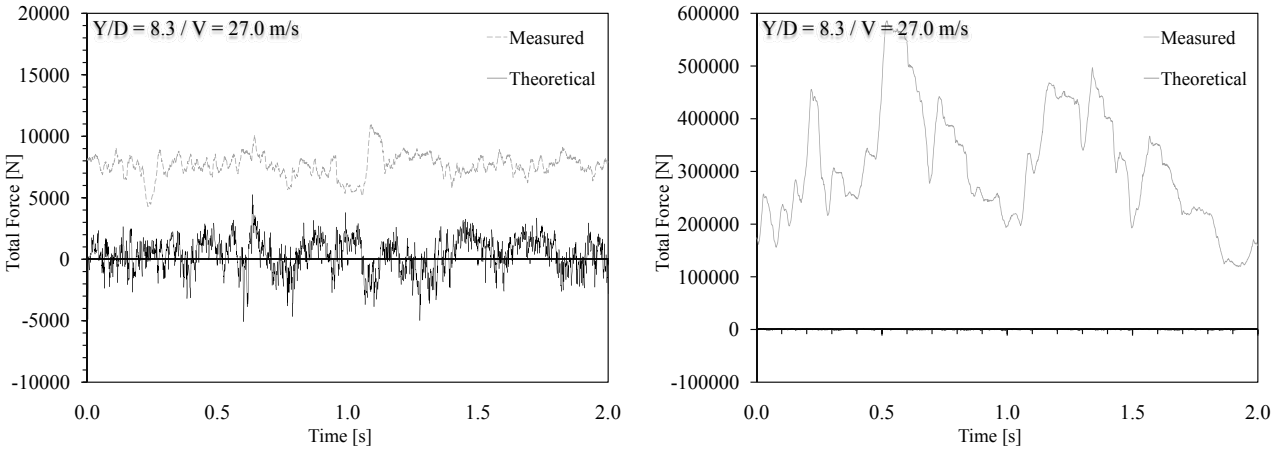

Figure 7.19: Comparison between theoretical total force (computed with the pressures acting on the block) and measured total force (computed with displacements of block) for a Y/D ratio of 8.3 and a jet velocity of 27.0 m/s. Configuration CR (left) and configuration SI (right).

The method based on the displacement measurement cannot be used due to the added mass influence. The added mass has been used to compute the measured total force. The dynamic block impulsion grows proportionally with the added mass and, as a consequence, the difference between the force acting on the block upper face and the force acting underneath the block increases as well (a larger added mass generates larger force differences between the upper and lower block face).

The added mass is a virtual mass (the inertia of the fluid entrained by the accelerating body) that has to be "moved" by the block in its movements. The added mass influences the displacements but does not affect the pressures acting on the block. Hence, this method cannot be used to compute the total force (the pressures are not directly related to the added mass).

7.1.3 Conclusion

7.1.3.1 Added mass

The added mass is an important parameter that has to be taken into account for the dynamic block impulsion computation. The added mass influences the amplitude of the vertical displacements.

The added mass evolution as a function of the jet velocity has a different behavior if the block is solicited by a symmetrical jet (jet impact on the block center) or an asymmetrical jet (jet impact on the block side: right or left side, corner or radial).

For configurations with the jet impact on the block center, the added mass coefficient α_{am} is almost constant for all water depths and all jet velocities and ranges between 2 and 4.

The added mass coefficients obtained for configurations with the jet impact not on the block center (asymmetrical impact) show a different behavior and the values are situated in another order of magnitude. The added mass evolution as a function of the jet velocity is similar to the observed displacements of block. Generally, the block begins to move up for jet velocities larger than 7.4-9.8 m/s. Jet velocities lower than 4.9-7.4 m/s are related to coefficients ranging between 150 and 350. These small jet velocities generate small displacements (10^{-3}-10^{-2} mm): it is like the block does not move. When the jet velocity increases, the displacements increase as well and the added mass coefficient decreases. This behavior is valid for all asymmetrical jets that have been tested except for configuration RR (where the jet impact between the center and the corner of the block). This different behavior for configuration RR is related to the pressure combination needed to compute the theoretical uplift. As explained before, the added mass influences the amplitude of the vertical displacements. Hence, when the displacements are quite inexistent (10^{-3}-10^{-2} mm) the added mass has a larger value and when the vertical displacements of block increase their amplitude the added mass is smaller.

For larger jet velocities, the added mass coefficient decrease from 300 to 5. The added mass evolution as a function of the jet velocity depends from the jet impact position and the water depths. Each tested configuration and water depth (core, transition and developed jets) has its own equation to estimate the added mass coefficient. Hence, a unique equation could not be defined.

The added mass coefficients obtained experimentally using the LCH facility (from the dynamic block impulsion equation: Eq. (5.22)) are very different from literature values (Chapter 2.4). The added mass increases when the distance between a body, moving in a quite fluid, and the surrounded bodies decreases (these bodies could be still or moving). The same phenomenon appears when the body approaches a boundary condition (as an example: the boat skull that approaches the bottom of the river). More two bodies (or more bodies) approach and more the added mass increases.

The highly instrumented block is strongly confined in the measurement box (Chapter 3.2.2): the block is surrounded on five of its six faces by the measurement box. The distance between

the block and its surrounding is 1 mm, that mean the two bodies (block and measurement box) are very close. Moreover, the block is not only strongly surrounded by another body (measurement box) but directly is loaded by jet on its free surface (block upper face), that pushes it inside the central cavity of the measurement box.

When the block moves up, due to the dynamic impulsion, the pressure inside the fissure decreases. This pressure decrease attracts the block to the bottom of the central cavity (like suction). The water situated inside the vertical fissure has to flow under the block to fill up the empty space generated by the vertical displacement. This phenomenon influences the added mass coefficient: more this suction phenomena is stronger and more the added mass is larger. The behavior of this pressure drop, when the block is ejected from the central cavity, has been explained in Chapter 5.7.3.1. This phenomenon explained in Chapter 5.7.3.1 is not completely representative of the real test conditions: the fissure was filled up with water but on the plunge pool was empty and the jet did not load the block. The block has been moved up for approximately 6 mm. In real-life test conditions, the vertical displacement ranges between 10^{-3}-10^{-2} mm and it changes direction and amplitude for each increment of time. These fast displacements in both directions (positive and negative), cannot reproduce the same pressure drop that has been observed due to the small time interval between each measurements ($\Delta t_{\Delta pulse} = 0.001\ s$). The suction phenomenon is present under the block but not so strong as can be expected. This suction reduce its effect with an increase of the displacement (growth of the fissure under the block)

The cross analysis between pressures and block uplift evolution did not allow to observe this pressure drop, due to the fast vertical fluctuations of the block. The analysis of the pressure evolution acting underneath the block, cannot explain alone the vertical displacements because there are other forces that have to be considered.

An asymmetrical jet may generate some very small rotations of the block (inside the central cavity), that may modify the block solicitations. If the block gets stuck inside the central cavity, the pressures acting underneath change (F_{down}) and as well the friction coefficient changes (μ_s increase). The block uplift may be reduced and the added mass coefficient increases.

The jet, before impacting on the block upper face, has to travel through the plunge pool. The interaction between the jet and the water cushion generate some large eddies and as well an oscillating jump in the plunge pool. The jet impacting the plunge pool introduces some air that modifies the water characteristics. With an increase of the jet velocity, these two phenomena take more importance. This strong aerated 3-dimensional turbulent flow inside the plunge pool affects the added mass: more this turbulent flow increases and more the added mass decreases. In literature, the added mass coefficient has been determined for bodies moving in a stagnant fluid and not for a body moving in a strong turbulent fluid.

Our case is very different: a body moving in a fluid under strongly confinement and subject of a strong opposite flow. A situation similar at the tests performed with the experimental

facility may be the following: a submarine moving in a fluid that fires a torpedo or a missile in immersion. The torpedo is strongly confined in the torpedo tube with an opposite flow acting on the torpedo head. The difference with our facility is related to the torpedo movement inside the torpedo tube: in our case this movement is generated by the pressure difference between the upper and the lower face of the block and in the torpedo case is generated by an injection of compressed air.

The strong confinement and the high jet velocities acting on the block generate these large values for the added mass coefficients.

The added mass concept as to be integrated in the scour model developed by Bollaert (2002b) in the block impulsion module to estimate the block uplift generated by the hydrodynamic impulsion.

7.1.3.2 Pressure reduction coefficient

The influence of the pressure reduction coefficient takes more importance for configurations where the jet is asymmetrical. The jet impacts on the block extremity (left side, right side, corner and radial). The surface where the pressures are unknown is larger than the surface where the pressures are known (Figure 5.5). The surface where no pressure measurements have been made is situated in the wall jet region where the pressures could be negative (at the extremity of the pressure exponential distribution).

The added mass coefficient and the pressure reduction coefficient have been calibrated for a time interval of 30 s. The two coefficients represent a mean value for this time interval. In reality, the two coefficients change and are not constant for each time increment. The added mass is not the same if the block moves up or moves down. Define a coefficient changing each time is not practical and not feasible for computation. A mean value is easier for computing the dynamic block impulsion for a given period of time.

The same remarks are valid as well for the pressure reduction coefficient. The coefficient changes for each time increment. It could be positive for a time increment and negative for the time step. Knowing the exact evolution of the coefficient for each time step is not important for the computation. As explained for to the added mass coefficient a mean value is easier for computing the dynamic block impulsion

7.1.3.3 Dynamic block impulsion computed with mean and maximum pressures

The computation performed with the mean pressure provides a stationary result for the block uplift because the computation input was only a pressure value. For all jet configurations, all water depths and all jet velocity the computed uplift provide very small values in the order of 10^{-3} to 10^{-5} mm. Following the results the block may moves up for some combinations of water depths and jet velocities. The uplift time evolution may be estimate multiplying the computed uplift value by a time interval. If the interval of time used to compute the mean pressure (30 s) will be use, maximum uplift is overestimate for configuration with the jet impacting

on the block center and underestimate for the other configurations. Using the time interval necessary at the pressure waves to travel inside the fissure (two directions) the total uplift is always smaller than the measured values. For the maximal pressure, the computed uplift is always negative and the block remains in contact with the central cavity bottom.

7.1.3.4 Dynamic block impulsion computed with components of pressure fluctuations

The block uplift computed with the fluctuating components of pressures for configurations with the jet impacting on the block center (CE and CR) show a good similitude between theoretical and measured uplift. The uplift time evolution can be well estimated with the fluctuating components of pressure. The configuration with the jet impact not in the block center (SR, SL, RR and CN) did not show the same behavior: the theoretical uplift diverges from the measured uplift. The theoretical uplift is negative and the block remains in contact with the central cavity bottom. The forces not generated by the pressures acting on the block upper and lower face are now predominant in the dynamic uplift computation because generally are larger than the forces generated by the pressures acting on the block. The forces acting on the block upper and lower face are now only generated by fluctuating components of the pressure.

This different behavior may be related to the way that the block is loaded: symmetrical for the jet impacting on the block center and asymmetrical for the other configurations. An asymmetrical jet may generate small rotations inside the central cavity that affect the block displacements. These small block rotations may affect as well the pressures acting on the block and influence the pressure fluctuations.

Normally when the block impulse is positive, the block should move up and vice versa when the impulse is negative the block should move down. This behavior has been observed for configurations where pressures have been recorded simultaneously to the displacements: jet impact on the block center (configurations CE and CR) and jet impact on the block right side (SI and SR).

The other configurations (SL, CN and RR) are affected by a combination of pressures recorded with different jet impacts. The pressures acting on the block upper face have not been recorded simultaneously with the pressures recorded under the block, as well the block response (displacements and accelerations). This time difference breaks the direct relationship between the pressures acting on the block and the block responses. Sometimes the block impulse is not directly related to the displacements: if the block impulse changes direction very fast, the block does not have time to realize this direction change and it continue in its precedent movement.

To have a similarity between theoretical and measured uplift, the complete pressure signal has to been used in combination with the added mass and the pressure reduction coefficient.

7.1.4 Remarks

To widen the knowledge in the field of the added mass and to optimize the dynamic block computation, the added mass coefficient for the experimental facility has to be determined experimentally. Korotkin (2009) proposed different techniques to estimate experimentally the added mass. As an example, the experimental techniques based on small oscillations or on electro-hydrodynamic analogy (EHDA) for 3-dimensional body. There exists some numerical software for the added masses computation based on the method of finite elements that allow to describe numerically the highly complicated interactions of bodies moving in fluids.

The dynamic block impulsion should be computed without the combination of pressures recorded with different configurations. That's mean, new tests with the transducers located always radially outwards from the stagnation point (jet impact position on the block) should be performed. These new measurements allow to eliminate the time difference that breaks the direct relationship between pressures acting on the block and block responses (displacement and accelerations).

7.2 Influence of the "passive" air entrainment by the free falling jet

7.2.1 Introduction

The experimental facility is subjected at three main air entrainment phenomena:

- Air entrainment during the jet trajectory in the air;
- Air entrainment at jet impact on the plunge pool;
- Air release and/or resolution from water.

The process of air entrainment during the jet trajectory in the air has been extensively studied and depends mainly on jet characteristics at issuance such as velocity, geometry and turbulence intensity (Ervine and Falvey (1987) and Zaman (1999)). Additional air is dragged into the pool when the jet impacts the plunge pool surface. McKeogh and Ervine (1981) described the mechanisms of air entrainment in a plunge pool for jets with different turbulence intensities (from laminar to rough turbulent). The diffusion of rough turbulent plunging jets inside a water pool has been object of systematic research by several authors (Henderson et al. (1970), Hartung and Häusler (1973), McKeogh and Ervine (1981), Ervine and Falvey (1987), Bonetto and Lahey (1993) and Bohrer et al. (1998)). Bin (1993) performed a comprehensive review of air entrainment by plunging liquid jets, independently of their turbulence level, which constitutes a good reference. Several investigators (Van de Sande and Smith (1973), Chanson (1996) and Ervine (1998)) discussed the different mechanisms of air entrainment at the plunge point. The approach outlined by Ervine (1998) is particularly interesting because it directly relates to the each mechanisms of air entrainment to a mathematical expression for quantify the air that is entrained.

Manso (2006) investigate the behavior of air bubble in depth-limited plunge pool for the present experimental facility. It performs some air concentration measurement, with an optic-probe, in three different regions in the plunge pool: in the impinging region, in the wall jet region and in the plunging jet region

Exist another source able to introduce air in the system (jet plus plunge pool): the air dissolute in the water, but the quantity are small.

The air content inside the 3-dimensional fissure cannot be direct measured. However, several indirect methods exist (Bollaert (2002b)). For high jet velocities (maximum 30 m/s), the mean air content inside the fissure can fluctuate between 1 and 10%. These larger differences in air concentration are related to the flow conditions in the plunge pool: for developed jets, a turbulent shear layer containing a larger volume of free air (bubbles) impacts the fissure entrance, because for core jets the air is only present during low-frequency turbulences that temporarily diffuse the jet and entrain air into the fissure. Two mechanisms of air bubble transfer from the plunge pool into a 3-dimensional fissure are: convective air bubble transfer and air bubble transfer by release and/or resolution from the water (Bollaert (2002b)). The

first mechanism is based on the ideal gas law (Henry's law) and depends on the free air presents in the water. The second mechanism correspond to the air dissolved in the water that come out from the solution (water-air) when the pressure as a sudden decrease. Vice versa, the opposite phenomena happen when the pressure show a sudden increase, the air is dissolved in the water. This phenomenon depends on a large number of parameters and is strongly to be predicted. This phenomenon depends on the pressure presents in the liquid.

7.2.2 Configurations

This section analyses the influence air entrained by natural suction of the jet ("passive" air entrainment) during the jet trajectory in the air. Two configurations have been analyzed both equipped with lateral guides having eight contact points and free to move:

- Jet impact position on the block corner (CN);
- Jet impact position on the block corner with passive air entrainment (ACN).

The two configurations were the same (same jet position on the block corner, same lateral guides and block free to move along the vertical axis) but for the ACN configuration a passive jet aeration system has been installed at the nozzle of the LCH experimental facility.

At the end of the water supply conduit (the experimental facility has been explained in Chapter 3.2) a new 72 mm nozzle has been installed. This nozzle has the same geometry of the existing nozzle, but at 50 mm from the water supply conduit lid, six holes of 10 mm diameter have been perforated (Figure 3.16 on the center). Inside these holes, six aluminum pipes of 10 mm diameter and 50 mm length have been inserted. The so obtained passive jet aeration system has been explained in Chapter 3.7.

Both configurations generate natural air entrainment during the jet trajectory in the air (from the nozzle exit to the impact with plunge pool surface) and at the jet impact on the plunge pool surface. For configuration ACN, the air entrained by the passive aeration system must be addict at the natural air entrainment: Table 3.3 summarizes the passive jet aeration concentrations.

The influence of the passive jet aeration by suction on the pressure measurements and on the block uplift has been analyzed. Natural jet aeration has not been measured because was the same for all configurations (the conditions for natural aeration were always the same; some values can be found in Manso (2006)).

Only the pressure measurements performed with three pressure transducers are analyzed in this section: transducer N° 312 near the fissure entrance on the block upper face (at 25 mm), transducer N° 313 inside the vertical fissure (at 50 mm from the plunge pool bottom) and transducer N° 318 underneath the block on the same vertical axis as transducer N° 312 (Figure 6.46).

The analysis results have been illustrated for a core (Y/D = 2.8), a transition (Y/D = 5.6) a developed jet (Y/D = 8.3) and three jet velocities (4.9, 12.3 and 19.6 m/s).

For configuration CN detailed results are explained in Chapter 6.4.

7.2.3 Pressure field surrounding the block

Figures 7.20, 7.21, 7.22 and 7.23 show the pressure field comparison between the two configurations.

By analyzing the pressure field acting on the block, both configurations show approximately the same mean values as a function of the jet velocity. For both configurations, the mean pressure evolution, as a function of the jet velocity, is almost superposed with small difference (less than 0.02 Bar) all around the block.

However, maximum and minimum pressures show some difference between the configuration with only the natural air entrainment (CN) and the configuration with natural and passive air entrainment (ACN). Maximum and minimum pressures show similar evolution as function of the jet velocity but the pressure values are different.

At the plunge pool bottom, configuration ACN (transducer N° 312) show pressure difference approximately of 1 Bar (maximum pressure) for jet velocities larger than 12.3 m/s. This behavior could be observed for core (Y/D = 2.8) and transition jets (Y/D = 5.6). A similar behavior could be observed as well for minimum pressures but the difference are smaller (∼0.15 Bar). It' seem that the passive air entrainment influence the extreme pressure values (maximum and minimum) but not mean values.

Transducer N° 309 (located at the block center) shows lower pressures and small differences. The lower pressures are related to its position from the stagnation point. Transducer N° 309 is located in wall jet region at 142 mm from the stagnation point and transducer N° 312 is located at 104 mm from the same point (at the boundary between impingement region and wall jet region). As can be observed by the pressure measurements and in literature, the pressure generated in this region loads the block in a different way. In the wall jet region the pressures can reach negative values and are more subjected to the influence of the large eddies and oscillating hydraulic jump generated inside the plunge pool. The difference between maximum and minimum pressures appear but is small (∼0.1 Bar).

The four transducers located on the block upper face are not aligned radially outwards from the stagnation point but are located perpendicularly at one side of the block (with distances between 104 and 142 mm from the stagnation point). Hence, is not possible to obtain the real pressure distribution acting on the block. It is difficult to estimate the real effect of the passive air entrainment onto the pressures acting on the block upper face, but it seems that the passive air entrainment influence the extreme pressure values (maximum and minimum).

Inside the 3-dimensional fissure, as explained before the mean pressure is practically superposed for both configurations. For both configurations, the pressure evolution, as a function of the jet velocity is almost the same. However, maximum and minimum pressures show some difference. Near the fissure entrance (transducer N° 313), the jet with passive air entrainment (ACN) generates higher pressures but the difference it's not so large as observed on the plunge pool (normally ∼0.1 Bar but with a maximum difference of 0.25 Bar for core jet). Minimum

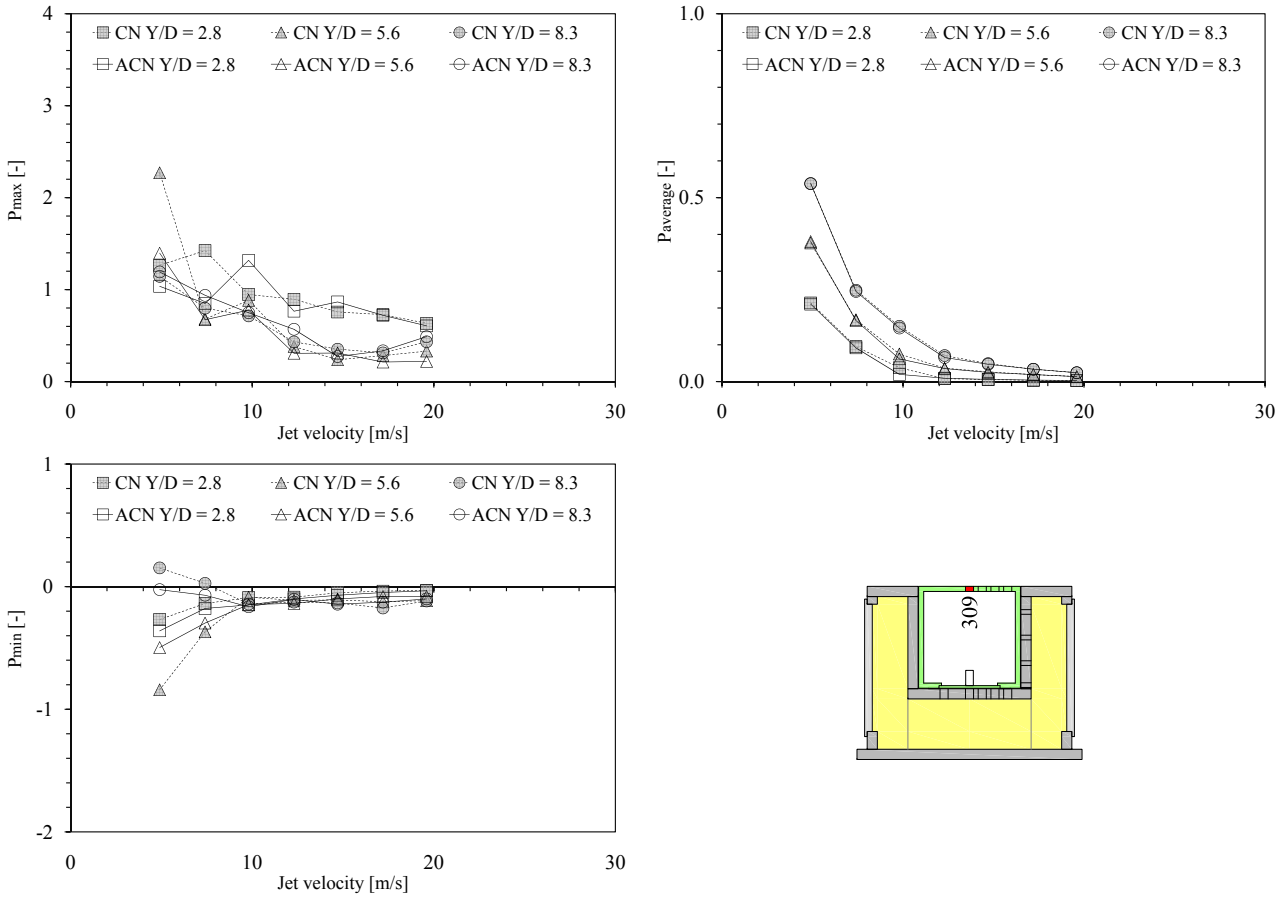

Figure 7.20: Influence of passive jet aeration on the pressure field surrounding the block. Normalized pressure measured with transducer N° 309 for configurations CN (without passive air entrainment) and ACN (with passive air entrainment) as a function of jet velocity (2.5-19.6 m/s) and Y/D ratio (2.8, 5.6 and 8.3). Maximum pressure (top left), mean pressure (top right), minimum pressure (bottom left) and transducer location (bottom right).

pressures show as well differences but the two configurations are very close. Moving along the vertical fissure and going underneath the block, the pressures recorded for configuration ACN show lower maximum values. The evolution as a function of the jet velocity is similar for both configurations but are shifted vertically (approximately 0.1 Bar). It seems that inside the fissure the passive air entrainment reduce the amplitude of maximum pressures fluctuations. The pressure waves travelling inside the fissure compress and decompress the air bubbles present in the water. This mix flow (water-air) influences the pressure propagation and the pressure fluctuations inside the fissure. Hence, maximum pressures are reduced because the pressure acting inside the fissure are influenced by the air bubbles (these bubbles act like springs inside the fissure).

As before, the transducers located underneath the block are not aligned radially outwards from the stagnation point but are located perpendicularly. These locations cannot allow the reconstruct the real pressure field acting under the block. To have a better relationship between pressures acting onto the block upper and lower face, the transducers should have another

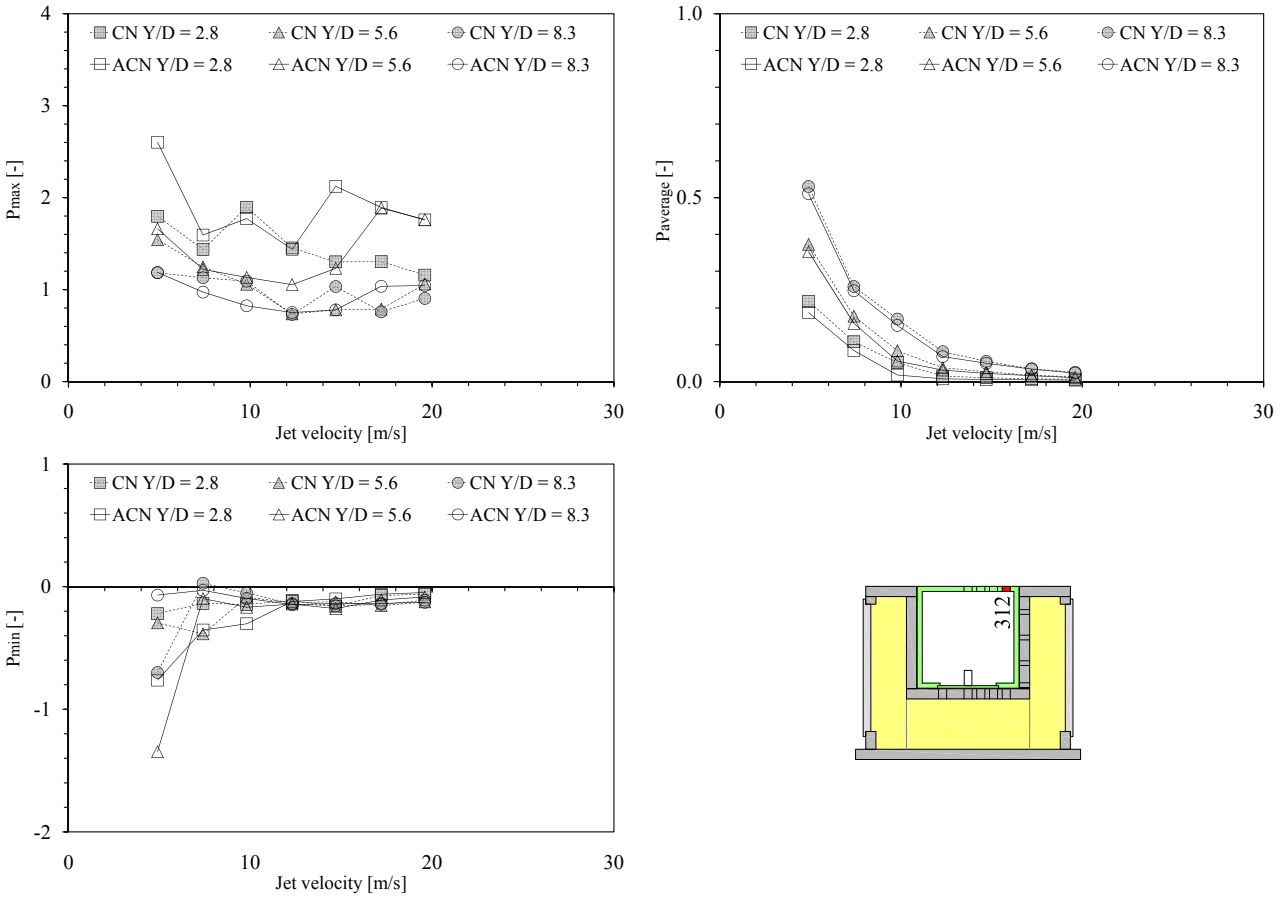

Figure 7.21: Influence of passive jet aeration on the pressure field surrounding the block. Normalized pressure measured with transducer N° 312 for configurations CN (without passive air entrainment) and ACN (with passive air entrainment) as a function of jet velocity (2.5-19.6 m/s) and Y/D ratio (2.8, 5.6 and 8.3). Maximum pressure (top left), mean pressure (top right), minimum pressure (bottom left) and transducer location (bottom right).

location (radially outwards from the block corner). As before, it is difficult to estimate the real effect of the passive air entrainment onto the pressures acting inside the 3-dimensional fissure, but it seems as before that the passive air entrainment influence maximum pressures.

7.2.4 Pressure coefficients

Figure 7.24 summarizes the comparison between the different pressure coefficients for the two configurations (mean pressure coefficient C_p, turbulent pressure fluctuation coefficient $C_{p'}$, positive extreme fluctuation coefficient C_p^+, negative extreme fluctuation coefficient C_p^-, positive extreme pressure coefficient $C_{p,max}$ and negative extreme pressure coefficient $C_{p,min}$).

The pressure coefficients computed for the two configurations allow to analyze the influence of the air entrainment (equations are explained in Chapter 5.2.2). The theoretical curves, developed by Ervine's (Ervine et al. (1997)), are plotted on Figure 7.24. These curves are considerate as reference for pressure recorded at the plunge pool bottom and have been developed

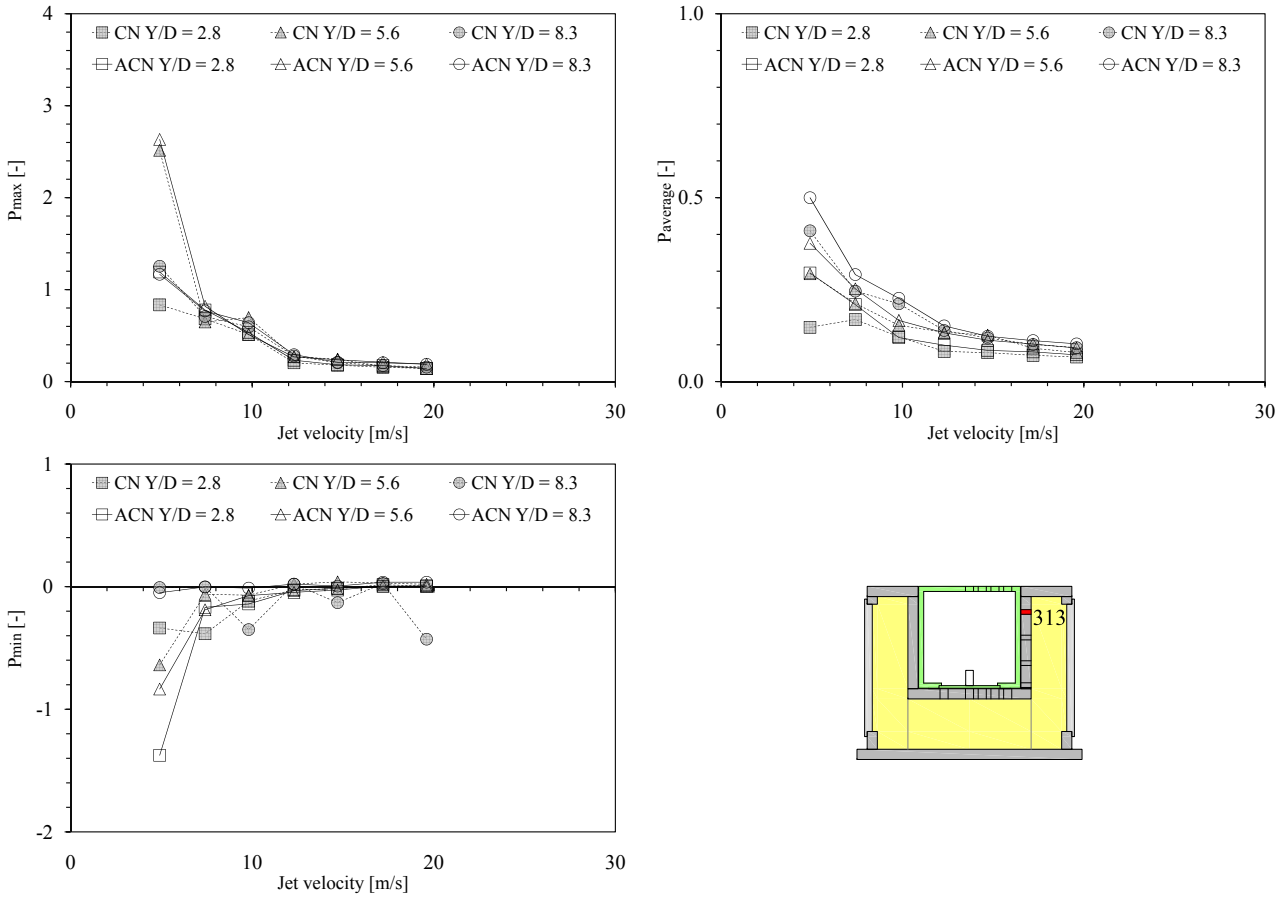

Figure 7.22: Influence of passive jet aeration on the pressure field surrounding the block. Normalized pressure measured with transducer N° 313 for configurations CN (without passive air entrainment) and ACN (with passive air entrainment) as a function of jet velocity (2.5-19.6 m/s) and Y/D ratio (2.8, 5.6 and 8.3). Maximum pressure (top left), mean pressure (top right), minimum pressure (bottom left) and transducer location (bottom right).

for transducers located radially outwards from the stagnation point. In our case, as explained in Chapter 6.4, transducers are de-axed (Figure 6.46) and are located at the boundary between impingement region and wall jet region. In this region, the wall pressure decreases and the jet energy is converted into velocity (deflected flow in the wall jet region) as explained in Cola (1966). Hence, the pressure coefficients are lower than the expected values for transducers located near the stagnation point and in the impingement region.

Figure 7.24 top left shows the mean pressure coefficients (C_p) computed for both configurations (CN only natural air entrainment and ACN natural and passive air entrainment). The coefficients computed on the block upper face (at the plunge pool bottom) for core, transition and developed jet are lower than the theoretical curves (as explained before).

The mean pressure coefficients computed inside the fissure (along the vertical fissure and underneath the block) are larger than the corresponding coefficients computed at the plunge pool bottom: the mean pressure acting underneath the block is higher than the mean pressure recorded at the plunge pool bottom. Hence, the mean pressure coefficients are higher than at

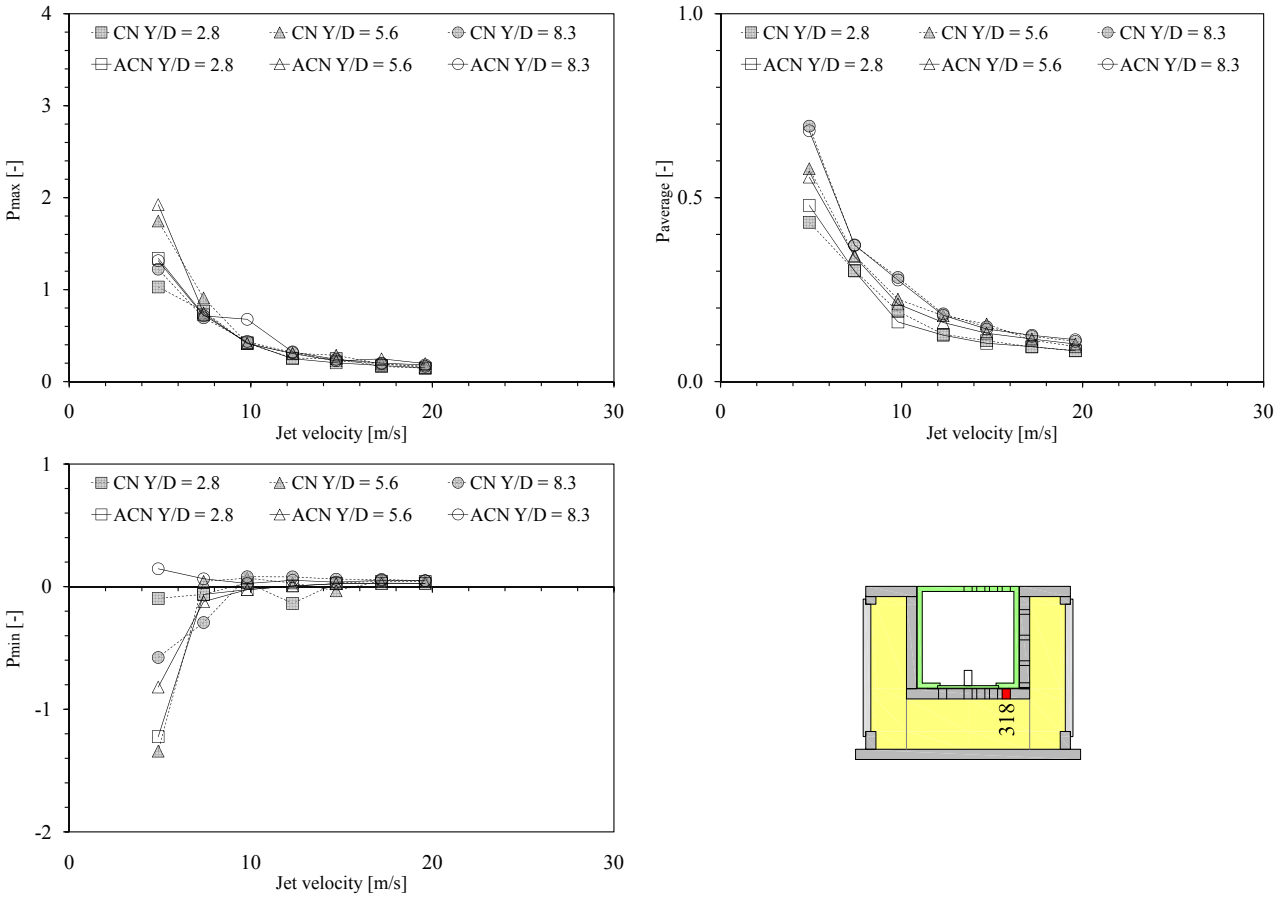

Figure 7.23: Influence of passive jet aeration on the pressure field surrounding the block. Normalized pressure measured with transducer N° 318 for configurations CN (without passive air entrainment) and ACN (with passive air entrainment) as a function of jet velocity (2.5-19.6 m/s) and Y/D ratio (2.8, 5.6 and 8.3). Maximum pressure (top left), mean pressure (top right), minimum pressure (bottom left) and transducer location (bottom right).

the plunge pool bottom. As explained before, the pressure transducers are not located radially outwards from the stagnation point and did not represent the real pressure field acting onto the block. If the transducers were installed radially, the mean coefficients computed on the block upper face will be higher than inside the fissure.

By analyzing the pressure field acting around the block appears that the mean pressure is almost the same, the coefficients computed for both configurations are very close. The differences between coefficients are related to the small pressure difference recorded by the pressure transducers.

Figure 7.24 top right shows the turbulent pressure fluctuations coefficients ($C_{p'}$) computed for both configurations. The coefficients computed all around the block are in agreement with the theoretical curve. Some small difference could be observed for coefficients computed with the same test conditions (water depth and jet velocity) but for different air entrainment. The differences between the coefficients decrease as a function of the jet velocity. Normally, the

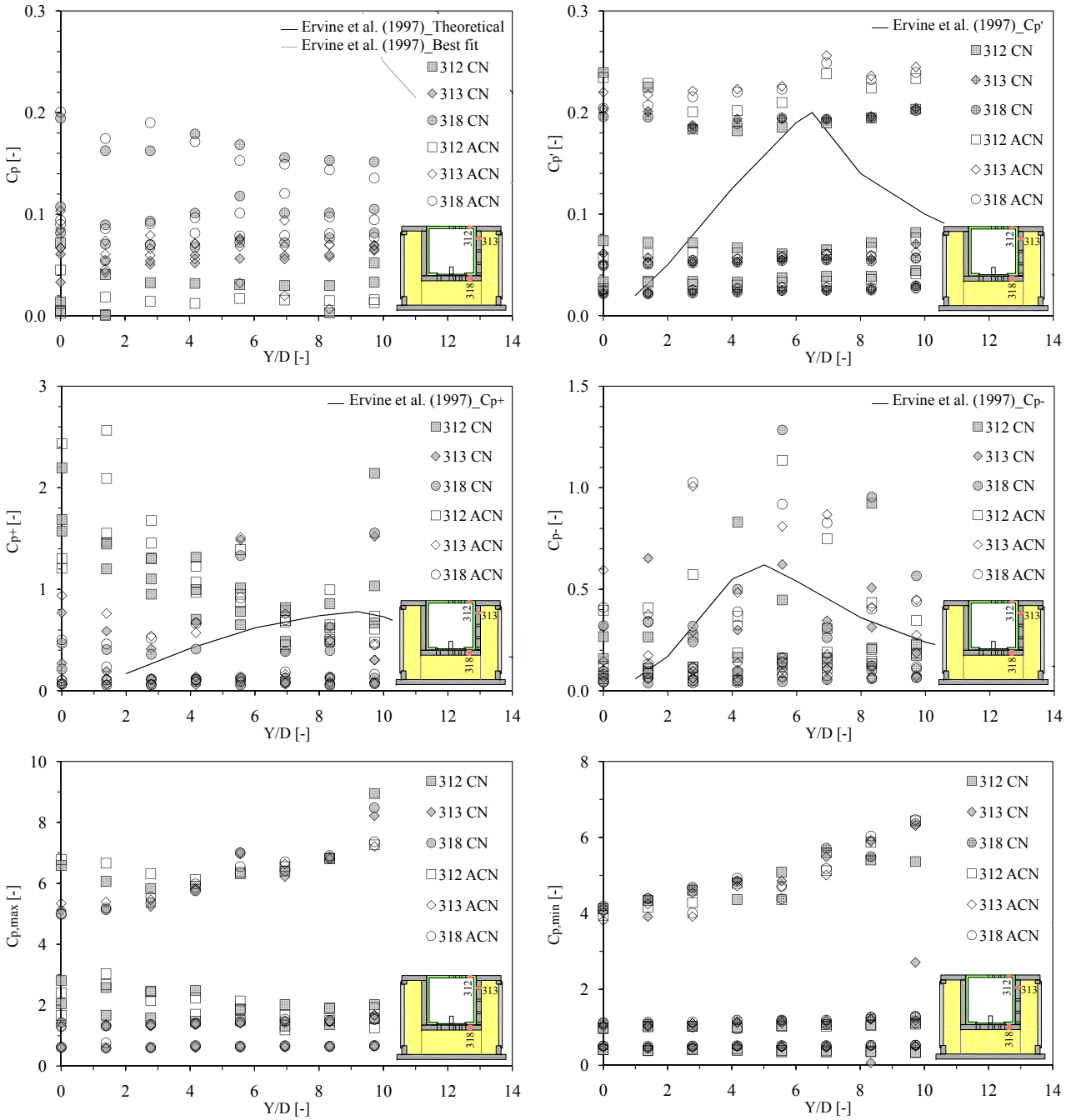

Figure 7.24: Influence of passive jet aeration on the pressure coefficients for configurations CN (without passive air entrainment) and ACN (with passive air entrainment) as a function of jet velocity (2.5-19.6 m/s) and Y/D ratio (0-9.7). Mean pressure coefficient C_p (top left); Turbulent pressure fluctuation coefficient $C_{p'}$ (top right); Positive extreme pressure fluctuation coefficient C_p^+ (middle left); Negative extreme pressure fluctuation coefficient C_p^- (middle right); Positive extreme pressure coefficient $C_{p,max}$ (bottom left); Negative extreme pressure coefficient $C_{p,min}$ (bottom right).

larger turbulence values are generated by the jet subjected at the natural and passive air entrainment (ACN).

Small differences in coefficients values have been observed for all transducers (at the plunge pool bottom and inside the fissure) but larger differences may be expected due to passive

air entrainment that modify flow and water conditions inside plunge pool and fissure. The measurements show that the pressure fluctuations are similar for all transducers, independently by their relative position from the stagnation point. It's seem that for transition jets ($4 < Y/D < 6$) the turbulence deceases weakly and the return at the same values observed for core jet for Y/D ratios larger than 6 (developed jets).

For both configurations, the larger coefficients are generated by jet velocities lower than 7.4 m/s as has been observed before.

Figure 7.24 middle left shows the positive extreme pressure fluctuation coefficients (C_p^+) computed for both configurations. The coefficients computed for Y/D ratios lower than 6 (core and transition jets) and for small jet velocities (lower than 7.4 m/s) are larger than the theoretical curves. These observations are valid for both configurations.

The pressures recorded at the plunge pool bottom (with transducer N° 312) show the highest coefficient values (for core, transition and developed jets). With an increase of the jet velocity, the positive extreme fluctuations at the plunge pool bottom decrease. Inside the fissure, the positive extreme fluctuations are smaller than at the plunge pool bottom and decrease as a function of the jet velocity. The differences between the two configurations decrease with an increase of the jet velocity and the water depth.

Normally, the configuration subjected at the natural and passive air entrainment (ACN) shows the larger values all around the block (as observed before in the pressure field analysis).

Figure 7.24 middle right shows the negative extreme pressure fluctuation coefficients (C_p^-) computed for both configurations. For jet velocities up to 7.4 m/s, the computed coefficients are larger than the Ervine's curve. As observed before (positive extreme pressure fluctuation coefficient), the configuration subject at the natural and passive air entrainment (ACN) shows the larger values all around the block with some exceptions. When the jet velocity and the water depth increase, the coefficient differences between the two configuration decreases.

Figure 7.24 bottom left, shows the positive extreme pressure coefficients ($C_{p,max}$) computed for both configurations. As observed in the pressure field analysis, at the plunge pool bottom (transducer N° 312) maximum pressures are larger than inside the fissure (transducers N° 313 and N° 318). Configuration ACN shows the larger values, but the difference with the configuration CN decreases as a function of the jet velocity and the water depth. Inside the fissure, the positive extreme pressure is almost the same for a given jet velocity and water depth.

Figure 7.24 bottom right shows the negative extreme pressure coefficients ($C_{p,min}$) computed for both configurations. The coefficient values are similar for both configurations. The larger coefficient values are generated by jet velocities up to 7.4 m/s, as observed before. The negative extreme pressures at the plunge pool and inside the fissure are almost the same, hence the coefficients are very close.

7.2.5 Displacements and accelerations of block

For both configurations maximum uplift was approximately 160 mm. For both configurations the block moves up for jet velocities larger than 7.4-9.8 m/s and reaches the transducer upper limit for a jet velocity of 12.3 m/s. Maximum uplift has been reached for a jet velocity of 19.6 m/s. The passive air entrainment did not affect the block behavior (when the block starts its vertical movement and the value of maximum uplift). Figure 7.25 shows the mean vertical displacement for the two configurations.

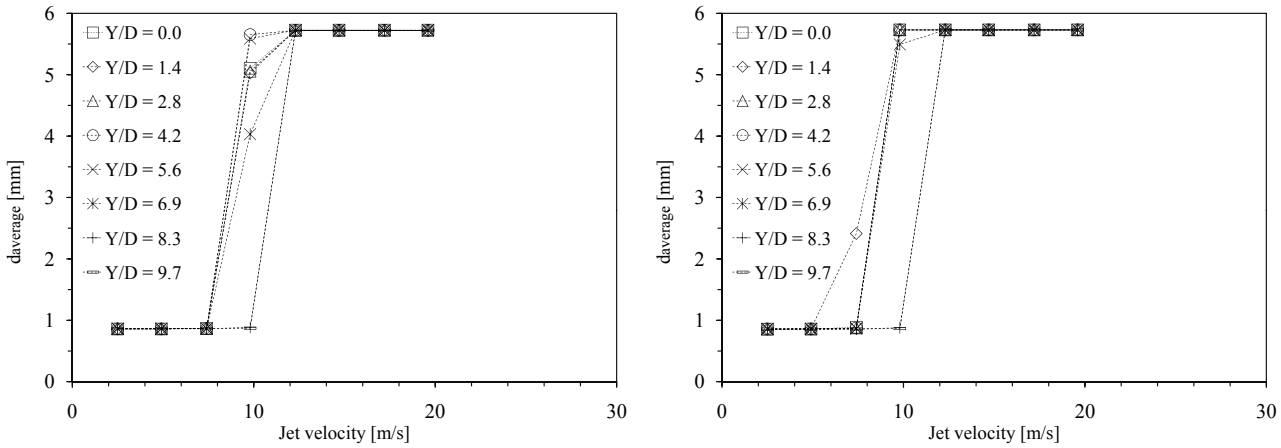

Figure 7.25: Influence of passive jet aeration on mean displacements of block as a function of jet velocity (2.5-19.6 m/s) and Y/D ratio (0-9.7). Configuration CN without passive air entrainment (left) and configuration ACN with passive air entrainment (right).The block initial position corresponds to a distance of ∼0.85 mm.

The accelerations recorded inside the block show a similar behavior for both configurations. The accelerations follow the block vertical movements: when the block starts to move up the accelerations increase to reach a new mean value though the block continues in its vertical movements the acceleration did not change and remain approximately constant. Configuration ACN shows the highest accelerations (for all jet velocities and all water depths). Mean accelerations are almost the same and show the same evolution as a function of the jet velocity. For both configurations, minimum accelerations are affected by some electrical noises that influence the minimum value (lower limit of the accelerometer -1000 g). Figure 7.26 shows the mean acceleration for the two configurations.

The passive air entrainment did not influence the block response (displacements and accelerations) for the two analyzed configurations.

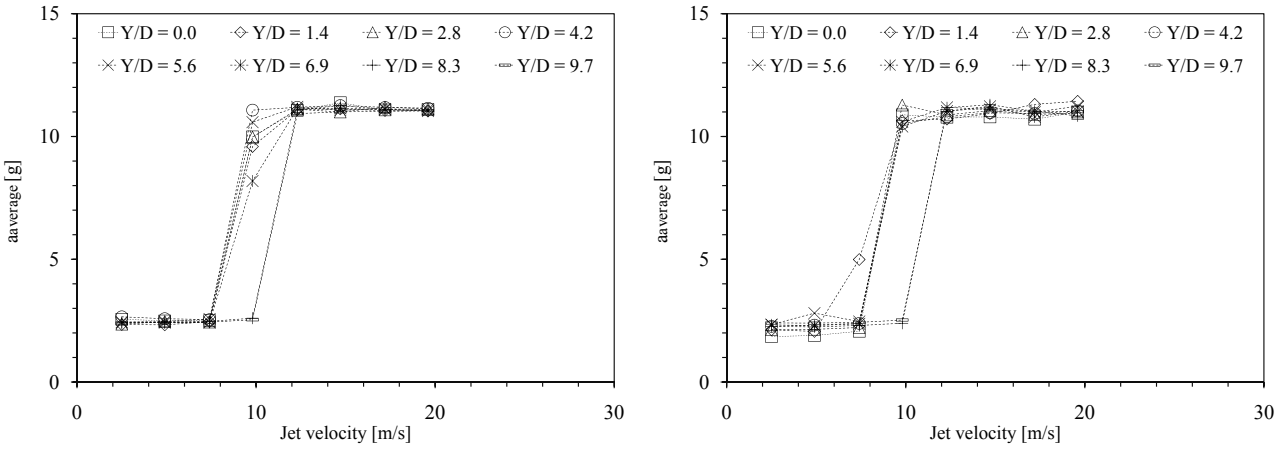

Figure 7.26: Influence of passive jet aeration on mean accelerations of block as a function of jet velocity (2.5-19.6 m/s) and Y/D ratio (0-9.7). Configuration CN without passive air entrainment (left) and configuration ACN with passive air entrainment (right).

7.2.6 Power Spectral Density

Figures 7.27, 7.28 and 7.29 show the power spectral density comparison between the two configurations (transducers N° 312, N° 313 and N° 318). In figures 7.27, 7.28 and 7.29, the continuous line corresponds to the configuration with the natural air entrainment (CN) and the dashed line to the configuration with natural and passive air entrainment (ACN).

As has been observed previously for all configurations, when the jet velocity increases, the energy per frequency increases proportionally (the energy is related to jet kinetic energy at the entrance in the plunge pool).

The power spectral density behavior is different for transducers situated at the plunge pool bottom (as an example: N° 312) compared to transducers situated inside the 3-dimensional fissure (as an example: N° 313 and N° 318). These observations are valid for core, transition and developed jets.

The pressure transducer fixed on the block upper face (transducer N° 312, Figure 7.27) has a behavior that is similar to previous observations (Chapter 6.4.5).

The low frequency part of the PSD signal ($f < 10$ Hz) looks almost similar for all jet velocities. The energy per frequency decreases slowly with a slope of approximately -2/3. For higher frequencies ($f > 10$ Hz) the spectral content decreases with a -1 slope. For jet velocities larger than 7.4 m/s, the configuration with natural air entrainment (CN) has an energy content higher than the configuration with natural and passive air entrainment (ACN), for each frequency. For jet velocities lower than 7.4 m/s, configuration ACN has the higher energy content. The PSD shows a vertical shift (different energy content) as a function of frequency and the signal evolution is almost the same along the whole frequency range.

The pressure transducers situated inside the 3-dimensional fissure (along the vertical fissure N° 313, Figure 7.28 and underneath the block N° 318, Figure 7.29) show a different behavior than transducer N° 312 situated at the plunge pool bottom. The energy per frequency is lower

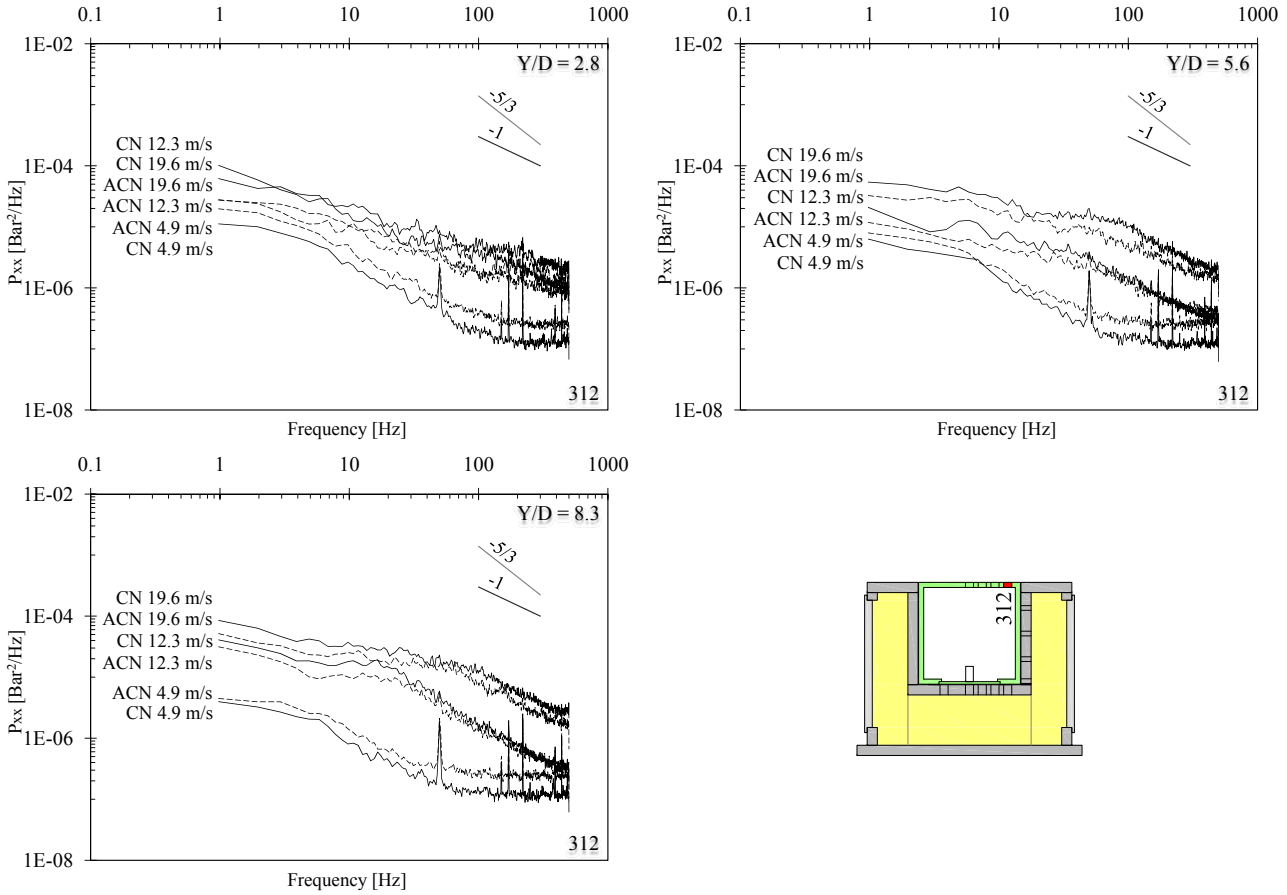

Figure 7.27: Influence of passive jet aeration on the non-dimensional spectral content (PSD) computed for configurations CN (without passive air entrainment, continuous line) and ACN (with passive air entrainment, dashed line) as a function of jet velocity (4.9, 12.3 and 19.6 m/s) and Y/D ratio (2.8, 5.6 and 8.3). Transducer N° 312. Core jet (top left), transition jet (top right), developed jet (bottom left) and transducer location (bottom right).

than at the plunge pool bottom, for the same jet velocity. With an increase of frequency, three zones can be distinguished in the PSD signal: a first zone up to 8-15 Hz, a second zone between 8-15 and 100 Hz and the third zone beyond 100 Hz. In the first zone, the energy decreases slowly with a slope approximately situated between -2/3 and -1. In the second zone, the energy decrease with a different slope, approximately situated between -5/3 and -6/3 in a small frequency range (between 8-15 and 40-60 Hz). In the third zone, the energy reaches a constant value similar for all jet velocities.

Inside the fissure, the difference between the two configurations could be described by using the same three zones. For frequencies up to 8-15 Hz, the configuration with natural and passive air entrainment (ACN) shows normally more energy for the same frequency. Between 8-15 and 100 Hz, the two configurations have almost the same energy per frequency. For frequencies large than 100 Hz, configuration ACN shows more energy per frequency. The PSD evolution as a function of the frequency is almost the same for both configurations.

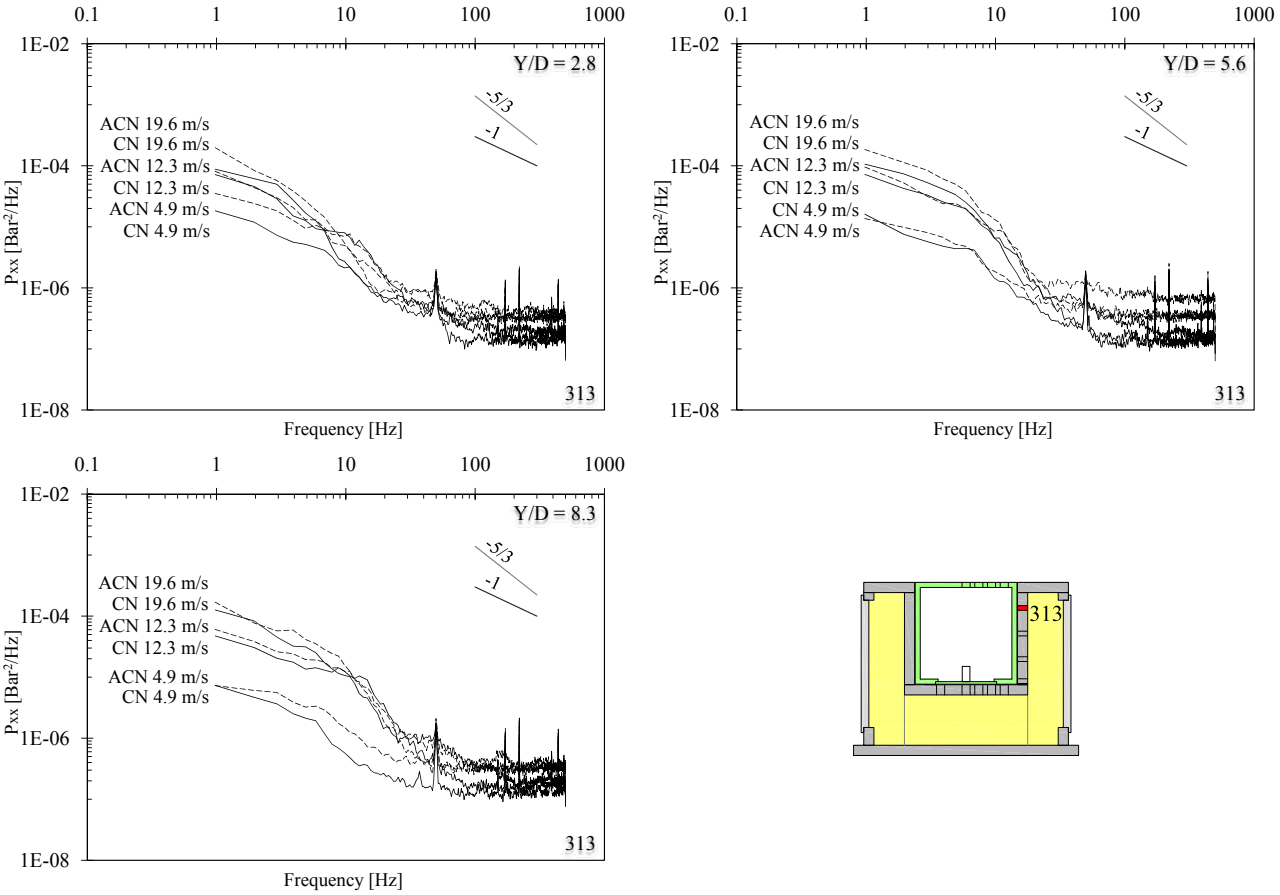

Figure 7.28: Influence of passive jet aeration on the non-dimensional spectral content (PSD) computed for configurations CN (without passive air entrainment, continuous line) and ACN (with passive air entrainment, dashed line) as a function of jet velocity (4.9, 12.3 and 19.6 m/s) and Y/D ratio (2.8, 5.6 and 8.3). Transducer N° 313. Core jet (top left), transition jet (top right), developed jet (bottom left) and transducer location (bottom right).

At the plunge pool, the passive air entrainment reduces the energy per frequency for jet velocities larger than 7.4 m/s. This behavior may be related to the different flow conditions inside the plunge pool generate by a new mixture of water and air (more air in the water). The jet may be destabilized by the passive air entrainment that modifies its structures. Another possibility may be the oscillating hydraulic jump present in the plunge pool, which affects the pressures acting on the block due to the different mixture water-air.

Inside the 3-dimensional fissure, the passive air entrainment influence the lower (f < 8-15 Hz) and higher (f > 100 Hz) frequencies in the PSD signal. The air penetrated inside the fissure modifies the response of the fissure at lower and higher frequency.

7.2.7 Dynamic block impulsion

The dynamic block impulsion for both configurations has been analyzed in Chapter 5.4.

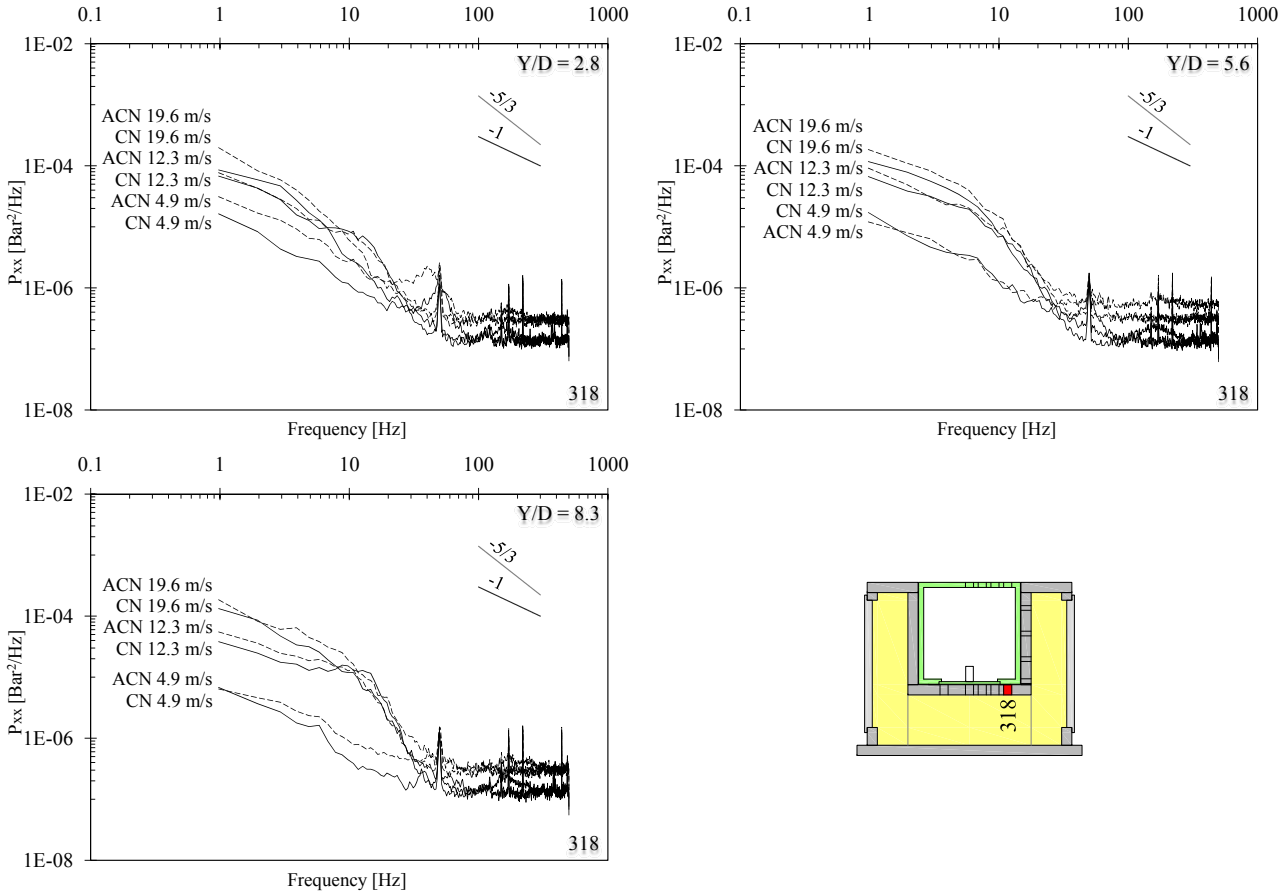

Figure 7.29: Influence of passive jet aeration on the non-dimensional spectral content (PSD) computed for configurations CN (without passive air entrainment, continuous line) and ACN (with passive air entrainment, dashed line) as a function of jet velocity (4.9, 12.3 and 19.6 m/s) and Y/D ratio (2.8, 5.6 and 8.3). Transducer N° 318. Core jet (top left), transition jet (top right), developed jet (bottom left) and transducer location (bottom right).

7.2.8 Conclusions

For the first time, the pressure field surrounding an experimentally rock block (the highly instrumented block) solicited by a water jet has been measured. This block was solicited by a water jet that has been naturally aerated, without (CN) and with a suction-based passive aeration system (ACN).

By analyzing the pressure field acting on the block, mean pressures for both configurations are practically superposed with small differences all around the block. However, maximum and minimum pressures show some difference between the two configurations. Maximum and minimum pressures show similar evolution as function of the jet velocity but the pressure values are different. This phenomenon has been observed as well inside the fissure but the differences between maximum and minimum pressure values are smaller.

The four transducers located on the block upper face are not aligned radially outwards from the stagnation point but are located far away and perpendicularly from one block side. Hence,

is not possible to obtain the real exponential pressure distribution acting on the block upper face (centred at the stagnation point).

It is difficult to estimate the real effect of the passive air entrainment on the pressures acting on the block upper face and inside the fissure, but it seems that it influences the extreme pressure values (maximum and minimum).

The computed pressure coefficients have been compared for both configurations using the theoretical curves developed by Ervine et al. (1997). For the tests performed with the present experimental facility, the transducers are "de-axed" and are located between the impingement region and the wall jet region. Hence, the pressure coefficients are lower than the expected values for transducers situated at stagnation point and in impingement region. This reference was used to evaluate the results obtained by the transducers situated inside the fissure, while it was originally developed for plunge pool bottoms only. However, our results are in reasonable agreement with this reference.

The influence of the passive air entrainment on the pressure coefficients seems quite small. Normally the configuration with natural and passive air entrainment (ACN) show the larger coefficients values but the differences are small (they are related to the small pressure differences recorded by the pressure transducers and observed in the pressure field).

The smallest jet velocities (up to 7.4 m/s) generate the largest coefficients differences, but this fact is related to the equations used to compute the coefficients (Chapter 5.2.2): the pressure coefficients are normalized with the jet kinetic energy at impact on the water surface.

For both configurations, the largest uplift was approximately 160 mm. The block vertical displacements show the same behavior for both configurations: the block moves up for jet velocities larger than 7.4-9.8 m/s and reaches the largest uplift for a jet velocity of 19.6 m/s.

The accelerations show a similar behavior for both configurations and follow the block vertical evolution. The configuration with natural and passive air entrainment (ACN) shows highest accelerations (for all jet velocities and water depths). Mean acceleration is similar for both configurations. As a result, the passive air entrainment did not influence the block vertical displacements and the accelerations for the analyzed configurations.

The power spectral density (PSD) analyses show a different behavior for transducers located in the plunge pool and inside the 3-dimensional fissure. The remarks made for configuration CN are valid as well for configuration ACN, as an example: difference behavior at the plunge pool bottom and inside the fissure, energy evolution as a function of frequencies.

At the plunge pool bottom, for jet velocities larger than 7.4 m/s, the configuration with the natural air entrainment (CN) shows an energy content larger than the other configuration (ACN). For jet velocities lower than 7.4 m/s, it is the configuration ACN that shows this behavior. The PSD shows a vertical shift (different energy content) as a function of frequency and the signal evolution is almost the same along the frequency range.

Inside the fissure, the difference between the two configurations could be described by using

the same three zones: for frequencies lower than 8-15 Hz, the configuration with natural and passive air entrainment (ACN) shows normally more energy for the same frequency, between 8-15 and 100 Hz, the two configurations have almost the same energy per frequency and for frequencies large than 100 Hz, configuration ACN shows more energy per frequency. The PSD evolution as a function of the frequency is quasi similar for both configurations.

The analysis of these configurations (jet position on the block corner, lateral guides with eight contact points and the block free to move along the vertical axis) did not allow to find a relationship between block solicitations and passive air entrainment. The pressure field acting around the block shows that the passive air entrainment influences the extreme pressure values (maximum and minimum) but mean pressure is practically superposed for both jet aeration configurations (for all water depths and jet velocities). The pressure coefficients are weakly influence by the passive air entrainment. Normally, the larger coefficients values are related at this configuration but the differences are small. The power spectral density shows a difference between the two configurations: there are some differences in the energy per frequency at plunge pool and inside the fissure. The energy differences, between the two configurations, are not so large to modify the block behavior and its response to the solicitations applies on its body.

7.2.9 Remarks

A thorough analysis of the influence of the jet aeration on the block solicitation has to be made in future. The same tests with same configurations have to be performed, but modify the transducers location onto the block upper face and inside the 3-dimensional fissure. The transducers have to be installed, where is possible, radially outwards from the stagnation point, to be able, to reconstruct the pressure distribution on the block upper face and inside the fissure. These measurements have to allow to perform a better analysis of the influence of the jet aeration, as an example: pressure field surrounding the block and dynamic block impulsion (direct relationship between solicitations and block response).

Further configurations have to be investigated: these configurations are characterized by a different jet impact position on the block upper face (on the block center, on the block left and right side ...). Transducers locations have to be adapted for each configuration and not as in this research project where transducers had always the same location regardless the stagnation point (radially outwards from the stagnation point and with the first transducer located near this point).

Another accelerometer (more precise) and others displacement transducers (with a wider measurement range) would be installed in the present experimental facility to broaden the results range.

7.3 Influence of lateral guides fixed on the block lateral faces: two or eight contact points

To guide the block in its vertical movements (the only degree of freedom of the block), a couple of bronze guides have been installed on the block side faces (two guides on each face, Figures 3.5 and 4.3). To evaluate their influence, two different lateral guides have been tested. The lateral guides are described in Chapter 4.2.1.3. Four configurations with the same parameters (jet impact position and block degree of freedom) but different lateral guides have been analyzed.

Jet impact position on the block center:

- Block equipped with lateral guides having two contact points (CE);
- Block equipped with lateral guides having eight contact points (CR).

Jet impact position on the block right hand side:

- Block equipped with lateral guides having two contact points (SI);
- Block equipped with lateral guides having eight contact points (SR).

The four configurations are described in Chapter 4.3.

The detailed results are explained in Chapters 6.2 and 6.3 for configurations with lateral guides having eight contact points (CR and SR).

To illustrate the analysis of the influence of lateral guides, only the results of three transducers are reproduced: on the block upper face transducer N° 310 or N° 312, located at 25 mm from the stagnation point, the first transducer inside the vertical fissure at 50 mm from the plunge pool bottom (N° 313) and transducer N° 321 situated underneath the block on the center.

On the block upper face, for configurations with the jet impact on the block center (CE and CR) transducer N° 310 is analyzed, whereas for configurations with the jet impact on the block right side (SI and SR) transducer N° 312 is analyzed. The two transducers are both situated at the same distance from the stagnation point and their measurements may be compared.

The pressure distribution underneath the block is almost constant, as observed before (Chapters 6.2 and 6.3).

The results are illustrated for a core (Y/D = 2.8), a transition (Y/D = 5.6) and a developed jet (Y/D = 8.3) with four jet velocities (4.9, 12.3, 19.6 and 27.0 m/s).

7.3.1 Pressure field surrounding the block

7.3.1.1 Jet impact on the block center with two (CE) and eight (CR) contact points lateral guides

Figures 7.30, 7.31 and 7.32 show the pressure field comparison between configurations with the jet impact on the block center (CE and CR).

The analyses of the pressure field (surrounding the block) allow to confirm that the lateral guides (with two or eight contact points) do not affect the pressures acting around the block for configurations with the jet impact on the block center. Maximum, mean and minimum pressure evolutions are similar for both configurations as a function of the jet velocity. On the block upper face underneath the block with the increasing of the jet velocity some differences may be observed for the same water depth but different configurations. Maximum and minimum pressures show some variations in the largest pressure values for jet velocities above 17.2-19.6 m/s. The orders of magnitude of these variations reached a maximum of 0.2 Bar.

Mean pressures for both configurations are very close though some small pressure differences can be observed, but may be neglected due to their order of magnitude.

The same observation can be made for all pressure transducers situated around the block and for the three jet types (core, transition and developed jets).

7.3.1.2 Jet impact on the block right hand side with two (SI) and eight (SR) contact points lateral guides

Figures 7.33, 7.34 and 7.35 show the pressure field comparison between configurations with the jet impact on the block right side.

The remarks that have been made for the previous configurations (jet impact on the block center, Chapter 7.3.1.1) are also valid for configurations with jet impact on the block right side.

The analyses of the pressure field confirm that the lateral guides (with two or eight contact points) do not affect the pressures acting around the block for configurations with the jet impact on the block right side.

7.3.2 Displacements of block

The four configurations show a similar behavior: the block starts to move along the vertical axis for jet velocities larger than 4.9-7.4 m/s and reaches normally the largest displacement for a jet velocity of 27.0 m/s. The initial distance between the bottom of the central cavity and the block lower face is approximately 0.85 mm.

7.3.2.1 Jet impact on the block center with two (CE) and eight (CR) contact points lateral guides

Figure 7.36 shows the evolution of maximum and mean displacement for configurations with jet impact on the block center.

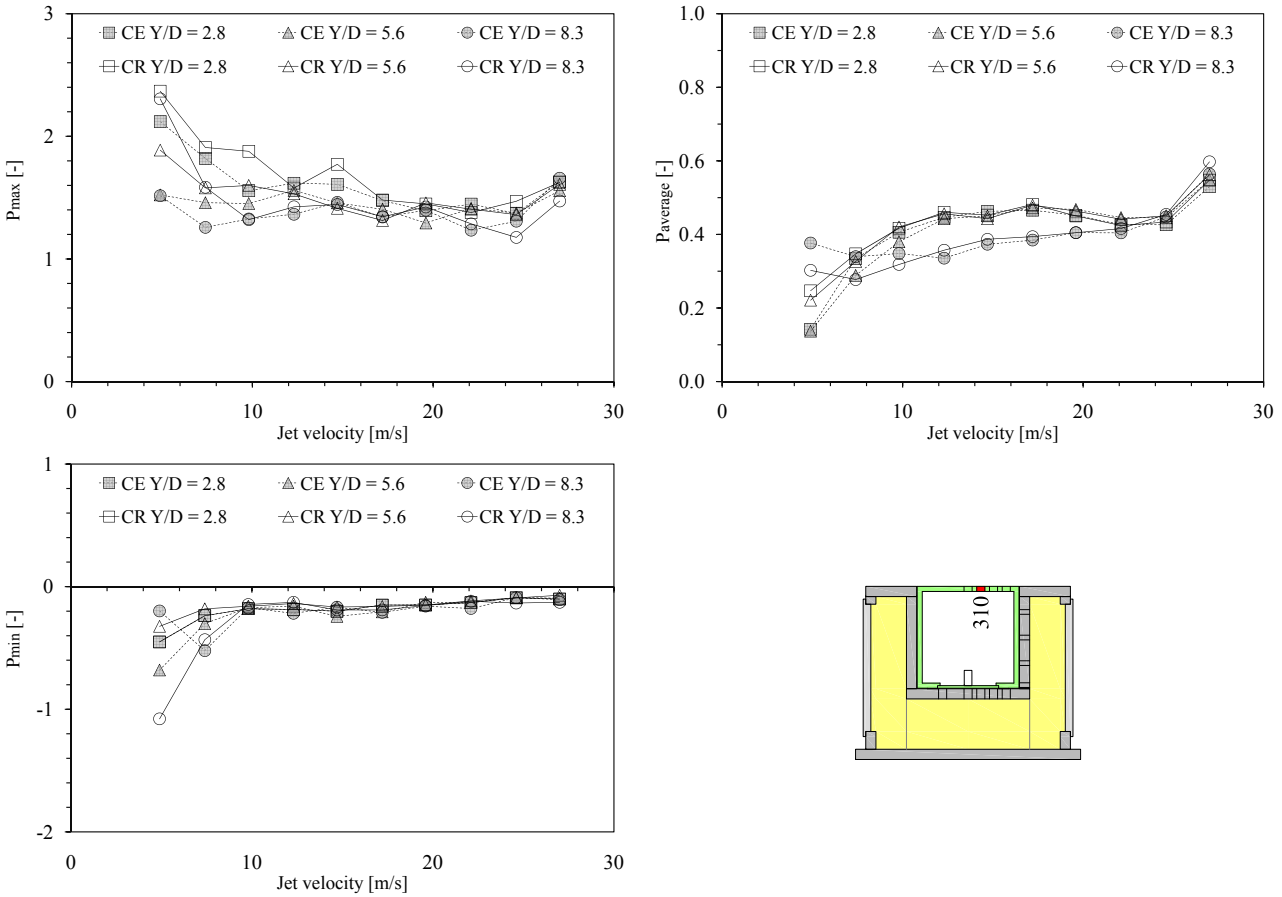

Figure 7.30: Influence of the type of lateral guide on the pressure field surrounding the block. Normalized pressure measured with transducer N° 310 for configurations CE and CR (jet impact on the block center) as a function of jet velocity (2.5-27.0 m/s) and Y/D ratio (2.8, 5.6 and 8.3). Maximum pressure (top left), mean pressure (top right), minimum pressure (bottom left) and transducer location (bottom right).

There are some small differences between both configurations: the mean displacement shows a different evolution with an increase of jet velocity. The block starts to move for jet velocities larger than 9.8 m/s: for smaller velocities, the block is in its initial position (in contact with central cavity bottom) and when the jet velocity increases, it reaches a new equilibrium position. This is the block behavior for configuration CR. For configuration CE, the mean pressure is almost constant along the whole range of jet velocities. Maximum and mean values are similar for both configurations. Minimum displacements correspond to the initial position of the block (in contact with the bottom of the central cavity).

Maximum displacements show a similar evolution for both configurations as a function of the jet velocity and show some small differences (values fluctuations between configurations). Maximum displacement is almost the same for both configurations and all water depth and ranges between 0.96 and 1.03 mm.

The analysis of the vertical displacements did not show an influence of the type of lateral guide on the block displacements for configurations with the jet impact on the block center.

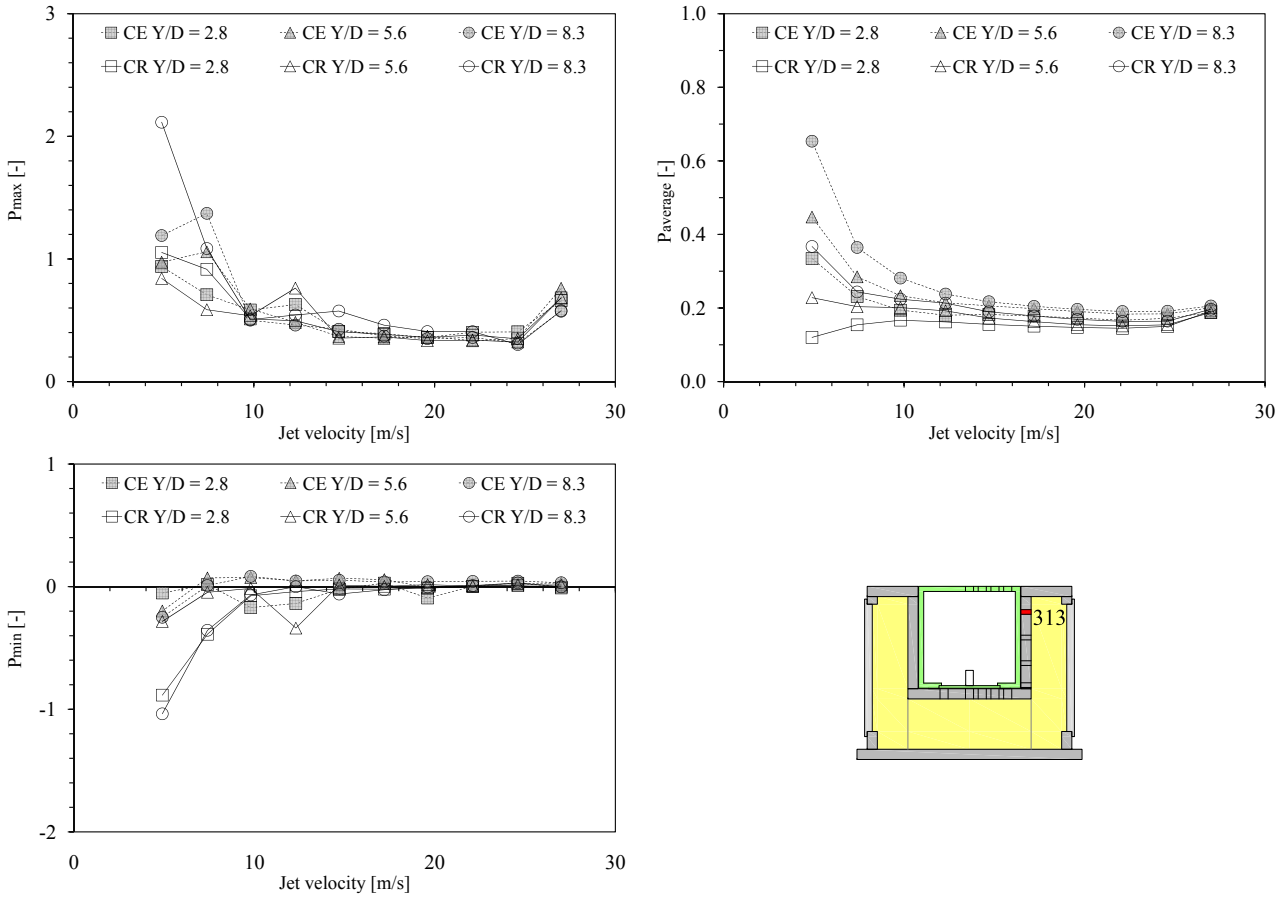

Figure 7.31: Influence of the type of lateral guide on the pressure field surrounding the block. Normalized pressure measured with transducer N° 313 for configurations CE and CR (jet impact on the block center) as a function of jet velocity (2.5-27.0 m/s) and Y/D ratio (2.8, 5.6 and 8.3). Maximum pressure (top left), mean pressure (top right), minimum pressure (bottom left) and transducer location (bottom right).

7.3.2.2 Jet impact on the block right side with two (SI) and eight (SR) contact points lateral guides

Figure 7.37 shows the evolution of maximum and mean displacement for configurations with the jet impact on the block right side.

The jet impact on the block right side shows a different behavior between the two configurations: configuration SI (equipped with the lateral guides having two contact points) shows larger vertical displacements than configuration SR (equipped with lateral guides having eight contact points). Maximum and mean vertical displacements are different, but the evolution along the whole range of jet velocities is similar.

The two lateral guides differ in the friction surface between the block and the central cavity walls (situated in the measurement box). The two contact points lateral guide (SI) has a contact surface of $\sim$3 cm^2 and the eight contact points lateral guide (SR) has a contact surface of $\sim$6 cm^2 (approximately the double). The friction force is larger for the eight contact points lateral guide. More friction means that the block vertical displacements should be smaller as have been observed for the configuration with eight contact points (SR).

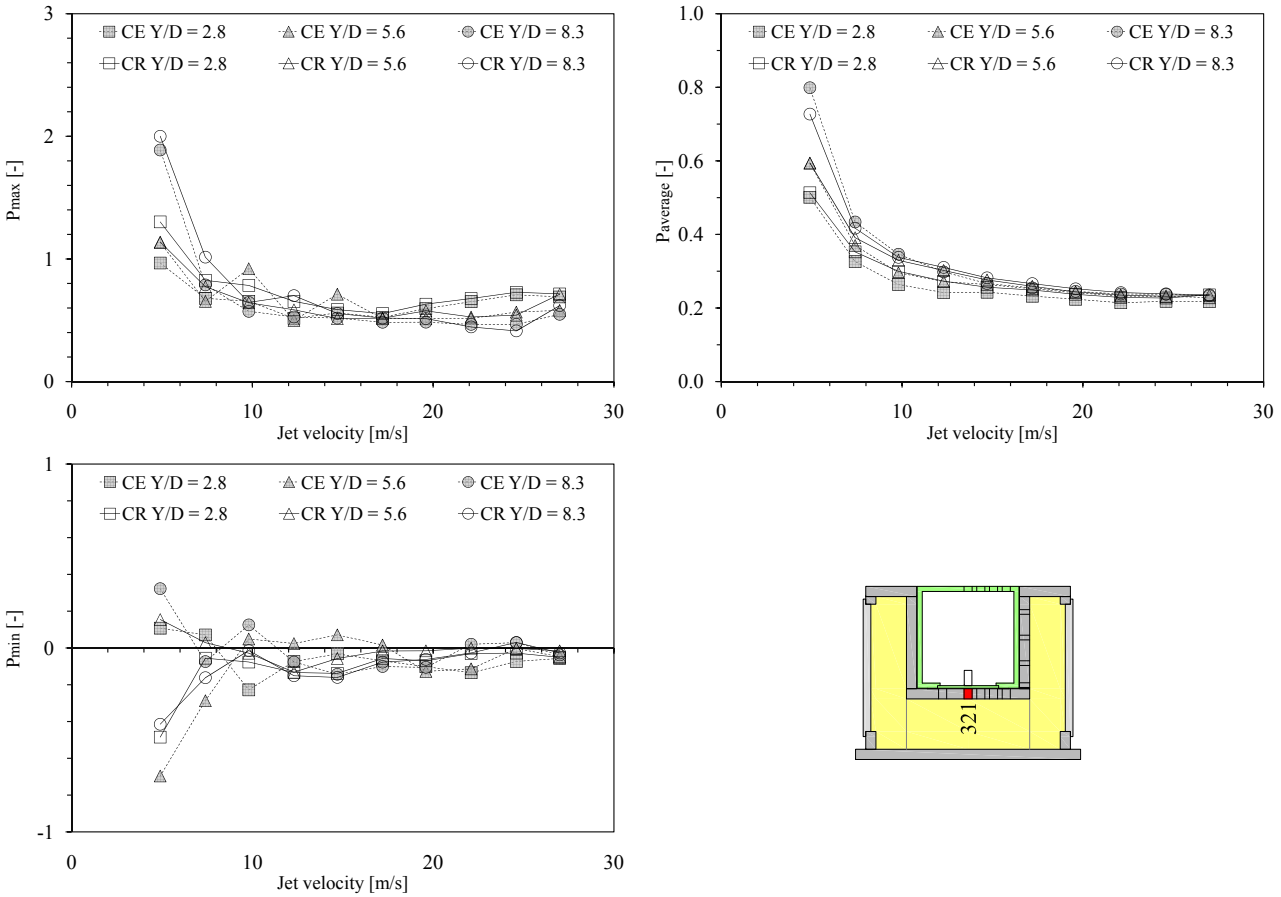

Figure 7.32: Influence of the type of lateral guide on the pressure field surrounding the block. Normalized pressure measured with transducer N° 321 for configurations CE and CR (jet impact on the block center) as a function of jet velocity (2.5-27.0 m/s) and Y/D ratio (2.8, 5.6 and 8.3). Maximum pressure (top left), mean pressure (top right), minimum pressure (bottom left) and transducer location (bottom right).

The influence of the friction was not observed for the previous configurations (jet impact on the block center, Chapter 7.3.2.1): maximum and mean displacements were almost the same. It is important to remark that the block is solicited in another way: when the jet impacts on the block center the block is loaded symmetrically and when the jet impacts on the right or left side is loaded asymmetrically. At the same time the jet loads directly the vertical fissure.

The jet impacting on the block center pushes the block inside the central cavity and maintains it in this position. These block solicitations generate small displacements (as has been observed in Chapter 7.3.2.1). The pressure distribution generated by the jet acts completely on the block upper face and the surface where the pressure could be negative is small (Figure 5.5). When the jet impacts asymmetrically on the block upper face (right or left side), it generates the same pressure distribution, but only half of this pressure acts directly on the block, the other half acts on the measurement box. In this case, the surface where the pressure could be negative is larger and the block could have larger vertical displacements, as has been observed (Figure 7.37). For these "large" displacements (some millimeters), the friction effect is more

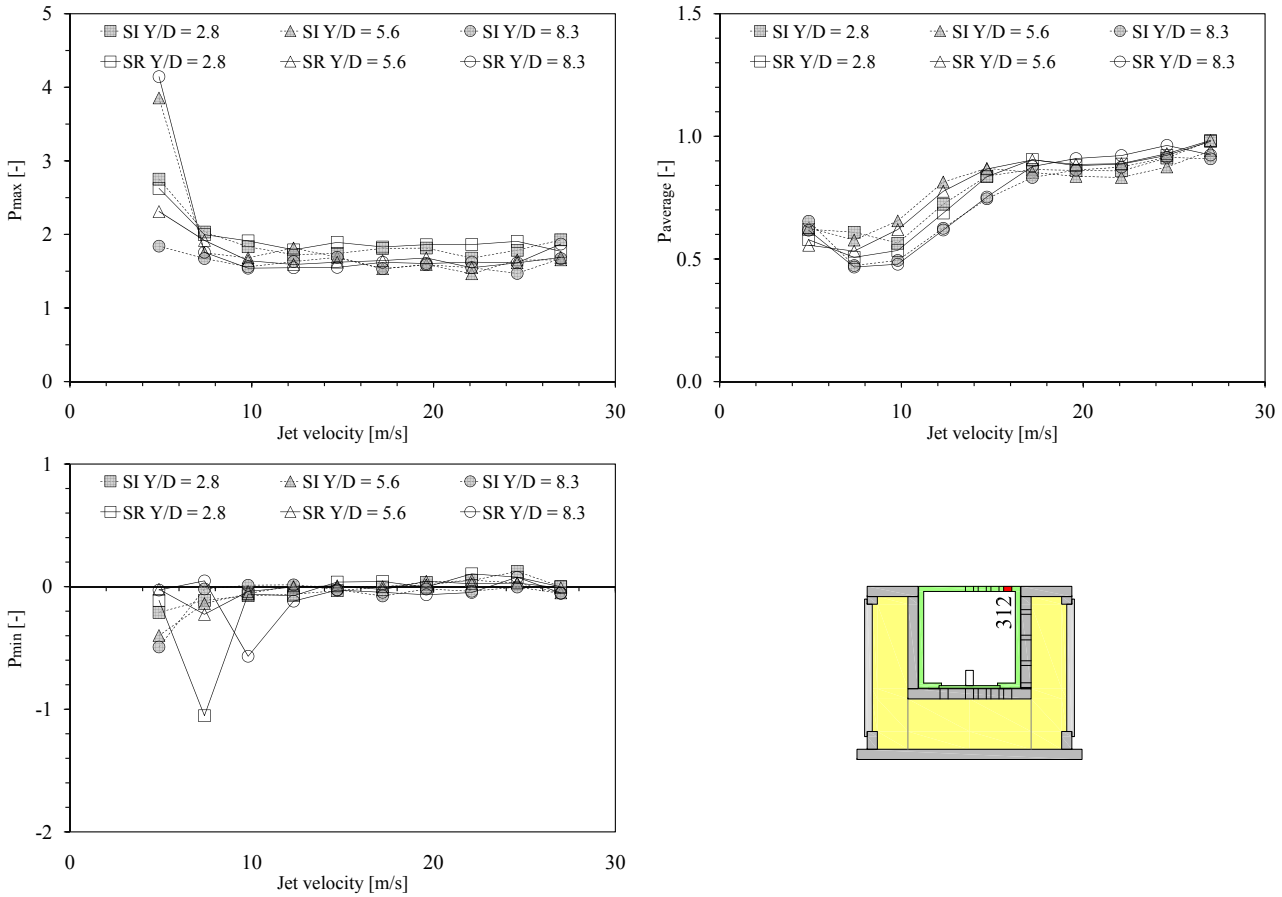

Figure 7.33: Influence of the type of lateral guide on the pressure field surrounding the block. Normalized pressure measured with transducer N° 312 for configurations SI and SR (jet impact on the block right hand side) as a function of jet velocity (2.5-27.0 m/s) and Y/D ratio (2.8, 5.6 and 8.3). Maximum pressure (top left), mean pressure (top right), minimum pressure (bottom left) and transducer location (bottom right).

important and this effect can be observed (configurations SI and SR).

The analysis of the vertical displacements show an influence of the type of lateral guide on the vertical displacements of block for configurations with the jet impact on the right side (SI and SR).The difference of the contact surface (between the block and the measurement box, friction force) modify the resulting vertical displacements. This effect was not observed for configurations with the jet impact on the block center (CE and CR).

The friction coefficient that has been measured for the two lateral guides are very close (Chapter 5.3.4: lateral guide with two contact points $\mu_k = 0.29$ and lateral guide with eight contact points $\mu_k = 0.32$). These coefficients cannot be the only reason for this large difference in the block response. It may be that the block is subjected to some small rotations inside the central cavity that influence the friction force acting on the block and they depend on the type of lateral guide fixed on the block. These rotations may affect the block displacements due to different block rotations, generated by the different type of lateral guides. For the two contact

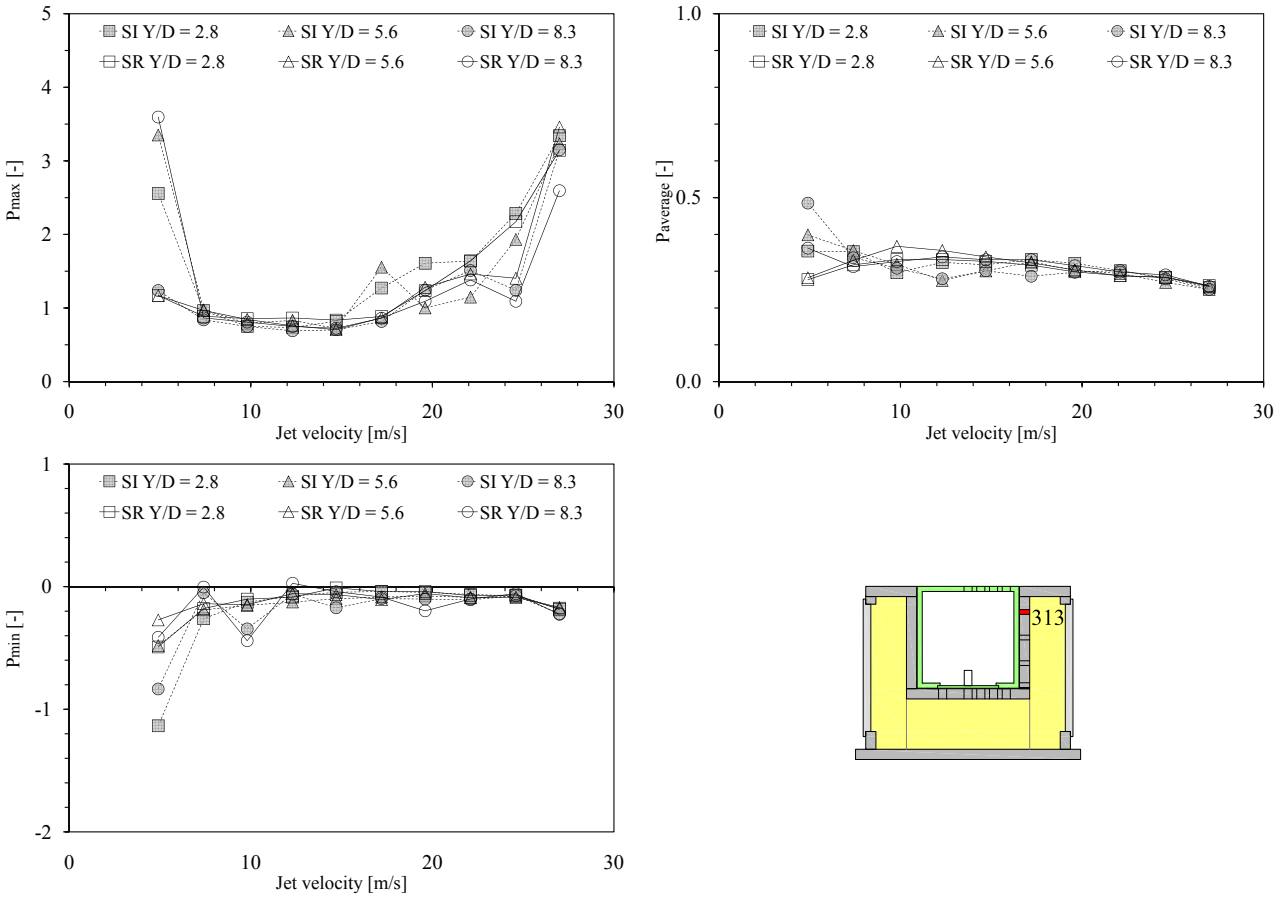

Figure 7.34: Influence of the type of lateral guide on the pressure field surrounding the block. Normalized pressure measured with transducer N° 312 for configurations SI and SR (jet impact on the block right hand side) as a function of jet velocity (2.5-27.0 m/s) and Y/D ratio (2.8, 5.6 and 8.3). Maximum pressure (top left), mean pressure (top right), minimum pressure (bottom left) and transducer location (bottom right).

points lateral guide the block may rotate differently than with the eight contact points lateral guide. These rotations may increase the friction force acting on the block and they can change the force intensity at each increment of time. If the block is loaded with the same conditions (water depth and jet velocity), these small rotations may be not the same and the influence onto the block displacement different (phenomenon not reproductive).

The geometry of the lateral guide fixed may influence the jet propagation inside the 3-dimensional fissure and then the displacements of block. The lateral guides with eight contact points generate different jet propagation inside the vertical fissure: they generate a kind of confinement inside the vertical fissure because the space where the water can flow horizontally is reduced related to the lateral guides with two contact points (Figure 4.3). Inside the vertical fissure, the water flow is guided better with the eight contact points lateral guides. The lateral guides with two contact points generate a better horizontal connection because the space between the two extremities of the lateral guide is free of contact points. However an influence of the different jet penetration inside the fissure was not observed for the four configurations.

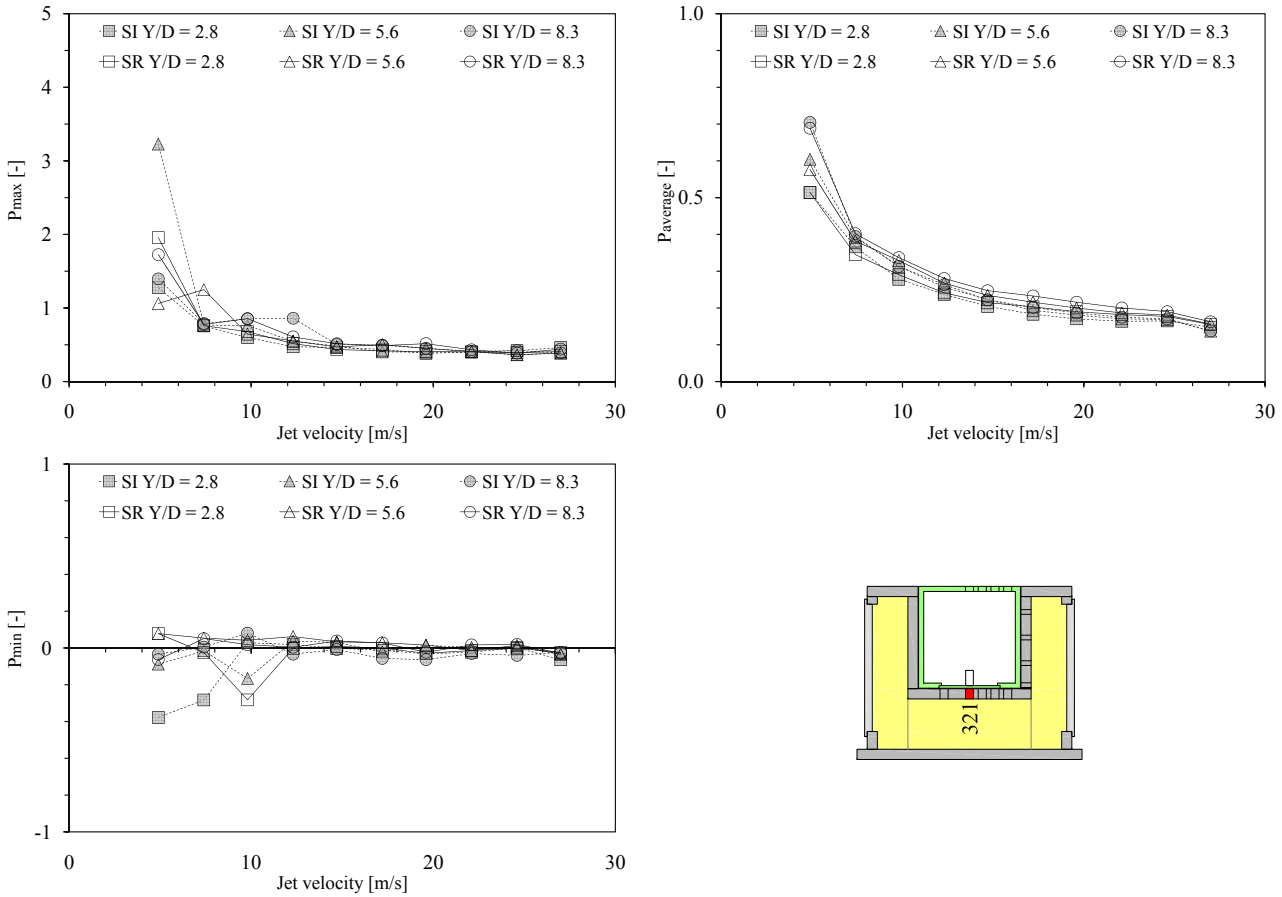

Figure 7.35: Influence of the type of lateral guide on the pressure field surrounding the block. Normalized pressure measured with transducer N° 312 for configurations SI and SR (jet impact on the block right hand side) as a function of jet velocity (2.5-27.0 m/s) and Y/D ratio (2.8, 5.6 and 8.3). Maximum pressure (top left), mean pressure (top right), minimum pressure (bottom left) and transducer location (bottom right).

7.3.3 Power Spectral Density

7.3.3.1 Jet impact on the block center with two (CE) and eight (CR) contact points lateral guides

Figures 7.38, 7.39 and 7.40 show the power spectral density comparison between two configurations. In Figures 7.38, 7.39 and 7.40 the continuous line correspond to the configuration equipped with lateral guides having two contact points (CE) and the dashed line correspond to the configuration equipped with lateral guides having eight contact points (CR).

Both configurations show the same behavior for all transducers (as well for the transducer that are not plotted in this section). Observations that have been made in Chapter 6.2.5 for configuration CR are valid as well for configuration CE.

As observed before, the power spectral density behavior could be separated in two groups: one for transducers situated at the plunge pool bottom (N°s 309 to 312) and another one for transducers situated inside the 3-dimensional fissure (N°s 313 to 321). These observations are valid for core, transition and developed jets. The energy is related to the pressure field

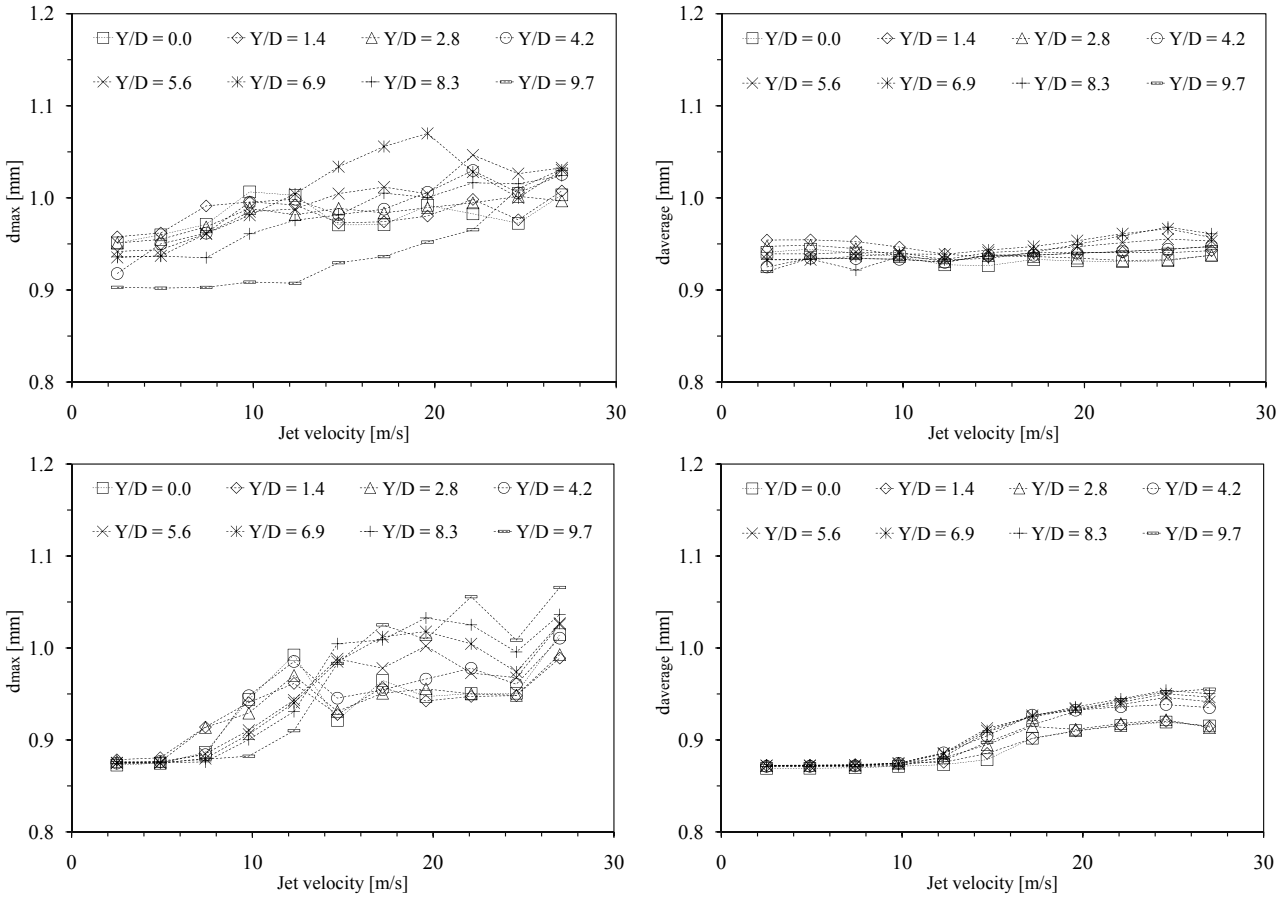

Figure 7.36: Influence of the type of lateral guide on the displacements of block for configurations CE and CR (jet impact on the block center) as a function of jet velocity (2.5-27.0 m/s) and Y/D ratio (0-9.7). Maximum (top left) and mean (top right) displacements for configuration CE, maximum (bottom left) and mean (bottom right) displacements for configuration CR. The block initial position corresponds to a distance of ∼0.85 mm.

surrounding the block.

The PSD signal for the pressure transducers fixed on the block looks quite similar for all jet velocities. The energy per frequency decreases slowly with a slope of approximately -2/3. For higher frequencies ($f > 10$ Hz) the spectral content decreases with a -1 slope.

The pressure transducers situated inside the 3-dimensional fissure (along the vertical fissure and underneath the block) show a different behavior. The energy per frequency is lower than at the plunge pool bottom for the same jet velocity, as can be expected. Most part of the energy is dissipated in the plunge pool. With an increase of frequencies, two zones can be distinguished: a first zone up to 8-10 Hz and a second zone above 8-10 Hz. In the first zone, the energy decreases slowly with a slope situated between -1/3 and -2/3. In the second zone, two different peaks may be detected in the PSD signal: the first peak between 10-20 and 80-100 Hz and the second peak between 80-100 and 200-300 Hz. For small jet velocities, the first peak appears but not the second. When the velocity increases, the first peak disappear and the second peak appear. The two peaks appear in the PSD signal for core, transition and developed jet. The second peak (at higher frequency) is stronger than the first peak. None of the two peaks appear

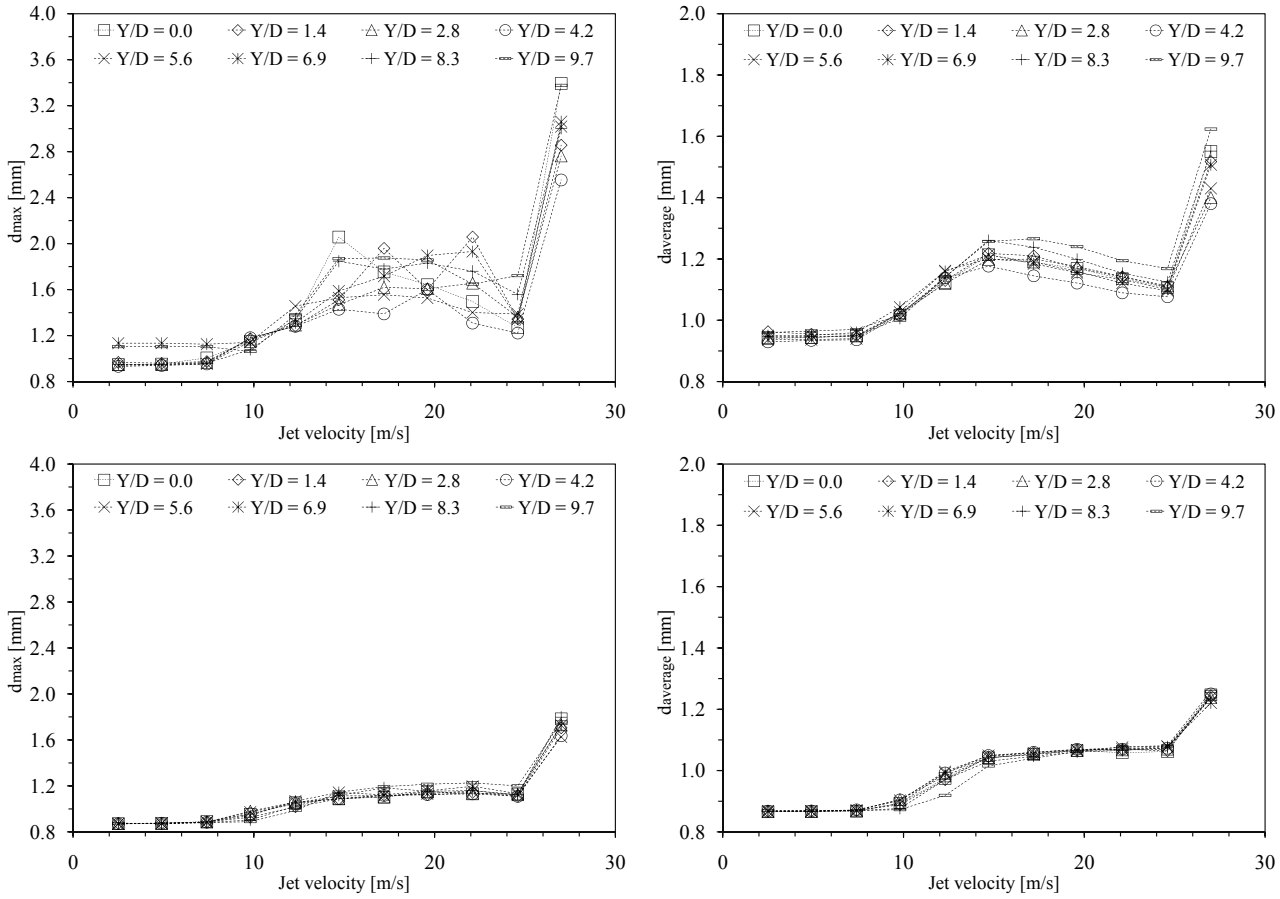

Figure 7.37: Influence of the type of lateral guide on the displacements of block for configurations SI and SR (jet impact on the block right hand side) as a function of jet velocity (2.5-27.0 m/s) and Y/D ratio (0-9.7). Maximum (top left) and mean (top right) displacements for configuration SI, maximum (bottom left) and mean (bottom right) displacements for configuration SR. The block initial position corresponds to a distance of ∼0.85 mm.

in the PSD of the surface pressure signal as such they are not present at the plunge pool bottom.

The PSD signal for transducers situated on the block upper face (N° 310) is practically the same for both configurations. The PSD signals for each jet velocity are superposed with very small differences (Figure 7.38).

Inside the 3-dimensional fissure, some differences in the PSD signal have been observed (transducers N° 313 and N° 321). These small differences decrease with an increase of frequencies and jet velocity (Figures 7.39 and 7.40). For frequencies lower than 80-100 Hz normally is the configuration equipped with lateral guides having eight contact points that has more energy per frequencies. These differences in the PSD signal for the two configurations decrease from the fissure entrance to underneath the block.

On the block upper face, the analysis of the power spectral density does not show an influence of the type of lateral guide on the PSD signal, but inside the fissure some difference appears for frequencies lower than 80-100 Hz. These differences decrease with an increase of the jet velocity and distance from the plunge pool bottom.

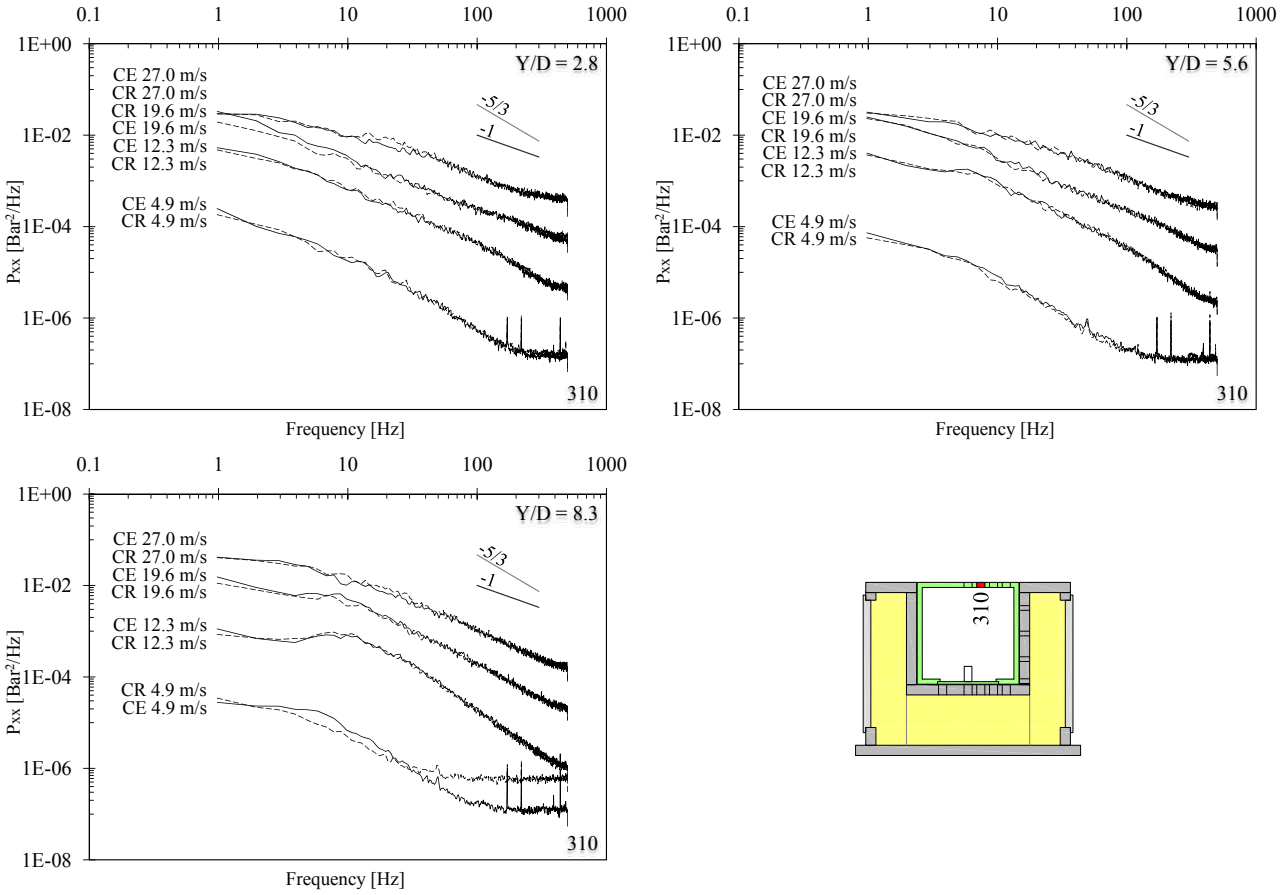

Figure 7.38: Influence of the type of lateral guide on the non-dimensional spectral content (PSD) computed for configurations with the jet impact on the block center CE (continuous line) and CR (dashed line) as a function of jet velocity (4.9, 12.3, 19.6 and 27.0 m/s) and Y/D ratio (2.8, 5.6 and 8.3). Transducer N° 310. Core jet (top left), transition jet (top right), developed jet (bottom left) and transducer location (bottom right).

7.3.3.2 Jet impact on the block right side with two (SI) and eight (SR) contact points lateral guides

Figures 7.41, 7.42 and 7.43 show the power spectral comparison for the same water depths and jet velocities than the previous Chapter 7.3.3.1. Only the transducer situated on the block upper face has been changed, to be also located at 25 mm from the stagnation point (N° 312). In Figures 7.41, 7.42 and 7.43 the continuous line correspond to the configuration equipped with lateral guides having two contact points (SI) and the dashed line correspond to the configuration equipped with lateral guides having eight contact points (SR).

The two configurations show the same behavior for all transducers located around the block. The observations that have been made in Chapter 6.3.5 for configuration SR are valid as well for configuration SI.

As observed for configurations with the jet impact on the block center, the power spectral density shows a different behavior between plunge pool bottom and 3-dimensional fissure.

At the plunge bottom, the energy decreases slowly with a different slope for frequency smaller than 10 Hz (approximately -2/3 slope) and above 10 Hz (-1 slope). Inside the fissure,

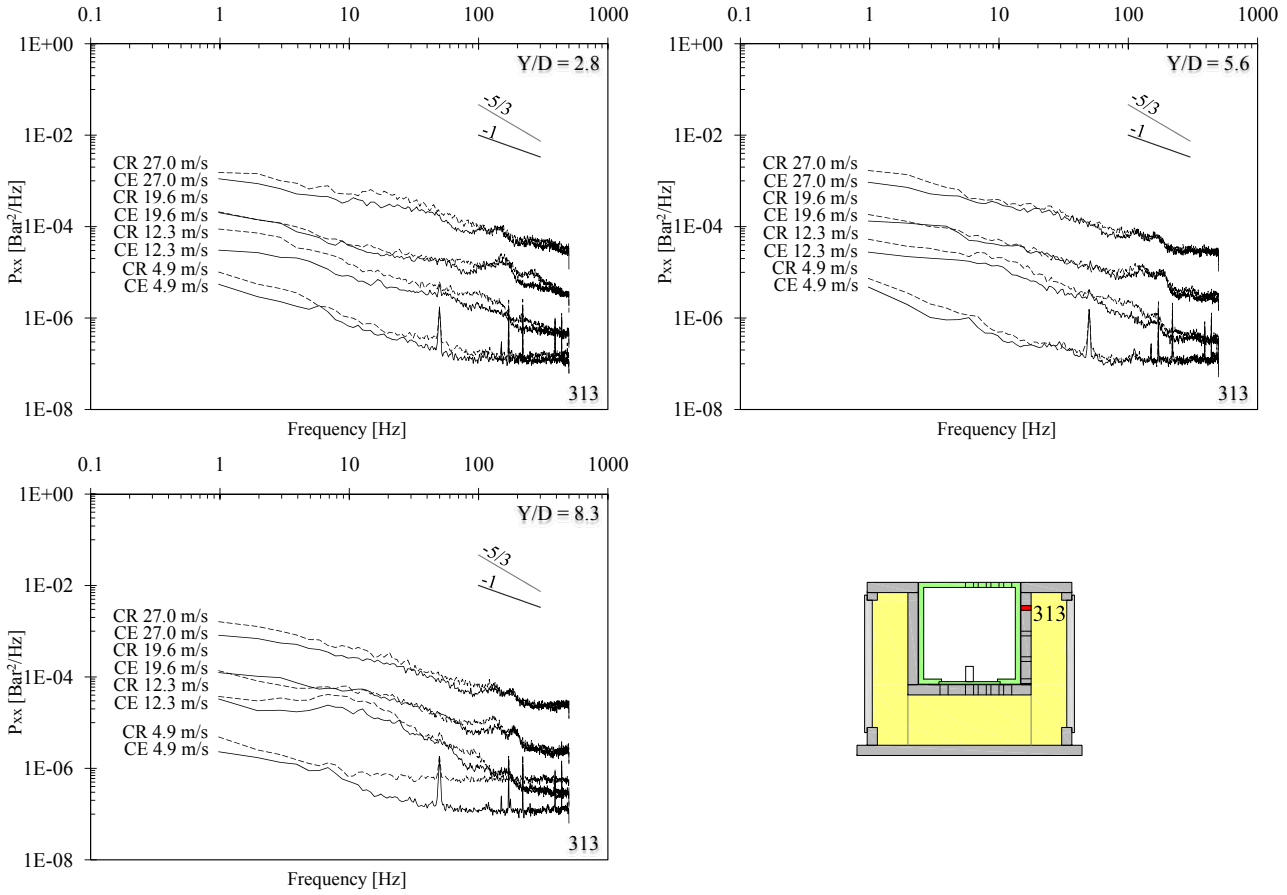

Figure 7.39: Influence of the type of lateral guide on the non-dimensional spectral content (PSD) computed for configurations with the jet impact on the block center CE (continuous line) and CR (dashed line) as a function of jet velocity (4.9, 12.3, 19.6 and 27.0 m/s) and Y/D ratio (2.8, 5.6 and 8.3). Transducer N° 313. Core jet (top left), transition jet (top right), developed jet (bottom left) and transducer location (bottom right).

the energy per frequency is lower than at the plunge pool bottom for the same jet velocity. With an increase of frequency, the two zones can be distinguished: a first zone up to 8-10 Hz and a second zone above 8-10 Hz. In the first zone, the energy decreases slowly with a slope situated between -1/3 and -2/3 and in the second zone, two different peaks may be detected. The two peaks appear in the PSD signal for core, transition and developed jet. The first peak (at low frequency) is stronger than the second peak. For configuration with the jet impact on the block center (CE and CR) the second peak was the stronger.

As has been observed for configurations with the jet impact on the block center, the PSD signal for the transducer situated on the block upper face (N° 312) is practically the same for both configurations. The PSD signals for each jet velocity are superposed with very small differences (Figure 7.38).

Inside the 3-dimensional fissure, some differences in the PSD signal have been observed (Figures 7.42 and 7.43). Along the vertical fissure is the configuration SR that show more energy for frequencies lower than 50-80 Hz, however underneath the block is configuration SI. That may be related to the different block responses observed in Chapter 7.3.2.

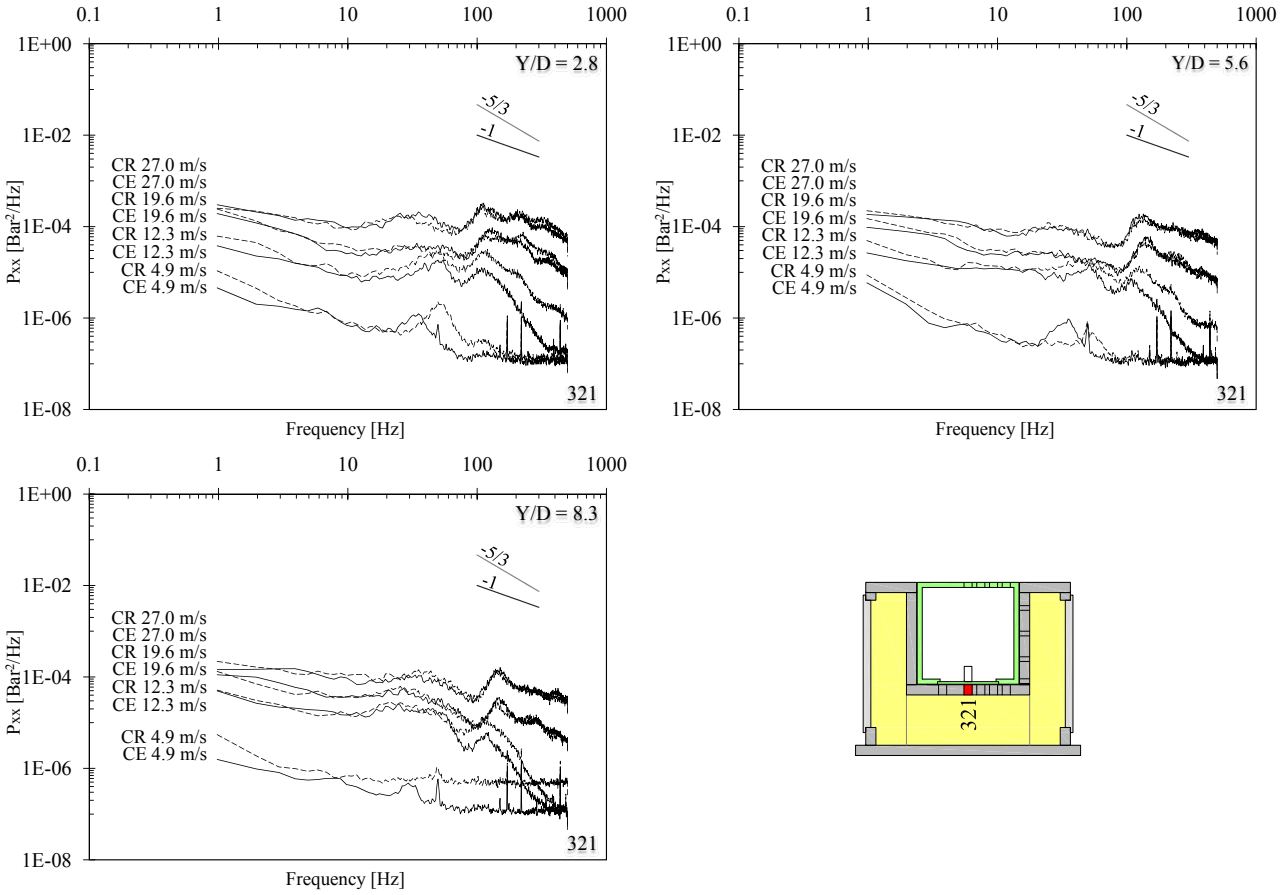

Figure 7.40: Influence of the type of lateral guide on the non-dimensional spectral content (PSD) computed for configurations with the jet impact on the block center CE (continuous line) and CR (dashed line) as a function of jet velocity (4.9, 12.3, 19.6 and 27.0 m/s) and Y/D ratio (2.8, 5.6 and 8.3). Transducer N° 321. Core jet (top left), transition jet (top right), developed jet (bottom left) and transducer location (bottom right).

As observed for the jet impacting on the block center, at the plunge pool bottom the power spectral density does not show an influence of the type of lateral guides. Inside the fissure some difference appears for frequencies lower than 50-80 Hz. Along the vertical fissure is the configuration with the two contact points lateral guides that show more energy per frequencies whereas underneath the block is the other type of lateral guides that shows this phenomenon.

7.3.4 Dynamic block impulsion

The dynamic block impulsion for both configurations has been analyzed in Chapter 5.4.

7.3.5 Conclusions

The analyses of the pressure field (surrounding the block) show that the lateral guides (with two or eight contact points) did not affect the pressures acting around the block for both jet impacts (jet impact on the block center and on the block right side). The evolution of maximum, mean and minimum pressures, as a function of jet velocity, is almost the same for both

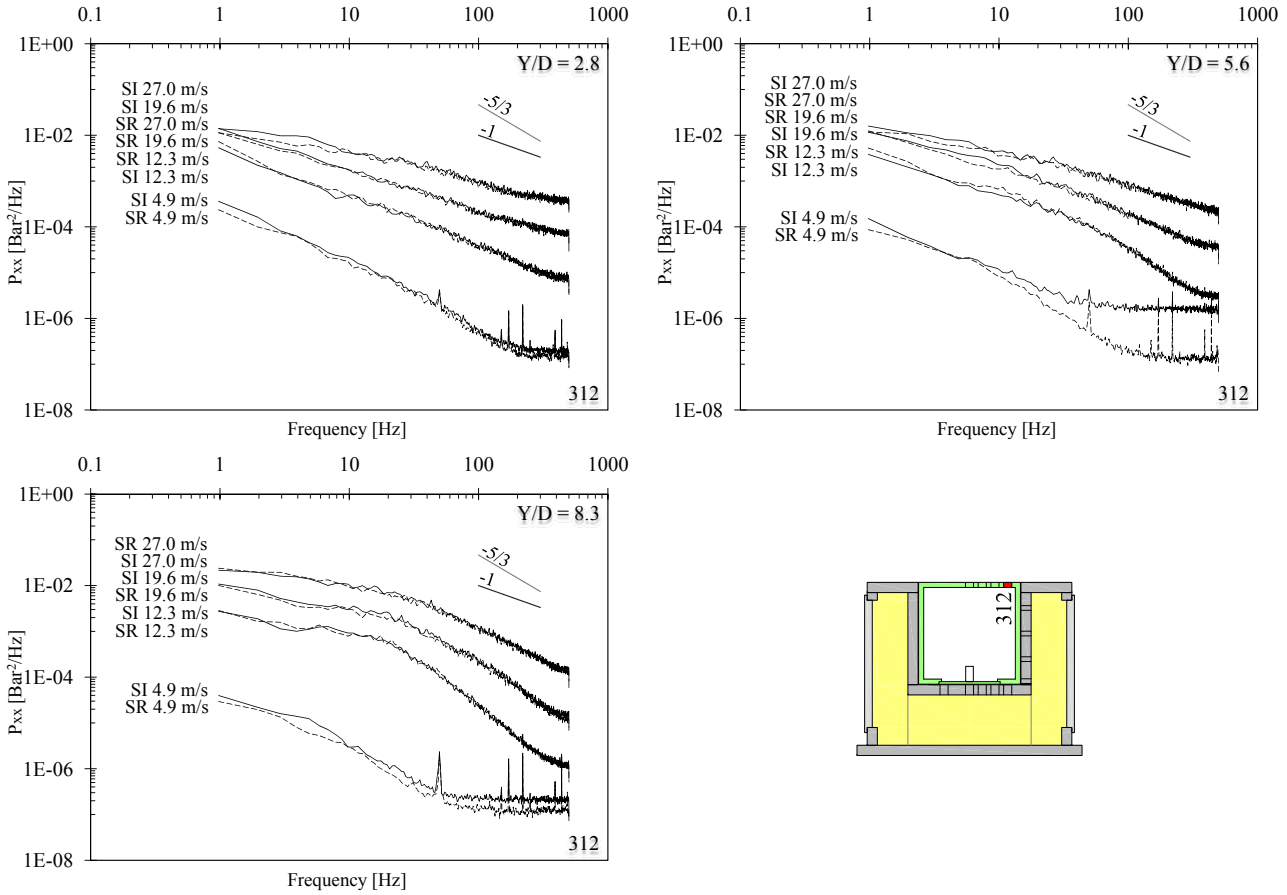

Figure 7.41: Influence of the type of lateral guide on the non-dimensional spectral content (PSD) computed for configurations with the jet impact on the block right side SI (continuous line) and SR (dashed line) as a function of jet velocity (4.9, 12.3, 19.6 and 27.0 m/s) and Y/D ratio (2.8, 5.6 and 8.3). Transducer N° 312. Core jet (top left), transition jet (top right), developed jet (bottom left) and transducer location (bottom right).

configurations. Some small pressure differences could be observed, but could be neglected due to their small order of magnitude.

The analysis of the block response show an influence of the type of lateral guide on the block displacements for configurations with the jet impact on the block right side (SI and SR). The two types of lateral guides differ in the friction surface between the block and the central cavity walls. The friction force computed for both configurations is very close due to the small difference in the friction coefficient used to compute these forces. For this jet impact (block right side), the two configurations show a large difference in the block responses that may be related to these friction coefficients, but is not the case for configurations with the jet impacting on the block center. These coefficients cannot be the only reason for this large difference in the block response. It may be that the block is subjected to some small rotations inside the central cavity that influence the friction force acting on the block and they depend on the type of lateral guide fixed on the block. These rotations may affect the block displacement due to a different block rotations generated by different lateral guides and jet impact position:

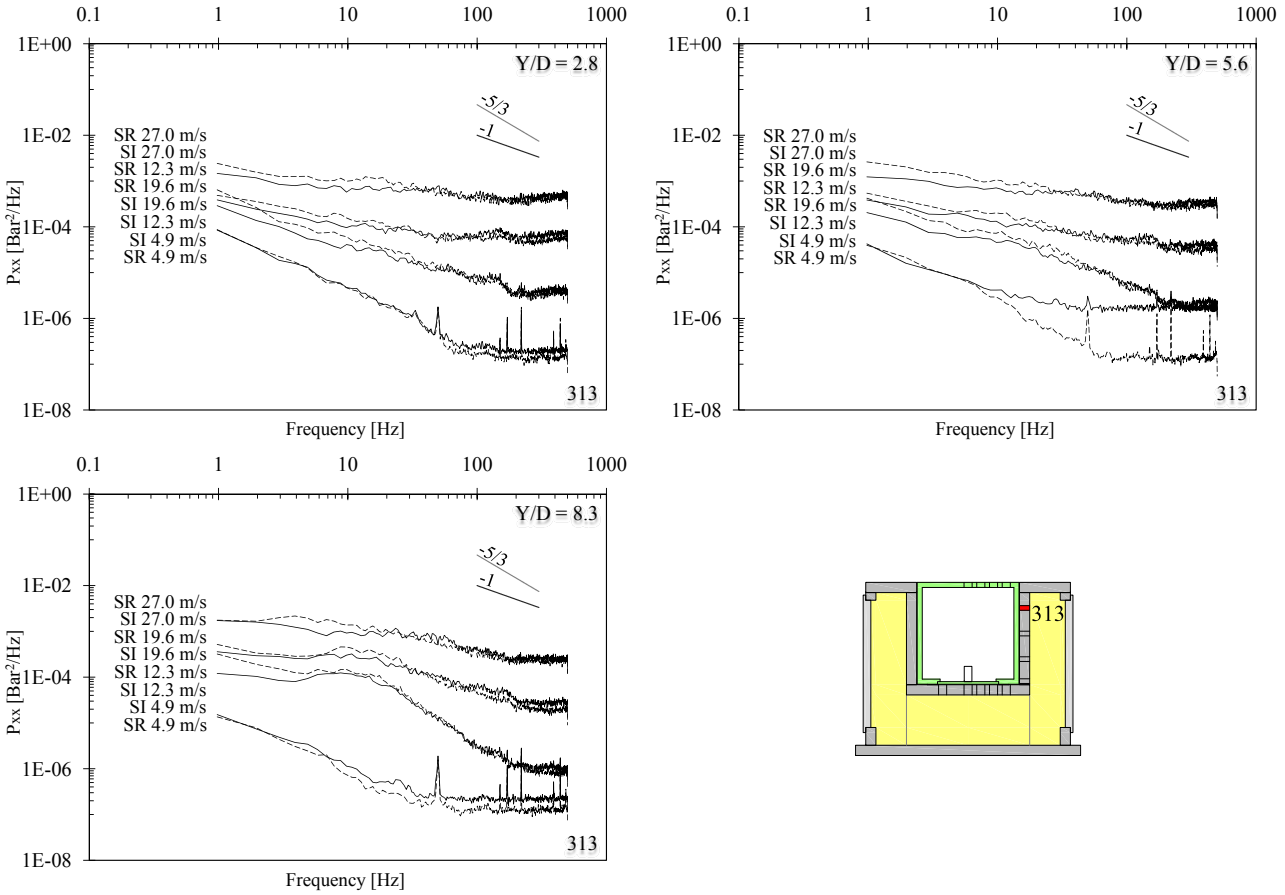

Figure 7.42: Influence of the type of lateral guide on the non-dimensional spectral content (PSD) computed for configurations with the jet impact on the block right side SI (continuous line) and SR (dashed line) as a function of jet velocity (4.9, 12.3, 19.6 and 27.0 m/s) and Y/D ratio (2.8, 5.6 and 8.3). Transducer N° 313. Core jet (top left), transition jet (top right), developed jet (bottom left) and transducer location (bottom right).

for the two contact points lateral guides the block may rotate differently than for the block equipped with the eight contact points lateral guides. An influence of the jet penetration inside the fissure generated by the different lateral guides was not observed for the four configurations.

The power spectral density (PSD) signal for the transducers situated on the block upper face is practically the same for the four configurations. The two signals are practically superposed for all jet velocities. Inside the 3-dimensional fissure, some differences in the PSD signal have been observed. For all configurations these small differences decrease with an increase of frequencies and jet velocity. Along the vertical fissure are always the configurations equipped with lateral guides having eight contact points that show the larger energy content for frequencies lower than 80-100 Hz. Whereas underneath the block for the jet impact on the block center is the configuration with the eight contact points lateral guides and for the jet impact on the block right side is the configuration with the two contact points lateral guides. That may be related to the different block responses observed for configurations with jet impact on the right side. These differences in the PSD signal decrease from the fissure entrance to underneath the block

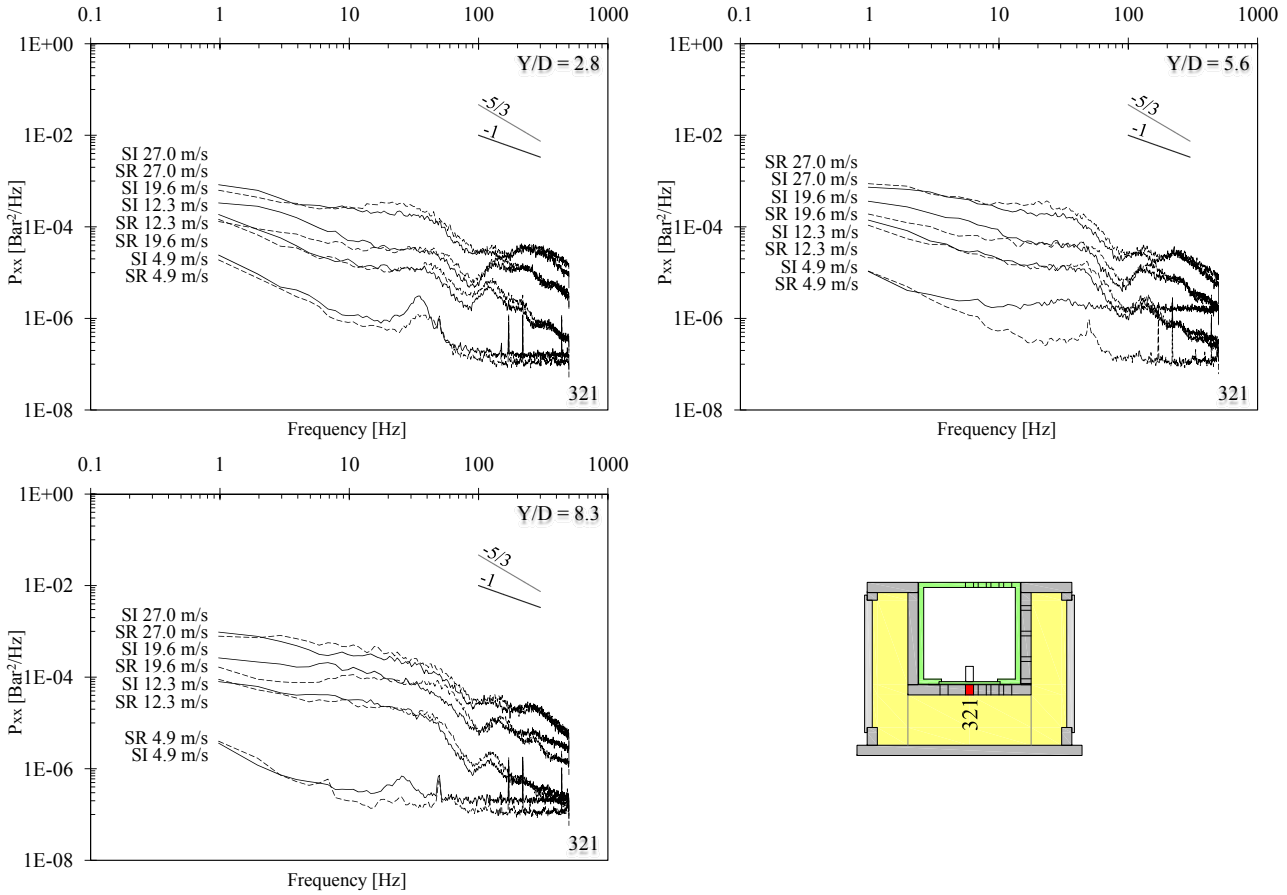

Figure 7.43: Influence of the type of lateral guide on the non-dimensional spectral content (PSD) computed for configurations with the jet impact on the block right side SI (continuous line) and SR (dashed line) as a function of jet velocity (4.9, 12.3, 19.6 and 27.0 m/s) and Y/D ratio (2.8, 5.6 and 8.3). Transducer N° 321. Core jet (top left), transition jet (top right), developed jet (bottom left) and transducer location (bottom right).

7.3.6 Remarks

To have a thorough evaluation of the influence of the type of lateral guides, other tests with the two contact point lateral guides may be performed. They have to be analyzed using the test almost performed during this research project. The further configurations may be a jet impact on the block corner and a jet impact between the center and the corner of the block with the transducers located radially outwards from the stagnation point.

7.4 Influence of the degree of freedom of the block

To investigate the influence of the degree of freedom of the block on the pressure field acting inside the 3-dimensional fissure, a system to fix the block has been developed. The block was fixed inside the central cavity of the measurement box using two rigid steel profiles. Those have been designed to reduce their influence on the water flow near the plunge pool bottom. This system is explained in Chapter 4.2.1.2 and is illustrated by Figures 4.2 and 4.4 on the left.

Three configurations of jet impact position on the block have been analyzed for two different degrees of freedom: block free to move along the vertical axis and block fixed. For all configurations the block was equipped with lateral guides having eight contact points.

Jet impact position on the block center:

- Block *free to move* (CR);
- Block *fixed* (CR_F).

Jet impact position on the block right hand side:

- Block *free to move* (SR);
- Block *fixed* (SR_F).

Jet impact position on the block corner:

- Block *free to move* (CN);
- Block *fixed* (CN_F).

The main characteristics of the three configurations are described in Chapter 4.3.

The detailed results are explained in Chapters 6.2, 6.3 and 6.4 for configurations with the block free to move (CR, SR and CN).

Three transducers have been used to illustrate the influence of the degree of freedom of the block. The transducers were the same that have been used to analyze the influence of the type of lateral guide (Chapter 7.3): transducer N° 310 for configurations CR and CR_F and transducer N° 312 for configurations SR, SR_F, CN and CN_F (both transducers are located at 25 mm from the stagnation point). Inside the 3-dimensional fissure, two transducers have been illustrated: transducer N° 313 at 50 mm from the plunge pool bottom along the vertical fissure and transducer N° 321 situated underneath the block on the block center (Figure 4.8).

The results are illustrated for a core (Y/D = 2.8), a transition (Y/D = 5.6) and a developed jet (Y/D = 8.3) with four jet velocities (4.9, 12.3, 19.6 and 27.0 m/s).

7.4.1 Pressure field surrounding the block

7.4.1.1 Jet impact on the block center with the block free to move (CR) and the block fixed (CR_F)

Figures 7.44, 7.45 and 7.46 show the influence of the degree of freedom on the pressure field for configuration with the jet impact on the block center (CR and CR_F).

On the block upper face (transducer N° 310) the influence of the block degree of freedom can be neglected. The pressures recorded for different degrees of freedom are almost similar. Core jets (Y/D $<$ 4) show some differences for jet velocities larger than 14.7 m/s. These pressures differences (for maximum pressure) may be generated by some pressure fluctuations acting on the plunge pool bottom. The system developed to fix the block may influence the flow conditions near the bottom on deflecting the flow, although they have been designed to minimize their influence on the flow. This flow deflection may modify the behavior of the large eddies that are generated inside the plunge pool (interaction between impinging jet, bottom flow and water cushion presents in the plunge pool). At the same time, the oscillating hydraulic jump moving from the plunge pool wall to the block center may be affect by this modification of the flow conditions inside the plunge pool. This change of the flow in the plunge pool may generate these pressures differences.

Mean and minimum pressures show the same evolution and similar values along the whole range of jet velocity.

Similar behavior has been observed for the other transducers located on the block upper face.

Transducer N° 313, located inside the vertical fissure, shows a different behavior as a function of the degree of freedom: for jet velocities larger than 12.3-14.7 m/s, the configuration with the fixed block shows higher pressure values (maximum, mean and minimum) than the configuration with the block free to move. Developed jets (Y/D $>$ 6) generate the most extreme pressure values (maximum, mean and minimum). This observation allows classifying the jets as a function of the water depth: the recorded pressures decrease with a decrease of the water depth (developed jet, transition jet and core jet). The recorded pressures are influenced by the jet solicitations and by the water depth in the plunge pool.

Underneath the block (transducer N° 321), the pressure evolution is similar to transducer N° 313 at the fissure entrance: the pressure increases as a function of jet velocity (maximum and mean pressure) and the pressure differences between both degrees of freedom reach large values ($\sim$1 Bar). For jet velocities larger than 12.3-14.7 m/s, the configuration with the fixed block shows higher pressure values than the configuration with the free block. Inside the fissure, the mean pressure shows a difference of approximately 0.2-0.3 Bar for the largest jet velocity (27.0 m/s).

The system installed to fix the block generates this different response of the fissure (different pressure field).The pressures acting underneath the block cannot be transmitted to the block to generate a vertical movement (the energy is transformed from pressure to vertical displacement).

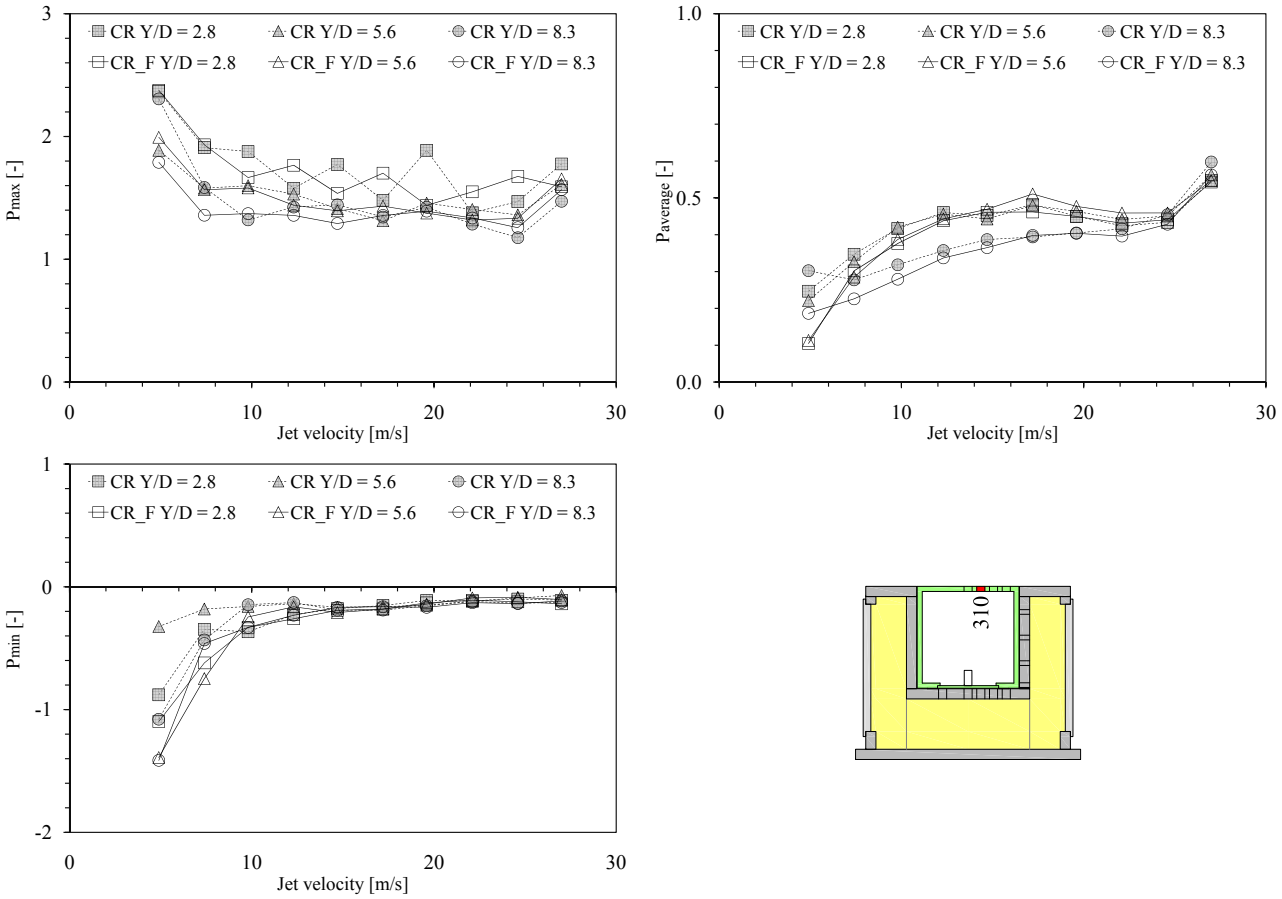

Figure 7.44: Influence of the degree of freedom of the block. Normalized pressure measured with transducer N° 310 for configurations CR (block free to move) and CR_F (block fixed) as a function of jet velocity (2.5-27.0 m/s) and Y/D ratio (2.8, 5.6 and 8.3). Maximum pressure (top left), mean pressure (top right), minimum pressure (bottom left) and transducer location (bottom right).

The block movements are stopped and the pressure is obliged to increase inside the surrounding fissure. These pressures, acting around the block, generate a force that tries to eject the block outside the central cavity. This force cannot produce a vertical movement and is transmitted to the measurement box via the system fixing the block in the central cavity. This system is rigid enough to prevent any deformation and as any vertical movements. Hence, the fixed block is submitted a higher pressures solicitations than the free block.

7.4.1.2 Jet impact on the block right side with the block free to move (SR) and the block fixed (SR_F)

Figures 7.47, 7.48 and 7.49 show the influence of the degree of freedom on the pressure field for configuration with the jet impact on the block right side (SR and SR_F).

As observed for the previous configuration, on the block upper face (transducer N° 312) the pressures have a similar behavior for both degrees of freedom: the influence of the degree of freedom could be neglected and the pressures recorded are similar. Only maximum pressures show some differences that could be generated by some pressure extreme fluctuations acting

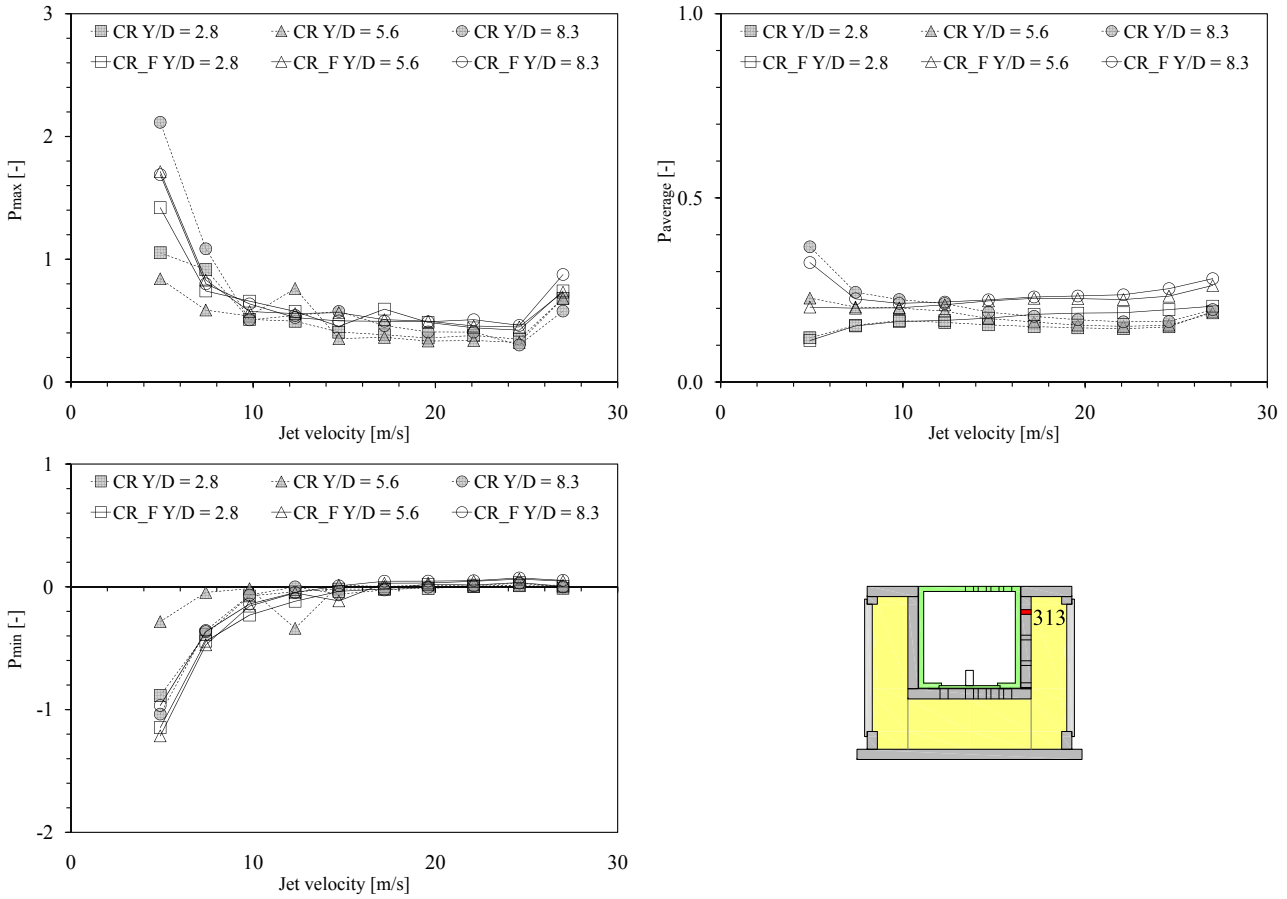

Figure 7.45: Influence of the degree of freedom of the block. Normalized pressure measured with transducer N° 313 for configurations CR (block free to move) and CR_F (block fixed) as a function of jet velocity (2.5-27.0 m/s) and Y/D ratio (2.8, 5.6 and 8.3). Maximum pressure (top left), mean pressure (top right), minimum pressure (bottom left) and transducer location (bottom right).

on the block. As explained before, the system developed to fix the block may influence the flow inside the plunge pool and, as consequences, generated these pressure fluctuations at the bottom.

Along the vertical fissure (transducer N° 313) the difference between the two degrees of freedom is more visible: mean pressures show clearly a different evolution as a function of the jet velocity (mean values for both degrees of freedom increase but with a different trend). The configuration with the fixed block shows the larger pressure values. Maximum and minimum pressures are influence by the jet position impact (directly on the fissure vertical axis) that generates some pressure peaks (positive and negative) near the fissure entrance. As explained before, this peak may be related at a "cavitation" phenomenon or at a compression-decompression phenomenon of the air bubbles present into the water that appears near the fissures entrance and generates these extreme pressures peaks. Maximum pressures are smaller for the configuration with fixed block.

Underneath the block (transducer N° 321), the configuration with fixed block shows the highest pressures (maximum, mean and minimum) for jet velocities above 9.8-12.3 m/s. For a

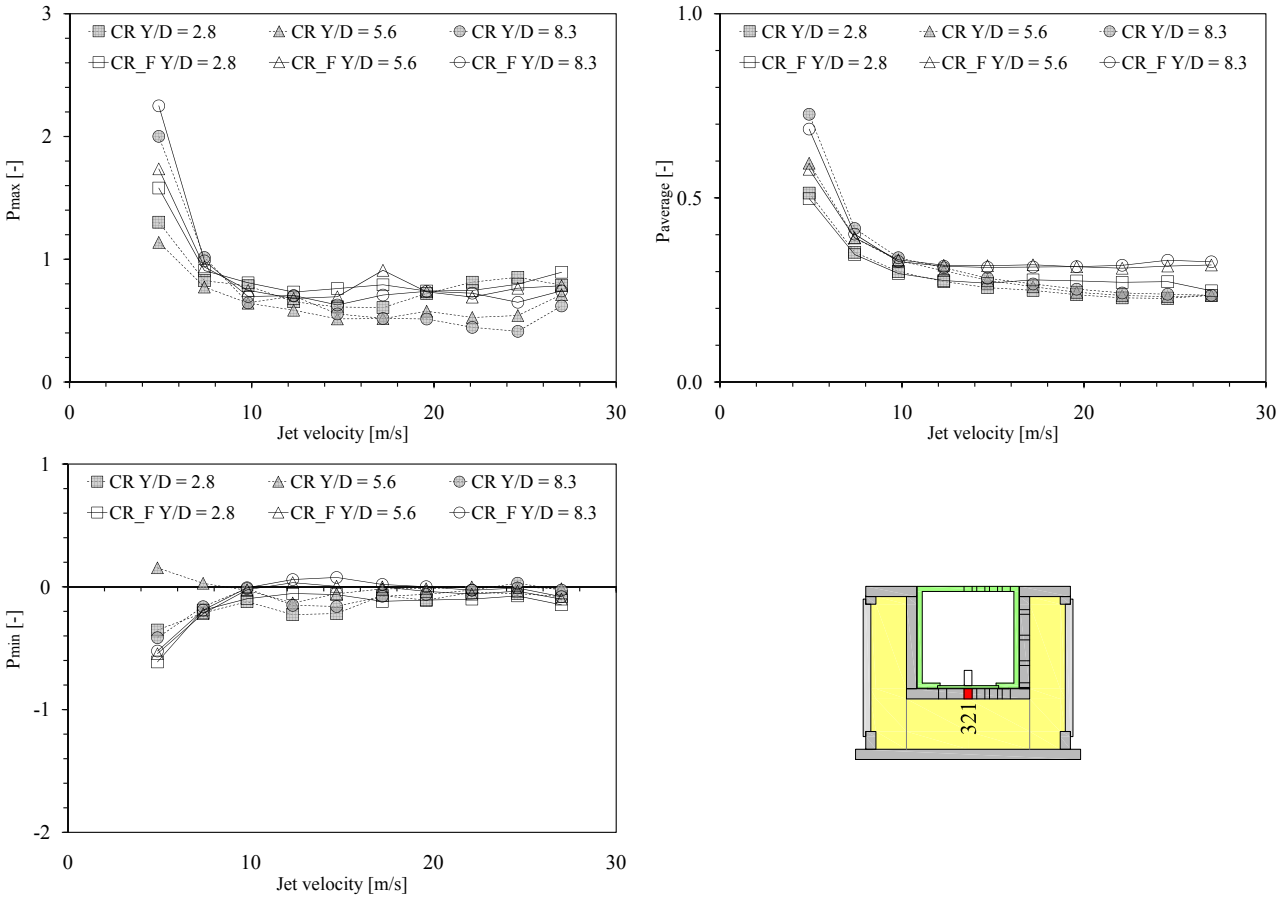

Figure 7.46: Influence of the degree of freedom of the block. Normalized pressure measured with transducer N° 321 for configurations CR (block free to move) and CR_F (block fixed) as a function of jet velocity (2.5-27.0 m/s) and Y/D ratio (2.8, 5.6 and 8.3). Maximum pressure (top left), mean pressure (top right), minimum pressure (bottom left) and transducer location (bottom right).

jet velocity of 27.0 m/s, this pressure difference reaches ∼1.5 Bar and for mean pressure reaches ∼0.8 Bar. The jet impact on the vertical fissure axis (SR) increases the pressures acting inside the fissure related to the configuration with the jet impacting on the block center (CR).

7.4.1.3 Jet impact on the block corner with the block free to move (CN) and the block fixed (CN_F)

Figures 7.50, 7.51 and 7.52 show the influence of the degree of freedom on the pressure field for configuration with the jet impact on the block corner (CN and CN_F).

Due to the block larger movements, the configuration with the block free to move (CN) has been tested with a maximum jet velocity of 19.6 m/s and the configuration with the fixed block (CN_F) has been tested up to the largest jet velocity (27.0 m/s)

On the block upper face (transducer N° 312) until the jet velocity reaches 19.6 m/s, the measured pressures (maximum, mean and minimum) are similar and follow the same trend for both degrees of freedom. For jet velocities above 19.6 m/s, only the pressures measurements for the configuration with fixed block are available. As observed before, the influence of the

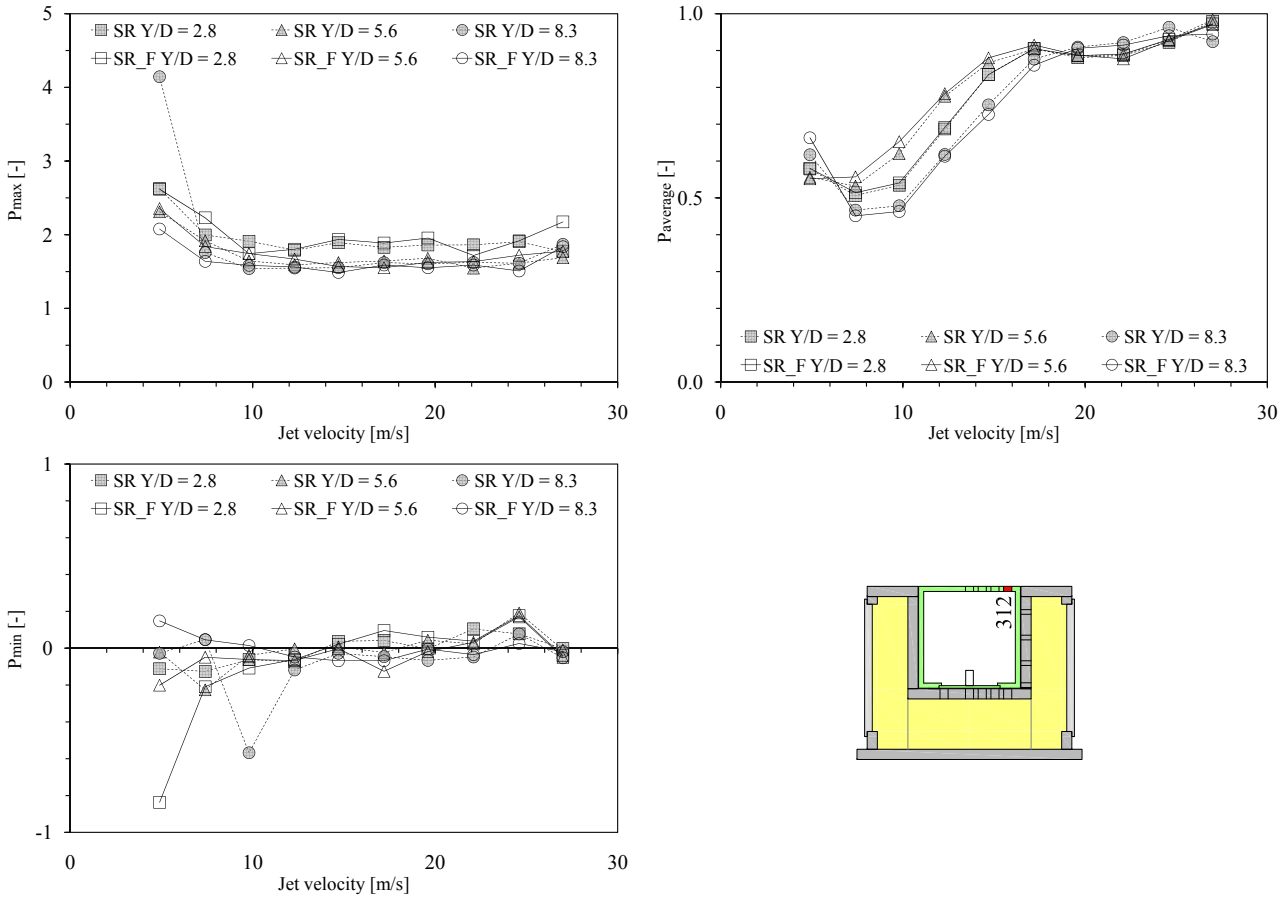

Figure 7.47: Influence of the degree of freedom of the block. Normalized pressure measured with transducer N° 312 for configurations SR (block free to move) and SR_F (block fixed) as a function of jet velocity (2.5-27.0 m/s) and Y/D ratio (2.8, 5.6 and 8.3). Maximum pressure (top left), mean pressure (top right), minimum pressure (bottom left) and transducer location (bottom right).

block degree of freedom could be neglected on the block upper face.

As observed for the two previous configurations, along the vertical fissure (transducer N° 313), the configuration with fixed block shows larger maximum and mean pressures (for jet velocities above 9.8 m/s). Minimum pressures show same trend and same values for both degrees of freedom.

Underneath the block (transducer N° 321), the configuration with the fixed block show a stronger pressure increase. Extrapolating the pressure evolution (for the block free to move), maximum pressures may show a difference of ∼2-2.5 Bar for the largest jet velocity and mean values may show a difference of ∼0.8 Bar for the same jet velocity.

Inside the 3-dimensional fissure, the jet impact on the block corner generates the stronger pressure increase related to the other jet configurations. The configurations with the jet impact on the block right side (SR) and with jet impact on the block corner (CN) load directly the fissure. The jet impact on the block corner loads two vertical faces of the block and the jet impact on the right side only one vertical face. The jet may penetrate better inside the fissure because the fissure length (where the jet can penetrate) is quite the double related to the jet

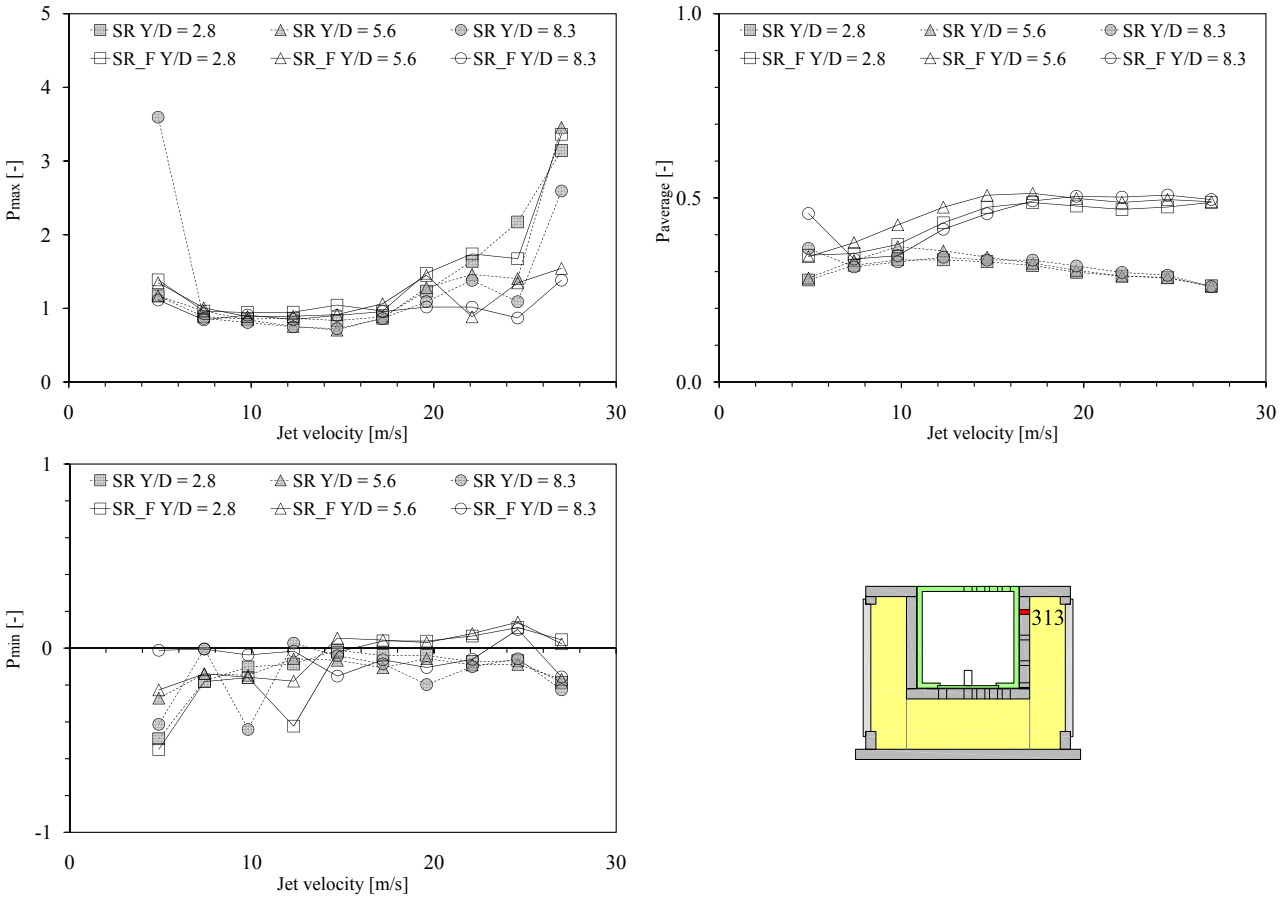

Figure 7.48: Influence of the degree of freedom of the block. Normalized pressure measured with transducer N° 313 for configurations SR (block free to move) and SR_F (block fixed) as a function of jet velocity (2.5-27.0 m/s) and Y/D ratio (2.8, 5.6 and 8.3). Maximum pressure (top left), mean pressure (top right), minimum pressure (bottom left) and transducer location (bottom right).

impact on the block right side. The water flow penetrating inside the fissure is practically double than for the jet impacting on the right side. This flow acts like a piston underneath the block and ejects the block outside of the central cavity, as has been observed in Chapters 6.4.4.1 and 7.1.2.4.

7.4.2 Pressure coefficients

The three configurations show almost the same behavior for the two degrees of freedom (free or fixed). The observations made for the configuration with the jet impact on the right side (SR and SR_F) are valid for the other two (impact on center CR and on the corner CN).

Figure 7.53 shows the six pressure coefficients computed for configurations SR (free) and SR_F (fixed). Some differences appear between the three configurations, but are not related to the behavior of free or fixed block but on the coefficient values (depending on the pressure field, Chapters 7.4.1.1, 7.4.1.2 and 7.4.1.3).

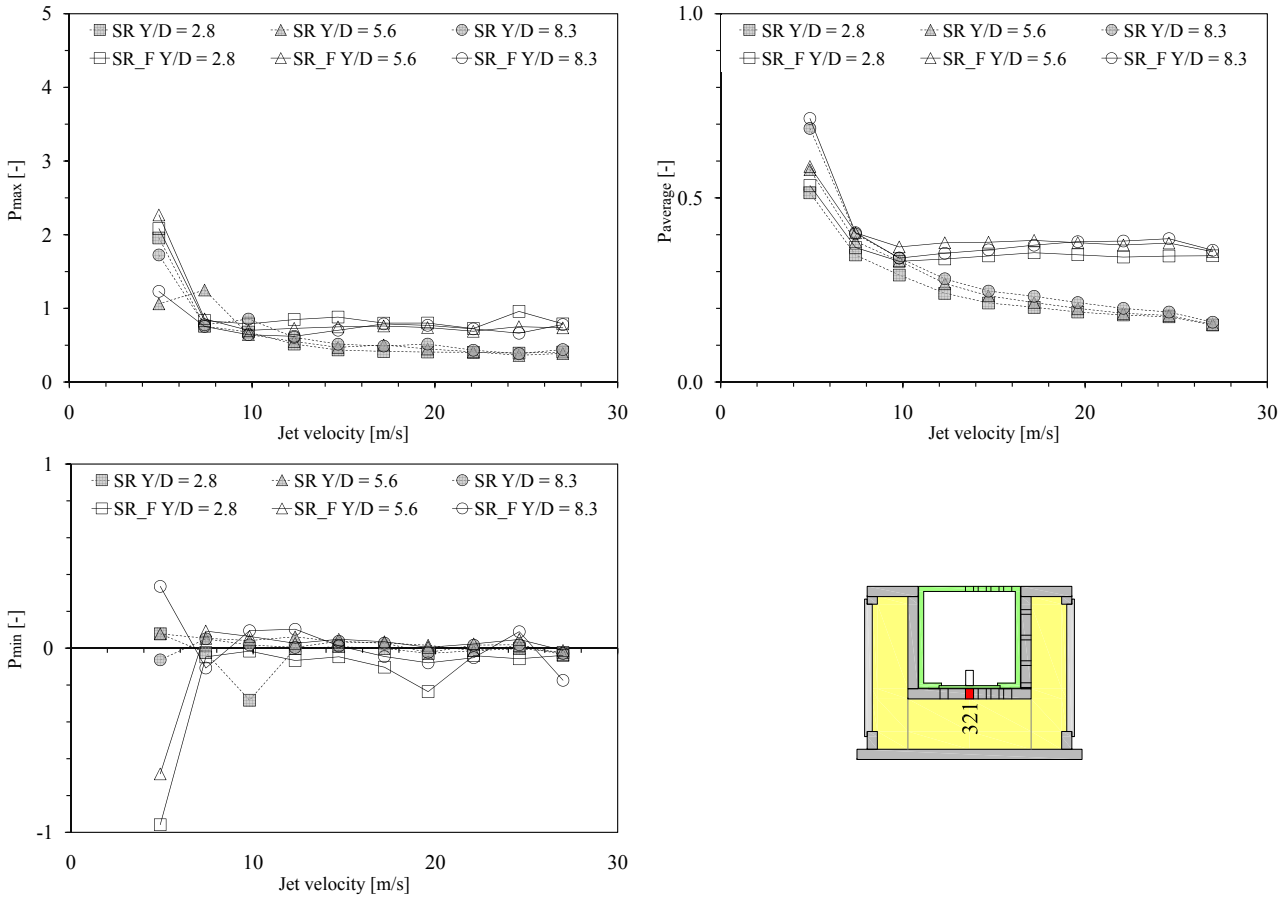

Figure 7.49: Influence of the degree of freedom of the block. Normalized pressure measured with transducer N° 321 for configurations SR (block free to move) and SR_F (block fixed) as a function of jet velocity (2.5-27.0 m/s) and Y/D ratio (2.8, 5.6 and 8.3). Maximum pressure (top left), mean pressure (top right), minimum pressure (bottom left) and transducer location (bottom right).

The mean pressure coefficients C_p (Figure 7.53 top left) computed on the block upper face (transducer N° 312) show almost the same values for the two degrees of freedom. As observed in previous chapter, the mean pressure acting on the block upper face is similar, independently if the block is free to move or fixed.

Inside the 3-dimensional fissure (transducers N° 313 and N° 321), is the configuration with fixed block that show higher coefficient values (SR_F). The pressure field analysis (Chapter 7.4.1.2) explains these results: the pressures recorded inside the fissure for the fixed block are higher than for the block free to move. Hence, the respective coefficients are larger. For configurations SR and SR_F, the maximum difference reaches ∼0.2. For configurations with jet impact on the block center (CR and CR_F) this difference is smaller (maximum ∼0.1) and configurations with jet impact on the block corner (CN and CN_F) have the same order of magnitude of configurations SR and SR_F.

The turbulent pressure fluctuations coefficients $C_{p'}$ (Figure 7.53 top right) show almost the same behavior for the three configurations and the two degrees of freedom. As explained for

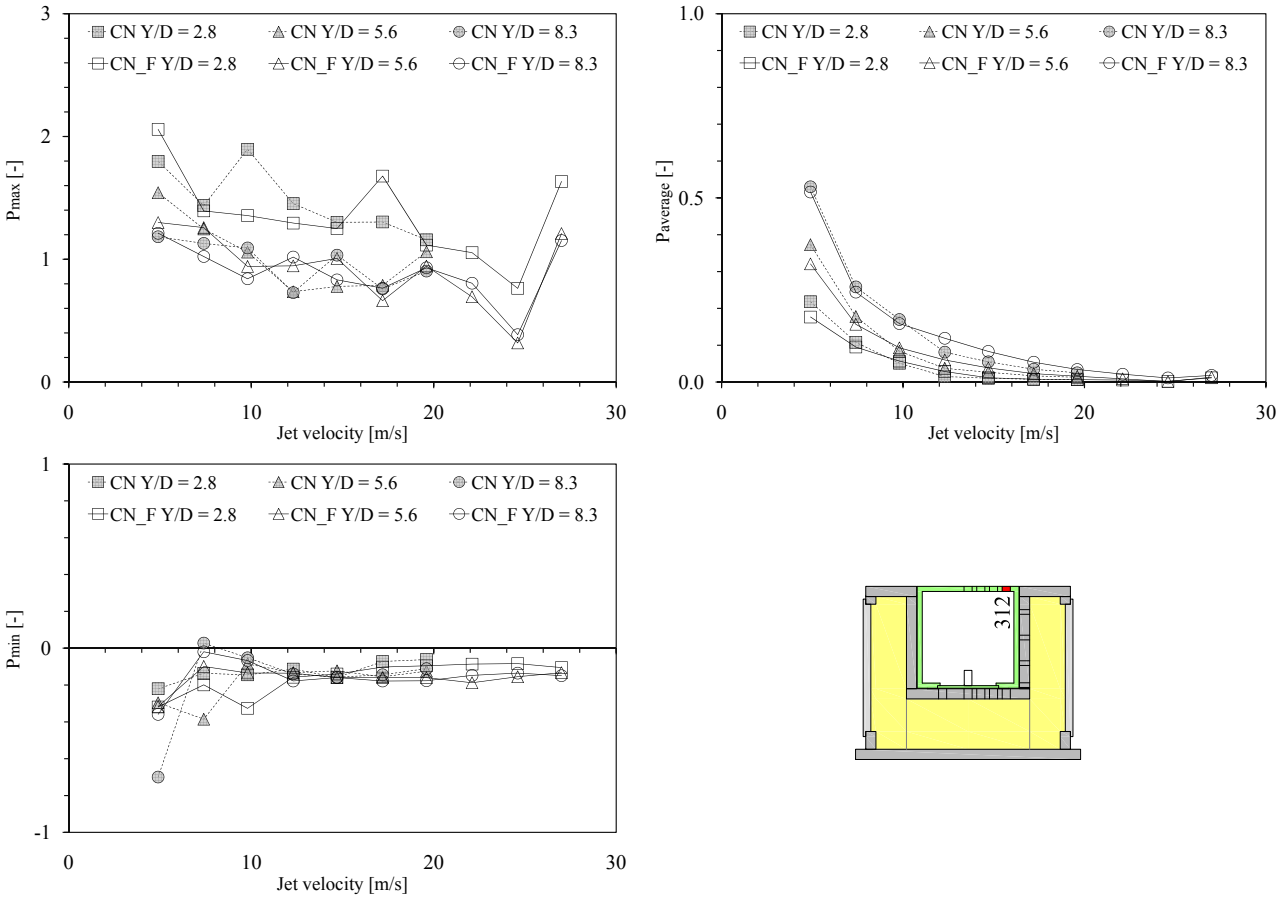

Figure 7.50: Influence of the degree of freedom of the block. Normalized pressure measured with transducer N° 312 for configurations CN (block free to move) and CN_F (block fixed) as a function of jet velocity (CN: 2.5-19.6 m/s and CN_F: 2.5-27.0 m/s) and Y/D ratio (2.8, 5.6 and 8.3). Maximum pressure (top left), mean pressure (top right), minimum pressure (bottom left) and transducer location (bottom right).

the mean pressure coefficient, the coefficients computed on the block upper face are similar for both degrees of freedom (N° 312). It seems that the turbulence did not change at the plunge pool bottom. Inside the fissure (N° 313 and N° 321), is the configuration with fixed block that shows the larger coefficients (SR_F) and the largest difference between the two block degrees of freedom is approximately 0.02, for all configurations. The turbulence fluctuations acting around the block are not affected by the block degree of freedom.

The positive extreme pressure fluctuation coefficients C_p^+ (Figure 7.53 middle left) show the same behavior that has been observed for the two previous coefficients (C_p and $C_{p'}$). On the block upper face (N° 312), the computed coefficients are closer and showing small differences that are generated by the small pressure differences observed in the pressure field analysis. Some random positive fluctuations may solicit the plunge pool bottom. As explained before, these pressure fluctuations may be generated by the system used to fix the block that modifies the flow conditions inside the plunge pool. Inside the fissure (N° 313 and N° 321), configuration SR shows larger positive extreme pressure fluctuations for the transducer situated near

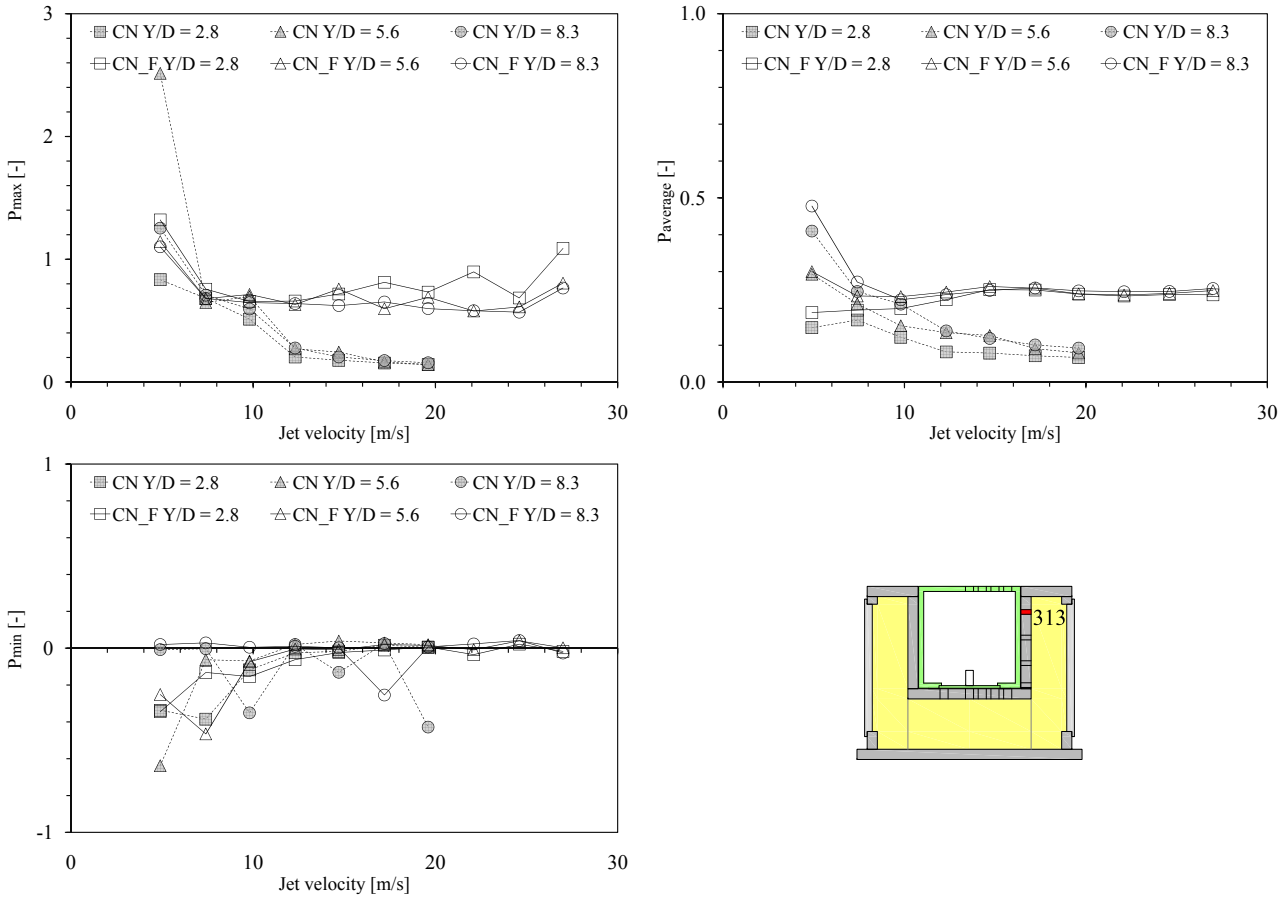

Figure 7.51: Influence of the degree of freedom of the block. Normalized pressure measured with transducer N° 313 for configurations CN (block free to move) and CN_F (block fixed) as a function of jet velocity (CN: 2.5-19.6 m/s and CN_F: 2.5-27.0 m/s) and Y/D ratio (2.8, 5.6 and 8.3). Maximum pressure (top left), mean pressure (top right), minimum pressure (bottom left) and transducer location (bottom right).

the fissure entrance. These extreme values may be related to a "cavitation" phenomenon or a compression-decompression phenomenon of the air bubbles present into the water that appears near the fissures entrance and generates these extreme pressures peak, as explained before. The coefficient differences, between the block free to move and fixed, reaches a maximum value of 2 (jet velocity of 27.0 m/s). This larger difference between coefficients is only related to configuration SR: the other jet configurations (block center CR and block corner CN) did not show this extreme difference in the coefficient values (maximum ∼0.1-0.2). The fixed block generates highest positive pressure fluctuations inside the 3-dimensional fissure and these values are concentrated near the fissure entrance.

The negative extreme pressure fluctuation coefficients C_p^- (Figure 7.53 middle right) computed on the block upper face (N° 312) are closer for both degrees of freedom, with small differences that have been observed in the pressure field. Inside the fissure (N° 313 and N° 321), as before, the configuration with fixed block shows larger negative extreme pressure fluctuations. Some random negative extreme pressure generates larger coefficients. For all configurations,

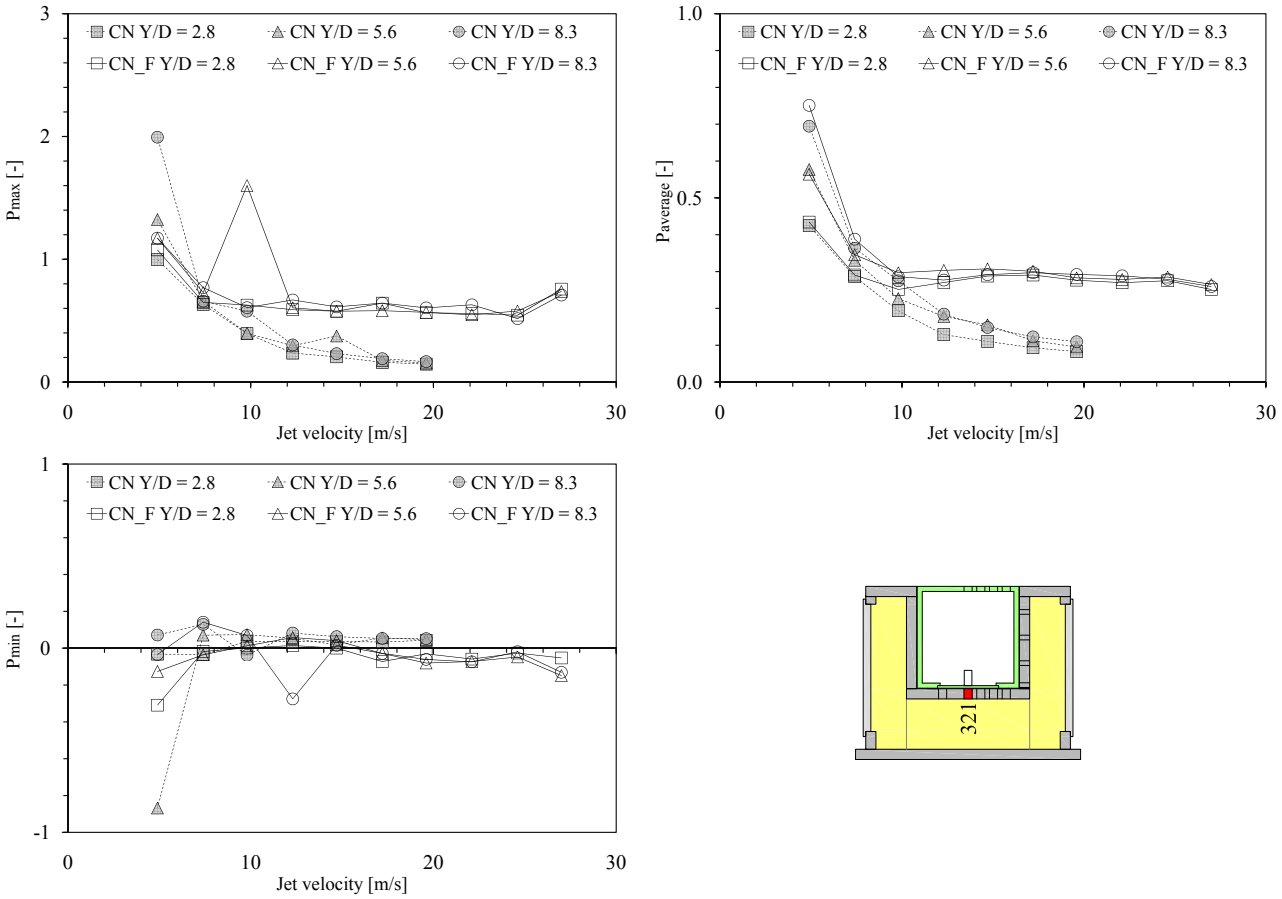

Figure 7.52: Influence of the degree of freedom of the block. Normalized pressure measured with transducer N° 321 for configurations CN (block free to move) and CN_F (block fixed) as a function of jet velocity (CN: 2.5-19.6 m/s and CN_F: 2.5-27.0 m/s) and Y/D ratio (2.8, 5.6 and 8.3). Maximum pressure (top left), mean pressure (top right), minimum pressure (bottom left) and transducer location (bottom right).

the maximum difference between the block free to move or fixed, reaches ∼0.2. As observed before, the fixed block generates highest negative pressure fluctuations inside the fissure.

The positive extreme pressure coefficients $C_{p,max}$ (Figure 7.53 bottom left) computed on the block upper face (N° 312) show similar values for both degrees of freedom (differences could be observed and are generate by the pressure fluctuations). Along the vertical fissure (N° 313) the larger coefficients are not related to one specific degree of freedom (free or fixed) but change as a function of the jet velocity. Underneath the block (N° 321), the configuration with the fixed block shows larger positive extreme pressure (for all configurations, the maximum difference reaches ∼0.3-0.4).

The negative extreme pressure coefficients $C_{p,min}$ (Figure 7.53 bottom right) computed on the block upper face (N° 312) show similar values for both degrees of freedom. Inside the fissure (N° 313 and N° 321), the fixed block shows larger negative extreme pressure (maximum difference reaches ∼0.3 and is related to the transducer situated underneath the block).

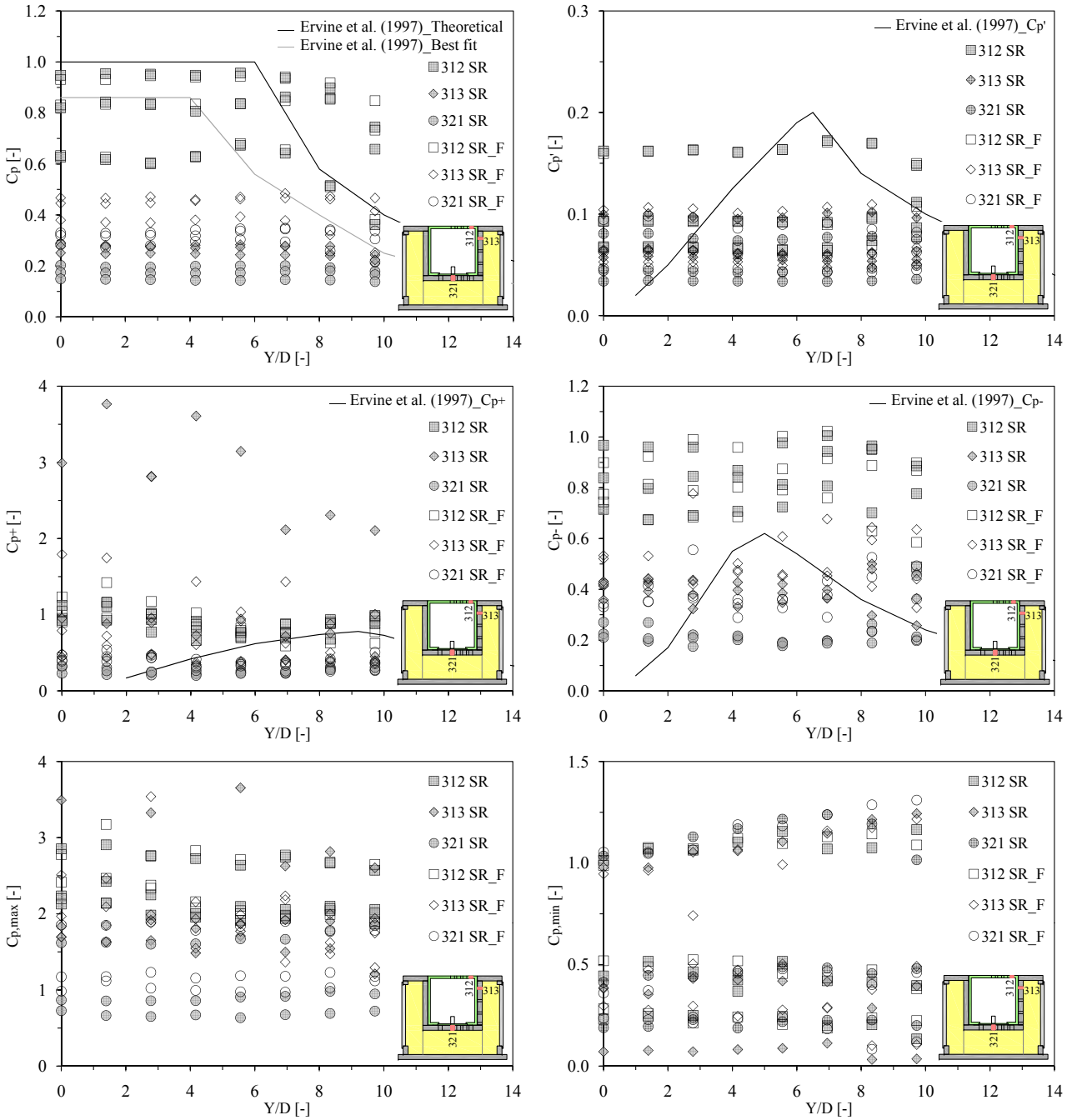

Figure 7.53: Influence of the degree of freedom of the block for configurations SR (block free to move) and SR_F (block fixed) as a function of jet velocity (2.5-27.0 m/s) and Y/D ratio (0-9.7) Mean pressure coefficient C_p (top left); Turbulent pressure fluctuation coefficient $C_{p'}$ (top right); Positive extreme pressure fluctuation coefficient C_p^+ (middle left); Negative extreme pressure fluctuation coefficient C_p^- (middle right); Positive extreme pressure coefficient $C_{p,max}$ (bottom left); Negative extreme pressure coefficient $C_{p,min}$ (bottom right).

These observations are valid for other transducers fixed around the block, water depths and jet velocities. As observed for all configurations the highest coefficient values are generated by jet velocities lower than 7.4 m/s due to the coefficient normalization by the jet kinetic energy at the plunge pool surface.

7.4.3 Power Spectral Density

7.4.3.1 Jet impact on the block center with the block free to move (CR) and the block fixed (CR_F)

In Figures 7.54, 7.55 and 7.56 the continuous line correspond to configuration with the block free to move along the vertical axis (CR) and the dashed line correspond to configuration with the block fixed (CR_F).

The PSD signal for the transducer situated on the block upper face (N° 310) is practically the same for both degrees of freedom. The two signals, illustrated for the same jet velocity, are superposed with small differences (Figure 7.54). The block degree of freedom did not affect the pressure field on the block upper face, as has been observed before.

Along the vertical fissure (N° 313) and underneath the block (N° 321) there are some differences between the two degrees of freedom: generally the configuration with fixed block shows a higher energy content per frequency. In Chapter 7.4.1.1 the pressure field has been analyzed and inside the 3-dimensional fissure a pressure difference between the two degrees of freedom has been detected. Inside the fissure, the pressure increases when the block is not free to move along the vertical axis. This pressure growth influences the energy content in the PSD signal. Along the vertical fissure the PSD signal shows a vertical shift (different energy content per frequency) but underneath the block for frequency greater than 20-40 Hz, the PSD signal changes: the energy increase as a function of the jet velocity and two peaks appear. These peaks range between 50 and 250 Hz. The first peak (between 50 and 150 Hz) is always presents and the second peaks (between 150 and 250 Hz) appears with an increase of the jet velocity. As observed in Chapter 6.2.5, the first peak could correspond to the natural period of an open ended fissure (range 22-72 Hz) but the second peak did not correspond to the block eigenfrequencies (5-9 Hz). The 50 Hz frequency correspond to the electric alimentation frequency. The second peak may be related to a resonance phenomenon underneath the block due to the block is not free to move. The increase of the pressure inside the fissure and the fixed block modify the power spectral density signal inside the 3-dimensional fissure.

Core, transition and developed jets show the same behavior and these observations could be applied for the other transducers and water depths.

7.4.3.2 Jet impact on the block right side with the block free to move (SR) and the block fixed (SR_F)

In Figures 7.57, 7.58 and 7.59 the continuous line correspond to configuration with the block free to move along the vertical axis (SR) and the dashed line correspond to configuration with the block fixed (SR_F).

As observed in Chapter 7.4.3.1, the degree of freedom did not affect the power spectral density on the block upper face (N° 312) but only inside the 3-dimensional fissure (N° 313 and N° 321). On the block upper face, the two signals (free block and fixed block) are superposed with small differences (Figure 7.57). Inside the fissure the configuration with the fixed block shows a higher energy content per frequency. Along the vertical fissure the power spectral

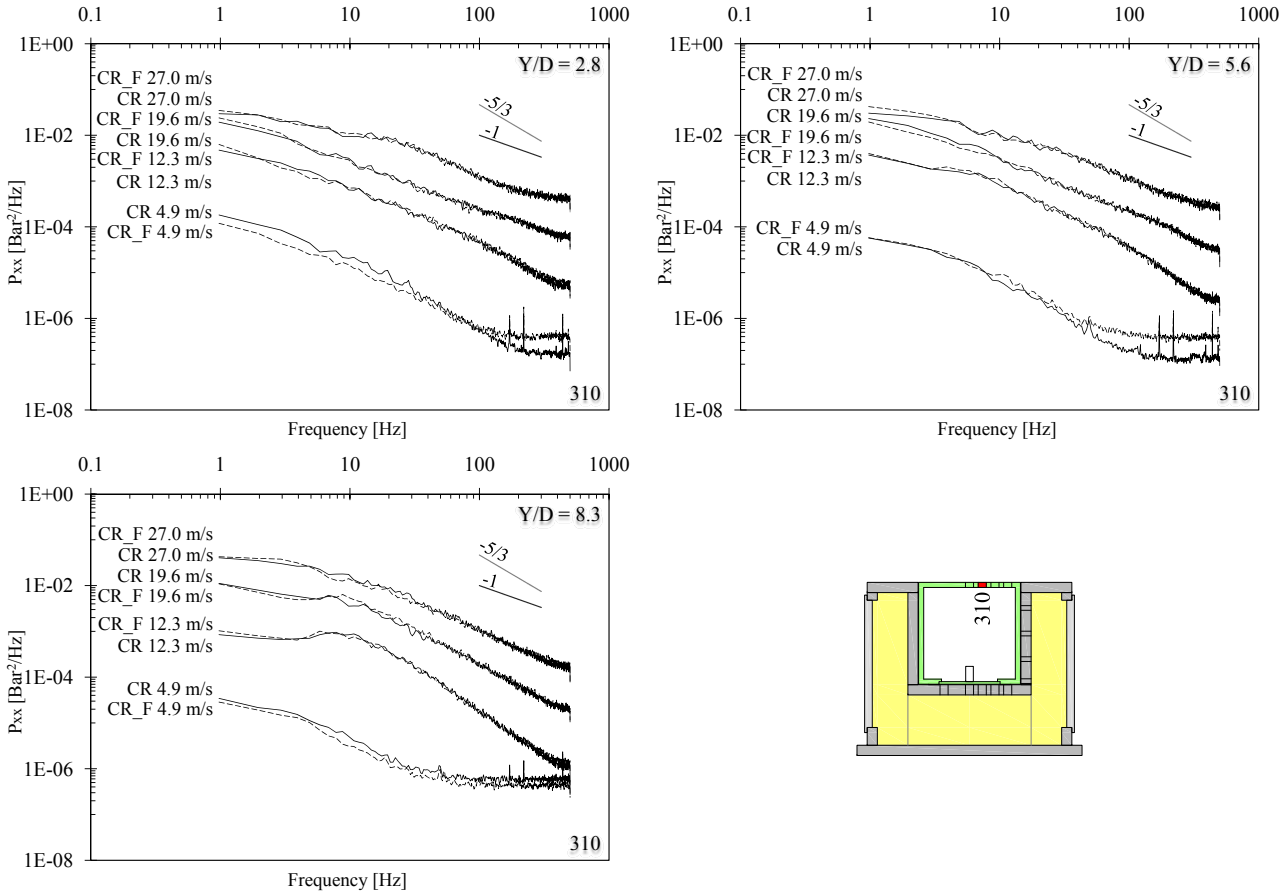

Figure 7.54: Influence of the degree of freedom of the block on the non-dimensional spectral content (PSD) computed for configurations CR (block free to move, continuous line) and CR_F (block fixed, dashed line) as a function of jet velocity (4.9, 12.3, 19.6 and 27.0 m/s) and Y/D ratio (2.8, 5.6 and 8.3). Transducer N° 310. Core jet (top left), transition jet (top right), developed jet (bottom left) and transducer location (bottom right).

density shows a vertical shift (different energy content) but underneath the block for frequency greater than 20-40 Hz the PSD signal changes, as observed for the configuration with the jet impact on the block center (CR). Also the same two peaks appear (Chapter 6.3.5) and range between 50 and 250 Hz.

As before, core, transition and developed jets show the same behavior and this observation are valid for the other transducers and the other water levels.

7.4.3.3 Jet impact on the block corner with the block free to move (CN) and the block fixed (CN_F)

In Figures 7.60, 7.61 and 7.62 the continuous line correspond to configuration with the block free to move along the vertical axis (CN) and the dashed line correspond to configuration with the block fixed (CN_F).

Transducer N° 312, located on the block upper face (at 104 mm from the stagnation point on the block corner), shows a different energy content as a function of the degree of freedom: when the block is fixed (CN_F), the power spectral density shows a higher energy content related to

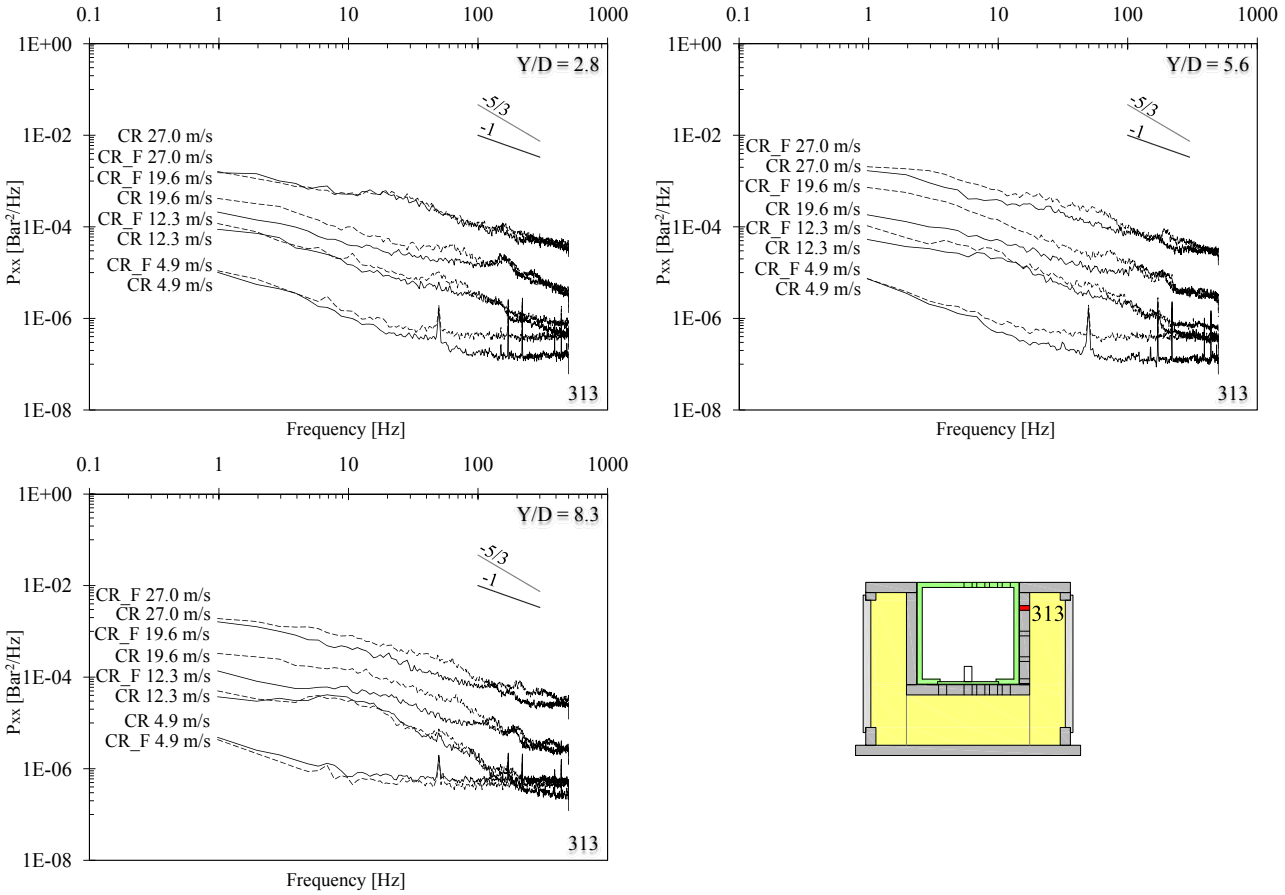

Figure 7.55: Influence of the degree of freedom of the block on the non-dimensional spectral content (PSD) computed for configurations CR (block free to move, continuous line) and CR_F (block fixed, dashed line) as a function of jet velocity (4.9, 12.3, 19.6 and 27.0 m/s) and Y/D ratio (2.8, 5.6 and 8.3). Transducer N° 313. Core jet (top left), transition jet (top right), developed jet (bottom left) and transducer location (bottom right).

configuration with the block free to move (CN). The frequency evolution is similar for the two degrees of freedom, but is vertically shifted (energy).

Along the vertical fissure (N° 313) and underneath the block (N° 321), as before, the fixed block shows higher energy per frequency that increase with jet velocity. This increase of energy, as a function of the jet velocity, is more pronounced than for the two other configurations (CR and SR). The transducers are not loaded in the same way for the three configurations due to the different positions of the stagnation point. The pressures could be similar but the solicitations may not be exactly the same (as an example: fluctuations and turbulence). This is the reason of this different energy growth. At the same time, the pressure field inside the fissure is not the same for both degrees of freedom (fixed block generates higher pressure).

As observed before, along the vertical fissure the power spectral density shows a vertical shift but underneath the block for frequency greater than 10-20 Hz the PSD signal change. Two peaks appear and range between 50 and 250 Hz.

As before, core, transition and developed jets show the same behavior and this observation are valid for the other transducers and the other water levels.

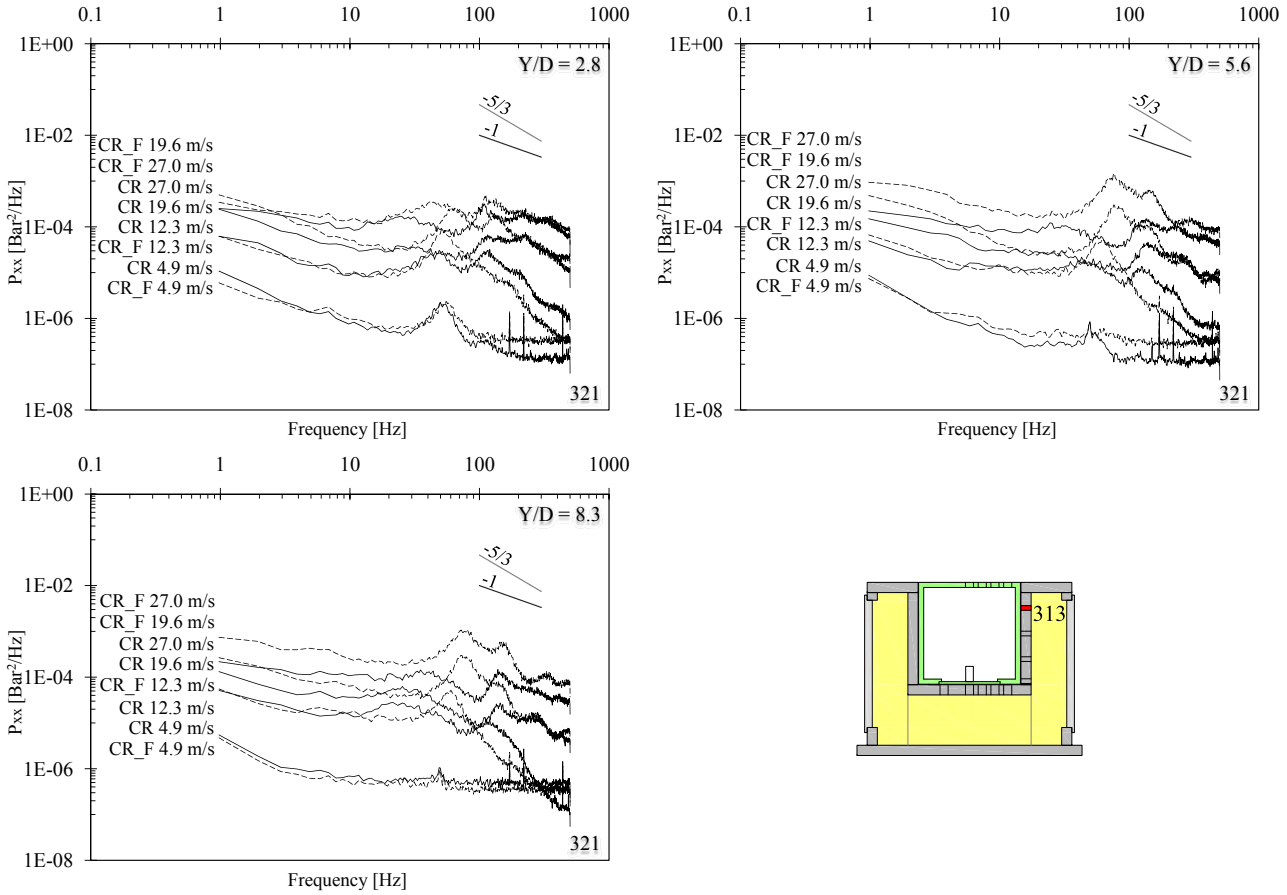

Figure 7.56: Influence of the degree of freedom of the block on the non-dimensional spectral content (PSD) computed for configurations CR (block free to move, continuous line) and CR_F (block fixed, dashed line) as a function of jet velocity (4.9, 12.3, 19.6 and 27.0 m/s) and Y/D ratio (2.8, 5.6 and 8.3). Transducer N° 321. Core jet (top left), transition jet (top right), developed jet (bottom left) and transducer location (bottom right).

7.4.4 Conclusions

The degree of freedom of the block did not affect the pressure field acting on the block upper face. However, the pressures inside the 3-dimensional fissure are strongly affected. More the jet impact approaches and loads directly the 3-dimensional fissure (jet impact on the block left or right side and on the corner) and more the pressures acting inside the fissure increase, related to configurations with the block free to move along the vertical axis. The jet impact near the fissure entrance generates a better jet penetration inside the fissure.

The system installed to fix the block generates this different response of the fissure (different pressure field). The block movements are stopped and the pressure inside the fissure could not be transmitted to the block to generate a vertical movement. Hence, the fixed block is submitted to higher pressures solicitations than the free block.

In nature, the pressures loading (hydrodynamic fracturing) generated by the jet impact on or near the fissure entrance, generate a series of pressure peaks (maximum and minimum) that could break the rock mass with instantaneous or brittle crack propagation (open-close fissure process or fatigue). The cyclic solicitations of the pressures, govern rock fissure propagation by

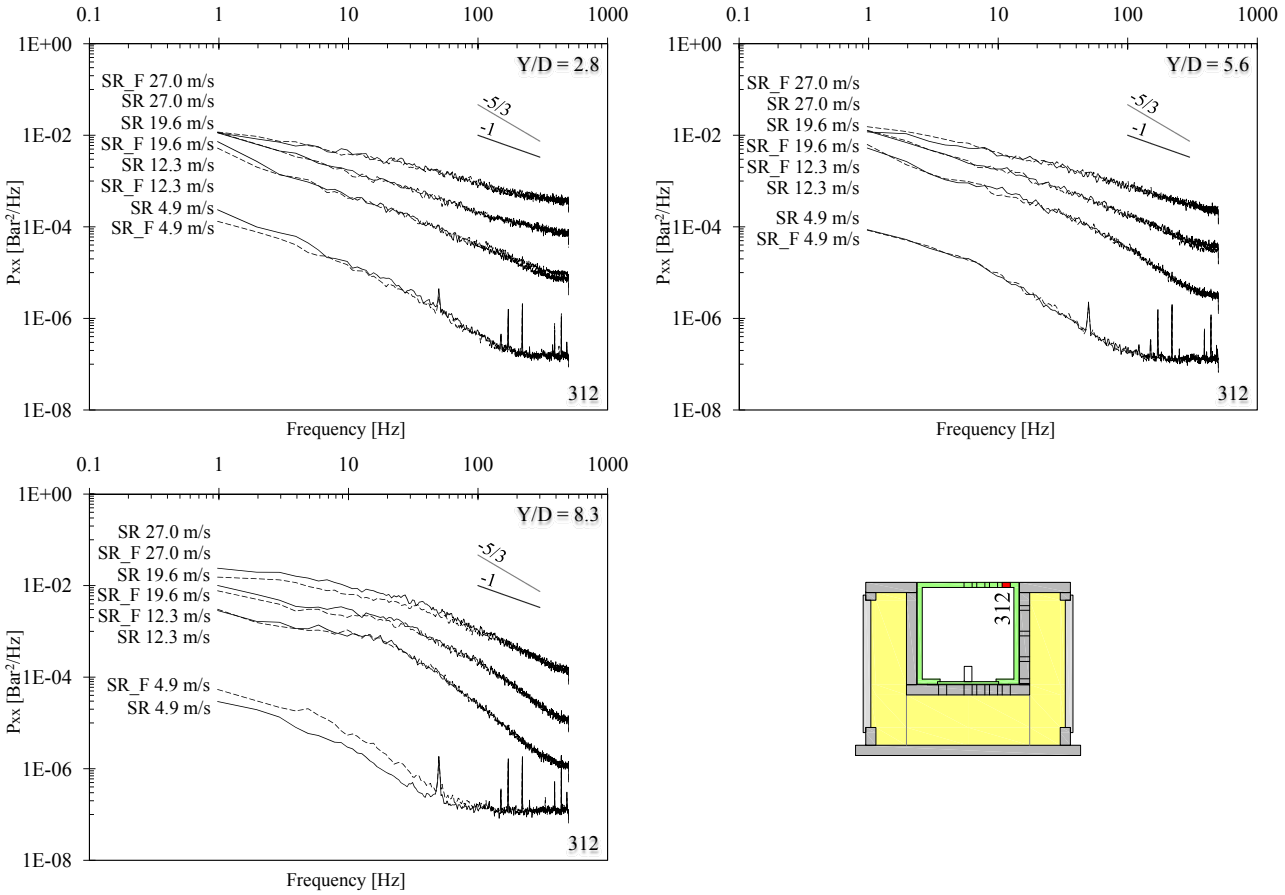

Figure 7.57: Influence of the degree of freedom of the block on the non-dimensional spectral content (PSD) computed for configurations SR (block free to move, continuous line) and SR_F (block fixed, dashed line) as a function of jet velocity (4.9, 12.3, 19.6 and 27.0 m/s) and Y/D ratio (2.8, 5.6 and 8.3). Transducer N° 312. Core jet (top left), transition jet (top right), developed jet (bottom left) and transducer location (bottom right).

fatigue effects. After a certain time, the rock mass break-up in small blocks due to the progressive fissure growth. Then the block is subjected to the hydrodynamic uplift that tries to eject its outside of the rock mass (pressure differences acting between upper and lower block faces). If these phenomenons continue, the score holes increase his horizontal and vertical dimensions. The observed pressures increase, inside the fissure, could be integrated in the scouring model developed by Bollaert (2002b) in the rock mass module to estimate the rock mass fracturation. The hydrodynamic loading inside the fissure allow to compute the intensity factor K_I that will be compared to the critical intensity factor K_{IC} to evaluate if the fissure grows or is stable.

The jet impacting on the block corner is the configuration most dangerous for fissure and scour propagation because: firstly, this configuration has generated the largest observed vertical uplift and secondly, it is this configuration that generates the larger pressure difference as a function of the degree of freedom inside the 3-dimensional fissure.

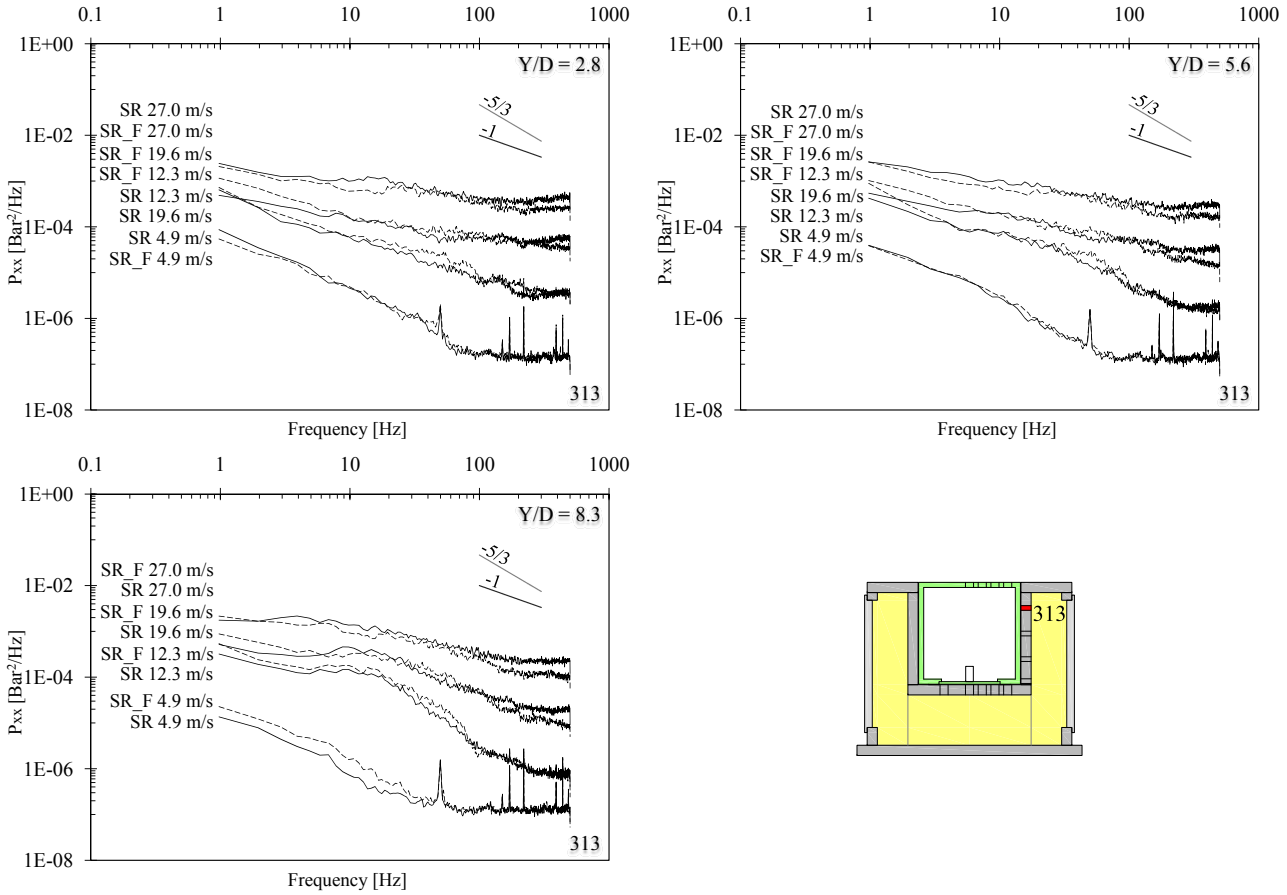

Figure 7.58: Influence of the degree of freedom of the block on the non-dimensional spectral content (PSD) computed for configurations SR (block free to move, continuous line) and SR_F (block fixed, dashed line) as a function of jet velocity (4.9, 12.3, 19.6 and 27.0 m/s) and Y/D ratio (2.8, 5.6 and 8.3). Transducer N° 313. Core jet (top left), transition jet (top right), developed jet (bottom left) and transducer location (bottom right).

The pressure coefficients analyses reveal that all configurations with the fixed block generate larger pressure coefficient values inside the fissure (but with small difference except near the fissure entrance). The block upper face is practically not influenced by the degree of freedom of the block, as has been observed in the pressure field analysis. Inside the fissure, the fixed block generates larger: mean pressure, positive and negative extreme pressure fluctuations and positive and negative extreme pressure. The turbulence fluctuations acting around the block are not affected by the degree of freedom. The system installed to fix the block generates this different fissure response: the pressures acting underneath the block could not be transmitted to the block to generate a vertical movement and generate a pressure increase inside the fissure (fluctuations, mean value).

The power spectral density signal on the block upper face (from N° 309 to N° 312) for configurations CR (center impact) and SR (right side impact) is practically superposed with small differences for both degrees of freedom (free and fixed). The configuration with the jet impact on the block corner (CN) shows a different behavior as a function of the degree of

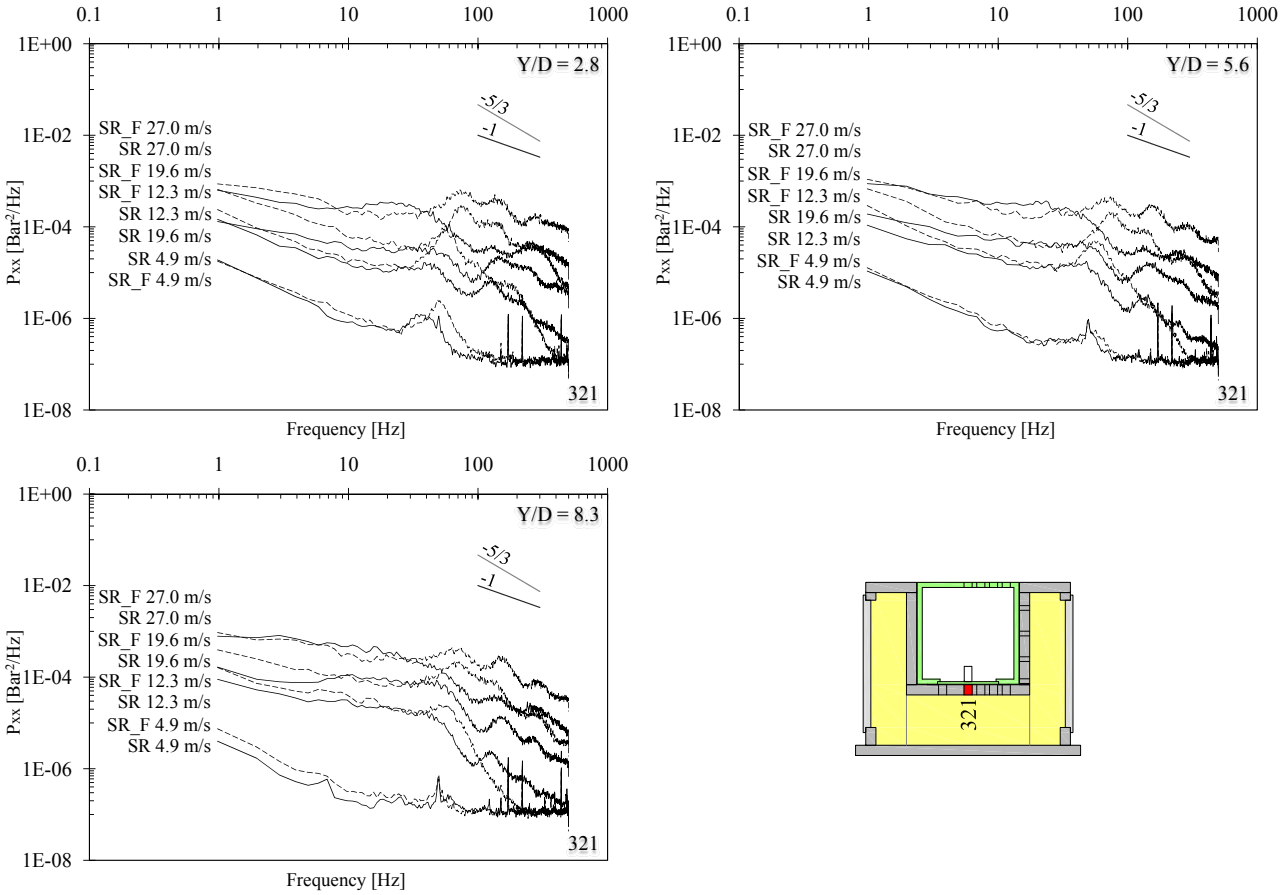

Figure 7.59: Influence of the degree of freedom of the block on the non-dimensional spectral content (PSD) computed for configurations SR (block free to move, continuous line) and SR_F (block fixed, dashed line) as a function of jet velocity (4.9, 12.3, 19.6 and 27.0 m/s) and Y/D ratio (2.8, 5.6 and 8.3). Transducer N° 321. Core jet (top left), transition jet (top right), developed jet (bottom left) and transducer location (bottom right).

freedom: the fixed block (CN_F) has higher energy content per frequency than the block free to move (CN). The frequency evolution is similar but is vertically shifted.

There are some differences between the two degrees of freedom inside the fissure and at the plunge pool bottom: the fixed block shows generally a higher energy content per frequency independently by the jet configuration. The different pressure field, acting inside the 3-dimensional fissure, influences the power spectral density signal. Inside the fissure, the pressure increases when the block is not free to move along the vertical axis and the energy as well increase in the PSD.

Along the vertical fissure the PSD shows a vertical shift (different energy content) but underneath the block for frequencies greater than 20-40 Hz the PSD signal changes: the energy increase with an increase of the jet velocity and two peaks appear. These peaks range between 50 and 250 Hz. The first peak (between 50 and 150 Hz) is always presents and could correspond to the natural period of an open ended fissure (range 22-72 Hz) and the second peaks (between 150 and 250 Hz) appears with an increase of the jet velocity and is not so clear defined.

Core, transition and developed jets show the same behavior.

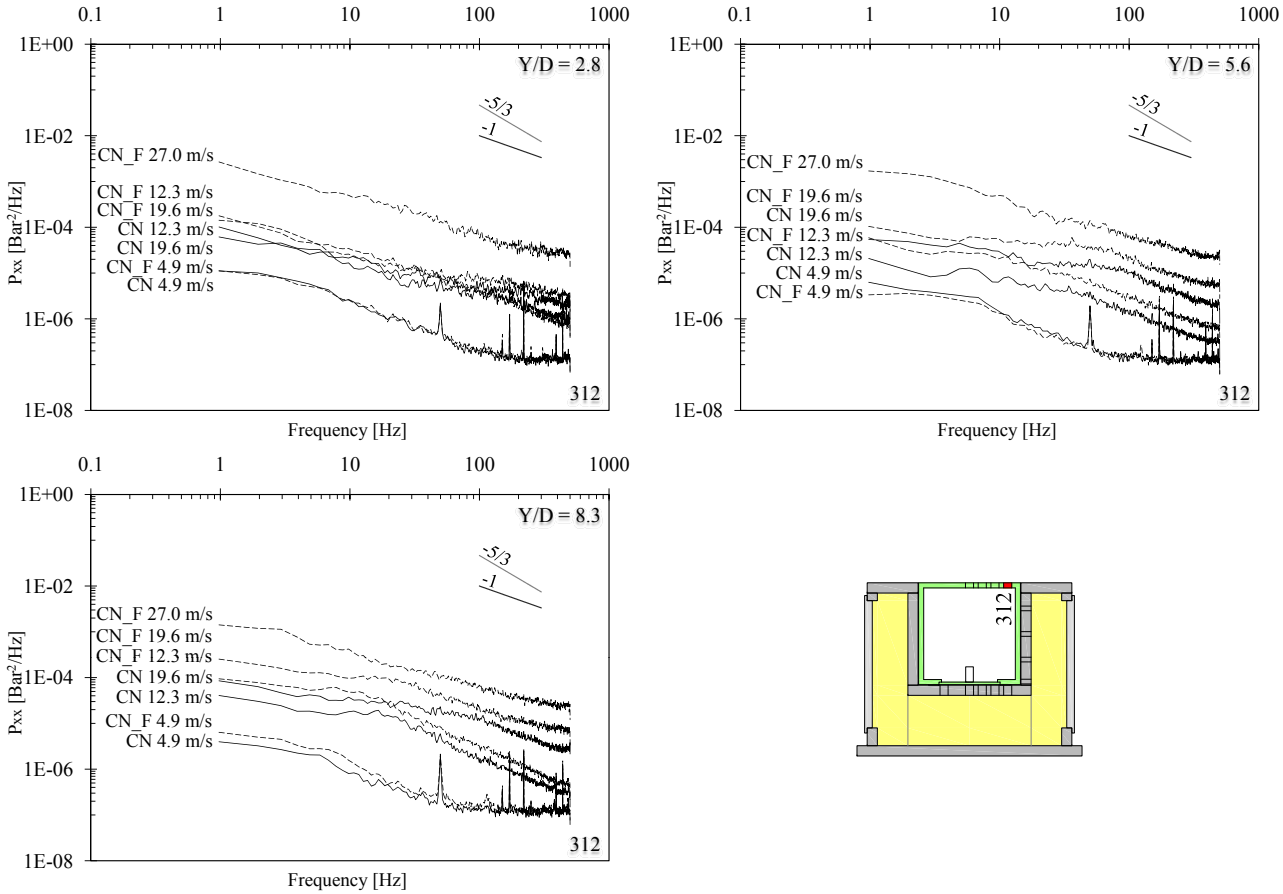

Figure 7.60: Influence of the degree of freedom of the block on the non-dimensional spectral content (PSD) computed for configurations CN (block free to move, continuous line) and CN_F (block fixed, dashed line) as a function of jet velocity (CN: 4.9, 12.3 and 19.6 m/s and CN_F up to 27.0 m/s) and Y/D ratio (2.8, 5.6 and 8.3). Transducer Nº 312. Core jet (top left), transition jet (top right), developed jet (bottom left) and transducer location (bottom right).

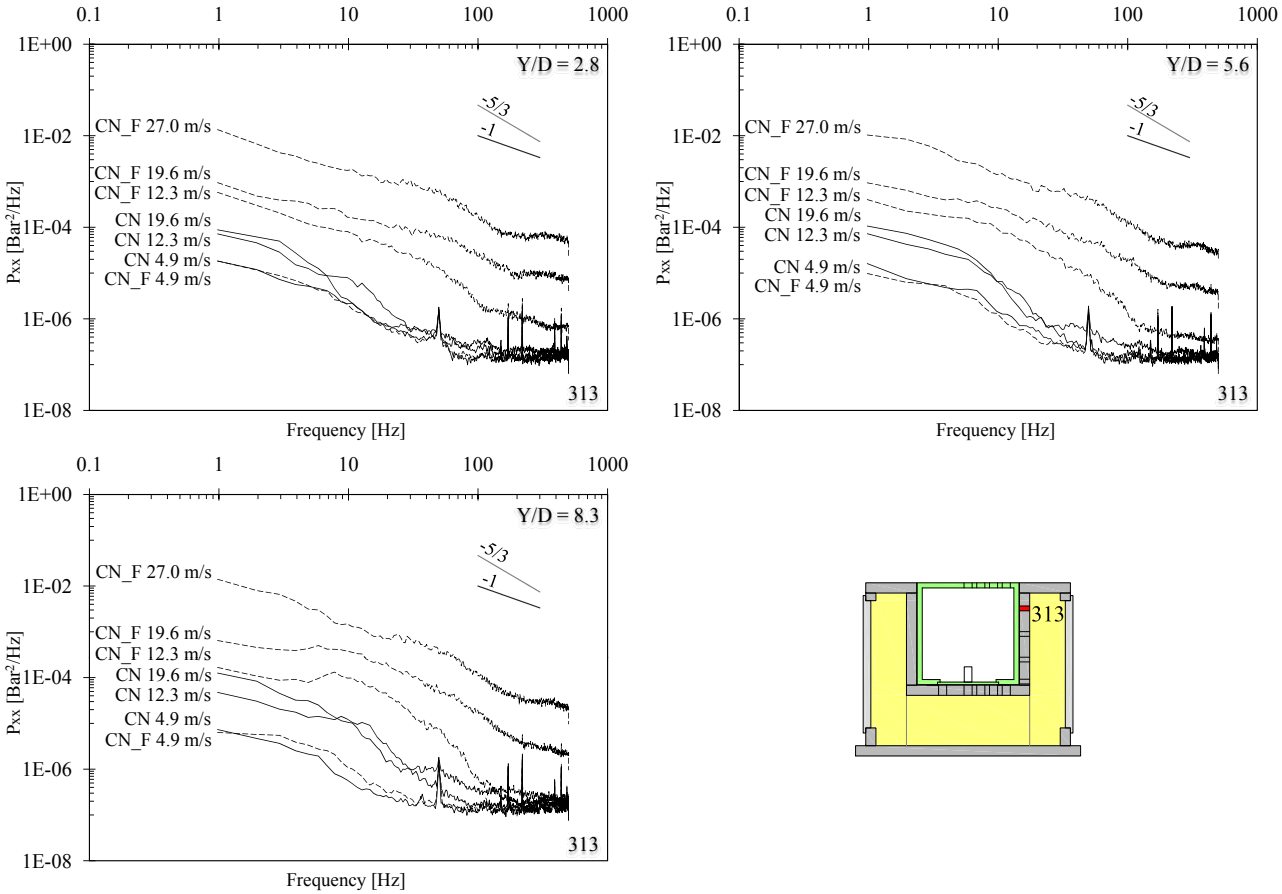

Figure 7.61: Influence of the degree of freedom of the block on the non-dimensional spectral content (PSD) computed for configurations CN (block free to move, continuous line) and CN_F (block fixed, dashed line) as a function of jet velocity (CN: 4.9, 12.3 and 19.6 m/s and CN_F up to 27.0 m/s) and Y/D ratio (2.8, 5.6 and 8.3). Transducer Nº 313. Core jet (top left), transition jet (top right), developed jet (bottom left) and transducer location (bottom right).

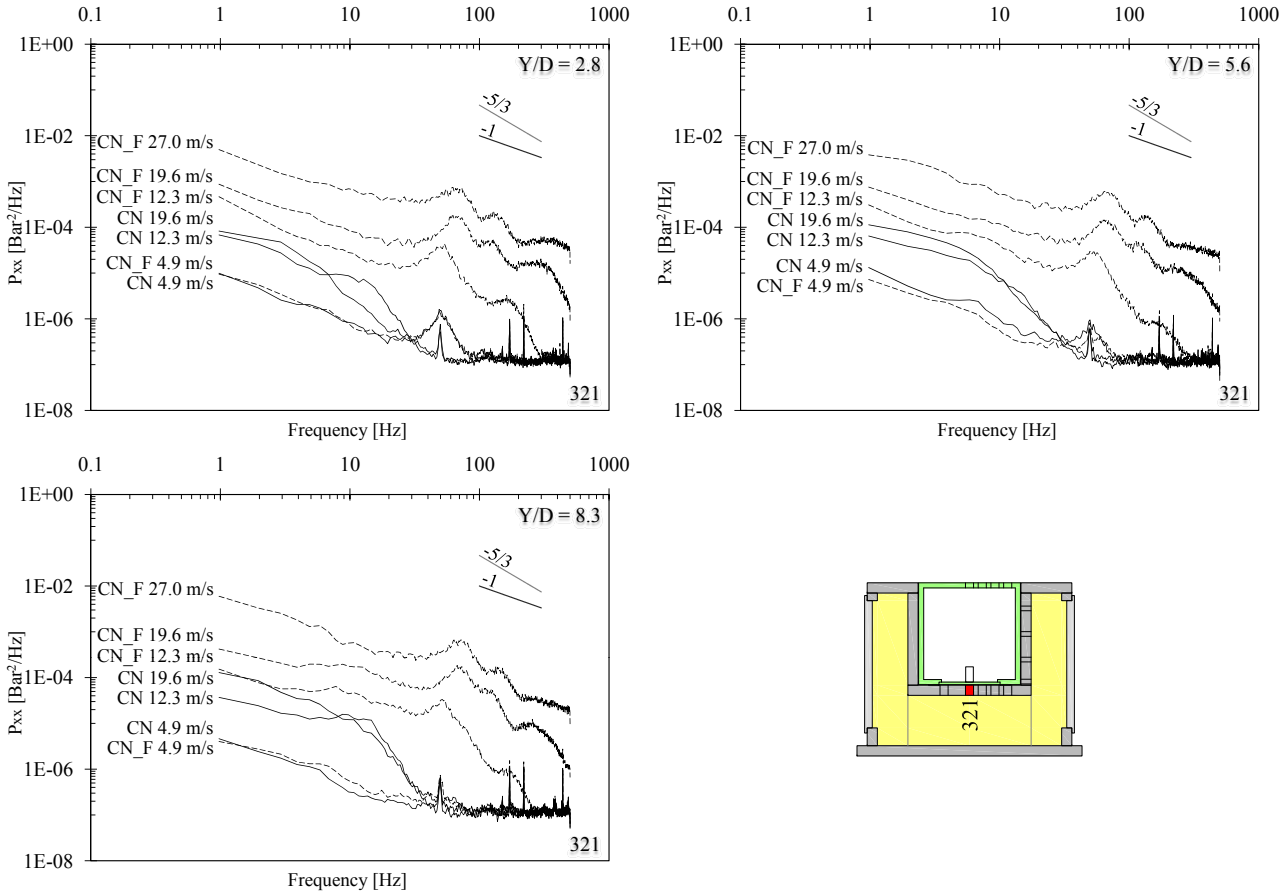

Figure 7.62: Influence of the degree of freedom of the block on the non-dimensional spectral content (PSD) computed for configurations CN (block free to move, continuous line) and CN_F (block fixed, dashed line) as a function of jet velocity (CN: 4.9, 12.3 and 19.6 m/s and CN_F up to 27.0 m/s) and Y/D ratio (2.8, 5.6 and 8.3). Transducer Nº 321. Core jet (top left), transition jet (top right), developed jet (bottom left) and transducer location (bottom right).

7.5 Analysis of on the block rotations

7.5.1 Introduction

The analysis of the influence of dynamic block impulsion (Chapter 7.1), influence of the lateral guide type (Chapter 7.3) and influence of the degree of freedom of block (Chapter 7.4) show a possible new phenomenon that has to be investigate: the block rotation inside the central cavity when it is loaded by an asymmetrical jet.

An asymmetrical jet may generate small rotations (infinitesimal) inside the central cavity that influence the block displacements. These small rotations may influence as well the pressures acting on the block and the friction force acting between the block and the walls of the central cavity. A symmetrical jet is not subject to these small rotations, as has been observed previously (Chapter 7.3).

The new experimental set-up, measurement box and highly instrumented block (Chapter 3.2.2), was built with a construction tolerance of ± 0.01 mm. This tolerance corresponds to a maximum rotation of $\pm 0.003^{o}$.

7.5.2 Pressure field generated by a symmetric and an asymmetrical jet

To investigate if these rotations may influence the pressure field surrounding the block, four configurations have been analyzed.

These configurations allow to reconstruct the pressure field acting on the block upper face (exponential distribution, Chapter 5.1.1.3) and inside the 3-dimensional fissure. Two configurations have the jet impact on the block center and two configurations have the jet impact on the block right side. The block is free moves along the vertical axis. The configurations are explained in Chapter 4.3.1.

Block equipped with lateral guides having two contact points:

- Jet impact position on the block center (CE);
- Jet impact position on the block right hand side (SI).

Block equipped with lateral guides having eight contact points:

- Jet impact position on the block center (CR);
- Jet impact position on the block right hand side (SR).

To avoid the influence of the type of lateral guide (Chapter 7.3), configurations have been compared pairwise (same lateral guide but not the jet impact position): configuration CE with SI and configuration CR with SR.

The stagnation point on the block upper face is not the same due to the different jet impact position. The pressure distributions have been plotted radially outwards from a hypothetic stagnation point on the block center for the upper and lower face and are situated on the same vertical plane.

The pressure transducers, for configurations CE and CR cover a range between 0 and 75 mm from the stagnation point and for configurations SI and SR cover a range between 25 and 100 mm (for transducers and stagnation point location see Figures 6.1 and 6.24).

Figures 7.63 and 7.64 show the pressure field comparison for configurations CE and SI (equipped with lateral guide having two contact points).

On the block upper face, is the configuration with the jet impact on the block right side that shows higher pressure values (maximum and mean) for all water depths and all jet velocities. Whereas, underneath the block is the configuration with the jet impact on the block center that shows higher pressure values for all water depths and all jet velocities.

The pressure distribution on the block upper face should be similar due to the same jet characteristics at impact, however some differences appear with an increase of the jet velocity. The pressures acting on the block have similar evolution but not same values. The pressure differences, between the two configurations, disappear radially outwards from the stagnation point and reach an equivalent value for all configurations, water depths and jet velocities.

The different location of the jet impact influences the pressures values. The fissure entrance may generate some flow perturbations that increase the pressures recorded on the block: the incoming flow cannot penetrate completely inside the fissure and some small eddies may be generated near the fissure entrance. These small eddies may propagate onto the plunge pool bottom and generate these pressures differences.

Underneath the block, the configuration with the jet impact on the block center (CE) shows higher pressure values. The configuration with the jet impact on the block right side (SR) loads directly the fissure and the water flow can penetrate inside the fissure with higher velocity than for configuration CE. For the jet impact on the block center, is not the jet that solicits directly the fissure but are the pressure fluctuations acting on the plunge pool bottom. At the same time, the flow velocity inside the fissure is smaller (generated by pressure differences at the fissure entrances). The flow inside the fissure may be governed by these pressures differences. The jet impact on the fissure (SI) generates higher flow velocities and smaller pressure on the block lower face, as has been observed.

As observed for maximum pressures, mean pressures acting on the block lower face show a similar evolution but not the same values. The differences increase as a function of the jet velocity. The mean pressure is quite constant underneath the block for both configurations.

Figures 7.65 and 7.66 show the pressure field comparison for configurations CR and SR (equipped with lateral guide having eight contact points).

The remarks performed for the previous configurations (CE and SI) are also valid for configurations CR and SR equipped with a different type of lateral guide (eight contact points).

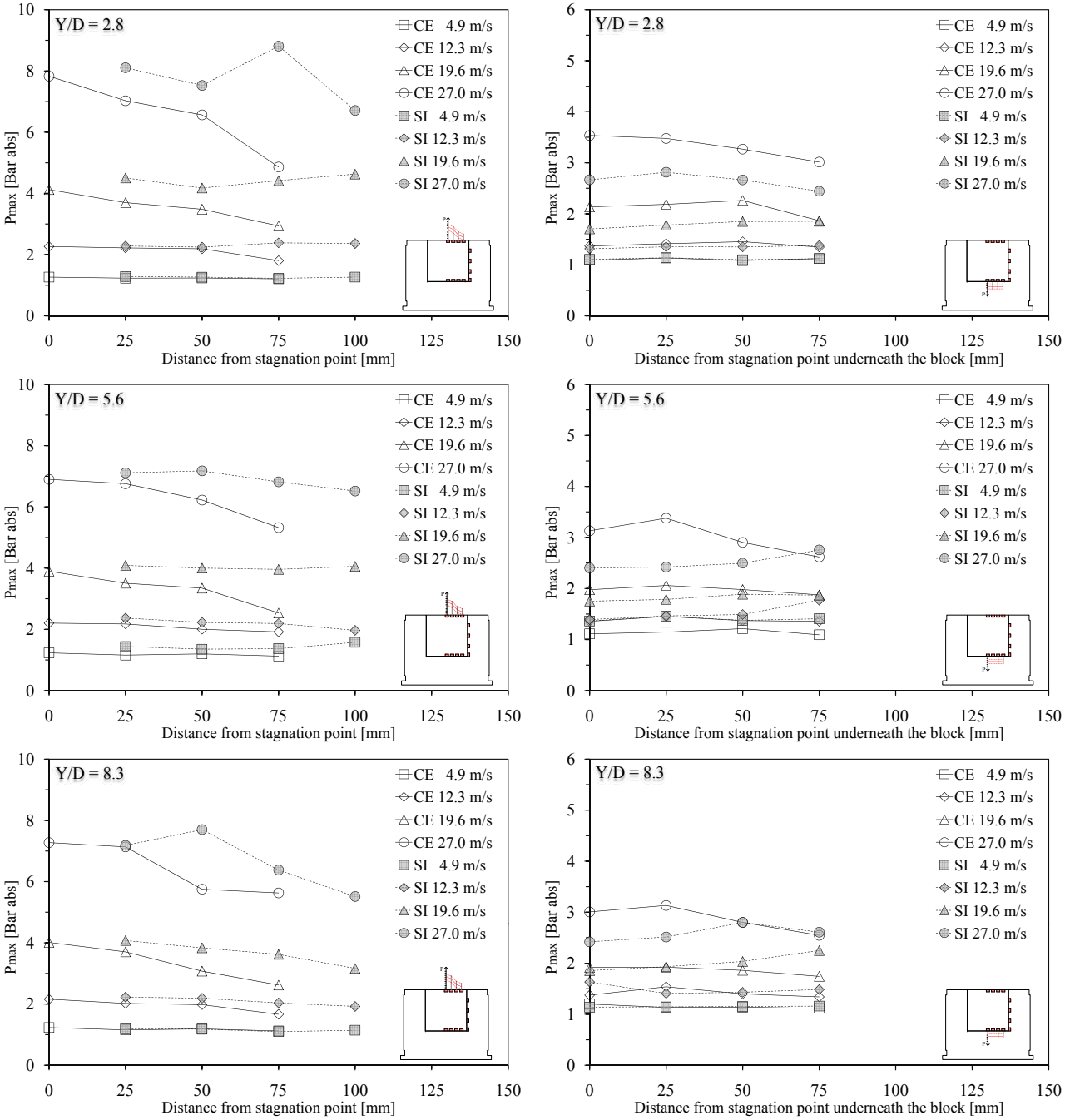

Figure 7.63: Comparison of the pressure field surrounding the block for configurations CE (jet impact on the block center) and SI (jet impact on the block right side) as a function of jet velocity (4.9, 12.3, 19.6 and 27.0 m/s) and Y/D ratio (2.8, 5.6 and 8.3). Maximum pressures acting on the block upper face (left column) and underneath the block (right column). Core jet (first row), transition jet (second row) and developed jet (third row). Pressures are expressed in absolute Bar.

The pressures (maximum and mean) and its spatially distribution (radially outwards from the stagnation point) are similar to the previous configurations. That means, the pressure field is not influence by the type of lateral guide but it is influenced only by the jet location on the block upper face.

If these rotations appear, some difference may be observed in the pressure field, but is not

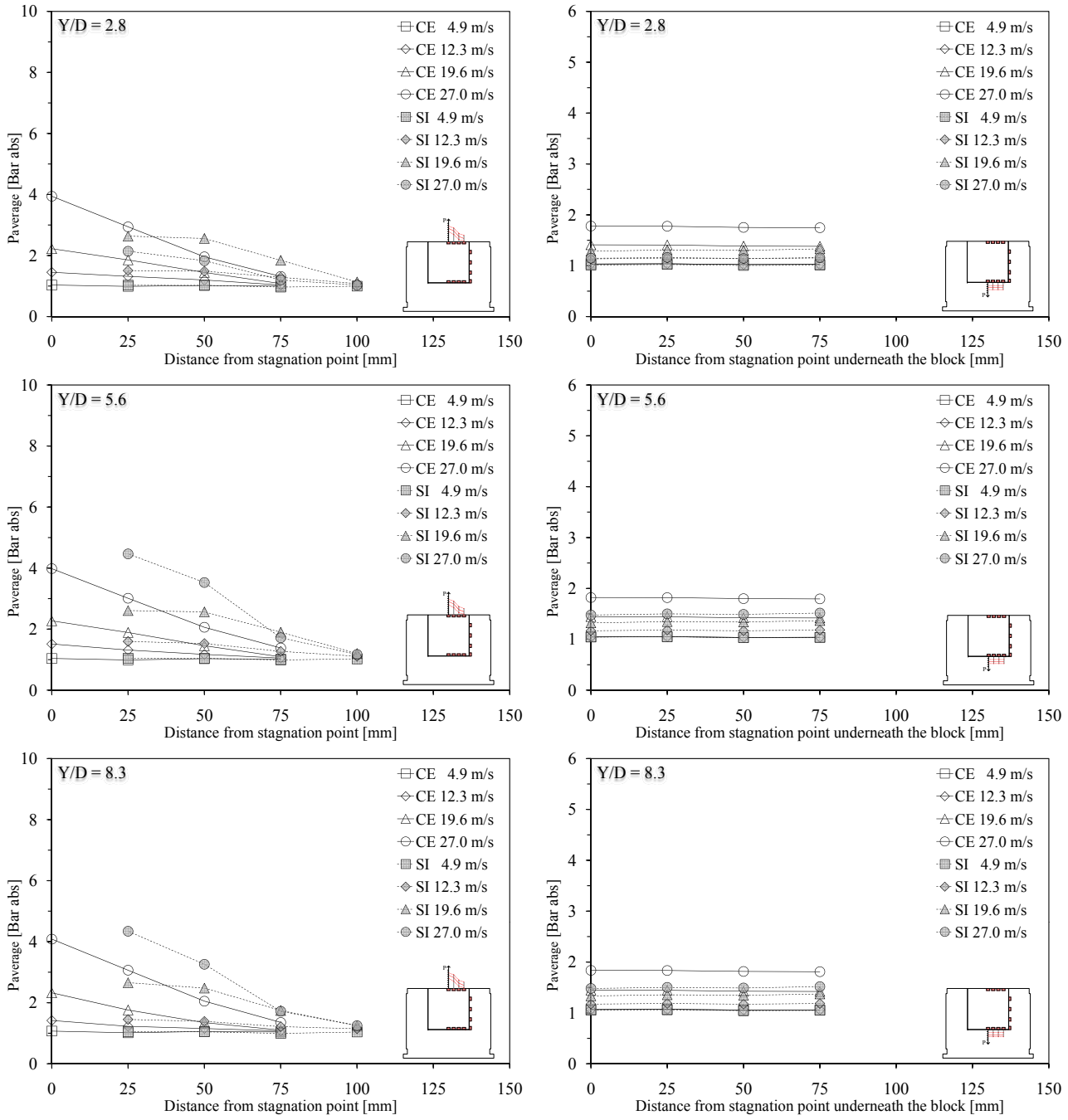

Figure 7.64: Comparison of the pressure field surrounding the block for configurations CE (jet impact on the block center) and SI (jet impact on the block right side) as a function of jet velocity (4.9, 12.3, 19.6 and 27.0 m/s) and Y/D ratio (2.8, 5.6 and 8.3). Mean pressures acting on the block upper face (left column) and underneath the block (right column). Core jet (first row), transition jet (second row) and developed jet (third row). Pressures are expressed in absolute Bar.

the case for these four configurations. The mean pressure evolution is similar for all configurations with some small difference in the trend line. Maximum pressures are more subjected to the pressure fluctuations acting on the block, but show a similar behavior for both types of lateral guides.

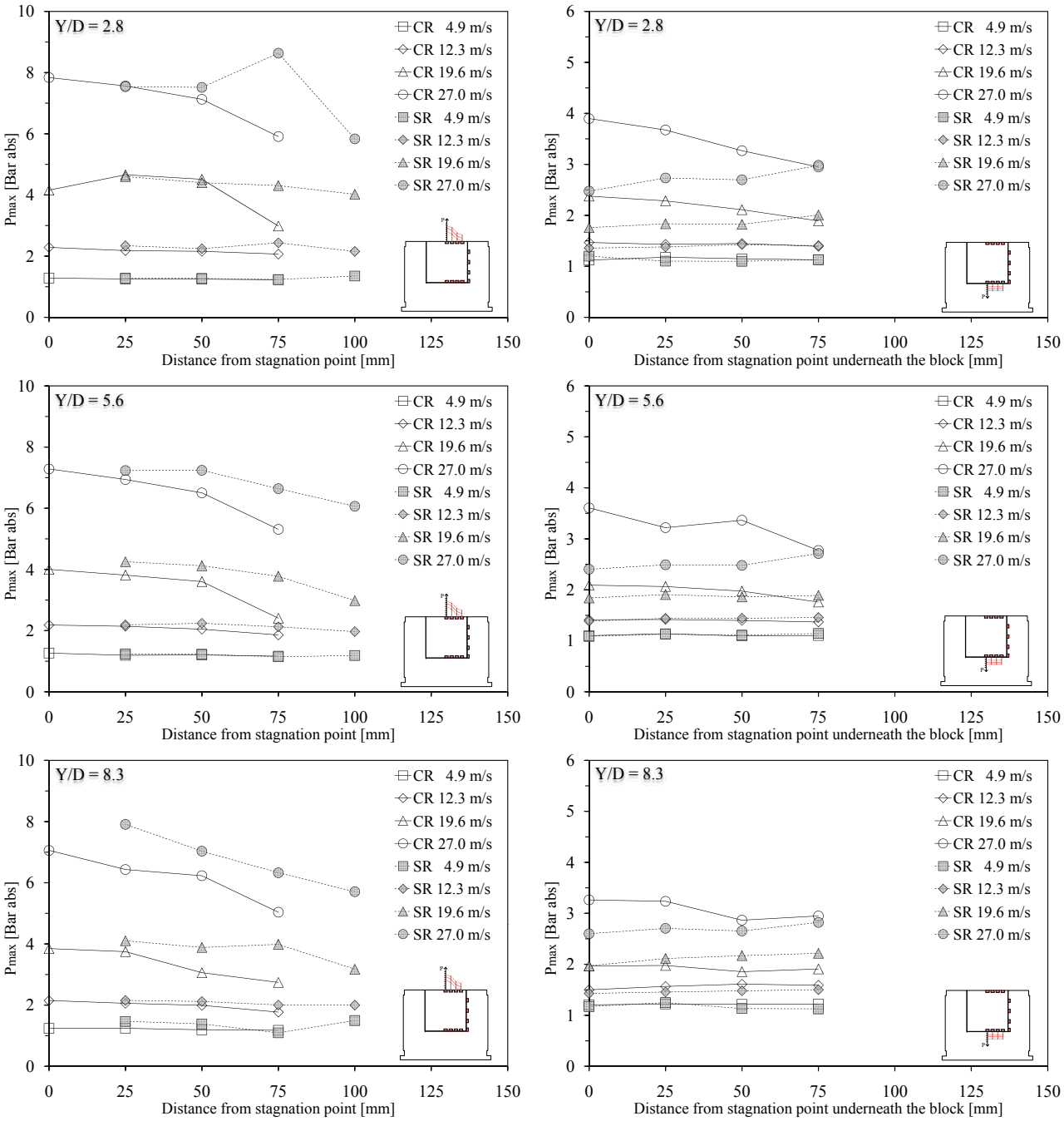

Figure 7.65: Comparison of the pressure field surrounding the block for configurations CR (jet impact on the block center) and SS (jet impact on the block right side) as a function of jet velocity (4.9, 12.3, 19.6 and 27.0 m/s) and Y/D ratio (2.8, 5.6 and 8.3). Maximum pressures acting on the block upper face (left column) and underneath the block (right column). Core jet (first row), transition jet (second row) and developed jet (third row). Pressures are expressed in absolute Bar.

From the pressure field analysis is not possible to prove the existences of these block rotations, but this did not mean that they are not presents.

These rotations may change direction each time and they influences, on the block behavior, is not constant for a time interval.

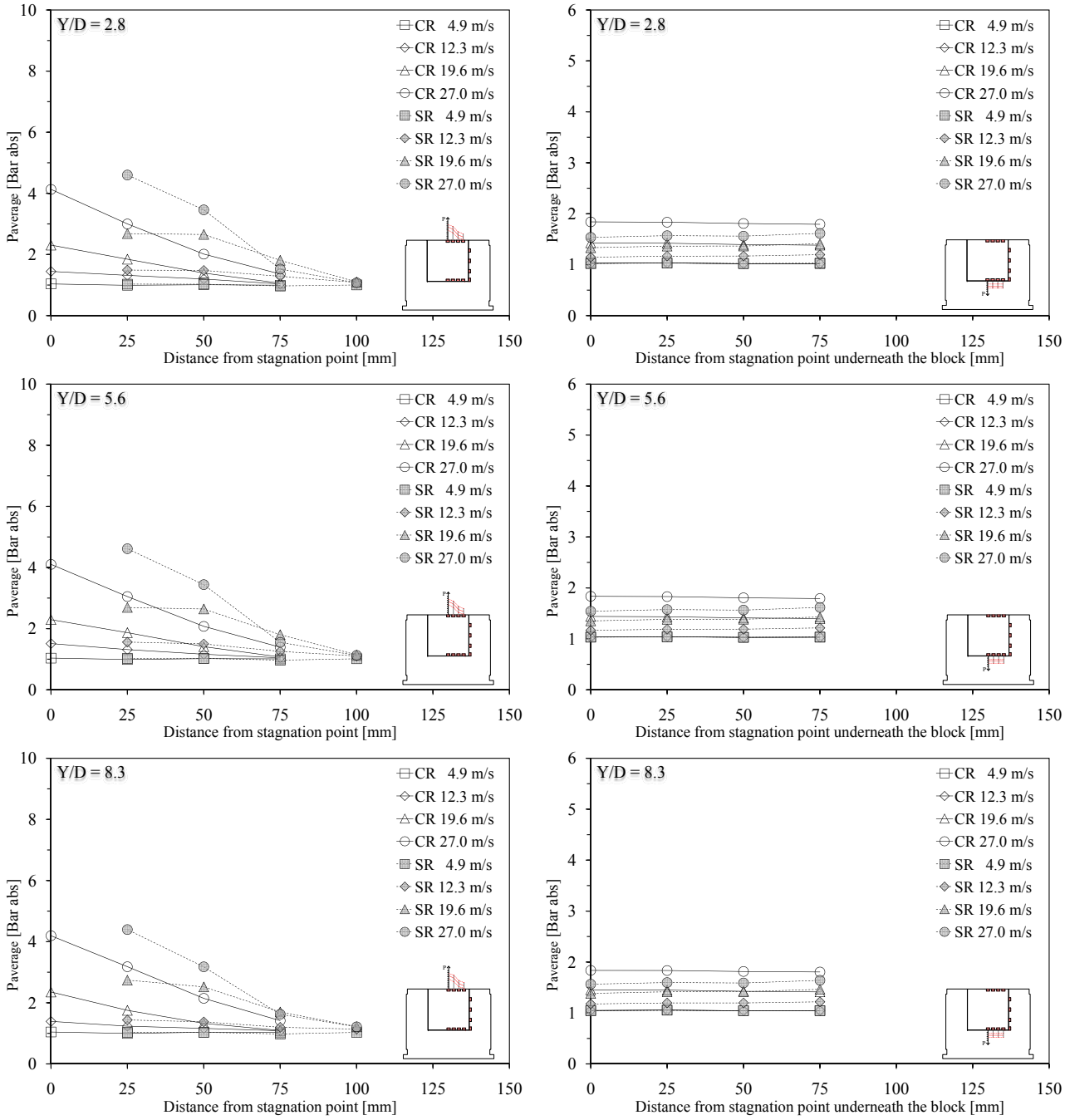

Figure 7.66: Comparison of the pressure field surrounding the block for configurations CR (jet impact on the block center) and SR (jet impact on the block right side) as a function of jet velocity (4.9, 12.3, 19.6 and 27.0 m/s) and Y/D ratio (2.8, 5.6 and 8.3). Mean pressures acting on the block upper face (left column) and underneath the block (right column). Core jet (first row), transition jet (second row) and developed jet (third row). Pressures are expressed in absolute Bar.

7.5.3 Displacements of block

The block displacements have been explained in Chapters 6.2.4 and 6.3.4.1 for configurations CR and SR.

The block displacements have been analyzed in Chapter 7.3.2.

Figure 7.67 shows the evolution of maximum and mean displacements for configurations with the jet impact on the block center (CE and CR).

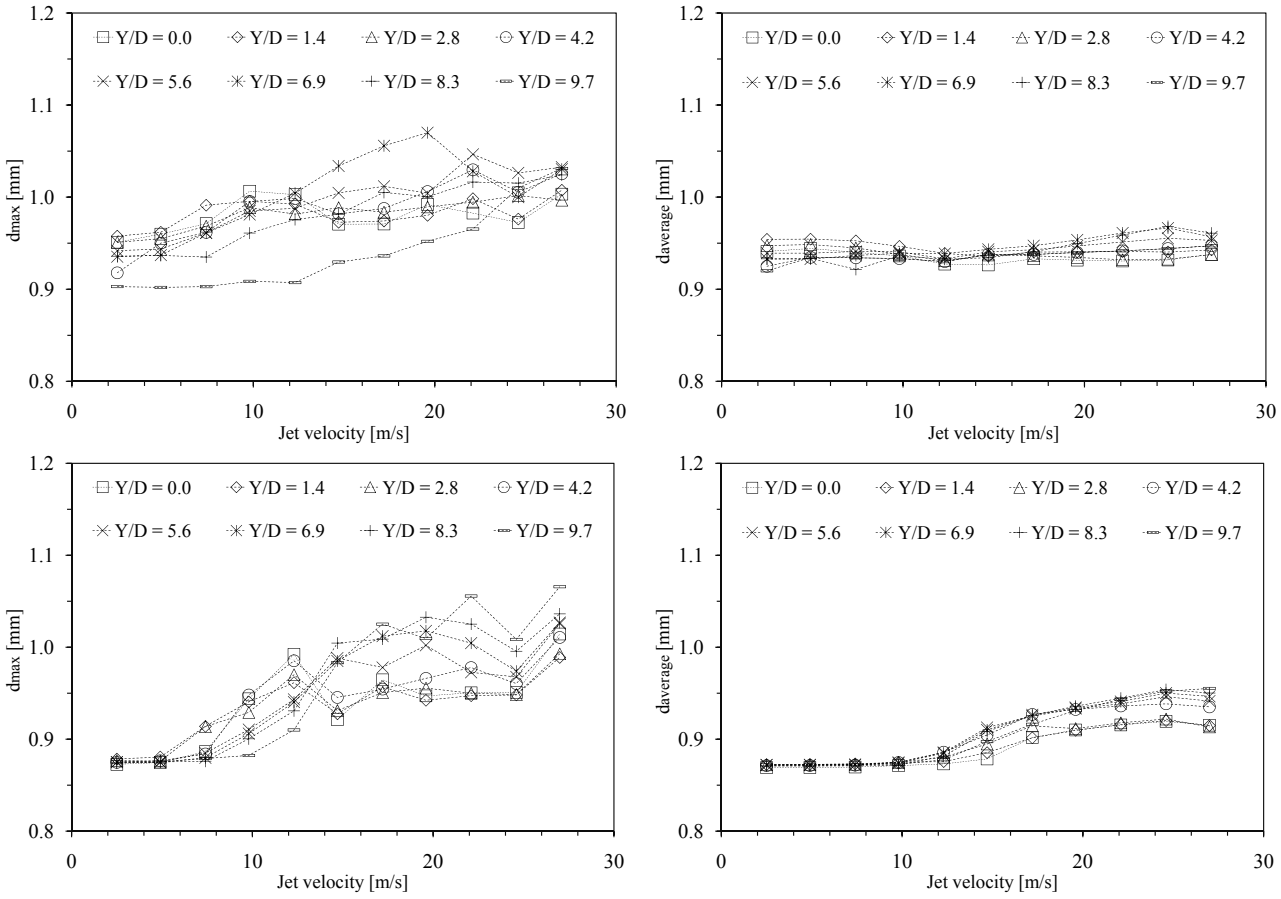

Figure 7.67: Comparison of block displacements for configurations CE and CR (jet impact on the block center) as a function of jet velocity (2.5-27.0 m/s) and Y/D ratio (0-9.7). Maximum (top left) and mean displacements (top right) for configuration CE. Maximum (bottom left) and mean displacements (bottom right) for configuration CR. The block initial position corresponds to a distance of ∼0.85 mm.

There are some small differences between both configurations: mean displacement shows a different evolution with an increase of the jet velocity. For configuration CR, the block begins to move for jet velocities larger than 9.8 m/s. For smaller velocities, the block is in its initial position. When the jet velocity increases, it reaches a new equilibrium position. Maximum and mean displacements follow this evolution as a function of the jet velocity. For configuration CE, mean pressure is almost constant along the whole range of jet velocity. Maximum and mean values are similar for both configurations.

The observed differences in the block movements are in the order of magnitude of 10^{-2} mm. The block may be not pushed inside the central cavity in the same way for both configurations, or the block lower face moves down due to the temperature changes (lid dilatation).

For the largest jet velocity (27.0 m/s), the displacement growth suddenly and this growth is more accentuate for configuration CR.

Figure 7.68 shows the evolution of maximum and mean displacement for configurations with the jet impact on the block right side.

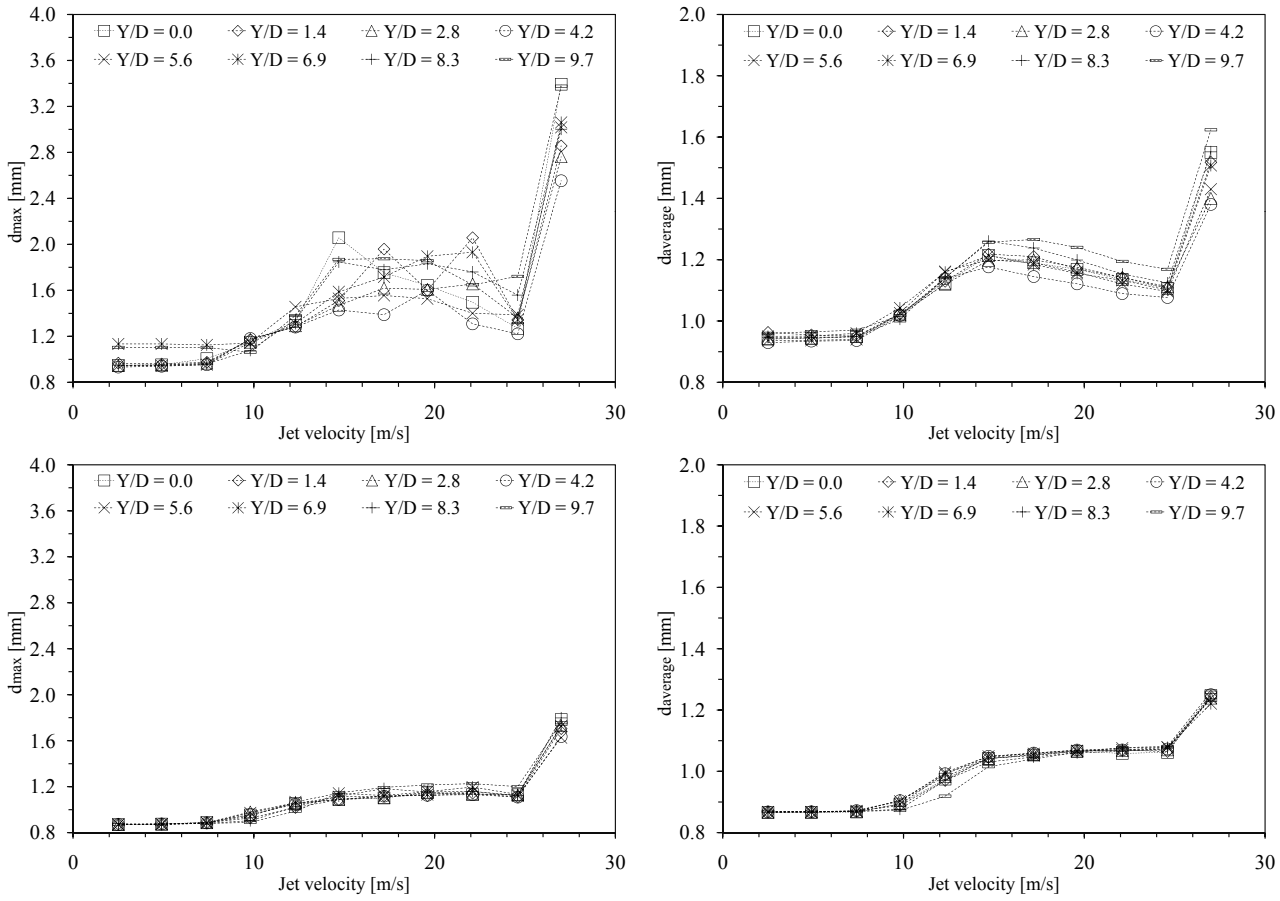

Figure 7.68: Comparison of block displacements for configurations SI and SR (jet impact on the block right hand side) as a function of jet velocity (2.5-27.0 m/s) and Y/D ratio (0-9.7). Maximum (top left) and mean displacements (top right) for configuration SI. Maximum (bottom left) and mean displacements (bottom right) for configuration SR. The block initial position corresponds to a distance of ∼0.85 mm.

The jet impact on the block right side shows a different behavior than the configurations with the jet impact on the block center: configuration SI shows larger vertical displacements than configuration SR. Maximum and mean displacements are different, but the evolution along the whole range of jet velocity is similar. As observed before, the largest jet velocity corresponds normally to a larger increase of the block uplift (before it was smaller).

The block is in equilibrium for jet velocities lower than 7.4-9.8 m/s (in contact with the central cavity bottom), then it moves up and find a new equilibrium position that is quite

constant. At this moment the block may get stuck for a certain time in the cavity and the displacements are limited. For the largest jet velocity (27.0 m/s), the block is again free and suddenly moves up.

To have a thorough analysis of this possible phenomenon, the time evolution of displacements has been analyzed for several water depths and jet velocities. This evolution did not show this phenomenon, the block fluctuates (up and down) under the pressure solicitations. Exactly the same behavior has been observed for the previous configurations.

It is not evident to affirm, if this different displacement behavior is related to the type of lateral guides or to the block rotations. It is strange that for the largest jet velocity the block shows this sudden large displacement, but it is present for all configurations (more accentuate for asymmetric jet impacts).

Figure 7.69 shows the evolution of maximum and mean displacements for configuration with jet impact on the block left side. As observed before, the block solicited on the left side shows displacements larger than if it was solicited on the right side. The pressure field could not be compared due to the transducers location on the block upper face (between 100 and 175 mm from the stagnation point). Configurations SL and SI/SR should have a similar pressure field and the displacements should as well be similar, but is not the case: configuration SL shows larger displacements than the other two. The lateral guides are the same, which means that the friction force should already be equal. These differences may be related to small rotations of the block.

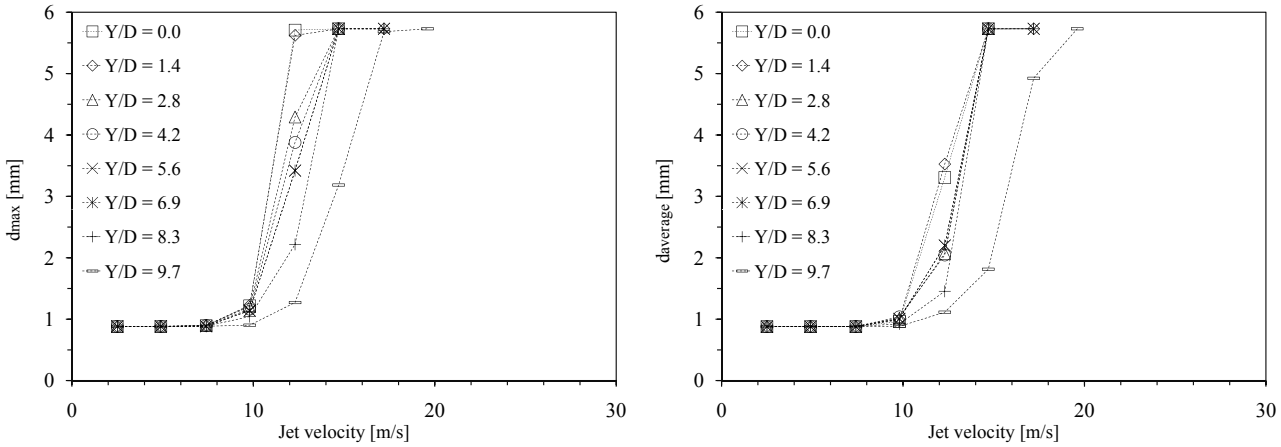

Figure 7.69: Block displacements for configurations SL (jet impact on the block left hand side) as a function of jet velocity (2.5-14.7 m/s) and Y/D ratio (0-9.7). Maximum (left) and mean displacements (right). The block initial position corresponds to a distance of ∼0.85 mm.

The differences, observed between configurations SI and SR (right side impact), may be related to the block lateral guides that modify the friction force acting on the block or by the

small block rotations. The kinetic friction coefficient measured and summarized in Chapter 5.3.4 is similar for both lateral guide (two contact points: $\mu_k = 0.29$ and eight contact points: $\mu_k = 0.32$) and cannot be the source of this difference on the block movements.

The small rotations may be the source of the differences between configurations SR and SL (right side and left side impact) because the friction force is almost the same (same lateral guide).

7.5.4 Dynamic block impulsion

In Chapter 7.1 the dynamic block impulsion has been analyzed for symmetric an asymmetric jet configurations.

The added mass coefficient shows a different behavior if the jet impacts on the block center or is "de-axed". The coefficient is quite constant along the whole range of jet velocities. It is small for symmetric jet impacts (CE and CR) but for asymmetric solicitations (SI, SR, SL, RR, CN and ACN) the coefficient has another order of magnitude. Small jet velocities (equal to small displacements) needed large coefficients and large jet velocities (equal to large displacements) needed small coefficients. As explained before in Chapter 7.1, the added mass coefficient decrease with an increase of jet velocity, as was observed as well for the pressure reduction coefficient (define the pressures acting on the block surface where no pressure measurements have been made).

The added mass influences the amplitude of block movements. A large coefficient generates small displacements, but for the same jet velocity if the block is loaded by a symmetrical or asymmetrical jet, the added mass coefficients show another order of magnitude (Table 7.1).

The order of magnitude of the added mass coefficients is similar for all jet impact soliciting the block asymmetrically, independently where is situated this impact. Moreover, if the block is not loaded symmetrical, the surface where the pressures are unknown increases and it is influenced by the pressure reduction coefficient. This coefficient modifies the force acting on the block upper face (F_{up}) that could be positive or negative (boundary between impinging region and wall jet region at the extremity of the exponential distribution).

The block impulsion analysis highlights a different behavior for the two coefficients, but is not possible to affirm if it is related to the block rotations or only to the different solicitations generated by the asymmetric jet impact on the block.

7.5.5 Conclusions

Pressure field, displacements and dynamic block uplift analysis did not allow to confirm or to eliminate the existence of these small rotations of the block. It seems that something happens in the central cavity, but with the performed measurements it is difficult to find a relationship between asymmetric jet impact and different block response.

To observe very small rotations, a more precise accelerometer should be installed inside the block, which hast to be able to record data along 2- or 3-axis (record the block rotations).

Chapter 8

Practical relevance

8.1 Introduction

Dynamic block impulsion is one of the phenomenon that governs the rock scour downstream of hydraulic structure in general, and high head dams in particular. This scour process depends also on the rock characteristics (in-situ stresses, Young's modulus ...) and the fissure characteristics (geometry, persistence, roughness, aperture and filling material), as has been explained by Bollaert (2002b). For a single rock block founded in the fissured rock mass, the phenomenon has been explained in Chapter 5.4. Based on the present work, it was found that the added mass is also an important parameter and should be integrated in the computation of the block impulsion, as explained in Chapter 7.1.

By analyzing the block impulsion, the added mass, for the present experimental facility, shows two different behaviors as a function of the jet solicitations (symmetrical or asymmetrical jet impacts). Symmetrical jet impacts are characterized by rather small added mass coefficients, independent of the jet type (core, transition or developed jets or Y/D ratio) and the jet velocity. The pressure reduction coefficients are quite constant for all parameters (Y/D ratio and jet velocity) because the surface where no pressures have been measured is small related to the total block surface. Asymmetrical jet impacts show a different behavior. The added mass coefficients for small jet velocities show large values and then for larger jet velocities it decreases. The coefficient begins to decrease when the block moves up (7.4-9.8 m/s), independently of the jet configuration (left or right side, corner or radial). The pressure reduction coefficient has more influence for an asymmetrical jet impact because the surface where the pressures are unknown is larger. The coefficient decreases as a function of the jet velocity (reaching also negative values for large jet velocities) but until the block begins to move the coefficient shows an increase of its values.

In the following, net force, block impulsion and block uplift are illustrated for three configurations (jet impact on the block center CR, on the right side SR and on the corner CN). The illustrated values summarize the results for core (Y/D = 2.8 or Y = 0.2 m), transition (Y/D = 5.6 or Y = 0.4 m) and developed jets (Y/D = 8.3 or Y = 0.6 m) and four jet velocities (4.9,

12.3, 19.6 and 27.0 m/s). Net force, block impulsion and block uplift have been computed for configurations equipped with lateral guides having eight contact points (Chapter 4.2.1.3). This type of lateral guide has a "larger" friction coefficient as explained in Chapter 5.3.4, although the difference between the two types is small: μ_k equal at 0.29 (two contact points) and at 0.32 (eight contact points). In nature, the friction coefficient may be larger due to the characteristics of the surrounding fissure.

The net uplift coefficient C_{up} is computed for the same configurations and parameters (water depths but for all jet velocities).

8.2 Net force, net impulsion and uplift

Figures 8.1 to 8.3 may be used to estimate the block uplift for similar test/prototypal conditions: jet impact positions, Y/D ratios and jet velocities. These values have been computed using the present experimental facility (flow conditions, plunge pool geometry, block geometry, block weight, fissure geometry, added mass and pressure reduction coefficient). Some adaptions may be necessary for practical use (as an example if the block weight is different or the friction coefficient is different). If other assumptions have to be made (for the added mass and the pressure reduction coefficients), the complete computation of the dynamic uplift has to be performed (Chapter 5.4).

Maximum, mean and minimum values of net force, block net impulsion and block uplift are illustrated by Figures 8.1 to 8.3. A positive value means that the block moves up and, vice versa, a negative value means that it moves down in the central cavity (Figure 5.4).

Maximum and minimum values correspond to a time interval of 10^{-3} s (it corresponds to the acquisition frequency $f = 1$ kHz). The mean value was computed for a time interval of ~65.5 s (2^{16} samples or 65'536 samples recorded at 1 kHz). Net impulsion and block uplift have to be multiply for a time interval to obtain an estimation of the final possible displacement.

The large difference that appears between configurations CR and SR/CN is related to the block solicitations (symmetric and asymmetric jet impact) and to the added mass coefficients. Configuration CR shows larger values for the net force acting on the block (all forces acting on the block are explained in Chapter 5.3). The uncertainty on the pressure acting on the block upper face, where no measurements have been made, is less. Configurations SR and CN show similar values, but configuration CN has smaller values due to the larger surface where the pressures are unknown.

The net force acting on the block is directly linked to the block impulsion, and the impulsion is directly linked to the block uplift. The uplift values are strongly affected by the added mass: the impulsion is divided by the sum of the block mass and the added mass. More the added mass is larger and more the impulsion is smaller. For symmetric jets, maximum and minimum block uplift are approximately $\pm$ 10^{-2} mm and mean value is approximately 10^{-3} mm (quite zero). For asymmetric jets, maximum and minimum block uplift are very small (10^{-3} mm) and mean value is practically zero.

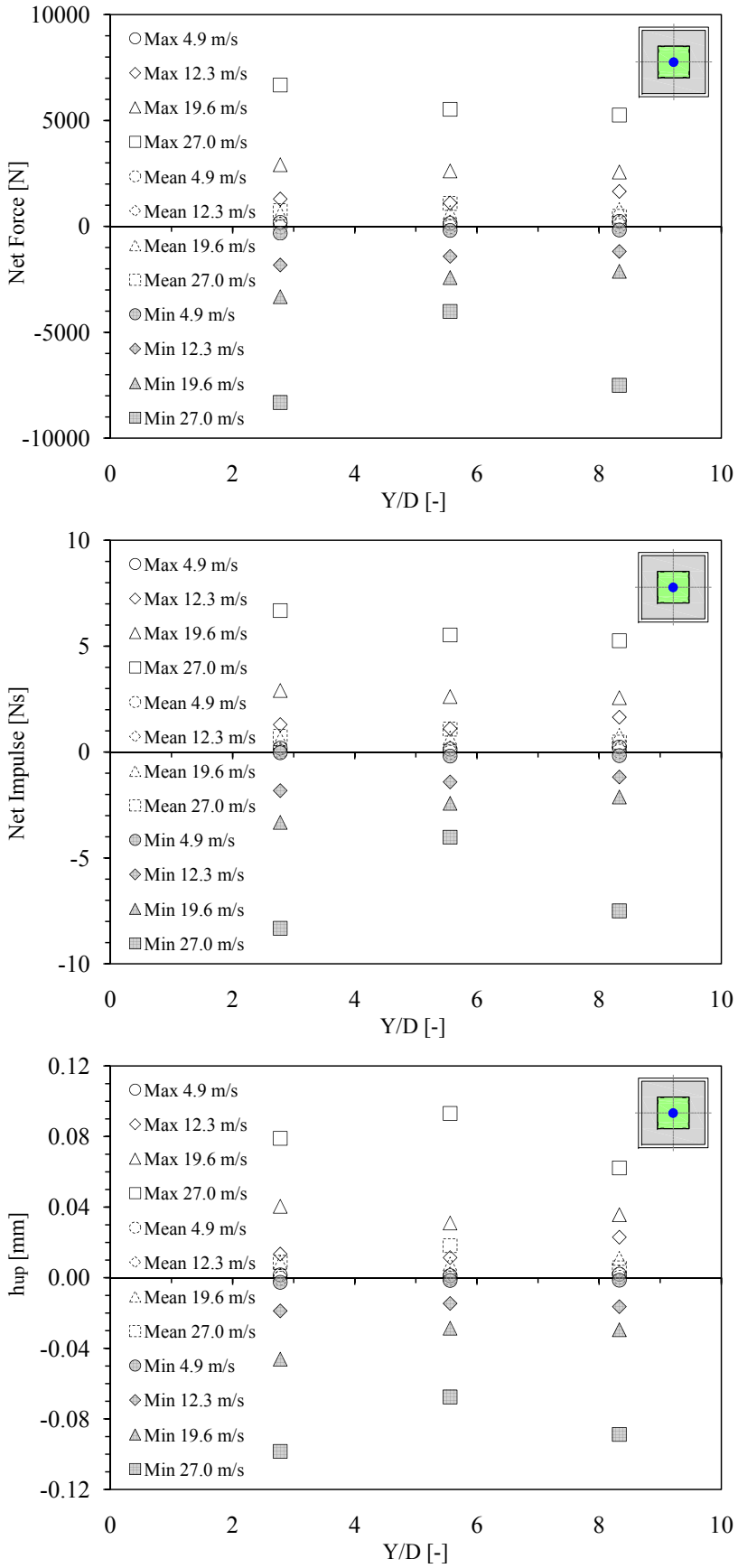

Figure 8.1: Block net force acting on the block (top), net impulsion (center) and block uplift (bottom) for configuration CR (jet impact on the block center), four jet velocities (4.9, 12.3, 19.6 and 27.0 m/s) and three water depths (Y = 0.2, 0.4 and 0.6 m or Y/D = 2.8, 5.6 and 8.3).

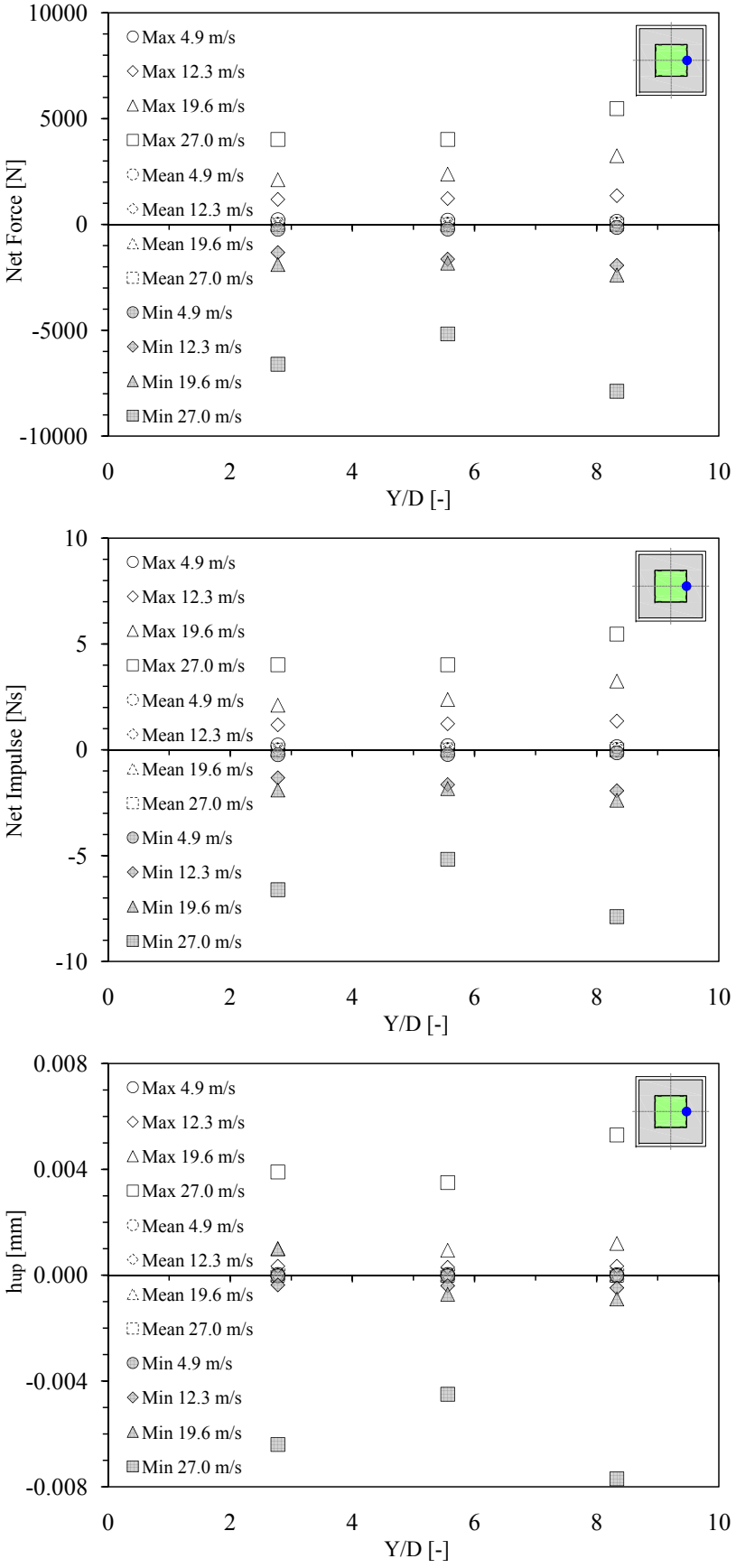

Figure 8.2: Block net force acting on the block (top), net impulsion (center) and block uplift (bottom) for configuration SR (jet impact on the block right hand side), four jet velocities (4.9, 12.3, 19.6 and 27.0 m/s) and three water depths (Y = 0.2, 0.4 and 0.6 m or Y/D = 2.8, 5.6 and 8.3).

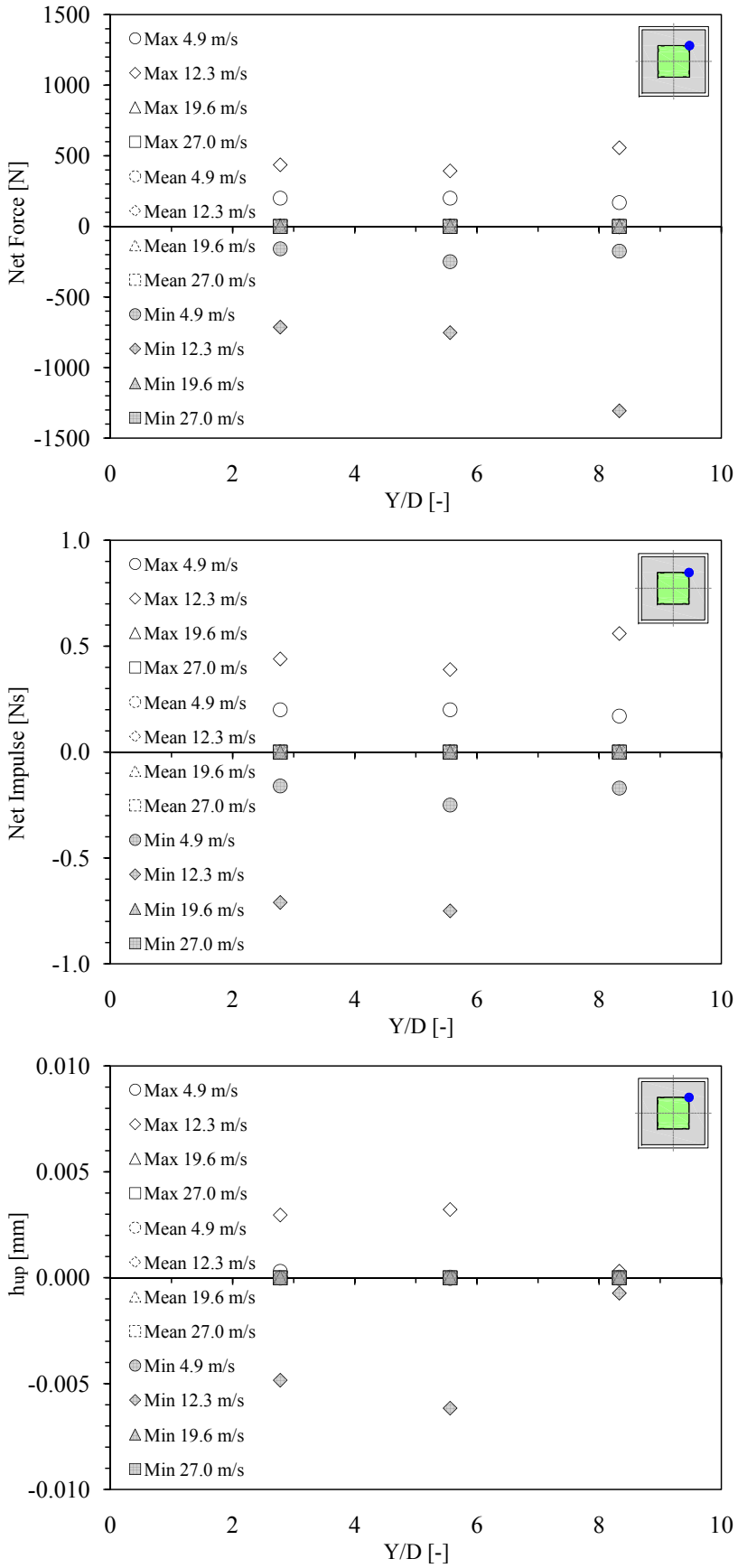

Figure 8.3: Block net force acting on the block (top), net impulsion (center) and block uplift (bottom) for configuration CN (jet impact on the block corner), four jet velocities (4.9, 12.3, 19.6 and 27.0 m/s) and three water depths (Y = 0.2, 0.4 and 0.6 m or Y/D = 2.8, 5.6 and 8.3).

8.3 Time evolution

As an example, Figures 8.4 and 8.5 show the time evolution of the pressure acting on the block, the net force, the block impulsion and the block uplift for configuration SR (jet impact on the right side) with a Y/D ratio of 8.3 (Y = 0.6 m) and jet velocities of 12.3 and 27.0 m/s. The time interval is the same for all graphs in Figures 8.4 and 8.5.

The pressures are relative values (without atmospheric pressure) and are normalized by the kinetic energy at the jet impact ($V_I^2/2 \cdot g$). The pressure signal of three transducers are plotted on Figures 8.4 and 8.5 top left (N° 309 on the block center, N° 312 at 25 mm from the fissure entrance and N° 321). Transducers N° 309 and N° 312 are located on the block upper face and they show the pressure acting radially outwards from the stagnation point. Transducer N° 321 shows the pressure signal underneath the block (is almost similar for all transducers located underneath the block).

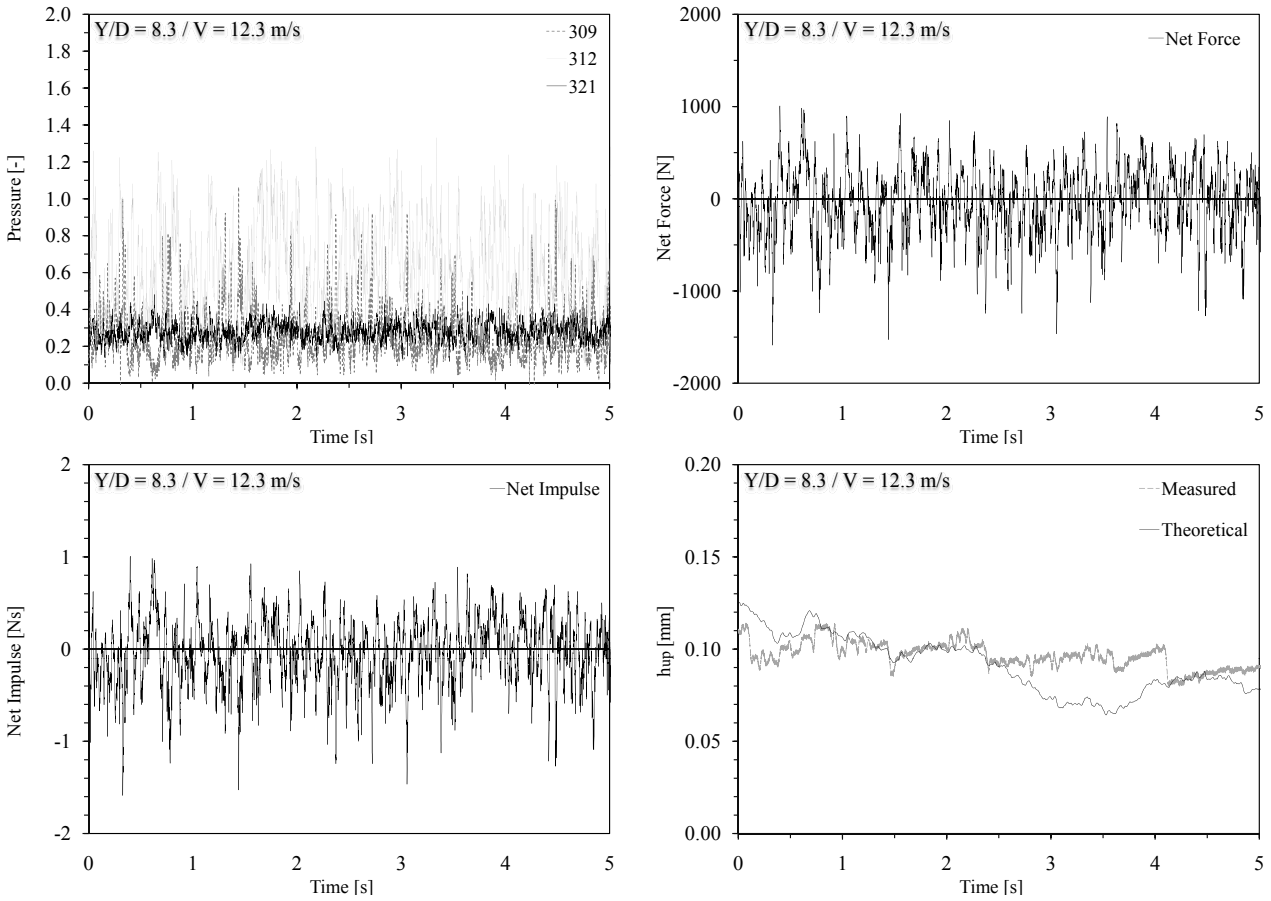

Figure 8.4: Time evolution of normalized pressure for three transducers (top left), net force acting on the block (top right), block impulsion (bottom left) and block uplift measured and computed (bottom left) for configuration SR (jet impact on the right hand side), Y/D = 8.3 (Y = 0.6 m) and a jet velocity of 12.3 m/s.

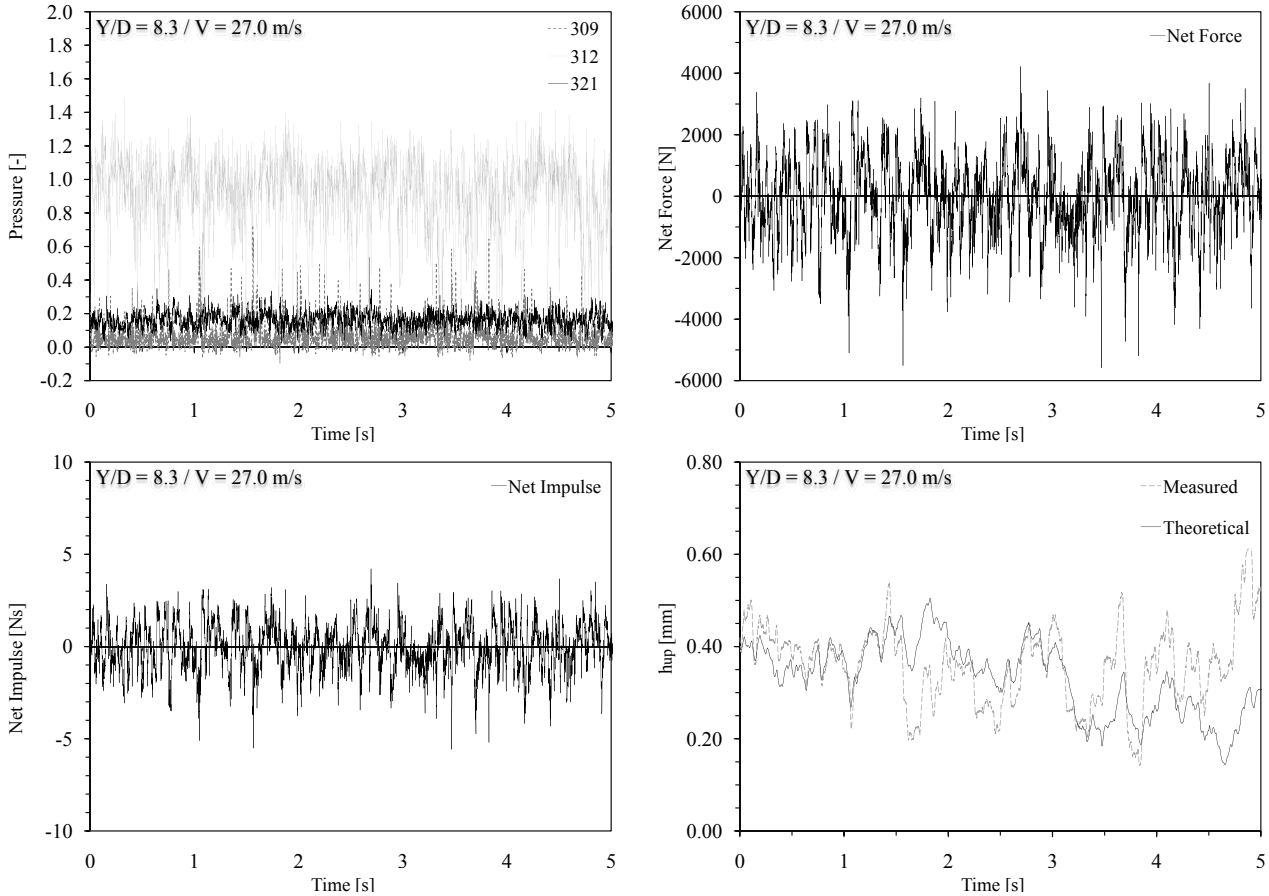

Figure 8.5: Time evolution of normalized pressure for three transducers (top left), net force acting on the block (top right), block impulsion (bottom left) and block uplift measured and computed (bottom left) for configuration SR (jet impact on the right hand side), Y/D = 8.3 (Y = 0.6 m) and a jet velocity of 27.0 m/s.

8.4 Net uplift coefficient C_{up}

Bollaert (2002b) defined the net uplift coefficients C_{up}, for an open-ended fissure (D-joint), as the maximum difference between the pressure acting at the fissure first bend (near the central cavity bottom) and the average value of the pressures acting near the fissure entrance at the plunge pool bottom (Figure 1.4). Those correspond to the maximum net instantaneous uplift pressure that has been measured on the simulated rock block. The net uplift coefficient equation could be written as follows:

$$C_{up} = \frac{p_{max,fissure\_end} - \overline{p}_{plunge\_pool}}{\alpha \cdot \frac{V_I^2}{2 \cdot g}} \tag{8.1}$$

where $p_{max,fissure\_end}$ is the maximum pressure at the first fissure bend, $\overline{p}_{plunge\_pool}$ the mean pressure at the plunge pool bottom near the fissure entrance, V_I the jet velocity at the impact on the water surface in the plunge pool, g the gravity acceleration and α the velocity profile correction parameter that has been considered equal to 1.

Bollaert (2002b) performed a literature review of this coefficient. Based upon his own measurements, he found values for submerged jets in a range of 0.8 to 1.6. He compared this values with actual design criteria, which consider a C_{up} of 0.5-1.0 as the maximum possible value. Bellin and Fiorotto (1995) made measurements of net uplift forces on concrete slabs and proposed an absolute maximum value of 0.5. Liu et al. (1998) measured net uplift pressures on simulated rock blocks of 2 to 4 times the root-mean-square value corresponding to uplift coefficient values in a range of 0.5 to 1.0. By applying a maximum underpressure underneath the rock block together with a zero pressure at the whole block upper face, the physically maximum plausible value could be obtained: 1.0. This, however, is not possible in practice.

Bollaert (2002b) solicited directly the fissure with the jet impact. In this work, the jet impact on the block upper face changes position as a function of the configuration. Not all configurations load directly the vertical fissure surrounding the block. To take into account this aspect and the pressure distribution on the block upper face, the net uplift coefficient has been computed with pressures that have been spatially average. The mean pressure acting on the block upper face corresponds to the mean value of each transducers (on the block upper face: N°s 309 to 312) pondered with their surface of influence (similar at the concept to compute the pressure integration on the block, as explained in Chapter 5.3.3). Maximum pressure corresponds to the maximum value recorded with the four transducers located underneath the block (N°s 318 to 321). Whether an average of the maximum pressures values is used to compute the coefficient, the result did not change.

Figure 8.6 shows the net uplift coefficient computed for the three configurations (CR, SR and CN).

The net uplift coefficient decrease as a function of the jet velocity for the three configurations. The kinetic energy, which normalized the coefficient, increases quadratically with the

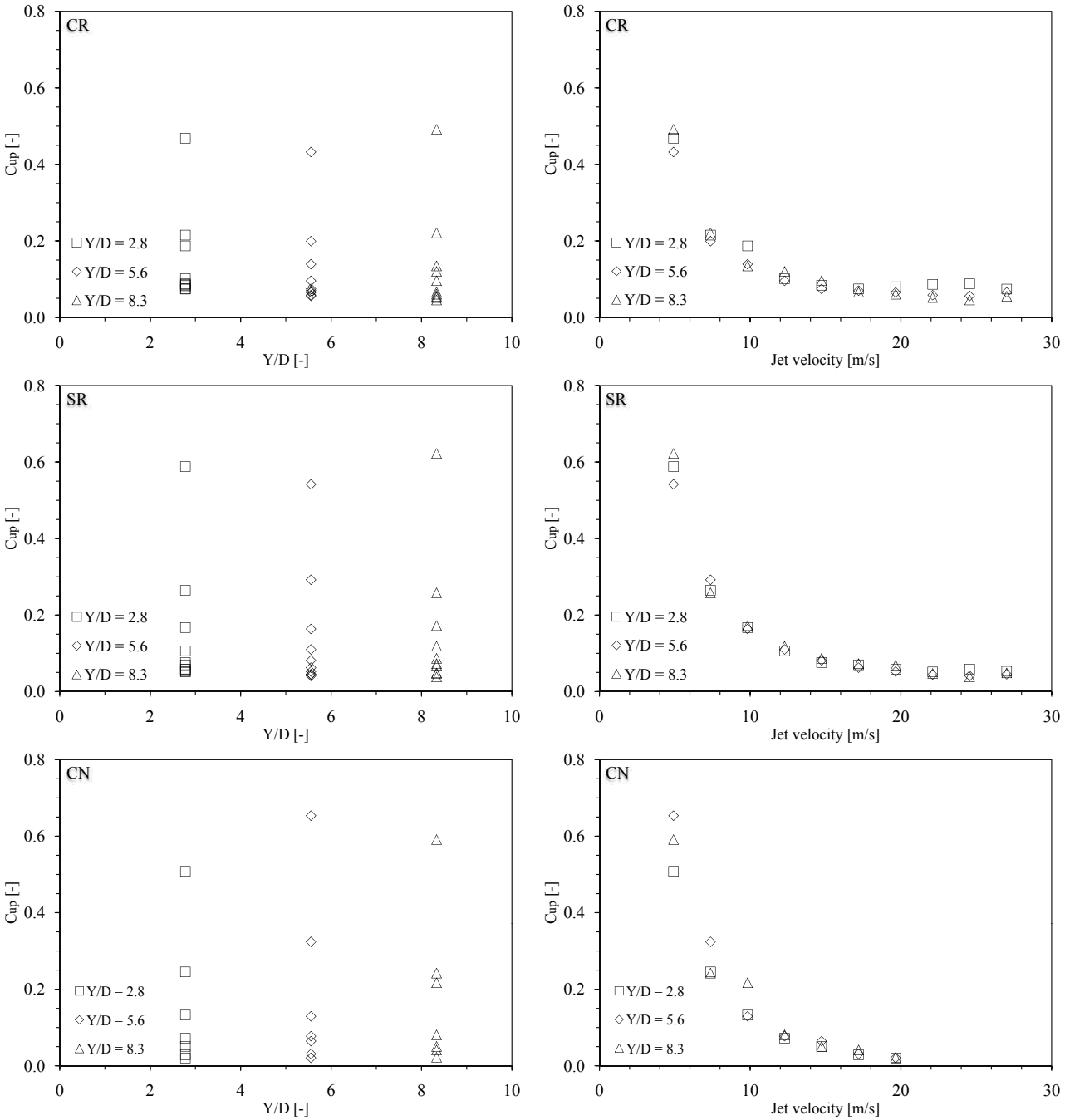

Figure 8.6: Net uplift coefficient computed for configurations CR (first row), SR (second row) and CN (third row) as a function of the Y/D ratio (left) and as a function of the jet velocity (right). Three water depths (Y/D = 2.8, 5.6 and 8.3 or Y = 0.2, 0.4 and 0.6 m) and jet velocities ranging between 4.9 and 27.0 m/s for configurations CR and SR and only up to 19.6 m/s for configuration CN.

jet velocity. Hence, the larger jet velocities show small coefficient values. However, the difference between maximum and mean pressure increases as a function of the jet velocity. Core, transition and developed jets show a similar behavior.

The computed coefficient values are smaller than the values found by Bollaert (2002b), but situated in the literature range. He computed the coefficient only for a single measurement point

and did not take into to account the spatial distribution of the pressure. Near the stagnation point (jet impact point) the pressure values are the largest and decrease radially outwards. The importance of these largest values on the mean pressure that has been spatially average (the surface where these pressures act on the block upper face) is small. More the distance from the stagnation point increase (the pressure decreases radially outward) and more the surface where these pressures act becomes larger. Hence, the mean pressure is not so large on the block upper face.

The coefficient changes radially outwards from the stagnation point for pressures recorded with transducers located on the same vertical axis (as an example: transducers N^o 309 and N^o 321). The pressures measured at or near the stagnation point are largest (maximum and mean). Underneath the block the pressure increases as a function of the jet velocity and is almost constant on the whole block lower face. Hence, the coefficient increases from the stagnation point moving radially outwards. With an increase of the jet velocity, the coefficient computed near the stagnation point decreases (may reach negative values) and faraway from the stagnation point it increases.

For the illustrated three configurations and for the three jet types (core, transition and developed jets), the net uplift coefficient decreases as a function of the jet velocity and ranges between 0 and 0.6.

Chapter 9

Conclusions and outlook

9.1 Concluding remarks

The influence of high-velocity water jets impacting on "artificial rock block" surrounded a by fissured "rock mass" has been investigated. A new experimental facility was constructed and integrated in the existing LCH experimental facility. The "artificial rock block" was simulated by a highly instrumented steel block having a cubic shape and an apparent density similar to the rock density. The fissured rock mass was simulated by a measurement box that surrounded the block with a full interconnected 3-dimensional fissure of 1 mm thickness.

For the first time, the pressure field surrounding the block and it responses to the hydrodynamic solicitations (vertical displacements and accelerations) have been measured simultaneously. The block and the 3-dimensional fissure have been solicited with several jet impact positions (symmetrical and asymmetrical), water depths (core, transition and developed jets, Y/D ratio ranging between 0 and 9.7) and near-prototype jet velocities (2.5-27 m/s). The influences of different parameters have been analyzed as a function of the water depth (Y/D ratio) and the jet velocity.

9.1.1 Pressure field surrounding the block for block free to move with natural air entrainment

The pressure field acting on the block upper face (at the plunge pool bottom) was an exponential distribution centred at the stagnation point, as proposed in literature. This distribution is independently of the jet impact position: the pressure decreases quickly from the stagnation point radially outwards. The boundary between the impinging region and the wall jet region may be fixed at 100-120 mm from the stagnation point (following the pressure measurement performed on the block upper face).

The pressure field acting inside the 3-dimensional fissure (along the vertical fissure and underneath the block) is almost constant for a given water depth and jet velocity. The pressure increases as a function of the water depth and jet velocity. The pressure acting inside the

vertical fissure shows a weak increase as a function of the distance from the plunge pool (water load). Maximum and minimum extreme pressures are localized near the fissure entrance where a weak a "cavitation" phenomenon or by a compression-decompression phenomenon of the air bubbles present into the water near the fissure entrance may appear. This behavior is more evident for jets impacting on the block side, directly on the fissure axis. Underneath the block the pressure acting on the whole lower face of the block is almost constant (maximum, mean and minimum pressure) and increases as a function of the jet velocity.

The pressure values recorded inside the fissure are lower than the values recorded on the block upper face and no transient amplifications have been detected.

9.1.2 Pressure coefficients

The pressure coefficients computed for the transducers situated on the block upper faces are in reasonable agreement with the theoretical curves proposed by Ervine et al. (1997) and with previous pressure records made by Bollaert (2002b) and Manso (2006). Ervine's curves have been developed using measurements performed at the plunge pool bottom only. The pressure coefficients computed for transducers located inside the 3-dimensional fissure show lower values than at the plunge pool bottom. Mean, turbulent, positive or negative extreme fluctuations and positive or negative extreme pressures did not solicit the fissure as at the plunge pool bottom. The extreme values are attenuated inside the fissure, except near the fissure entrance.

Jet velocities lower than 7.4 m/s generate high coefficient values that did not match with the previous measurements present in literature (the kinetic energy that normalizes the coefficients is probably too small).

9.1.3 Block displacements and accelerations

For all Y/D ratios and all configurations, the block moves up and reaches a new equilibrium position for jet velocities greater than 7.4-9.8 m/s. For lower jet velocities, the block, after its vertical displacements, systematically returns to its initial position (in contact with central cavity bottom). For jet velocities larger than 7.4-9.8 m/s the block always finds a new equilibrium position (not in contact with central cavity bottom anymore).

The vertical displacements are strongly influenced by the jet impact position: the more the jet is asymmetrical (the jet impact point moves from the block center to the block extremities) the larger are the block displacements.

The jet impact on the block corner generates the largest displacement, reaching ∼160 mm (jet velocities: 17.2-19.6 m/s). When the jet impact on the block center, the maximum displacement reaches only some 10^{-2} mm (jet velocity: 27.0 m/s).

The accelerations are related to the block displacements and show a similar behavior, but minimum accelerations are affected by electrical noise generating incongruous values that reach the acceleration lower limits. There are some uncertainties on the recorded accelerations due theses incongruous values that may affect as well mean and maximum accelerations.

9.1.4 Power Spectral Density

The Power Spectral Density (PSD) shows a different behavior between transducers situated on the block upper face and inside the 3-dimensional fissure.

The pressure transducers located on the block upper face (at the plunge pool bottom) have a behavior similar to previous literature observations (Bollaert (2002b) and Manso (2006)). At the plunge pool bottom the low frequency part of the PSD signal ($f <$ 8-10 Hz) looks quite similar for all jet velocities. The energy per frequency decreases slowly with a slope of approximately -2/3 and faster for higher frequencies with a -1 slope.

Inside the fissure, the energy per frequency is lower than at the plunge pool bottom for the same jet velocity (as observed in the pressure field). With an increase of the frequency, two zones can be distinguished: a first zone up to 8-10 Hz and a second zone for frequencies higher than 8-10 Hz. In the first zone, the energy decreases slowly with a slope approximately situated between -1/3 and -2/3. In the second zone, two different peaks may be detected in the PSD signal: the first peak (between 10-20 and 80-100 Hz) is related to the fissure natural frequency and the second peak (between 80-100 and 200-300 Hz) is not so clearly definable. At low jet velocities, the first peak appears but not the second. When the jet velocity increases, the first peak disappears and the second peak appears. Based on the wave celerity $c_w = 1000\ m/s$, and the fissure length $L_F = 0.604\ m$ and the air concentration $C_{air} = 0.02 - 0.4$ the eigenfrequency of the joint is about 22-72 Hz. The block eigenfrequency has been detected experimentally and it ranges between 5 and 9 Hz with a peak around 7 Hz.

9.1.5 Dynamic impulsion on a rock block

The analysis of the dynamic block impulsion reveals the importance of the added mass. The added mass influences the amplitude of the vertical displacements and has to be integrated in the computation of the block impulsion.

The uplift computed from the pressure measurements, is in good agreement with the measured uplift (recorded with the displacement transducers) if an added mass and pressure reduction coefficient are taken into account. The pressure reduction coefficient influences the slope of the displacements and represents the pressure acting on the block upper face where no pressure measurements have been made (it had less influence).

The added mass shows a different behavior if the block is solicited by a symmetrical jet (jet impact on the block center) compared to an asymmetrical jet (jet impact on the block side: right side, left side, corner or radial). For configurations with the jet impacting on the block center, the added mass coefficient α_{am} is almost constant for all water depths and all jet velocities. However, for asymmetric jets the added mass coefficient α_{am} follows the behavior of the block displacements: before the block begins to move (jet velocities lower than 7.4-9.8 m/s) the added mass shows largest values. When it moves, the coefficient progressively decreases as a function of the jet velocity. The added mass coefficient depends on the jet impact position, the water depths and the jet velocities. Each tested configuration and water depth (core, tran-

sition and developed jets) has its own equation to estimate the added mass coefficient. Hence, a unique equation could not be defined.

The added mass coefficients obtained experimentally using the present facility are very different from literature values. The latter have mostly been determined for bodies moving in a stagnant fluid and not for a body moving in a strong turbulent fluid. Also, the closer two bodies are, the higher the added mass is. The highly instrumented block is strongly confined in the measurement box: the block is surrounded on five of its six faces by the measurement box (fissure thickness 1 mm). Moreover, the block is directly loaded by the jet on its free surface. An asymmetrical jet may generate some infinitesimal rotations of the block that could modify the block responses and provide additional added mass.

The strong confinement, the high-velocities of the jet and these possible small rotations might be directly related to these large values for the added mass coefficient.

The pressure reduction coefficient takes more influence, in the computation, for configurations with an asymmetrical jet impact (on the block left or right side, corner and radial). The surface where the pressures are unknown is larger related to the surface where the pressures are known. Hence, the pressures acting on the block are influenced by this coefficient. For a symmetric jet impact, this coefficient is less important because the surface where the pressures are unknown is smaller.

The added mass coefficient and the pressure reduction coefficient have been calibrated for a time interval of 30 s. The two coefficients represent a mean value but in reality they change and are not constant for each time increment. To compute the dynamic block impulsion is not comfortable using coefficients that change at each time increment.

For computations performed with only the mean pressure (without the pressure fluctuations) the block uplift corresponds to small values for all jet configurations, water depths and jet velocity (in the order of 10^{-3} and 10^{-5} mm). Analyzing the results, the block may move up for some combinations of water depths and jet velocities. The uplift evolution (or maximal uplift) may be estimated by multiplying the computed uplift with a time interval (as an example the time interval used to calibrate the two coefficients or the time interval necessary at the pressure waves to travel inside the fissure).

The uplift computed with maximum pressures is always negative and the block remains in contact with the central cavity bottom.

The block uplift computed with the pressure fluctuating components, for configurations with jet impact on the block center, is in good agreement with the measured uplift. Unfortunately, for configurations with a jet impact not on the block center, the theoretical uplift diverges from the measured uplift. This different behavior may be related to the way that the block is loaded: an asymmetric jet may generate small rotations inside the central cavity that affect the block displacements. These small rotations may affect as well the pressure acting on the block and

influence the pressure fluctuations.

When the block impulse is positive, normally the block should move upwards and downwards when the impulse is negative. This behavior has been observed for configurations where the pressures have been recorded simultaneously to the displacements (CE, CR, SI and SR). Other configurations (SL, CN and RR) combine pressures recorded for different jet configurations, which breaks the direct relationship between pressures and corresponding displacements.

To have a good similarity between theoretical and measured uplift, the complete pressure signal has to be used, in combination with the added mass and the pressure reduction coefficient. The concept of the added mass has to be integrated in the scour model developed by Bollaert (2002b) to predict the correct block impulsion, more in detail in the sub module dynamic impulsion.

9.1.6 Influence of the "passive" air entrainment by the free falling jet

For the first time, the pressure field surrounding an "artificial rock block" loaded by a water jet naturally aerated, without and with a suction-based passive aeration system has been measured. Simultaneously the block responses have been recorded (displacements and accelerations).

By analyzing the pressure field acting on the block, the mean pressure values for both configurations are practically superposed with small differences all around the block. However, maximum and minimum pressures show some differences between the two configurations. Maximum and minimum pressures show similar evolution as a function of the jet velocity but the pressure values are different. This phenomenon has been observed as well inside the fissure but the differences between maximum and minimum pressure values are smaller.

The influence of the passive air entrainment on the pressure coefficients seems quite small. Normally the configuration with natural and passive air entrainment shows the larger coefficients values (they are related to the small pressure differences recorded by the pressure transducers).

The block vertical displacements show the same behavior for both configurations: the block begins to move for jet velocities larger than 7.4-9.8 m/s and reaches the maximum uplift for a jet velocity of 19.6 m/s (approximately 160 mm). The accelerations show a similar behavior. The configuration with natural and passive air entrainment shows highest accelerations (for all jet velocities and water depths) and the mean acceleration is similar.

The power spectral density (PSD) analyze shows a different behavior for transducers situated in the plunge pool and inside the 3-dimensional fissure. At the plunge pool bottom, for jet velocities larger than 7.4 m/s, the configuration with the natural air entrainment shows an energy content larger than the configuration with natural and passive air entrainment. But for jet velocities lower than 7.4 m/s, it is the configuration with the natural and passive air entrainment that shows this behavior. The PSD shows a vertical shift (different energy content)

and the signal evolution is almost the same along the whole frequency range.

Inside the fissure, the difference between the two configurations could be described using three zones: for frequencies lower than 8-15 Hz, the configuration with natural and passive air entrainment shows normally more energy for the same frequency, between 8-15 and 100 Hz, the two configurations have almost the same energy per frequency and for frequencies large than 100 Hz, configuration with natural and passive air entrainment shows more energy per frequency. The PSD evolution as a function of the frequency is quasi similar for both configurations.

The analysis of these configurations (jet position on the block corner, lateral guides with eight contact points and block free to move along the vertical axis) did not allow to find a relationship between block responses and passive air entrainment. However, some influences of the passive air entrainment have been detected.

The pressure field acting around the block shows that the passive air entrainment influences the extreme pressure values (maximum and minimum) but the mean pressure is practically superposed for both jet aeration configurations (for all water depths and jet velocities).

The pressure coefficients are weakly influenced by the passive air entrainment. Normally, the larger coefficients are related at this configuration but the differences are small.

The passive air entrainment did not influence the displacements and the accelerations of the block for the analyzed configurations.

The power spectral density shows the existence of some differences in the energy content per frequency between the plunge pool and the fissure. The energy differences, between the two configurations, are not so large to modify the block behavior and its response to the solicitations.

The four transducers located on the block upper face are not aligned radially outwards from the stagnation point but are located perpendicularly and far away (with distances between 104 and 142 mm from this point). Hence, is not possible to estimate the real effect of the passive air entrainment on the block and fissure response.

9.1.7 Influence of the lateral guides

The analysis of the pressure field surrounding the block shows that the lateral guides (with two or eight contact points) did not affect the pressures acting around the block for configurations with the jet impact on the block center. The evolution of maximum, mean and minimum pressure, as a function of jet velocity, is almost the same for both configurations (some small pressure differences could be observed, but could be neglected due to their small order of magnitude).

However, for configurations with the jet impact on the block right side and equipped with lateral guides having two or eight contact points some differences appear in the block displacements. The two types of lateral guides, differ in the friction surface between the block and

the central cavity walls (situated in the measurement box), but from the measurement of the friction coefficient this difference is small. The block solicited by a symmetrical jet impact (jet impact on the block centre) did not show an influence of the different friction forces acting on the block: maximum and mean displacements are almost the same. The block solicited by an asymmetrical jet (jet impact on the block right side) shows an influence of the type of lateral guide. On one hand, these differences may be related to the different friction forces acting on the block. On the other hand these differences may be generated by small rotations of the block inside the central cavity that increase the friction force.

The geometry of the lateral guides did not affect the jet penetration inside the 3-dimensional fissure and, as a consequence, the block displacements.

The power spectral density signal for transducers located on the block upper face is practically the same for the compared configurations. The two signals are superposed for all jet velocities and show very small differences. Inside the 3-dimensional fissure, small differences have been observed in the PSD signal and their decrease with an increase of frequency. For frequencies lower than $\sim$50 Hz, the configuration with lateral guides having eight contact points shows more energy per frequency. These small differences decrease from the fissure entrance to underneath the block.

9.1.8 Degree of freedom of the block (free or fixed block)

The degree of freedom of the block did not affect the pressure field acting on the block upper face. However, the pressures inside the 3-dimensional fissure are strongly affected. The more the jet impact approaches and loads directly the 3-dimensional fissure (jet impact on the block left or right side and on the corner), the more the pressures acting inside the fissure increase, related to configurations with the block free to move along the vertical axis. The system installed to fix the block generates this different response of the fissure (different pressure field).

In nature, these pressures (hydrodynamic fracturing) generated by the jet impact on or near the fissure entrance, could break the rock mass with instantaneous or fissure propagation (open-close fissure process or fatigue) and then the block is subjected to the dynamic block uplift that tries to eject it outside the rock foundation.

The jet impacting on the block corner is the most dangerous configuration for fissure and scour propagation. Firstly, this configuration generates the largest observed uplift and secondly, it is this configuration that generates the largest pressure differences inside the 3-dimensional fissure as a function of the degree of freedom.

The pressure coefficients analyses show that all configurations with the fixed block generate larger coefficient values inside the fissure (but with small differences, except near the fissure entrance). The block upper face is practically not influenced by the degree of freedom of the block, as has been observed in the pressure field analysis.

The power spectral density signal on the block upper face for configurations with a jet impact on the block center and on the right side is practically superposed with small differences for both degree of freedom (free and fixed). The configuration with the jet impact on the block corner shows a different behavior as a function of the degree of freedom: the fixed block has higher energy per frequency than the block free to move (it is related to the pressure increase). The frequency evolution is similar for both degrees of freedom, but is vertically shifted.

There are some differences between the two degrees of freedom inside the fissure and at the plunge pool bottom: the fixed block shows generally a higher energy content per frequency independent of the jet configuration. The different pressure field, acting inside the 3-dimensional fissure, influences the power spectral density signal. Inside the fissure, the pressure increases when the block is not free to move and the energy as well increase in the PSD.

Along the vertical fissure the PSD shows a vertical shift (different energy content) but underneath the block, for frequencies greater than 20-40 Hz, the PSD signal changes: the energy increases with an increase of the jet velocity and two peaks appear. These peaks range between 50 and 250 Hz. The first peak (between 50 and 150 Hz) is always present and could correspond to the natural period of an open ended fissure (between 22 and 72 Hz) and the second peak (between 150 and 250 Hz) appears with an increase of the jet velocity and is not so clearly definable. Core, transition and developed jets show the same behavior.

9.2 Outlook for future researches

The following subject could be the topic for future researches.

9.2.1 Dynamic impulsion on a rock block

To widen the knowledge in the field of the added mass and to optimize the dynamic block computation, the added mass coefficient for a 3-dimensional block strongly confined and loaded by a high-velocity jet could be determined experimentally (the presents experimental facility).

Korotkin (2009) proposes different techniques to estimate experimentally the added mass that may be applied for the present facility. As an example, the experimental techniques based onto the small oscillations or onto the electro-hydrodynamic analogy (EHDA) for 3-dimensional body. Other techniques may exist and may be applied to define the added mass (literature review).

Compute the dynamic block impulsion without the combination of pressures recorded with different configurations and perform new tests with transducers located radially outwards from the stagnation point. These new measurements allow to eliminate the time difference that breaks the direct relationship between the pressures acting on the block and the corresponding displacements and accelerations.

Another accelerometer and others displacement transducers (with a wider measurement range) have to be install in the highly instrumented block and the measurements box to broaden the results range.

9.2.2 Influence of the "passive" air entrainment by the free falling jet

The influence of the jet aeration on the block solicitation was studied for one configuration which allowed to improve somewhat the knowledge along the air-axis on the "knowledge cube" proposed by Bollaert (2002b), Bollaert and Schleiss (2003a) and Schleiss and Annandale (2007) (Figure 1.3).

The same tests with the same configurations should be performed, but changing the transducers locations on the block upper face and inside the 3-dimensional fissure. These transducers location have to be adapted for each configuration (centred on the stagnation point and distributed radially outwards). This distribution allows to reconstruct the pressure distribution on the block upper face and inside the fissure.

Further configurations have to be investigated which are characterized by a different jet impact positions on the block upper face (on the block center, on the block left or right side, on the block corner and between the center and the corner of the block).

9.2.3 Block rotations

To analyze possible small rotations of the block, an additional accelerometer should be installed inside the block which is able to record data along 2- or 3-axis (record the block rotations).

9.2.4 Influence of the plunge pool geometry

A flat plunge pool is present only at the beginning of the erosion process. With the progression of the rock scour the jet becomes laterally confined in to highly irregular hole shape. Lateral confinements of the jets (Manso (2006)) could be studied by installing cylinders inside the plunge pool. These confinement are characterized by the diameter D_c and the height t as explained in Manso (2006).

The influence of the lateral confinement on the block dynamic uplift computation has to be investigated. The different shape of the plunge pool (different flow conditions inside the plunge pool) may influence the added mass values that have to be taken into account for the computation. The same configuration (as an example with the jet impact on the block right side or on the block corner) but with different lateral confinement (diameter or height) have to be investigated to analyze the evolution of the added mass as function of the water depth and jet velocity.

9.2.5 Fissure thickness

The fissure thickens may be modified to analyze its influence on the block (displacements and accelerations) and on the fissure response (pressure field). The fissure thickens may be reduce to 0.5 mm (actually 1 mm).

Bibliography

Abramovich, G. N. (1963). *The theory of turbulent jets*. Massachusetts Institute of Technology (MIT) Press, USA.

Akhmedov, T. K. (1968). Local erosion of fissured rock at the downstream end of spillways. *Gidrotekhnicheskoe Stroitelstvo*, 9:44–48.

Akhmedov, T. K. (1988). Calculation of the depth of scour in rock downstream of a spillway. *Water Power and Dam Construction*, 12:25–27.

Aki, S. (1988). jiyu rakka suimuyaku no mizu-kusshon koka mi kansuru kenkyu (Study of the efficiencyof water cushioning in free-falling jets). *Denryoku chuo kenkyujo hokoku (Journal of the Research Institute for Hydroelectric Power Stations)*, page 7.

Akram, M. and Karfakis, M. (1987). Rock fracture toughness and fracture energy in aqueous chemical environments. In *Proceedings of 28th US Symposium on Rock Mechanics*, pages 211–230. A.A. Balkema, Rotterdam, Netherlands.

Albertson, M. L., Dai, Y. B., Jensen, R. A., and Rouse, H. (1950). Diffusion of submerged jets. In *Transactions of ASCE*, volume 115, pages 639–664. American Society of Civil Engineers (ASCE), USA.

Allievi, L. (1903). Teoria generale del moto perturbato dell'acqua nei tubi in pressione. In *Annali della Societa degli Ingegneri ed Architetti Italiani*. Milano, Italy.

Altinbilek, H. D. and Okyay, S. (1973). Localized scour in a horizontal sand bed under vertical jets. In *Proceedings of XV IAHR Congress, Istambul, Turkey*, pages 99–106. International Association for Hydro-Environment Engineering and Research (IAHR).

Amanian, N. (1993). *Scour below a flip bucket spillway*. Ph.D. Thesis, Utah State University, USA.

Amanian, N. and Urroz, G. E. (1993). Design of pre-excavated scour hole below flip bucket spillways. In *Hydraulic Engineering '93*, volume 1, pages 856–860. American Society of Civil Engineers (ASCE), USA.

Amelung, M. (1996). *Auskolkung klueftiger Felssohlen durch Entlastungsstrahlen*. Ph.D. Thesis, TU Braunschweig, Germany.

Amri, A. E. and Verrette, J. L. (2005). Étude quantitative de l'érosion en aval des dissipateurs d'énergie type auge. *Canadian Journal of Civil Engineering*, 32(2):400–412.

André, S. (2004). High velocity aerated flows on stepped chutes with macro-roughness elements. In *Communication N^o 20*. A.J. Schleiss (ed.), Laboratory of Hydraulic Constructions (LCH), École Polytechnique Fédérale de Lausanne (EPFL), Switzerland (ISSN 1661-1179).

Annandale, G. W. (1995). Erodibility. *Journal of Hydraulic Research*, 33(4):471–494.

Annandale, G. W. (2005). Discussion of "Fluvial entrainment of protruding fractured rock" by S.E. Coleman, B.W. Melville and L. Gore. *Journal of Hydraulic Engineering*, 131(2):142–144.

Annandale, G. W. (2007). Current state-of-the-art of rock scour technology. In *Proceedings of Geo-Denver 2007: New Peaks in Geotechnics*, volume 230 of *Geotechnics of Soil Erosion (GSP 167)*, pages 1–12. American Society of Civil Engineers (ASCE), USA.

Annandale, G. W. (2010). Wall jet scour in rock. In *Proceedings of Fifth International Conference on Scour and Erosion (ICSE-5)*, pages 70–71. American Society of Civil Engineers (ASCE), USA.

Annandale, G. W. and Schleiss, A. J. (2007). Predicting rock scour: Part 2. *International Water Power & Dam Construction*, 10:38–41.

Annandale, G. W., Wittler, R. J., Ruff, J. F., and Lewis, T. M. (1998). Prototype validation of erodibility index for scour in fractured rock media. In *Proceeding of International Water Resources Engineering Conference*, volume 2, pages 1096–1101. American Society of Civil Engineers (ASCE), USA.

Armengou, J. (1991). *Disipacion de energia hidraulica a pie de presa en presas boveda*. Ph.D. Thesis, Universitat Politechnica de Catalunya, Barcellona, Spain.

Armenio, V., Toscano, P., and Fiorotto, V. (1999). On the effects of a negative step in pressure fluctuations at the bottom of a hydraulic jump. *Journal of Hydraulic Research*, 38(5):359–368.

Arndt, R. E. A. and Ippen, A. T. (1970). Turbulence measurements in liquids using an improved total pressure probe. *Journal of Hydraulic Research*, 8(2):131–158.

Asadollahi, P., Tonon, F., Federspiel, M. P. E. A., and Schleiss, A. J. (2011). Prediction of rock block stability and scour depth in plunge pools. *Journal of Hydraulic Research*, Accept to publication.

Atkinson, B. K. (1987). *Fracture Mechanics of Rock*. Academic Press Inc., London, UK.

Attari, J., Arefi, F., and Golzari, F. (2002). A review on physical models of scour holes below large dams in iran. In *Rock scour due to falling high-velocity jets*, pages 73–80. A. J. Schleiss and E. F. R. Bollaert (ed.), A.A. Balkema - Swets & Zeitlinger, Netherlands.

Bai, K. J. (1977). The added mass of a two-dimensional cylinders heaving in water of finite depth. *Journal of Fluid Mechanics*, 81:85–105.

Ballio, F., Franzetti, S., and Tanda, M. G. (1994). Pressure fluctuations induced by turbulent circular jets impinging on a flat plate. *Excerpta*, 7:41–59.

Barata, J. M. M., Duraco, D. F. G., Heitor, M. V., and McGuirk, J. J. (1993). On the analysis of an impinging jet on ground effects. *Experiments in Fluids*, 15:117–129.

Bearman, P. W. (1972). An investigation of the forces on flat plates normal to a turbulent flow. *Journal of Fluid Mechanics*, 46:177–198.

Bellin, A. and Fiorotto, V. (1995). Direct dynamic force measurement on slabs in spillway stilling basins. *Journal of Hydraulic Engineering*, 121(10):686–693.

Beltaos, S. (1976a). Oblique impingement of circular turbulent jets. *Journal of Hydraulic Research*, 14(1):27–36.

Beltaos, S. (1976b). Oblique impingement of plane turbulent jets. *Journal of the Hydraulic Division*, 100(HY10):1177–1192.

Beltaos, S. and Rajaratnam, N. (1973). Plane turbulent impinging jets. *Journal of Hydraulic Research*, 11(1):29–59.

Beltaos, S. and Rajaratnam, N. (1974). Impinging circular turbulent jets. *Journal of the Hydraulics Division*, 100(10):1313–1328.

Beltaos, S. and Rajaratnam, N. (1977). Impingement of axisymmetric developing jets. *Journal of Hydraulic Research*, 15(4):311–326.

Bendat, J. S. and Piersol, A. G. (1971). *Random data: Analysis and measuremenst procedures*. J. Whiley & Sons Ltd., New York, USA.

Bendat, J. S. and Piersol, A. G. (1980). *Engineering applications of correlation and spectral Analysis*. J. Whiley & Sons Ltd., New York, USA.

Bergant, A. and Simpson, A. R. (1999). Pipeline column separation flow regimes. *Journal of Hydraulic Engineering*, 125(8):835–848.

Bin, A. K. (1984). Air entrainment by plunging jets. In *Proceedings of Scale Effects in Modeling Hydraulic Structures*, volume 5.5, pages 1–6.

Bin, A. K. (1988). Minimum air entrainement velocity of vertical plunging jets. *Chemical Engineering Science*, 43(2):379–389.

Bin, A. K. (1993). Gas entrainment by plunging liquid jets. *Chemical Engineering Science*, 48(21):3585–3630.

Blevins, R. D. (2001). *Formulas for natural frequency and mode shape*. Krieger Publishing Company, USA.

Boes, R. (2000). *Zweiphasenstroemung und energieumsetzung an grosskaskaden*. Ph.D. Thesis, Mitteilungen de Versuchsanstalt fur Wasserbau, Hydrologie und Glaziologie (VAW), ETH Zürich, Switzerland.

Boes, R. M. and Hager, W. H. (1998). Fiber-optical experimentation in two-phase cascade flow. In *Proceeding of International RCC Dams Seminar*. K. Hansen (ed.), USA.

Bohrer, J. G. (1996). *Plunge pool velocity prediction of jets formed by overtopping steep dams*. Ph.D. Thesis, Colorado States University, USA.

Bohrer, J. G., Abt, S. R., and Wittler, R. J. (1998). Predicting plunge pool velocity decay of free falling, rectangular jet. *Journal of Hydraulic Engineering*, 124(10):1043–1048.

Bollaert, E. F. R. (2002a). The influence of plunge pool air entrainment on the presence of free air in rock joints. In *Rock scour due to falling high-velocity jets*, pages 137–151. A.J. Schleiss and E.F.R. Bollaert (ed.), A.A. Balkema - Swets & Zeitlinger, Netherlands.

Bollaert, E. F. R. (2002b). Transient water pressures in joints and formation of rock scour due to high-velocity jet impact. In *Communication N^o 13*. A.J. Schleiss (ed.), Laboratory of Hydraulic Constructions (LCH), École Polytechnique Fédérale de Lausanne (EPFL), Switzerland (ISSN 1661-1179).

Bollaert, E. F. R. (2004a). A comprehensive model to evaluate scour formation in plunge pools. *Hydropower and Dams*, 1:94–101.

Bollaert, E. F. R. (2004b). A new procedure to evaluate dynamic uplift of concrete linings or rock blocks in plunge pools. In *Hydraulics of Dams and River Structures*, pages 125–132. Yazdandooszt & Attari (ed.), Taylor & Francis Group, UK, London, UK.

Bollaert, E. F. R. (2008). Discussion of "Jet impact geometry and plunge pool dimensions effects on dynamic presssures at pool sidewalls" by S.M. Borgheri and P. Zarnani. *Canadian Journal of Civil Engineering*, 35(11):1347–1348.

Bollaert, E. F. R., Falvey, H. T., and Schleiss, A. J. (2002). Assessment of turbulent jet impingement on rocky riverbeds: The particular properties of a near-prototype physical model study. In *Proceedings of International Conference on Fluvial Hydraulic: Riverflow 2002*, pages 395–403. D.Z.Y. Bousmar, Lavoisier, France.

Bollaert, E. F. R., Manso, P. F. A., and Schleiss, A. J. (2004). Dynamic pressure fluctuations at real-life plunge pool bottoms. In *Hydraulics of Dams and River Structures*, pages 117–124. Yazdandooszt & Attari (ed.), Rotterdam, Netherlands.

Bollaert, E. F. R., Manso, P. F. A., and Schleiss, A. J. (2009). Discussion of "Effect of jet aeration on hydrodynamic forces on pluge pool floors" by A.N. Pinheiro and J.F. Melo. *Canadian Journal of Civil Engineering*, 36:524–526.

Bollaert, E. F. R. and Schleiss, A. J. (2001). Discussion of "Simulation of scour process in plunging pool of loose bed-material" by Y. Jai, T. Kitamura and S.S.Y. Wang. *Journal of Hydraulic Engineering*, 128(7):721–723.

Bollaert, E. F. R. and Schleiss, A. J. (2002). *Rock scour due to falling high-velocity jets*. A.J. Schleiss and E.F.R. Bollaert (ed.), A.A. Balkema - Swets & Zeitlinger, Netherlands.

Bollaert, E. F. R. and Schleiss, A. J. (2003a). Scour of rock due to the impact of plunging high velocity jets. Part 1: A state-of-the-art review. *Journal of Hydraulic Research*, 41(5):451–464.

Bollaert, E. F. R. and Schleiss, A. J. (2003b). Scour of rock due to the impact of plunging high velocity jets. Part 2: Experimental results of dynamic pressures at pool bottoms and in one- and two-dimensional closed end rock joints. *Journal of Hydraulic Research*, 41(5):465–480.

Bollaert, E. F. R. and Schleiss, A. J. (2005). Physically based model for evaluation of rock scour due to high-velocity jet impact. *Journal of Hydraulic Engineering*, 131(3):153–165.

Bollaert, E. F. R. and Schleiss, A. J. (2011). Discussion of "Closure problem to jet scour" by G.J.C.M. Hoffmans. *Journal of Hydraulic Research*, 49(2):279–280.

Bonetto, F., Drew, D., and Lahey, R. T. J. (1994). The analysis of a plunging liquid jet. The air entrainement process. *Chemical Engineering Communications*, 130:11–29.

Bonetto, F. and Lahey, R. T. J. (1993). An experimental study of air carryunder due to a plunging liquid jet. *International Journal of Multiphase Flow*, 19(2):281–294.

Borgheri, S. M. and Zarnani, P. (2008). Jet impact geometry and plunge pool dimensions effects on dynamic pressures at pool side walls. *Canadian Journal of Civil Engineering*, 35(4):408–417.

Bormann, N. E. (1988). Physical model of local scour at grade-control structures. In *Proceeding of ASCE National Conference on Hydraulic Engineering*, pages 1129–1134. American Society of Civil Engineers (ASCE), USA.

Bormann, N. E. and Julien, P. Y. (1991). Scour downstream of grade-control structures. *Journal of Hydraulic Engineering*, 117(5):579–594.

Bower, C. E. and Tsai, F. Y. (1969). Fluctuanting pressures in spillways stilling basins. *Journal of Hydraulics Division*, 95(6):2071–2079.

Bradshaw, P. and Love, E. M. (1961). *The normal impingement of a circular air jet on a flat surface*, volume 3205. Ministry of Aviation, Her Majesty's Stationery Office, London, UK.

Brattberg, T. and Chanson, H. (1998). Air entrapment and air bubble dispersion at two-dimensional plunging water jets. *Chemical Engineering Science*, 53(24):4113–4127.

Brennen, C. E. (1982). *A Review of added mass and fluid inertial forces*. Technical report, CR 82.010, Department of the Navy, Naval Civil Engineering Laboratory, USA.

Breusers, H. N. C. (1963). Discussion of "Sediment transport mechanics: erosion of sediment". *Journal of Hydraulic Division*, 89(HY1).

Breusers, H. N. C. (1967). Time scale of two-dimensional local scour. In *Proceedings of XII IAHR Congress, Fort Collins, USA*. International Association for Hydro-Environment Engineering and Research (IAHR).

Breusers, H. N. C. and Raudkivi, A. J. (1991). *Scouring*, volume 2. IAHR Hydraulic Structures Design Manual, A.A. Balkema, Rotterdam, Netherlands.

Brito, S., Infanti, N., and Vargas Jr, E. d. A. (1991). Studies of erosion processes downstream of concerte spillways. In *Proceedings of 7^{th} International Congress on Rock Mechanics, Aachen, Germany*, volume 2. Stabiliy of rock slopes: Underground construction in rock, pages 1261–1266.

Bui, H. H., Sako, K., and Fukagawa, R. (2007). Numerical simulation of soil-water interaction using smoothed particle hydrodynamics (SPH) method. *Journal of Terramechanics*, 44:339–346.

Burattini, P., Antonia, R. A., Rajagopalan, S., and Stephens, M. (2004). Effect of initial conditions on the near-field development of a round jet. *Experiments in Fluids*, 37:56–64.

Burdine, N. T. (1963). Rock failure under dynamic loading conditions. *Society Petrol Engineering Journal*, 3(1):1–8.

Cain, P. and Wood, I. R. (1981). Instrumentation for aerated flow on spillways. *Journal of Hydraulic Engineering*, 107(11):1407–1424.

Canepa, S. and Hager, W. H. (2003). Effect of air content on plunge pool scour. *Journal of Hydraulic Engineering*, 129(5):358–365.

Carbone, V., Regnoli, G., Martines, E., and Antoni, V. (2000). Intermittency and self-similarity in plasma edge fluctuations. *Physics of Plasmas*, 7(2):445–447.

Carreras, B. A., Milligen, B. P., Pedrosa, M. A., Balbin, R., Hidalgo, C., Newman, D. E., Sanchez, E., Frances, M., Garcia-Cortes, I., Bleuel, J., Endler, M., Riccardi, C., Davies, S., Matthews, G. F., Martines, E., Antoni, V., Latten, A., and Klinger, T. (1998). Self-similarity of the plasma edge fluctuations. *Physics of Plasmas*, 5(10):3632–3643.

Cartellier, A. (1992). Simultaneous void fraction measurement, bubble velocity and size estimate using a single optical probe in gas-liquid two-phase flows. *Review of Scientific Instruments*, 63(11):5442–5453.

Cartellier, A. and Achard, J. L. (1991). Local phase detection probes in fluid/fluid two-phase flows. *Review of Scientific Instruments*, 62(2):279–303.

Castillo Elsitdié, L. G. (1989). *Metodología experimental y numérica para la caracterización del campo de presiones en los disipadores de energía hidráulica. Aplicación al vertido libre en presas bóveda.* Ph.D. Thesis, Universitat Politecnica de Catalunya, Barcelona, Spain.

Castillo Elsitdié, L. G. (2002). Parametrical analysis of the ultimate scour and mean dynamic pressures at plunge pools. In *Rock scour due to falling high-velocity jets*, pages 95–104. A.J. Schleiss and E.F.R. Bollaert (ed.), A.A. Balkema - Swets & Zeitlinger, Netherlands.

Castillo Elsitdié, L. G. (2006). Aerated jets and pressure fluctuations in plunge pools. In *Proceedings of 7th International Conference on HydroScience and Engineering (ICHE 2006)*, pages 1–23. M. Piasecki (ed.), College of Engineering Drexel University, USA.

Castillo Elsitdié, L. G. (2007). Pressure characterization of undeveloped and developed jets in shallow and deep pool. In *Proceedings of XXXII IAHR Congress, Venezia, Italy*, volume 2, pages 645–655. International Association for Hydro-Environment Engineering and Research (IAHR).

Castillo Elsitdié, L. G., Puertas, J., and Dolz, J. (1999). Discussion of "Pressures fluctuations on plunge pool floors" by D.A. Ervine, H.T. Falvey and W.A. Withers. *Journal of Hydraulic Research*, 37(2):272–277.

Castillo Elsitdié, L. G., Puertas, J., and Dolz, J. (2007). Discussion of "Scour of rock due to the impact of plunging high velocity jets. Part I: A state-of-the-art review" by E.F.R. Bollaert and A.J. Schleiss. *Journal of Hydraulic Research*, 45(6):853–858.

Chanson, H. (1995). Air entrainement in two-dimesnional turbulent shear flows with partially developed inflow conditions. *International Journal of Multiphase Flow*, 21(6):1107–1121.

Chanson, H. (1996). *Air bubble entrainment in free surface turbulent shear flows.* Elsevier Science Publishers, Amsterdam, Netherlands.

Chanson, H. (2004a). Air-water flows in water engineering and hydraulic structures. Basic processes and metrology. In *Hydraulics of dams and river structures*, pages 3–16. Yazdandooszt & Attari (ed.), Taylor & Francis Group, UK.

Chanson, H. (2004b). The compressibility of extra-high-velocity aerated flow. *Journal of Hydraulic Research*, 42(2):213–215.

Chanson, H., Aoki, S., and Hoque, A. (2004). Physical modelling and similitude of air bubble entrainment at vertical circular plunging jets. *Chemical Engineering Science*, 59:747–758.

Chanson, H. and Brattberg, T. (1997). *Experimental investigation of air bubble entrainement in developing shear layers*, volume CH48/97. The University of Queensland, Brisbane, Australia.

Chassaing, P. (2000). *Turbulence en mécanique des fluides. Analyse du phénoméne en vue de sa modélisation a l'usage de l'ingénieur*. POLYTECH. Cépadues-Editions, Toulouse.

Chee, S. P. and Kung, T. (1971). Stable profiles of plunge basins. *Journal of the American Water Resources Association*, 7(2):303–308.

Chee, S. P., Strelchuk, D. L., and Kung, T. (1972). Configurations of water basin for energy dissipation. In *Proceedings of 86th Annual Congress of Engineering Institute of Canada*. Saskatoon, Canada.

Chee, S. P. and Yuen, E. M. (1985). Erosion of unconsolidated gravel beds. *Canadian Journal of Civil Engineering*, 12:559–566.

Chung, H. and Chen, S. S. (1982). *Hydrodynamic mass*. Technical report, COHF-840647-9, Components Technology Division, Argonne National Laboratory, USA.

Clanet, C. and Lasheras, J. C. (1997). Depth of penetration of bubbles entrained by a plunging water jet. *Physics of Fluids*, 9(7):1864–1866.

Cola, R. (1965). Energy dissipation of a high-velocity vertical jet entering a basin. In *Proceedings of XI IAHR Congress, Leningrad, URSS*, volume I, paper 1.52, pages 1–13. International Association for Hydro-Environment Engineering and Research (IAHR).

Cola, R. (1966). Diffusione di un getto piano verticale in un bacino d'acqua d'altezza limitata. *L'energia elettrica*, 11:649–664.

Coleman, S. E., Melville, B. W., and Gore, L. (2003). Fluvial entrainment of protruding fractured rock. *Journal of Hydraulic engineering*, 129(11):871–884.

Comte-Bellot, G. and Corrsin, S. (1966). The use of a contraction to improve the isotropy of grid-generated turbulence. *Journal of Fluid Mechanics*, 25(4):657–682.

Costin, L. S. and Holcomb, D. J. (1981). Time-dependent failure of rock under cyclic loading. *Tectonophysics*, 79:279–296.

Covas, D., Ramos, H., and Almeida, A. B. (2005). Impulse response method for solving hydraulic transients in viscoelastic pipes. In *Proceedings of XXXI IAHR Congress, Seoul,*

South Korea, volume 1, pages 676–686. International Association for Hydro-Environment Engineering and Research (IAHR).

Cummings, P. D. and Chanson, H. (1997). Air entrainment in the developing flow region of plunging jets. Part 2: Experimental. *Journal of Fluids Engineering*, 119(9):603–608.

Cunha, L. V. and Lencastre, A. C. (1966). La dissipation de l'énergie dans un évacuateur en saut de ski, observationde l'érosion. In *LNEC Publication nº 288 & Proceedings of the XI IAHR Congress, Leningrad, URSS*. International Association for Hydro-Environment Engineering and Research (IAHR).

Daviers, J. T. (1972). *Turbulence Phenomena*. Academic Press Inc., New York (USA) and London (UK).

De Vries, F. and Volkart, P. U. (1988). Field measurements of pressure fluctuations in a high head bottom outlet structure. In *Proceedings of Model-Prototype Correlation of Hydraulic Structures*, pages 199–209. American Society of Civil Engineers (ASCE), USA.

Doddiah, D., Albertson, M. L., and Thomas, R. (1953). Scour from jets. In *Proceedings of Minnesota International Hydraulics Conference*. American Society of Civil Engineers (ASCE), USA.

Elder, R. A. (1961). Model-prototype turbulence scaling. In *Proceedings of IX IAHR Congress, Dubrovnik, Croatia*, pages 24–31. International Association for Hydro-Environment Engineering and Research (IAHR).

Ervine, D. A. (1976). The entrainment of air in water. *Water Power and Dam Construction*, 28(12):27–30.

Ervine, D. A. (1998). Air entrainment in hydraulic structures: A review. In *Proceedings of Institution of Civil Engineers, Water and Maritime Engineering*, volume 130, pages 142–153.

Ervine, D. A. and Elsawy, E. M. (1975). The effect of a falling nappe on river aeration. In *Proceedings of XVI IAHR Congress, Sau Paulo, Brazil*, volume 3, pages 390–398. International Association for Hydro-Environment Engineering and Research (IAHR).

Ervine, D. A. and Falvey, H. R. (1988). Aeration in jets and high velocity flows. In *Proceedings of Model-Prototype Correlation of Hydraulic Structures*, pages 22–55. P.H. Burgi (ed.), American Society of Civil Engineers (ASCE), USA.

Ervine, D. A. and Falvey, H. T. (1987). Behaviour of turbulent water jets in the atmosphere and in plunge pools. In *Proceedings of Institution of Civil Engineers (ICE)*, volume 83, pages 295–314.

Ervine, D. A., Falvey, H. T., and Withers, W. (1997). Pressure fluctuations on plunge pool floors. *Journal of Hydraulic Research*, 35(2):257–279.

Ervine, D. A., McKeogh, E., and Elsawy, E. M. (1980). Effect of turbulence intensity on the rate of air entrainment by plungins water jets. In *Proceedings of Institution of Civil Engineers (ICE)*, volume 2, pages 425–445.

Ewalds, H. L. and Wanhill, R. J. H. (1986). *Fracture Mechanics*. Delftse Uitgevers Maatschappij, Netherlands.

Ewing, D. J. F. Allowing for free air in waterhammer analysis. In *Proceedings of 3th International Conference on Pressure Surges*, pages 127–146. Canterbury, UK.

Fahlbusch, F. E. (1994). Scour in rock riverbeds downstream of large dams. *International Journal on Hydropower and Dams*, 46(7):30–32.

Falvey, H. T. (1980). Air-water flow in hydraulic structures. In *Engineering Monograph Nº 41*. Bureau of Reclamation,USA.

Falvey, H. T. (1990). Cavitation in chutes and spillways. In *Engineering Monograph Nº 42*. Bureau of Reclamation,USA.

Falvey, H. T. and Ervine, D. A. (1988). Aeration in jets and high-velocity flows. In *Proceedings Sof ymposium Model-Prototype Correlation*, pages 25–55. American Society of Civil Engineers (ASCE), USA.

Farhoudi, J. and Narayanan, R. (1991). Force on slab beneath hydraulic jump. *Journal of Hydraulic Engineering*, 117(1):64–82.

Federspiel, M. P. E. A., Bollaert, E. F. R., and Schleiss, A. J. (2009). Response of an intelligent block to symmetrical core jet impact. In *Proceedings of XXXIII IAHR Congress, Vancouver, Canada*, pages 3573–3580. International Association for Hydro-Environment Engineering and Research (IAHR).

Federspiel, M. P. E. A., Bollaert, E. F. R., and Schleiss, A. J. (2010). Experiments on the reponse of a rock block in a plunge pool loaded by a symmetrical jet impact. In *Proceedings of Ist European IAHR Congress, Edinburgh, Scotland*. International Association for Hydro-Environment Engineering and Research (IAHR).

Federspiel, M. P. E. A., Bollaert, E. F. R., and Schleiss, A. J. (2011). Dynamic response of a rock block in a plunge pool due to asymmetrical impact of a high-velocity jet. In *Proceedings of XXXIV IAHR Congress, Brisbaine, Australia*. International Association for Hydro-Environment Engineering and Research (IAHR).

Ferrando, A. M. and Rico, J. R. (2002). On the incipient aerated flow in chutes and spillways. *Journal of Hydraulic Research*, 40(1):95–97.

Fiorotto, V. and Caroni, E. (2007). Discussion of "Forces on plunge pool slabs: Influence of joints location and width" by J.F. Melo, A.N. Pinheiro and C.M. Ramos. *Journal of Hydraulic Engineering*, 133(10):1182–1184.

Fiorotto, V. and Rinaldo, A. (1988). Sul dimensionamento delle protezioni di fondo in bacini di dissipazione a risalto: nuovi risultati teorici e sperimentali. *Giornale del Genio Civile*, 7/8/9:179–201.

Fiorotto, V. and Rinaldo, A. (1992a). Fluctuating uplift and lining design in spillway stilling basins. *Journal of Hydraulic Engineering*, 118(4):578–596.

Fiorotto, V. and Rinaldo, A. (1992b). Turbulent pressure fluctuations below hydraulic jumps. *Journal of Hydraulic Research*, 30(4):499–520.

Fiorotto, V. and Salandin, P. (2000). Design of anchored slabs in spillway stilling basins. *Journal of Hydraulic Engineering*, 126(7):502–512.

Flagg, C. N. and Newman, J. N. (1971). Sway added mass coefficients for rectangular profiles in shallow water. *Journal of Ship Research*, 15:257–265.

Franzetti, S. and Tanda, M. G. (1984). Getti deviati a simmetria assiale. In *Memorie e studi dell'Istituto di Idraulica e Costruzioni Idrauliche del Politecnico di Milano*, number 324. Politecnico di Milano, Italy.

Franzetti, S. and Tanda, M. G. (1987a). Analysis of turbulent pressure fluctuation caused by a circular impinging jet. In *Proceedings of International Symposium on New Technology in Model Testing in Hydraulic Research*, pages 85–91.

Franzetti, S. and Tanda, M. G. (1987b). Caratteristiche idrodinamiche di getti d'acqua assialsimmetrici deviati esterni e sommersi. In *Memorie e studi dell'Istituto di Idraulica e Costruzioni Idrauliche del Politecnico di Milano*, number 335. Politecnico di Milano, Italy.

Furstenburg, L., Huraut, J. P., Blake, K. R. K., and Zwanborn, J. A. (1991). The influence of foundation conditions on spillway and plunge pool design at Katse dam. In *Proceedings of XVII ICOLD Congress, Vienna, Austria*, volume Q.66 R93, pages 1727–1743. International Commission on Large Dam (ICOLD).

Gilard, V. and Brizzi, L.-E. (2005). Slot jet impinging on a concave curved wall. *Journal of Fluids Engineering*, 127(5):595–603.

Goodmann, R. E. (1980). *Introduction to Rock Mechanics*. J. Whiley & Sons Ltd., USA.

Griffith, A. A. (1921). The phenomenon of rupture and flow in solids. *Philosophical Transactions of the Royal Society of London, UK*, 221(A):163–198.

Gruber, C. and Willy, B. (1998). *Mécanique générale*. PPUR: Presses Politechniques et Universitaires Romandes, Lausanne, Switzerland.

Gunko, F. G. (1967). Macroturbulence of flows below spillways of medium head dams and their protection against undermining. In *Proceedings of XII IAHR Congress, Fort Collins, USA*, volume 2, pages 135–143. International Association for Hydro-Environment Engineering and Research (IAHR).

Gunko, F. G., Burkov, A. F., Isachenko, N. B., Rubinstein, G. L., Soloviova, A. G., and Yuditskii, G. A. (1965). Research on the hydraulic regime and local scour of river bed below spillways of high-head dams. In *Proceedings of XI IAHR Congress, Leningrad, URSS*, volume 1, pages 1–14. International Association for Hydro-Environment Engineering and Research (IAHR).

Gutmark, G. E., Wolfshtein, M., and Wygnanski, I. (1978). The plane turbulent impinging jet. *Journal of Fluid Mechanics*, 88(4):737–756.

Hager, W. H. (1998). Plunge pool scour: early history and hydraulicians. *Journal of Hydraulic Engineering*, 124(12):1185–1187.

Haimson, B. C. and M., K. C. (1971). Mechanical behavior of rock under cyclic fatigue. In *Proceedings of 13th Symposium on Rock Mechanics*, pages 845–863.

Halliwell, A. R. (1963). Velocity of a waterhammer wave in an elastic pipe. *Journal of the Hydraulics Division*, 89(HY4):1–21.

Hardy, H. R. and Chugh, Y. P. (1970). Failure of geologic materials under low cycle fatigue. In *Proceedings of 6th Canadian Symposium on Rock Mechanics*, pages 14–25.

Hartung, F. and Häusler, E. (1973). Scours, stilling basins and downstream protection under free overfall jets at dams. In *Proceedings of XI Congress on Large Dams, Madrid, Spain*, pages 39–56. International Commission on Large Dam (ICOLD).

Häusler, E. (1966). Dynamishe Wassserdrücke auf Tosbeckenplatten infolge freier Uberfallstrahlen bei Talsperren. *Die Wasserwirtschaft*, 2.

Hay, D. (1988). Model-prototype correlation: Hydraulic structures. In *Proceedings of International Symposium on Model-Prototype Correlation of Hydraulic Structures*, pages 1–24. P.H. Burgi (ed.), American Society of Civil Engineers (ASCE), USA.

Henderson, J. B., McCarthy, M. J., and Molloy, N. A. (1970). Entrainment by plunging jets. In *Proceeding of CHEMECA '70*, volume 2, pages 86–100.

Hinze, J. O. (1959). *Turbulence*. McGraw-Hill, UK, USA.

Ho, C.-M. and Nosseir, N. S. (1981). Dynamics of an impinging jet: the feedback phenomena. *Journal of Fluid Mechanics*, 105:119–142.

Ho, C.-M., Plocher, D. A., and Leve, H. L. (1977). Surface pressure fluctuation generated by a jet impinging on a curved plate. *AIAA Journal*, 15(9):1348–1350.

Hoagland, R. G., Hahn, G. T., and Rosenfield, A. R. (1973). Influence of microstructure on fracture propagation in rock. *Rock Mechanics and Rock Engineering*, 5(2):77–106.

Hoffmans, G. J. C. M. (1994a). Scour due to plunging jets. In *Report W-DWW-94-302*. Ministry of Transport, Public Works and Water Management, Road and Hydraulic Engineering Division, Netherlands.

Hoffmans, G. J. C. M. (1994b). Scour due to submerged jets. In *Report W-DWW-94-302*. Ministry of Transport, Public Works and Water Management, Road and Hydraulic Engineering Division, Netherlands.

Hoffmans, G. J. C. M. (1998). Jet scour in equilibrium phase. *Journal of Hydraulic Engineering*, 124(4):430–437.

Hoffmans, G. J. C. M. (2010a). Closure problem to jet scour. *Journal of Hydraulic Research*, 47(1):100–109.

Hoffmans, G. J. C. M. (2010b). Stability of stones under uniform flow. *Journal of Hydraulic Engineering*, 136(2):129–136.

Hoffmans, G. J. C. M. and Verheij, H. J. (1997). *Scour Manual*. A.A. Balkema, Rotterdam, Netherlands.

Holdhusen, J. S. (1948). Discussion of "Diffusion of submerged jets" by Albertson et al. *Transactions of the American Society of Civil Engineers (ASCE)*, Paper N° 2409:665–671.

Hubbert, M. K. and Willis, D. G. (1957). Mechanics of hydraulic fracturing. *American Association of Petroleum Geologists*, 210:153–162.

Huot, J. P., Rey, C., and Arbey, H. (1986). Experimental analysis of the pressure field induced on a square cylinder by a turbulent flow. *Journal of Fluid Mechanics*, 162:283–298.

Jaeger, C. (1977). *Fluid transients: in hydro-electric engineering practice*. Blackie & Son Ltd., Glasgow and London, UK.

Jaeger, C. and Cook, N. G. W. W. (1979). *Fundamentals of Rock Mechanics*. Chapman and Hall, New York, USA.

Jai, Y., Kitamura, T., and Wang, S. S. Y. (2001). Simulation of scour process in plunging pool of loose bed-material. *Journal of Hydraulic Engineering*, 127(3):219–229.

Jarvis, P. J. (1970). *A study in the mechanics of aeration at weirs*. Ph.D. Thesis, University of Newcastle upon Tyne, UK.

Jenkner, W. R. (1971). Über die druckstossgeschwindigkeit in Rohrleitungen mit quadratischen und rechteckigen Querschnitten. *Scweizerische Bauzeitung*, 89:99–103.

Johnson, G. (1967). The effect of entrained air in the scouring capacity of water jets. In *Proceedings of XII IAHR Congress, Fort Collins, USA*, volume 3, pages 218–226. International Association for Hydro-Environment Engineering and Research (IAHR).

Johnson, G. (1977). Use of a weakly cohesive material for scale model scour tests in flood spillway design. In *Proceedings of the XVII IAHR Congress, Baden-Baden, Switzerland*, volume 4, pages 509–512. International Association for Hydro-Environment Engineering and Research (IAHR).

Juon, R. and Hager, W. H. (2000). Flip bucket without and with deflectors. *Journal of Hydraulic Engineering*, 126(11):837–845.

Kamoi, A. and Tanaka, H. (1972). Measurements of wall shear stress, wall pressure and fluctuations in the stagnation region produced by oblique jet impingement. In *Proceedings of Fluid Dynamic Measurements in the Industrial and Medical Environments*, volume 1, pages 217–227. D.J. Cockrell (ed.), University press, UK.

Karimipanah, T. (1996). *Turbulent jets in confined spaces*. Ph.D. Thesis, Royal Institute of Technology, Sweden.

King, D. L. (1967). Analysis of random pressure fluctuations in stilling basins. In *Proceedings of XII IAHR Congress, Fort Collins, USA*, volume 2, pages 210–217. International Association for Hydro-Environment Engineering and Research (IAHR).

Kirschke, D. Universitä Karlsruhue, Germany.

Knowles, K. and Myszko, M. (1998). Turbulence measurements in radial wall-jets. *Experimental Thermal and Fluid Sciences*, 17:71–78.

Kobus, H. (1984). Local air entrainment and detrainment. In *Proceedings of Scale effects in modelling hydraulic structures*, volume 4, pages 1–10. International Association for Hydro-Environment Engineering and Research (IAHR).

Kobus, H., Leister, P., and Westrich, B. (1979). Flow field and scouring effects on steady and pulsating jets impinging on a movable bed. *Journal of Hydraulic Research*, 17(3):175–192.

Kolmogorov, A. N. (1941a). *Russian Academy of Science Monograph*, volume 30. Doklady Akademii Nauk, URSS.

Kolmogorov, A. N. (1941b). *Russian Academy of Science Monograph*, volume 31. Doklady Akademii Nauk, URSS.

Kolmogorov, A. N. (1941c). *Russian Academy of Science Monograph*, volume 32. Doklady Akademii Nauk, URSS.

Korotkin, A. I. (2009). Added masses of ship structures. In *Fluid Mechanics and Its Applications*, volume 88. Springer, Germany.

Kraatz, W. (1965). Flow characteristics of a free circular water jet. In *Proceedings of XI IAHR Congress, Leningrad, URSS*, volume 1. International Association for Hydro-Environment Engineering and Research (IAHR).

Kraichnan, R. H. (1974). On kolmogorov inertial-range theories. *Journal of Fluid Mechanics*, 62(Part 2):305–330.

Kraichnan, R. H. (1975). Statistical dynamics of two-dimensional flow. *Journal of Fluid Mechanics*, 67(Part 1):155–175.

Landreth, C. C. and Adrian, R. J. (1990). Impingement of a low reynolds number turbulent circular jet onto a flat plate at normal incidence. *Experiments in Fluids*, 9(1-2):74–84.

Lelliavsky, S. (1955). *An introduction to fluvial hydraulics*. Constable & Co. Ltd., London, UK.

Lemos, F. (1982). Behaviour of hydraulic structures of some dams built in narrow valleys (in Portuguese). In *Translation of the International Symposium on the Layout of Dams in Narrow Gorges*, pages 241–252. International Commission on Large Dam (ICOLD).

Lencastre, A. (1961). *Memoria Nº 174. Descarregadores de lamina livre: bases para o seu estudo e dimensionamento*. Laboratorio Nacional de Engenharia Civil (LNEC), Lisboa, Portugal.

Lesleighter, E. J. (1988). Cavitation in hydraulic structures. In *Proceeding of International Symposium on Model-Prototype Correlation of Hydraulic Structures*, pages 74–94.

Lesser, M. B. and Field, J. E. (1983). The impact of compressible liquids. *Annual Reviews Fluid Mechanics*, 15:97–122.

Levi, E. (1995). *The science of water: the foundation of modern hydraulics*. American Society of Civil Engineers (ASCE), USA.

Levy, J. J. (1961). Effet dynamique d'un courant á haute turbulence sur les ouvrages hydrauliques et sur le lit des riviéres. In *Proceedings of IX IAHR Congress, Dubrovnik, Croatia*, pages 133–140. International Association for Hydro-Environment Engineering and Research (IAHR).

Lewis, T. M. (1996). *Prediction of velocities within jets formed by overtopping steep dams*. Ph.D. Thesis, Colorado States University, USA.

Li, A. H. and Liu, P. Q. (2010). Mechanism of rock-bed scour due to impinging jet. *Journal of Hydraulic Research*, 48(1):14–22.

Lin, S. P. and Reitz, R. D. (1998). Drop and spray formation from liquid jet. *Annual Reviews Fluid Mechanics*, 30:85–105.

Lin, T. J. and Donnelly, H. G. (1966). Gas bubble entrainment by plunging laminar liquid jets. *Associate Institute of Chemical Engineers Journal*, 12(3):563–571.

Liu, P. Q. (1999). *Mechanism of energy dissipation and hydraulic design for plunge pools downstream of large dams*. China Institute of Water Resourcesand Hydropower Research, Beijing, China.

Liu, P. Q. (2005). A new method for calculating depth of scour pit caused by overflow water jets. *Journal of Hydraulic Research*, 43(6):695–701.

Liu, P. Q., Dong, J., and Yu, C. (1998). Experimental investigations of fluctuation uplift on rock blocks at the bottom of the scour pool downstream of Three Gorges spillway. *Journal of Hydraulic Research*, 36(1):55.

Liu, P. Q., Gao, J., Li, Z., and Li, Y. (1997). Mechanism of energy dissipation and hydraulic design for plunge pools downstream of large dams. In *Proceedings of XXVII IAHR Congress, San Francisco, USA*, pages 417–422. International Association for Hydro-Environment Engineering and Research (IAHR).

Liu, P. Q. and Li, A. H. (2007). Model discussion of pressure fluctuations propagation within lining slab joints in stilling basins. *Journal of Hydraulic Engineering*, 7:618–624.

Liu, P. Q., Li, F., and Yin, W. (2003). Experimental study on controlling parameters of flow patterns downstream of high dams. volume D, pages 839–844. International Association for Hydro-Environment Engineering and Research (IAHR).

Liu, P. Q., Wang, S., and Li, L. (2000). Investigation of fracture behavior during rock mass failure. *International Journal of Rock Mechanics and Minin Sciences*, 37:489–497.

Locher, F. A. and Hsu, S. T. (1984). Energy dissipation at high-dams. In *Developments in Hydraulic Engineering*, volume 2 of *Hydraulic Engineering Periodicals*, pages 183–238. P. Novak (ed.), Elsevier Science Publishers, Amsterdam, Netherlands.

Löfdahl, L. and Gad-el Hak, M. (1999). MEMS-based pressure and shear stress sensors for turbulent flows. *Measurement Science and Technology*, 10(8):665–686.

Lopardo, R. A. (1988a). Prototype instrumentation for pressure fluctuations. In *Proceedings of Model-Prototype Correlation of Hydraulic Structures*, pages 267–275. American Society of Civil Engineers (ASCE), USA.

Lopardo, R. A. (1988b). Stilling basin pressure fluctuations. In *Proceedings of Model-Prototype Correlation of Hydraulic Structures*, pages 56–73. American Society of Civil Engineers (ASCE), USA.

Lopardo, R. A. and Henning, R. E. (1985). Experimental advances on pressure fluctuations beneath hydraulic jumps. In *Proceedings of XXI IAHR Congress, Melbourne, Australia*, volume 3, pages 633–638. International Association for Hydro-Environment Engineering and Research (IAHR).

Lopardo, R. A., Lio, F. C., and Vernet, G. F. (1984). Model-prototype comparisons on pressure fluctuations in hydraulic jump energy dissipators. In *Proceedings of Symposium on the Scale Effects in Modelling of Hydraulic Structures*, number 5.7, pages 7.2.1–7.2.5. International Association for Hydro-Environment Engineering and Research (IAHR).

Lyons, R. G. (1997). *Understanding digital signal processing.* Addison Wesley Longman Inc., USA.

Machado, L. I. (1982). O sistema de dissipacao de energia proposto para a barragem de Xingo. In *Translation of the International Symposium on the Layout of Dams in Narrow Gorges.* International Commission on Large Dam (ICOLD).

Malmström, T. G., Kirkpatrick, A. T., Christensen, B., and Knappmiller, K. D. (1997). Centreline velocity decay measurements in low-velocity asymmetric jets. *Journal of Fluid Mechanics*, 346:363–377.

Mandelbrot, B. B. (2002). *Gaussian self-affinity and fractals.* Springer, Germany.

Manso, P. F. A. (2006). The influence of pool geometry and induced flow patterns in rock scour by high-velocity plunging jets. In *Communication N^o 25.* A. J. Schleiss (ed.), Laboratory of Hydraulic Constructions (LCH), École Polytechnique Fédérale de Lausanne (EPFL), Switzerland (ISSN 1661-1179).

Manso, P. F. A., Bollaert, E. F. R., and Schleiss, A. J. (2004a). Experimental investigation on high-velocity jet characteristics and its influence on plunge pool scour. In *Hydraulics of dams and river structures*, pages 173–180. Yazdandooszt & Attari (ed.), A.A. Balkema, Netherlands.

Manso, P. F. A., Bollaert, E. F. R., and Schleiss, A. J. (2004b). Influence of rock scour geometry on dynamic pressures due to jet impact. In *Proceeding of the 2nd International Conference on Scour and Erosion.*

Manso, P. F. A., Bollaert, E. F. R., and Schleiss, A. J. (2005). Dynamic pressures generated by plunging jets in confined pools under extreme flood discharges. In *Proceedings of XXXI IAHR Congress, Seoul, South Korea*, volume D, pages 2848–2860. International Association for Hydro-Environment Engineering and Research (IAHR).

Manso, P. F. A., Bollaert, E. F. R., and Schleiss, A. J. (2007a). Impact pressures of turbulent high-velocity, jets plunging in pools with flat bottom. *Experiments in Fluids*, 42:49–60.

Manso, P. F. A., Bollaert, E. F. R., and Schleiss, A. J. (2008). Evaluation of high-velocity plunging jet-issuing characteristics as a basis for plunge pool analysis. *Journal of Hydraulic Research*, 46(2):147–157.

Manso, P. F. A., Bollaert, E. F. R., and Schleiss, A. J. (2009). Influence of plunge pool geometry on high-velocity jet impact pressures and pressure propagation inside fissured rock media. *Journal of Hydraulic Engineering*, 135(10):783–792.

Manso, P. F. A., Fiorotto, V., Bollaert, E. F. R., and Schleiss, A. J. (2004c). Discussion of "Effect of jet air content on plunge pool scour" by S. Canepa and W.H. Hager. *Journal of Hydraulic Engineering*, 130(11):1128–1130.

Manso, P. F. A., Fiorotto, V., and Schleiss, A. J. (2007b). The influence of rock fissure opening dimensions in plunge pool scour. In *Proceedings of XXXII IAHR Congress, Venezia, Italy*, volume C. International Association for Hydro-Environment Engineering and Research (IAHR).

Manso, P. F. A., Marques, M., Almeida, F., Canellas, A., and Bottelho, M. (2007c). Rock scour downstream ski-jumps: comparison of prototype observations with analytical and physical-model estimation. In *Proceedings of XXXII IAHR Congress, Venezia, Italy*. International Association for Hydro-Environment Engineering and Research (IAHR).

Manso, P. F. A., Schleiss, A. J., Boillat, J.-L., and Bollaert, E. F. R. (2006a). Large-scale motion induced by turbulent plunging jets in pools created by scouring of the riverbed. In *Proceedings of International Conference on Fluvial Hydraulics River Flow 2006*, pages 657–666.

Manso, P. F. A., Schleiss, A. J., Bollaert, E. F. R., and Matos, J. (2006b). Experimental investigation on plunging jets: The behaviour of entrained air bubbles in the vicinity of a flat bottom. In *Proceedings of International Symposium on Hydraulics structures, Ciudad Guayana, Venezuela*, pages 370–379.

Marth, R. (2009). *Ausbreitung dynamischer Druckbelastungen infolge brechender Wellen in Fugen von Kistenschutzbauwerken*. Ph.D. Thesis, Technischen Universität Berlin, Germany.

Martin, C. S. and Padmanabhan, M. (1979). Pressure pulse propagation in two-component slug flow. *Journal of Fluids Engineering*, 101:44–52.

Martins, R. (1973a). Contribution to the knowledge on the scour action of free jets on rocky riverbeds. In *Proceedings of XI Congress on Large Dams, Madrid, Spain*, volume Q41 R44, pages 799–814. International Commission on Large Dam (ICOLD).

Martins, R. (1973b). *Memoria LNEC Nº 424. Scouring action of free jets downstream of hydraulic structures (in Portuguese)*. Laboratorio Nacional de Engenharia Civil (LNEC), Lisbon, Portugal.

Martins, R. (1975). Scouring of rocky riverbeds and free-jet spillways. *International Water Power and Dam Construction*, 27(4):152–153.

Martins, R., editor (1977). *Memoria LNEC Nº 486. Kinematics of the free jet in the field of hydraulic structures (in Portuguese)*. Laboratorio Nacional de Engenharia Civil (LNEC), Lisbon, Portugal.

Mason, P. J. (1983). Energy dissipating crest splitters for concrete dams. *Water Power and Dam Construction*, 35(11):37–40.

Mason, P. J. (1989). Effects of air entrainment on plunge pool scour. *Journal of Hydraulic Engineering*, 115(3):385–399.

Mason, P. J. (1993). Practical guidelines for the design of flip buckets and plunge pools. *Water Power and Dam Construction*, 45(9/10):40–45.

Mason, P. J. and Arumugam, K. (1985). Free jet scour below dams and flip buckets. *Journal of Hydraulic Engineering*, 111(2):220–235.

Matos, J., Frizell, K., André, S., and Frizell, W. (2002). On the performance of velocity measurement techniques in air-water flows. In *Proceedings of Hydraulic Measurements and Experimental Methods*, volume 113, page 58. T.L. Wahl, C.A. Pugh, K.A. Oberg and T.B. Vermeyen (ed.), American Society of Civil Engineers (ASCE), USA.

May, R. W. P. and Willoughby, I. R. (1991). Impact pressures in plunge basins due to vertical falling jets. In *Report SR242*. HR-Wallingford, UK.

McKeogh, E. J. (1978). *A study of air entrainment using plunging water jets*. Ph.D. Thesis, Queens University, Belfast, Ireland.

McKeogh, E. J. and Elsawy, E. M. (1980). Air retained in pool by plunging water jet. *Journal of the Hydraulic Division*, 106(10):1577–1593.

McKeogh, E. J. and Ervine, D. A. (1981). Air entrainment rate and diffusion pattern of plunging liquid jets. *Chemical Engineering Science*, 36:1161–1172.

Melo, J. F. (2001). *Hydrodynamic loads acting on floor slabs of energy dissipation basins by plunging jets (in Portuguese)*. Ph.D. Thesis, Instituto Superior Tecnico (IST), Lisbon, Portugal.

Melo, J. F. (2002). Reduction of plunge pool floor dynamic pressure due to jet air entrainment. In *Rock scour due to falling high-velocity jets*, pages 125–136. A.J. Schleiss and E.F.R. Bollaert (ed.), A.A. Balkema - Swets & Zeitlinger, Netherlands.

Melo, J. F., Pinheiro, A. N., and Ramos, C. M. (2006). Forces on plunge pool slabs: influence of joints location and width. *Journal of Hydraulic Engineering*, 132(1):49–60.

Mih, W. C. and Kabir, J. (1983). Impingement of water jets on nonuniform streambed. *Journal of Hydraulic Engineering*, 109(4):536–548.

Mirtskhula, T. E., Dolidze, I. V., and Magomeda, A. V. (1967). Mechanism and computation of local and general scour in non cohesive, cohesive soils and rock beds. In *Proceedings of XII IAHR Congress, Fort Collins, USA*, volume 3, pages 169–176. International Association for Hydro-Environment Engineering and Research (IAHR).

Mitosek, M. (2000). Study of transient vapor cavitation in series pipe systems. *Journal of Hydraulic Engineering*, 126(12):904–911.

Montgomery, R. A. (1984). *Investigations into rock erosion by high-velocity water flows*. Ph.D. Thesis, The Royal Institute of Technology, Sweden.

Newman, J. J. and Raju, I. (1981). An empirical stress-intensity factor equation for the surface crack. *Engineering Fracture Mechanics*, 15(1-2):185–192.

Nezu, I. and Nakagawa, H. (1993). *Turbulence in open-channel flows*. IAHR Monograph series. A.A. Balkema, Rotterdam, Netherlands.

Ohl, C. D., Oguz, H. N., and Prosperetti, A. (2000). Mechanism of air entrainment by a disturbed liquid jet. *Physics in Fluids*, 12(7):1710–1714.

Otto, B. (1989). *Scour potential of highly stressed sheet-jointed rocks under obliquely impinging jets*. Ph.D. Thesis, James Cook University of North Queensland, Townsville, Australia.

Pagliara, S., Amidei, M., and Minor, H.-E. (2008). Hydraulics of 3D plunge pool scour. *Journal of Hydraulic Engineering*, 134(9):1275–1284.

Pagliara, S., Hager, W. H., and Minor, H.-E. (2006). Hydraulics of plane plunge pool scour. *Journal of Hydraulic Engineering*, 132(5):450–461.

Pagliara, S. and Palermo, M. (2008). Plane plunge pool scour with protection structures. *Journal of Hydro-Environment Research*, 2(3):182–191.

Pagliara, S., Palermo, M., and Carnacina, I. (2011). Scour process due to symmetric dam spillways crossing jets. *International Journal of River Basin Management*, 9(1):31–42.

Pagliara, S., Roy, D., and Palermo, M. (2009). Effect of jet air content on 3D plunge pool scour. In *Proceedings of XXXIII IAHR Congress, Vancouver, Canada*, pages 3588–3595. International Association for Hydro-Environment Engineering and Research (IAHR).

Paris, P. C. and Sih, G. C. (1965). Stress analysis of craks. In *Fracture toughness testing and its applications*, volume STP 381, pages 63–77. ASTM Committee E24, USA.

Patton, K. T. (1965a). *An experimental investigation of hydrodynamic mass and mechanical impedences*. Ph.D. Thesis, University of Rhode Island, Rhode Island, USA.

Patton, K. T. (1965b). Tables of hydrodynamic mass factors for translational motion. *American Society of Mechanical Engineers*, Paper 65, WN/UNT-2:1–7.

Pearsall, I. S. (1966). The velocity of waterhammer waves. In *Proceedings of Symposium on Surges in Pipelines*, volume 180-3E, pages 12–20. Institut of Mechanical Engineering, USA.

Pinheiro, A. N. (1995). *Accoes hidrodininamicas em soleiras de bacias de dissipacao de energia por ressalto*. Ph.D. Thesis, Instituto Superior Tecnico (IST), Lisbon, Portugal.

Pinheiro, A. N. and Melo, J. F. (2008). Effect of jet aeration on hydrodynamic forces on plunge pool flors. *Canadian Journal of Civil Engineering*, 35(5):521–530.

Pinto, N. and Neidert, S. H. (1982). Model-prototype conformity in aerated spillway flow. In *Proceedings of International Conference on Hydraulic Modelling*, pages 273–284. BHRA Group, UK.

Pope, S. B. (2000). *Turbulence flows*. Cambridge University Press, UK.

Poreh, M. and Hefez, E. (1967). Initial scour and sediment motion due to an impinging submerged jet. In *Proceedings of XII IAHR Congress, Fort Collins, USA*, volume 3, pages 169–176. International Association for Hydro-Environment Engineering and Research (IAHR).

Puertas, J. (1994). *Hydraulic criteria for the design of energy dissipation basins in arch dams with free crest overfall*. Ph.D. Thesis, Universitat Politecnica de Catalunya, Barcelona, Spain.

Puertas, J. and Dolz, J. Pressure fields due to the impingement of free falling jets on a riverbed. In *Rock scour due to falling high-velocity jets*, pages 105–114. A.J. Schleiss and E.F.R. Bollaert (ed.), A.A. Balkema - Swets & Zeitlinger, Netherlands.

Puertas, J. and Dolz, J. (2005). Plunge pool pressures due to a falling rectangular jet. *Journal of Hydraulic engineering*, 131(5):404–407.

Quintela, A. C. (1981). *Hidraulica*. Fundacao Calouste Gulbenkian, Portugal, 4$^{\text{th}}$ edition.

Quintela, A. C. and Cruz, A. A. (1982). Cahora-Bassa dam spillway. Conception, hydraulic model studies and prototype behaviour. In *Translation of the International Symposium on the Layout of Dams in Narrow Gorges*, pages 301–309. International Commission on Large Dam (ICOLD).

Quintela, A. C., Cruz, A. A., and Fernandes, J. S. (1987). Cahora-Bassa dam spilway. Design and prototype behaviour (in Portuguese). In *Iberian-American Conference on Hydraulic Schemes*, pages 197–206.

Rajaratnam, N. (1976). *Turbulent jets*, volume 5 of *Developments in Water Science*. Elsevier Science Publishers, Amsterdam, Netherlands.

Rajaratnam, N. (1981). Erosion by plane turbulent plane jets. *Journal of Hydraulic Engineering*, 19(4):339–358.

Rajaratnam, N. and Mazurek, K. A. (2002). Erosion of a polysterene bed by obliquely impinging circular turbulent air jets. *Journal of Hydraulic Research*, 40(6):709–716.

Rajaratnam, N. and Mazurek, K. A. (2003). Erosion of sand by circular impinging water jets with small tailwater. *Journal of Hydraulic Engineering*, 129(3):225–229.

Rajaratnam, N. and Mazurek, K. A. (2005). Impingement of circular turbulent jets on rough boundaries. *Journal of Hydraulic Engineering*, 43(6):689–695.

Ramos, C. M. (1979). Statistical characteristics of the pressure field of crossed flows in energy dissipation structures. In *Proceedings of XI ICOLD Congress, Madrid, Spain*, volume Q41-R3, pages 39–56. International Commission on Large Dam (ICOLD).

Ramos, C. M. (1982). Energy dissipation on free jet spillways. Bases for its study in hydraulic models. In *Translation of the International Symposium on the Layout of Dams in Narrow Gorges*, volume 1, pages 263–268. International Commission on Large Dam (ICOLD).

Reeve, L. N. (1932). Erosion below Conowingo dam proves value of model tests. *Engineering News-Record*, 108:127–130.

Reinus, E. (1986). Rock erosion. *Water Power and Dam Construction*, 38(6):43–48.

Renna, F., Fratino, U., and Matos, J. (2005). Air-water flow features in skimming flow over steeply sloping stepped spillways. In *Proceedings of XXXI IAHR Congress, Seoul, South Korea*, pages 2664–2674. International Association for Hydro-Environment Engineering and Research (IAHR).

Resch, F. J. and Leutheusser, H. J. (1971). Mesures de turbulence dans le ressaut hydraulique. *La Houille Blanche*, 4:17–31.

Reynolds, A. J. (1974). *Turbulent Flows in Engineering*. J. Wiley & Sons Limited, London, UK.

Ribeiro, A. A. (1975). The macroturbulence downstream a stilling basin. Erosion (scouring). In *Proceedings of XVII IAHR Congress, Sao Paulo, Brazil*, volume 5, pages 96–99. International Association for Hydro-Environment Engineering and Research (IAHR).

Richards, J. R., Lenhoff, A. M., and Beris, A. N. (1994). Dynamic breakup of liquid-liquid jets. *Physics Fluids*, 6(8):2640–2655.

Riman, I. S. and Kreps, R. L. (1947). Added masses of bodies of various shape. In *Proceedings of Central Institute of Aero- and Hydro-dynamics*, volume 635, pages 1–46.

Rinaldi, P. and Valentin, F. (2005). Non-dimensional scaling of turbulent jets in confined spaces. In *Environmental Hydraulics and Sustainable Water Management*, pages 319–324. Lee & Lam (ed.), Taylor and Francis Group, UK.

Rotta, J. C. (1972). *Turbulente Strömungen*. B.G. Teubner (ed.), Stuttgart, Germany.

Rouse, H. (1940). Criteria for similarity in the transportation of sediment. In *Proceedings of First Hydraulic Conference*, volume 20, pages 33–49. University of Iowa, USA.

Rouse, H., Howe, J., and Metzler, D. (1951). Experimental investigations of fire monitors and nozzles. In *Proceedings of ASCE Hydraulics Division*, volume 77, pages 1–29. American Society of Civil Engineers (ASCE).

Rouse, H., Sio, T. T., and Nagaratnam, S. (1959). Turbulence characteristics of the hydraulic jump. *Translation of the American Society of Civil Engineers (ASCE)*, 124:926–950.

Rubinstein, G. L. (1963). Laboratory investigation of local erosion on channel beds below high overflow dams. In *Proceedings of Hydraulics of High Head Water Discharge Structures*. M.L. Gosenergoizdat.

Salehi-Neyshabouri, A. A., Silva, A. M. F. d., and Barron, R. (2003). Numerical simulation of scour by a free falling jet. *Journal of Hydraulic Research*, 41(5):533–539.

Sanchez-Bribiesca, J. L. and Fuentes-Mariles, O. A. (1979). Experimental analysis of macro-turbulence effects on the lining of stilling basins. In *Proceedings of XXXIII Congress on Large Dams, New Delhi, India*, volume Q50-R6, pages 85–103. International Commission on Large Dam (ICOLD).

Sarkaria, G. S., Piasentin, C., Fiorini, A. S., and Carvalho, E. (2003). Operational efficiency of large spillways: eight Brasilian case studies. *International Journal on Hydropower and Dams*, 55(4):47–57.

Sarpkaya, T. (1960). Added masses of lenses and parallel plates. *Journal of Engineering Mechanical Division*, 86(EM3):141–151.

Schleiss, A. J. (1985). *Bemessung von Druckstollen, Teil I: Literatur, Grundlagen, Felshydraulik insbesondere Sickerströmungen durch Auskleidung und Fels*. Mitteilungen de Versuchsanstalt fur Wasserbau, Hydrologie und Glaziologie (VAW) N° 78, ETH Zürich, Switzerland.

Schleiss, A. J. (2002). Scour evaluation in pace and time. The challenge of dam designers. In *Rock scour due to falling high-velocity jets*, pages 3–22. A.J. Schleiss and E.F.R. Bollaert (ed.), A.A. Balkema - Swets & Zeitlinger, Netherlands.

Schleiss, A. J. and Annandale, G. W. (2007). Predicting rock scour: Part 1. *International Water Power & Dam Construction*, 9:22–26.

Schwartz, W. H. and Cosart, W. P. (1961). The two-dimensional turbulent wall jet. *Journal of Fluid Mechanics*, 10:481–495.

Schweitzer, P. H. (1937). Mechanism of disintegration of liquid jets. *Journal of Applied Physics*, 8:513–521.

Schweitzer, P. H. and Szebehely, V. G. (1950). Gas evolution in liquids and cavitation. *Journal of Applied Physics*, 21:1218–1224.

Sedov, L. I. (1966). *Planar problems of hydrodynamics and aerodynamic*. Nauka (ed.), Moscow, URRS.

Sene, K. J. (1988). Air entrainment by plunging jets. *Chemical Engineering Science*, 43(10):2615–2623.

Sene, K. J., Hunt, J. C. R., and Thomas, N. H. (1994). The role of coherent structures in bubble transport by turbulent shear flows. *Journal of Fluid Mechanics*, 259:219–240.

Simoes, G. F. and Vargas Jr, E. d. A. (2001). Analysis of erosion processes downstream of spillways in large dams. In *Proceedings of 38th US Rock Mechanics Symposium, Washington D.C., USA*, volume 1 & 2, pages 959–966.

Simons, D. B. and Stevens, M. A. (1971). Scour control in rock basins at culvert outlets. In *River Mechanics*, volume 2, chapter 24. H.W. Shen (ed.), USA.

Spurr, K. J. W. (1985). Energy approach to estimating scour downstream of a large dam. *International Water Power and Dam Construction*, 37(11):81–89.

Stearns, S. D. (2003). *Digital Signal Processing with examples in MATLAB*. CRC Press, Taylor & Francis Group, UK.

Stein, O. R., Julien, P. Y., and Alonso, C. V. (1993). Mechanics of jet scour downstream of a headcut. *Journal of Hydraulich Research*, 31(6):723–738.

Stelson, T. E. and Mavis, F. T. (1955). Virtual mass and acceleration in fluids. *Proceedings of American Society of Civil Engineers (ASCE)*, 81:670–1/670–9.

Stokes, G. G. (1851). On the effect of the internal friction of fluids on the motion of pendulums. In *Transactions of the Cambridge Philosophical Society*, volume IX, Part 8. McGraw Hill, UK.

Streeter, V. L. and Wylie, E. B. (1983). *Fluid Mechanics*. Civil and Mechanical Engineering Series. McGraw Hill, UK.

Swaffield, J. A. and Boldy, A. P. (1993). *Pressure surge in pipe and duct systems*. Avebury Technical, UK.

Tao, C. G., JiYong, L., and Xingrong, L. (1985). *Efeito doimpacto, no leito do rio, da lamina descarregada sobre uma barragem-abobada (translation from chinese by de J.A.P. Campos)*. Laboratorio Nacional de Engenharia Civil (LNEC), Lisboa, Portugal.

Taraimovich, I. I. (1979). Deformations of channels below high-head spillways on rock foundations. *Power Technology and Engineering (formerly Hydrotechnical Construction)*, 12(9):917–923.

Taraimovich, I. I. (1981). Calculation of local scour of rock foundations by high-velocity flows. *Power Technology and Engineering (formerly Hydrotechnical Construction)*, 14(8):791–797.

Tennekes, H. and Lumley, J. L. (1972). *A First Course in Turbulence*. Massachusetts Institute of Technology (MIT) Press, USA.

Thomas, N. H. (1983). Entrapment and transport of bubbles by transient large eddies in multi-phase turbulent shear flows. In *Proceedings of International Conference on Physical Modelling of Multi-phase Flow*, pages 169–184. BHRA Group, UK.

Thorley, A. R. D. and Guymer, G. (1976). Pressure surge propagation in thick-walled conduits of rectangular cross section. *Journal of Fluids Engineering*, 98(3):455–460.

Toso, J. W. and Bowers, C. E. (1988). Extreme pressures in hydraulic-jump stilling basins. *Journal of Hydraulic Engineering*, 114(8):829–843.

Ursino, N., Salandin, P., and Da Leppo, L. (2003). Fluctuating pressures at the bottom of a plunge pool. In *Proceedings of XXX IAHR Congress, Thessaloniki, Greece*, volume C, pages 191–198. International Association for Hydro-Environment Engineering and Research (IAHR).

Van de Donk, J. A. C. (1981). *Water aeration with plunging jets*. Ph.D. Thesis, Technische Hogeschool Delft, Netherlands.

Van de Sande, E. and Smith, J. M. (1973). Surface entrainment of air by high velocity water jets. *Chemical Engineering Journal*, 28(5):1161–1168.

Van de Sande, E. and Smith, J. M. (1976a). Jet break-up and air entrainement by low velocity turbulent jets. *Chemical Engineering Science*, 31:219–224.

Van de Sande, E. and Smith, J. M. (1976b). Mass transfer from plunging water jets. *Chemical Engineering Journal*, 10(3):225–233.

Vasiliev, O. F. and Buckreyev, V. I. (1967). Statistical characteristics of pressure fluctuations in the region of hydraulic jump. In *Proceedings of XII IAHR Congress, Fort Collins, USA*, volume 2, pages 1–8. International Association for Hydro-Environment Engineering and Research (IAHR).

Veronese, A. (1937). *Erosion of a bed downstream from an outlet*. Colorado A & M College (ed.), USA.

Viscaino, A. C. and Sànchez Bribiesca, J. S. (1979). Turbulent effects on the lining of stilling basin. In *Proceedings of XVII IAHR Congress, Madrid, Spain*, volume 11, pages 1575–1592. International Association for Hydro-Environment Engineering and Research (IAHR).

Vischer, D. L. and Hager, W. H. (1995). Energy dissipators. In *IAHR Hydraulic Structures Design Manual*. A.A. Balkema, Rotterdam, Netherlands.

Vischer, D. L. and Hager, W. H. (1998). *Dam Hydraulics*. J. Whiley & Sons Ltd., UK.

Vorobjov, P. S. (1966). Experimental investigation of added masses of parallelepipeds on shallow water. In *Proceedings of Novosibirsk Institute of Water Transport*, volume 21, pages 3–9.

Weilin, X., Huasheng, L., Yongquan, Y., and Chigong, W. (2002). Turbulent flow and energy dissipation in plunge pool of high arch dam. *Journal of Hydraulic Research*, 40(4):471–476.

Weilin, X., Jun, D., Jingxue, Q., Shanjun, L., and Wei, W. (2004). Experimental investigation on influence of aeration on plane jet scour. *Journal of Hydraulic Engineering*, 130(2):160–164.

Whittaker, B. N., Singh, R. N., and Sun, G. (1992). *Rock Fracture Mechanics*. Elsevier Science Publishers, Amsterdam, Netherlands.

Whittaker, J. G. and Schleiss, A. J. (1984). *Scour related to energy dissipators for high head structures*, volume 73. Mitteilungen de Versuchsanstalt fur Wasserbau, Hydrologie und Glaziologie (VAW), ETH Zürich, Switzerland.

Wiggert, D. C. and Sundquist, M. J. (1979). The effect of gaseous cavitation on fluid transients. *Journal of Fluids Engineering*, 101:79–86.

Wisner, P. (1966). Role of the froude number in the study of air entrainment. In *Proceedings of XI IAHR Congress, Leningrad, URSS*, number 1.15. International Association for Hydro-Environment Engineering and Research (IAHR).

Wisner, P., Radu, M., and Armences, G. (1967). Note sur les méthodes d'étude sur modele réduit des affouillements locaux des lits rocheux. In *Proceedings of XII IAHR Congress, Fort Collins, USA*, volume 3. International Association for Hydro-Environment Engineering and Research (IAHR).

Withers, W. (1991). *Pressure fluctuations in the plunge pool of an impinging jet spillway*. Ph.D. Thesis, Universy of Glasgow, Scotland.

Wood, I. R. (1991). *Air entrainment in free-surface flows*, volume 4 of *Hydraulic structures design manual*. A.A. Balkema, Rotterdam, Netherlands.

Wood, I. R., Ackers, P., and Loveless, J. (1983). General method for critical point on spillways. *Journal of Hydraulic Engineering*, 109(2):308–312.

Wylie, E. B. and Streeter, V. L. (1978). *Fluid Transients*. McGraw Hill, UK.

Xu-Duo-Ming (1983). *Pressao no fundo de um canal devido ao choque de um jacto plano, e suas caracteristicas de fluctuacao (translation from chinese by de J.A.P. Campos)*. Laboratorio Nacional de Engenharia Civil (LNEC), Lisboa, Portugal.

Yu, Y. T. (1945). Virtual masses of rectangular plates and parallelepipeds in water. *Journal of Applied Physics*, 16(11):724–729.

Yuditskii, G. A. (1963a). Actual pressure on the channel bottom below ski-jump spillways. *Izvestiya Vsesoyuznogo Nauchno-Issledovatel-Skogo Instuta Gidrotekhiki*, 67:231–240.

Yuditskii, G. A. (1963b). *Memoria LNEC Nº 442. Accao hidrodinamica de uma lamina descarregada sobre blocos de um leito rochoso e condicoes de rotura deste (in Portuguese), translated from "Izvestiya Vsesoyuznogo Nauchno-Issledovatel-Skogo Instuta Gidrotekhiki"*. Laboratorio Nacional de Engenharia Civil (LNEC), Lisboa, Portugal.

Yuditskii, G. A. (1971). *Experimental prediction of rock bed scour below a ski-jump spillway dam (translated from the russian)*. IPST, Jerusalem.

Yuen, E. M. (1984). *Clear water scour by high-velocity jets*. Ph.D. Thesis, Department of Civil Engineering, University of Windsor, Ontario,Canada.

Zaman, K. B. M. Q. (1999). Spreading characteristics of compressible jets from nozzles of various geometries. *Journal of Fluid Mechanics*, 383:197–228.

Zhao, J. F. and Li, W. (2000). Investigation of the compressibility of extra-high-velocity aerated flows. *Journal of Hydraulic Research*, 38(5):351–358.

Zhu, Y., Oguz, H. N., and Prosperetti, A. (2000). On the mechanism of air entrainment by liquid jets at a free surface. *Journal of fluid Mechanics*, 404:151–177.

Notations

Roman Lower Case

a	Block acceleration / Body dimension
$a_{\Delta pulse}$	Uplift acceleration
b	Body dimension
c	Structural damping / Viscous damping coefficient
c_{air}	Pressure wave celerity in the air
c_{mix}	Pressure wave celerity for a mixed fluid
c_w	Pressure wave celerity in the water
dt	Time increment
e	Distance between the water "reservoir" bottom and the lower face of the floating body
f	Frequency / Vibration frequency
f_n	Natural frequency
$f_{n,b}$	Block natural frequency
f_{vs}	Frequency of vortex shedding
g	Gravitational acceleration
h_{up}	Block uplift
k	Spring constant / System stiffness
l	Crack length
m	Body mass
m_b	Block mass
m_{am}	Added mass
p	Total pressure
p_{max}	Maximum pressure
$\overline{p}$	Mean pressure
p_{min}	Minimum pressure
p'	Pressure fluctuations
x, y, z	Coordinates
x	Displacement of the body from the equilibrium position

Roman Capital

A	Amplitude
A_{xx}	Added mass
B_{xx}	Water dumping
C_s	Skewness
CL	Characteristic length for the Strouhal number (i.e. hydraulic diameter)
C_p	Mean pressure coefficient
$C_{p'}$	Turbulent pressure fluctuation coefficient
C_p^+	Positive extreme pressure fluctuation coefficient
C_p^-	Negative extreme pressure fluctuation coefficient
$C_{p,max}$	Positive extreme pressure coefficient
$C_{p,min}$	Negative extreme pressure coefficient
C_{air}	Air concentration
D	Nozzle diameter / Jet diameter at the nozzle
F_{up}	Pressure force acting on the block upper face
F_{shear}	Shear force
F_{am}	Added mass force
F_{down}	Pressure force acting underneath the block
F_{ar}	Buoyancy force acting on the block
Fr	Froude number ($Fr = U/\sqrt[2]{\rho \cdot D}$)
G_b	Block weight
$I_{\Delta pulse}$	Block net impulsion
K_I	Critical intensity factor (crack propagation)
K_{IC}	Intensity factor (crack propagation)
Ku	Kurtosis coefficient
L	Jet travel distance in the air
L_b	Jet break-up length in the air
L_F	Characteristic fracture length
P_{xx}	Power Spectral Density (PSD)
Q	Flow discharge / Quality factor for a damped oscillator
Re	Reynolds number ($Re = U \cdot D/\nu$)
S_b	Block surface (horizontal surface)
St	Strouhal number ($St = f_{vs} \cdot CL/U$)
T_n	Fissure natural period
Tu	Jet turbulence intensity
U, U_0	Mean flow velocity
V, V_0	Jet velocity at the nozzle
V_I	Jet velocity at the impact on the plunge pool water surfance

Roman Capital

V_b	Block volume
$V_{\Delta pulse}$	Block uplift velocity
Var	Variance
W_b	Block immerged weight
We	Weber number ($We = \rho \cdot U^2 \cdot D/\sigma$)
Y	Plunge pool water depth

Greek symbols

α	Velocity profile correction for the pressure coefficient calculation
α_{am}	Added mass coefficient
β	Volumetric air-to-water ratio ($= Q_{air}/Q_w$)
$\Delta t_{\Delta pulse}$	Pressure pulse time
μ_k	Kinetic friction coefficient
μ_s	Static friction coefficient
ν_w	Water kinematic viscosity
ω_d	Damped natural (angular) frequency
ω_n	Angular frequency
Ω_{peak}	Resonance frequency
ξ	Damping ratio
ρ_{air}	Air density
ρ_b	Block density
ρ_{mix}	Air-water mixture density
ρ_w	Water density
σ	Standard deviation
σ_w	Water surface tension
σ_p	Pressure standard deviation
θ_x, θ_y, θ_z	Rotation around the x-, y- and z-axis
ϕ	Phase

Acronyms

FFT	Fast Fourier Transformation
PRC	Pressure Reduction Coefficient
PSD	Power Spectra Density
SDoF	Single degree of freedom

Acknowledgements

This research project was performed at the Laboratory of Hydraulic Constructions of the École Polytechnique Fédérale de Lausanne under the supervision of Prof. Dr Anton J. Schleiss and Dr Erik F.R. Bollaert. I would like to express my gratitude to Prof. Schleiss to have given me the opportunity to perform this research project after my studies on civil engineering in the same institute. I really appreciated his support, his technical and scientific advice. It was a great pleasure to work with him. My gratitude also goes to Dr Bollaert for his open mind thinking, the scientific advices and the technical comments during all my research.

This project was funded by the Swiss National Science Foundation (SNSF) project number FN 200021-112620 with the extension FN 200020-129606.

Michel Teuscher was the man who built this sophisticated experimental facility (the highly instrumented block and the measurement box) and who modified the existing experimental facility. Without him this work would not have been performed. He was always ready to help when any kinds of problems occurred: *"Houston I have a problem!!!! "* Thank you so much :)

I thank also the other members of the technical team that helped me and my facility. My thanks go to: PanPam, Jean-Marc, Laurent, Virgile, Jonathan, Grégory and Shawna.

Not to forget, Louis Schneiter firstly and then Cédric Bron who gave me some advice for the data acquisition equipment of the facility.

I thank Dr Mohammed Farhat of the Laboratory of Hydraulic Machinery (LMH) of EPFL for his support for the calibration of the pressure transducers.

This thesis gave me the opportunity to extend my stay in this beautiful city for a wonderful five-year experience. Apart from the professional life, my stay in Lausanne was a really interesting time in my personal life. In these years I had the opportunity to get in touch with a lot of people coming from all around the world.

I would like to thank all my friends of the LCH, pasts and presents: Alex, Ana Margarida,

Azin, Burkhard, Erica, Fadi, Fréd, Javier, Jean-Marc, Jolanda, José Pedro, Juliano, Marcelo, Markus, Mathias, Martin, Michael, Michael, Milad, Mona, Pedro, Philippe, Rafael, Ramesh, Rémi, Sabrina, Sameh, Stéphane, Sylvain, Tamara, Théodora, Tobias, Violaine, Walter ... I'm sorry in case I have forgotten some of you!!!!

A special thanks to Giovanni, my office colleague, for his eternal good spirit and readiness to answer to my "stupid" questions :)

Jean-Louis Boillat for his enthusiasm in discovering new horizons, his optimistic point of view, and his interesting discussions during the project meetings and coffee-breaks: Every time I learned something new from our discussions! Thanks a lot :)

The secretary team to make all work with a smile: Caroline, Martine, Christelle, Sonia and Scarlett.

The SPLEEN volley team for the relaxing moments during the lunch breaks: Nicolas, Damien, Rafal, Jean-Marc, Ronny, Lena, Michael, Emanuele, Lucia, Markus, Guillaume, Tomas ... champions of the internal tournament for the season 2008-2009 and two times at the second place.

IOOOOBOMBULEEEEEEE

This work is dedicated to my loving parents, my mother Eliana and my father Marco, my sisters Sonja and Lucia and my grandparents Ginetta and Giovanni✞.

Non ci sono abbastanza parole per ringraziarvi di tutto
quello che avete fatto per me in tutti questi anni!!!!
Dirvi grazie mille non basta!!!!
Matteo

Not to forget two new family members my brother in law Ugo and the little Sara.

I would thank my beloved Nicoletta with all my heart for her incredible support during these last two years and especially in the last months of the thesis drafting.

Grazie con tutto il mio cuore dolce fanciulla!!!!
Doc

And last but not least, Striscia who helped me in the mouse management during the drafting time.

My friends in Switzerland and abroad.

Appendix

Data base and graphical representation of all performed experiments

The following data with graphical representation are available on request at the Laboratory of Hydraulic Constructions (LCH) of the École Polytechnique Fédérale de Lausanne (EPFL) for all performed experiments (see Figure 4.7):

- Configuration description
- Pressure field surrounding the block
- Pressure coefficients
  - Mean pressure coefficient C_p
  - Turbulent pressure fluctuation coefficient $C_{p'}$
  - Positive extreme pressure fluctuation coefficient C_p^+
  - Negative extreme pressure fluctuation coefficient C_p^-
  - Positive extreme pressure coefficient $C_{p,max}$
  - Negative extreme pressure coefficient $C_{p,min}$
- Displacements and accelerations of block
  - Displacements of block
  - Accelerations of block
- Power Spectral Density
- Dynamic block impulsion

The tested configurations are:

- Two contact points at lateral guides
    - Jet impact position on the block center with the block free to move (CE);
    - Jet impact position on the block right hand side with the block free to move (SI).
- Eight contact points at lateral guides
    - Jet impact position on the block center with the block fixed (CR_F);
    - Jet impact position on the block right hand side with the block fixed (SR_F);
    - Jet impact position on the block left hand side with the block free to move (SL);
    - Jet impact position on the block left hand with the block fixed (SL_F);
    - Jet impact position on the block corner with the block fixed (CN_F);
    - Jet impact position radial (between the center and the corner of the block) with the block free to move (RR);
    - Jet impact position radial (between the center and the corner of the block) with the block fixed (RR_F).
- Passive air entrainment and eight contact points at lateral guides
    - Jet impact position on the block corner with the block free to move (ACN).

Curriculum Vitae

Curriculum Vitae

PERSONAL DATA

FEDERSPIEL Matteo Paolo Elia Antonio

Nationality: Swiss
Born in Sorengo (Switzerland), 20.9.1978
Native: Mesocco (GR) and Pregassona (TI)
Marital state: Unmarried

Professions

Architect STS
Civil Engineer EPFL
PhD in Civil Engineer EPFL

Private address
Via Probello 2F
CH-6963 Pregassona
Switzerland
Phone: ++41'91'972'54'81
Mobile: ++41'79'295'78'88
e-mail: matteo.federspiel@bluewin.ch

Professional address
Laboratoire de Construction
Hydrauliques (LCH)
EPFL-ENAC-ICC-LCH
Station 18
CH-1015 Lausanne
Switzerland
Phone: ++41'21'693'63'34
Fax: ++41'21'693'22'64
e-mail: matteo.federspiel@epfl.ch

EDUCATION

09.2006 - 09.2011	PhD student, Environment Doctoral Program (EDEN) at the Ecole Polytechnique Fédérale in Lausanne (EPFL), Switzerland
10.1999 - 07.2006	Ecole Polytechnique Fédérale in Lausanne (EPFL), Switzerland, faculty of Civil Engineering, graduated in July 2006
09.1993 - 06.1999	Scuola Tecnica Superiore (STS) in Lugano, Switzerland, faculty of Architecture, graduated in June 1999
	First and secondary school in Ticino (Pregassona - Lugano), Switzerland

PROFESSIONAL EXPERIENCES

09.2006 - 09.2011	Civil engineer and assistant at the Laboratory of Hydraulic Construction (LCH) of the EPFL Preliminary analysis of projects, hydraulic models construction and hydraulic models tests. Assistant for semester courses, semester projects and Master projects
07.2004 - 09.2004	Summer practical: Studio d'ingegneria Mauri T. & Banci F., Via Boschina 19, 6963 Pregassona (TI), Switzerland Support on some structural and hydraulic projects
06.1999 - 07.1999	Summer work: Studio d'architettura Prof. M. Campi e F. Pessina, Architetti FAS e associati, Via Casserinetta 28, 6900 Lugano, Switzerland Supporton a architecture project
07.1994 - 07.1996	Studio d'architettura Prof. M. Campi e F. Pessina, Architetti FAS e associati, Via Casserinetta 28, 6900 Lugano Compulsory practical stage during the formation at the STS (second and third years)

DISTINCTIONS AND AWARDS

07.2006	EPFL	Prof. Dr Stucky award for an innovative project in the field of hydraulic construction (Master project: Dam and Hydropower plant of Sazbon, Iran)
06.1999	STS	Giuseppe and Valentina Maraini award (best average of the Architecture section) OTIA award (best graduate work of the Architecture section: Multipurpose building in Ciani Garden, Lugano, Switzerland) Schindler AG award (best graduate work of the Architecture section)

LANGUAGES

Italian	Mother tongue
French	Fluent
German	Fair
English	Fair (Level B2)
Japanese	Basic (Level A1)

SOFTWARE

Office	Microsoft Office (Word, Excel, PowerPoint …)
Mathematics	Matlab
Draw	AutoCAD, ArchiCAD, Autodesk Inventor Professional 11
DAQ	LabVIEW
Hydraulic	HEC-RAS, Flow 3D (basic)
Text	ProText, TeXnicCenter

ACTIVITY

Military instruction: officer of the Swiss Air Force (Air Defence System: SM Gr DCA m 32) as “Enemy/Info” Officer (rank: captain)

Airplane Private Pilot Licence PPL(A)_VFR (Private Pilot Licence Airplane_Visual Flight Rules) obtained in March 2000

INTERESTS

Sport	Karate (FKSI - Skotokan Karate Pregassona) - Brown belt Bike (road and mountain bike) Mountain trekking Volley
Reading	Books (action, adventure, history, science fiction, fantasy …) Scientific magazines (construction, car, aircrafts, defence …)

PUBLICATIONS

M. P. E. A. Federspiel, E. F. R. Bollaert, and A. J. Schleiss. *Experiments on the response of a rock block in a plunge pool loaded by a symmetrical jet impact*. In 34rd IAHR Congress Water Engineering for a Sustainable Environment, 26 June-01 July 2011, Brisbaine, Australia

M. Bieri, M. Federspiel, J.-L. Boillat, B. Houdant, L. Faramond and F. Delorme. *Energy dissipation downstream of Piano Key Weirs - Case study of Gloriettes Dam (France)*. Workshop on labyrinth and piano key weirs, 9-11 February 2011, Liège, Belgique

M. Bieri, M. Federspiel, J.-L. Boillat, B. Houdant, and F. Delorme. *Spillway capacity upgrade of Gloriettes Dam: Environmental integration and energy dissipation*. Hydropower & Dams, Issue Five 2010, pp. 88-93

Giovanni De Cesare, Milad Daneshvari, Matteo Federspiel, Mathias Malquarti, Gaël Epely Chauvin et Anton Schleiss. *Etude sur modele physique et numerique des evacuateurs de crue et des fosses d'erosion du barrage de Koman en Albanie.* SimHydro 2010: Modèles Hydrauliques et Incertitudes, Sophia Antipolis, Nice, France, 2-4 juin 2010

Giovanni De Cesare, Juliano M. Ribeiro, Sameh A. Kantoush, Matteo P.E.A. Federspiel. *River intake and desander efficiency testing on a physical model using UVP and LSPIV*. In 7th International Symposium on Ultrasonic Doppler Methods for Fluid Mechanics and Fluid Engineering, 7-9 April 2010, Göteborg, Sweden

M. P. E. A. Federspiel, E. F. R. Bollaert, and A. J. Schleiss. *Experiments on the repons of a rock block in a plunge pool loaded by a symmetrical jet impact*. In Proceedings of the 1st European IAHR Congress, 4-6 May 2010, Edinburgh, Scotland

Pooyan Asadollahi, Fulvio Tonon, Matteo P.E.A. Federspiel, and Anton J. Schleiss. *Prediction of rock block stability and scour depth under high-velocity water jet impact in plunge pools*. Submitted for publication to the Journal of Hydraulic Research

M. Bieri, M. Federspiel, J.-L. Boillat, B. Houdant, and F. Delorme. *Spillway capacity upgrade of Gloriettes Dam: Environmental integration and energy dissipation*. In Proceedings of HYDRO 2009, 26-28 October 2009, Lyon, France

M. P. E. A. Federspiel, E. F. R. Bollaert, and A. J. Schleiss. *Response of an intelligent block to symmetrical core jet impact*. In 33rd IAHR Congress Water Engineering for a Sustainable Environment, 9-14 August 2009, pages 3573-3580, Vancouver, Canada

J. Jenzer, S. Carvalho Pereira, M. Federspiel, and J.-L. Boillat. *Modellversuche des Rhône bei Visp (Schweiz) unter Betrachtung mehrerer wasserbaulicher Aspekte*. In INTERPRAEVENT Science & Technology Board, editor, Protection of populated territories from floods, debris flow, mass movements and avalanches, volume 1, pages 131-139, Klagenfurt, Austria, 26-30 Mai 2008. International Research Society INTERPRAEVENT

CONGRESS AND PRESENTATIONS

M. P. E. A. Federspiel. *Response of an intelligent block to symmetrical core jet impact*. 33rd IAHR Congress Water Engineering for a Sustainable Environment, 9-14 August 2009, Vancouver, Canada

M. P. E. A. Federspiel, E. F. R. Bollaert, and A. J. Schleiss. *Experiments on the response of a rock block in a plunge pool loaded by a symmetrical jet impact*. 1st European IAHR Congress, 4-6 May 2010, Edinburgh, Scotland

ASSOCIATION MEMBER

Individual member of SIA (Swiss association of architects and civil engineering's), section Ticino since 2007.

Member of "Società Ticinese degli Ufficiali (Swiss Italian Officer Association)" since 2003.

Member of "AVIA Luftwaffe TI" (Air Force Officier Association) since 2003.

PROJECTS COLLABORATIONS

2010
Customer: Zambezi River Authority
Project: Kariba Dam
Country: Zambia-Zimbabwe
Professional service: Hydraulic model test of the existing scour hole and proposition of a new geometry to avoid the scour propagation.

2009
Customer: BKW (Bieler KraftWerke)
Project: Hagneck
Country: Switzerland
Professional service: Hydraulic model test of the new river dam and power plant.

2008
Customer: EDF (Electricité De France)
Project: Choranche Dam
Country: France
Professional service: Hydraulic model test of the existing spillway capacity as a function of the new PMF (Probable Maximum Flood). Numerical study on the scour hole propagation at the dam toe.

2008
Customer: Pöyry Ldt.
Project: Koman Dam
Country: Albania
Professional service: Hydraulic and numerical model test of spillways, scour holes propagation and erosion of the dam toe.

2007
Customer: Colenco
Project: Teesta IV HEP
Country: India
Professional service: Hydraulic model test of river dam, water intakes and desanders.

2007
Customer: EDF (Electricité De France)
Project: Gloriettes Dam
Country: France
Professional service: Hydraulic model test of existing (free crest) and new spillways (PKW-Piano Key Weir). Design and validation of the new restitution channel.

2007
Customer: Nordostschweizerische Kraftwerke AG
Project: Pump storage power plant of Linth-Limmern
Country: Switzerland
Professional service: Hydraulic model test of the intake structures of the lower basin Limmernsee and the upper basin Muttsee.

2007
Customer: Gemeinde Ingenbohl-Brunnen
Project: Wylerbrücke on the Muota River
Country: Switzerland
Professional service: Hydraulic model test to evaluate the danger of destruction of the historical wood bridge.

2006
Customer: Aare Tessin AG für Elektrizität (atel)
Project: Pump storage power plant of Nant de Drance
Country: Switzerland
Professional service: Hydraulic model test of the intake structures of the lower and upper basin.

2006
Customer: Vallis canton
Project: Third correction of the Rhone River, sector Visp-Grosseya
Country: Switzerland
Professional service: Hydraulic model test to evaluate the new hydraulic structures at the confluence of Rhone and Vispa Rivers.

COURSES ASSISTANT

2007-2011	Construction law Prof. Dr A.J. Schleiss, Prof. J-L. Zufferey and Dr L. Mouvet
2007 and 2011	Dams Prof. Dr A.J. Schleiss
2006-2007	Hydraulic Structures Prof. Dr A.J. Schleiss
2006-2007	Urban hydraulics Dr J-L. Boillat

SEMESTER PROJECTS ASSISTANT

2010 Winter	Construction project: Sazbon Dam, Iran
2009 Summer	Construction project: Sazbon Dam, Iran
2008 Summer	Construction project: Bakhtiyari Dam, Iran
2008 Summer	Construction project: River re-naturalization Sorge-Chamberonne, Switzerland
2007 Summer	Construction project: River re-naturalization Sorge-Chamberonne, Switzerland

MASTER PROJECTS ASSISTANT

2010	Dam and hydropower plant of Nam Bak, Laos in collaboration with Pöyry Ldt
2009	Analysis of the pressure generated by high-velocity jet: experimental study (Federspiel PhD facility) and practical application (Koman Dam, Albania)
2008	Dam and hydropower plant of Kersan III, Iran
2007	Dam and hydropower plant of Bakhtiyari, Iran